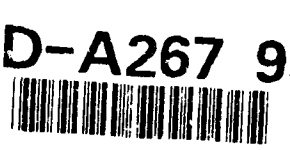

AGARD-CP-531

AGARD-CP-531

AGARD

ADVISORY GROUP FOR AEROSPACE RESEARCH & DEVELOPMENT
7 RUE ANCELLE 92200 NEUILLY SUR SEINE FRANCE

AGARD CONFERENCE PROCEEDINGS 531

Smart Structures for Aircraft and Spacecraft

(Les Structures Intelligentes pour les Aéronefs et les Vaisseaux Spatiaux)

Papers presented at the 75th Meeting of the AGARD Structures and Materials Panel, held in Lindau, Germany from 5th—7th October 1992.

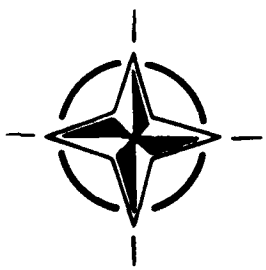

NORTH ATLANTIC TREATY ORGANIZATION

Published April 1993

Distribution and Availability on Back Cover

AGARD

ADVISORY GROUP FOR AEROSPACE RESEARCH & DEVELOPMENT

7 RUE ANCELLE 92200 NEUILLY SUR SEINE FRANCE

AGARD CONFERENCE PROCEEDINGS 531

Smart Structures for Aircraft and Spacecraft

(Les Structures Intelligentes pour les Aéronefs et les Vaisseaux Spatiaux)

Papers presented at the 75th Meeting of the AGARD Structures and Materials Panel, held in Lindau, Germany from 5th—7th October 1992.

North Atlantic Treaty Organization
Organisation du Traité de l'Atlantique Nord

The Mission of AGARD

According to its Charter, the mission of AGARD is to bring together the leading personalities of the NATO nations in the fields of science and technology relating to aerospace for the following purposes:

- Recommending effective ways for the member nations to use their research and development capabilities for the common benefit of the NATO community;
- Providing scientific and technical advice and assistance to the Military Committee in the field of aerospace research and development (with particular regard to its military application);
- Continuously stimulating advances in the aerospace sciences relevant to strengthening the common defence posture;
- Improving the co-operation among member nations in aerospace research and development;
- Exchange of scientific and technical information;
- Providing assistance to member nations for the purpose of increasing their scientific and technical potential;
- Rendering scientific and technical assistance, as requested, to other NATO bodies and to member nations in connection with research and development problems in the aerospace field.

The highest authority within AGARD is the National Delegates Board consisting of officially appointed senior representatives from each member nation. The mission of AGARD is carried out through the Panels which are composed of experts appointed by the National Delegates, the Consultant and Exchange Programme and the Aerospace Applications Studies Programme. The results of AGARD work are reported to the member nations and the NATO Authorities through the AGARD series of publications of which this is one.

Participation in AGARD activities is by invitation only and is normally limited to citizens of the NATO nations.

Published April 1993

ISBN 92-835-0701-X

Printed by Specialised Printing Services Limited
40 Chigwell Lane, Loughton, Essex IG10 3TZ

Preface

The "Smart Structures" technology offers extremely attractive advantages in the design, development and operation of aerospace structures. A structure which is capable of sensing its environment and responding to it appropriately will be miles ahead of passive structures whose performance is limited by constant material constraints.

In the field of sensors, mainly for structural fault detection and health monitoring, progress has already advanced to industrial applications which will give great relief to aircraft maintenance operations. The next application we will probably see is related to vibration suppression which was already investigated during the "Active Control Technology" efforts a few years ago.

The papers which are collected in this report give an excellent overview of the state-of-the-art as well as specific detailed descriptions of specific applications.

Préface

Les technologies des "structures intelligentes" offrent des avantages très attrayants pour la conception, le développement et la mise en oeuvre des structures aérospatiales. Une structure qui est capable d'appréhender son milieu et d'y répondre d'une façon appropriée devancera facilement les structures passives, dont les performances sont limitées par des contraintes permanentes de matériaux.

Dans le domaine des capteurs, principalement pour la détection de défauts et le contrôle de l'intégrité des matériaux, les progrès réalisés ont déjà permis des applications industrielles qui doivent servir à alléger les procédures de maintenance des avions. La prochaine application prévisible concerne l'élimination des vibrations, lequel sujet a déjà fait l'objet de recherches dans le cadre des activités du Panel relatives à la "Conception automatique généralisée" (CAG) il y a quelques années.

Les communications réunies dans ce rapport donnent un excellent aperçu de l'état de l'art dans ce domaine, ainsi que des descriptions détaillées de certaines applications.

L. Chesta
Chairman

Structures and Materials Panel

Chairman: Mr Roger Labourdette
Directeur Scientifique des
Structures
ONERA
29, Avenue de la Div. Leclerc
92322 Châtillon
France

Deputy Chairman: Dip. Ing. O. Sensburg
Chief Engineer for
Structures
MBB Flugzeuge /FE
Postfach 80 11 60
8000 Munich 80
Germany

SUB-COMMITTEE

Chairman: Dr-Ing. L. Chesta
ALENIA, Settore Aeronautica
Gruppo Aerei Difesa
Corso Marche 41 — C.P. 432
10146 Torino
Italy

Members

D. Chaumette	FR	H.H. Ottens	NL
J.P. Cornand	FR	S. Paipetis	GR
M. Curbillon	FR	D.B. Paul	US
M. Doruk	TU	R. Potter	UK
W. Elber	US	A. Rodriguez-Villa	SP
H. Försching	GE	T. Ronald	US
R. Freymann	LU	M. Rother	GE
E. Fuente	SP	A. Salvetti	IT
J.J. Glaser	CA	P. Santini	IT
A. Guemes	SP	O. Sensburg	GE
J.J. Kacprzynski	CA	A.F. Tovar de Lemos	PO
W.C. Kessler	US	S.L. Venneri	US
M.J. Kilshaw	UK	J. Waldman	US
R. Kochendörfer	GE	A.P. Ward	UK
R. Labourdette	FR	T.P. Watterson	UK
P. Marchese	IT	H. Zocher	GE
M.L. Minges	US	R.J. Zwaan	NL

PANEL EXECUTIVE

Dr Jose M. Carballal, Spain

Mail from Europe:
AGARD—OTAN
Attn: SMP Executive
7, rue Ancelle
92200 Neuilly-sur-Seine
France

Mail from US and Canada:
AGARD—NATO
Attn: SMP Executive
Unit 21551
APO AE 09777

Tel: 33(1)47 48 57 90 & 57 92
Telex: 610176 (France)
Telefax: 33(1) 47 38 57 99

Contents

† Not available at time of printing.

Technical Evaluation Report

by

R.F. O'Connell
19462 Citronia Street
Northridge
California 91324
United States

G.R. Tomlinson
University of Manchester
Department of Engineering Dynamics
Simon Building, Oxford Road
Manchester M13 9PL
United Kingdom

INTRODUCTION

The technology referred to by the terms "Smart Structures", "Smart Materials", "Intelligent Structures", etc, is one which has generated a great deal of interest in the Structures/Materials communities in recent years. The concept of a structure with the capability of sensing and automatically responding to its environment is one which offers the potential of extremely attractive advantages in the design, development and operation of aerospace structures. As with most state of the art advances, these advantages will not be achieved without a great deal of painstaking research and development. This emerging discipline combines, as do many other recent technologies, elements of many of the traditional disciplines involved in the design and development of aerospace vehicles. The implementation of Smart Structures technologies will, in fact, involve the close co-operation of nearly all the disciplines currently involved in the design/development activity. In view of this, the Structures and Materials Panel of AGARD conducted the Specialists' Meeting on Smart Structures for Aircraft and Spacecraft reported herein.

CONTENT OF PRESENTATIONS

Session I: State of the Art and Future of Smart Structures in Aerospace

Of the seven papers presented in this session, three were overview presentations giving an assessment of the present state of the art and future applications of Smart Structures technology, and some of the short term and long term benefits to be derived. In addition, a number of problem areas were examined and the requirements for progressing the discipline were discussed.

One paper described the use of piezoceramics in the active control of helicopter rotors and blades, and concludes that a factor of 10 increase in the reaction force capability of the material is needed.

Three papers concentrated on spacecraft issues. One discussed the use of adaptive structures in the shape control and vibration control of spacecraft. Another outlined a planned test of a sensor on a spacecraft to detect laser, rf and x-ray related events. The third provided an insight into the problems of excitation, modal identification and sensor location in space structures.

Session II: Sensors and Actuators

Of the nine papers presented in this session, three dealt with fibre optic sensing techniques used in the monitoring of composite structures. Strain monitoring, temperature monitoring and impact damage monitoring of structural systems were described. Two of the papers addressed the use of fibre optic techniques in monitoring the cure condition of composite materials. One of these also included electrical, acoustic and viscosity sensors for monitoring the processing of composite materials, and indicated that the water content of these materials could be monitored in service.

Two papers discussed the use of piezoelectric and electrostrictive materials as sensors and actuators, primarily for vibration control and active damping. One paper explored the use of polymeric gels for electromechanical transduction, although it appeared that at the present none meets the requirements.

Two of the papers in this session dealt with the use of shape memory alloys for adaptive control surfaces and actuators, and illuminated some of the difficulties such as response time encountered in the use of these materials.

Session III: Structural Defect Detection

The first of the five papers presented in this session gave an overview of the subject of structural defect detection, beginning with a description of current methods. The requirements for future systems were then discussed, along with a road map detailing the means of meeting these requirements with Smart Structures.

Three papers discussed the techniques of structural health monitoring of composite structures using embedded fibre optic sensors. The present status of these sensors was explained, together with the requirements of further development. Two of these papers described relevant test programs, and one paper included a description of an optical fibre with an electrostrictive coating performing as an integrated sensor/actuator.

One paper dealt with the use of neural networks in health monitoring. The architecture of a network to detect structural faults in terms of input strain data was described, and the process of enabling the network to "learn" to recognise the strain patterns of the relevant structural faults was outlined. An example was given, showing a neural network developed from finite element simulations of a series of mathematically simulated structural faults, being successfully applied to experimental data for accurate fault location.

Session IV: Smart Technology Control System

One paper presented an overview of Smart Structures research at the USAF Wright Laboratory pertaining to sensory structures, multi-functional structures and active structures. The current state of the art, potential for the use of Smart Structures and technology needs in this area was also discussed. Another paper gave a general summary of the status of active control technology and the state of the art of predicting loads caused by flight control changes.

Three papers addressed the use of Smart Structures technology in the control of space systems. One presentation described the use of adaptive space structures for shape control and vibration control, and the second discussed the equations of motion of multibody space systems and related control applications. The third paper described an experiment using piezoelectric sensors and actuators to augment the damping of an elastomechanical system.

The remaining five papers covered a variety of subjects. One paper examined the use of active control of nose landing gear damping characteristics of an aircraft to improve ride quality. Another discussed the development of an algorithm for an adaptive digital filter used in vibration control. A third described ground and flight tests using fibre optic strain sensors. One paper discussed the use of distributed sensors and actuators for mode control in superflight air vehicles and the related control algorithms; another examined the use of finite element representations of piezoelectric devices and shape memory alloys.

ROUND TABLE DISCUSSIONS

The round table was composed of:

L. Chesta	Alenia, IT
O. Sensburg	MBB-DASA, GE
J. Kaprzcynski	IAR, NRC, CA
E. Crawley	MIT, US
B. Wada	JPL, US
W. Schmidt	MBB-DASA, GE
A. Janizewski	EOARD, US Air Force, US
R.F. O'Connell	Evaluator
G.R. Tomlinson	Evaluator

The discussions were prefaced by introductory remarks by the evaluators giving a brief summary of the presentations and reviewing the various applications of Smart Structures technology covered by the presentations. The potential pay-offs were cited, along with some of the deficiencies and problem areas to be addressed. One aspect which received attention was the difference between the difficulties associated with spacecraft and aircraft. In aircraft the load paths are more difficult to identify than in the case of spacecraft. In addition, the actuation forces required for control of vibration/position in spacecraft are in general lower, making the application of Smart Materials more attractive for control purposes. This led to the view that Smart Materials had several current limitations in relation to aircraft applications such as low actuation forces and low response times (for shape memory alloys). It was likely that the first real applications for Smart technology would be in Health Monitoring of aircraft structures. The advances being made in data processing using techniques such as Neural Networks meant that fault patterns could be rapidly deduced from different types of Smart sensors and the analysis carried out on dedicated small computers.

The financial input required to drive the Smart technology forward had to be project driven and there was a general feeling that more applications were required in order to ensure the research advances being made resulted in an effective technology transfer to industry.

ASSESSMENT OF PRESENTATIONS

The presentations were generally of high quality, and served to provide an excellent guide to the status, scope and future of Smart Structures technology. The overview papers were very good, and gave a comprehensive view of the discipline. The projections of future applications and pay-offs were particularly useful. The descriptions of the deficiencies, problems and needs were also excellent. It would appear that more attention could have been given to the means by which progress in the technology could be accomplished in order to achieve the long term benefits.

The papers directed to more specialised subjects were likewise of high quality, and in general seemed to cover the topics adequately. In most cases, deficiencies in the presently available materials were noted, and the required improvements identified. Again, the means of achieving these improvements are areas in which further efforts are necessary.

RECOMMENDATIONS

In achieving the projected pay-offs resulting from Smart Structures, very significant cost and weight are anticipated. If this is to be the case, a great deal of attention must be given to the reliability of the systems. The failure modes of such systems must be identified, and must be minimised to the greatest possible extent. In the case of health monitoring applications, the objective is to reduce inspections on both new and repaired structures and thereby reduce maintenance costs. Similarly, the use of Smart Structures to improve performance and/or to reduce structural weight implies that the combined structural systems have a reliability commensurate with that of the unaugmented structure. The failure of such systems to perform the intended function has serious safety implications, and the combined structure/sensor/actuator/controller systems must be treated in the same context as present material systems. A related consideration will be that of convincing the various regulatory agencies of the safety of these systems.

While this is a formidable task, it should also be kept in mind that the development of Smart Structures must proceed as rapidly as possible. The current political and economic constraints dictate a very limited number of new vehicle designs, both in spacecraft and aircraft. One obvious implication of this is that, if the technology is not sufficiently mature for inclusion in a particular design effort, it may be many years before such an opportunity presents itself again.

In view of this, it is recommended that Workshop activity be formulated to:

1. provide a roadmap of the various applications in terms of the time frame in order that these applications might be sufficiently mature for inclusion in a new design,
2. propose, insofar as is possible, the means of achieving this design readiness,
3. identify projected aerospace design efforts which could benefit from such applications, including the estimated time the applications would be required, and
4. determine to what extent any chronological imcompatibilities could be corrected.

SMART STRUCTURES
A TECHNOLOGY FOR NEXT GENERATION AIRCRAFT

by

W. Schmidt and **Chr. Boller**
Deutsche Aerospace
Military Aircraft Division
P.O. Box 80 11 60
8000 Munich 80
Germany

SUMMARY

Performance of aircraft structures has progressed in a sequence of steps during the past. Since composite materials have gained broad application because of significant technological improvement it is timely to look for the next step in improvement of aircraft performance. It is very likely that this step is related to smart structures technology. Smart structures technology is able to meet various aircraft design objectives such as improved military aircraft effectiveness through improved aircraft capabilities and reduced life cycle cost or reduced direct operating cost of civil aircraft through improvement in performance, fuel consumption and aircraft maintainability. Active/adaptive structures, structure health monitoring and structure integrated avionics are the three areas which are felt to be the areas where smart structures technology is most benefical. Ways for cooperation between various engineering and natural sciences, being a major driving force for the success of smart structures, are described as well as some laboratory scale experiments which have been recently performed. It is felt that an increased effort of engineers in various fields towards realization of smart structures can be a new rewarding challenge for the aircraft industry in developing next generation aircraft.

ABBREVIATIONS

CFRP	Carbon Fibre Reinforced Polymer
DASA	Deutsche Aerospace
DOC	Direct Operating Cost
LCC	Life Cycle Cost
NDT	Non Destructive Testing

INTRODUCTION

The performance of aircraft structures during the past century has progressed in a sequence of steps which were mainly due to a change in applied material (Fig.1). Starting from wood, cloth and wires as fundamental structural materials, metals - and here especially aluminium alloys - were soon identified in a second step to provide higher strength and environmental stability. The continuous need for light weight construction and the ability to tailor strength of components according to structural needs led to fibre reinforced polymer composites, which can be considered as the third step in aircraft structure performance development.

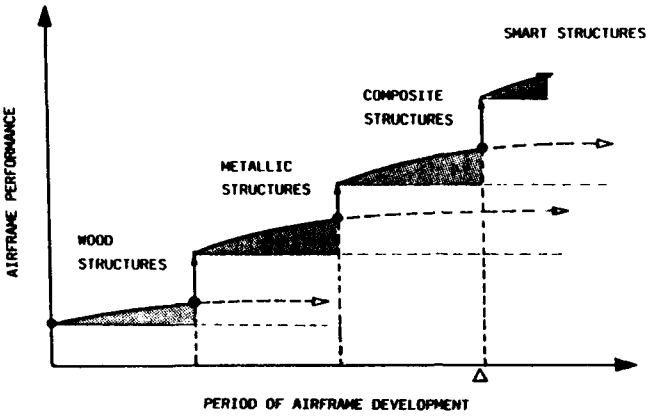

Fig. 1 Trend of Airframe Performance

Each of these steps starts at some degree of development and during the time further improvements are achieved until development is close to a saturation point. This incident is then the verge to the next step in aircraft performance developement when considering materials applied.

Composite materials have gained increased applicability in aircraft structures because of improved strength, manufacturing technology and cost. Even though further improvement can be expected it is certainly not wrong to assume that composite materials are close to their saturation point in technological development. It is therefore timely to consider the next technological step in airframe performance which is very likely to be smart structures.

Various definitions of smart structures were given in the past where a definition by Breitbach [1] has been widely accepted in and outside Germany. According to this definition the evolutionary process of smart (synonyms are: adaptive, multifunctional, intelligent, etc.) structures (Fig.2) started with a structure being subjected to external disturbances and responding in a passive way. Such a structure is defined to become active as soon as it is able to recognize these external disturbances by specific, mainly monofunctional sensors and depending on the severity and consequences of the disturbances the sensor signals can be transmitted to a controller which processes and generates signals in real time allowing the structure to respond actively by use of an actuator.

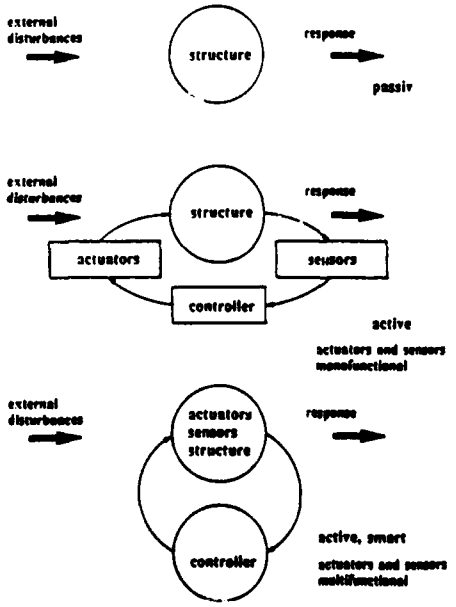

Fig. 2 Smart Structures Technology - Evolutionary Process

Sensor, controller and actuator, key elements of an active structure, which do not all three have to be present in one system, are nowadays available as extrinsic elements and functions. Examples for sensors include strain gauges, load cells, thermocouples etc. while the actuators applied are based on electrical heating, motors or hydraulic systems. Controllers are mainly electric circuits and electronic elements including often human control. Examples for systems which include all three key elements and being commercially available are cooling and heating systems, automatic gears, deicing systems for aircraft or active shock absorbers.

A structure is defined to be smart when sensor, actuator and possibly even controller become an integral part - or in other words an intrinsic function - of the structure or structural material respectively. The integration of sensing and actuating functions has already become reality when considering smart materials such as piezoelectric ceramics and polymers, shape memory materials, electrorheological fluids or magnetostrictive materials. When considering future material development organically modified ceramics, nanostructures or generally materials modified on a molecular basis are included. The final vision is that future structural materials will sense their condition themselves and will be able to react with the help of a controlling process where the controlling process being based on advanced electronics and data processing techniques will usually still not be an integral part of the structure from a materials point of view.

Smart structures technology was mainly initiated for spacecraft applications. Whithin the past few years areas such as military aircraft, helicopters and commercial aircraft have also started to explore the benefits of this technology for their purposes. Other technical areas with major interest in smart structures are automobiles, civil engineering including power plants and medicine.

That smart materials and structures have gained large interest not only in North-America and Japan shows the following list of activities within Deutsche Aerospace (DASA):

Daimler- Benz Research (DASA Lab.)	Smart/Adaptive Materials (Piezoelectrics, Shape Memory Alloys, Advanced/Smart Composites); Sensor Technology
DASA Military Aircraft	Smart Structures (Aircraft Health and Usage Monitoring, Active/Adaptive Structures, Structure-Integrated Avionics)
DASA Space Systems	Control and Simulation Algorithms
Eurocopter Deutschland	Active Rotor Blade Control

Various cooperations and contacts with universities and research centers have been established where DLR, the German Aeronautical Establishment is playing a major initiative role in Germany.

The following paragraphs describe how smart structures technology can meet aircraft design objectives and what strategies are pursued in view of next generation aircraft.

AIRCRAFT DESIGN OBJECTIVES

Aircraft design objectives differ significantly depending on the aircraft configurations considered. Subsonic transport aircraft are designed for economy, military aircraft for agility, helicopters for

vertical flight and super- and hypersonic transport aircraft for speed. An objective common to all of these aircraft configurations is however minimization of cost.

A lot of thought has been and is still spent on technological improvement which main aircraft configurations demand [2]. A summary of these demands combined with the impact of smart structures technology is given in the following for military and commerical aircraft.

Military Aircraft

Military aircraft effectiveness is best defined in terms of life cycle cost (LCC). The objective is improved survivability which is achieved by development of the aircraft's capabilities and availability. Major development work in aircraft's capabilities is focussed on:

- improvement of system performance
- better range
- better manoeuvrability and
- better sensor capability

where smart structures technology can significantly influence the latter three aspects. Aircraft's availability can be increased by improvements in:

- reliability
- maintainability and
- ease of turn-round

where the aspects of reliability and maintainability are those being most significantly influenced by smart structures technology.

Life cycle cost, the term to express military aircraft effectiveness can be divided into two major parts:

- acquisition cost and
- operational cost.

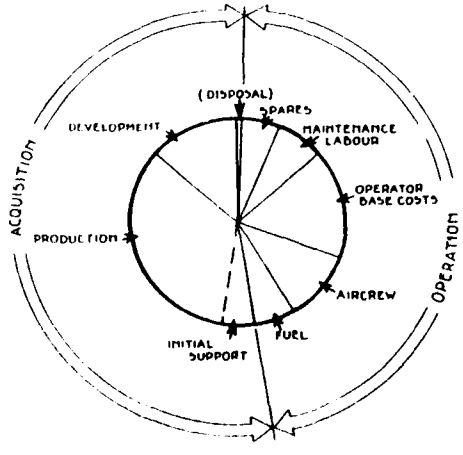

Source: EUROMART Study

Fig. 3 Life Cycle Cost (LCC) Breakdown for a Typical Military Aircraft (Assumes 25 years in service)

Fig.3 shows an example of a life cycle cost breakdown for a typical military aircraft assuming 25 years in service. For existing aircraft types these cost values are known to the aircraft operator. When a new aircraft or technology is introduced, the operator will therefore compare the new life cycle cost (LCC_{new}) with the actual (LCC_{actual}) which will lead him to three major possibilities only being accepted when the following conditions are fullfilled:

1.) $LCC_{new} < LCC_{actual}$

No decrease in technological capabilities or availability.

2.) $LCC_{new} = LCC_{actual}$

There must be at least an improvement in technological capabilities or availability with no decrease in the other.

3.) $LCC_{new} > LCC_{actual}$

Outstanding improvement in technological capabilities and/or availability, possibly even tailored to the needs and wishes of the operator.

Returning to smart structures technology, in-flight health monitoring systems is a good example to show how this technology can affect LCC (Fig.4).

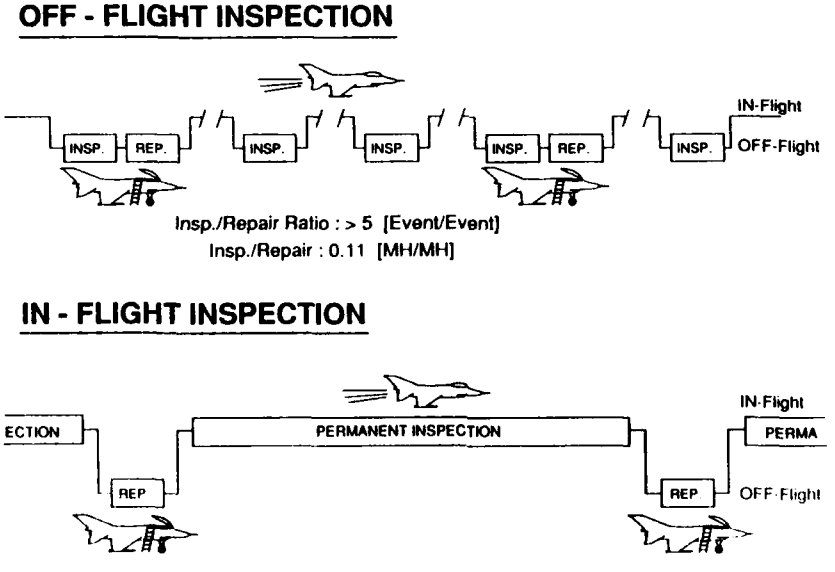

Fig. 4 Improved Availability through Automated In-Flight Structure Monitoring

Health monitoring of aircraft is the major part of aircraft inspection. To prevent the aircraft from critical damage inspection is performed in fixed intervals. Work is mainly done manually using hand held equipment. Aircraft operation is only accepted to be economical when repair is identified in less than 1 out of 5 inspections (Inspection/Repair Ratio: >5). The average manpower cost for inspection of an aircraft is approximately 11% of the manpower cost required for repair. This inspection cost can be reduced with a health monitoring system, especially when the cost for the system is less than the actual inspection cost relative to the capabilities of the health monitoring system. When health

monitoring can even be performed during flight or in-service further benefits arise such as better availability and on condition maintenance. As inspection is now permanently performed, the inspection to repair ratio mentioned before goes up to a very large value (mathematically to infinity), which is not a measure of improved security but a measure of having taken full advantage of the aircraft's technical availability and therefore a measure for economy. More quantitative values on aircraft maintenance cost are given in [3].

Commercial Aircraft

Major objectives for commercial/competitive air transport is to meet operational requirements of

- safety
- environment
- punctuality and
- comfort.

These requirements have to be met in conjunction with minimization of direct operating cost (DOC). Similar to LCC mentioned before DOC is composed of aircraft production and aircraft operational cost. Fig. 5 is a compilation of competitive air transport demands for continuous

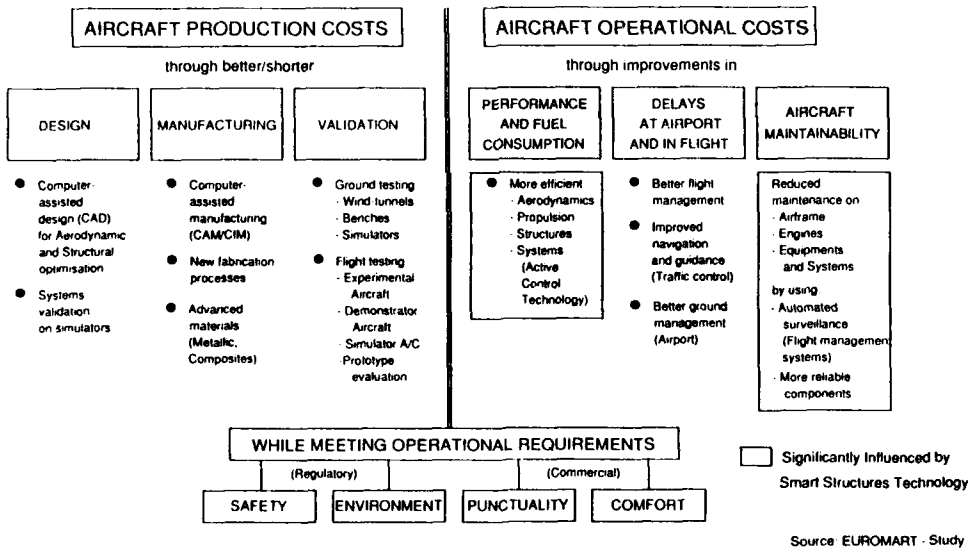

Fig. 5 Competitive Air Transport Demands Continuous Improvement in...

improvements in various cost driving areas which was set up by a team effort of the European aircraft industry and the Commission of the European Community [2]. When looking for areas where smart structures technology could contribute to reduce cost 'Performance and Fuel Consumption' and 'Aircraft Maintainability' are the areas of significant influence. A reduction in aircraft production cost or aircraft price by using smart structures technology is not likely to be expected.

Within large aircraft manufacturing industries (e.g. Airbus Industries) a lot of thought has been spent on how improved technology can reduce DOC of a commercial aircraft. Fig. 6 shows a typical DOC breakdown using 1987 cost for an Airbus A320 on a 500 nm trip. Smart structures technology can significantly influence aspects such as 'Reduced Maintenance', 'Fuel Savings' and 'Reduced

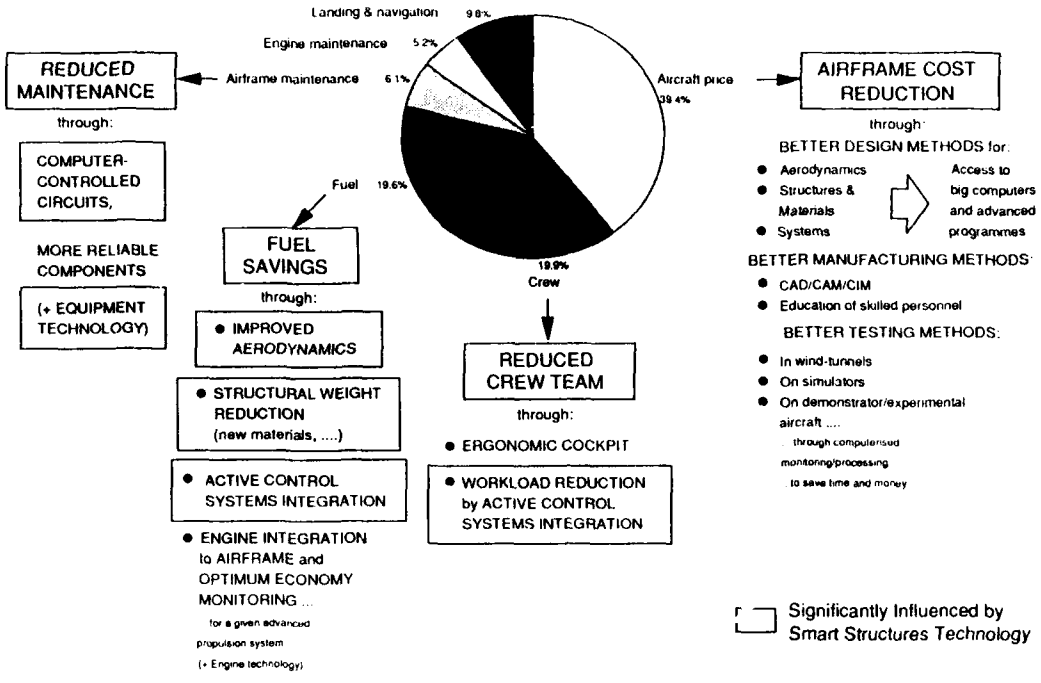

Fig. 6 How improved technology can reduce the direct operating cost (DOC) of a commerical aircraft. (Chart shows a typical DOC breakdown (using 1987 costs) for an Airbus A-320 on a 500 n mi trip.) Source: Airbus Industrie

Crew Team' which in all is close to 50% of DOC and therefore worth to be considered. A selection of examples how to achieve this will therefore be given in the following.

THE SMART STRUCTURES CHALLENGE

Smart structures are still at a very initial stage of their development. Various concepts have been and are still proposed for performing large research programs in North-America, Japan and Europe and a lot of laboratory research work is going on which has especially shown first results in the area of spacecraft application. Within the following paragraphs some ideas are described on how smart structures technology can be introduced to next generation aircraft and possibly even become benefical to existing ones.

Possible Smart Structures Applications in Aircraft

When considering smart structures and materials application in aircraft a large number of areas can be identified. Fig. 7 is a compilation of various applications starting from cabin noise reduction and ending up with structure-integrated avionics and processing all major data in a central data processing unit.

When trying to group these different areas three major topics can be identified:

- Active/Adaptive-Structures applied to cabin noise reduction, vibration and flutter suppression of engines, wings and fin, variation in wing geometries for optimized aerodynamical behaviour including automated positioning of flaps and slats.
- Aircraft (Structures, Engine, Systems and Equipment) Health Monitoring Systems, able to detect, localise and validate deterioration due to fatigue, corrosion, impacts, mishandling, wear, temperature or other environmental conditions.

- Structure-Integrated Avionics which includes integration of existing antennas into aircraft structures improving aerodynamic behaviour, avoiding additional antenna housing and possibly even making use of the antennas' stiffness for structural purposes.

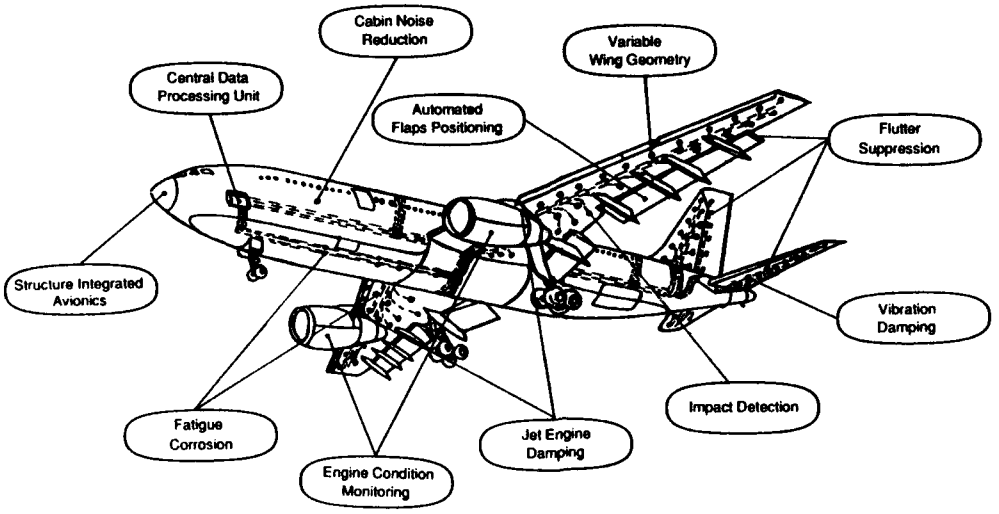

Fig. 7 Areas of Application of Smart Structures and Materials in Aircraft

These three topics have also been the focal points when smart structures research work started within Deutsche Aerospace Military Aircraft. (Fig.8).

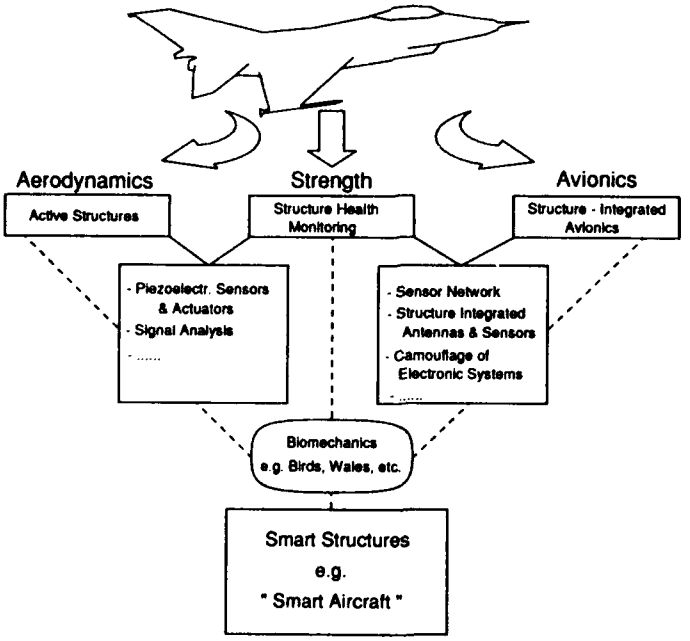

Fig. 8 DASA Mil. Aircraft Smart Structures Activities

From ongoing research and development work problems common to these different topics were identified and are used as links for ongoing and future research work. Examples of such links includes improvement of piezoelectric sensors' and actuators' potential or advanced signal processing when thinking of active structures and structure health monitoring or sensor networks, structure

integrated antennas and sensors, or camouflage of electronic systems when thinking of links between structure health monitoring and structure-integrated avionics. These links can be consolidated by studying and possibly integrating solutions dealt within areas usually not included into engineering science such as biomechanics. Following this strategy is felt to be a suitable way how to achieve the objective of developing applicable smart structures even leading in the end to a "smart aircraft".

Another view which exhibits that the three topics structure health monitoring, active structures and structure-integrated avionics are highly interacting when considering smart structures technology is shown in Fig.9.

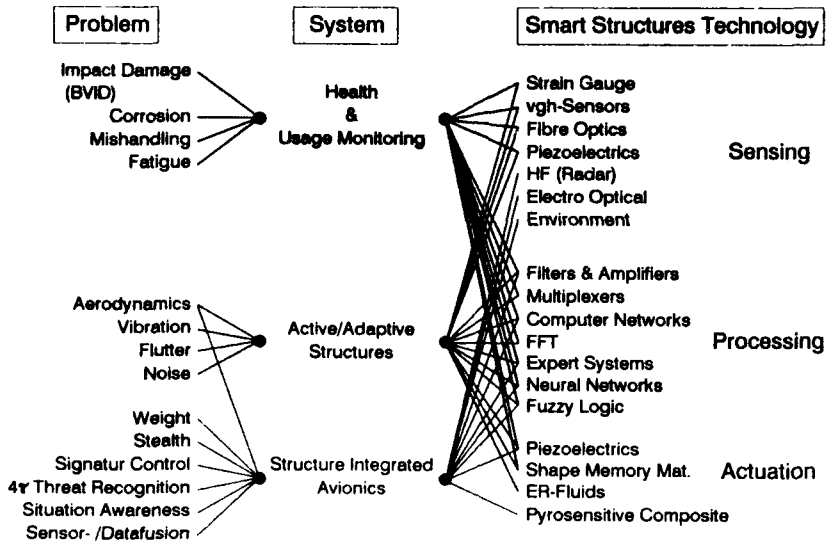

Fig. 9 Smart Structures Technology in Aircraft

Starting from a variety of problems still to be solved within aircraft design links can be drawn to smart structure systems which themselves are linked to a broad spectrum of smart structures and materials technology. It can be seen that investment into sensing, processing and actuation technology, the three elements of smart structures technology, can be beneficial for more than one system. It further proves that strong links between system development and smart structures technology can be advantageous for system development in short term.

As smart structures is not limited to structural engineering, areas such as materials science, electronics and sensors, actuators and control algorithms, computer science, NDT, dynamics, etc. have to be included in addition to the links already mentioned before. Fig. 10 gives two examples on how to establish interacting teams for development of smart structures. Only successful cooperation between people, sciences, companies/institutions and nations can lead to valuable smart structures.

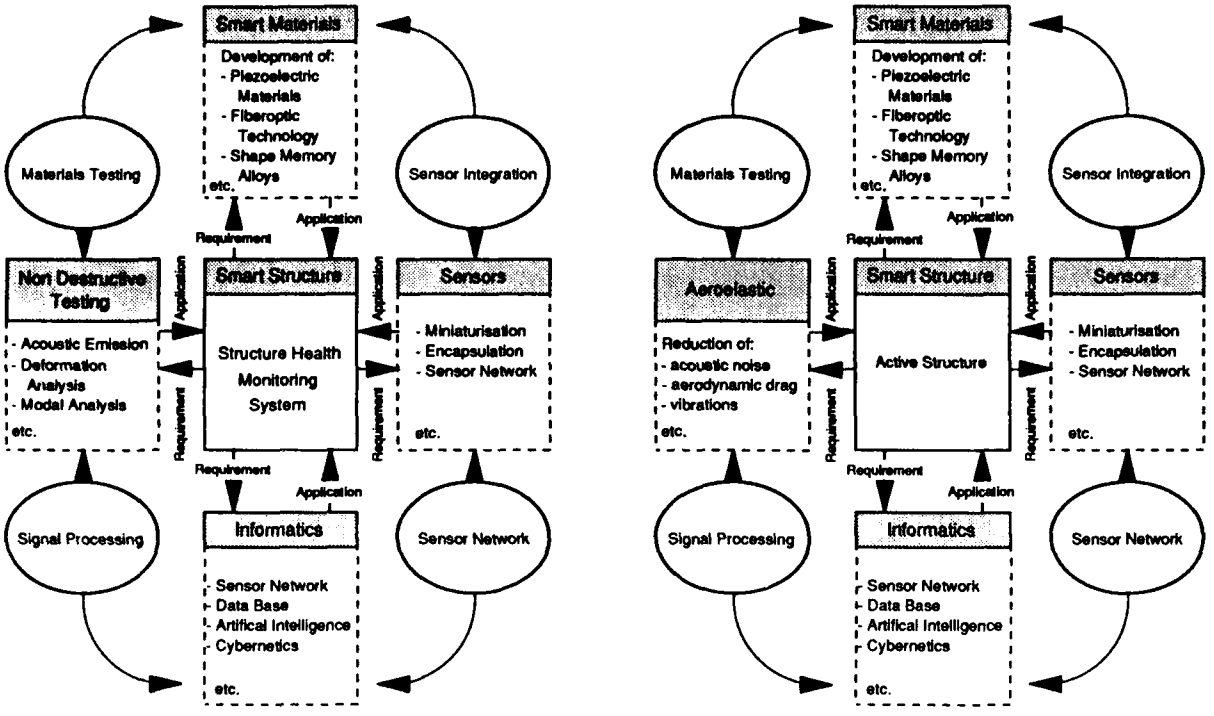

Fig. 10 Cooperation in Smart Structures Development

Laboratory Scale Examples

As smart structures development is still at a laboratory stage some examples and ideas are described where work is actually going on within Deutsche Aerospace.

Active/Adaptive Structures

Active/adaptive structures technology solves structural problems which cannot be handled by passive metallic or even optimized composite structures. It is strongly dependent on development and performance of smart materials and its potential can only fully be explored when used as an integrated design element from the initial stage of product design.

Actual research work is concentrated on two areas, shape control and active vibration damping. Fig. 11 shows an example for active vibration damping. A cantilever beam made of carbon fibre reinforced polymer (CFRP) was selected and equiped with an accelerometer (sensor) and an actuator made of piezoelectric ceramics. Sensor signals were fed into the signal generator which generated the signal for the actuator. The test objective was to look at the control process, bonding of the actuators and the actuator performance. The result shows that damping is significantly increased when using the piezoeletric actuator with control.

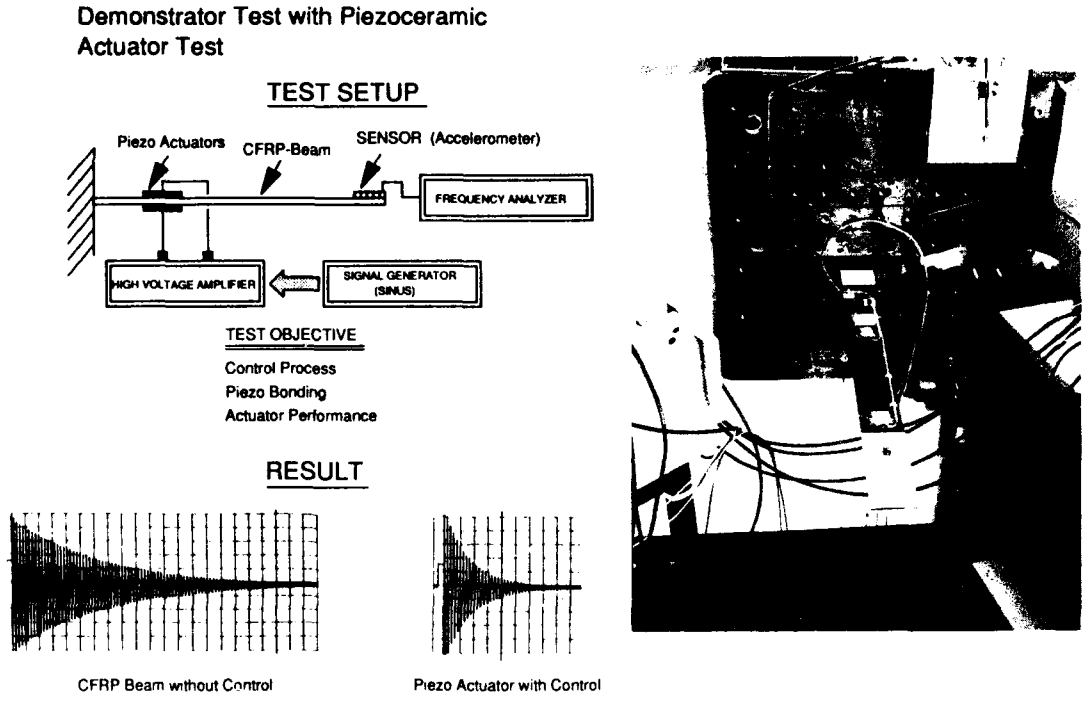

Fig. 11 Active/Adaptive Structures

Another example which is more related to shape control is based on use of shape memory alloys. Fig. 12 shows an example where a wire made of shape memory alloys has been wound around a bar. This solution on which Daimler-Benz Research DASA Central Laboratories holds a patent allows to introduce torsion and could be used for rotor blade control or flaps positioning.

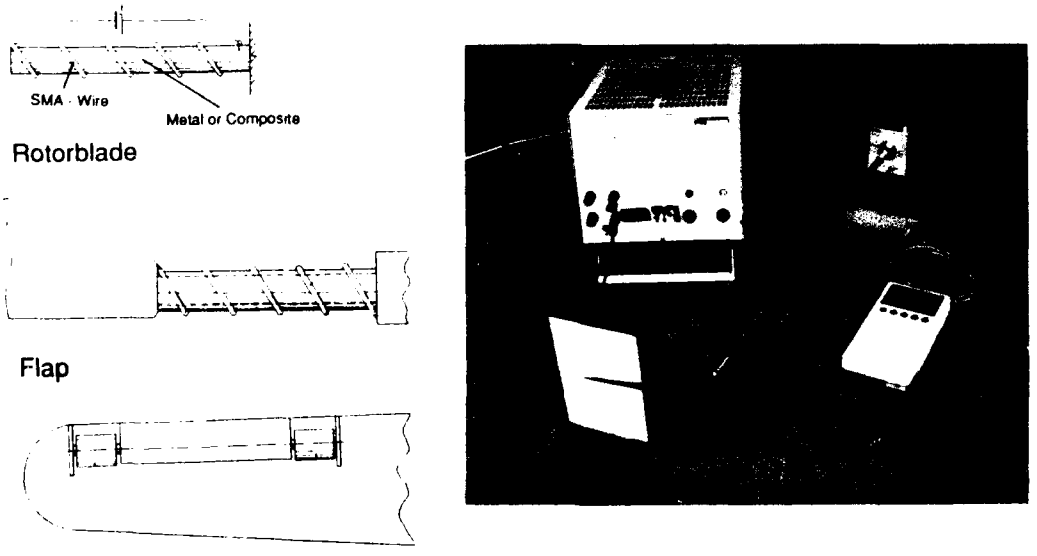

Fig. 12 SMA - Torsionbar

Structure Health Monitoring

Much effort has been spent in the past to obtain information on the actual condition (health) of aircraft structures. Based on strain gauges and flight parameters load sequences were determined allowing to estimate fatigue damage accumulated. Structure health monitoring systems of the next

generation which will be based on smart structures technology will allow on-condition and in-situ monitoring of damage resulting from

- impacts (especially in fibre reinforced polymers)
- corrosion
- fatigue and
- mishandling including misrepair.

Parameters to be monitored can be strain, vibration modes or acoustic emission. A broader view on health monitoring systems is given in [3].

Monitoring of engineering structures is conventionally performed in a way that sensors are bonded on the structure's surface. Strains, vibrations, acoustic waves etc. resulting from structural behaviour and being changed because of structural damage are measured. When using smart materials sensors can become an integral part of the material. This has the advantage that sensors are better protected against environmental effects and that their stiffness can contribute to the structural stiffness. They have to be low cost because repairability of such integrated sensors is more or less excluded. Furthermore a much higher amount of sensors than required have to be included into the structure allowing graceful degradation of the sensors during the structure's service life. Fig. 13 shows an example for conventional and smart health monitoring when including the sensor functions into a composite material.

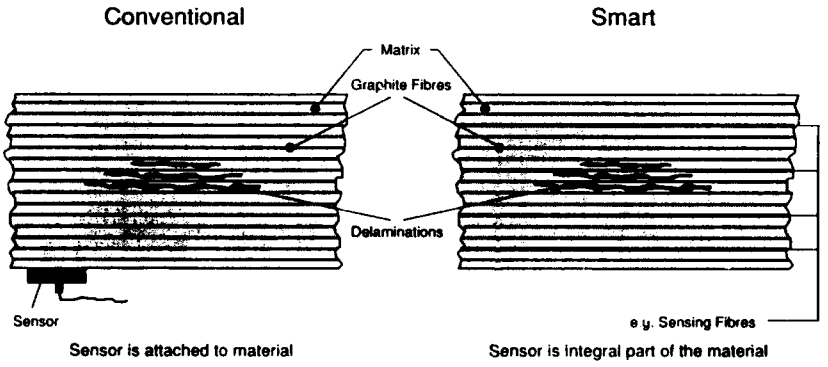

Fig. 13 Composites Health Monitoring

Structure health monitoring does however not just consist of integrating sensors into the structure. It also includes application of advanced/smart sensors with intelligent signal preprocessing using the most recent development in microelectronics and advanced data processing as well as visualisation. This allows to handle large quantities of data which is the case when monitoring large structures such as a composite wing. Fig. 14 illustrates such a strategy which is actually been followed within DASA for composite parts under impact loading. At this stage plates of simple geometric shape with low cost piezoelectric sensors still bonded onto the plate's surface are impact tested. Future research work aims at integrating the sensor function into the material, testing structural components and establishing data processing and visualisation tools which shall finally lead to an applicable structure health monitoring system for aircraft components.

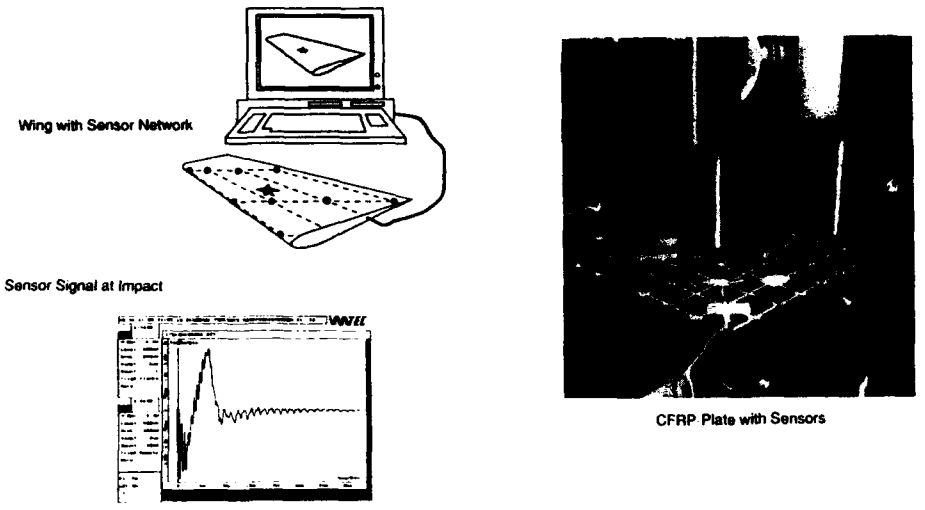

Fig. 14 Structure Health Monitoring Using Network Based on Piezoelectric Sensors

CONCLUSIONS

During the last ten years enormous achievements have been gained in minimization of sensors and actuators. Small light weight powerful computers are installed in flying vehicles now which allow onboard real time assessment of flight parameters, loads, stresses etc.. Optimal control laws with minimal control force requirements are applied and will offer large weight reduction benefits.

Regarding next generation aircraft the following conclusions can be drawn:

- There is a significant potential to improve military effectiveness and to reduce LCC as well as DOC of civil aircraft by application of smart structures and materials technology.
- Active control technologies together with aeroelastic tailoring, structural and damping combined with smart materials applied in the design process will lead to active/adaptive structures yielding much lighter design.
- Structure health monitoring based on smart structures technology will support development towards automated in-situ monitoring of damage even on-board the aircraft and in-flight. This will allow to reduce maintenance cost, improve operational capability and availability and even lead to lighter design because of better knowledge of structural damage behaviour.
- Aircraft will benefit from structure-integrated avionics including weight and volume savings, improved aerodynamics, reduced signature and possible 4 Π coverage.

Altogether cooperation between people, sciences, companies/institutions and nations is a major driving force for development of smart structures. Smart structures' success heavily depends on it. Development of this technology has just started and the increased effort of engineers in all fields will be a new rewarding challenge for the aircraft industry.

ACKNOWLEDGEMENTS

The authors would like to express their appreciation to DLR Göttingen, DASA Central Laboratories and DASA Military Aircraft Avionics Department for their cooperation in providing material for preparing this paper.

REFERENCES

[1] Breitbach E.J., "Research Status on Adaptive Structures in Europe", in: Pocs. of 2nd Joint Japan/U.S. Conference on Adaptive Structures, Nagoya/Japan, Nov. 1991

[2] "European Cooperative Measures for Aeronautical Research Technology" (EUROMART), Study Report, (1988)

[3] Boller Chr., Dilger R., "In-Flight Aircraft Structure Health Monitoring Based on Smart Structures Technology", Paper 17, This volume

ADAPTIVE STRUCTURES FOR SPACECRAFT A USAF PERSPECTIVE

Alok Das
Phillips Laboratory (AFMC)
OLAC PL/VTS
Edwards AFB, CA 93523-5000, USA

Glenn Ormbrek
Wright Laboratory (AFMC)
WL/MLB
Wright-Patterson AFB, OH 45433-6508, USA

and

Michael Obal
Strategic Defense Initiative Organization
SDIO/TNI
The Pentagon, Washington D.C. 20301-7100, USA

SUMMARY

The precise pointing / shape control needs of future space systems coupled with a 10 - 20 year life requirement and very stringent limitation on system weight has motivated a new approach in control system design. This approach, referred to as "adaptive structures," exploits recent breakthroughs in advanced composite materials, sensors and actuators, and intelligent control concepts to provide an integrated structure / controller.

1. INTRODUCTION

Dynamics and control of flexible space structures has been an area of active research for the past 15 years. For a period of time, the impetus for this work was based on the perceived need for relatively large spacecraft, either deployed or assembled in space, requiring precise pointing or shape control. These Large Space Structure (LSS) missions fell in two broad, overlapping categories. First, the large optical systems, such as Space Based Laser (see Figure 1), were characterized by a relatively stiff structure up to a few tens of meters in diameter. Their need to obtain precise performance from large optics, which must be rapidly retargeted and operated in the presence of severe on-board disturbances, causes the most demanding controls / structures interactions (CSI). On the other hand, large space antenna systems, such as Space Based Radar (SBR) and Large Deployable Reflector, consisted of a flexible structure up to 100 meters in size [1,2]. Figure 2 shows a conceptual design of a corporate fed SBR. All the proposed concepts required the spacecraft to be packaged for launch and unfolded once in orbit. The dynamics of the unfolding process and shape determination / control of the large antenna were a primary concern.

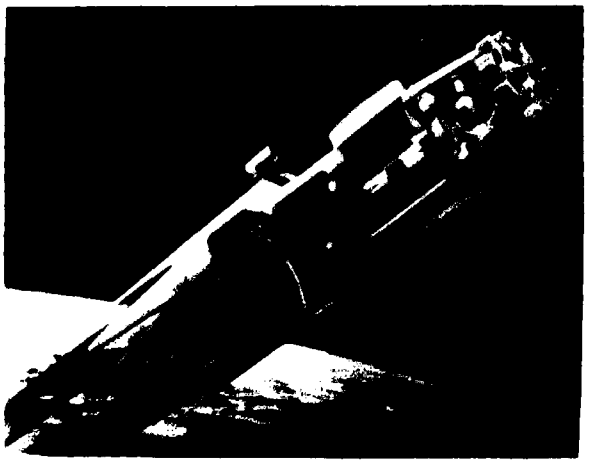

Figure 1 Conceptual Design of Space Based Laser

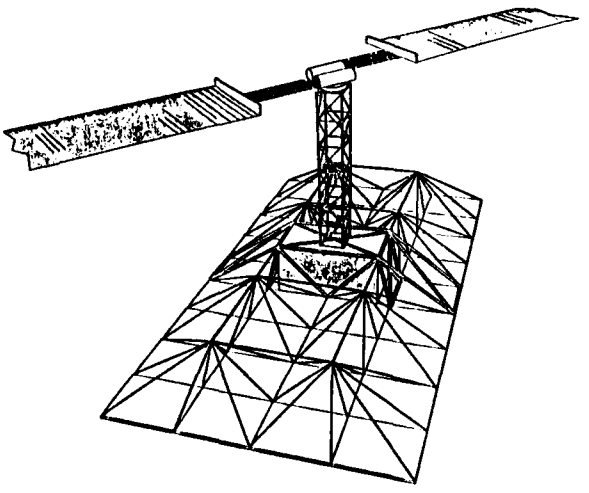

Figure 2 A Phased Array Corporate Fed SBR Concept

Thus, the dynamics and control requirements were driven by proposed systems; many of which were very large in

size, and due to the cost of putting mass into orbit weighed as little as possible, thus making them inherently flexible. Furthermore, many of these missions called for very precise pointing and shape control, often in the presence of severe on-board or environmentally induced disturbances resulting in severe controls / structures interaction. It was recognized that a solution to this problem was well beyond the existing state-of-the-art in vibration and shape control resulting in sustained National Aeronautics and Space Administration (NASA) and Department of Defense (DoD) funded LSS technology development programs.

By the mid to late 1980s it had become apparent that many of the perceived *near-term* DoD system applications of the LSS technology such as, SBR, had failed to materialize. However, the need for increased precision from existing surveillance and communication satellite platforms provided a new near-term outlet for LSS technology. These satellites do not require a global application of vibration suppression to the entire structure. Instead, the vibration concerns are localized to specific spacecraft components. Most of the modeling and control algorithms developed for LSS are applicable to these smaller satellites. Unfortunately, their smaller size and limited power availability puts a severe limitation on the allowable weight and power of the vibration control system. Also in the Strategic Defense Initiative Organization (SDIO) arena, the recent change in mission architecture has shifted the focus away from larger Directed Energy Weapon systems. The new architecture, referred to as Global Protection Against Limited Strikes (GPALS) utilizes a large number of small space-based autonomous surveillance and defensive satellites. These satellites are required to react quickly and perform optimally after remaining dormant for an extended period of time. None of these elements will receive scheduled maintenance and are expected to operate over a 10-15 year life with minimal ground support. The need for health and threat monitoring combined with static / dynamic structural control for such systems has been described by Obal and Sater in a recent paper [3]. This requires the development of an autonomous on-board control and health monitoring system that continuously monitors spacecraft health, detects the threat environment and evaluates its impact on the satellite; observes significant changes in key performance parameters, and autonomously reconfigures to compensate for these changes. Finally, the weight penalty imposed by the health monitoring and vibration control system is of particular concern for the near-term SDIO systems, where the system weight plays a crucial role in determining the feasibility of the concept.

The United States Air Force (USAF) in cooperation with SDIO has developed an adaptive structures approach for this application. A number of recently developed technologies combine to enable the adaptive structures approach. These include advances in high modulus composite materials, resulting in lightweight, yet stiff, thermally stable structures; sensors and actuators, including distributed fiber optic sensors, piezoelectric sensors/actuators embedded inside the layers of the composite structure, and shape memory alloy actuators; and intelligent control concepts, including neural networks for autonomous system identification, rapid failure detection, and control system reconfiguration.

This paper traces the development of vibration suppression technology from a USAF perspective, leading to the joint SDIO/USAF adaptive structures program.

2. BACKGROUND

In the early to mid 1970s, some of the initial work in LSS vibration suppression relied on the application of existing methodologies (developed for aircraft flutter suppression) to spacecraft with a rigid central hub and light, flexible appendages. Often the spacecraft was treated as rigid for the purpose of attitude control system design. Subsequently, the performance of the resulting controller was evaluated in the presence of structural flexibility. If necessary, the controller was then appropriately modified to account for the flexible modes. Typically, there was sufficient separation between the control system bandwidth and the first flexible mode so that their interaction could be safely ignored.

When the notion of large antenna and power generation satellites was introduced, it was quickly realized that such systems were inherently flexible and could not be modeled as a rigid hub with flexible appendages. This resulted in a flurry of papers out of which the well recognized characteristics of LSS took form, namely, (i) an inherently flexible structure with a large number of lightly damped, closely spaced structural modes; (ii) stringent vibration suppression and shape control requirements resulting in a controller bandwidth which includes a significant number of flexible modes; (iii) frequency, and to a greater extent mode shapes, of the higher modes not accurately known, and; (iv) typically, the structure is packaged into a compact form for launch and unfolded into its operational form once in orbit . Further details are provided in references [4,5].

By the mid 1970s, the volume of research in this field had grown to the point of requiring a specialized conference. Recognizing this need, Prof. Leonard Meirovitch of Virginia Polytechnic Institute and State University chaired a Symposium on Dynamics and Control of Large Flexible Spacecraft in June 1977 [6]. This biennial symposium remains a popular watering hole for researchers active in this field. Also, in 1977 The Charles Stark Draper Laboratory (CSDL) conducted a state-of-the-art assessment of passive and active suppression of vibration for precision space structures [7]. The results of this assessment showed that the achievable damping of 1 to 3% was insufficient to meet the needs of the proposed systems [8].

Table 1. ACOSS Program Summary (Strunce and Carman [7])

Company	Control Theory	Control Design & Analysis	Experiments
Control Dynamics	Sampling Phenomena Stability	Digital Control Digital Implementation	
Convair	Model Error Sensitivity Suppression (MESS)	MESS Disturbance Accommodation	Flyswatter Plate (IR&D)
Draper	Reduced-Order Modeling Reduced-Order Controller Output Feedback Sensor/Actuator Placement Optimal Slewing Maneuvers High Resolution System Identification	Structural Damping Augmentation Modern Modal Control (MMC) SDA/MMC, Actuator Synthesis Disturbance Rejection Sensor/Actuator Placemant Optimal Slewing Maneuvers High Resolution System Identification	Beam (IR&D)
Honeywell	System Identification	Singular Values	
Hughes	Electronic damping	Electronic Damping	Hollow Cylinder
Lockheed	Low Authority Control (LAC) High Authority Control (HAC) Modal Cost Analysis (MCA)	LAC, HAC, LAC/HAC Frequency Shaping System Identification	Mini-Beam,Maxi-Beam Vertical Pipe Circular Plate Wheel (frame) Toysat, POC
TRW	Stability Ensuring Methodology System Identification Adaptive Control	Stability Ensuring Methodology System Identification	Plate (IR&D)

This study motivated the Defense Advanced Research Projects Agency (DARPA) to initiate the Active Control of Space Structures (ACOSS) program in 1979. The objectives of this focused program were to develop a unified technology base in structural dynamics and control for precision LSS and to demonstrate this technology through simulations and proof-of-concept ground experiments [8]. Up to eight research teams were funded under ACOSS at various times starting in late 1978 and ending in 1982 when this program was prematurely terminated. Table 1,which is from a 1983 paper by Strunce and Carman [8] summarizes the accomplishments of ACOSS. A number of today's well known vibration suppression techniques were developed and refined at this time, such as, Model Error Sensitivity Suppression (MESS), Low Authority Control (LAC), High Authority Control (HAC), and the combined HAC/LAC technique. Also, to assess the performance, sensitivity, and hardware requirements of various active structural control techniques, the CSDL developed two finite element evaluation models. First, a low order model of a 10-member tetrahedral structure [9] and second, a simplified optical system with associated performance measures and tolerances [10] were commonly known as Draper Models #1 and #2, respectively. The Draper Model #2 (shown in Figure 3) was the first systematic attempt to create an unclassified detailed model of an optical system and it was extensively used in literature over the next few years. In addition, under ACOSS and company Independent Research and Development (IR&D) funding, a number of simple proof-of-concept experiments on beams and plates were also successfully performed. Unfortunately, the planned experiments on three-dimensional structures were abandoned due to the early termination of the program. In spite of its early termination, the ACOSS program was responsible for focussing the LSS technology development towards precision space structures and it had a major impact on the scope and direction of the research which followed.

Running concurrently with the ACOSS program were the NASA funded activities in Large Space Systems Technology (LSST). This program looked at the technology needs of systems considered near-term at that point, such as, large antennas and space platforms [1]. Much of this work was documented in proceedings of the

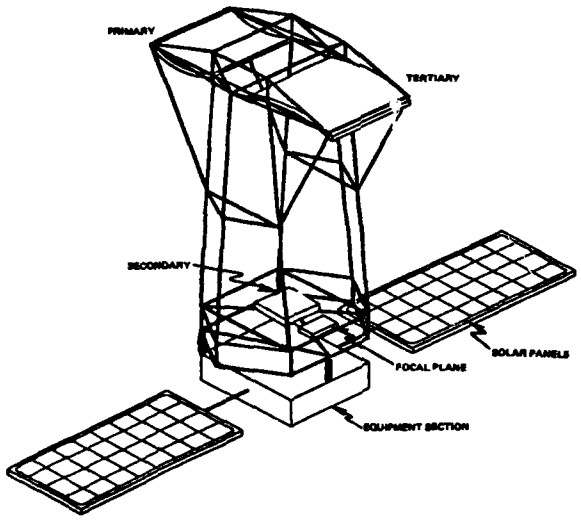

Figure 3 Draper Model #2

NASA sponsored annual workshops held at the NASA Langley Research Center starting in 1979 [11-15]. With the focus on large antenna applications, NASA selected a number of deployable structural concepts for further study. Starting in 1979, two of these concepts, the wrap-rib [16] and the hoop/column [17], were selected for a design and development program with a 100-meter diameter class of application in mind. The program ended in 1985 with technology readiness ground demonstration experiments. A 15-meter hoop-column antenna structure, capable of deployment / stow cycles, was developed and used for static / dynamic tests and to assess the active control requirements.

After the end of the ACOSS program, the focus of Department of Defense (DoD) and NASA funded follow-on efforts slowly shifted to hardware demonstrations. In 1983, taking off from where ACOSS finished, both the Air Force Astronautics Laboratory (AFAL) and the Air Force Flight Dynamics Laboratory initiated a number of hardware programs to demonstrate active and passive damping methodologies on simplified three dimensional test beds. Large angle retargeting of flexible structures was selected by AFAL and CSDL for a systematic methodology development and hardware demonstration program. An experimental structure consisting of a rigid hub with four flexible appendages, supported on an air bearing was developed [18,19]. Figure 4 shows the final configuration of this experiment. A number of sensing and actuation components such as cold gas thrusters, proof-mass actuators, hub torquer, and distributed piezoelectric film actuators were used to demonstrate spacecraft retargeting with vibration suppression. It is interesting to note that large angle retargeting continues to be an area of active research to this day. See Reference 20 for a recent survey of ground-based experiments in this field.

Experiments like those on the AFAL/CSDL structure and other NASA / DoD facilities [21,22] in the mid 1980s were essential for the gradual progression in the development of LSS technology. However, these experiments concentrated on methodology demonstration with little concern about the weight and power requirements or about the space survivability of the resulting control system. In fact, in many such experiments, the control actuators outweighed the structure they were controlling! The same was true for the associated control electronics and computers. Thus, at this point, although the control methodology had been developed and demonstrated and could be considered ready for application, the control hardware was at least 5-10 years away from reaching maturity.

Figure 4 AFAL/CSDL Large Angle Retargeting Experiment

Cooperation between NASA and DoD has continued with the *long-term* goal of developing and demonstrating controls - structure interaction technology for the next generation of precision space structures. To this end, a number of realistic, complementary, three dimensional test-beds have been developed at the participating NASA and AF research centers. Since 1990, the two organizations have a joint Guest Investigator (GI) Program for the ground demonstration and validation of emerging structures and controls technology. Five contracts covering a broad spectrum of CSI issues have been awarded and the experimental demonstrations are on-going at three NASA /AF experimental facilities. One of these facilities, located at the Phillips Laboratory, is the Advanced Space Structure Technology Research Experiments (ASTREX) test bed. Central to the ASTREX facility is a three-axis large-angle retargeting

capability and a powerful real-time control computer. The experimental structure consists of a dynamically scaled model of a three-mirror space-based laser beam expander. The current configuration of this experiment is shown in Figure 5. For further details on this facility, see Ref. 23.

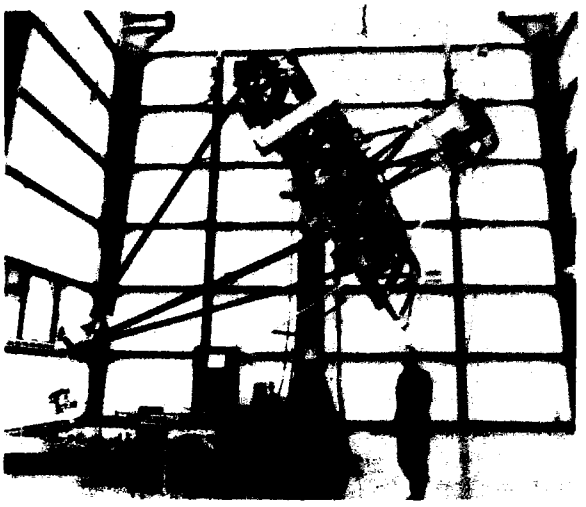

Figure 5 Current Configuration of the ASTREX Testbed

Also, since 1986, NASA and DoD have jointly sponsored the Controls / Structures Interaction Technology conference to promote timely dissemation of technical information [24-26].

3. ADAPTIVE STRUCTURES

In addition to the long-term requirements of precision large space structures, the new SDIO GPALS architecture imposed performance and reliability constraints on near-term systems which were beyond existing state-of-the-art. None of the space based assets in the GPALS architecture will receive scheduled maintenance. The vibration suppression system aboard these satellites will be required to autonomously track changes in the system dynamics and retune itself to deliver the required performance. These changes in system dynamics could come from many causes: inherent uncertainties in the knowledge of plant dynamics; gradual changes due to outgassing and ageing of the structure; sudden damage to the structure due to a threat environment; and/or changes in the components of the control system itself, such as, degradation or failures in one or more sensor / actuator. As an example of environmentally induced changes in system dynamics, Figure 6 shows the transfer functions for a relatively small, stiff composite structure (the structure is part of ACTEX flight experiment described later). These transfer functions, taken at room temperature before and after the structure was thermally cycled, show approximately 5% change in the modal frequency. Changes in system dynamics and the associated degradation in controller performance will be the rule rather than an exception. As a solution to this problem, the SDIO Materials and Structures (M&S) Program has proposed an adaptive structures approach that combines health and environmental monitoring with static and dynamic structural control [3].

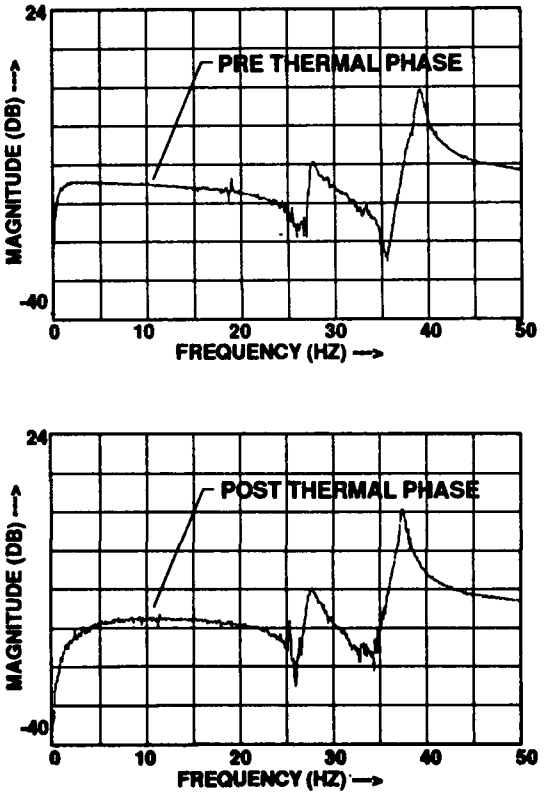

Figure 6 Effect of Thermal Cycling on the Modal Characteristics of ACTEX Flight Structure

The SDIO M & S program has adopted a new concept for Adaptive Structures (for details see Reference 3 by Obal and Sater). Different types of sensors, either embedded in or attached to certain structures, are used for several functions, such as, structural health monitoring for identification, status, and propagation of cracks; threat and natural environment measurements; and monitoring of system states. The sensory information obtained from measurements and subsystem diagnostics is processed and stored. This information, in conjunction with actuators, can be used for static shape control or active vibration suppression. Applications of this technology are only now becoming achievable as a result of developments in

microprocessors and miniature sensors / actuators. Thus lightweight, miniaturized sensors and actuators, health monitoring and intelligent control software, along with advanced composite materials form the cornerstones of the adaptive structures approach. Each of these will be discussed in more detail later. A pictorial representation of the M & S adaptive structures concept is reproduced here in figure 7 (from Reference 3).

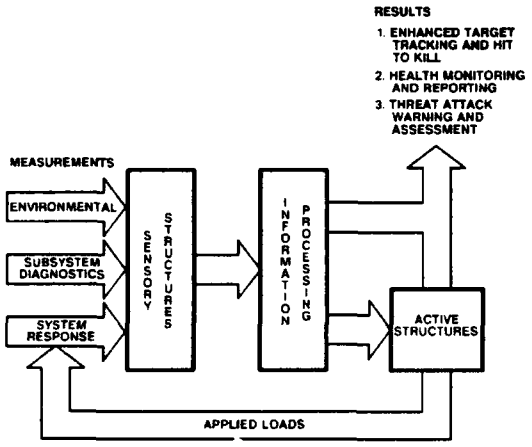

Figure 7 SDIO M & S Concept for Adaptive Structures

Although adaptive structures offer some very attractive features for these complex, autonomous systems, there still are many issues to be resolved. Some of these issues will be discussed in the sections that follow. Finally, in order for system designers to accept this technology, it must be minimally intrusive to the design in terms of weight, power, and reliability. These are some of the issues being addressed under the joint SDIO/USAF program.

3.1 Advanced Composites

As discussed earlier, the proposed near-term systems call for high precision from the structure. Not only must the structure be designed stiff to minimize unwanted distortions; it must also, in certain applications, provide accurate static alignment between specific points. In addition, these accuracies have to be maintained over long exposures to large variations in temperature, vacuum, and radiation. These requirements may apply to the entire structure or only to selected components, such as an optical bench where boresight alignment between sensors and line-of-sight jitter are of prime importance. A number of structural design concepts have been developed to address these requirements (see Reference 27 for an excellent description of some of these concepts and issues). Of course structural design and proper material selection go hand in hand. The availability of advanced composites has provided the structural designer with a very powerful tool. For example, with proper choice of graphite fiber and orientation of the various layers, one can literally tailor the properties of the resulting structure. Thus desirable properties such as light-weight, high-stiffness, thermal stability, low outgassing, good thermal conductivity, high-temperature resistance, high corrosion resistance, etc. could be traded to produce an optimized structure. Graphite fiber reinforced polymer composites (FRPC) such as graphite thermosets and graphite thermoplastics along with metal-matrix and carbon-carbon composites form a class of promising materials for spacecraft applications. However, graphite thermosets have continued to be by far most popular for such applications.

A graphite fiber reinforced polymer composite and graphite-reinforced aluminium are expected to, and indeed do, outperform their respective unreinforced matrix polymer and matrix "monolithic" aluminium in terms of strength and elastic properties. A simple comparison of composite properties to reinforcements alone is not meaningful for graphitic fibers which have tensile strength and modulus in excess of the composite, but are brittle and deficient in compression. High modulus graphite fiber, followed by pyrolytic graphite, most nearly approaches the extremes in tensile modulus and theoretical maximum strength of the single crystal. The degree to which fibers can approach this theoretical limit is determined by the purity of the fiber, presence of contaminants, and proper aligning of planes in filaments. Impurities affect the statistical variation in strength properties of filaments through the creation of flaw sites. The future availability of synthetic fibers promises to eliminate these contaminants. Typical fibers in use today include T-300, AS-4, IM-7, GY-70, P-75 and P-100. Fiber types are those predominantly derived from polyacrylonitrile (PAN) or pitch precursors.

The most common thermosetting resins are epoxies, bismaleimides and polyimides with epoxies being the most widely used in spacecraft. Thermal allowable is the main distinguishing feature among these thermosets. Two polymeric resins attracting a lot of attention because of improved resistance to matrix cracking (from solar thermocycling) and possessing very low outgassing characteristics are polycyanate resin and polyetheretherketone (PEEK) resin. Polycyanates are thermosets and PEEK is a thermoplastic. Peak temperature for processing of graphite/PEEK composites is 390° C, far above that of graphite/epoxy thermosets.

Graphite-thermoset composites have been widely used in military and commercial satellites. Their applications have progressed from limited use in component and subsystem designs to various structural applications. These applications include antenna support structure, waveguide and multihorn feed support tower and parabolic

reflectors [28]. With the popularity of advanced composites as the material of choice for the construction of spacecraft, it became possible to embed the vibration suppression and health monitoring sensors/actuators within the layers of the composite material. This provides a truly integrated, survivable control system. However, this new demand of transducer embedability imposes an additional constraint during the composite material selection. Since the embedded transducer has to survive the composite processing, the peak processing temperature should be kept low enough to not impact the transducer performance. Recent attempts to embed piezo ceramic actuators into graphite/PEEK composites were unsuccessful. The high processing temperature of the peek thermoplastic depoled the actuators resulting in a significant loss in actuation capability. On the positive side, piezo ceramic transducers have been successfully encapsulated in a variety of graphite-thermosets, including polycyanates.

3.2 Integrated Sensors and Actuators

Integrated sensors and actuators are very important components of an adaptive structure. Thus, the weight and power requirements of these transducers is of prime importance. The impact of excessive sensor and actuator weight became apparent in the mid 1980s. This and other factors resulted in shifting the focus from high authority point devices, such as proof-mass actuators and reaction wheels, to a search for devices which can provide distributed sensing and control.

Bailey and Hubbard [29] investigated the use of piezoelectric distributed actuators for structural damping augmentation. The piezoelectric material used was a PVF_2 film bonded directly onto the structure. The PVF_2 actuator was shown to provide a high level of damping at low vibration levels, however, its low authority made it impractical for most applications [30]. Crawley and de Luis [31] compared a variety of piezoelectric materials for possible use as actuators. A number of factors were used in the comparison, including embedability in composites, ratio of strain to applied voltage, and a performance criteria derived by maximizing the actuator effectiveness. The superiority of piezoelectric ceramics over other piezoelectric materials such as polymer film was conclusively demonstrated by this comparison. Concurrently, Hanagud, Obal and Meyyappa [32] investigated the use of piezo ceramic sensors and actuators for active damping of a cantilevered beam. A procedure to quantify the effects of active damping was developed and experimentally verified. It was through the effort of these and other investigators that the feasibility of this important technology was demonstrated.

In 1988, in an attempt to advance the technology of lightweight composite structures with embedded control systems from bench-scale proof-of-concept demonstrations to closer to actual applications in space, the USAF Phillips Laboratory (PL) in cooperation with SDIO, initiated the ACESA (Advanced Composites with Embedded Sensors and Actuators) program. Overall goals for the program included design, fabrication, and demonstration of composite components containing embedded sensors and actuators. A variety of sensing and actuation mechanisms were evaluated, including fiber optic, strain gauge, piezoelectric and electro restrictive ceramics, and shape memory alloys [33, 34]. This evaluation led to the selection of piezoelectric ceramics for sensors and actuators. Factors such as extreme strain sensitivity, ability to use simple drive electronics, and relative maturity of the basic technology led to this selection. A number of practical issues such as sensor / actuator encapsulation techniques, procedure for embedding the encapsulated devices in graphite epoxy composite structures, and the effect of thermal/vacuum and mechanical loading on the resulting structure were studied. System level demonstration of the technology was recently performed using the ASTREX facility. For this purpose, the three 17-ft long, 5-in diameter composite tubes comprising the secondary mirror support metering truss were targeted for active control. Equivalent active composite members tubes (with flattened sides to facilitate embedding of flat piezo ceramic wafers) and supporting control electronics were fabricated and integrated into the testbed. Figure 8 shows the layout of a string of actuators including colocated and nearly colocated sensors. As shown, these encapsulated strings were embedded in flattened sections along the length of the tube on all four

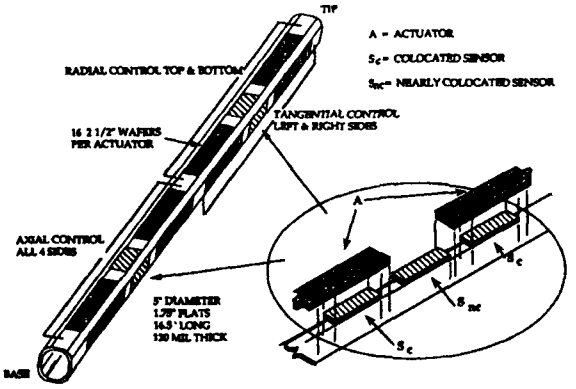

Figure 8 Layout of Embedded Piezo Ceramic Sensors and Actuators used on ASTREX Structure

sides. These sensor/actuator strings can be paired in various ways to provide radial, axial, or tangential control of the tube. Transfer functions taken with realistic sustained disturbances located near the secondary mirror showed a dramatic reduction in the magnitude of targeted structural modes. In many cases, the modes were overdamped by the control system. A representative set of

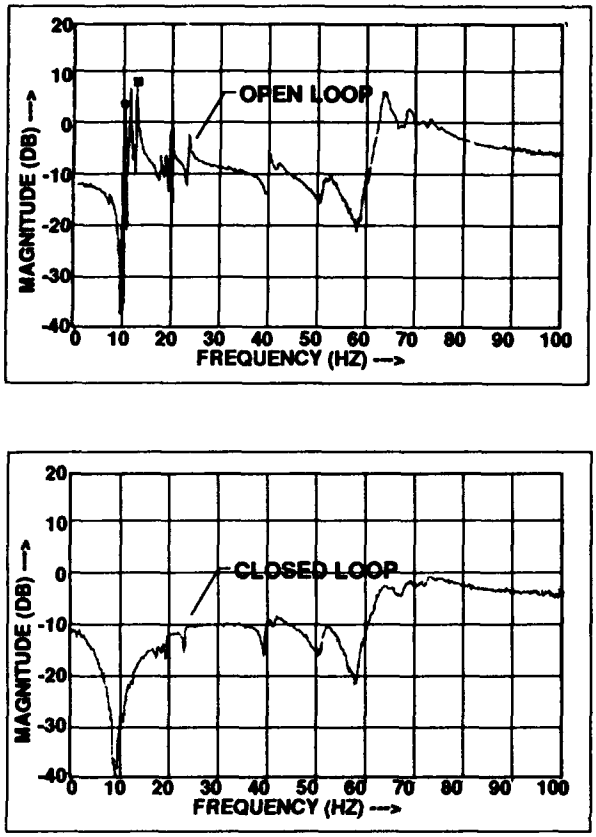

Figure 9 Representative Transfer Function of a Sensor / Actuator pair with Active Controller OFF and ON

transfer functions with active control OFF (Open Loop) and ON (Closed Loop) are shown in Figure 9.

Although a number of very important practical issues related to embedded sensors and actuators were addressed in the ACESA program, little or no importance was placed on the size or the power requirements of the associated electronics. Current SDIO near-term systems have extremely stringent constraints on power and weight, thus requiring significant reduction in active vibration system weight and power requirements. Also the option of embedding sensors and actuators will not be available in every application. This could be due either to the incompatibility of the sensors / actuators with processing temperatures of the selected structural material, or the requirement of retrofitting an existing structure. For these reasons, a concept for a space-durable modular patch is being developed. The patch integrates sensing, actuation, and control / power conditioning electronics into a self contained package that can be either bonded to or embedded within the structure [35]. The match box size patch will be designed to interface directly with the spacecraft power system (unregulated 28 volt power), require less than 10 watts to operate, and have minimal external interface requirements. An individual patch could be used to provide local vibration suppression or made to work with other patches in a global manner. It is anticipated that the modular control patch will reduce the weight and volume of the control system by up to 90% compared to current technology. Figure 10 shows a leading concept for the patch currently under consideration. This concept uses a multichip module, consisting of a custom ASIC with analog input conditioning and compensator electronics, and a high voltage drive amplifier. Overall dimensions of the chip which will contain all necessary power conditioning and control electronics are expected to be within 3.3 cm X 1.7 cm. Design and fabrication of the multichip module is expected to begin in early 1993.

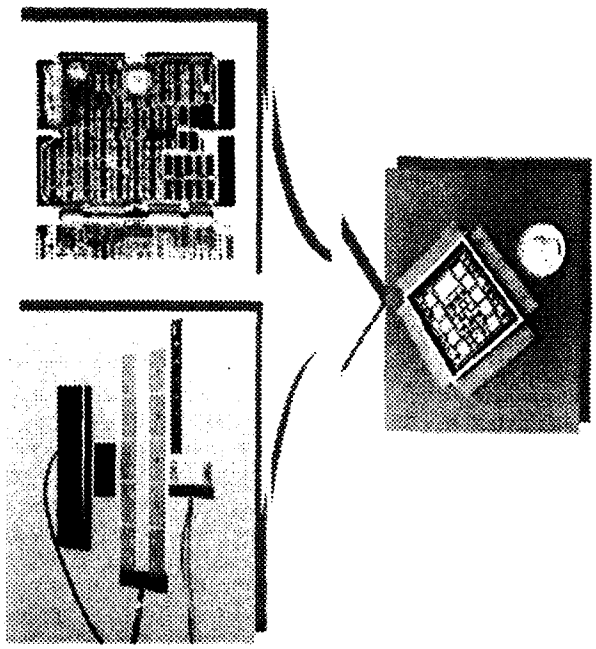

Figure 10 A Concept for Modular Control Patch Using Piezo Ceramic Sensor / Actuator and Multichip Module

3.3 Intelligent Control

As mentioned earlier, the long life and minimal ground support requirements of the GPALS and other near-term spacecraft require the development of an on-board health monitoring and autonomous control system. Such a system should be capable of autonomously monitoring the health of the satellite subsystems, the threat environment and its impact on the satellite, and detect any significant changes in key performance parameters. These

changes could be gradual due to aging of the spacecraft structure or mechanical components, or sudden due to threat (either natural or hostile) induced damage to components. The components of the control system itself, such as sensors or actuators could demonstrate degradation in performance. The objective of the on-board intelligent controller is to identify changes in key performance parameters, determine the source of the change if possible, and retune / reconfigure the control system. This should return the control system to full performance, or if that is not possible, to a graceful degradation in performance.

Research in intelligent control for precision space structures is progressing along a number of complementary paths; two of these are described here. de Luis et al [36] investigated highly distributed actuator, sensor, and processor networks integrated with the structure. This approach makes a large number of sensors and actuators available to the control system designer. It also allows implementing distributed control logic with the computational load shared among a number of distributed processors. In such a control architecture, the failure of an individual sensor or actuator becomes much less critical to the overall performance, providing a degree of fault tolerance.

More recently, work has also started in the use of neural networks for autonomous system identification along with rapid failure detection and control system reconfiguration [37, 38]. Hyland used a neural controller consisting of two blocks: a system replicator block, which autonomously builds a model of the plant with no prior information; and a control adaptor network which adapts the system dynamic compensation to produce the desired closed loop response. Preliminary experiments in system identification and control have produced encouraging results. However, on-going investigations have barely scratched the surface and much more work has to be done before the true potential of this technology can be assessed. With this in mind, in 1991 PL initiated a focussed program in neural network controller methodology development, proof-of-concept experiments, and system level demonstrations.

4. TECHNOLOGY DEMONSTRATION EXPERIMENTS

Finally, ground based and on-orbit technology demonstration experiments form an important component of the overall adaptive structures effort. The long-term survivability and fault tolerance of any emerging technology, like adaptive structures, to space environment must be adequately demonstrated before it can be considered mature for applications in operational space systems. Many of the space environmental effects such as thermal cycling, vacuum, and radiation can largely be simulated in ground based test chambers. However, in order to access the long-term effects of simultaneous exposure to a combination of environmental effects, on-orbit experiments become necessary. A series of generic technology demonstration and specific technology application experiments are on-going. The testing phase of each experiment includes ground based functional, performance, and environmental tests, followed by extended on-orbit demonstrations.

The Advanced Control Technology Experiment (ACTEX) has been designed to demonstrate active vibration suppression using embedded piezo ceramic actuators, a technology developed under the ACESA program. This experiment is scheduled to fly as a secondary payload on a DoD satellite in 1994. The test structure consists of a cantilevered graphite epoxy tripod with embedded piezo ceramics, approximately 60 cm X 30 cm X 25 cm in size (see figure 11). It is designed to be externally mounted on the payload deck of a host satellite and will thus be exposed unprotected to the rigors of space environment. The structure is well instrumented with accelerometers and thermistors in order to determine the dynamics of the structure and evaluate the performance of the control system over a wide range of orbital environments and over a long orbital life. Orbital life of 2-3 years is anticipated.

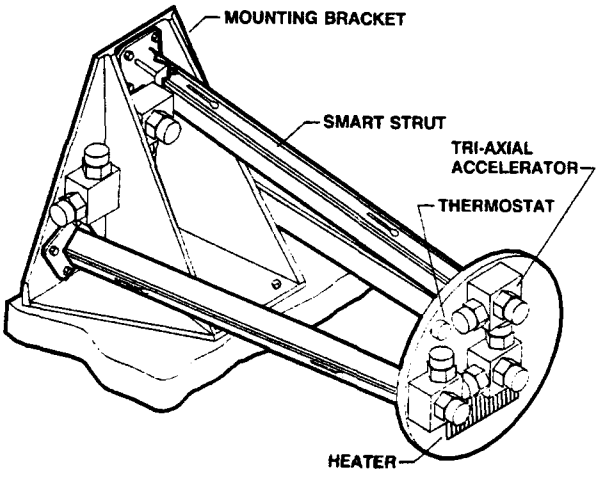

Figure 11 Forward View of the ACTEX Tripod Structure Showing the Location of Various Instrumentation

Besides conducting on-orbit structural characterization and vibration suppression experiments, the structure is equipped with a mechanism to change the dynamics of the tripod by stiffening a set of flexures. This changes the frequency of the first two modes by 10% and 20% respectively. This capability will be used to demonstrate the ability of the control system to adapt to significant changes in system dynamics, an important requirement for future systems.

Figure 12 shows the effect of active damping measured on the tripod structure. Typically, as expected, damping between 10% to 20% has been observed for the targeted modes.

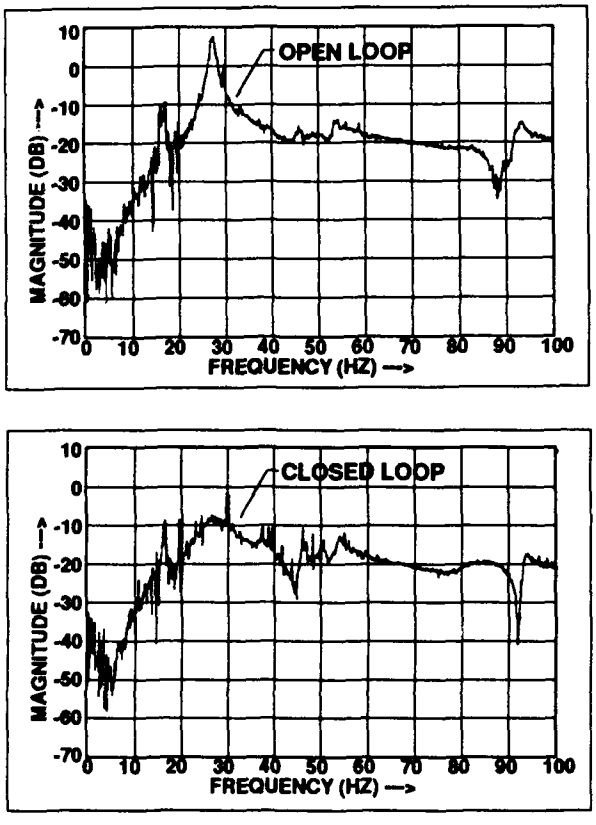

Figure 12 Typical Open Loop and Closed Loop Transfer Functions Measured on the ACTEX Tripod Structure

ACTEX was planned and executed as a low cost flight experiment with minimal redundancy, quality assurance and documentation. It was felt that low cost and rapid turnaround were essential for sustained funding for such an experiment. The entire design, fabrication, and ground testing of the experiment was successfully completed over a 1-year period ending in July 1992.

Whereas the ACTEX experiment will demonstrate the maturity of generic adaptive structures technology, two other experiments are investigating specific applications. Sensor jitter has always been a matter of grave concern for optical surveillance systems and GPALS space assets are no exception. Typically, Stirling cycle cryocoolers are used to keep the infrared space surveillance sensors at their operating temperature. Unfortunately in many cases, one of the leading sources of jitter, given a quiescent spacecraft, is the cryocooler itself [3]. Cryocooler generated vibrations can reach the sensor focal plane array through two alternate paths: first, the cryocooler cold finger is in thermal contact with the sensor focal array via a copper strap, which can also provide a path for vibrations; second, the common structure to which both the cryocooler and the sensor are mounted also serves as a path for transmitting vibrations.

Although a number of approaches existed to reduce the effect of the latter, cold finger bourne vibrations could only be reduced using a compliant thermal strap at the cost of additional thermal load on the cryocooler. Recently the Jet Propulsion Laboratory (JPL), under SDIO M&S funding, demonstrated a novel method for reducing these vibrations. Small sections of curved, thin piezo ceramic actuators are bonded onto the root of the cold finger, which is at room temperature during operation. It is anticipated that these actuators will reduce the lateral vibrations of the cold finger by a factor of 2 to 5 in the 0 to 200 Hz range. Based on this approach, a flight experiment is currently under fabrication at JPL. See Figure 13 for a schematic of the experiment.

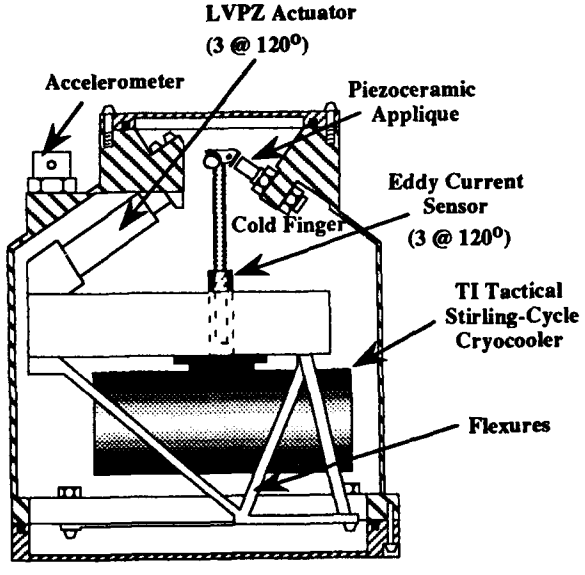

Figure 13 A Schematic of Cryocooler Cold Finger Vibration Suppression Experiment

An alternate approach for vibration reduction is also demonstrated on this experiment. The cryocooler is mounted on three low voltage piezo stacks, equally spaced 120° apart. Thus the entire cryocooler can be rotated to keep the tip of the cold finger from moving. The experiment is scheduled to fly on a British technology demonstration satellite in late 1993 or early 1994 to

obtain space durability data in a high radiation environment. It will demonstrate an important technology for GPALS systems where cryocooler induced vibrations may lead to increased sensor jitter.

Besides cryocoolers, another major source of spacecraft line-of-sight jitter is the solar array system. The solar array vibrations can be caused either by stepper motors used in array drive, or by satellite housekeeping activities such as attitude control thruster firings. Under the SDIO funded Advanced Materials Applications to Space Structures (AMASS) program, structurally integral active and passive vibration damping techniques are being applied to a representative yoke-type solar array support system. Again, active damping is provided via embedded piezo ceramic sensor/actuator technology developed under the ACESA program. In this case, the solar array yoke struts have been constructed using graphite-polycyanate. As mentioned earlier, this new thermoset resin exhibits lower outgassing and higher resistance to microcracking than other thermosets. Viscoelastic passive damping materials have been used to provide over 10% of critical damping in the joint between the solar array drive assembly and the spacecraft bus. Three different viscoelastic materials had to be used to provide the desired damping over a temperature range of 30 to 120° F. A schematic of the passively damped solar array drive assembly and the actively damped solar array yoke is shown in Figure 14.

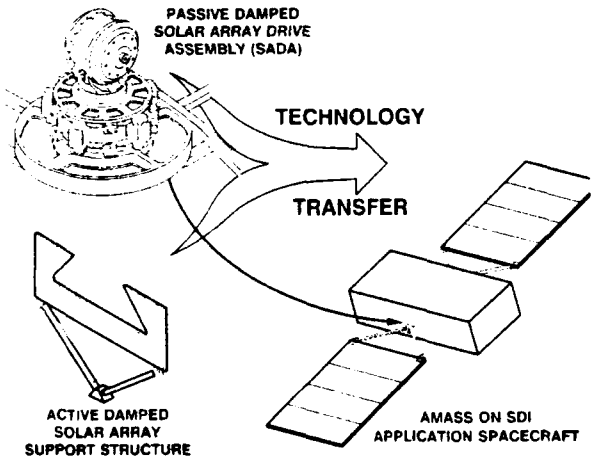

Figure 14 Application of Active and Passive Vibration Damping Technology to a Solar Array Drive System

The vibration suppression hardware developed under AMASS is currently undergoing extensive testing in a laboratory environment. These experiments have conclusively demonstrated the maturity of this technology for flight application. A number of options for on-orbit demonstration of the technology are being explored.

Finally, a number of new adaptive structures technology application experiments are under consideration. In one such application, a precision optical bench is proposed for development. This bench will use high modulus advanced composites with co-cured viscoelastic damping to provide a stiff, yet damped surface for mounting optical sensors. The entire optical platform will then be mounted on active isolation mounts to isolate it from spacecraft bus bourne vibrations.

5. CONCLUSIONS

The preceding sections of this paper have surveyed the development of vibration suppression technology for large space structures, leading to the joint SDIO/USAF adaptive structures program. This adaptive structures approach provides a mechanism for autonomous on-orbit health and threat monitoring combined with static / dynamic structural control; an important requirement for many future systems. It is anticipated that future work will continue to focus on application of this important technology to DoD systems.

6. REFERENCES

1. James, R. L., "Large Space Systems Technology Overview," in "Large Space Systems Technology - 1980," NASA Conference Publication 2168, Vol. I, 1980, pp 1-8.

2. Tolivar, A. F. and Wang, S. J., "Control of Large Space Antennas," in "Large Space Antenna Systems Technology - 1982," NASA Conference Publication 2269, Part 2, 1983, pp 583-599.

3. Obal, M. and Sater, J. M., "Adaptive Structures Programs for the Strategic Defense Initiative Organization," Proceedings of the 33rd Structures, Structural Dynamics, and Materials Conference, Dallas, Texas, April 1992.

4. Gupta, N. K., Lyons, M. G., Aubrun, J-N. and Margulies, G., "Modeling, Control and System Identification Meyhods for Flexible Structures," in "Spacecraft Pointing and Position Control," AGARD-AG-260, November 1981, pp12-1 to 12-41.

5. Balas, M. J., "Trends in Large Space Structures Control Theory: Fondest Hopes, Wildest Dreams," IEEE Transactions on Automatic Control, Vol. AC-27, No. 3, June 1982, pp 522-535.

6. Meriovitch, L., editor, "Proceedings of the 1st VPI&SU/AIAA Symposium on Dynamics and Control of large Flexible Spacecraft," Blacksburg, Virginia, June 13-15, 1977.

7. Strunce, R. R. and Carman, R. W., "Active Control of Space Structures (ACOSS) A Status Report," The Charles Stark Draper Laboratory report CSDL-P-1707, February 1983.

8. Strunce, R. R. and Carman, R. W., "Active Control of Space Structures (ACOSS) A Status Report," The Charles Stark Draper Laboratory report CSDL-P-1707, February 1983.

9. ACOSS Four (Active Control of Space Structures) Theory, RADC-TR-80-78, Rome Air Development Center, Griffiss AFB, New York, April 1980.

10. ACOSS Eleven (Active Control of Space Structures), RADC-TR-84-185, Rome Air Development Center, Griffiss AFB, New York, September 1984.

11. Large Space Systems Technology, Part 1 & 2, NASA CP-2118, 1980.

12. Large Space Systems Technology - 1980, Part 1 & 2, NASA CP-2168, 1980.

13. Large Space Systems Technology - 1981, Part 1 & 2, NASA CP-2215, 1982.

14. Large Space Antenna Systems Technology - 1982, Part 1 & 2, NASA CP-2269, 1983.

15. Large Space Antenna Systems Technology - 1984, Part 1 & 2, NASA CP-2368, 1985.

16. Freeland, R. E., Garcia, N. F. and Iwamoto, H., "Wrap-Rib Antenna Technology Development," in "Large Space Antenna Systems Technology - 1984," NASA CP-2368, Part 1, 1985, pp 139-166.

17. Campbell, T. G., Butler, D. H., Belvin, K. and Allen, B. B., "Development of the 15-meter Hoop/Column Antenna System," in "large Space Antenna Systems Technology - 1984," NASA CP-2368, Part 1, 1985, pp 167-212.

18. Bailey, T., Gruzen, A. and Madden, P., "RCS/Linear Discrete Actuator Study," AFAL-TR-88-039, Air Force Astronautics Laboratory, Edwards AFB, California, August 1988.

19. Floyd, M. A. , "Single-Step Optimal Control of Large Space Structures," The Charles Stark Draper Laboratory report CSDL-T-840, April 1984.

20. Das, A. "Large-Angle Maneuver Experiments in Ground-Based Laboratories," in "Mechanics and Control of Large Flexible Structures," Junkins, J. L., editor, Progress in Astronautics and Aeronautics, Vol. 129, 1990.

21. Williams, J. P., "Slew Maneuvers on the SCOLE Laboratory Facility," NASA CP-2447, Part 2, 1986, pp 851-867.

22. Pearson, J. and Yuen, W., "Active Control Evaluation for Spacecraft (ACES)," in "NASA/DoD Control/Structures Interaction Technology - 1986," NASA CP-2447, Part 1, 1986, pp 67-84.

23. Das, A., et, al., "ASTREX - A Unique Facility for CSI Research," Proceedings of the 29th IEEE Conference on Decision and Control, December 1990.

24. NASA/DOD Controls/Structures Interaction Technology - 1986, NASA CP-2447, Part 1 & 2, 1986.

25. NASA/DOD Control/Structures Interaction Technology 1987, AFWAL-TR-88-3052, Flight Dynamics Laboratory, Wright-Patterson AFB, Ohio, 1988.

26. NASA/DOD Controls/Structures Interaction Technology 1989, NASA CP-3041, 1989.

27. Hedgepeth, J. M., "Critical Requirements for the Design of Large Space Structures," NASA CR-3484, November 1981.

28. Rawal, S. P. and Misra M. S., "Measurement of Mechanical and Thermophysical Properties of Dimensionally Stable Materials for Space Applications," NASA CR-189552, Martin Marietta Astronautics Group, Denver, Colorado, February 1992.

29. Bailey, T., and Hubbard, J. E., "Piezoelectric-Polymer Active Vibration Control of a Cantilever Beam," Journal of Guidance, Control, and Dynamics, Vol. 8, No. 5, Sept.-Oct. 1985.

30. Bailey, T., Gruzen, A., and Madden, P., "RCS/Piezoelectric Distributed Actuator Study," Air Force Astronautics Lab., Edwards AFB, CA, AFAL-TR-88-038, Aug. 1988.

31. Crawley, E. F., de Luis, J., "The Use of Piezoelectric Actuators as Elements of Intelligent Structures," AIAA Journal, Vol 25, No. 10, Oct 1987, pp 1373-1385.

32. Hanagud, S., Obal, M. W., and Meyyappa, M.,"Electronic Damping Techniques and Active Vibration Control," AIAA Paper 85-0752, 1985.

33. Bronowicki, A. J., Mendenhall, T. L., Betros, R. E., Wyse, R. E., and Innis, J. W., "ACESA Structural Control System Design," 1st Joint US/Japan

Conference on Adaptive Structures, Maui, Hawaii, Nov 1990.

34. Bronowicki, A., Betros, R., and Dvorsky, G., "Encapsulation Technique to Enhance Actuator Performance in Composite Beams," Presented at the 1990 NASA/DoD CSI Conference, Orlando, FL.

35. Griffin, S. F., Denoyer, K. K., and Yost, B. J., "Smart Patch Piezoelectric Actuator Issues," presented at the 1992 NASA / DoD Controls-Structures Interaction Technology Conference, Lake Tahoe, Nevada.

36. de Luis, J., Crawley, E. F., and Hall, S. R., "Design and Implementation of Optimal Controllers for Intelligent Structures Using Infinite Order Structural Models," MIT Report, SSL # 3-89, Jan 1989.

37. Hyland, D., "Neural Network Architecture for On-Line Identification and Adaptively Optimized Control," Proceedings of the 30th IEEE Conference on Decision and Control, December 1991, Brighton, England, pp 2552-2557.

38. Wang, S. J., Boussalis, D., Pineda, F., and Antsaklis, P. J., "Autonomous Spacecraft Control Using Neural Networks," Annual Report of Investigations Carried Out Under the Director's Discretionary Fund, Jet Propulsion Laboratory, Pasadena, Ca, JPL D-9387, June 1992.

DYNAMIC TESTS ON THE NASA LANGLEY CSI EVOLUTIONARY MODEL

by

H. Troidl
Industrieanlagen-Betriebsgesellschaft
IABG
Ottobrunn
Germany

K.B. Elliott
NASA Langley Research Center
Mail Stop 230
Hampton VA23665-5225
United States

SUMMARY

A modal analysis study, representing one of the anticipated "Cooperative Spacecraft Structural Dynamics Experiments on the NASA Langley CSI Evolutionary Model", has been carried out as a sub-task under the NASA/DLR collaboration in dynamics and control of large space systems. The CSI evolutionary testbed (CEM) is designed for the development of Controls-Structures Interaction (CSI) technology to improve space science platform pointing. For orbiting space structures like large flexible trusses, new identification challenges arise due to their specific dynamic characteristics (low frequencies and high modal density) on the one hand, and the limited possibilities of exciting such structures and measuring their responses on orbit on the other. The main objective of this study was to investigate the modal identification potential of several different types of forcing functions that could possibly be realized with on-board excitation equipment using a minimum number of exciter locations as well as response locations. These locations were defined in an analytical test prediction process used to study the implications of measuring and analysing the responses thus produced. It turned out that broadband excitation is needed for a general modal survey, but if only certain modes are of particular interest, combinations of exponentially decaying sine functions provide favourable excitation conditions as they allow to concentrate the available energy on the modes being of special interest. From a practical point-of-view structural nonlinearities as well as noisy measurements make the analysis more difficult, especially in the low frequency range and when the modes are closely spaced.

1. INTRODUCTION

Future space missions will require new methodology for controlling space structures. The challenge lies in their complexity, extreme flexibility, size, and accuracy requirements. Optics of large space telescopes will have to be assembled in orbit and kept focused and pointed, science platforms will contain several instruments and antennas which must be pointed independently, while each of the instruments is affecting the performance of each other, and any space station will be extremely flexible and will have subsystems which are sensitive to motion or vibration and are subject to a variety of disturbances.

As a consequence spacecraft structural dynamics, with its heavy impact on spacecraft control, has become a topic of increasing importance in the recent years. This increasing importance is a result of the need for reliable analytical structural models for pointing precision, flight path control, vibration reduction, structural dynamic analysis, control system design and health monitoring.

While spacecrafts launched to date undergo excessive testing, including system identification studies to improve their mathematical models, often using full flight hardware, for large space structures on-orbit testing in their subsequent assembly stages will become necessary [1,2]. These structures will be characterized by low mass, high flexibility, high modal density, low natural frequencies, nonlinearities and low damping. Due to the zero-g environment, rigid-body motions will interact with flexible body motions of the structure. Reduced "controllability", as the excitation is limited to only certain forcing functions as well as exciter locations, and a confined "observability", due to the limited number of sensors resulting from weight and cost considerations, are the problems dynamicists will have to cope with [3]. Disturbances arising, for example, from changes in temperature will allow only certain restricted time windows for data acquisition [4].

2. CURRENT RESEARCH WORK

The subject of on-orbit testing of space structures is being considered by several programs. The Controls-Structures Interaction (CSI) program [5] is a focused technology program that is examining ways to improve spacecraft stability and pointing performance. The program is examining three areas: spacecraft structure and controller design, spacecraft ground testing, and flight verification.

The Dynamic Scale Model Technology (DSMT) [6] concentrates on research to adapt the use of scale models, which are currently used in aircraft and have been used in several large launch vehicles, as a tech-

nology to support large spacecraft ground verification.

Perhaps the most amount of work on on-orbit testing has been performed in relation to the Space Station Freedom (SSF). NASA is planning an on-orbit modal test of Space Station Freedom, termed the "Space Station Structural Characterization Experiment" (SSSCE) [7], which would consist of a series of modal tests on the evolving space station structure. Results from the experiment could be used to correlate analytical models and to evaluate modeling and testing methods for large space structures. Some work has already been done comparing modal identification techniques [8], selecting suitable techniques like the polyreference method [9] and the Eigenvalue Realization Algorithm (ERA) [10], and adapting these methods for this particalur problem. Blelloch et al. [11] have developed a Modal Test Simulation (MTSIM) software tool to simulate on-orbit testing of Space Station Freedom using an SSF finite element model. The structure is assumed to be excited by reaction control system jet firings using random and modulated random forcing functions. Specific work has been done by Kim [12] and Kim et al. [13] designing random excitation individually for each configuration of the SSF which could be used with a free-decay time-domain technique for the on-orbit modal identification.

Efficient sensor placement for on-orbit modal identification as well as mode-order reduction, taking into account that the structure will be assembled sequentially or even modified after years of operation, is discussed by Kammer et al. [14]. The authors propose to select a limited number of dynamically important target modes using the amount of mass in each mode shape participating in each of the six rigid body directions (effective mass) as the main criterion. As the effective mass is identically zero for free-free systems a Graig-Bampton representation (see [14]) is generated by constraining the sequentially assembled structure at the actuator locations and the interface points to the next phase. Fixed interface modes are computed and ranked according to their importance using a measure called "effective excitation mass". The sensor placement problem is approached from the standpoint of the estimation theory.

A simulated on-orbit modal test has been performed on the JPL Precision Truss by Chen et al. [15], using active members as the excitation source. The authors point out that active members, as opposed to reaction jet facilities or momentum wheels, would not considerably increase the weight and volume of the spacecraft. Only elastic motions would be excited, thus decoupling rigid-body dynamics from the modes of interest, which often are the flexible ones. Their results indicate that such a test can produce as good or even better modal parameters as those obtained using conventional excitation techniques.

3. OBJECTIVES OF THIS STUDY

The NASA LaRC CSI Evolutionary Model (CEM) [16] offers the opportunity to study and solve some problems of the on-orbit identification sub-technology task. The structure, shown in Fig. 1, is a double-cruciform truss (about 16 m long) with two vertical towers. It was designed to study problems related to multi-sensor space platforms.

The study reported here focuses on the investigation of the modal identification potential of different types of forcing functions and the development of excitation functions which will allow the concentration of the available energy into one, two, or several selected target modes by tuning the frequency content of one or more exciter forces to the corresponding mode frequencies. The forces may be applied by reaction jets, momentum wheels, or internal force producing devices. The target frequencies are initially taken from a mathematical structural model. As these frequencies do not necessarily coincide with the real-life frequencies of the structure, the effects of a frequency mismatch and the possibilities of a frequency updating are considered.

4. DESCRIPTION OF THE CSI EVOLUTIONARY MODEL TESTBED

NASA Langley's CSI Evolutionary Model Phase 0 is a testbed for the development of CSI technology to improve space science platform pointing. The evolutionary nature of this testbed permits the study of global line-of-sight pointing in phases 0 and 1, whereas multi-payload pointing systems will be studied beginning with phase 2.

The CEM has been designed to possess dynamic properties typical of spacecraft platforms proposed for remote sensing and communications. As such, unwanted interactions between sensor pointing control systems and the flexible body dynamics of the platform can be qualitatively assessed. Figure 1 shows the phase 0 version structural platform consisting of a long truss-bus and several appendages with varying degrees of flexibility. The truss-bus is constructed from 62 0.3 m cubical bays. Four horizontal appendages consist of 10 bays each. Two vertical towers consist of 11 bays and four bays, respectively. The truss is made from aluminum tubes and node balls. Threaded steel rods connect the tubes to the node balls. In addition to the truss, the structure contains a reflector, which had been included to simulate large appendages typical for space platforms. The reflector is a 5 m diameter ribbed structure with a flat mirror at its center.

A low-powered laser is mounted to the eleven bay vertical tower such that the beam reflects upon the reflector's mirrored surface. The beam reflection is measured by a photo-diode array attached directly above the reflector at the ceiling. This laser-reflector-detector system enables the global line-of-sight pointing to be measured.

The structure is suspended by two cables. These cables are attached to two support

points in the ceiling of the test facility. The primary suspension cables are yoked such that four points on the CEM are connected to the suspension system. Two linear extension springs are attached near the ceiling to reduce the effect of the suspension system on the CEM flexible body dynamics.

Several different types of sensors and actuators are available for use with the CEM testbed for both control and system identification (ID). The primary sensors are accelerometers. Two types of accelerometers are available: 18 servo accelerometers which can be used for low-frequency system ID, and a total of 195 piezo-film accelerometers for acceleration measurements above 1 Hz. A maximum of 16 air thrusters at 8 locations can be used to excite the structure. They are operated in pairs (forming together an "exciter") to insure pure translational forces when mounted on opposite sides of a truss bay. Each thruster produces a peak load of 10 N.

5. TEST PROGRAM

The test program was characterized by the variants of the excitation conditions. Three fundamentally different types of forcing functions were applied using the air thrusters as exciters:

- band-limited random noise
- impulse
- sum of exponentially decaying sinusoids

Random Excitation

This type of excitation was characterized by a uniform distribution of energy over the frequency range of interest. Four pairs of air thrusters were selected to simultaneously apply an uncorrelated excitation to the structure. The band-limited random excitation spectrum was defined by a constant power spectral density between the lower and upper frequencies of interest. In this case, the lower and upper cut-off frequencies were chosen to be 0.04 and 10 Hz, respectively. The CEM analytical model was used to size the magnitude of the excitation at a level that would keep the structure's response within predifined safety limits. For averaging purposes, the test was repeated 20 times resulting in approximately 1 hour of testing time.

Impulse Excitation

Impulse excitation was applied to the structure using each of the four thruster pairs, individually. The impulse was defined by its magnitude and duration. These parameters were chosen to produce an impulse with sufficient energy over the frequency range of interest (0-10 Hz). Five test runs, at each of the exciter locations, were performed for averaging purposes. The duration of each test was about 160 seconds.

Exponentially Decaying Sinusoidal Excitation

This is a selective type of transient excitation which may be tuned to particular modes of special interest. It is defined by a sum of exponentially decaying sinusoids:

$$p(t) = \sum_{i=1}^{n} p_i * e^{-\alpha_i t} * \sin(2\pi f_i t), \qquad (1)$$

with p_i = initial amplitude of component i
f_i = frequency of component i
α_i = decay rate of component i
n = number of components (target frequencies)

The frequencies of the exponentially decaying sinusoids refer to the selected target flexible-body modes of vibration, predicted with the CEM finite element model and eventually updated using the preliminary data analysis results of the preceeding excitation cases.

This type of excitation was applied to the structure using each of the thruster pairs separately. For each excitation location, the excitation frequencies, f_i, were chosen to coincide with the estimated eigenfrequencies of the selected modes. As in the impulse excitation case, each test was repeated five times for averaging purposes.

To study the effect of a mismatch of the excitation frequencies with the true structural eigenfrequencies, two additional tests were performed at a single excitation location. In the first test, the excitation frequencies were detuned a small amount, whereas, in the second test, the excitation frequencies were detuned a considerably larger amount.

The choice of the decay rates, α_i, must take into account both the modal damping properties of the test article and the data acquisition requirements with regard to leakage effects. From the latter point of view it is desirable to have high values of α_i to ensure a quick decay of the response amplitudes. On the other hand, a low decay rate is desirable to put a maximum of excitation energy into the structure. By way of an analytical simulation it was found out that 1 percent is a reasonable order of magnitude. The duration of each test was approximately 160 seconds.

Figure 2 gives a graphical representation of the frequency contents of the three types of forcing functions descibed above. The random excitation, in Fig. 2a, is characterized by a constant power spectral density between the upper and lower frequency bounds. The impulse excitation, Fig. 2b, shows a loss of power when approaching the upper frequency bound. The characteristic peaks in the third function, Fig. 2c, which corresponds to the decaying sinusoidal excitation, show the concentration of energy at the frequencies of interest.

6. ANALYTICAL TEST PREDICTIONS

The existing NASTRAN finite-element model of the CEM has been used for the pre-test analysis. Although this model does not predict the CEM dynamics exactly, there is a reasonably good agreement below 5 Hz and for several global modes above 5 Hz.

The FEM, shown in Fig. 3, has about 650 grid points with almost 4000 degrees-of-freedom. The model contains about 1600 bar elements, representing the truss structure, some rod elements, representing the supporting cables, about 100 plate elements, modeling parts of the reflector and the thrusters, about 40 spring elements, modeling the air supply hose stiffness, and some concentrated masses. Eighty-six modes were predicted below 50 Hz. Thirty-six of these modes are below 10 Hz. An example plot of the first truss-bus Z-axis bending mode is shown in Fig. 4.

Selection of Target Modes

Since the object of this work was to study excitation techniques and not to completely identify the CEM, the frequency range of interest was confined to below 10 Hz. Of the thirty-six modes below 10 Hz, twelve can be considered "global". For this study, a "global" mode is a mode which exhibits most of its motion in the truss or reflector. Table 1 lists all predicted frequencies below 10 Hz. The "global" modes are marked with an asterisk. These twelve "global" modes were chosen as the target modes.

Selection of Response Locations

A simple iterative procedure was used to select and minimize the number of response locations. The procedure began with defining a primary set of locations from which the final set was chosen in order to achieve a sufficient level of mode shape observability.

The primary response location set was generated by analyzing the target mode shapes and identifying the locations of the maximum displacements on the truss-bus and appendages. Sixteen locations were identified using this method. Additionally, eight locations on the reflector were added to the primary set; four locations were evenly spaced at the ends of the ribs, and four locations were located next to the mirror. Two additional locations were picked at the branching points of the two suspension cables. These locations were included to provide information on the suspension cable modes. As a final addition, the driving point locations were also chosen. In summary, the primary location set consisted of 24 tri-axial response locations and 4 uni-axial drive-point response locations. These locations are shown in Fig. 5.

Once the primary response location set was identified, the response locations were fine-tuned through the following procedure. First, a FEM substructure was constructed using Guyan reduction and the primary location set as the master degrees-of-freedom. Next, the mode shapes for this reduced model were computed and compared with the original model's mode shapes using the Modal Assurance Criterion (MAC) [17]. Perfectly correlated mode shapes have a MAC value of 1 while uncorrelated shapes have a MAC value of 0. By iterating on the sensor location (modifying locations and recomputing/correlating the reduced model's mode shapes), a target MAC value of 0.95 was achieved for all the target modes.

Selection of Exciter Locations

An attempt was made to minimize the number of exciters needed to properly excite the target modes. For that purpose forced responses were computed for all of the selected response locations and given excitation functions at any of the available 8 exciter locations. From this data, mode indicator functions and power spectra [17] were computed. The mode indicator function (MIF) provides a tool to detect and locate, by frequency, normal modes of vibration. The power spectrum (or significance function, SIF, which is the square root of the power spectrum, normalized to its maximum value) indicates how strong a mode is excited. The combination of these two tools provides a means for assessing each exciter location's contribution to exciting the target modes. By comparing MIF and SIF functions, redundant exciters may be systematically eliminated.

MIFs and SIFs were calculated for all load cases and compared in detail. For example, the upper part of Fig. 6 shows an overlay of the MIFs computed using an impulse excitation applied, separately, to all of the available eight exciter locations. The lower part of Fig. 6 shows the remaining MIFs after systematically eliminating four exciters. Apart from the frequency ranges around 8 Hz and around 9.5 Hz, the plots illustrate that, despite the elimination of four exciters, all the dominant modes were excited.

The SIFs show the same trend with the added information that none of the exciter locations excites the modes well in the frequency band of 8 Hz to 9.5 Hz.

A summary of the modes which can be excited by any one of the selected exciters is given in Table 1. A "Y" indicates that the mode is excitable, and a "-" means not excitable. The positions of the selected exciters 1, 2, 6 and 7 and the respective force directions are shown in Fig. 5.

Prediction of Test Results

Two typical examples of calculated responses are given in Fig. 7. The curves displayed in the two plots are totally different, although they refer to the same response location. This is due to the different types of excitation forces which were used to excite the structure. In the first case, an impulse was used. A relatively small amount of energy is put into the structure due to the short duration of the impulse. This results in a low excitation level (see left curve). In the second case the decaying sine type of excitation had been employed. The three target frequencies 1.5 Hz, 1.9 Hz and 4 Hz were chosen to construct the forcing function. The α_i were set to 1 percent. As can be seen easily from the second curve the

response amplitudes are much higher and the decay rate is much lower compared to the first one. This accounts for a clearly improved excitation of the target frequencies.

7. TEST RESULTS

Once the test program was completed, the test data were available in the form of time histories. These time histories were post-processed into frequency response functions. The frequency response functions were then analyzed using a combination of direct parameter, complex exponential, and polyreference techniques [17] to derive modal parameters and mode shapes. In the following discussion the random excitation case will be used to present a general analysis of the structure. This will be followed by a comparison of the excitations in determining the modal parameters of the target modes. The discussion ends with an analysis of the effect of frequency mismatch using the decaying-sine excitation.

Using the multi-point random excitation (all four exciters active), mode indicator and significance functions were computed. These functions are shown in Fig. 8. In general, four effects are illustrated in these plots:

1) The structure has a high modal density in the analysis frequency range. This is illustrated by the number of peaks in the MIF plot.
2) There appears to be a significant amount of noise below 1 Hz. This is indicated by the rising "noise floor" below 1 Hz in the MIF plot.
3) The multiple peaks, which are grouped around a single frequency in the MIF, may indicate nonlinearities.
4) The differences in the number of peaks between the MIF and SIF plots show that only a low number of modes were excited well enough for an easy identification.

A general identification was performed using the random excitation data. The results are given in Table 2. This table presents the modal parameters of the existing analytical model, the identified modal parameters, the relative differences between the test and analysis frequencies, and a short description of the mode shapes. The identification of the rigid body modes (eigenfrequencies below 1 Hz) was difficult due to noisy measurements. However, most of the noise could be attributed to the piezo-film sensors which do not produce reliable signals below 1 Hz. By using the servo-accelerometers alone, which have good response down to DC, the rigid body modal parameters could be estimated. The fundamental flexible modes at 1.47, 1.74 and 1.88 Hz, as well as a few higher "truss" modes, could be identified easily. These modes also correlated very well with the analytical model. In contrast modes with significant reflector motion were not easily identified, and they did not correlate well with the analytical model. Two fundamental "reflector" modes, "Y-bending" and "umbrella mode", have no representation in the finite element model. On the other hand a number of analytical "reflector" modes could not be identified. This might be a consequence of inadequate excitation of the reflector.

The identification results corresponding to the target modes using the three different excitations can be described as follows: The identified frequencies do not differ very much between the excitation cases. This indicates that there is sufficient energy provided by any of the excitations to estimate frequencies. However, the damping and mode shape estimates do differ. In general, the estimated damping is higher for the random excitation case. This is most likely caused by the signal processing, required to eliminate leakage in the frequency response computation [17]. The random excitation case also required the longest test and post-processing time because of the larger number of averages required to obtain a satifactory confidence on the frequency response function. The best mode shape estimates of the target modes were produced using the decaying sine data. The improved mode shapes can be attributed to the concentration of excitation energy at these target modes. In both the random and the impulse excitation cases the excitation energy is spread evenly over the frequency range, while the decaying sine excitation attempted to concentrate the energy around the target modes. However, the decaying sine excitation produces better target mode information at the expense of the non-target modes.

It should be noted that the test and processing time for both the impulse excitation and the decaying sine excitation did not differ. However, the impulse excitation case produced data sets that were more inconsistent (different identification results depending on the shaker location) than the decaying sine excitation. This may be attributed to nonlinearities which were much more detrimental to the analysis in the impulse tests than in the decaying sine and random tests. Another reason might be a lower signal-to-noise ratio for the impulse data due to the lower level of relevant energy input to the structure.

The final test involved the analysis of the effect of a frequency mismatch between excitation and modal frequency in the decaying sine excitation. Four target frequencies were used to generate an excitation: 1.51, 1.91, 5.38 and 8.37 Hz. These frequencies were then detuned by 5 and 20 percent, respectively. Auto-power spectra of these three excitations (marked with "1", "2", and "3") as well as of the corresponding driving point responses are shown in Fig. 9. The frequency shifts cause the excitation level to vary considerably for certain target frequencies as can be seen from the horizontal arrows marking the values of the response spectra at the target frequencies. The considerable drop of the response amplitudes due to the frequency mismatch generally will adversely effect the identification result. In fact, the third bending mode at 8.4 Hz could not be identified any more after a frequency shift of 20 percent.

8. CONCLUSIONS

The following conclusions can be drawn from the work performed:

1) Forcing functions which consist of exponentially decaying sinusoids proved to be favourable excitations for the identification of a limited number of target modes. No repetition for averaging purposes is needed, leading to a considerable reduction in testing time compared to random excitation testing.

2) Frequency mismatches due to modeling errors do not significantly influence the identification results at a level less then 5 percent. However, higher frequency shifts could prevent a successful identification. Therefore, a pre-test using broad-band excitation for the determination of realistic eigenfrequency and damping values may be useful.

3) Identification results may be poor for the structural components which can not be excited directly.

4) The method used to select a suitable set of sensor locations was both straightforward and effective.

5) Noisy measurements as well as structural nonlinearities obviously, but not surprisingly, may cause identification problems.

ACKNOWLEDGEMENTS

The research summarized in this paper was conducted under the NASA/DLR collaboration in dynamics and control of large space systems. The authors wish to thank the NASA Langley Research Center for the test execution and a very good cooperation.

9. REFERENCES

1. Hanks, B.R. and Pinson, L.D., "Large Space Structures Raise Testing Challenges", American Institude of Aeronautics and Astronautics (AIAA), October 1983, pp 34-40

2. Denman, E.D. et al, "Identification of Large Space Structures On Orbit", ASCE Report, AFRPL TR-86-054, New York, NY, September 1986

3. Schenk, A., Pappa, R.S., "Practical Aspects of On-Orbit Modal Identification Using Free-Decay Data", Proc. of the Int. ESA Conference on "Spacecraft Structures and Mechanical Testing", Noordwijk, The Netherlands, 24-26 April 1991, (EAS SP-321, October 1991)

4. Pappa R.S., "Identification for Large Space Structures", Proc. of the 8th Int. Modal Analysis Conference, Kissimmee, FL, Jan. 29 - Feb. 1, 1990, Vol. 1, pp 15-24

5. "Controls-Structures Interaction - A New Approach to Spacecraft Design", NASA Headquarters, Materials and Structures Division, Office of Aeronautics, Exploration, and Technology, Washington, DC 20546, Rev. 8/90

6. Hanks B.R. and Gilbert M.G., "Research on the Structural Dynamics and Control of Flexible Spacecraft", Presented at the International Forum on Aeroelasticity and Structural Dynamics, Aachen, Germany, June 5, 1991, pp 265-274

7. Cooper P.A. and Johnson J.W., "Space Station Freedom On-Orbit Modal Identification Experiment - An Update", Presented at the 2nd USAF/NASA Workshop on System Identification and Health Monitoring of Precision Space Structures, Pasadena, Ca, March 1990, pp 683-714

8. Juang J.-N. and Pappa R.S., "A Comparative Overview of Modal Testing and System Identification for Control of Structures", Shock and Vibration Digest, Vol. 20, No. 6, June 1988, pp 4-15

9. Vold H., Kundrat J., Rocklin G.T. and Russell R., "A Multi-Input Modal Estimation Algorithm for Mini-Computers", SAE International Congress & Exposition, Detroit, Michigan, February 1992

10. Juang J.-N. and Pappa R.S.,"An Eigensystem Realization Algorithm (ERA) for Modal Parameter Identification", JPL Workshop on Identification of Flexible Space Structures, San Diego, CA, June 1984

11. Blelloch P., Engelhardt C., Hunt D. L., "Simulation of On-Orbit Modal Tests of Large Space Structures", Kissimmee, FL, Jan. 29 - Feb. 1, 1990, Vol. 2, pp 926-932

12. Kim H.M., "System Identification for Large Space Structures", Ph.D. Thesis, The University of Texas, Austin, TX, Dec. 1988, 156 p.

13. Kim H.M. and Doiron H.H., "Random Excitation for On-Orbit Modal Identification of Large Space Structures", Presented at the International Forum on Aeroelasticity and Structural Dynamics, Aachen, Germany, June 5, 1991, pp 223-230

14. Kammer, D.C. and Triller, M.J., "Efficient Sensor Placement for On-Orbit Identification of Sequentially Assembled Large Space Structures", Int. Journ. of Analytical and Experimental Modal Analysis", Vol. 7, No. 2, April 1992, pp 95-109

15. Chen, J.-Ch. and Fanson, J.L., "On-Orbit Vibration Testing for Space Structures", Proc. of the 40th Congress of the Int. Astronautical Federation, Oct. 7-13, 1989, Malaga, Spain, (IAF-89-333)

16. Belvin, W.K., Elliott, K.B., Bruner, A., Sulla, J. and Bailey, J., "The LaRC CSI Phase-0 Evolutionary Model Testbed - Design and Experimental Results", Proceedings of the 4th Annual NASA/DOD CSI Conference, Orlando, FL, Nov. 1990, WL-TR-91-3103, January 1991, pp 553-567

17. I-DEAS Test User's Guide, Level VI, SDRC, 1990

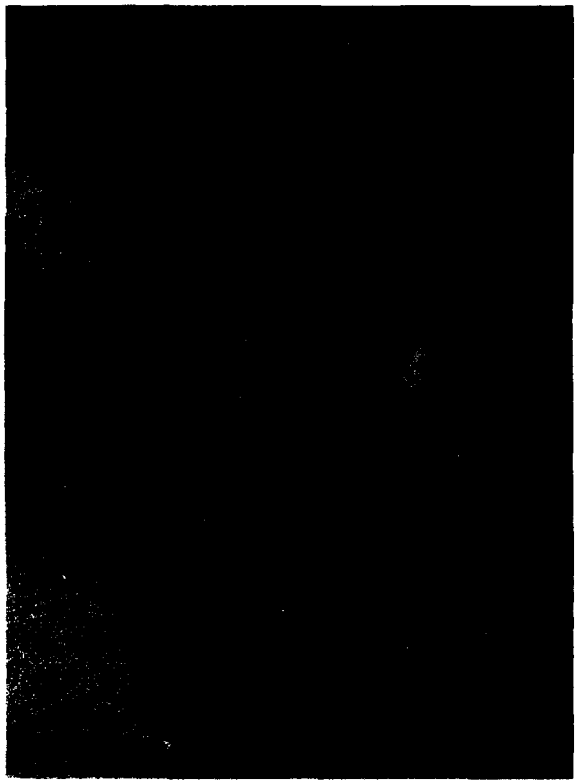

Figure 1. NASA Langley's CSI evolutionary testbed

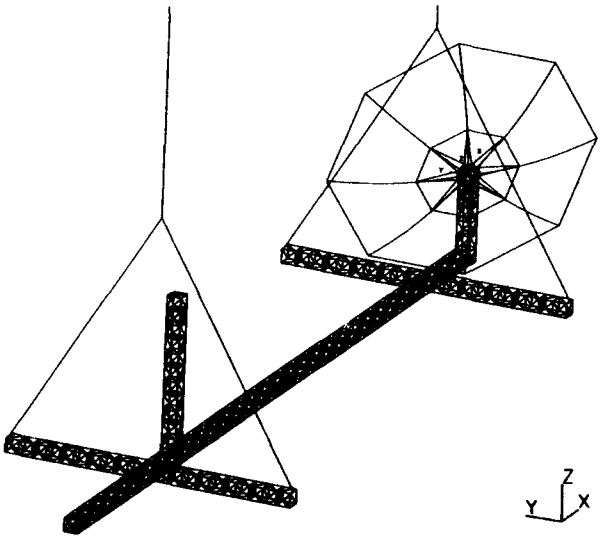

Figure 3. Finite element model of NASA Langley's CSI evolutionary model

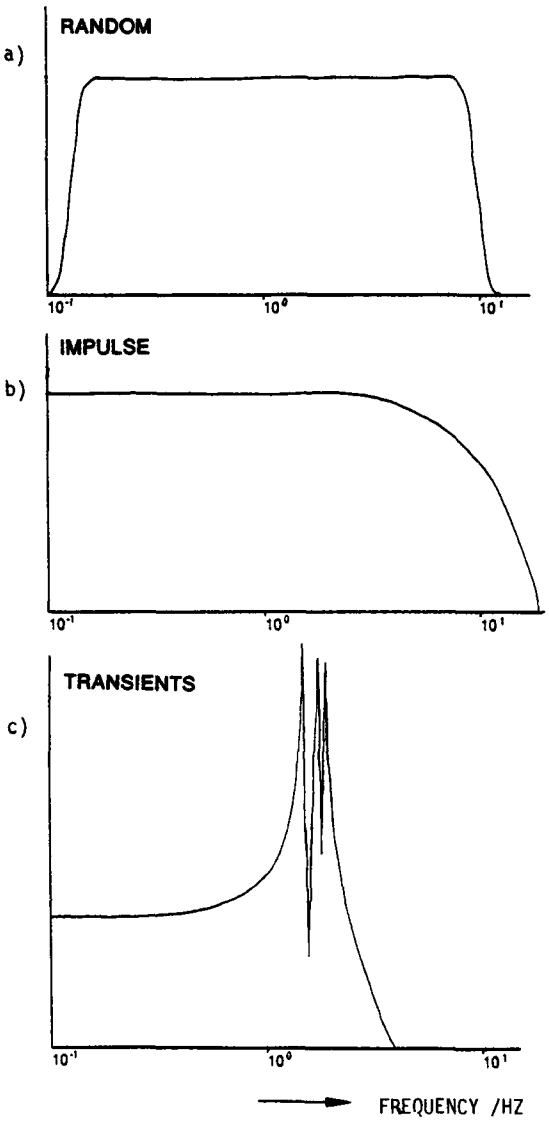

Figure 2. Schematic spectral representation of the exciter forcing functions a) random, b) impulse, c) exponentially decaying sinusoids

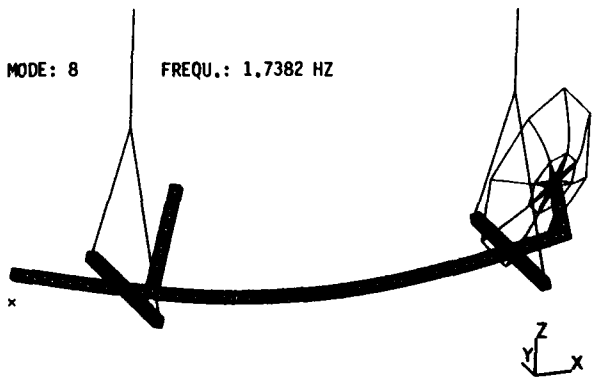

Figure 4. Typical analytical mode shape calculated with the CEM finite element model

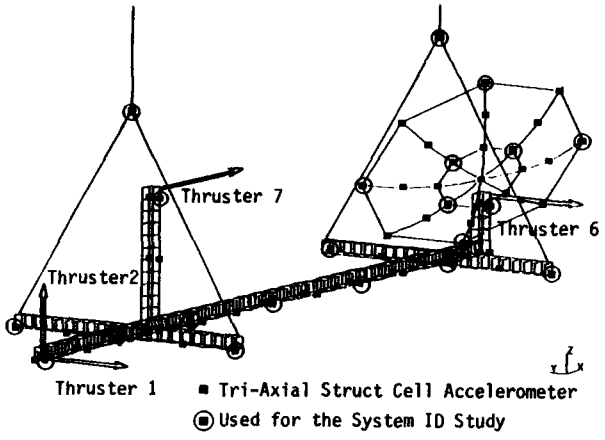

Figure 5. Locations of tri-axial accelerometers and selected pairs of thrusters

MODE NO.	FREQUENCY [HZ]	PAIR OF THRUSTERS 1	2	6	7
1	0.147	Y	-	-	Y
2	0.149	Y	-	-	Y
3	0.155	Y	-	-	Y
4	0.730	-	-	-	Y
5	0.748	-	Y	-	-
6	0.874	-	-	Y	-
7 *	1.473	Y	-	-	-
8 *	1.738	-	Y	-	-
9 *	1.882	Y	-	-	-
10	2.294	Y	-	-	-
11	2.535	-	-	Y	-
12	2.829	-	Y	-	-
13	3.419	-	-	-	Y
14	3.486	-	-	-	Y
15	3.582	-	-	-	Y
16	4.008	Y	-	-	-
17 *	4.032	-	-	Y	-
18	4.201	Y	-	-	-
19 *	4.391	-	Y	-	-
20	5.028	Y	Y	Y	Y
21	5.034	Y	Y	Y	Y
22 *	5.498	Y	-	-	-
23	6.178	-	Y	-	-
24 *	6.229	-	-	Y	-
25 *	6.471	-	-	-	Y
26 *	6.670	-	-	-	Y
27 *	7.372	-	Y	-	-
28 *	8.291	-	-	Y	-
29 *	8.405	Y	-	-	-
30	8.450	-	-	-	Y
31	8.823	-	-	Y	-
32	8.922	-	-	-	Y
33	8.966	Y	-	-	-
34	9.215	-	Y	-	-
35	9.527	Y	-	-	-
36	9.834	-	-	Y	-

*) Modes of special interest
Y) Mode can be excited

Table 1. Modes of special interest and the ability to excite them with the selected pairs of thrusters

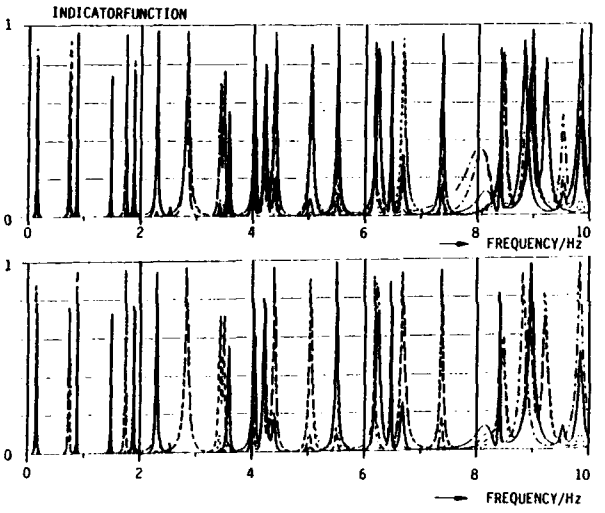

Figure 6. Calculated MIFs for impulse excitation applied to all available eight exciter locations (upper plot) and four selected exciters (lower plot)

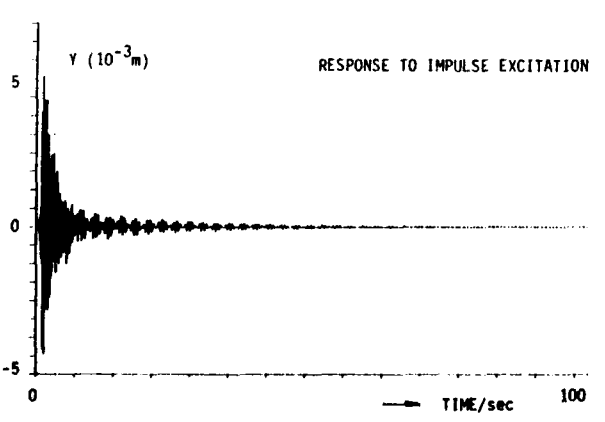

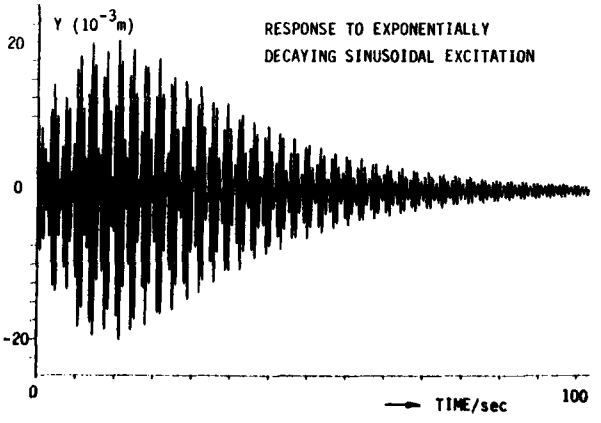

Figure 7. Calculated responses at a certain response location using a) impulse, b) exponentially decaying sinusoidal excitation

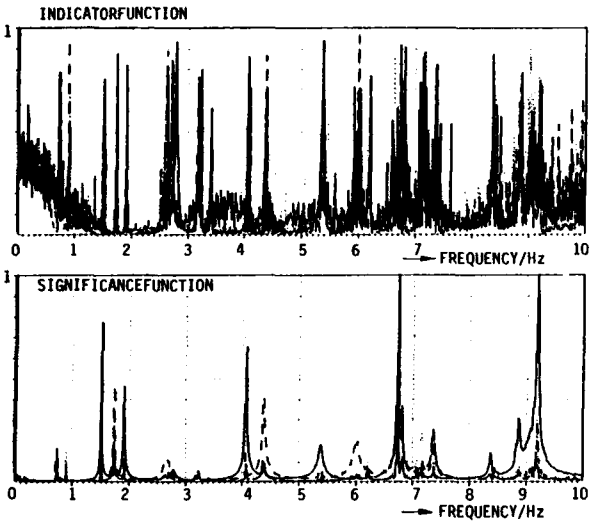

Figure 8. Indicator and significance functions for the multi-point random excitation test

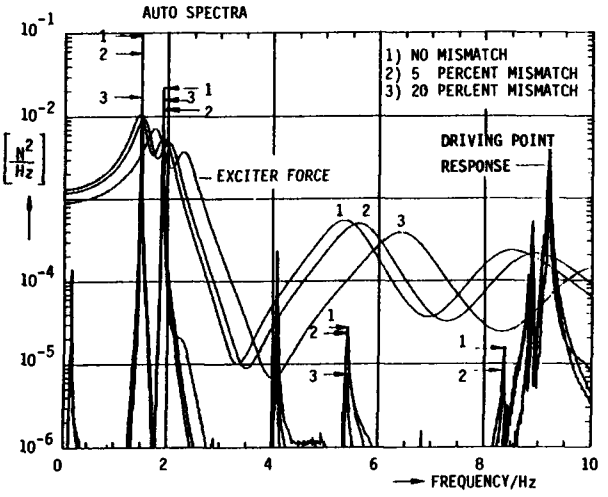

Figure 9. Effect of a frequency mismatch on the identification potential of exponentially decaying sinusoidal excitation

ANALYTICAL MODEL FREQUENCY [HZ]	DAMPING [%]	RANDOM TEST FREQUENCY [HZ]	DAMP. [%]	FREQUENCY DIFFERENCE [%]	DESCRIPTION OF THE IDENTIFIED MODE SHAPE
0.147	5.7	0.167	4.0	-12.0	RIGIB BODY X-TRANSLATION
0.149	7.5	0.162	4.4	-8.0	RIGID BODY Y-TRANSLATION
0.155	7.5	0.182	5.5	-14.6	RIGID BODY Z-ROTATION
0.730	0.7	0.730	1.0	0.7	RIGIB BODY Y-ROTATION
0.748	*0.7*	*0.748*	*1.0*	*0.4*	RIGID BODY Z-TRANSLATION
0.874	0.2	0.901	0.4	-3.1	RIGID BODY X-ROTATION
1.473	0.2	1.506	0.2	-2.2	TRUSS X-TORSION
1.738	0.3	1.733	0.4	0.3	TRUSS 1ST Z-BENDING
1.883	0.3	1.908	0.4	-1.3	TRUSS 1ST Y-BENDING
-----	---	2.782	1.6	---	REFLECTOR Y-BENDING
2.839	0.1	3.180	0.5	-10.7	REFLECTOR X-BENDING
3.419	0.1	3.228	0.4		SUSPENSION CABLE X-BENDING
3.486	0.1	3.234	0.3		LINEAR COMB. OF CORRESP. FE-MODES
-----	---	3.409	0.4	---	REFLECTOR UMBRELLA-MODE
4.032	0.1	4.070	0.3	-0.9	TRUSS 2ND Y-BENDING
4.392	0.1	4.381	0.5	0.3	TRUSS 2ND Z-BENDING
5.501	0.1	5.376	0.7	2.3	REFLECTOR TORSIONAL MODE
6.179	0.1	6.001	0.9	3.0	REFL. UMBRELLA-MODE 1)
6.231	0.1	7.160	0.7	-13.0	REFLECTOR Y-BENDING 1)
6.471	0.1	6.207	0.3	4.2	HORIZONTAL APPENDAGES X-BENDING
6.670	0.1	6.739	0.2	-1.0	TOWER X-BENDING
7.372	0.1	7.368	0.4	0.1	TRUSS 3RD Z-BENDING
8.368	0.1	8.293	0.3	-0.8	TRUSS 3RD Y-BENDING
8.456	0.1	8.870	0.4	-4.7	REFLECTOR X-BENDING 1)
8.966	0.1	9.188	0.2	-2.4	TRUSS AND APPEND. LOCAL BENDING

1) REFLECTOR'S RIBBED STRUCTURE MOVING OUT-OF-PHASE VS. MIRROR AT ITS CENTER

Table 2. Comparison of the modal parameters identified using random excitation and those of the existing analytical model

Smart Materials for Helicopter Rotor Active Control

H. Strehlow, H. Rapp
Eurocopter Deutschland GmbH
P.O. Box 80 11 40
8000 München 80, Germany

SUMMARY

A major improvement of helicopter performance and comfort can be achieved by the implementation of rotor active control technology (RACT). Especially the introduction of individual blade control (IBC) is a subject of current research activities. But the breakthrough of this technology is still missing due to the lack of appropriate rotating blade actuation systems. Smart materials may open a new possibility for the realisation of rotor active control.

A survey of current hydraulic individual blade actuation systems shows that these are very complicated and heavy. Blade actuation by smart materials offers the chance for an electrical system integrated into the blade itself. A study of different blade actuation systems shows that in principle there is the possibility of achieving this goal. But, today the available materials are not ready for real "smart" applications. The preferred materials - piezoceramics - show a too low tension strength and very low active strains. Therefore, at this time the only feasible blade actuation system for individual blade control seems to be a hinged flap at the outer third of a rotor blade. This flap can be controlled by a smart (piezoelectric) actuator. Estimations have shown that such a system will work in the desired way.

LIST OF SYMBOLS

C_{ij}	stiffness coefficients, N/mm^2
S_{ij}	compliance coefficients, mm^2/N
e_{ij}	piezoelectric coefficients, N/Vmm
d_{ij}	piezoelectric strain coefficient, mm/V
E_i	electric field, V/mm
a_i	thermoelastic coefficient, N/mm^{2}K
A	cross section area, m^2
$C_{M\delta}$	aerodynamic coefficient
D	modal damping
EI	bending stiffness, Nm^2
I	generalized blade inertia, kgm^2
R	rotor radius, m
U	voltage, V
ΔT	temperature difference, K
K	gain
b, c	blade semichord, chord, mm
d	generalized blade damping, Nms
d	lever arm length, mm
l, t	length, width and thickness, mm
h	distance of piezo layers, mm
r, s	geometrical dimensions, mm
w	end deflection of a bar, mm
α_m	thermal coefficient of expansion, 1/K
β	end deflection angle (slope) of a bar
ε_i	longitudinal strain
γ	lock number
γ_{ij}	shear strain
σ_i	longitudinal stress, N/mm^2
τ_{ij}	shear stress, N/mm^2
θ, δ	twisting, deflection angle
ω	fundamental blade natural frequency, 1/s
η	generalized coordinate
Φ'	slope of the fundamental bending mode
Ω	nominal rotor speed, 1/s
ζ	equivalent blade lead-lag deflection

Subscript:

0	structure without piezoceramic material
E	electrical
N	Neck
p	piezoceramic material
ζ	lead-lag bending

1. INTRODUCTION

One of the most recent trends and promising concepts is the incorporation of smart materials technology in the construction of the next generation rotary-wing aircraft. There are three areas where smart materials are likely to play an important role for future aircraft:

- Rotorcraft Health & Usage Monitoring,
  - System Monitoring,
  - Vibration Signature,
- Blade Shape Control,
- Rotor Active Control,
  - Blade Impedance Control,
  - Individual Blade Control.

The development of reliable low cost health and usage monitoring systems (HUMS) for helicopters requires appropriate small mechanical (micro) sensors and sophisticated electronics signal processing. "Smart sensors" - a combination of miniaturized sensors and integrated circuits - offer a very attractive potential for system monitoring and vibration signature.

The performance of modern helicopters has been improved by special aerodynamic profiles. A further optimization may be possible by blade shape control. For instance the dynamic stall flutter behaviour of the retreating blade may be changed by modifying the blade profile. Smart materials offer the chance to realize such advanced concepts.

The realisation of helicopter rotor active control concepts is a challenge for the helicopter engineers for a long time. The application of servo-hydraulic actuation systems has posed many technical problems especially when active blade control in the rotating system is required.

In this paper results of a feasibility study are presented which has been performed at Eurocopter Deutschland GmbH (ECD). The goal was to find out potential applications of smart materials actuation systems for helicopter rotor active control.

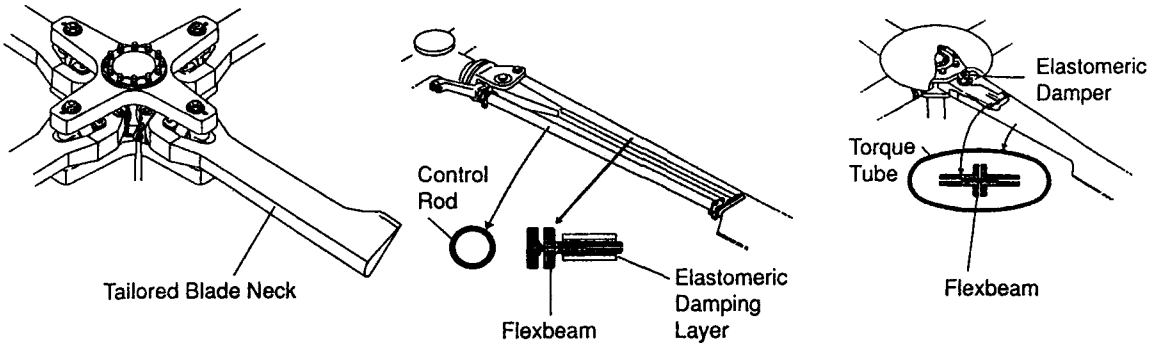

Hingeless Rotor with Elastomeric Pitch Bearings

Bearingless Rotor with Control Rod

Bearingless Rotor with Torque Tube

Fig. 1: Modern Rotor Systems

2. ROTOR CONCEPTS AND SMART ACTUATION

The proper integration of smart materials technology in modern helicopter rotor concepts is the key for the design of efficient, simple and reliable rotor actuation systems. Before this difficult task can be attacked some details of modern main rotor designs are presented and different goals of rotor active control technology are listed. Finally the most promising rotor blade control concept is identified and important requirements for the envisaged realisation by smart materials are noted.

2.1 Hingeless and Bearingless Rotors - State-of-the-Art

In the last two decades the application of composite and elastomeric materials has had the most beneficial impact on the design of new helicopter rotor systems. These new materials have made it feasible to develop and manufacture advanced rotor systems of reduced complexity by eliminating partly or totally conventional blade root hinges and bearings. Figure 1 shows the main components of modern rotor systems.

They will be discussed shortly for better understanding the needs and expectations of helicopter engineers on smart materials. The soft inplane hingeless and bearingless rotor concepts (Figure 1) can be characterized in the following way:

Hingeless rotor system: The flapwise and chordwise bending motions of the rigidly attached composite blades are facilitated by elastic deformations of the blade neck. Blade pitch control is achieved by using elastomeric pitch bearings and conventional pitch root control linkages in the rotating system. For adequate lead-lag blade damping a mechanical damping device is provided. (Note: Fig. 1 left, the fluid damper is not shown).

Bearingless rotor system: The elimination of all blade bearings is achieved by using a special designed composite flexbeam which accomplishes both bending and torsional blade motions. The pitch control forces applied to the pushrods are transmitted as torsional moment to the outer part of the blade via a stiff control rod and tube, respectively. For adequate blade lead-lag damping a viscoelastic shear damper is implemented using elastomeric materials with a high loss factor.

Both the hingeless and the bearingless rotor systems are equipped with a conventional swashplate and hydraulic actuation systems for primary flight control tasks.

The three rotor designs, shown in Figure 1, were developed by MBB - now Eurocopter Deutschland (ECD). They are more fully discussed in Ref. 1 to 3. A comprehensive review of bearingless main rotor (BMR) technologies in Europe and the USA is given in Ref. 4. There it is stated that the main goal of this new rotor concept is simplicity because of the favourable implications for rotor system weight, cost, reliability and maintainability. Figure 2 shows the ECD's BMR-design which was successfully flight tested on a BO108 prototype helicopter.

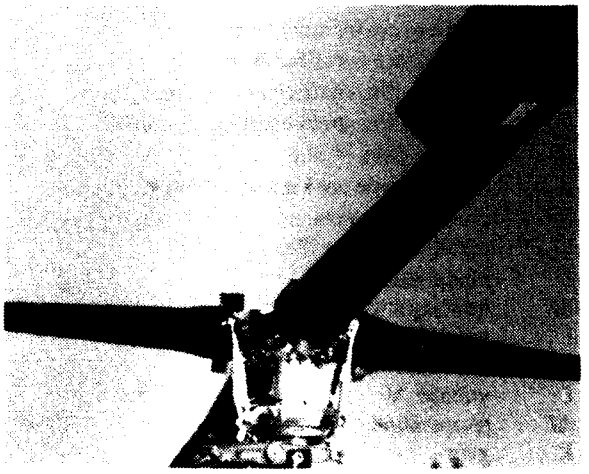

Fig. 2: Bearingless Main Rotor on an ECD-BO108

2.2 The "Ideal" Smart Rotor - Prospect

Thus, modern rotor hubs loose their bearings - concluded in Ref. 4 - by using composite and elastomeric materials. But what about the future? Recently at a workshop on rotorcraft dynamics and aeroelasticity (Ref. 5) the following two questions are posed:

"Can smart materials make helicopters better?"
Or: "How can we make the rotor better?"

Due to Ref. 5, the "ideal" smart rotor concept could look like Fig. 3.

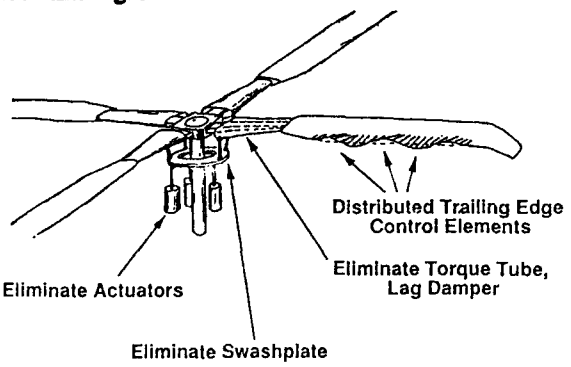

Fig. 3: Smart Helicopter Rotor

The smart rotor has lost both the bearings and the control linkages. The conventional collective and cyclic blade controls through a swashplate and hydraulic actuators in the fixed system are replaced by "smart" blade trailing edge flap actuation in the rotating system. This control concept is principally able to fulfil all needs coming from the flight mechanics (primary rotor flight control) and the aeromechanics (servo-aeroelastic blade controls).

The following Table 1 collects the most typical design characteristics of the three rotor concepts discussed so far.

Table 1: Design characteristics of rotor concepts

	Hingeless Rotor	Bearingless Rotor	Smart Rotor
Flap/lag hinge	eliminated	eliminated	eliminated
Pitch hinge	elastomeric	eliminated	eliminated
Mechanical lead-lag damper	fluid damper	elastomeric damper	eliminated
Mechanical primary flight control links	swashplate, pitch horn	swashplate, pitch horn, control tube	eliminated

The "ideal" rotor concept is a very ambitious concept of the future and currently studied mainly by research institutes (Georgia Tech, USA, for instance, see Ref. 6).

2.3 Individual Blade Control - Status

The activities of the helicopter industry in Europe as well as in the USA are concentrated on concepts which promise major improvements of helicopter performance and comfort by implementation of rotor active control technologies (RACT). They do not have the replacement of the conventional flight control systems with swashplate actuation as their near term goal. Especially the introduction of individual blade control (IBC) with limited authority is subject of intensive research activities worldwide.

In a research programme started in 1989 between ECD and HFW (Henschel Flugzeug Werke) a full scale IBC system was implemented at the BO105 helicopter and flight tested successfully, Ref. 7 and 8. This system uses servo-hydraulic pitch link actuators in the rotating system. The actuators replace the conventional pitch link rods of the BO105 hingeless rotor system, whereas the collective and cyclic control is fully maintained.

The control authority of the IBC actuators was limited to ±0.4° pitch displacement at the blade root due to safety consideration. A separate hydraulic power supply was installed in the fixed system. Thus, both a hydraulic and an electrical slipring are needed for the power and control signal transfer between the rotating and the non-rotating system. Figure 4 reveals some more details of the HFW-IBC concept. This system is currently prepared for full scale open loop tests in the NASA Ames 40 by 80 ft wind tunnel.

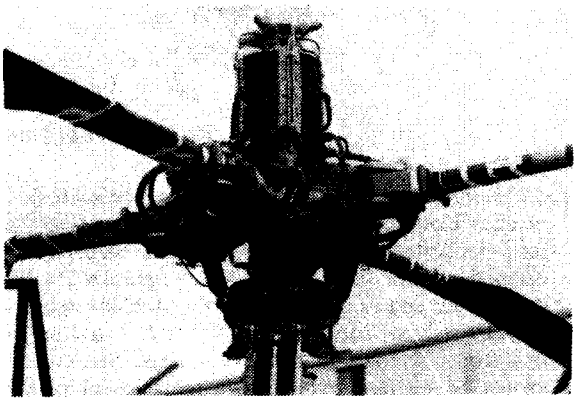

Fig. 4: Individual Blade Control System at a BO105 Rotor

The HFW system is the most spectacular attempt to realize hydraulic driven individual blade actuation concepts. Other activities are reported in the literature with emphasis on model rotor research activities. But the breakthrough of the IBC technology is still missing due to the lack of simple and reliable rotating blade actuation systems.

2.4 Smart Rotor Blade Actuation - Goals

Rotor active control technology (RACT) has a broad scope. The interest of ECD is concentrated on the development of technologies that may have impact on the expansion of the flight envelope of the next generation helicopters, see Ref. 7 to 9. An overview of the various RACT-goals is given in Fig. 5 using rotating induced strain actuation systems (smart materials).

In Figure 5 two different blade control concepts are shown:

Blade Impedance Control: The capability of changing the blade stiffness, damping and mass characteristics by using fully integrated smart composite structures is a very demanding task. The realisation of a rotor with variable hub stiffness (tuning of blade flap bending natural frequency) or introduction of artificial blade lead-lag damping for providing adequate aeromechanical stability margins of soft inplane rotor systems may be achieved solely by smart blade neck or blade attachment bending actuators.

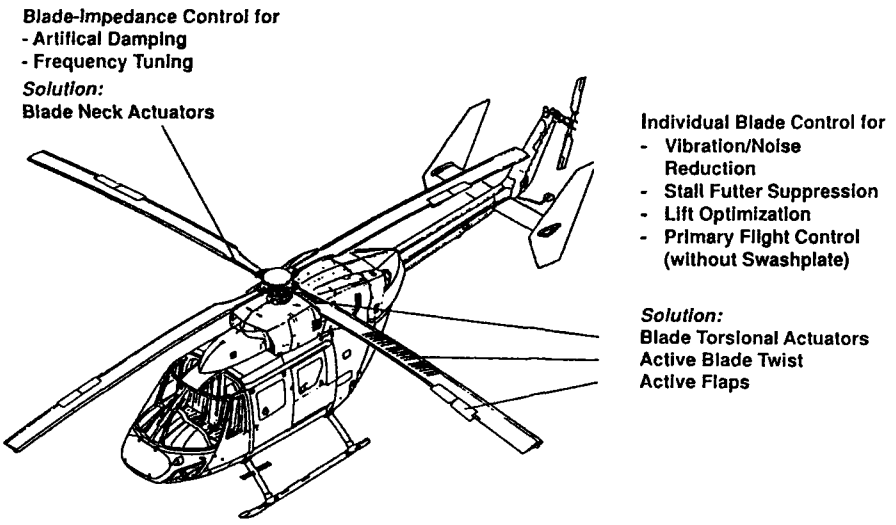

Fig. 5: Rotor active control technology - Goals

Individual Blade Control: Controlling the lift distribution of each blade individually by actively changing the torsional deflections and flap of the blade respectively offers the possibilities to control and optimize the lift distribution and to suppress aeroelastic blade oscillations by stability augmentation and disturbance rejection feedback controllers. Since a smart IBC-system cannot be realized by a simple replacement of the existing rotating pitch link rods, new concepts have to be developed. In principle the smart IBC may be accomplished by designing

- blade neck torsional actuators (hingeless rotors),
- active control rods (bearingless rotors),
- fully integrated smart structures for distributed blade torsional control,
- smart blade flap actuation systems for blade lift and torsional control.

For helicopter rotor active control by smart materials the IBC-concept is judged to be more efficient than the "plain" impedance control concept. The active control of the blade aerodynamic load distribution by relative small torsional deflections results in high control forces. Smart IBC-concepts are studied in Ref. 5 and Ref. 10 to 13. The principle and possibilities of smart impedance control applied to flexible structures are outlined in Ref. 14. An overview of the current and planned European activities is gathered in Ref. 15.

In this paper the feasibility of a smart IBC-system for servo-aeroelastic rotor blade control purposes is investigated. This system should be adaptable to ECD's hingeless or bearingless rotors and should allow the investigation of means for rotor performance enhancements, stall flutter suppression and comfort improvement by vibration and noise control. In addition improving the aeromechanical stability with respect to ground and air resonance should be possible using active blade lead-lag damping augmentation or active equivalent pitch-lead coupling.

The following requirements are used as guidelines in the feasibility study:

Active blade torsional deflection: $\pm(1 + 2)^\circ$ (at radial position 0.7 R),

Active blade flap deflection: $\pm(4 + 6)^\circ$ (10%-flap at outboard position).

Active blade modal damping augmentation: 2% (lead-lag bending mode).

Actuator bandwidth needed: up to 100Hz.

3. SMART MATERIALS FOR HELICOPTER APPLICATIONS

Helicopter applications require special properties of the used smart materials. Especially for the individual blade control, the materials have to react very quickly to reach the necessary actuator bandwidth. Furthermore the materials have to endure the strains of the structure where the smart materials are bonded to. In the following, the available smart materials and the possible candidates for helicopter blade actuation systems are reviewed.

3.1 Available Smart Materials

The research on smart materials has just begun. So there is an increasing number of candidate materials and material systems which may be suited for smart structure actuators. Some of these are

Piezopolymers,
Piezoceramics,
Electrostrictive ceramics,
Magnetostrictive rare earth alloys,
Shape memory alloys.

Each of these materials has its special properties and with this its most suited field of application. Piezoelectric materials and the magnetostrictive rare earth alloys are of special interest for actuators in a helicopter rotor system. These materials show a high potential of inducing forces into structures, and they allow the moderate control frequencies (up to 100 Hz), needed for helicopter rotor active control.

Shape memory alloys actually show high stiffness too and a larger active strain than piezoelectric and magnetostrictive materials, but due to the necessity of heating up the material the dynamic response frequency is much lower. Therefore, these materials can only be used for quasi-static applications. Furthermore, their active strain

cannot be controlled exactly, because the temperature-strain characteristic is very steep and the accurate controlling of the temperature within one degree is very difficult.

Electrostrictive materials are similar to the piezoceramic materials, but their active strains are smaller. They are not further considered.

The magnetostrictive rare earth alloys show a high stiffness and a rather large active strain. These materials are controlled by a magnetic field, which must be created by a coil and an electrical current. Magnetostrictive materials are expensive and as they always need the magnetic coil such systems are heavy.

For these reasons, the most favourable candidate material for the use as actuator in the helicopter rotor seems to be the piezoceramic material. This is because of the relative high stiffness (Young's modulus) and resulting from this due to the capacity of inducing high forces. Unfortunately, the active strain of the material when subjected to an electrical field is rather small. Today, the maximum piezoelectric strain for an electrical field of 1000 V/mm is about 0.5‰ in the 3-direction and 0.25‰ in the 1- or 2-direction, respectively.

Piezopolymers have a much lower stiffness, but a higher active strain and better strength properties. Further investigations must show, whether these materials can be used as actuator materials, too.

At the horizon there is coming up a new class of piezoelectric materials, made from a gel. It is expected that these materials have better properties than the piezoceramics. The important piezoelectric strain coefficients will be a factor of 10 higher than those of piezoceramics.

Therefore, in the following piezoceramic material is considered to be the smart material for helicopter rotor active control.

3.2 Piezoceramic Materials

Piezoceramic materials induce an electrical voltage if they are subjected to mechanical strains. On the other hand, if a voltage is applied at two opposite sides of the material, it reacts with mechanical deformation. This behaviour is known as piezoelectric effect and it can be used for sensors and actuators equally. This attracts special attention to these materials for control applications.

3.2.1 *Material Law*

Piezoceramics can be considered as orthotropic material like a composite unidirectional laminate. In a plane perpendicular to the orientation of the piezoceramic, it has even isotropic properties (transversely isotropic material in the plane 1-2 of Fig. 6). The constitutive equation of such a material is given by Equation 1.

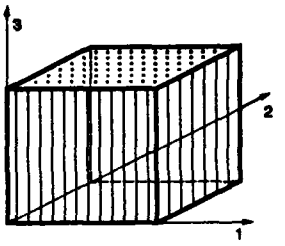

Fig. 6: Piezoceramic material

$$\begin{bmatrix}\sigma_1\\ \sigma_2\\ \sigma_3\\ \tau_{23}\\ \tau_{31}\\ \tau_{12}\end{bmatrix} = \begin{bmatrix} C_{11} & C_{12} & C_{13} & 0 & 0 & 0\\ C_{12} & C_{11} & C_{13} & 0 & 0 & 0\\ C_{13} & C_{13} & C_{33} & 0 & 0 & 0\\ 0 & 0 & 0 & C_{44} & 0 & 0\\ 0 & 0 & 0 & 0 & C_{44} & 0\\ 0 & 0 & 0 & 0 & 0 & \frac{C_{11}-C_{12}}{2}\end{bmatrix}\begin{bmatrix}\varepsilon_1\\ \varepsilon_2\\ \varepsilon_3\\ \gamma_{23}\\ \gamma_{31}\\ \gamma_{12}\end{bmatrix} - \begin{bmatrix} 0 & 0 & e_{31}\\ 0 & 0 & e_{31}\\ 0 & 0 & e_{33}\\ 0 & e_{15} & 0\\ e_{15} & 0 & 0\\ 0 & 0 & 0\end{bmatrix}\begin{bmatrix}E_1\\ E_2\\ E_3\end{bmatrix} - \begin{bmatrix}a_1\\ a_2\\ a_3\\ 0\\ 0\\ 0\end{bmatrix}\Delta T. \qquad (1)$$

In this equation the influence of an applied electrical field E_i is shown by the coefficients e_{ij}. One can see that these electrical strains act like thermal strains with one difference: For orthotropic material there is no temperature induced shear deformation. However, the piezoelectric material shows such shear deformation if an electrical field E_1 or E_2 is applied. For structural mechanics this is no difficulty, as orthotropy is a special case of anisotropy, and anisotropic materials show shear strains due to temperature, too. Therefore every theory which can handle thermal strains and anisotropic materials is suited to describe the behaviour of a piezoceramic material as an actuator. Of course, also the interaction of piezoceramic materials and other materials can be investigated. By substituting a new coefficient b_i for the sum of the thermal and the piezoelectric strains

$$\begin{bmatrix}b_1\\ b_2\\ b_3\\ b_4\\ b_5\\ b_6\end{bmatrix}\Delta T = \begin{bmatrix} 0 & 0 & e_{31}\\ 0 & 0 & e_{31}\\ 0 & 0 & e_{33}\\ 0 & e_{15} & 0\\ e_{15} & 0 & 0\\ 0 & 0 & 0\end{bmatrix}\begin{bmatrix}E_1\\ E_2\\ E_3\end{bmatrix} + \begin{bmatrix}a_1\\ a_2\\ a_3\\ 0\\ 0\\ 0\end{bmatrix}\Delta T \qquad (2)$$

and writing these new coefficients b_i as a function of the piezoelectric and thermal coefficients

$$b_{1,2} = \frac{1}{\Delta T}e_{31}E_3 + a_{1,2}, \qquad b_3 = \frac{1}{\Delta T}e_{33}E_3 + a_3,$$

$$b_4 = \frac{1}{\Delta T}e_{15}E_2, \qquad b_5 = \frac{1}{\Delta T}e_{15}E_1, \qquad b_6 = 0 \qquad (3)$$

a new ordinary thermoelastic material equation for anisotropic materials is given which can be used in any structural analysis (e.g. the classical lamination theory):

$$\begin{bmatrix}\sigma_1\\ \sigma_2\\ \sigma_3\\ \tau_{23}\\ \tau_{31}\\ \tau_{12}\end{bmatrix} = \begin{bmatrix} C_{11} & C_{12} & C_{13} & 0 & 0 & 0\\ C_{12} & C_{11} & C_{13} & 0 & 0 & 0\\ C_{13} & C_{13} & C_{33} & 0 & 0 & 0\\ 0 & 0 & 0 & C_{44} & 0 & 0\\ 0 & 0 & 0 & 0 & C_{44} & 0\\ 0 & 0 & 0 & 0 & 0 & \frac{C_{11}-C_{12}}{2}\end{bmatrix}\begin{bmatrix}\varepsilon_1\\ \varepsilon_2\\ \varepsilon_3\\ \gamma_{23}\\ \gamma_{31}\\ \gamma_{12}\end{bmatrix} - \begin{bmatrix}b_1\\ b_2\\ b_3\\ b_4\\ b_5\\ b_6\end{bmatrix}\Delta T. \qquad (4)$$

Herewith, the effect of the piezoceramic material in combination with any other material can be investigated. Sometimes the material equation written in terms of stresses is useful. In such an equation, the thermal and the piezoelectric strains are included explicitly.

$$\begin{bmatrix}\varepsilon_1\\ \varepsilon_2\\ \varepsilon_3\\ \gamma_{23}\\ \gamma_{31}\\ \gamma_{12}\end{bmatrix} = \begin{bmatrix} S_{11} & S_{12} & S_{13} & 0 & 0 & 0\\ S_{12} & S_{11} & S_{13} & 0 & 0 & 0\\ S_{13} & S_{13} & S_{33} & 0 & 0 & 0\\ 0 & 0 & 0 & S_{44} & 0 & 0\\ 0 & 0 & 0 & 0 & S_{44} & 0\\ 0 & 0 & 0 & 0 & 0 & S_{66}\end{bmatrix}\begin{bmatrix}\sigma_1\\ \sigma_2\\ \sigma_3\\ \tau_{23}\\ \tau_{31}\\ \tau_{12}\end{bmatrix} + \begin{bmatrix} 0 & 0 & d_{31}\\ 0 & 0 & d_{31}\\ 0 & 0 & d_{33}\\ 0 & d_{15} & 0\\ d_{15} & 0 & 0\\ 0 & 0 & 0\end{bmatrix}\begin{bmatrix}E_1\\ E_2\\ E_3\end{bmatrix} + \begin{bmatrix}\alpha_{T1}\\ \alpha_{T2}\\ \alpha_{T3}\\ 0\\ 0\\ 0\end{bmatrix}\Delta T. \qquad (5)$$

This equation shows two different types of piezoelectric strains:

1. If an electric field E_3 is applied the material reacts with longitudinal strain ε_1, ε_2 and ε_3. This deformation behaviour can be compared directly to the thermal expansion.
2. If an electrical field E_1 or E_2 is applied, the material reacts with shear strain γ_{31} and γ_{23} respectively. For orthotropic materials, there is no corresponding thermal deformation, but anisotropic materials have such a form of thermal deformation. So, with respect to the piezoelectric deformation, these materials have to be considered as anisotropic.

For the use as actuator in helicopter rotor blades both types of piezoelectric effects are investigated, regardless of the possibility of realisation. Further details on piezoelectric materials are given in Ref. 16 and 17.

3.2.2 *Material Data*

Typical data of piezoceramic material are shown in the following table:

Young's modulus in 1-direction:	66000 N/mm²,
Young's modulus in 2-direction:	66000 N/mm²,
Young's modulus in 3-direction:	55000 N/mm²,
Shear modulus in 12-direction:	26000 N/mm²,
Compression strength:	600 N/mm²,
Tension strength:	80 N/mm²,

Piezoelectric strain coefficient d_{31}: -2.5 10^{-7} mm/V,

Piezoelectric strain coefficient d_{33}: 5.0 10^{-7} mm/V,

Piezoelectric strain coefficient d_{15}: 8.0 10^{-7} mm/V.

With a reasonable maximum electrical field of 1000 V/mm the maximum active piezoelectrical strain ε_E is 0.25 ‰ and 0.50 ‰ respectively, the maximum shear strain is 0.80 ‰.

4. ROTOR ACTIVE CONTROL BY SMART MATERIALS - FUNDAMENTALS

The application of strain induced piezoceramic blade actuation systems can be accomplished in different ways. Of course, the smartest way is a full integration of the actuator into the blade itself. For the feasibility study simplified induced strain actuation models of beam- or plate-like composite structures for bending and torsion are needed. Therefore in this section the mechanics of strain induced actuators ideally bonded on (composite) bars and plates are given and the formulas for estimating the strain induced deformation are derived. A similar but more sophisticated approach is used in Ref. 18 to 20.

4.1 Bending of Bars by Piezoceramics

One application of piezoceramic material is the bending of bars or plates. Figure 7 shows a section of a rectangular bar (the rotor blade can be considered as a bar). The top and bottom side is covered with piezoelectric material. If an electrical field is applied to the piezo plates in such a manner that the top plate reacts with extension and the bottom plate reacts with contraction, the shown bending strains are induced to the bar.

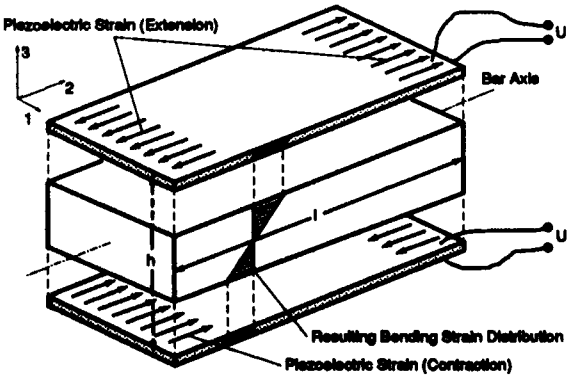

Fig. 7: Bending of a rectangular bar

If the bar with the length l is built in at one end, the deformation w and the deflection angle β at the other end can be calculated by the formula:

$$w = \frac{l^2}{h}\frac{1}{1+\frac{EI_0}{EI_P}}\varepsilon_E, \qquad \beta = \frac{l}{h}\frac{2}{1+\frac{EI_0}{EI_P}}\varepsilon_E. \tag{6}$$

Herein EI_0 denotes the bending stiffness of the bar without the piezo plates while EI_P denotes the bending stiffness of the two piezo plates itself. The piezoelectric strain ε_E follows from the piezoelectric strain coefficient d_{31} and the applied electric field E_3:

$$\varepsilon_E = d_{31}E_3. \tag{7}$$

If the bending stiffness of the bar is small compared to the stiffness of the piezo plates, the Equations 6 simplify to

$$w = \frac{l^2}{h}\varepsilon_E, \qquad \beta = \frac{2l}{h}\varepsilon_E. \tag{8}$$

4.2 Torsion of Bars by Piezoceramics

Generation of twist in a bar by piezoceramics is more complicated. Twisting of a bar can be achieved by inducing shear deformation on the surfaces of the bar according to Fig. 8.

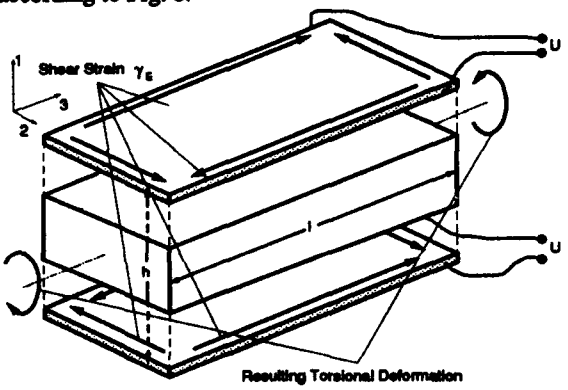

Fig. 8: Torsion of a rectangular bar

If the stiffness of a rectangular bar is neglected and shear strain is introduced only at the upper and the lower face of the bar, the twisting angle can be calculated by

$$\theta = \frac{l}{h}\gamma_E. \tag{9}$$

Because of ignoring the torsional stiffness of the bar, Equation 9 represents an upper bound of the real twisting angle.

From Equation 5 one can see, that piezoceramic material is able to create shear deformations directly by means of the electric field E_1 and E_2 in combination with the piezoelectric strain coefficient d_{15}. However, for practical applications this effect cannot be used. The piezoelectric effect will be destroyed, if large electrical fields E_1 or E_2 are applied (depolarisation). Therefore, shear deformation has to be generated by use of the longitudinal strain ε_1, ε_2 and ε_3 created by the electrical field E_3.

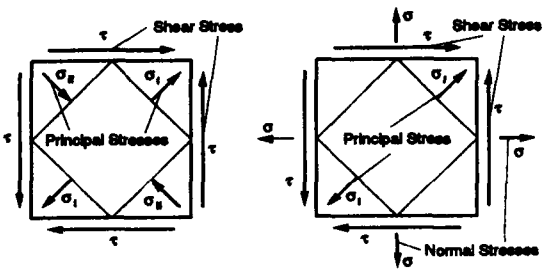

$$\sigma_I = -\sigma_{II} = \tau \qquad \sigma_{II} = 0: \quad \tau = \frac{\sigma_I}{2}, \quad \sigma = \frac{\sigma_I}{2}$$

Fig. 9: Normal and shear stresses

From Figure 9 it can be seen, that for a pure state of shear stress the principal stresses in the directions I and II are tension and compression of the same magnitude. If only one of these normal stresses is present (e.g. the tension stress σ_I, the compression stress σ_{II} shall be zero), shear stresses exist too, but together with normal stresses. The stresses can be derived from Mohr's circle. For most applications, the additional normal stresses do not matter. So, shear deformation can be generated if it is possible to introduce a longitudinal strain in the 45° direction (Fig. 10).

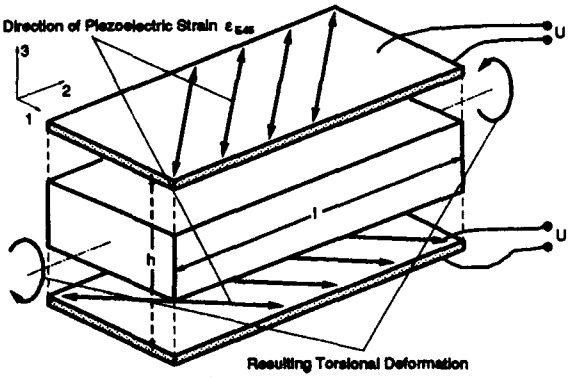

Fig. 10: Torsion of a rectangular bar by longitudinal strains

The maximum twisting angle (under ignoring of the torsional stiffness of the bar) then can be calculated with $\gamma = \varepsilon_{45}$:

$$\theta = \frac{l}{h}\varepsilon_{E45}. \tag{10}$$

4.3 Active Rotor Blade Control by Piezoceramic Actuator/Sensor-Systems

The application of the piezoceramic bending and torsion actuators for an active rotor blade feedback control system is in principal straightforward and best explained for a hingeless rotor system. For this rotor system a simple collocated blade neck actuator/sensor arrangement can be used for both bending and torsion, as shown by the following two examples:

Active lead-lag blade damping: The bonding of piezoceramic materials on both sides of the blade neck allows the active generation of bending strains and moments according to Fig. 7. The complete control system with the actuators/sensors is presented in Fig. 11. In this case a robust integral feedback controller may be used for lead-lag damping augmentation. The benefits of this control concept are described in Ref. 21 for example.

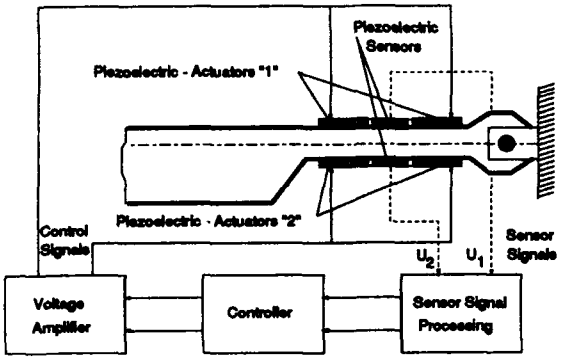

Fig. 11: Active blade neck bending for lead-lag damping augmentation (principle)

Individual blade control: The use of "directional" bonded piezoceramic materials (antisymmetric angle-ply "laminate") in the blade neck area provides the means for generating torsional deflections according to Fig. 10. The control concept with the smart actuator/sensor-system is shown in Fig. 12.

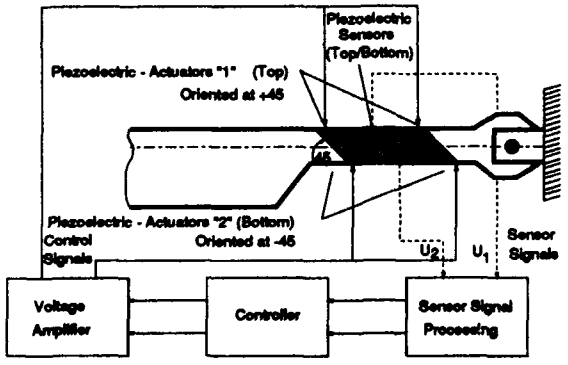

Fig. 12: Active blade neck twisting for IBC (principle)

It should be noted that the design of the feedback controller, the selection of (smart) sensors, the data processing system and the layout of the high voltage amplifier was not subject of the feasibility study. This work has to be done later if appropriate blade actuation systems are actually designed.

5. SMART ROTOR BLADE ACTUATION - FEASIBILITY STUDY

The feasibility of smart rotor blade actuation is investigated now for the hingeless and bearingless rotor systems. The design parameters are oriented on ECD's rotor hub designs presented at the beginning, see Fig. 1.

5.1 Generation of Damping and Twist at the Blade Neck

Strain induced blade neck actuators are in principle well suited for hingeless rotors to (1.) increase the modal lead-lag damping of the fundamental inplane blade bending mode and to (2.) generate torsional inputs for individual blade control. The rotor data used in the following two subsections are similar to the data of the Tiger hingeless main rotor presented in Fig. 13. More information related to this soft inplane fibre elastomeric 13 m diameter rotor with a fluid blade damper to prevent ground and air resonance can be found in Ref. 1.

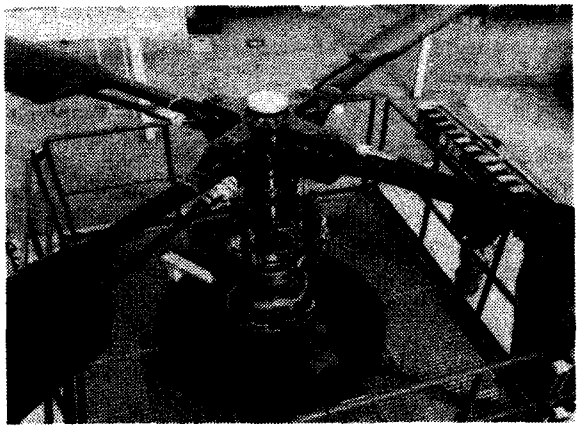

Fig. 13: Hingeless fibre-elastomeric main rotor

For applications in the blade neck section, the smart material must sustain the strain level in that area. Typical strain levels are 3 to 7 ‰. Actual piezoceramics cannot endure such strains in tension. Prestressing the material may improve such situation, but it will hardly solve it. For future applications, the tension strength of such materials has to be improved.

5.1.1 *Bending the Blade Neck*

The bending actuation of the blade neck is achieved by surface bonded piezoceramics (Fig. 14) on both sides and appropriate voltage control.

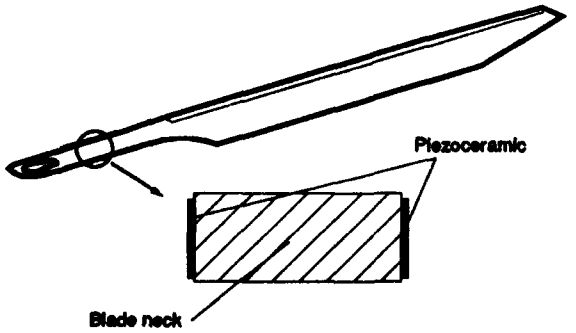

Fig. 14: Rotor blade with piezoceramic lead-lag bending actuator

The problem of modal damping augmentation by piezoelectric actuators has been extensively investigated in the literature. In Ref. 18 a dynamic beam model is analytically derived using simple rate feedback. In order to apply this

theory to the blade damping problem some definitions are given. The blade modal damping of the fundamental blade lead-lag bending mode is defined by

$$D_\zeta = \frac{d_\zeta}{2\omega_\zeta I_\zeta}. \qquad (11)$$

Herein ω_ζ, d_ζ and I_ζ denote the blade natural frequency, the generalized damping and the generalized inertia respectively. The corresponding blade modal deflection is determined by

$$u(r,t) = \Phi_\zeta(r) \cdot \eta_\zeta(t) \qquad (12)$$

with the mode shape Φ_ζ - normalized to 1 m blade tip deflection - and the generalized coordinate η_ζ. With these definitions the estimation of the generalized blade damping at the actuator saturation limits reads as

$$d_\zeta = \frac{\varepsilon_{E_{max}}}{\omega_\zeta \hat{\eta}_{\zeta,max}} \cdot \frac{1}{1+\frac{EI_{\zeta N}}{EI_p}} \cdot \frac{2EI_{\zeta N}}{t_N} (\Phi_\zeta'(r_2) - \Phi_\zeta'(r_1)). \qquad (13)$$

The bending stiffness of the blade neck and the actuators are denoted as $EI_{\zeta N}$ and EI_p respectively. The later is approximated by

$$EI_p = \frac{1}{2} t_N^2 t_p h_N E_p, \qquad (14)$$

where t_N and h_N denote the width and height of the blade neck, t_p describes the thickness of the piezo plates.

The maximum generalized blade lead-lag amplitude is estimated by the equivalent rigid body angular deflection (amplitude $\hat{\zeta}$) about an equivalent hinge with the offset a_ζ

$$\hat{\eta}_{\zeta,max} = \frac{(R - a_\zeta)}{1\text{ m}} \cdot \hat{\zeta}_{max}. \qquad \text{(R=Rotor radius)} \qquad (15)$$

The mode shape - deflection, slope, curvature - of the Tiger blade at nominal rotor speed is presented in Fig. 15. As can be seen the piezoceramic blade neck actuators are optimally attached in regions with high slope. In Table 2 all numerical data are collected which are needed for the estimation of the active lead-lag damping capacity of smart piezoceramic blade neck actuation.

Table 2: Tiger data for active lead-lag modal damping augmentation

Mean blade neck bending stiffness	EI_ζ	: $2.2 \cdot 10^5$ Nm^2
Slope of 1st bending mode		
at neck beginning ($r = 0.65m$)	Φ_ζ'	: 0.046
at neck end ($r = 1.20m$)	Φ_ζ'	: 0.145
Generalized blade inertia	I_ζ	: 16.4 kgm^2
1st natural bending frequency	ω_ζ	: 23.8 1/s
Rotor radius	R	: 6.5 m
Equivalent hinge offset	a_ζ	: 0.91 m
Width of blade neck	t_N	: 0.110 m
Height of blade neck	h_N	: 0.060 m
Thickness of piezo plate	t_p	: 0.001 m

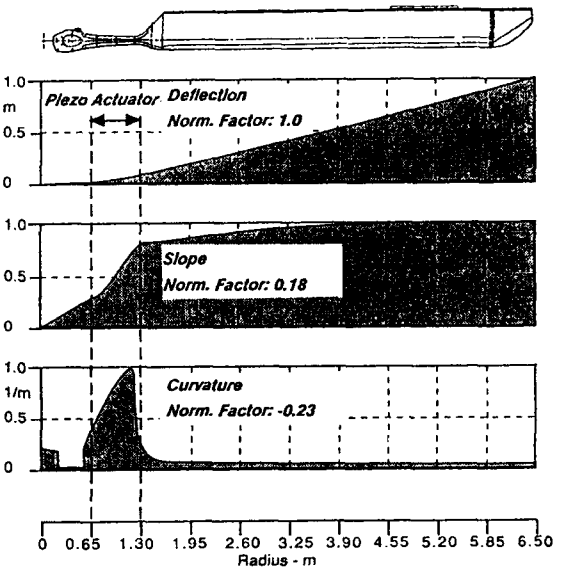

Fig. 15: Modal data of the lead-lag bending mode of a hingeless rotor blade (Fundamental frequency: 3.8 Hz at 100% rotor speed)

The calculated maximum active blade modal damping values are plotted in Fig. 16 for different lead-lag blade amplitudes. Obviously the envisaged damping augmentation of 2% cannot be achieved by this simple arrangement. A multilayered actuation system may improve the situation but was not further investigated due to the general limitations of piezoceramics bonded at high strained blade necks.

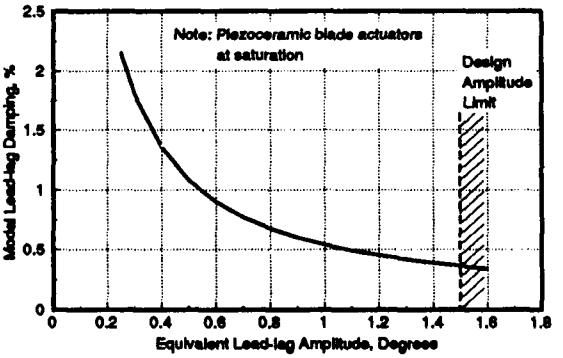

Fig. 16: Active blade lead-lag damping augmentation versus amplitude

5.1.2 *Twisting the Blade Neck*

The application of "directional" attached piezoceramics in the blade neck (Fig. 17) is studied next in more detail. Object of this investigation is to have a measure for the maximum torsional deformation, one can reach with the use of piezoceramic material.

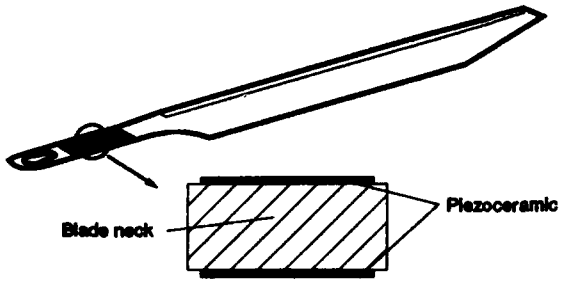

Fig. 17: Rotor blade with piezoceramic twisting actuator

For a typical piezoceramic material with the material data given in 3.2.2, the maximum twisting angle for a bar with a thickness of 60 mm (see later, Fig. 23) can be calculated according to Equation 10 to about 0.24 °/m. This value is valid if the torsional stiffness of the bar itself is neglected and when one succeeds to direct all the piezoelectric strain (0.25 ‰) into the 45° direction. In reality not all the piezoelectric strain can be directed into the 45° direction. Additionally, the torsional stiffness restrains the deformation, so that the real twisting angle always will be less.

The behaviour of piezoceramic material in the 1-2 plane is isotropic, this means, the strains in all directions in this plane are the same. To direct these strains in the 45° direction, different methods exist.

Methods for Inducing Shear Strain

One method suggested in Ref. 10 is to attach the piezo strips only partially to the blade neck (Fig. 18 and 19). With that, the stiffness in direction of the bonding line is partially decoupled from the stiffness perpendicular to the bonding line. In the direction of the bonding line the full stiffness is effective while perpendicular to this axis the effective stiffness depends from the ratio strip width to bonding width r/s. For a ratio of zero the stiffnesses are fully decoupled, the more realistic ratio of 0.5 yields a stiffness ratio of the same value.

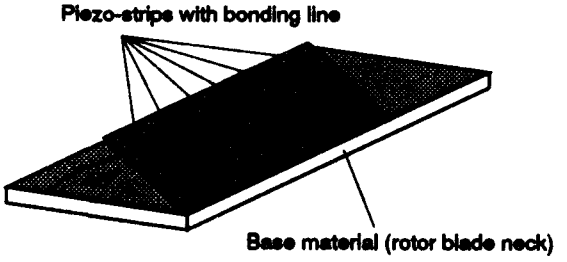

Fig. 18: Piezo strips, partially bonded, oriented under 45°

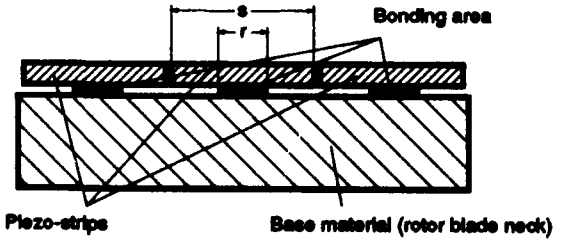

Fig. 19: Partially bonded piezo strips

These partially bonded piezo strips are a more academical solution, because they will cause trouble when loaded dynamically. Another solution is that one shown in Figure 20. The piezo strips are bonded over the whole area to the blade neck, but they cover only a part of the available area.

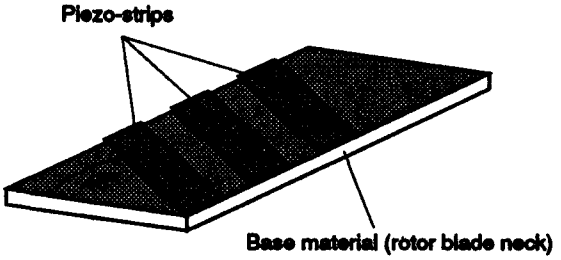

Fig. 20: Blade neck partially covered with piezo strips

Again, the strips are bonded under an angle of 45° to induce torsion. This method is good with respect to strength, but it has a poor efficiency.

A better possibility is the use of piezoceramics, sandwiched between two layers of unidirectional high modulus laminates (Fig. 21). These laminates nearly totally restrain the strain of the piezoceramics in the fiber direction, but do not have a remarkable influence perpendicular to that direction.

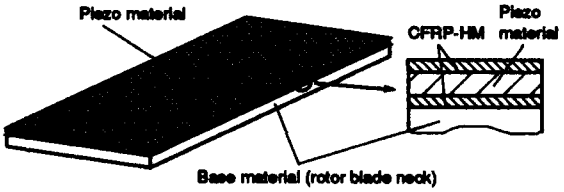

Fig. 21: Piezo strips sandwiched between two unidirectional layers

In this case, the piezoceramics and the unidirectional layers are bonded together over the whole area, the unidirectional layers have an orientation angle of 45° with respect to the blade axis. A disadvantage is a significant amount of coupling between axial force and torsion due to the angle of 45°.

The last very interesting solution is shown in Figure 22. In this case the shear deformation mode of the piezoceramic material is used. Though this effect cannot be used today for such an application, it is presented here to show the potential the materials have.

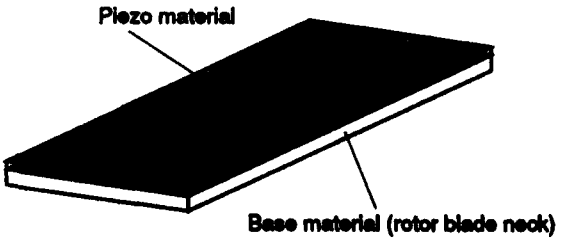

Fig. 22: Torsion induced by shear deformation

Active Twist Precalculations

All investigations are done by using the classical lamination theory (Ref. 22). Figure 23 shows a typical laminate of a rotor blade neck with applied piezoceramic material. The given dimensions are valid for the Tiger (in brackets for an advanced BO105) rotor blade.

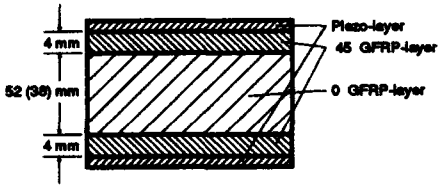

Fig. 23: Blade neck laminate

The twisting angle is calculated from the laminate stiffness matrix. For the laminate from Figure 23 and partially bonded piezo strips (r/s=0.5, Fig. 19) the twisting angle versus the thickness of the piezoceramic layer is shown in Figure 24. The maximum twisting angle which can be achieved with this configuration is about 0.041°/m for the Tiger rotor blade (0.053°/m for the advanced BO108 blade). Compared with the maximum possible twisting angle of 0.24°/m and 0.32°/m respectively (following from Equation 10) the efficiency of this configuration is very low.

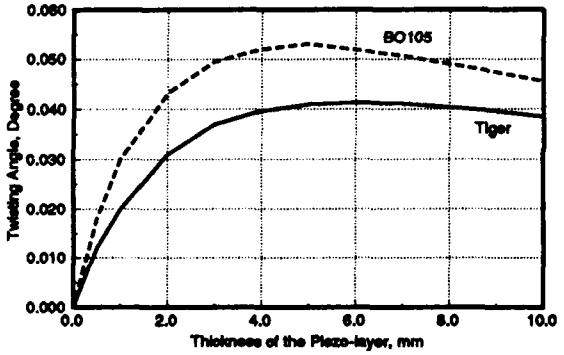

Fig. 24: Twisting angle versus thickness of piezoceramic layer

Figure 24 shows a maximum of the twisting angle. Due to the increasing stiffness of the piezo layer the twisting angle increases with increasing the thickness of the piezo layer, up to a maximum angle. Further increasing of the piezo thickness results in a decrease of the twisting angle because the increasing effective distance of the piezo layers prevails over the increasing stiffness. Due to Equation 10 this results in a decrease of the twisting angle. From this follows that for a specific configuration (laminate lay-up and geometry) a maximum twisting angle exist.

Therefore, optimization procedures, based on the lamination theory and numerical optimization procedures (Ref. 23) are particularly useful for the calculation of the twisting angle. With such tools the most efficient configuration of laminates and piezoceramics can be found very easy.

Active Twist Optimization

Objective of the current investigation is to determine the maximum twisting angle which can be reached with the available materials. The basis is the neck of the Tiger and the BO105 rotor blade (similar to Figure 23). A laminate with the thickness and the torsional stiffness of the real rotor blade neck is covered by layers of piezoceramic material. In the following investigations the laminate data of Table 3 are used.

Table 3: Laminate material data

Laminate	Young's Modulus 1 N/mm²	Youngs Modulus 2 N/mm²	Shear Modulus N/mm²	Poisson's Ratio -
GFRP, 0°	45200	11600	4400	0.27
GFRP, ±45°	13700	13700	12900	0.57
CFRP-HT, ±45°	16500	16500	34400	0.78
CFRP-UHM, 0°	420000	3700	3100	0.36

The necessary thickness of the piezoceramic layers t_{Piezo} and the resulting maximum twisting angle θ_{max} are determined for each of the following variants:

Variant 1: Piezo strips partially bonded (r/s=0.5)
Variant 2: Blade neck partially covered
Variant 3: Piezo strips sandwiched between CFRP-UD
Variant 4: Shear deformation

During the optimization procedure, the torsional stiffness of the laminate is held constant. This is necessary, as the piezoceramic material has a relatively high Young's modulus and therefore it has an influence on the stiffness which cannot be neglected. Constant torsional stiffness can be achieved by simultaneously changing the thicknesses of the individual laminate layers together with the thickness of the piezo layer. Strength constraints are not considered in this investigation. The results are shown in Table 4.

Table 4: Maximum twisting angles of a rotor blade

Variant			1	2	3	4
BO105	δ_{max}	°/m	0.07	0.02	0.25	0.42
	t_{Piezo}	mm	6.0	7.4	3.2	6.5
	$t_{45°\,UHM}$	mm	-	-	2.9	-
Tiger	δ_{max}	°/m	0.05	0.01	0.22	0.34
	t_{Piezo}	mm	9.1	11.3	4.4	13.6
	$t_{45°\,UHM}$	mm	-	-	5.9	-

All twisting angles are very low, compared to the angles, necessary for rotor active control. For the required ±2° blade twist at 0.7*R* an induced blade neck twist of about ±2°/m is necessary for both blades. Especially the first two variants (partially bonded and partially covered) have a very low efficiency concerning twisting due the piezoelectric effect. Better is Variant 3. With moderate thicknesses nearly 0.2 °/m twisting angle can be achieved.

The best efficiency shows Variant 4. However, at the present time the use of the piezoceramic shear deformation cannot be used. But the result shows, that in principle there is a potential, which is desirable to use. Furthermore, this method has the advantage of not inducing any coupling between tension and torsion. All other variants show a large amount of such coupling due to the artificial anisotropy of the piezoceramics, which cannot be neglected.

The results reveal that in principle inducing twist by means of piezoceramics will work. But there are some difficulties which prevent the application of these materials for this application. First, the tension strength is too low for the application of piezoceramics in the rotor blade neck section. As mentioned, the strain level is about 3 to 7‰, but the piezoceramic tension strength is only 1‰. Second, the maximum twisting angle obtainable with the current piezoceramics is much lower than the required angle of 2°. So, at this time the application of piezoceramic material at the neck of a rotor blade is not possible. For this application especially the tension strength of this material has to be improved by at least a factor of ten.

5.2 Generation of Twist through a Control Rod

If it is possible to decouple the torsion and the longitudinal strain, the strength requirement for current piezoceramic materials can be fulfilled. One possibility is to apply the piezoceramics at special control rods, which are loaded mainly in torsion. This concept seems to be especially suited for bearingless rotors. Figure 25 shows an experimental bearingless main rotor with a control rod, which was successfully flight tested on ECD's BO105 helicopter. Further details of this 9.80 m diameter rotor can be found in Ref. 2 and Ref. 4.

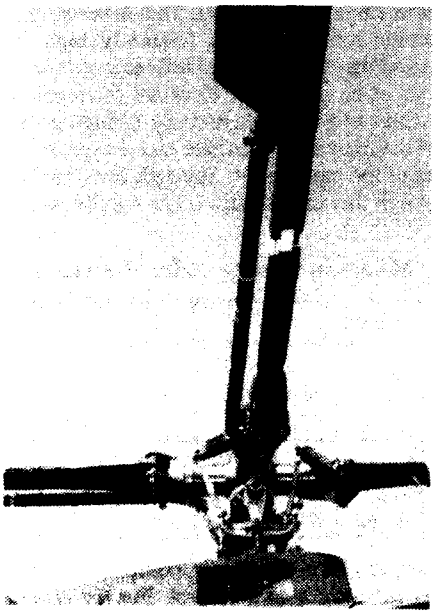

Fig. 25: Bearingless main rotor at a MBB BO105

The blade - control rod arrangement with piezoceramic material is shown symbolically in Fig. 26. The control rod is designed as a relatively stiff torsion tube with flexible bending couplings on both ends. Thus the rods are mainly loaded in torsion, there are only minor bending and centrifugal stresses present.

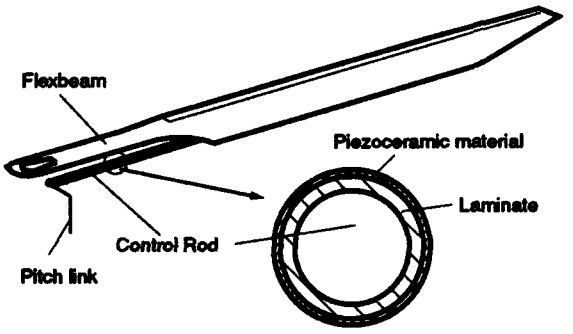

Fig. 26: Blade twisting by a control rod

The torsional angle θ for a circular tube with the radius r and the length l under pure shear deformation is given by

$$\theta = \frac{l}{r}\gamma. \tag{16}$$

Similar to Equation 9 and 10 twisting can be achieved too by a longitudinal strain $\varepsilon_{\pm 45}$ under an angle of 45° to the tube axis:

$$\theta = \frac{l}{r}\varepsilon_{\pm 45}. \tag{17}$$

This equation describes the maximum obtainable twisting angle of a circular tube when neglecting its torsional rigidity. With a maximum piezoelectric strain of 0.25‰ and a medium tube radius of 18 mm this yields a twisting angle of 0.8°/m. For real control tubes, this value will be lower due to the tube torsional stiffness.

From Table 4 it was concluded that the piezoceramic material sandwiched between CFRP-HM unidirectional laminate and oriented under 45° has the best deformation efficiency. Therefore, this configuration is further investigated for the control tube. Figure 27 shows the cross section of such a tube.

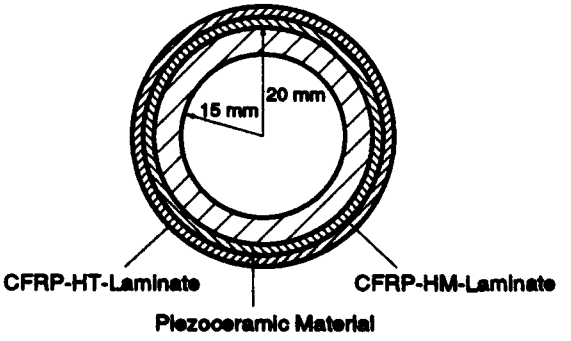

Fig. 27: Cross Section of a Control Tube

The twisting angles which can be reached with this configuration are shown in Figure 28. With reasonable thicknesses of the piezoceramic and the CFRP-HM layer, angles up to 0.2°/m can be obtained.

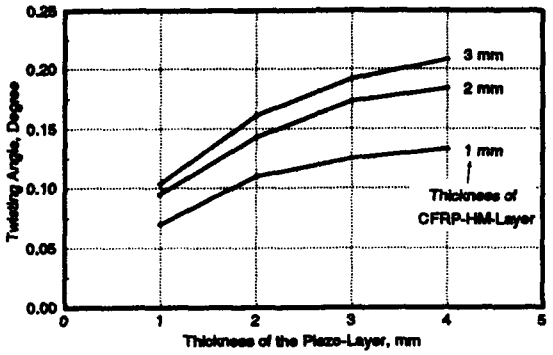

Fig. 28: Twisting Angles of a Control Tube

Though this value is small compared to the desirable value of 2°/m, new materials (e.g. piezo-gels) let hope that in the next future larger twisting angles can be reached. Moreover, due to the pure torsion load, the strength criteria of the piezoceramic materials if fulfilled. Therefore the active control rod is likely to become realizable.

In addition the active control rod can also be used for improving the blade lead-lag damping by using "position" feedback of the blade lead-lag motion:

$$\theta = K_{p\zeta} \cdot \zeta \tag{18}$$

where a negative control gain $K_{p\zeta}$ (pitch-lead coupling) is stabilizing. The resulting active blade lead-lag damping can be estimated by the following formula (derived in Ref. 25):

$$D_\zeta = -\frac{\gamma}{8}\frac{\beta_{el}}{\omega_\zeta/\Omega} \cdot K_{p\zeta}. \tag{19}$$

Herein γ, β_{el}, ω_ζ and Ω denote the blade lock number, the elastic flap angle, the first lead-lag bending frequency and the nominal rotor speed respectively. Already small gains ($K_{p\zeta} = -0.1 \ldots -0.2$) are effective to augment the blade lead-lag damping significantly if the rotor operates under high thrust conditions ($\beta_{el} > 0$). The design of improved feedback control laws for stabilizing soft inplane rotor systems by individual blade control has recently found strong interest in the helicopter community.

5.3 Generating Blade Lift and Twist by Active Flaps

Another method to achieve individual blade control by piezoceramic materials for both hingeless and bearingless rotors is the design of smart active blade flaps at the outer third of the rotor blade (Fig. 29)

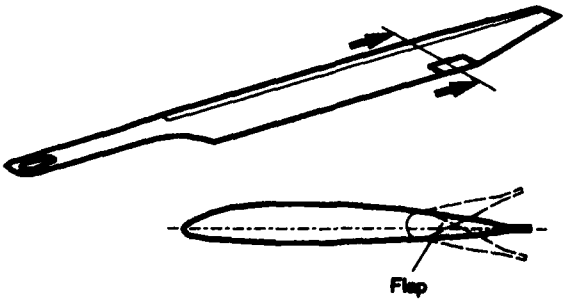

Fig. 29: Rotor blade with flap

Up to now helicopter rotor blade control by active flaps is only exceptionally applied due to the lack of appropriate actuation systems. The high g-level due to centrifugal forces at the blade outer part (above 100g) poses extreme practical problems for servo-hydraulic controlled blade flaps. This situation may now be changed by using smart blade flap actuation.

In the following, the feasibility of both a smart flap and a servo-flap with a smart bending actuator is investigated.

5.3.1 *Smart Blade Flap*

The aim of the smart piezoceramic blade flap is the realisation of a simple and efficient IBC system without additional hinges or linkages, see Fig. 3. Such a system can be adapted to different control tasks by using continuous multiple control elements distributed along the blade.

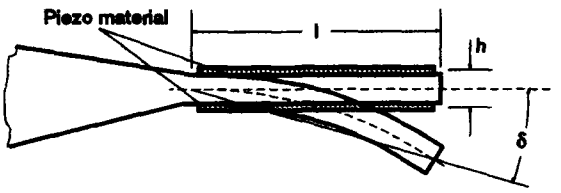

Fig. 30: Trailing edge flap

A simple solution for a smart flap is to enlarge the blade trailing edge to a flap. For such a flap of constant thickness the deflection angle due to the piezoelectric strain can be calculated very simple, if the stiffness of the flap and the aerodynamic loads are neglected:

$$\delta = \frac{l}{h}\varepsilon_g. \tag{20}$$

Note that this angle is only half of the tip angle value (compare Equation 8). With an active piezoelectric strain of 0.25 ‰ (chapter 3.2) the maximum deflection angle for a 10%-flap with a depth of l=30 mm (BO108 blade, chord: 300mm) and a distance between the piezo plates of h=1 mm can be calculated to 0.42 degree. This is much too less, compared to the desirable 6°. Therefore at this time the "smart" trailing edge flap cannot be realized for a helicopter rotor active control system.

The investigations in Ref. 5 of a more elaborated smart blade/flap come to the same negative conclusion: the realisation of smart rotor blade flaps with current piezoceramic material is not possible.

5.3.2 *Servo Flap with Smart Actuator*

Another concept to by-pass the high strain requirements of smart flaps is the active flap with piezo-actuator. This concept is investigated in detail in Ref. 12, using a piezoceramic bending-actuator for control of a hinged flap. A similar flap design is studied in Ref. 11, too.

The hinged flap, suggested in Ref. 12 is shown in Fig. 31. Here large flap deflections can be reached by a hinged flap and a mechanism, which transfers the motion of the piezoelectric bar to the flap.

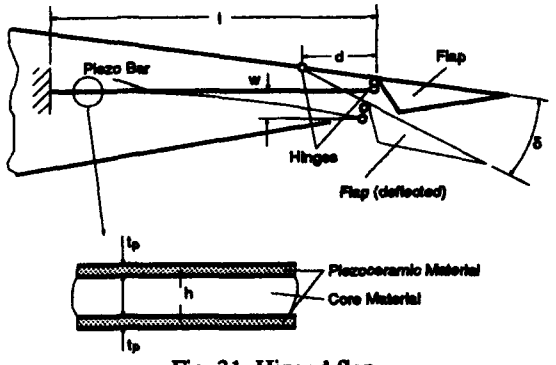

Fig. 31: Hinged flap

In this case the flap deflection angle δ is a function of the tip deflection w of the piezoelectric bar and the length d of the lever arm. With the geometry, given in Fig. 31 the following linearized relation between the flap angle δ and the tip deflection w of the piezoelectric bar exists:

$$\delta = \frac{w}{d}. \tag{21}$$

Neglecting first the flap aerodynamics the tip deflection w is solely determined by the piezo-bending actuator. Using Equation 6 the active flap angle δ can be easily derived:

$$\delta = \frac{l^2}{dh}\frac{1}{1+\frac{EI_0'}{EI_p'}}\varepsilon_E. \quad \text{(no airloads)} \tag{22}$$

Here the assumptions and notations concerning the bending actuator are the same as in Equation 6 and Fig. 7. For simplicity the two bending stiffnesses of the bar EI_0' and the piezo plates EI_p' are related to the width of the servo-flap. The parameter h is the mean distance of the two piezo plates, compare Fig. 31.

A more realistic flap angle estimation has to consider the effect of the aerodynamic flap hinge moment M_δ' (the prime is carried on M_δ' to denote the application to unit flap width). Thus the tip deflection w in Equation 21 is determined by the piezo-elastic loads of the actuator and the aerodynamic loads of the flap. Using the procedure of Ref. 12 the following formula can be derived for the piezo-controlled flap angle:

$$\delta = \frac{1}{1+\frac{M_\delta'}{3EI_p'\left(1+\frac{EI_0'}{EI_p'}\right)}\frac{l^2}{d^2}}\cdot\frac{l^2}{dh}\cdot\frac{1}{1+\frac{EI_0'}{EI_p'}}\cdot\varepsilon_E \tag{23}$$

The aerodynamic flap hinge moment coefficient M_δ' may be derived from quasi-steady incompressible aerodynamics (see Ref. 12):

$$M_\delta' = \rho V^2 b^2 C_{M\delta} \tag{24}$$

Here ρ is the air density, b the blade semichord, V a reference (design) velocity at $0.7R$ and $C_{M\delta}$ is a non-dimensional aerodynamic coefficient of the flap. For a 10% flap this coefficient assumes the value

$$C_{M\delta} = 0.01768. \tag{25}$$

For the feasibility study the following simplifications are in order:

$$EI_0' = 0 \quad \text{and} \quad EI_p' \approx E_p\frac{1}{2}h^2 t_p \tag{26}$$

where t_p is the thickness of the piezo-plates.

The "optimal" flap design, that means the flap with the highest possible flap angle δ, depends primarily on the lever arm length d which determines the kinematic angle amplification. The optimal lever arm length can be evaluated from Equation 23. This results in

$$d_{opt} = \frac{l}{h}\sqrt{\frac{2M_\delta l}{3E_p t_p}}. \tag{27}$$

The corresponding flap angle is given by

$$\delta_{opt} = \sqrt{\frac{3E_p t_p l}{8M_\delta}}\varepsilon_E. \tag{28}$$

These two design equations now allow to check the feasibility of active flaps for both the advanced BO108 blade and the Tiger blade. The reachable flap deflection angle δ is independent of the bar height. With the data of Table 5 and the material data given before, Fig. 32 shows the optimal deflection angle δ which can be reached with different lengths of the piezoelectric actuator (Equ. 28).

Table 5: Flap Design Data

	BO108	Tiger
Flap/Blade Chord Ratio	0.1	0.1
Blade Chord, $c = 2b$, mm	300	520
Design Speed $V = 0.7R\Omega$, m/s	153	150
Air Density ρ, kg/m^3	1.2	1.2
Piezo-Plate Thickness t_p, mm	1.0	1.0

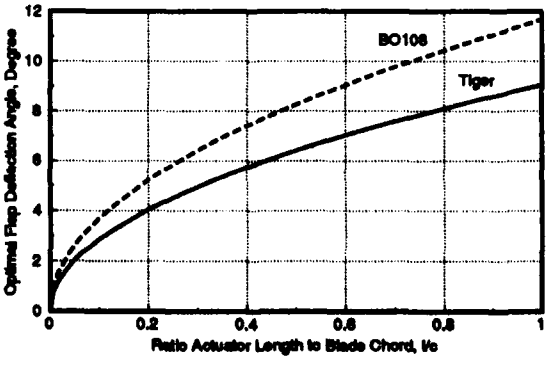

Fig. 32: Optimal deflection angle δ_{opt} versus relative actuator length

From Fig. 32 follows that an actuator length of $l = 0.4c$ is sufficient to get a deflection angle δ of about $\pm 6°$. The lever arm length, necessary for this deflection angle depends on the length of the piezo bar as well. Fig. 33 shows the optimal lever length d versus the actuator length for two different values of h at the actuator saturation limit.

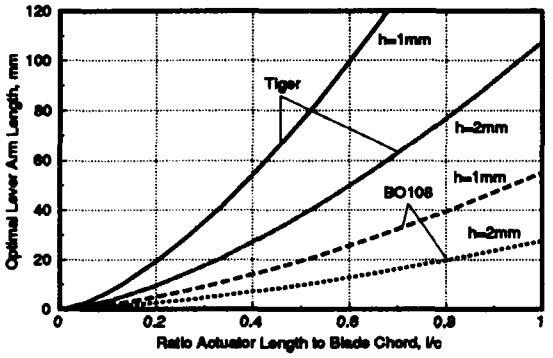

Fig. 33: Optimal lever arm length d_{opt} versus relative actuator length

For a value of $h = 1$ mm which means, that the two piezo plates, each 1 mm thick, are bonded together directly, and an actuator length $l = 0.4c$ the optimal lever arm length is about 53 mm and 13 mm for the Tiger and BO108 rotor blade respectively. These values seem to be feasible. Thus, the hinged servo flap with piezo actuation is capable to generate angles of $\pm 6°$ and may be the solution for future IBC-systems. Of course, the practical design may encounter great problems and the necessary hinges may introduce a new unwanted complexity into the rotor design that could "destroy" all the benefits of modern hingeless and bearingless rotor systems.

6. CONCLUSIONS

Smart materials offer the possibility of realizing helicopter rotor active control by electrical systems, which can be integrated into the rotor blade. It is shown that in principle strain induced actuation systems will work in the desired way. But at the present time the available materials are not ready for really "smart" helicopter rotor blade actuation systems.

The piezoceramics have a very low tension strength, so that they cannot be applied in areas where a high strain level occurs. An increase of the strength by a factor of 10 is necessary if these materials should be applied at the neck of hingeless rotor blades. To reach the twisting angles, necessary for individual blade control, the piezoelectric active strains have to be increased by a factor of at least 10, too. This is valid for both blade neck (hingeless rotors) and control rod (bearingless rotors) torsional actuation.

Also, smart flaps at the outer third of rotor blade cannot be realized at this time due to the very low active strain of the piezoceramics. The only way in getting higher deflection angles of flaps is to use hinged flaps. With a proper geometry such flaps can reach sufficient deflection angles, when controlled by a smart actuator (e.g. piezoceramic bending bar). For the next future this seems to be the most promising way to realize individual blade control for helicopters.

A real breakthrough of rotor active control technology (RACT) by strain induced smart blade actuation systems has to be postponed until better smart materials are available. But in the meantime even the current active materials seem to have a potential which the helicopter engineers may apply with benefit to the next generation of helicopter rotor systems.

7. REFERENCES

1 Seitz G., Krysinski T., **Overview of Tiger Dynamics Validation**, 48th Annual Forum and Technology Display, Washington D.C., June, 1992

2 Strehlow H., Frommlet H., **Entwicklung neuartiger lagerloser Rotorsysteme**, 4. BMFT-Statusseminar Luftfahrtforschung und Luftfahrttechnologie, München, Germany, April, 1986

3 Schimke D., Enenkl B., Allramseder E., **MBB BO108 Helicopter Ground and Flight Test Evaluation**, 15th European Rotorcraft Forum, Amsterdam, The Netherlands, September, 1989

4 Huber H., **"Will Rotor Hubs Lose Their Bearings?" A Survey of Bearingless Main Rotor Development**, 18th European Rotorcraft Forum, Avignon, France, September, 1992

5 Ormiston R.A., **Can Smart Materials Make Helicopters Better?**, Workshop on Dynamics & Aeroelastic Stability Modeling of Rotorcraft Systems, University of Maryland/Army Research Office, November, 1991

6 Schrage D.P., Oakes G., Jonnalagadda V.R.P., Anand V.R., **Development of an Individual Blade Control Computer Analysis**, Workshop on Dynamics & Aeroelastic Stability Modeling of Rotorcraft Systems, Boca Raton, Florida, November. 1987

7 Richter P., Eisbrecher H.D., Klöppel V., **Design and Test of Individual Blade Control Actuators**, 16th European Rotorcraft Forum, Glasgow, UK, September, 1990

8 Teves D., Klöppel V., Richter P., **Development of Active Control Technology in the Rotating System, Flight Testing and Theoretical Investigations**, 18th European Rotorcraft Forum, Avignon, France, September, 1992

9 Strehlow H., Mehlhose R., Znika P., **Passive & Active Vibration Control Activities in the German Helicopter Industry**, Aero Tech 92, Conference, Birmingham, UK, January, 1992

10 Barret R., **Intelligent Rotor Blade Actuation through Directionally Attached Piezoelectric Crystals**, 46th Annual Forum and Technology Display, Washington D.C., May, 1990

11 Chen P.C., Samak D.K., Chopra I., **Development of an Intelligent Rotor**, The Fourth Workshop on Dynamics and Aeroelastic Stability Modeling of Rotorcraft Systems, University of Maryland/Army Research Office, November, 1991

12 Spangler R.L., Hall S.R., **Piezoelectric Actuators for Helicopter Rotor Control**, MIT-SSL 1.89, Mass. Institute if Technology, Cambridge, Mass., January, 1989

13 Hanagud S., Babu G.L.N., Won C.C., Obal M.B., **Smart Structures for Helicopters**, 16th European Rotorcraft Forum, Glasgow, UK, September, 1990

14 Melcher J., Breitbach E., **New Approaches for Actively Controlling Large Flexible Space Structures**, European Forum on Aeroelasticity and Structural Dynamics, Aachen, Germany, April, 1989

15 Breitbach E.J., **Research Status on Adaptive Structures in Europe**, Second Joint Japan - U.S.A. Conference on Adaptive Structures, Nagoya, Japan, Nov. 12-14, 1991

16 Mason W.P., **Crystal Physics of Interaction Processes**, Academic Press, New York, London, 1966

17 Ikeda T., **Fundamentals of Piezoelectricity**, Oxford University Press, Oxford, 1990

18 Crawley E.F., de Luis J., **Use of Piezoelectric Actuators as Elements of Intelligent Structures**, AIAA Journal, Vol. 25, No. 10, 1987

19 Crawley E.F., Lazarus K.B., **Induced Strain Actuation of Isotropic and Anisotropic Plates**, 30th AIAA Structural, Structural Dynamics and Materials Conference, Mobile, Alabama, April, 1989

20 Crawley E.F., Anderson E.H., **Detailed Models of Piezoceramic Actuation of Beams**, 30th AIAA Structural, Structural Dynamics and Materials Conference, Mobile, Alabama, April, 1989

21 Preumont A., Dufour J.-P., Malekian C., **Active Damping by a Local Force Feedback with Piezoelectric Actuators**, Workshop on Smart Material Systems and Structures, Aachen, Germany, June, 1991

22 Tsai S.W., Hahn H.T., **Introduction to Composite Materials**, Technomic Publishing Co., Westport, Conn., 1980

23 Rapp H., **New Computer Codes for the Structural Analysis of Composite Helicopter Structures**, 16th European Rotorcraft Forum, Glasgow, UK, September, 1990

24 Sung C.-C., Varadan V.V., Bao X.-Q., Varadan V.K., **Active Control of Torsional Vibration Using Piezoceramic Sensors and Actuators**, AIAA-90-1130-CP, 1990

25 Hohenemser K.H., **Hingeless Rotorcraft Flight Dynamics**, AGARD-AG-197, 1974

INTELLIGENT STRUCTURES – A TECHNOLOGY OVERVIEW AND ASSESSMENT

by

Edward F. Crawley
Professor of Aeronautics and Astronautics
and
Mac Vicar Faculty Fellow
Space Engineering Research Center
Massachusetts Institute of Technology
77 Massachusetts Avenue
Cambridge, MA 02139
United States

SUMMARY

The paper presents a topical review of a decade of work toward the development of intelligent structures; i.e. structures with highly distributed actuators, sensors and processors. The background and status of the research in this area are covered, as are the evolution of the technology components: strain actuators, acceleration and strain sensors, processors and signal conditioning and control algorithms. The results of several system level experimental implementations are presented, as are the challenges for further development.

INTRODUCTION

The objective of this article is to present an overview and assessment of the technology leading to the development of intelligent structures. Intelligent structures are those which incorporate actuators and sensors that are highly integrated into the structure and have structural functionality, as well as highly integrated control logic, signal conditioning and power amplification electronics. Such actuating, sensing, and signal processing elements are incorporated into a structure for the purpose of influencing its states or characteristics (mechanical, thermal, optical, chemical, electrical or magnetic). For example, a mechanically intelligent structure is capable of altering both its mechanical states (its position or velocity) or its mechanical characteristics (its stiffness or damping).

Definition of Intelligent Structures

Intelligent structures are a subset of a much larger field of research, as shown in Figure 1 [Ref. 43]. Those structures which have actuators distributed throughout them are defined as adaptive. Definitive examples of such adaptive structures are conventional aircraft wings with articulated leading and trailing edge control surfaces, and robotic systems with articulated members. More advanced examples in current research include highly articulated adaptive space cranes.

The subset of structures which have sensors distributed throughout them are referred to as sensory. These structures have sensors which might detect displacements, strains or other mechanical states or properties, electromagnetic states or properties, temperature or heat flow, or the presence or accumulation of damage. Applications of this technology might include damage detection in long life civil engineering structures, or in devices which are stored for long periods but must always be ready for action, such as solid rocket motors.

The overlap of structures which contain actuators and sensors, and those which implicitly contain a closed-loop control system linking the actuators and sensors, are referred to as controlled structures. Any structure whose properties or states can be influenced by the presence of a closed-loop control system are included in this category. A subset of controlled-structures are active structures. Active structures are distinguished from controlled structures by highly distributed actuators which have structural functionality and are part of the load bearing system.

Intelligent structures are a subset of active structures which have highly distributed actuator and sensor systems with structural functionality and, in addition, distributed control functions and computing architecture. To date, such intelligent structures have not been built. The realization of intelligent structures is a goal which has motivated this technology assessment.

Development Background

There are three historical trends which have combined to establish the potential feasibility of intelligent structures. The first is a transition to laminated materials. In the past, structures were built up out of large pieces of monolithic material which were machined, forged, or formed to a final structural shape, making it difficult to imagine the incorporation of active elements. However, in the past thirty years a transition to laminated material technology has occurred. Laminated materials, which are built up from smaller constitutive elements, allow for the easy incorporation of active elements within the built up structural form.

Exploitation of the off diagonal terms in the material constitutive relations is a second trend which enables intelligent structures at this time. The full constitutive relations of a material include characterizations of its mechanical, optical, electromagnetic, chemical, physical and thermal properties. Nominally, researchers have focused only on block diagonal terms. For example, those interested in exploiting a material for its structural benefits have focused only on the mechanical

characterization, and those interested in exploiting its electrical properties have focused on the electrical characterization. However, much gain can be made by exploiting the off block diagonal terms in the constitutive relations, which for example, couple the mechanical and electrical properties. The characterization and exploitation of these off diagonal material constitutive relations has led to much of the progress in the creation of intelligent structures.

The third, and perhaps most obvious advance comes in the electrical engineering and computer science disciplines. These include the development of micro-electronics, bus architectures, switching circuitry, and fiber optic technology. Also central to the emergence of intelligent structures is the development of information processing, artificial intelligence and control disciplines. The sum of these three developing technologies (the transition to laminated materials, the exploitation of the off-diagonal terms in material constitutive relations, and the advances in micro electronics) has created the enabling infrastructure in which intelligent structures can develop.

CRITICAL COMPONENT TECHNOLOGIES

There are four component technologies critical to the evolution of intelligent structures and their application to devices. These four component technologies are: actuators for intelligent structures; sensory elements; control methodologies and algorithms; and controller architecture and implementation hardware. The remainder of this study will focus on these four component technologies, and their use in several typical intelligent structure applications.

Actuators for Intelligent Structures

Actuators for intelligent structures must be capable of being highly distributed and influencing the mechanical states of the structure. The ideal mechanical actuator would directly convert electrical inputs into strain or displacement in the host structure. Its primary performance parameters include its maximum achievable stroke or strain, stiffness, and bandwidth. Secondary performance parameters include linearity, temperature sensitivity, strength and density. These properties will be assessed and compared for several types of strain actuators. In addition, the availability of each actuator type will be considered [Ref. 14]. Currently, many types of strain actuators are available, including piezoceramics, piezoelectric films, electrostrictives and shape memory alloys.

The principal actuating mechanism of strain actuators is referred to as actuation strain. Actuation strain is the strain which is controllable and not due to stress. Actuation strains are produced by a variety of phenomena, with the most common but least controllable being temperature and moisture absorption. Other examples, which are less common but more useful for active control, include piezoelectricity, electrostriction, magnetostriction, and the shape memory effect. The latter four phenomena are desirable actuating mechanisms since they directly convert electrical signals into actuation strain.

Strain Actuator Modeling. The actuation strain enters into the constitutive relations in the same manner as do commonly modeled thermal strains. The constitutive relations dictate that the total strain in the actuator material is the sum of the mechanical strain induced by the stress, plus the controllable actuation strain. Once the strain is induced in the actuator, it must be converted to strain in the host structure. The strain in the host structure can be found from a number of different assumptions about the local strain deformation field. The simplest assumption for a surface mounted actuator is that of uniform strain in the actuation material, and linearly distributed strain throughout the host structure. Such a model is not very exact, but is useful for obtaining simple figures of merit by which actuators can be compared. The most useful and general model is the Bernoulli-Euler-Kirchoff assumption, in which the strain is linearly distributed throughout the actuator and host structure regardless of whether the actuator is surface mounted or embedded. Such modeling has been found useful for beams, plates and shell-like structures [Refs. 9, 10].

If there is concern about the ability of the actuator to transfer the strain through a bonding layer, a shear lag analysis of the bonding layer can be performed. The principle result of this analysis is the identification of the shear lag parameter, which must be kept small to allow for efficient transfer of strain to the host structure [Ref. 37]. The most general model is one which includes local shearing of the host structure. Fortunately, Saint Venant's principle makes such a detailed model unnecessary for predicting the overall deformation of strain actuated structures. However, such an analysis is necessary for accurately predicting the strain field near and around active elements. Once the constitutive relations of the actuator, the assumed local strain deformation field, and the imposition of equilibrium are found, the influence of the strain actuator on the host structure can be calculated. Such models had been derived for embedded actuators as well as actuators in plates and shells.

The simple uniform strain model produces a useful figure of merit for comparing the effectiveness of various actuation materials. This model predicts that the strain induced in the host structure is proportional to the product of the actuation strain, which can be commanded in the actuation material, and the reciprocal of one plus the stiffness ratio (stiffness of the structure to that of the actuator). This latter term is an impedance matching effect which simply indicates that the stiffness of the actuator must be comparable to the stiffness of the structure for effective strain transfer.

Comparison of Commercially Available Strain Actuators. Commercially available strain actuating materials are listed in Table 1. There are four broad classes of materials which can create actuation strains. The first two columns represent two material classes (a piezoceramic and a polymer film) which use the piezoelectric effect. Piezoelectricity can be thought of

as an interaction of the electrical field imposed upon the material with electrical monopoles in the material itself. When an electric field is applied, the monopoles are pulled in the appropriate direction, straining the material and creating a strain in the direction of the field. This fundamental relation of piezoelectricity between field and strain is linear to first order [Ref. 12]. The third column represents a material which creates actuation strain through electrostriction, which can be thought of as an interaction between the electric field and electric dipoles in the material which is inherently non-linear [Ref. 5]. The fourth column is a magnetostrictor, which represents a coupling between an applied magnetic field and magnetic dipoles in the material and is also inherently non-linear. The absence of magnetic monopoles explains the absence of the fourth effect, which would be the interaction between magnetic fields and magnetic monopoles in the material. Shape memory is a qualitatively different effect, in which the application of electrical current causes heating in the material, and associated with the heating is a phase change, and strain. In some materials the strain associated with phase changes can be recovered when the material cools, which is called the shape memory effect [Refs. 4, 27]. Many of the actuator materials can be embedded as discrete devices [Ref. 10], foils or fibers [Ref. 44].

All four of the material classes listed fulfill the basic strain actuator requirement of converting electrical inputs to strain in the material. A PZT is a common lead zirconate titanate piezoceramic material having a maximum actuation strain on the order of 1000 micro strain. PVDF is a polymer piezoelectric film which can produce about 700 microstrain, and PMN is a lead based electrostrictor which can create about a 1000 micro strain. Terfenol, a rare earth magnetic-like material, can create about 2000 microstrain at its non-linear maximum. And, nitinol (a nickel titanium alloy) can create up to 20,000 microstrain or 2% strain.

As seen in Table 1, the modulus of each materials is comparable to that of structural materials with the exception of the PVDF film, which has a significantly lower modulus. The next row in the table indicates the approximate strain which can be induced on the surface of an aluminum beam whose thickness is 10 times the thickness of the actuation material. This value indicates the range of strain which can be created in the host structure and is on the order of 3 to 500 micro strain with commercially available piezoelectric, electrostrictive, and magnetostrictive materials. In contrast, as much as 0.8% strain can be induced by the nitinol. However, the bandwidth of the nitinol is much lower than the other strain actuators because of the necessity to introduce heat into the material and especially because of the time constants associated with the removal of heat by cooling. The trade which must therefore be made is one of strain authority versus bandwidth. The piezoelectrics and electrostrictives have quite high bandwidths, effectively beyond the frequency range of structural and acoustic control applications. Terfenol has a moderate bandwidth because of the difficulty of creating a rapidly changing magnetic field to stimulate the magnetostrictive effective.

Sensory Elements

Sensory elements of intelligent structures must be capable of being highly distributed and sensing the mechanical states of the structure. The ideal sensor for a intelligent structure converts strain or displacement (or their temporal derivatives) directly into electrical outputs. The primary functional requirements for such sensors are their sensitivity to the strain or displacement, or their time derivatives, spatial resolution and bandwidth. Secondary requirements (which again might have to be compromised in order to reach primary requirements) include the transverse sensitivity, the temperature sensitivity, linearity and hysteresis, electromagnetic compatibility, and size of sensor packaging. Unlike actuators, which are so large and bulky that they have to be explicitly accommodated in the built up laminates, it is desirable to make sensors small that they can fit into intralaminar or otherwise unobtrusive positions.

Sensing Mechanisms. There are two generally types of sensors which can be used in intelligent structures, since they do not require an external reference. These are acceleration and strain sensors. Acceleration, of course, is measured against an inertial reference frame. Current technology allows the acquisition of integrated circuit chip-based accelerometers. These have been fabricated using silicon cantilever structures with piezoelectric capacitive, and electron tunneling detection mechanisms. Accelerometers are packaged in a way which allows them to be embedded in a structure or highly distributed over its surface. The output of the acceleration can be integrated once or twice in a high bypass manner to provide an inertial velocity or displacement at the point of measurements. Accelerometers are capable of making measurements over wide frequency ranges, including nearly quasi-static.

The alternative sensing scheme is to measure the strain or strain rate in the structure (or the deflection or velocity of one point relative to another). Strain can be sensed at a point in the structure or averaged over a larger finite area in order to yield some particularly desirable output with the assistance of a weighting function [Refs. 35, 31, 6, 28, 8]. Weighting functions can be chosen such that the output has frequency transfer function characteristics which are more desirable and unobtainable from temporal filtering of discrete point signals. The phase and amplitude characteristics of weighted discrete point signals are intimately related through the Bode integral theorem. However, because an area averaging sensor can be thought of as a device which can sense incoming strain waves before they reach the center point of the sensor, the device can in fact appear to be noncausal and thus violate the causality assumptions of the Bode integral theorem. This allows distributed strain sensors to have highly desirable roll-off characteristics with none of the associated undesirable phase loss. Note that such weighting functions can be applied to the output of any

sensing device, including fiber optic sensors, and does not rely on a shaped piezoelectric strain gauge sensor.

Two common weighting methods are modal sensors and discrete shaped sensors [Refs. 24, 26, 25]. Modal sensors use sensitivity weighting functions which are distributed in such a way as to mimic the strain pattern in one of the structural modes. Therefore, modal sensors may be very sensitive to one mode, and through orthogonality, be relatively insensitive to other modes. The frequency domain output is therefore concentrated in bandwidths associated with particular modes of the system.

An alternative to modal sensing is discrete shaped sensing, in which sensors cover a finite section of the structure [Ref. 2]. By using relatively simple weighting functions, such as triangular weighting or the Bartlett Window, discrete sensors can be made to roll-off rapidly in frequency, effectively acting as a low pass filter.

Commercially Available Sensors. Current commercially available sensing devices are listed in Table 2. Available sensing devices, which can be embedded in host structures, include traditional foil gauges, semiconductor strain gauges, embedded fiber optics, piezoelectric films and piezoceramics. Foil and semiconductor gauges rely on a change in resistivity associated with strain for their fundamental operation. Piezoelectric and piezoceramic devices use the piezoelectric effect which constitutes the coupling between the strain field and the voltage observed at the leads of the device. Fiber optic strain gauges rely on interferemetric effects to cause the optical output of the fiber to change with the strain [Refs. 42, 40]. The sensitivities, indicated in Table 2, range from approximately 30 volts per strain for the foil gauges, through 10^3 volts per strain for the semiconductors, to 10^4 volts per strain for the piezoelectric and piezoceramic gauges. Fiber optics have a fundamentally different relationship between the output and measurement which is expressed in degrees per strain (fiber optics produce roughly 10^6 degrees per strain). The bandwidths of almost all the devices extend over the range of conventional structural control.

Considering that commercially available strain gauges are comparable in terms of their primary functional requirements of sensitivity, localization, and bandwidth, the choice of which to use in intelligent structures must be based on the secondary considerations. These considerations includes embeddability (which eliminates the soft piezoelectric films), the ability to introduce weighting functions, and electromagnetic compatibility issues (which generally reduce the attractiveness of foil gauges). In the associated electronics, which must be incorporated in order to extract the strain signals, the last consideration tends to *prejudice against the fiber optics. The remaining* preferable strain sensors are therefore likely to be derivatives of the semiconductor based or piezoceramic devices, unless the signal conditioning electronics associated with embedded optics can be made small enough to accommodate wide spread distribution throughout a structure. Note that the sensitivities listed in Table 2 are made for reasonable excitation voltage, gauge length, and sensor thickness assumptions needed to place the various strain sensors into a common format.

Actuator-Sensor Synthesis. With certain types of actuators and sensors a level of synthesis can be achieved in which the same device can be used for both actuation and sensing [Ref. 19]. Shape memory alloy fibers have been used in this application, as have piezoelectrics. In the case of piezoelectrics, the embedded material is modeled by combining the actuator and sensor constitutive relations. In this configuration, the piezoelectric can be considered a generalized transformer between the structural states (stress and strain) and the electrical states (charge and voltage) [Ref. 18]. By making use of the properties of generalized transformers, the same device can be used as both an actuator and sensor through a technique referred to as simultaneous actuation and sensing, or sensuation [Ref. 13, 1]. Typical sensuating circuits compare the charge which appears across a reference capacitor with the charge which appears across the piezoelectric. Nominally, the difference corresponds to the strain in the piezoelectric. Signal conditioning circuits can be designed to return either the strain or the strain rate as an output signal. This scheme operates essentially by using a mechanical capacitor as an estimator to estimate part of the electrical states. Sensuation is advantageous for active control application since the actuator and sensor are a perfectly collocated pair.

Another form of actuator-sensor synthesis is the appropriate selection of actuators and sensors to simplify the structural control problem. In choosing a control scheme for a structure one can, in principle, select any form of actuator (i.e. applied force, applied moment or applied distributed strain) and any form of sensor (i.e. displacement, velocity or acceleration, slope, slope rate or acceleration, or strain, strain rate or acceleration). However, it may be that there is an optimal combination of these nine possible sensor outputs and three possible generalized force inputs which simplifies the structural control problem.

In order to examine this issue by example, the tip displacement of a cantilever beam was controlled by a discrete moment actuator at 1/10 the length of the beam from the root (which simulates the influence of a strain actuator over the region from the root to 1/10 of the length). The beam was modeled by assumed displacement finite elements and it was assumed that all of the displacement and rotations at the nodes were available as sensor outputs. Linear quadratic regulator theory was then applied, and the feedback from the nodal displacements and rotations to the discrete moment actuator was computed. By making use of the assumed displacement functions within the element, the continuous spatially distributed feedback gain function (or kernel) from displacement and displacement rate to the actuator can be calculated. The function shows no regular pattern of displacement feedback. When the displacement feedback function is twice integrated to

produce the equivalent strain feedback function, a much more regular pattern appears, diminishing approximately exponentially from root to tip. In another example, the optimal output feedback was calculated for the sinusoidal flexural modes in an infinite beam for distributed moment actuators. It was found that if transverse inertial velocity and strain were measured, the optimal output feedback for flexural waves of a uniform structure (assuming uniform weighting functions of the error) were exactly collocated. The simplicity of the strain feedback functions to strain actuation in these cases could imply that strain is a more natural input and output than displacement and force, and is certainly more easily achieved in a distributed manner for real structural forms.

Control Methodologies and Algorithms

The real intelligence of intelligent structures stems from their highly distributed control functionality. There are three levels of control methodology and algorithm design which must be considered for intelligent structures. These three levels are local control, global algorithmic control and higher cognitive functions. The objectives of local control are to add damping and/or absorb energy and minimize residual displacements. The objectives of global algorithmic control are to stabilize the structure, control shapes, and reject disturbances. In the future, controllers with higher cognitive functions will have objectives such as system identification, identification and diagnosis of component failures, the ability to reconfigure and adapt after failures, and eventually to learn [Ref. 41].

Optimal Local (Low-Authority) Control. In the design of local or low authority control, the principle issue is how to design the best controller, considering that hundreds or thousands of actuators and sensors may be distributed throughout the structure [Ref. 3]. Further, it may be desirable to use local connections to introduce some level of control (or add some damping) into the structure before attempting to close global feedback loops with large numbers of actuators and sensors. Here the choice of ideal local control is quite obvious. Perfect local control is accomplished by simulating the conditions of matched termination, so that all of the impinging energy is absorbed by the controller [Ref. 33]. However, simulating conditions of matched termination requires actuation and sensing of all independent cross sectional variables, which is usually not feasible in a structural controller. For example, in the case of a flexural wave such matched termination would require sensing of displacement and rotation, and actuating of moment and sheer at a point.

For the case of a system with a single output, the optimal compensator is found by matching the impedance of the compensator to the reciprocal of the complex conjugate of the dereverberated frequency transfer function [Refs. 29, 30]. The dereverberated transfer function of a structure at the observation point is obtained by ignoring the effects of reflections from discontinuities in the boundaries in the far field. This can be obtained by smoothing or averaging the normally calculated frequency transfer function of the structure. In a limited number of cases, such dereverberated transfer functions can also be calculated from wave propagation theory.

Unfortunately, the optimal single-input single-output compensator is unachievable because the resulting transfer function is usually non-causal. Therefore, it is necessary to use the best causal approximation. Approximations can match the amplitude and/or phase of the non-causal compensator over some specified frequency range, but not over the entire frequency range of interest. The exact procedure is to determine the transfer function from actuator to sensor, dereverberate the transfer function, and approximate the dereverberated function with a causal approximation.

Optimal Global (High-Authority) Control. While local control is useful for adding damping and low-authority control, global or high-authority control must be utilized for objectives such as disturbance rejection, shape control, and stabilization of the structure. In the design of global controllers, one issue is how to establish a control architecture for structures with a large number of actuators and sensors. There are two limiting cases. The first is a completely centralized controller in which the signals from all the sensors are fed through the structure to a centralized processor. The control inputs are then computed and fed back throughout the entire structure to the distributed actuators. The second is a completely decentralized design, which is essentially the same as the local control already discussed. The centralized design would have the best performance, but would be computationally inefficient. A single centralized processor would have to process signals at rates corresponding to the highest mode being controlled, and would have to read all of the inputs and calculate all of the outputs for the entire system. Obviously, such huge computational requirements (typically on the order of 100x100 to 1000x1000 at speeds of 1000 Hz) cannot be met, even with dedicated real time control computers (capable of computations on the order of 10x10 to 30x30 at roughly a 1000 Hz).

As a secondary consideration, the centralized scheme requires the passage of many relatively low level electrical signals, all the way from the original sensor to the centralized processing area. Thus the centralized scheme lacks both computational efficiency and consistently high signal-to-noise ratios. On the other hand, the decentralized scheme lacks good performance. And, although localized control can be used to add damping and reduce residuals, it cannot, in general, produce the type of performance achievable when information is fed back to actuators all over the structure. Therefore a compromise must be made between the two approaches. One such compromise is to use a scheme, midway between a completely centralized and completely decentralized control, which is referred to as a hierarchic or multi-level control architecture [Refs. 20, 21]. In this scheme there would be two levels of control, a centralized controller for overall performance and distributed processing for local control. Such a structure would be divided into finite control elements with local processors providing local

control using measurements made within the element and actuators within the element. An average representation of the shape within each element would then be passed on to the global processor for providing global high-authority control. This division of the control function into local and global control has been found to be quite practical, and from an engineering perspective completely reproduces the performance of a truly centralized structural controller.

Controller Architecture and Implementation Hardware

The presence of actuators and sensors and highly distributed control functionality throughout the structure implies that there must be a distributed computing architecture. The functional requirements for such a computing architecture include a bus architecture, an interconnection scheme, and a distributed processing arrangement. The bus architecture should be chosen to yield a high transmission rate of data in convenient (probably digital) form throughout the structure. The interconnections must be suitable for connecting a (potentially) large number of devices, actuators, sensors, and processors with the least degradation of structural integrity. If the actuators and sensors are embedded within the structure, the interconnections also should be embedded within the structure in order to avoid the necessity of running the electrical connections through otherwise structurally important plies. Finally, the processing requires that the functionality, which includes signal conditioning, amplification, D/A and A/D conversion, and digital computation be distributed throughout the structure. Secondary requirements include minimizing electrical magnetic interference, maintaining the mechanical strength and longevity of the structure and of the electronics components, and thermal and chemical compatibility of electronic components within the host structure.

Bus Architecture. Selection of the bus architecture will strongly reflect the hierarchic control architecture chosen. Typically structures will have distributed actuators and sensors which report (probably analog signals) to a local processor where the local control is calculated. These local processors then communicate over (probably digital) busses to the global processor. Trade studies have shown that distribution and embedding of a digital bus interface can simplify the overall interconnections in systems with more that 20 or 30 sensors and/or actuators [Ref. 45]. Thus a relatively small number of actuators and sensors move the design toward one of a bus architecture.

Processing Hardware and Material Integration. The next question which is: are there embeddable processors which can perform the functions of the local controller? Here we only have to look at commercially available single-chip microprocessors, such as the Intel 87C196KB. This processor has a central processing unit, A/D, D/A, sample and hold functions, multiplexors, a serial port, high speed digital input/output, and 16K of memory on a single chip. This commercially available device operates at 12 mega Hz and integrates nearly all of the electronic functionality required to implement local processing for a hierarchic controller. With 16 bit precision, 10 inputs and 10 outputs, this device can perform the calculations for an LQR controller at 3 kilohertz. Alternatively, for a ten-state LQG controller, it can perform these calculations at 1000 Hz. Thus the capabilities needed for the local processors are clearly achievable within the state-of-the-art.

The last question which must be answered is: can such micro-devices be embedded within a structural laminate? The issues here are: whether the device will survive the temperature and pressure cycles of the curing process; and whether it can survive the periodically applied strain fields of the operational environment as well as the temperature and humidity conditions of general operation. A preliminary investigation of this subject finds that the embedding of micro-devices is feasible within common structural laminates [Ref. 46]. Electronic devices without protective packaging have been embedded and cured in laminated test coupons. These coupons were subjected to quasi-static loads, and the first ply failure occurred at nearly 8,500 microstrain and subsequent ply damage was recorded up to nearly 13,000 microstrain. The electronic devices continued to function normally all the way to failure of the test coupon. Embedded, but chemically, electrically and mechanically isolated integrated circuits have been shown to function up to the breaking point of typical graphite epoxy laminates. The remaining challenges in this area are: the robustification of the electrical contacts on to and off of the device, which are subject to fatigue loading; the design for the long term temperature and hermicity environments; and the design of the signal and power conditioning electronics to minimize the heat dissipation into the structure.

APPLICATIONS FOR INTELLIGENT STRUCTURES

A wide variety of applications exist for intelligent structures technologies [Ref. 37]. These include aeroelastic control and maneuver enhancement, reduction of vibrations and structure borne noise [Refs. 17, 32], jitter reduction in precision pointing systems [Ref. 15], shape control of plates [Refs. 22, 38], trusses and lifting surfaces, isolation of offending machinery and sensitive instruments, and robotic control [Ref. 39].

Despite the fact that truly intelligent structures have not yet been built, a number of experimental implementations of intelligent structures component technologies have been built and demonstrated. Particularly, many researchers have investigated applications of distributed actuators and sensors and advance control algorithms. What is lacking to date is the distribution of the control and processing, but these parts of the technology are expected to evolve in time. Four examples found in the recent literature are discussed below: the aeroservoelastic control of a lifting surface, precision control of a truss, seismic and control of a building, and control of radiated sound.

In the first example, a typical high performance aircraft-like wing was built out of a graphite epoxy laminate with piezoelectric actuators distributed over 71% of its surfaces [Ref. 23]. The actuators were arranged into three banks which consisted of the vertical columns shown in Figure 2. The actuators were wired so as to induce bending in the laminate. Three tip displacements were used for displacement feedback. The controller implemented was a reduced order, 14 state, LQG controller. The control objective was gust disturbance rejection and flutter suppression.

Shown in Figure 3 are the analytically predicted and experimentally measured open and closed loop control. As can be seen, the DC response of the structure was reduced by almost 10db, which corresponds to approximately a factor of three stiffening in the structure due to the application of the closed-loop control. The first mode was virtually eliminated from dynamic consideration, being reduced 30 db from an already present 1% damping. The second mode, which was torsional, was less strongly influenced, with a 10db reduction. This was due to the fact that this mode was less controllable than the first or third mode. The third mode achieved a 20 db reduction. Overall the RMS response in bandwidth up to 100 hertz was reduced by about 15.4 db. This is an example of the relatively high gain control which can be introduced into a structure, and is probably the largest control authority which has yet been reported on a structural test article in experimental implementation.

The second example of a prototypical intelligent structure is the "dial-a-strut" or locally controlled strut, which is part of a precision control truss experiment (Figure 4) [Ref. 7]. In this case, the structure contains two active piezoelectric struts. Each strut has a collocated displacement and force feedback. By making measurements of the collocated displacement and force, the localized optimal impedance matching described earlier can be implemented. The control objective of this experiment was disturbance rejection of on board machinery noise, which would be typical of the need to reduce the jitter in a interferemetric spacecraft. Figure 5 shows typical transfer functions (open-loop and closed loop) for one, and two of the dial-a-struts. By comparing the open-loop and two strut closed-loop response, it can be seen that the first and second structural modes were significantly modified. Both the first and second mode response was reduced by 40 db. Note however that in this case the initial structural damping was quite light (roughly a few tenths of a percent). Thus the local collocated approximation to the optimal non-causal controller is seen to achieve good performance in a realistic structural configuration.

The seismic control of buildings is a considerably larger scale application of intelligent structures. Experiments were performed on a model building with a simulated earthquake disturbance (Figure 6) [Ref. 36]. Control was effected by an active shear brace incorporated into the structure. Five transverse accelerometers were used to monitor the control response of the structure, and two of them were used for feedback control. The control objective was to minimized building acceleration in response to the disturbance from a simulated large earthquake. Figure 7 shows the building excitation with and without the control system. As a result of the closed loop control, the damping factor was increased from nearly zero to twenty percent in the first three modes, with significant reduction in the low frequency component.

The final example considers the reduction of sound radiated into a room or aircraft cabin by active control of the plate and shell-like members which form the walls. To simulate this situation, a rectangular plate was placed inside a test chamber [Ref. 7]. The plate was controlled by three piezoceramic actuators placed as shown in Figure 8. Two PVDF piezoelectric film sensors were used to measure the vibration of the plate. The excitation source was an electromagnetic shaker which drove the plate at a known frequency corresponding to, for example, the excitation of an aircraft cabin wall from the rotation of the propeller outside the wall at a known RPM. In these cases, adaptive LMS algorithms are likely candidates for the control scheme. These schemes make use of knowledge of the frequency at which the primary excitation is occurring. The control objective in this example was narrow band reduction of the radiated far field noise. Figure 9 shows the radiated sound pressure level for the open-loop case, and the cases of one-piezoceramic actuator with one-sensor, and two piezoelectric actuators with two sensors. As can be seen from the diagram on the left, the radiated sound pressure level was reduced by about 30 db. The figure on the right indicates that this was achieved by principally reducing the response of the three-one mode, which corresponded to the frequency of the excitation source.

These four examples are but a few of the cases in which investigators throughout the world are now applying distributed actuation and sensing to a wide variety of control problems. It is encouraging that these early experiments show not only the feasibility of intelligent structures application, but remarkably good agreement between theory and experimental results as well. Of course, further experimentation is necessary to establish the technological limitations as well as the feasibility of distributing the processing and control architectures.

STATE-OF-THE-ART AND FUTURE NEEDS

Currently, all of the technologies needed for cost-effective application of intelligent structures have not been sufficiently developed. There are a number of difficult problems which remain. Some of the more important of these problems are discussed below.

Better Actuation Materials. In order to truly achieve the desirable level of control for many structural applications, actuation materials which have 3 to 10 times larger strain than those currently commercially available must be developed. Or materials should be developed similar to shape memory alloys, but with much higher bandwidth than those currently available. Alternatively, innovative uses of currently available materials, such as complex electrode patters which offer

higher strains in piezoelectric devices, need to be investigated.

Optimized Sensors. There is a great deal of work to be done in the design and the optimization of sensors to alleviate such problems as spillover, and to focus control effort on the bandwidths of interest through selective observability of the structure.

Inherently Structural Control Algorithms. Much of the theoretical work done for controlled structures has been by control theoreticians who view the structure as an already discretized matrix system. However, structures are inherently distributed parameter systems and experience has shown that gains are made by considering this inherent distribution, as well as the inherent bandedness of structures in their parametrized form.

Distributed Control. The proper distribution of control between a lower level and a higher level systems is still a subject which needs to be developed more completely, so that stability is guaranteed while performance is maintained.

Power Conditioning and Switching. Although it is conceivable that signal level electronics can be highly distributed through a system, power conditioning and switching requires dissipation of some amount of energy. In order to make a feasible system, this power conditioning and switching must be done in a way which minimizes the local heat load on the structure, so that the system can be embedded without thermally degrading the material.

Structurally Robust VLSI. Here the challenge is to take commercially available electronic components and develop innovative packaging techniques in which the interconnections to the silicon devices are structurally robust, so that these devices can survive the strain and fatigue environments of typical structures.

Minimized Impact on Host Structure. The presence of active elements (actuators, sensors and processors) impact the host structure by increasing the mass of the system and interfering with the load path, and potentially introducing new structural discontinuities which must be accommodated. This may potentially change the fatigue and fracture toughness characteristics of host material.

Hermicity of Embedded Components. The requirements for military electronic micro-devices are dominated by the need to keep the ambient chemical and humidity environment away from electrically active surfaces. Once these devices are embedded in a laminate, the challenge becomes to isolate their surfaces from both the ionic contamination of the structural matrix material and from the chemical and humidity environment of the ambient conditions, which can leak into the host material via the pathways created by the electrical connections.

Manufacturablity, Reliability and Repairability. These implementation question include: What is the difficulty of manufacturing intelligent structures, what is their in service liability, and how difficult is it (if possible at all) to repair such materials in service? Such issues will obviously have to be addressed before a widespread application of this technology is possible.

ANTICIPATED RESEARCH AND DEVELOPMENT

In the near future, it is expected that wide spread application of the current technology (the present generation of actuators, sensors, processors and control methods) will occur. In addition, near term improvements are expected in these areas. The breadth of application of this technology is expected to not only span the aerospace industry, but become widespread in the home construction, automotive, and machine tool industries as well.

In the more distant future, the evolution of a new physical-biological technology is anticipated. This technology will have two trends which are complementary. First the introduction of intelligence into the physical world, by the application of a machine electronic intelligence to otherwise unintelligent devices. Secondly the introduction of life into engineering application, i.e. the application of biological processes to the solution of engineering problems. One might envision, for example, that the engineering schools of the future will have in addition to their existing departments of civil, mechanical, electrical and aeronautical engineering, a department of applied biological engineering. Much as the steam engine drove the technology of the 19th century and electronics drove the technology of the 20th century, one can envision that the application of biological concepts to engineering will drive the technology of the 21st century. Engineering will cease to be the application of only the physical sciences for the betterment of mankind, and become the application of all science, including both the physical and life sciences, for the betterment of humanity.

REFERENCES

1. Anderson, E. H., Hagood, N. W., Goodliffe, J. M. "Self-Sensing Piezoelectric Actuation: Analysis and Application to Controlled Structures" AIAA Paper No. 92-2645, Presented at the 33rd AIAA . Structures, Structural Dynamics, and Materials Conference Dallas, TX, April, 1992.

2. Andersson, M. S., Crawley, E. F., "Discrete Shaped Strain Sensors for Intelligent Structures", AIAA Paper 92-2406, Presented at the 33rd SDM Conference, Dallas, TX, April 13-15, 1992.

3. Aubrun, J. N., "Theory of the Control of Structures by Low-Authority Controllers" *J. Guidance and Control*, Vol. 3 No. 5 pp. 444-451, Sept.-Oct 1980.

4. Baz, A., Iman, K. and McCoy, J. "The Dynamics of Helical Shape Memory Actuators" *J. of Intell.*

Mater. Syst. and Struct. Vol. 1, No. 1, January 1990.

5. Blackwood, G. H., Ealey, M. A., "Characterization of Electrostrictive Behavior in Lead Magnesium Niobate (PMN) Actuators at Low Temperatures" to appear in *Ferroelectrics*, January 1993.

6. Burke, S. E., Hubbard, J. E., Jr. "Spatial Filtering Concepts in Distributed Parameter Control" *J. of Dynamic Systems, Measurement, and Control*, Vol. 112 565-573, December 1990

7. Clark, R. L., Fuller, C. R., "Control of Sound Radiation with Adaptive Structures", *J. of Intell. Mater. Syst. and Struct.*, Vol. 2, pp. 431-452. July 1991.

8. Collins, S. A., Miller, D. W., von Flotow, A. H., "Distributed Sensors as Spatial Filters in Active Structural Control" submitted to *Journal of Sound and Vibration* .

9. Crawley, E. F., Anderson, E. H. "Detailed Models of Piezoceramic Actuation of Beams" *J. of Intelligent Material Systems and Structures*, Vol. 1, No. 1, Jan. 1990, pp. 4-25.

10. Crawley, E. F.., de Luis, J., "Use of Piezoelectric Actuators as Elements of Intelligent Structures," *AIAA Journal*, Vol. 25, No. 10, October, 1987, pp 1373-1385.

11. Crawley, E. F., Lazarus, K. B., "Induced Strain Actuation of Isotropic and Anisotropic Plates" *AIAA Journal*, Volume 29, Number 6, pp. 944-951, June 1991.

12. Cross, E. L., "Polarization Controlled Ferroelectric High Strain Actuators", *J. of Intell. Mater. Syst. and Struct.*, Vol. 2, pp. 241-260, July 1991.

13. Dosch, J. J., Inman, D. J., Garcia, E., "A Self-Sensing Piezoelectric Actuator for Collocated Control" *J. of Intell. Mater. Syst. and Struct.* Vol. 3 No. 1 pp. 166-185, January 1992.

14. Ealey, M. A., "Actuators: Design Fundamentals, Key Performance Specifications, and Parametric Trades", Proc. of the SPIE Conference on Active and Adaptive Optical Systems, 15433-32 (1991)

15. Fanson, J. L. Blackwood, G. H., and Chu, C-C., "Active -Member Control of a Precision Structure, " AIAA/ASME/ASCE/AHS 30th Structures, Dynamics, and Materials Conference, April 1989.

16. Fanson, J. L., Chu, C., Lurie, B. J., Smith, R. S., "Damping and Structural Control of the JPL Phase 0 Testbed Structure" *J. of Intell. Mater. Syst. and Struct.*, Vol. 2, pp. 281-300, July 1991.

17. Fuller, C. R., Gibbs, G. P., Silcox, R. J., "Simultaneous Active Control of Flexural and Extensional Waves in Beams", *J. of Intell. Mater. Syst. and Struct.* Vol 1. pp. 235-247, April 1990.

18. Hagood, N. W., Chung, W. H., von Flotow, A., "Modelling of Piezoelectric Actuator Dynamics for Active Structural Control", *J. of Intell. Mater. Syst. and Struct.* Vol. 1 pp. 327-354, July 1990.

19. Hagood, N. W., von Flotow, A., "Damping of Structural Vibrations with Piezoelectric Materials and Passive Electrical Networks" *J. of Sound and Vibration* (1991) 146 (2), 243-268.

20. Hall, S. R., Crawley, E. F., How, J. P., Ward, B. "Hierarchic Control Architecture for Intelligent Structures" *J. Guidance*, Vol 14., No. 3, pp. 503-512, May-June 1991.

21. How, J. P., Hall, S. R., "Local Control Design Methodologies for a Hierarchic Control Architecture" Presented at the Guidance, Navigation and Control Conference, New Orleans Aug. 12-14, 1991

22. Kashiwase, T., Tabata, M., Tsuchiya, K., Akishita, Sadao "Shape Control of Flexible Structures" *J. of Intell. Mater. Syst. and Struct.*, Vol. 2 - pp. 110-125 January 1991.

23. Lazarus, K. B., Crawley, E. F., "Multivariable High-Authority Control of Plate-like Active Structures", AIAA Paper No. 92-2529, Presented at the 33rd AIAA Conference on Structures, Structural Dynamics, and Materials, Dallas, TX, April 1992.

24. Lee, C. K., Moon, F. C., "Modal Sensors/Actuators", *J. of Applied Mechanics*, Vol. 57, pp. 434-441, June 1990.

25. Lee, C.-K, O'Sullivan, T. C., Chiang, W. -W, "Piezoelectric Strain Rate Sensor and Actuator Designs for Active Vibration Control"

26. Lee, C.-K, O'Sullivan, T. C., Chiang, W. -W, "Piezoelectric Modal Sensors and Actuators Achieving Critical Active Damping on a Cantilever Plate" 30th AIAA/ASME/ASCE/AHS Structures, Structural Dynamics, and Materials Conference, Mobile, Alabama, April 1989.

27. Liang, D., Rogers, C. A., "One-Dimensional Thermomechanical Constitutive Relations for Shape Memory Materials" J. of Intell. Mater. Syst. and Struct., Vol. 1, No. 2,. pp. 207-234, April 1990.

28. Lindner, D. K., Reichard, K. M., Baumann, W. T., Barsky, M. F., "Measurement and Control of Flexible Structures Using Distributed Sensors" Presented at the 29th Conference on Decision and Control, Honolulu, Hawaii, December 1990.

29. MacMartin, D. G., Hall, S. R., "Control of Uncertain Structures Using an H• Power Flow Approach" *J. Guidance* Vol. 14. No. 3, May-June 1991 pp. 521-530.

30. MacMartin, D. G., Miller, D. W., Hall, S. R. "Structural Control Using Active Broadband Impedance Matching" Conference on Recent Advances in Active Control of Sound and Vibration, Virginia Polytechnical Institute and State University, Blacksburg, VA, April 1991.

31. Miller, D. W., Collins, S. A., Peltzman, S. P., "Development of Spatially Convolving Sensors for Structural Control Applications" Proceedings of the AIAA/ASME/ASCE/AHS 31st Structures, Structural Dynamics, and Materials Conference, Long Beach, CA, April 2-4, 1990, pp. 1899-1906.

32. Miller, D. W., Hall, S. R., "Experimental Results Using Active Control of Traveling Wave Power Flow" *J. of Guidance, Control, and Dynamics*, Volume 14, Number 2, Pages 350-349, March-April 1991.

33. Miller, D. W., Hall, S. R., von Flotow, A. H., "Optimal Control of Power Flow at Structural Junctions" *J. of Sound and Vibration*, 140 (3), pp. 475-497, (1990).

34. Newnham, R. E., Ruschau, G. R., "Smart Electroceramics" *J. Am. Ceram. Soc.* 74[3] 463-80 1991.

35. Newnham, R. E., Safari, A., Giniewicz, J., Fox, B. H., "Composite Piezoelectric Sensors" *Ferroelectrics*, Vol. 60, pp. 15-21, 1984.

36. Nishimura, I., Abdel-Ghaffar, A.M., Masfri, S. F., Miller, R. K., Beck, J. L.., Caughey, T. K., Iwan, W. D., "An Experimental Study of the Active Control of a Building Model" *J. of Intell. Mater. Syst. and Struct.*, Vol. 3, No. 1, pp. 134-165, January 1992.

37. Pan, J., Hansen, C. H. Synder, S. D., "A Study of the Response of a Simply Supported Beam to Excitation by a Piezoelectric Actuator" *J. of Intell. Mater. Syst. and Struct.* Vol. 3 pp. 3-16, January 1992.

38. Rubenstein, S. P., Saunders, W. R., Ellis, G. K., Robertshaw, H. H., Baumann, W. T., "Demonstration of a LQG Vibration Controller for a Simply-Supported Plate"

39. Seki, H., "Piezoelectric Bimorph Micrograpper Capable of Force Sensing and Compliance Adjustment" 1992 Japan-USA Symposium on Flexible Automation.

40. Sirkis, James S., Haslach, Henry, W. Jr. "Complete Phase-Strain Model for Structurally Embedded Interferometric Optical Fiber Sensors", *J. of Intel. Mater. Syst. and Struct.*, Vol. 2-pp. 3-24 January 1991.

41. Takagi, T. "A Concept of Intelligent Materials", *J. of Intell. Mater. Syst. and Struct.*, Vol. 1 pp. 149-156, April 1990.

42. Turner, R. D., Valis, T. Hogg, W. D., Measures, R. M., "Fiber-Optic Strain Sensors for Smart Structures", *J. of Intell. Mater. Syst. and Struct.*, Vol. 1, pp. 26-49, January 1990.

43. Wada, B. K., Fanson, J. L., Crawley, E. F., "Adaptive Structures", *J. of Intell. Mater. Syst. and Struct.*, Vol. 1, pp. 157-174, April 1990.

44. Waller, D. J., Safari, A. "Lead Zirconate Titanate Fiber/Polymer Composites Prepared by a Replication Process" J. Am. Ceram. Soc. 73 (11) 3503-506 pp. (1990)

45. Warkentin, D. J., Crawley, E. F., "Prospects for Electronic Component Distribution in Intelligent Structures" Presented at the ADPA/ AIAA/ ASME/SPIE/ Conference on Active Materials and Adaptive Structures, November 1991, Alexandria, VA.

46. Warkentin, D. J.., Crawley, E. F.., Senturia, S. D. "The Feasibility of Embedded Electronics for Intelligent Structures," AIAA paper No. 91-1084, *Journal of Intelligent Material Systems and Structures*, Vol. 3, pp. 462-482, July 1992.

Table 1. Comparison of strain sensors

	PZT G-1195	PVDF	PMN	TERFENOL DZ	NITINOL
Actuation Mechanism	piezoceramic	piezo film	electrostrictor	magnetostrictor	shape alloy
Λ_{max}, μstrain	1000	700	1000	2000	20000
E, Msi	9	0.3	17	7	4 (m), 13 (a)
ε_{max},* μstrain	350	10	500	580	8500 (a)
bandwidth	high	high	high	moderate	low

* for a sheet of actuator bonded to aluminum beam (ts/ta=10) in bending assuming AC value of Λ

(m) = martensite (a) = austenite

Table 2. Comparison of actuation strain materials

	foil [a]	semiconductor [a]	fiber [b]	piezo film [c]	piezoceramic [c]
sensitivity	30 V/ε	1000 V/ε	10^6 °/ε	10^4 V/ε	$2x10^4$ V/ε
localization, in	0.008	0.03	~0.04	<0.04	<0.04
bandwidth	DC - acoustic	DC - acoustic	~DC - acoustic	~0.1 Hz - GHz	~0.1 Hz - GHz

a) 10 V excitation

b) 0.04 in interferometer gauge length

c) 0.001 in sensor thickness

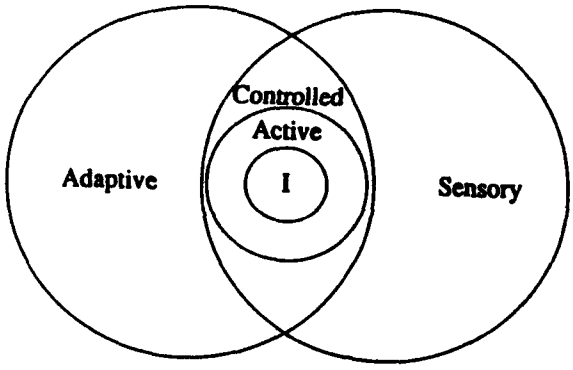

Figure 1. Intelligent Structures as a subset of active and controlled structures [Ref. 43]

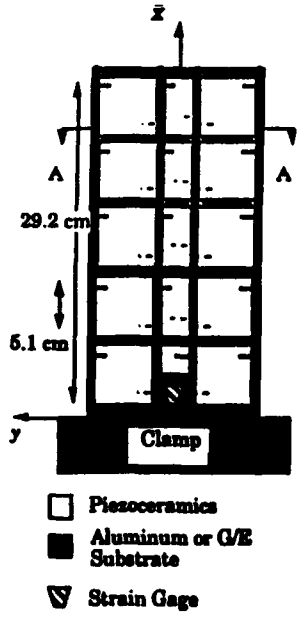

Figure 2. Active aeroservoelastic wing [Ref. 23]

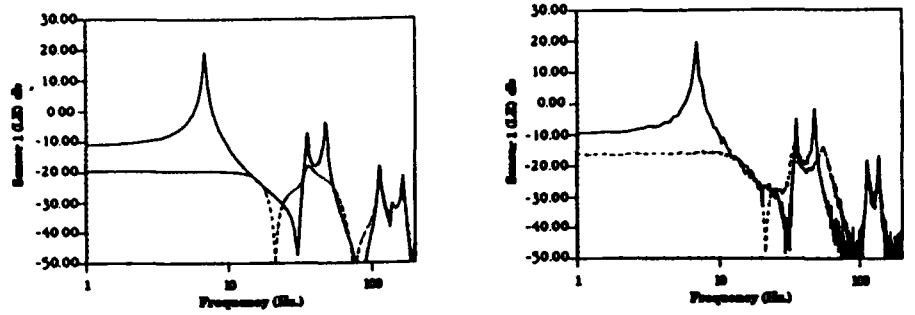

Analytical Prediction

Experimental Result

Figure 3. Comparison of the analytical prediction and experimental results of the open (solid) and closed loop (dashed) for bench top testing of the active wing [Ref. 23]

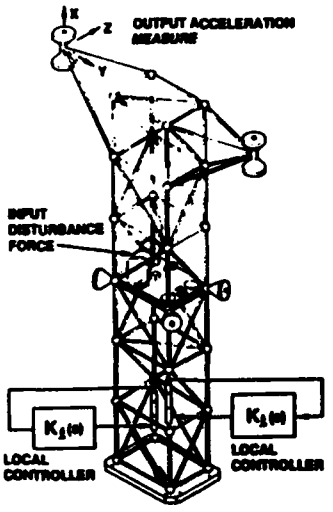

Figure 4. Precision truss with dial-a-strut [Ref 16]

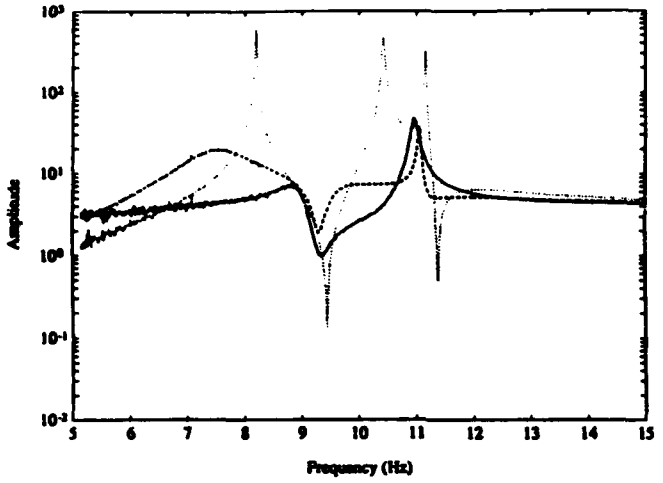

Figure 5. **Open loop (dotted) vs. closed loop for one (dashed) and two (solid) Dial-a-Struts [Ref 16]**

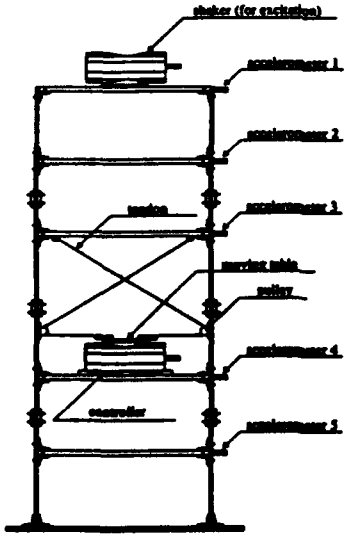

Figure 6. **Building model for controlled seismic response [Ref 36]**

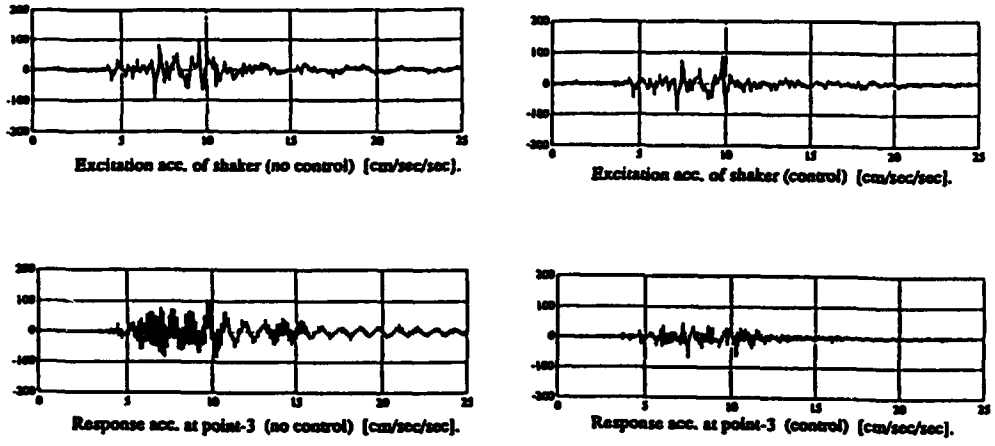

Figure 7. **Comparison of open and closed loop response of mid-building accelerometer under simulated seismic excitation [Ref 36]**

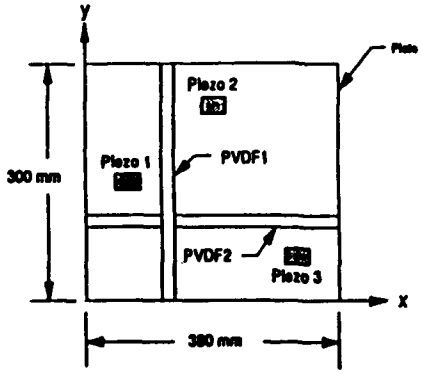

Figure 8. **Actively controlled panel for control of sound radiation [Ref 7]**

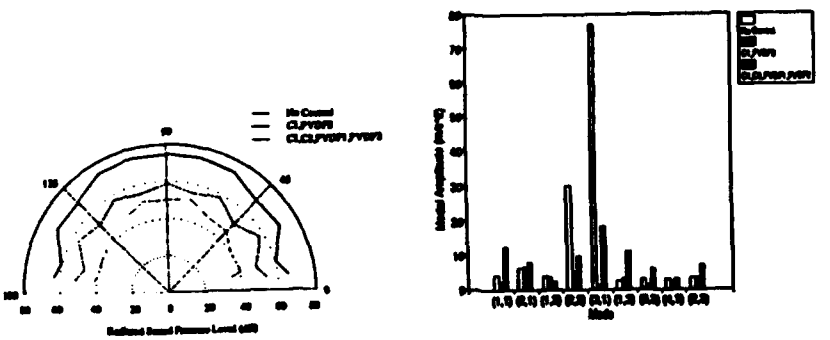

Figure 9. **Spatial distribution and frequency content of radiated sound with no control and two arrangements of control actuators and sensors [Ref 7]**

The Satellite Attack Warning and Assessment Flight Experiment (SAWAFE)

Michael Obal, Bill Saylor, Hugh S. Murray, Martin R. Sweet, Dan Holden and Calvin Moss
SDIO/TNI
The Pentagon
Washington, DC 20301-7100
USA

1. SUMMARY

A program to develop an advanced satellite health and status monitoring subsystem for detecting and discriminating hostile threats is described. The threats considered are laser, radio frequency and x-rays. The subsystem uses lightweight electronics and sensors that are imbedded in the satellite structure to minimize the integration impact on the host satellite. The novel sensor materials are described. The first of a series of flight experiments is also described.

2. INTRODUCTION

To accomplish the mission of GPALS in a cost effective manner will require real time mission monitoring and control capabilities beyond what is currently available. Essential to this task may be the requirement for sophisticated on orbit health and diagnostics systems that can supply real time higher order processed information on the status of each satellite element. This information would then provide the national command authorities with a continuous estimate of the weapon system's effectiveness.

One critical area of on orbit health monitoring is the identification and warning of tampering or attack on constellation satellite elements. As satellites in the constellation fail, the nature of the failure must quickly be determined. If analysis of the failure indicates tampering or attack, the constellation damage can be minimized by initiation of appropriate actions. Timely identification of tampering and attack may also provide early warning of a ballistic missile attack. The validity of attack threats to space assets is currently a major debate within the threat definition community given today's rapidly evolving global political environment. Though not the purpose of the paper to enter into this debate, it is the hypothesis that the proliferation of commercial lasers, sophisticated RF sources and nuclear technology make such threats to space assets in the next decade probable. Given this evolving threat environment, demonstrating to the SDIO space system programs that a reliable threat detection subsystem can be developed that will enhance the overall cost effectiveness of constellation management is of value.

Concepts involving attack warning for satellites have evolved over a number of years as the tactical and strategic military value of satellite surveillance and communication systems has increased. One Air Force project known as the Satellite On-orbit Attack Reporting System (SOARS) examined many aspects of satellite attack warning but, due to funding issues, is currently undergoing a reexamination of the original program goals. The SOARS system was not intended for SDIO type space assets since its sensors and support avionics were not constrained to meet the minimum required weight and power goals.

The Satellite Attack Warning and Assessment Flight Experiment (SAWAFE) is an SDIO/TNI funded project that will develop and demonstrate this particular critical component of a viable on-orbit health monitoring system. The technology goals are to define the nature of an attack (where, what physical means, intensity, etc.), provide awareness of tampering with the space platform or its primary sensors, and provide collateral information for failure analysis. Though similar to SOARS, SAWAFE aims to demonstrate a variety of new technologies such as "smart or sensory skins" to meet the required minimum weight and power goals. Of particular concern relevant to space assets is the ability to detect radio-frequency, laser and nuclear attacks against the satellite.

The approach taken in the SAWAFE program is to design a system that minimizes impact on the host satellite through the use of miniature sensors and low power and mass sensor conditioning and processing avionics. To achieve minimum system weight and power goals, all portions of a "typical" satellite structure were examined for sensor surface area and avionics volume. After a

variety of trades, the area selected was the outer surface structure of the satellite which usually consists of aluminum honeycomb sandwich panels with protective multilayer insulation. The term "smart or sensory skin" is used to define such an external structural member that not only carries load and provides thermal protection, but contains within it's volume a variety of sensors and avionics. Embedding the sensors into the volume thickness of a typical panel rather than as an additional avionic component provides a variety of system advantages such as: reduced avionic subsystem container parasitic weight, the elimination of antenna deployment mechanisms, decreased satellite response settling time during high slew rate maneuvers by reduced antenna appendages, and easier packing of multiple satellites in a launch vehicle.

Some of the design and development issues identified in using a sensory skin concept are: the EMI interaction between the widely differing sensors and supporting avionics, the thermal control and balance of the panel and as well as the overall system, the survivability of the sensors and avionics during launch when the panel is experiencing maximum load, sensor degradation in the space environment, and definition of a ground maintenance and test concept prior to launch. The SAWAFE program is a flight test intensive research program developed to investigate these issues.

The first generation SAWAFE is scheduled for a FY1994 launch on the US Air Force Space Test Program STEP 3 mission and will concentrate on demonstrating the space survivability and operability of "smart skin" laser, x-ray and RF sensors. The hardware will consist of an integrally mounted panel with embedded sensors and a separate electronics box used to control the experiments and collect data for transmission to the ground. The experiment will be an autonomous, high data rate payload that operates completely independently of the spacecraft computer. The sensor panel itself will be a structural member of the STEP 3 satellite.

During the mission, RF, laser, and x-ray sensor experiments will be conducted to measure sensor backgrounds in space and validate the sensor performance goals. The demonstration of data fusion and advanced signal extraction techniques will initially occur on the ground.

The SAWAFE system will draw heavily on other DoD/DOE-funded technology development. SAWAFE represents a significant advance in embedding a broadband RF antenna into a structural component of a spacecraft. The laser detector technology is the first space application of laser detectors developed for tactical DoD systems. The x-ray detector is an outgrowth of the advanced technology development for nuclear detonation, detection, and characterization. The use of fiber optic or CCD arrays, surface-mounted on a spacecraft to detect and characterize the x-ray fluence from a nuclear detonation, represents the next generation of detector technology. An attack recognition processor (ARP) is an extension of the adaptive event classification hardware and software being developed for FORTE and other programs.

Extensive ground testing will be used to characterize the response of the sensors, individually and as a system, to known ground sources. However, the trans-ionospheric propagation of event signals, the on-orbit material and functional performance of the sensors, and the operation of the ARP during flight can not be validated during ground testing.

The research and development products from the SAWAFE laser, RF, and x-ray sensors and the ARP will feed into the design of attack warning and assessment (AWA) technology for operational systems. The information from SAWAFE will also be useful to other space programs for characterizing the space background environment.

3. SENSOR TECHNOLOGIES

At the start of the SAWAFE program, a critical review of sensor technologies was undertaken. Based on existing technologies and development programs in place, additional sensor development was necessary to meet the programmatic goals. The following sections describe the sensor technologies that were chosen for development.

3.1 Laser Sensor Subsystem

3.1.1 Advantages of polymer film detectors

The need for a laser attack warning sensor that can be attached to, or integrated with, the spacecraft skin and thus minimize intrusion on the spacecraft suggests the use of a pyroelectric polymer film as an infrared laser detector. A

polymer such as polyvinyldenefluoride (PVDF) is available in very large pieces (on the order of 1 m^2) and in thicknesses from less than 10 microns up to 1 mm. The variety of available sizes, shapes, and thicknesses of the primary detector medium allows for considerable flexibility in choosing detector responsitivity and placement on the spacecraft surface. The film can be attached to curved surfaces; large aperture detectors can be fabricated for wide coverage; arbitrary shapes can be formed to take advantage of available surfaces; and because of simple fabrication procedures, several detectors can be positioned at different orientations over the spacecraft skin to obtain angle of arrival information. The polymer detector has been shown to be resistant to ultraviolet and ionizing radiation.

Pyroelectric polymers have lower pyroelectric activity coefficients than ceramic and crystalline materials; however, voltage responsitivities and detectivities equivalent to those of traditional materials can be achieved with polymers by using large areas and very thin detectors. Pyroelectrics are primarily transient radiation detectors. Their responses are greatly attenuated for temporal variations slower than the thermal time constant of the detector. Excellent rejection of low frequency variations in background radiation is achieved because of the low frequency attenuation. In space, where radiative losses dominate the thermal time constant, the thermal time constant is quite long, so that the frequency response covers a reasonably wide range. The high frequency cutoff of the pyroelectric response depends upon the detector capacitance and load resistance.

3.1.2 Comparison of thermal detectors

Thermal detectors such as pyroelectrics are inherently much less sensitive than photoconductive detectors. Thermal detectors, however, have a broad spectral response; they require very little power for operation; they are rugged, survivable, and easy to fabricate. The objectives of the SAWAFE system are to provide a non-intrusive sensor system and to provide a thermal sensor system with substantially improved performance compared to other thermal sensor systems. These objectives are accomplished by using pyroelectric polymers and solid-state/metal thermocouple junctions (Si/Au) to obtain good sensitivity and wide frequency response. Figure 1 compares the polymer/solid-state thermocouples with a low mass Type-K thermocouple junction previously developed for attack waning. For continuous wave (CW) response, the SAWAFE sensor is significantly more sensitive than the low mass Type K junctions, due to the larger Seebeck coefficient in the semiconductor/metal junction.

The polymer detector unit provides high transient responsitivity at input frequencies in the kilohertz range. The high rate is due to the extremely low mass heat capacity of the thin film and this rate is many times faster than that of a low mass thermocouple.

3.1.3 SAWAFE laser sensor concept

For an integrated skin sensor, multiple layer coatings can be deposited on the polymer to provide selective absorption at specific wavelengths of approximately quarter-wave layers of titania, alumina, and nickel. Figure 2 is an example of a typical mounting for a flight experiment. Different combinations of coatings show absorption peaks over a wide range of infrared wavelengths (Figure 3). Several of these coated polymer detectors were exposed on the STS-46 Space Shuttle EOIM-3 atomic oxygen test in July, 1992 to verify survivability of the polymer and coatings in low earth orbit. With coatings and electrodes, a polymer detector is approximately 10 microns thick. Electronics for preamplification is provided by surface mounted packages on flexible printed circuit board substrates to maintain conformability.

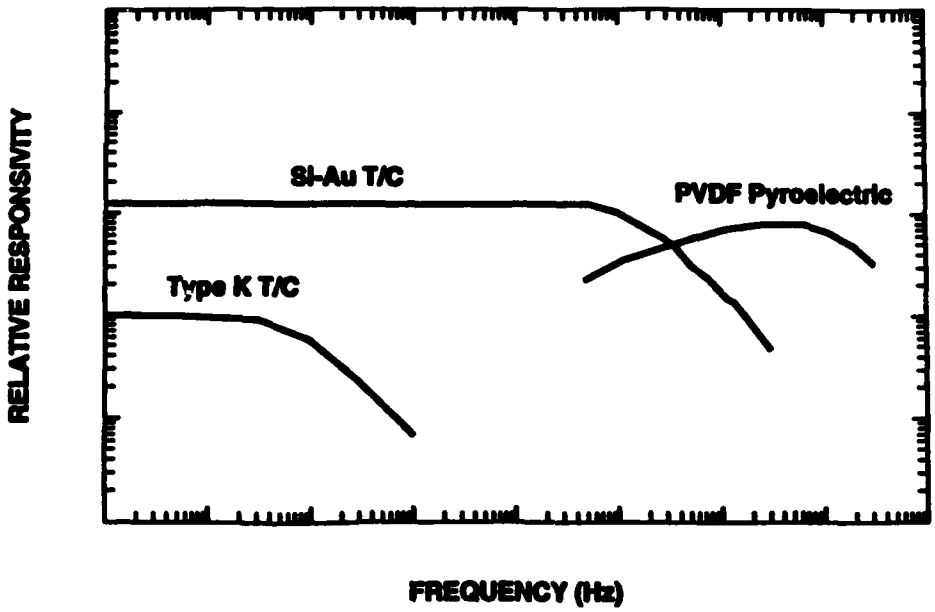

Figure 1. Comparison of polymer and solid state thermoplastics with low mass type-K thermocouple junction.

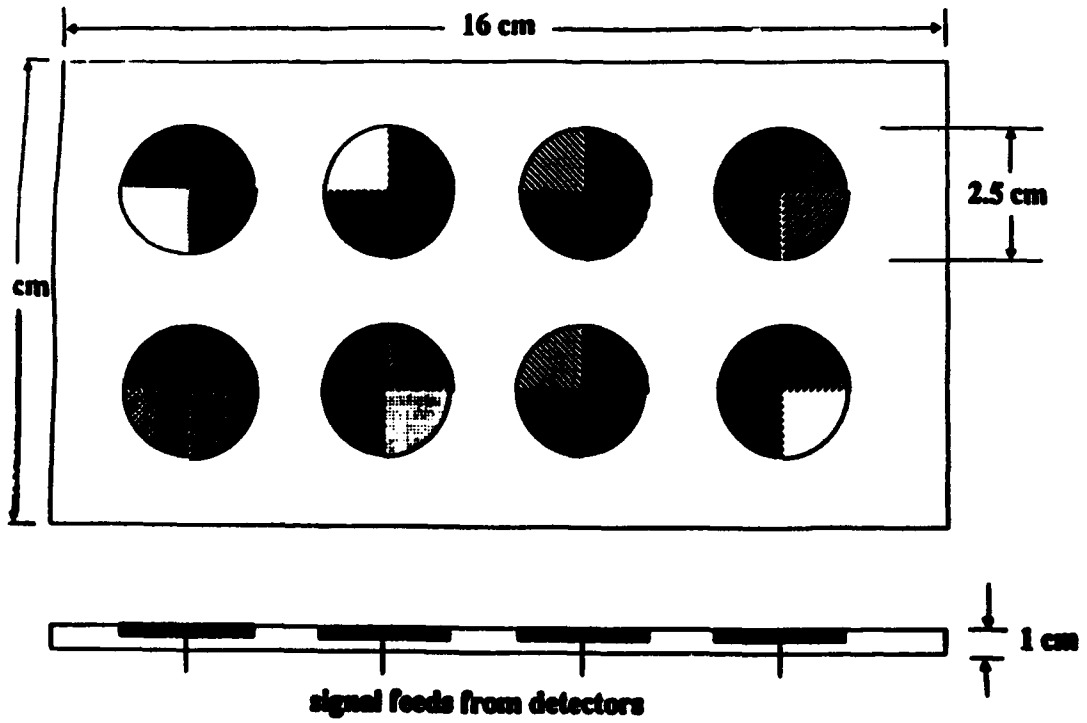

Figure 2. Laser sensor mounting options.

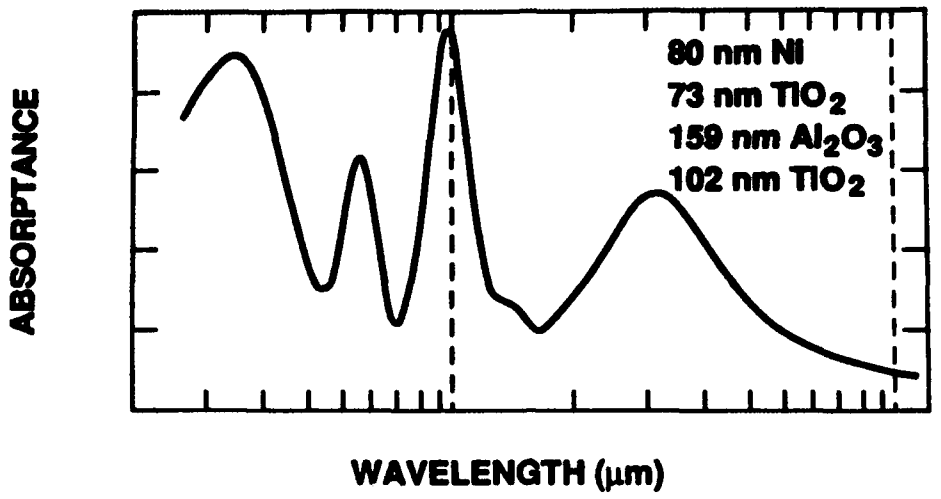

Figure 3. Typical performance of a laser detector given a combination of absorption coatings.

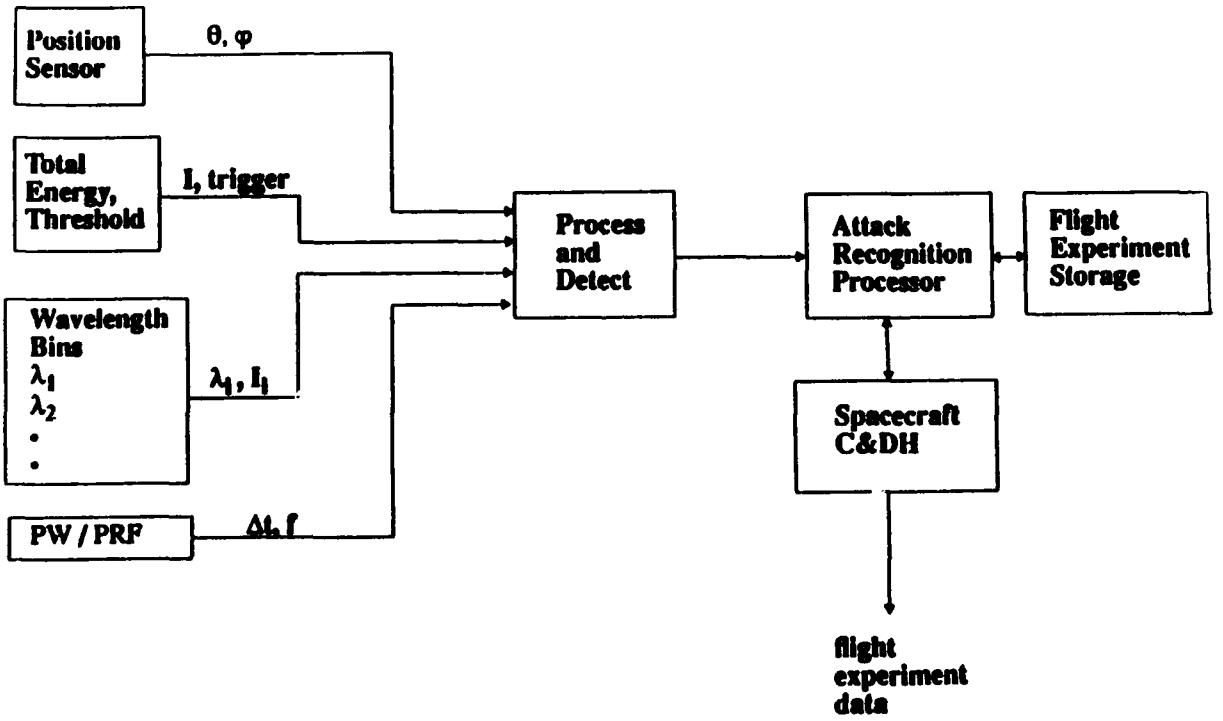

Figure 4. STEP-3 laser sensor experiment block diagram.

3.1.4 STEP-3 detectors
The STEP-3 flight is a near term test of SAWAFE laser sensor capabilities. The STEP-3 sensor system will be made of seven detectors. Five sensors consist of small disks of PVDF film on printed circuit boards (PCB) with surface-mount preamplifiers on the inner surface. Three of the disks will be covered with discrete interference filters to select specific wavelengths. One disk will be a broadband absorber, and one disk will be shielded from optical inputs to provide common mode rejection of nonoptical stimulation. The remaining two detectors will be Si/Au thermocouples to provide CW response indication. This modular detector approach allows for placing the detectors on the test panel wherever space is available, and to allow for testing the basic capability of the polymer sensor system using standard filters. Figure 4 is a schematic of the STEP 3 laser detector system.

3.2 RF Sensor Subsystem

The requirements for the RF threat sensor subsystem demand that it functions as a modern electronic support measures (ESM) system and yet be contained within the skin of the spacecraft. The resulting geometric configuration, mass, power, and environmental constraints for a minimum impact on spacecraft applications are significantly different from most ESM implementations. The signal environment is also quite different from conventional applications.

The need for broadband frequency coverage, at least one decade per antenna, with as wide as possible a field of view leads to the use of multi-arm spiral antennas. Because of thickness constraints on the integrated sensor panel, a resonant cavity design was not selected. The antenna must also be mounted on the electromagnetic exterior of the spacecraft with the choice of mounting substrate used based on a trade-off among mechanical, thermal , and electromagnetic properties. For example, high dielectric constant materials that would enhance antenna performance when used in thick enough configurations impose a significant mass penalty. For the STEP-3 flight experiment, the available space is limited to an 8 inch by 11 inch area.

The antenna design is placed on the surface of the substrate through the use of either adhesives, physical vapor deposition, or chemical vapor deposition processes. Depending on the material used, the exterior surface of the antenna may also require protection from atomic oxygen attack. Because of spacecraft charging phenomena, the antenna must have a resistive coating to allow for a continual charge bleedoff.

The technologies used in the receiver must be able to be miniaturized and reduced in power consumption for them to be further developed for spacecraft "smart skin" applications. The receiver used for the STEP-3 flight experiment is a compressive design which (Figure 5) includes several wide band receiver channels with detector circuits for pulse parameter estimation. Digital logic in the receiver estimates the parameters of the signal. The data are then used by the attack recognition processor to perform the signal characterization.

3.3 X-ray Sensor Subsystem

The purpose of the nuclear detonation (NUDET) detector in the satellite attack warning and assessment suite of sensors is to detect a NUDET that poses a threat to a satellite element or constellation area, and to determine the dose received by the particular host spacecraft.

Several detector types have been considered for the SAWAFE program. Silicon photodiodes have high sensitivity, small size, good linearity, provide fast signal timing for geolocation, and are moderately radiation hard. However, they are sensitive to electrostatic discharge and charged particles, they must be operated in a coincidence mode to prevent false alarms, and require multiple sensors with filters to measure the x-ray spectrum. The combination of scintillators and photodiodes also provides a detectors technology with good linearity, small size, and high sensitivity. However, it has a slow rise time (when used with an inorganic scintillator), is sensitive to electrostatic discharge and charged particles, requires multiple filters for spectral measurements, and requires multiple detectors for false alarm rate reduction. "High Z" sensors (e.g., CdTe, HgI_2, GaAs) share similar advantages and disadvantages. Thermal-based sensors (microcalorimeters) offer very high sensitivity and energy resolution, but require cooling to very low temperatures and have slow rise times.

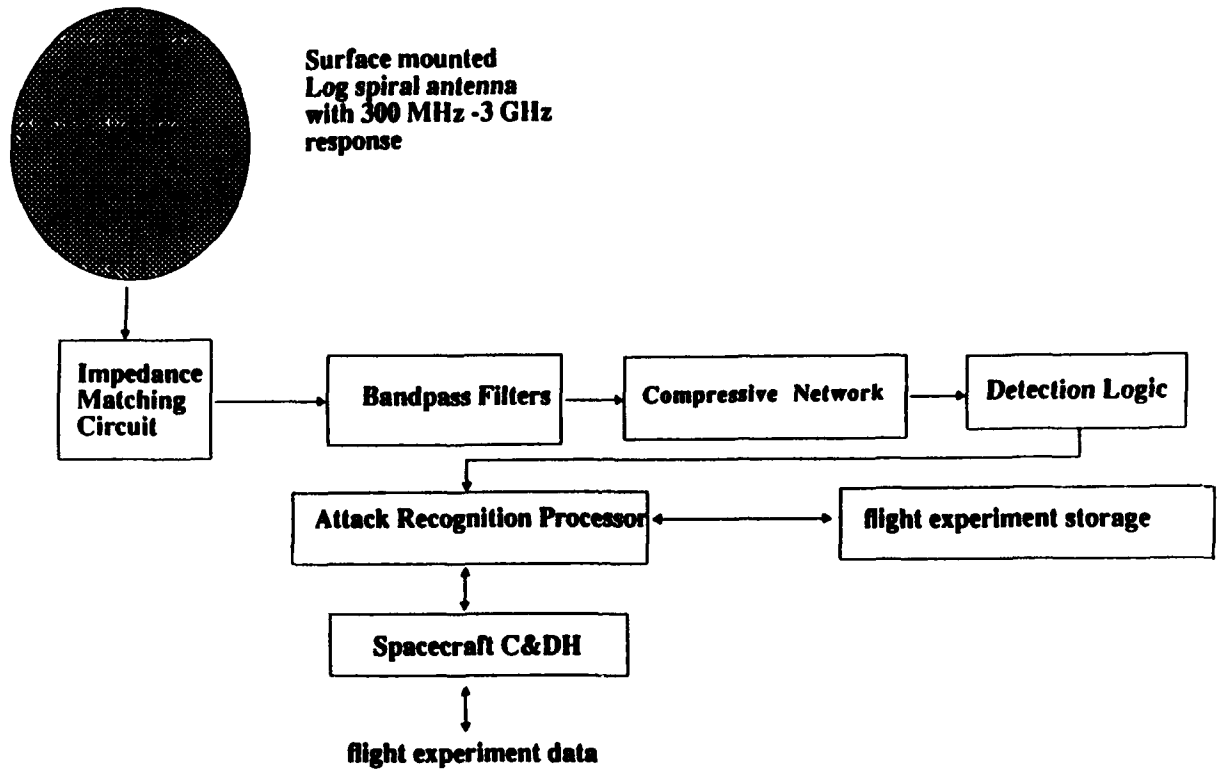

Figure 5. SAWAFE RF receiver exeperiment block diagram for STEP-3 flight experiment..

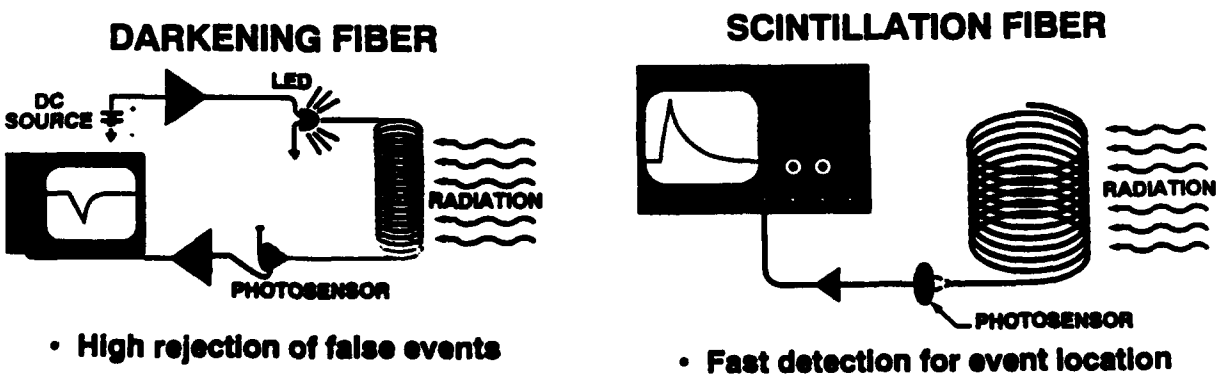

Figure 6. SAWAFE NUDET sensors for STEP-3 flight experiment..

The two technologies being developed under the SAWAFE program are charge-coupled detectors (CCDs) and fiber optics. The CCDs offer long term potential for a skin-mounted sensor that provides a direction vector to the source, high energy resolution, and can be implemented in a geometry that protects the sensor from radiation damage. However, the CCDs require cooling to -50° C and have a relatively slow response to multiple events.

Two types of fiber optics have been developed. Glass darkening fibers that have changes in their optical transmission properties when exposed to x-ray radiation are used in conjunction with light emitting diodes (LEDs) to measure received dose. The darkening occurs on the order of a few microseconds and the recovery time can be adjusted from microseconds to years as a function of the chemical composition of the fiber. The scintillation fiber is based on the same principle as an ordinary scintillator sensor but with important differences due to the geometry. The scintillating fiber is on the exterior of the spacecraft and the readout electronics can be on the inside of the spacecraft.

On the STEP-3 flight experiment, both darkening and scintillating fibers will be mounted on the surface of the RF antenna on the exterior of the sensor panel. (Figure 6) The fiber optics must be protected from atomic oxygen attack and spacecraft discharge with a coating thin enough to not attenuate the x-ray signals. The coating cannot be a highly conductive material, such as vapor deposited aluminum, because it will be placed over the RF antenna.

4. STEP-3 MISSION

The STEP-3 mission is a U.S. Air Force Space Test Program flight to provide a platform for several technology demonstration experiments. The satellite used as host platform is a small TRW/DSI satellite that will be launched from a Pegasus into low earth orbit between 30 to 60 degrees inclination. The SAWAFE hardware flown on this mission consists of an exterior panel (Figure 7) with embedded sensors and an internal avionics box that will run the experiments, collect data, and interface with the STEP-3 spacecraft computer.

4.1 Experiment Objectives

The primary objectives of the SAWAFE hardware and software on the STEP-3 mission are to demonstrate the functional operation and space survivability of the three sensor types, laser, RF, and x-ray, when mounted on an exterior spacecraft panel in low earth orbit. (Figure 8) Experiments will be conducted to measure the performance of the sensors and prototype signal detection circuitry. The sensors will collect significant amounts of data during the mission that will be used to characterize the natural and man-made background signals.

The sensors will each collect data for an entire orbit. Statistics will be generated to determine the signal background as a function of orbit location, time of day, and time of year. This information provides a basis for designing the follow-on SAWAFE systems. Other calibration experiments will also be performed to measure the absolute performance of the sensors in space as a function of time.

For most experiments, data from the sensor will be written into the FIFO (first in, first out) buffers on the instrument subsystem and transferred to the SAWAFE processor and solid-state data recorder (SSDR). At the start of the experiment, the raw data will be collected and passed through the ground station to the experimenters. The raw data will be used to generate signal identification algorithms that will distinguish among natural and man-made background signals and simulated threat signals.

4.2 Panel Design

The panel with the embedded SAWAFE sensors has three design objectives. First, the panel is to be a structural, load-bearing member of the host spacecraft. Second, the SAWAFE panel will have the various sensors mounted in a realistic configuration that is representative of potential applications of the developed technologies. Third, the panel design will have minimal impact on the spacecraft thermal or mass balance properties.

The final panel design and sensor layout represents a compromise among the design goals, the sensor mounting requirements, and the available space. The panel consists of a layer of Lockheed high thermal performance (HTP) insulation which is a rigid, composite fiber,

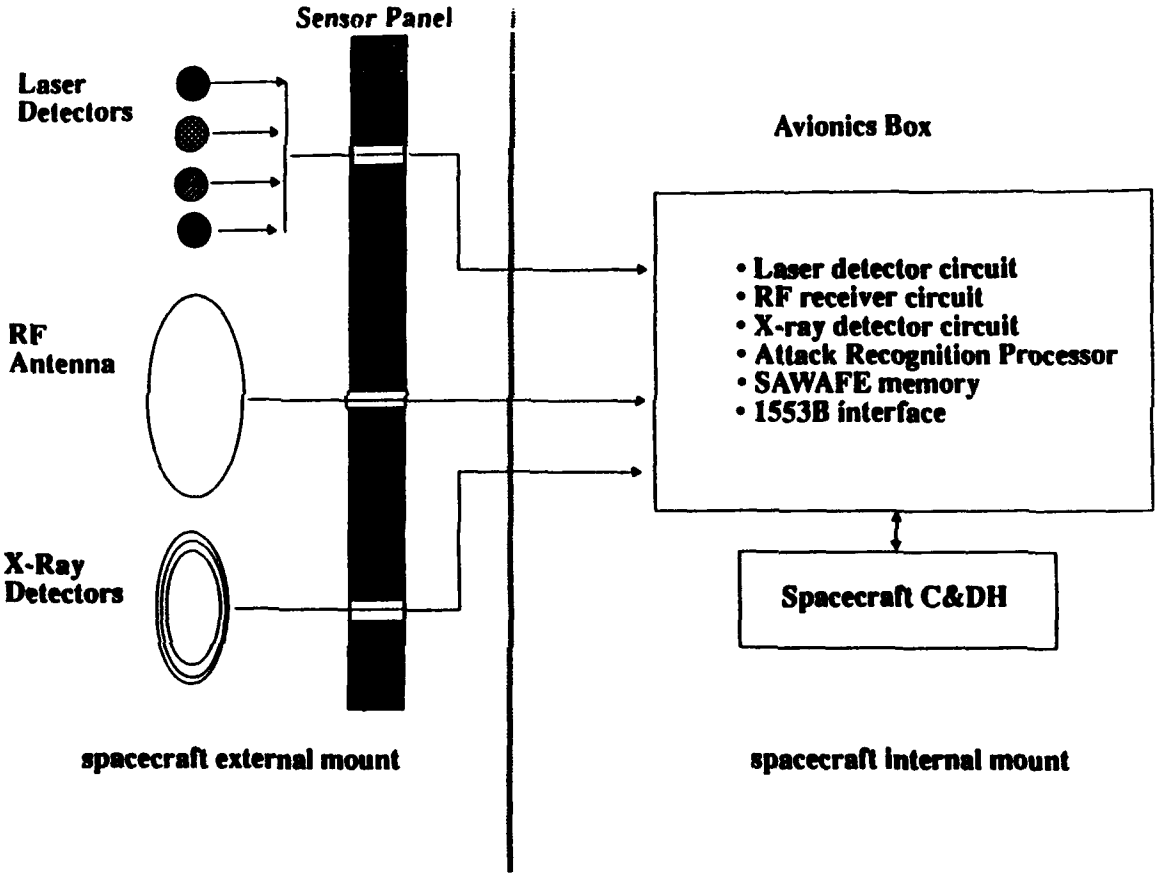

Figure 7. SAWAFE system layout for STEP-3 flight experiment.

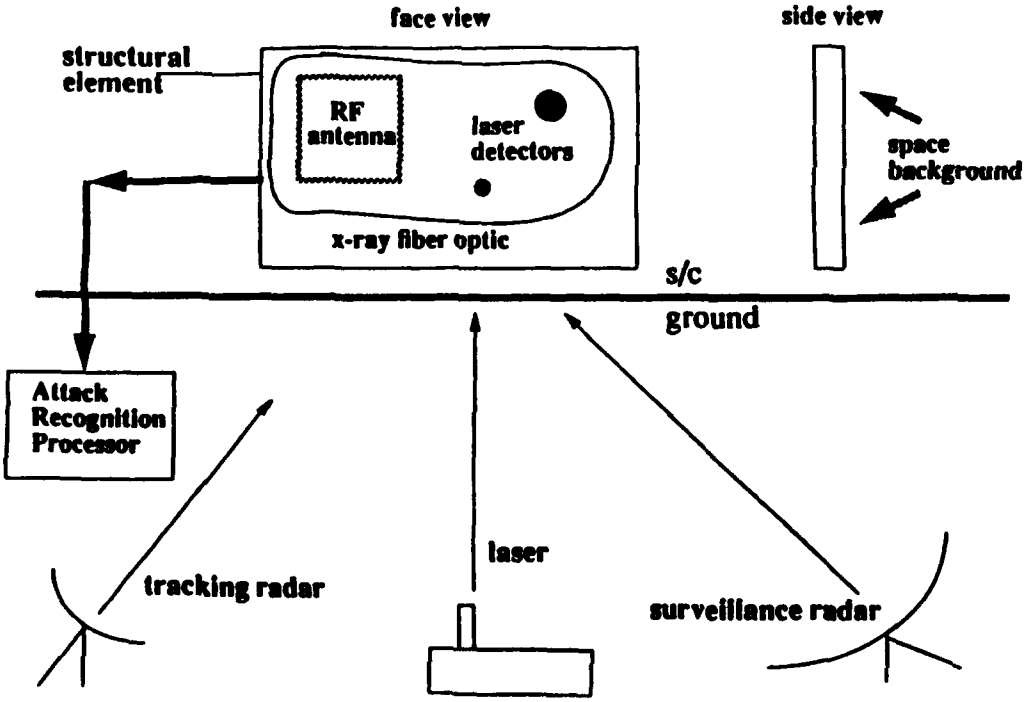

Figure 8. SAWAFE experiment concept for STEP-3 flight experiment.

ceramic insulation material based on the tiles developed for the Shuttle Transportation System. The HTP material has low density and dielectric constant.

The substrate is mounted on a 0.032 inch thick piece of aluminum plate that has dimensions of approximately 9 inches by 12 inches. The HTP is 8.0 inches by 10.25 inches. The HTP is attached to the aluminum plate with a layer of RTV adhesive, a layer of NOMEX felt for strain isolation, and another layer of RTV adhesive. (Figure 9)

The laser sensors are each contained within an aluminum sleeve approximately 1.25 inches in diameter. The HTP has holes machined in a pattern for the laser sensors and the laser sensors are epoxied into the holes. Because of the limited area, some of the laser sensors are placed between the arms of the spiral RF antenna. (Figure 10) Testing has shown that there is negligible impact on the antenna electromagnetic characteristics with this mounting configuration. The two-arm, spiral antenna for the STEP-3 panel will be attached to the surface of the HTP. The scintillating fiber and the darkening fiber will be wound into single layers and attached to the surface of the antenna with adhesive. By placing the laser sensors around the outside of the panel, fiber optics lengths of several meters (scintillating fiber) and approximately one hundred meters (darkening fiber) are used. The fibers are susceptible to atomic oxygen attack and several protective coatings are being tested to determine their applicability. These coatings must be opaque (to block stray light from adding noise to the detector circuits) and can not be highly conductive - or the underlying RF antenna will be shielded.

4.3 Avionics Design

The avionics design is centered around a high speed, 32-bit RISC (reduced instruction set computer) processor that gives the STEP-3 SAWAFE a significant processing capability (10 MIPS). The avionics is designed to be completely autonomous and does not require any spacecraft intervention for experiment control. The SAWAFE CPU (central processing unit) communicates with the spacecraft CPU over a MIL-STD-1553B serial interface. The SAWAFE receives a single 28 VDC connection from the spacecraft; all internal power control is done by the SAWAFE CPU. The CPU will autonomously cycle through various sensor experiments, record subsystem sensor data in its own 32 Mbyte SSDR, process raw data as appropriate and inform the spacecraft of experiment completion.

There are five separate experiments on the STEP-3 mission and, because of power and telemetry considerations, the experimental power will be cycled on and off numerous times during the mission life. The SAWAFE CPU includes 64 kbyte of PROM that contains a compressed form of the real time operating system (RTOS). There is also 1 Mbyte of non-volatile EEPROM and 1 Mbyte of SRAM. When the spacecraft controller supples 28 VDC to SAWAFE, the SAWAFE CPU initiates a "cold boot", checks the status of the EEPROM, transfers and decompresses the RTOS kernel from PROM to EEPROM (if necessary), and performs state-of-health checks on all of the sensor subsystems.

When the hardware and software are online and operational, SAWAFE will receive the commands that have been passed up from the experimenters through the ground station. The transmitted commands will cause SAWAFE to execute any of a number of separate or integrated sensor experiments.

The mechanical design of the avionics system is based on a "slice" architecture. (Figure 11) Each slice approximately 10 inches by 9 inches by 1 inch thick and is comprised of an exterior metal frame and two PCBs. The frame provides structural support and thermal dissipation for the PCBs. Each slice has two mounting bolts that are used to transfer heat to the mounting plate and to attach the slice to the mounting plate. Each slice includes a connector for the 32 bit processor global bus, power, and ground connections. Each sensor subsystem is built into one or more slices. A complete avionics box is formed when the slices for that flight experiment are placed together, end plates are attached, and bolts are run from one end to the other.

This design allows for rapid prototyping and fabrication of flight experiment components. Individual subsystems can be removed or added without requiring mechanical or electrical redesign.

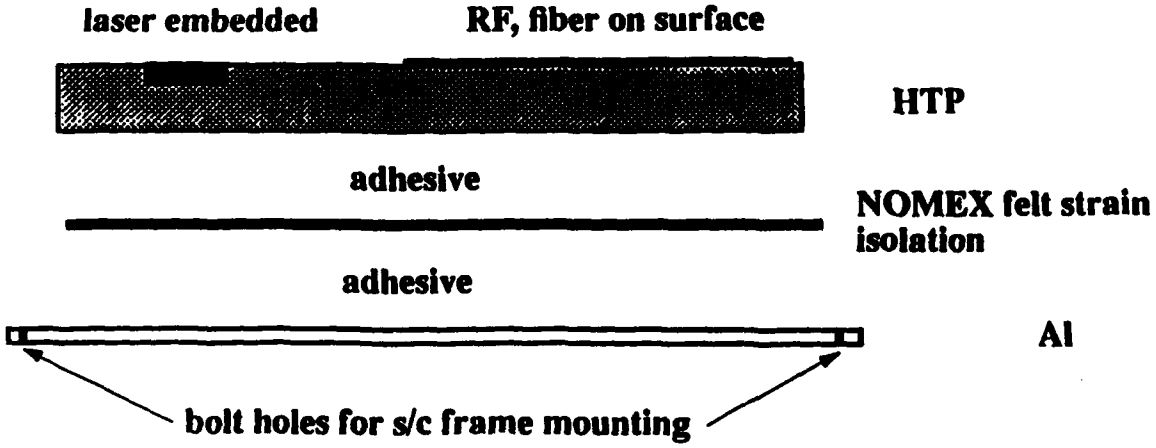

Figure 9. SAWAFE panel cross section concept for STEP-3 flight experiment.

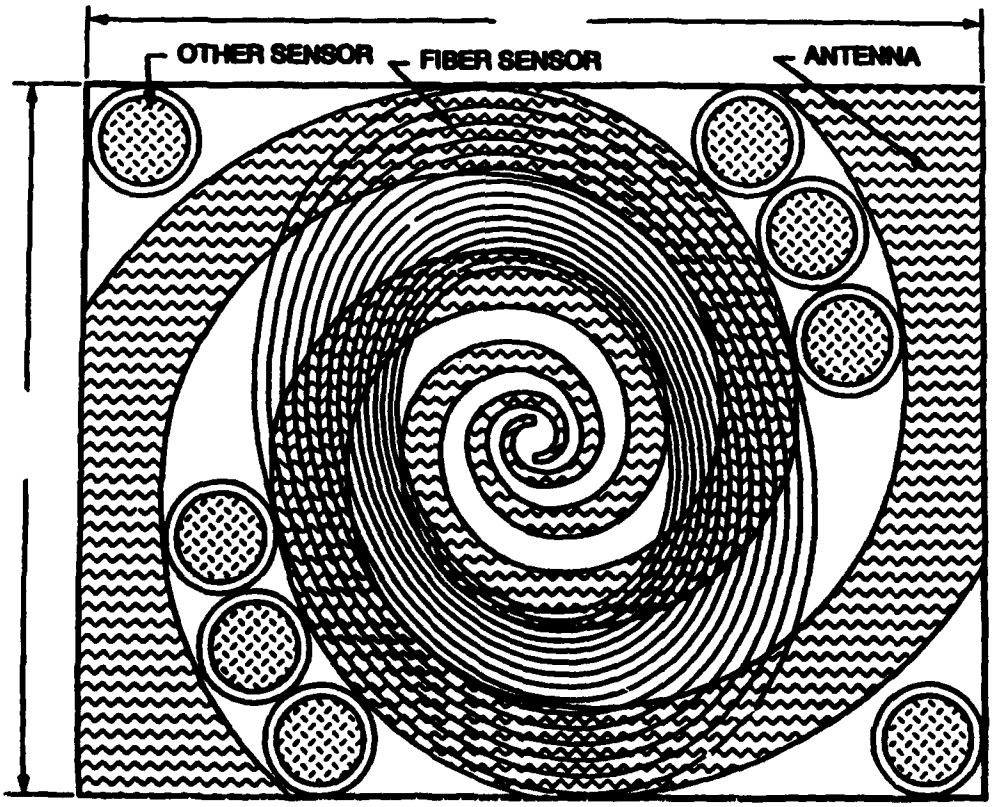

Figure 10. SAWAFE panel layout for STEP-3 flight experiment.

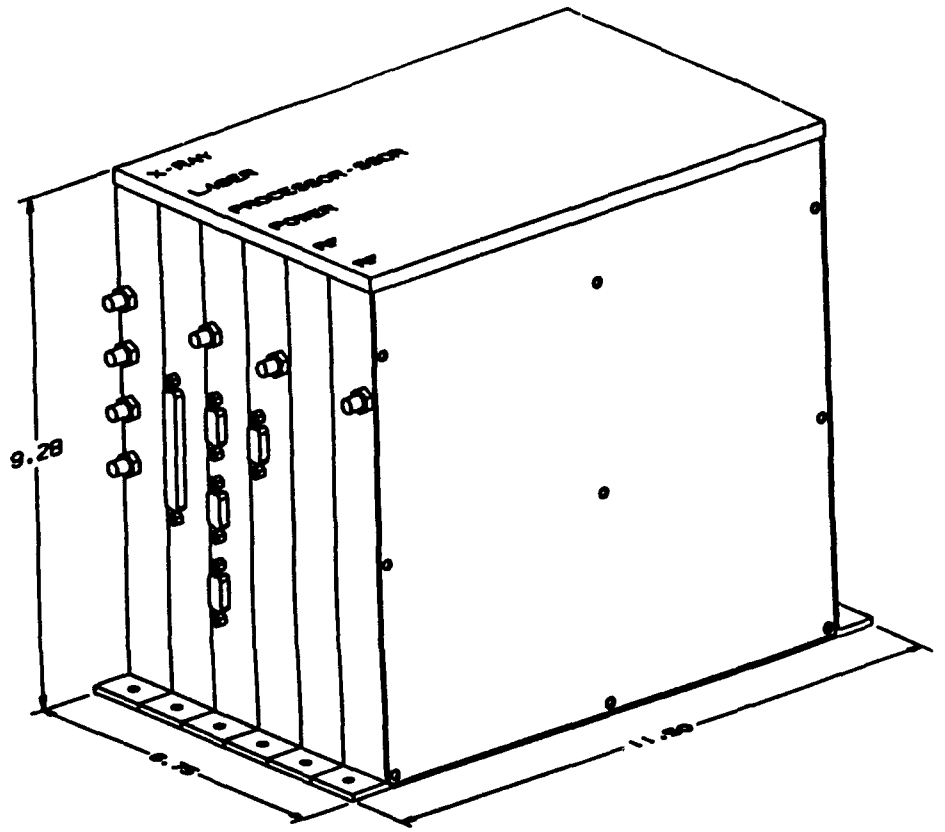

Figure 11. SAWAFE avionics subsystem concept.

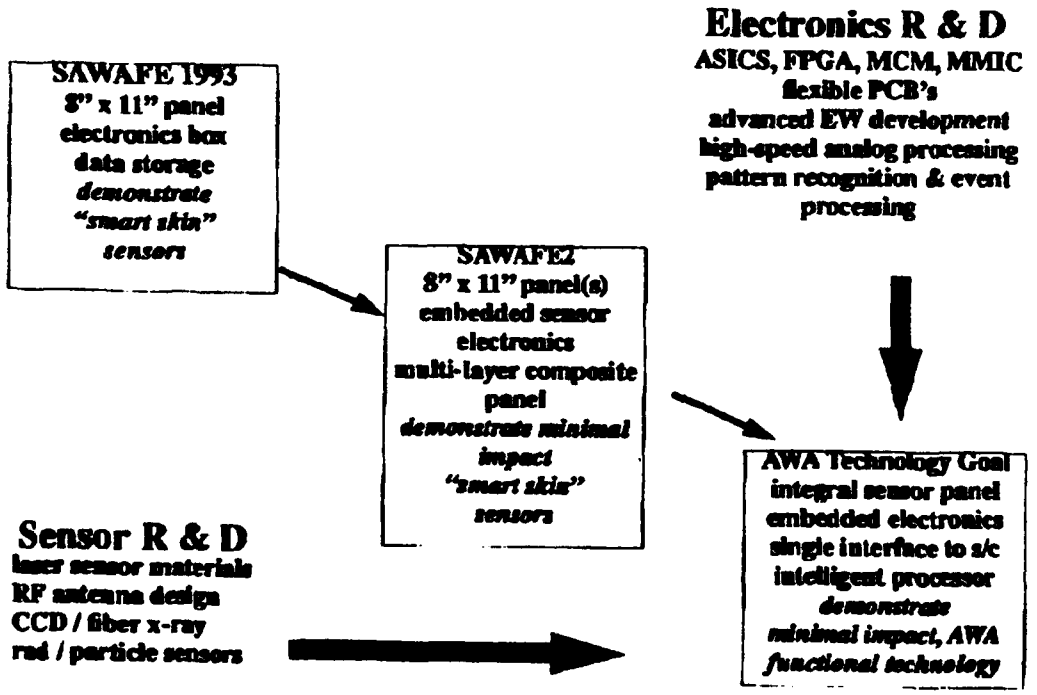

Figure 12. SAWAFE AWA technology evolution.

5. FUTURE EXPERIMENTS

The primary purpose of the first SAWAFE is to demonstrate the functionality and space durability of the skin-embedded sensors and to collect background and performance data. The next flight experiment will be designed to use more advanced panel construction techniques and to incorporate advances in electronic miniaturization. (Figure 12)

The panel will be representative of state-of-the-art designs for multilayer composites with embedded power and signal wires. This type of panel may be made in either a conformal or flat configuration. The laser, RF, and x-ray sensors embedded in the panel will be advanced versions of the sensors flown on STEP-3.

The sensor electronic circuitry, analog and digital, used for amplification, detection and discrimination of the sensor signal will be incorporated into specially designed components. Single application specific integrated circuits (ASICs) have already been made with multiple analog channels of preamplifiers, amplifiers, and peak-hold circuitry. Field programmable gate arrays (FPGAs) have also been used to place a corresponding number of digital detection circuits onto a single integrated circuit. Based on the success of the first (discrete component version) SAWAFE detection electronics, the necessary ASICs and FPGAs will be designed and fabricated. Flexible PCBs will be used as a mounting substrate and the entire assembly will be embedded in the panel. The miniaturized electronics will draw power from the embedded power lines and communicate over the embedded signal wires. Because of the experimental nature of the next flight experiment, the experiment controller and SSDR will be packaged into a single "slice" that may be attached to the back of the panel, or may be mounted separately in the spacecraft.

The third flight experiment in the program will be the demonstration of a fully operational technology. The attack recognition processor will be miniaturized and embedded in the panels along with the rest of the electronics and sensors. The only memory in the system will be the memory required to perform the attack warning and assessment mission in real time. The processor will have a bus connection that is compatible with the host spacecraft. The experimental plan for this flight will include the real time demonstration of signal detection, signal characterization, and threat assessment.

6. SUMMARY

The effectiveness of a future SDIO large constellation of surveillance and interceptor platforms may be dependent on a timely and accurate system for on orbit health monitoring capability. One critical component of such a capability will be autonomous attack warning and assessment. The technology used to implement this function must be easily integrated into the space platforms with minimal cost, schedule, and spacecraft integration impact. The SAWAFE program will develop and demonstrate these technologies through a series of autonomous flight experiments. The first SAWAFE payload on the STEP-3 mission will concentrate on demonstrating the functional performance of the "smart skin" in a space environment, and measuring the natural and man-made signal background for each sensor type. Follow-on flight experiments will demonstrate the functional performance of an operational attack warning and assessment system using miniaturized electronics embedded in prototype spacecraft structures.

7. ACKNOWLEDGEMENTS

The authors wish to thank Dr. Bob Kraus and Karen Kolen of W. J. Schafer Associates, Inc. for their outstanding support in compiling and producing this paper.

Optical Fibre Techniques for Structural Monitoring in Composites.

W. Craig Michie
B. Culshaw
D. Uttamchandani
Optoelectronics Division,
Department of Electronics and Electrical Engineering,
Royal College Building,
University of Strathclyde,
204 George St.,
Glasgow G1 1XW, UK.

Abstract.

The sensor technology to be used in smart structures must be compatible both operationally and mechanically with the material and the functional specification of the smart structure system. Fibre optic sensors are particularly attractive since they are mechanically robust and flexible. This paper will present an overview of work which has been carried out within the University of Strathclyde concerning the development of fibre optic sensing techniques for use in structural monitoring applications for composite material systems.

1. Introduction.

During the last decade a considerable expansion has been seen in research effort directed towards the development of smart structures and materials. The realisation of these systems requires a cross disciplinary understanding of aspects from mechanical engineering, system control, sensing, actuation and signal processing. The aim of this effort is the realisation of structures which will perform their own health and performance monitoring functions. A structure might issue a warning if a fault is discovered which it is unable to deal with or alternatively the structure might alter the shape or stiffness of its component members in order to damp out mechanical vibrations which are outwith the normal operating conditions of the structure. The applications of this technology are wide ranging from civil engineering through industries such as the petrochemical industry to aerospace and defence. The smart approach to system design offers the potential of improved process yield, safer working and operating conditions through the use of real time structural monitoring, increased efficiency by minimising component down time and performance improvements with associated cost reduction through weight minimisation as over engineering is eliminated. Much of the interest in smart materials has been driven from the needs of the aerospace industries. In particular the use of high performance composite materials in critical areas requires that these materials must be made to be reliable, and that they are seen to be reliable over the wide range of in service operating conditions. The adoption of these new materials in key areas has been relatively slow due to the fact that it has not been possible to have an in service indication of the health of these components. The development of the smart technology was seen as being a vehicle whereby these new materials could be effectively incorporated into primary structures since a real time up date of their state of health could be provided via the use of an embedded sensor network. This paper will review the work related to the development of these sensors within the University of Strathclyde. Within the university a considerable body of expertise has been established in the areas of fibre sensing and optical component development. Here the discussion will be restricted to the area of optical sensing methods for structural monitoring in composite materials.

2. Structural Monitoring in Composite Materials.

The first concerted effort undertaken within the university to examine the possibility of using optical fibre sensors to perform structural integrity measurements in composite materials was performed under a collaborative research programme OSTIC (Optical Sensing Technologies for Intelligent Composites)[1]. This program was in fact the first European programme to focus collaborative research onto this issue. The sensing aims of the programme were to demonstrate a quasi-distributed dynamic strain measurement within a composite material and secondly to implement a measurement scheme which, with the use of a single sensing fibre, would permit the simultaneous recovery of two quasi-static measurands (temperature and strain) to be achieved. The implementation of a quasi-distributed strain measurement was undertaken by the project

managers, Bertin et Cie., who developed a scheme based upon a coherence multiplexed polarimeter. This system will be described in full detail elsewhere in this meeting[2]. The University of Strathclyde was responsible for the latter investigation. Both of these sensing schemes were to be considered as a possible means for determining the state of cure of a Carbon Fibre Reinforced Plastic (CFRP) or Glass Fibre Reinforced Plastic (GFRP) structure by measuring the secondary effects (temperature and strain changes).

2.1 Simultaneous Measurement of Two Variables.

Optical fibres have stimulated considerable interest in their use as sensors due to their high sensitivity to a wide number of measurands, their immunity to electromagnetic interference, their capability for making distributed measurements and also because of their capacity for information transfer. These sensors are particularly attractive to users of composite materials due to their ability to withstand the dynamic range of strain excursion (up to 2%) which might be placed on a high performance composite component. The inherent sensitivity of optical fibre sensors to a wide range of measurands has been a key factor in their success. It is also true however that this sensitivity has inhibited their deployment in a large number of areas. In particular, under conditions where it is necessary to perform slowly varying or quasi-static measurements it is often the case that more than one measurand can influence the output of the optical sensor at the same time. At best this leads to a reduction in the measurement sensitivity and at worst this can cause a total corruption of the recovered data. During the early stages of the OSTIC programme a decision was made to address this particular issue. For the composite material needs the most appropriate measurement was felt to be an integrated measurement of temperature and strain variations. To this aim a target specification of simultaneous recovery with a resolution of 5 C and 100 $\mu\varepsilon$ was proposed.

Simultaneous recovery of information from two variables can be achieved by making two measurements on a single sensing fibre using two different approaches which have different sensitivities to the measurands of interest. In the present experiment the fibre was interrogated with a dual mode sensing scheme and a polarimeter. Investigation of these schemes had revealed that, for certain types of fibres, the relative sensitivities to temperature and strain changes were sufficiently different for measurements to be made which would allow these two variables to be discriminated. The implementation of the sensing scheme was as follows.

The sensitivity of the sensing fibre to changes in temperature and strain were first of all established independently of each other for both measurement techniques. This allowed the sensor to be represented in matrix form thus,

$$\begin{bmatrix} \Delta\phi_{POL} \\ \Delta\phi_{DUAL} \end{bmatrix} = \begin{bmatrix} \alpha_{\epsilon POL} & \alpha_{TPOL} \\ \alpha_{\epsilon DUAL} & \alpha_{TDUAL} \end{bmatrix} \begin{bmatrix} \Delta\epsilon \\ \Delta T \end{bmatrix} \quad (1)$$

where $\alpha_{\epsilon POL}$, $\alpha_{\epsilon DUAL}$, α_{TPOL} and α_{TDUAL} represent the individual strain and temperature sensitivities of the two sensing schemes, $\Delta\phi$ represents the phase changes seen by the dual mode and polarimetric signals, $\Delta\epsilon$ and ΔT are the applied strain and temperature changes. Provided that it is possible to invert this matrix, measurements of the total phase changes of the dual moded and the polarimeter signals can be used to uniquely specify changes in temperature and strain. Experimental data showing recovered temperature and strain variations for an unembedded sensing length of fibre is presented in Figure 1. Data recovery with an accuracy of approximately 10 $\mu\varepsilon$ and 2 C was achieved over the entire measurement cycle[3]. This sensing scheme was further evaluated in an embedded system: a section of fibre was embedded in a unidirectional CFRP composite coupon 320 mm by 25 mm by 55 mm. This coupon was subjected to a three point loading with simultaneous thermal cycling and the recovered data is displayed in Figure 2. The recovered temperature and strain information in this experiment was less accurate than in the unembedded situation, accuracies of around 35-50 $\mu\varepsilon$ and 5 C was achieved[3]. A number of reasons account for this discrepancy.

Batch to batch variations in the manufacture of the elliptical core fibre lead to variations in the sensitivities of both the polarimetric and dual moded sensing schemes. In the embedded system experiments, the sensitivities of the dual mode and polarimetric sensor were slightly different from the fibre used in the unembedded case. In particular the dual moded sensing scheme was found to be less sensitive to applied strain. The difference in these sensitivities was found to influence the conditioning of the fibre characteristic matrix making data recovery more difficult. In addition to this, the sensing length was shorter than in the previous case in order to be compatible with the maximum

permissable sample length. This has the effect of reducing the influence of the temperature changes and therefore this information is more difficult to recover. Thirdly, in order to perform the thermal cycling a heating coil was wrapped around the CFRP coupon and the coupon heated to around 100 C and left until isothermally stable. The coupon was then allowed to cool and a three point bending load applied. The glass transition temperature of the matrix resin used in the CFRP structure lies typically in the region of 130 C and consequently the modulus of the resin at elevated temperatures could be approximately half of its room temperature value. This leads to inaccurate strain transfer to the fibre during the initial stages of the cooling cycle.

These preliminary measurements of the embedded sensor performance indicate that it is possible to implement this form of sensor in an embedded configuration. Given the magnitude of the systematic errors associated with the experiment a reasonable agreement between the optical measurements and the reference data has been achieved. Future developments of this sensing scheme will take place around the implementation of an all fibre version of the sensor. It is expected that this will improve the reliability of the sensor and ease the deployment difficulties.

2.2 Multimode Fibre Optic Sensor Using Artificial Neural Networks.

Currently under progress within the Optoelectronics division is a project which involves the use of an artificial neural network to relate the changes in the speckle pattern at the output of a multimoded fibre to the strain applied to the fibre. The project aim is to identify an optimum technique for presenting the speckle pattern image to the input layer of the network, choosing the optimum layer number and nodes in the hidden layer and selecting an ouput layer to best represent the strain value. Absolute strain measurements of up to several hundred micro-strain using such multimode sensors with ANN processing are attainable.

Increasingly it is becoming possible to use Artificial Neural Networks (ANN's) in complex pattern recognition. The strain sensor described in the present section is one such problem. Light intensity patterns produced at the output of a multimoded optical fibre are complex in nature due to the interference of the many modes which propagate down the fibre length. Small strains exerted on the fibre will change its physical properties, such as length and refractive index, and hence alter the characteristics of the light as it travels along the fibre length[4]. These effects result in an alteration of the complex modal interference pattern at the fibre output[5]. A typical example of such a pattern is displayed in Figure 3. It is possible to produce unique patterns at the fibre output over a wide range of strain conditions and use the neural network as a means of relating a specific strain with a given pattern. This allows the construction of a simple yet effective strain sensor. The basic system under investigation consists of three blocks:a multimode fibre acting as a sensor; a digital signal processing of output pattern after acquisition and finally a neural network as the interface between the pattern and a strain value.

In order that repeatable strain measurements could be made, a multi-mode fibre was epoxy bonded to the surface of a cantilever beam which was then deflected giving strain value in the region off 0-300$\mu\varepsilon$. The patterns produced at the output of the fibre were then stored on a SUN work-station by means of a video camera and frame grabber. The patterns were processed using several digital signal processing techniques to simplify the resultant pattern thus enabling easier training of the neural network.

The neural network simulator used in this project was the Aspirin/Migraines package[6]. This package utilises a Generalised Delta Rule with back propagation[7]. Various neural network configurations are currently under investigation. Initially strain was output in binary format, this technique was used in work carried out by Grossman et.al. on a few moded sensor system[8]. Results obtained thus far indicate that the multimoded sensor system is more effective than the dual moded system giving a much improved sensitivity and range. This is due to the increased complexity of the modal patterns. Training of the ANN has varied in duration between a few minutes for some of the smaller networks up to a maximum of about one hour for the larger ones. Full details and results of this work will be published in the near future.

2.3 Impact Damage Detection and Location Using Optical Fibres.

Another line of investigation recently pursued at Strathclyde involves building an optical fibre sensor system capable of locating and detecting the magnitude of an impact occurring on a composite panel. The first phase of this activity has been concerned with designing a system for determining

impact *location* which operates by timing the arrival of impact generated acoustic waves at a sensor array. Electrically passive sensors have been targeted as of interest, and this has involved the use of multimode optical fibres as sensors. The acoustic sensitivity of such fibres, guiding coherent optical radiation, is well known[6].

Initially optical fibres were surface mounted along the edges of a metal panel. A multimode directional coupler was used to divide the optical power equally between two fibre sensors. The sensor outputs i.e. the speckle patterns were monitored by photoreceivers, one receiver dedicated to each sensor. The signals at the receiver outputs were then electronically processed to measure the difference in arrival times at the sensors, and from this a simple calculation yielded the impact origin. Using this relatively crude sensor, impacts of a few tenths of a Joule could be located with a resolution of +/-5cm. This project is currently in progress, but a more suitable fibre optic sensor system is now being evaluated. The design criteria are that the sensor must be lead-insensitive, demonstrate high sensitivity and dynamic range, and have a wide frequency response. Detailed results of this project will be presented elsewhere.

3. Cure Monitoring.

A key component to the development of smart structures based on thermoplastic epoxy resin based composite systems is a means of determining the cure state of these materials. As structural designs become more complex and material requirements for improved high temperature properties increase, the need for closer structural monitoring and control of the fabrication process is essential. Current practices rely heavily upon measurements of temperature and pressure conditions during the curing cycle of materials in order to ensure that the composite material structure is being sufficiently well cured. Batch to batch variations and changes in resin chemistry during storage can lead to components being held at high temperature for excessively long periods of time in order to guarantee that cure has been achieved. This can represent a considerable energy loss. There is clearly a need for a means of readily establishing the cure state of a composite structure, whether this be during the curing process or as a 'go:no go' test on a key element of the structure at the end of the manufacturing process. In order to achieve these aims measurement techniques as diverse as dielectric absorption[9], acoustic propagation[10], rheometry[11] and optical attenuation[12] have been investigated. Some of these measurement schemes are currently under development within the university however the present discussion is concerned only with techniques which are based on optical fibre sensors. One such method based on a means whereby the refractive index of the material might be accurately determined is currently under investigation.

During the curing process, epoxy resin based systems go through chemical changes which are reflected in changes in the refractive index of the material. If this change can be detected then in principal the cure state of the material can be determined. Optical measurement techniques which make use of this phenomena to induce a loss in the throughput of the optical signal as the index of the curing medium changes have been developed. While these measurements have been shown to be effective to some degree, they have considerable weaknesses. Being intensity based the resolution of the measurement is limited to the minimum resolvable change in intensity, it is also subject to influence from other loss mechanisms such as micro bending or down lead effects. Furthermore, the greater part of the index change takes place during the gelation phase of the epoxy system therefore during the latter stages, or during the post cure, the index changes are small. The resolution offered by the intensity based schemes is insufficient to indicate these changes.

Means of measurement of refractive index which can be made sensitive to index changes of 10^{-5} are currently being developed within the Optoelectronics group at the university[13]. These techniques are also under investigation with a view to applying these methods to cure monitoring[14].

3.1 Cure Monitor Operation.

The basic geometry of the device is as indicated in Figure 4. A high index overlay waveguide is evanescently coupled to a polished optical fibre. Efficient coupling between the optical fibre the overlay waveguide is achieved when the index of the highest order mode of the overlay waveguide (close to cut off) is matched to that of the fibre core. This condition can be realised by tuning any of the overlay waveguide parameters (thickness, index or operational wavelength). Under resonance conditions strong power transfer takes place between the fibre and the overlay waveguide (a typical trace of the transmission characteristics as a function of input wavelength is displayed in Figure 5). In addition to the above parameters it can be shown that the resonance

position is also a strong function of the index of the superstrate surrounding the overlay guide. Variations in this index have produced changes in the resonance centre wavelength of greater than 100 nm[13] and in principle this can be extended to around 500 nm with appropriate choices of materials. Making use of this property allows the refractive index of a material to be determined with accuracies of better than 10^{-5}. This approach offers the potential of monitoring the index of a curing resin based system. Although the present systems under investigation use cumbersome polished block technology, this is simply a means of facilitating the device development. The construction of these devices could be readily implemented with vacuum deposition of high index films onto D-type fibre. There remains however certain problems to be addressed before this measurement technique can be directly applied to the problem of measurement of cure state of composite material structures.

As the composite material undergoes the processing of the cure cycle, the refractive index of the resin systems changes from around 1.52 to 1.58 between the uncured and cured states. The refractive index measurement technique based on coupling to an overlay guide is effective only for superstrate indices which are lower than the effective index of the fibre core (1.45). A means must therefor be found of increasing the usable range of measurable indices. Several approaches to this problem are possible, including the manufacture of these devices using fibres of an alternative structure (for example Fluoride). In work being carried out at present, a thin film of low index material is deposited onto the overlay waveguide in order to buffer the overlay guide from the effect of the superstrate material.

A layer of high index ($n = 1.8$) was mounted onto a side polished block and polished to a thickness of approximately 30 μm. The tuning of the resonance positions as a function of overlay index measured for both the TE and TM polarisation states, these are displayed in Figure 6. A layer of CaF_2 of approximately 700 nm, corresponding to the evanescent field penetration depth was then deposited upon the overlay layer and the wavelength tunability measurements repeated, these measurements are also displayed in Figure 6. Examination of this figure shows clearly that the deposition of this film has extended the range of overlay indices during which the resonance position is tunable. Only when the superstrate index value exceeds 1.5 is lossy behaviour observed. Up until this value the resonance peaks are clearly discernable. While the extension of the measurement range does not extend to that required for cure measurements of current resins used in composite manufacture it is expected that a further increase can be achieved with the use of thicker layers. The layer thickness used at present represents approximately one penetration depth thickness, where the evanescent field strength falls to 1/e of its original value. It was not expected that much buffering effect would be observed for thickness of less than this value. Increasing the thickness of the low index layer should emphasise the buffering effect, up until the point where the superstrate index has no effect at all. It is not yet clear how much of an increase in operational range this will ultimately allow. A theoretical and experimental investigation are currently underway in order to determine this.

4. Conclusions.

This paper has reviewed work carried out within the Optoelectronics Division of the University of Strathclyde concerning the development of techniques suitable for structural monitoring of composite material systems. The work carried out to date has spanned a number of key areas within the smart structure concept, impact damage detection and location, measurement of quasi static parameters and material monitoring during manufacture. The results obtained to date represent the beginnings of the inter disciplinary collaboration that are necessary for the success of the smart structures technology. Future research will further develop this interdisciplinary cooperation with closer collaboration between constituent areas such as sensing, chemistry and signal processing. In order to close the loop and provide the necessary feedback to implement a truly smart structure, future research programmes will require closer interaction with control and actuation centres. Some preliminary work is already under way in this area coordinated by the Smart Structures Research Institute. Future research programmes will also target alternative smart systems for civil engineering applications. These areas will provide a valuable proving ground for the technology without having the high cost and high risk that is associated with development of primary components for the aerospace industry.

Acknowledgements.

This work was partially sponsored under the BRITE/OSTIC programme.

References.

1. B.Culshaw, W.C. Michie 'Fibre Optic Strain and Temperature Measurements in Composite Material-A review of the Ostic Programme'in 'Recent Advances in Sensory Materials and Their Applications'. Technomic April 1992.

2. P. Sansonetti et.al. 'Optical Fibre Monitoring of Composite Material with White Light Quasi-Distributed Polarimetric Sensor.' AGARD Specialists' Meeting on Smart Structures for Aircraft and Spacecraft., October 1992.

3. W.C. Michie, B. Culshaw, S.S. Roberts, R. Davidson,' Fibre Optic Technique for Simultaneous Measurement of Strain and Temperature Variation in Composite Materials.' ADPA/AIAA/ASME/SPIE Conference on Active Structures, IOP Publishing 1992 pp809-812.

4. Wilson and Hawkes, 'An Introduction to Opto-electronics', ch.8, 2ndEd., Prentice Hall, 1989.

5. Layton, M.R., Bucaro, J.L.'Optical Fibre Acoustic Sensor Utilising Mode-Mode Interference', Applied Optics, 18,666, March 1979.

6. Version 5 Aspirin/Migraines Manual, 1990.

7. Aleksander and Morton,' An Introduction to Neural Computing', ch.8, Chapman and Hall, 1991.

8. Grossman B. et.al. 'Proceedings of the 3rd annual Meeting of the International Society for Optical Engineering in Fiber Optic Smart Structures and Skins, San Jose, california, p205, Sept. 1990

9. Laiez, D. et.al.'Realtime dielectric measurement of network formation of crosslinked epoxy resin systems.'Plastics and Rubber Processing and Applications (1990)

10. R.T. Harrolds, Z.n. Sanjana 'Acoustic Waveguide for Smart Structures and Skins' Smart Structures and Skins II, SPIE vol 1170, Boston 1989, page 462.

11. Hayward, D. et.al.'The application of the Strathclyde rheometer to a variety of curing systems.'J.O.I. & Colour Chemistry Association (4):452, 1989.

12. Aframowitz, A.M. and Lamb K.Y.'Optical Properties of Curing Epoxies and Applications to a Fibre Optic Composite Cure Sensor', in Fibre Optic Smart Structures and Skins II, SPIE Volume 1170, Boston 1989, page 138.

13. W. Johnstone, G. Thursby, D. Moodie, K. McCallion 'Fibre Optic Refractometer Utilising Multimode Waveguide Overlay Devices', submitted to Optics Letters July 1992.

14. W.C. Michie, G.Thursby, W. Johnstone, B. Culshaw 'Optical techniques for determination of the state of cure of epoxy resin based systems' SPIE Smart Structures and Skins V, Boston 1992.

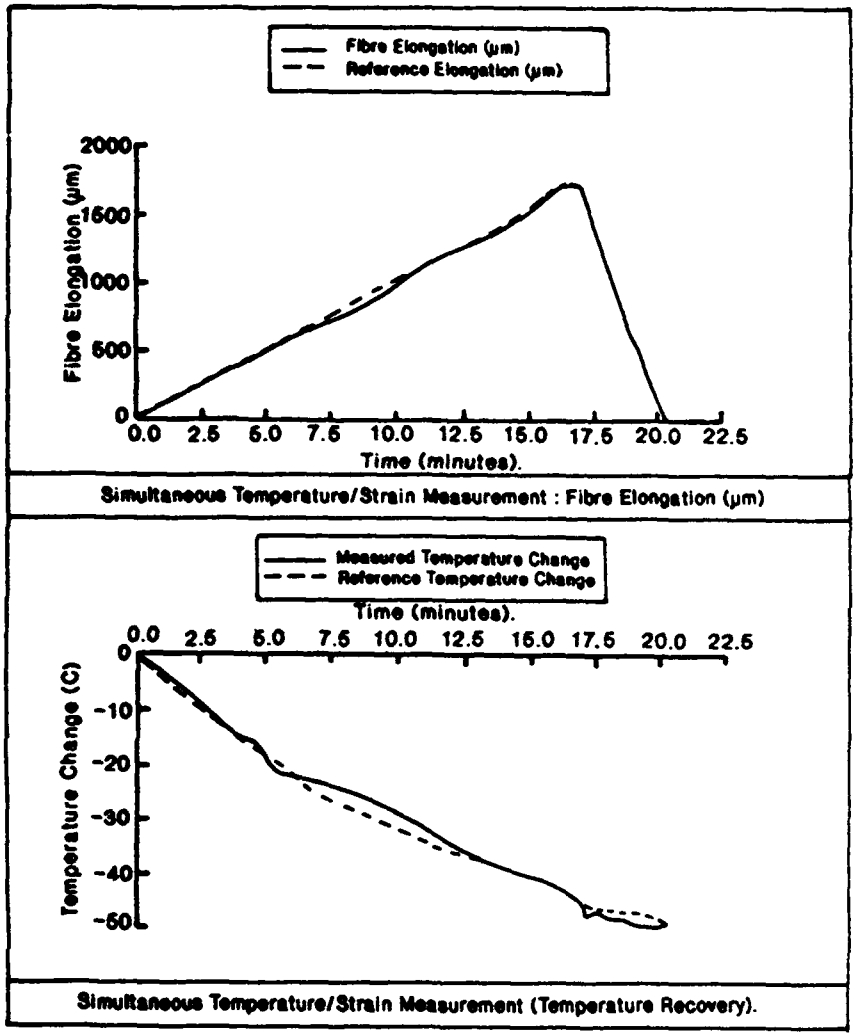

Figure 1:Temperature/Strain Recovery :Unembedded Sensor.

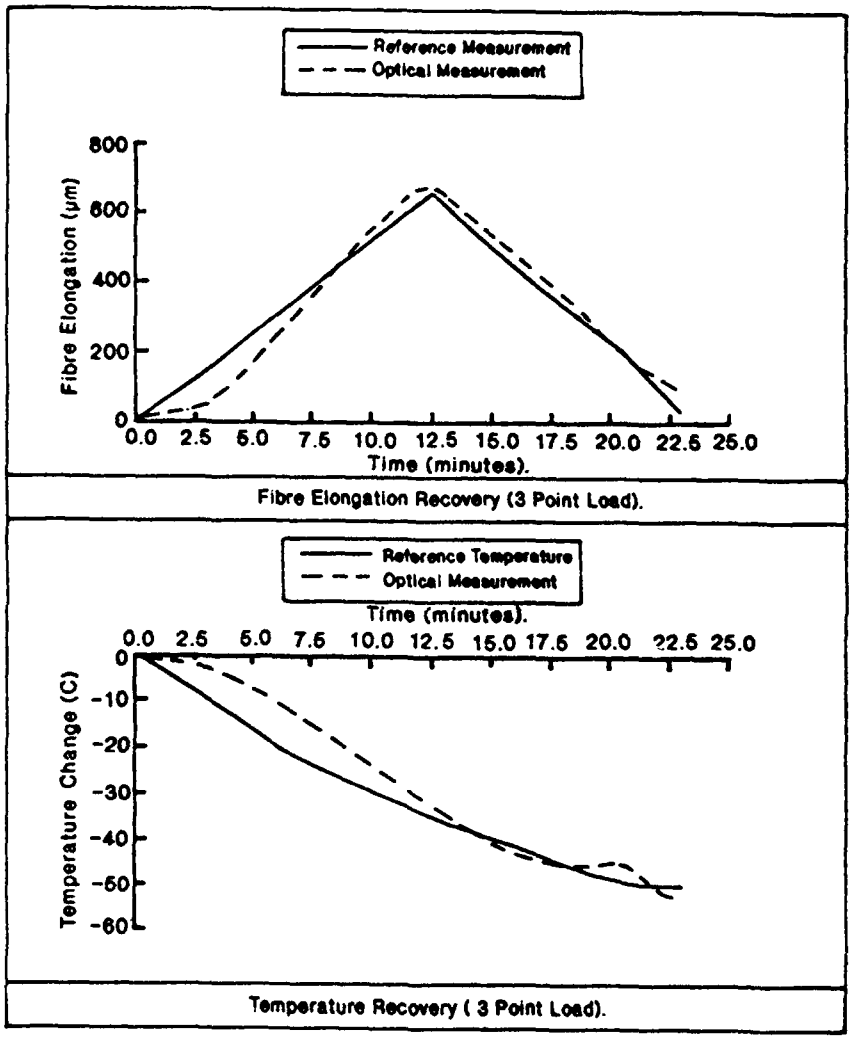

Figure 2:Temperature/Strain Recovery :Embedded Sensor.

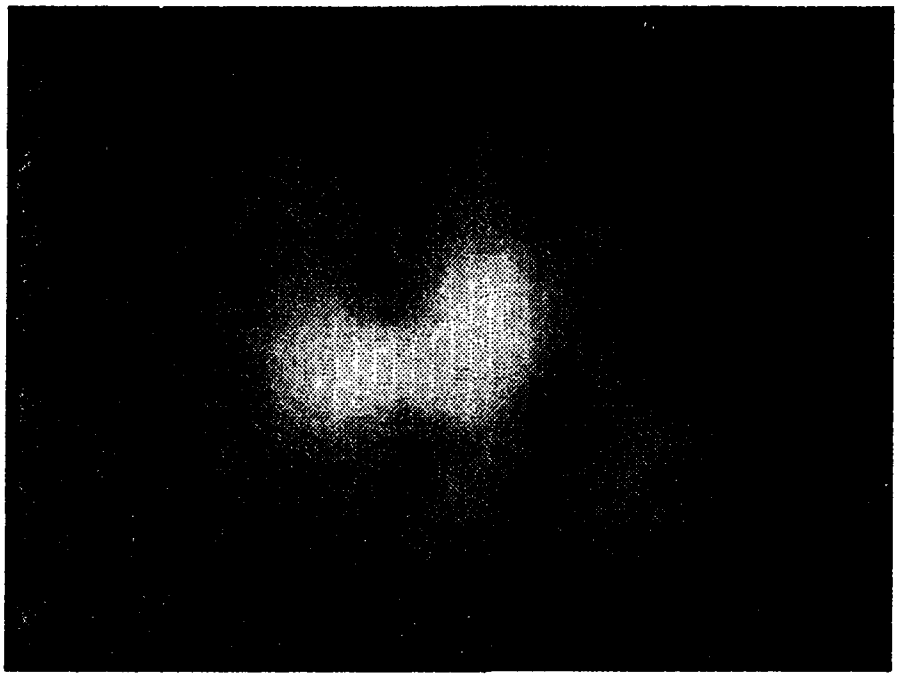

Figure 3: A Typical Speckle Pattern Output from a Multimoded Fibre.

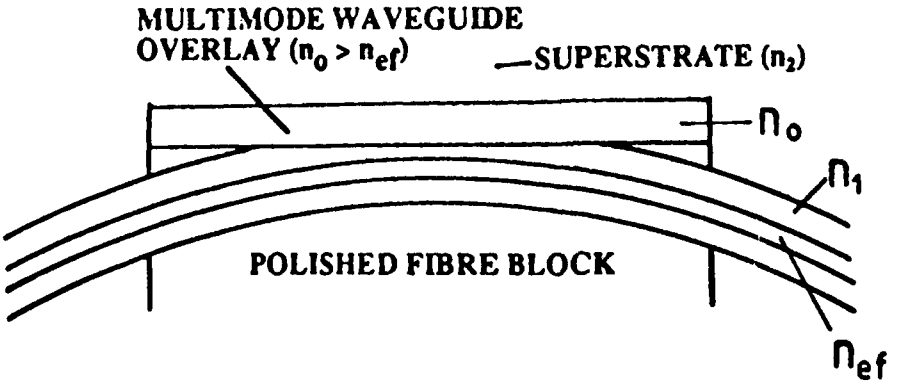

Figure 4: Schematic of Optical Refractometer/Cure Monitor.

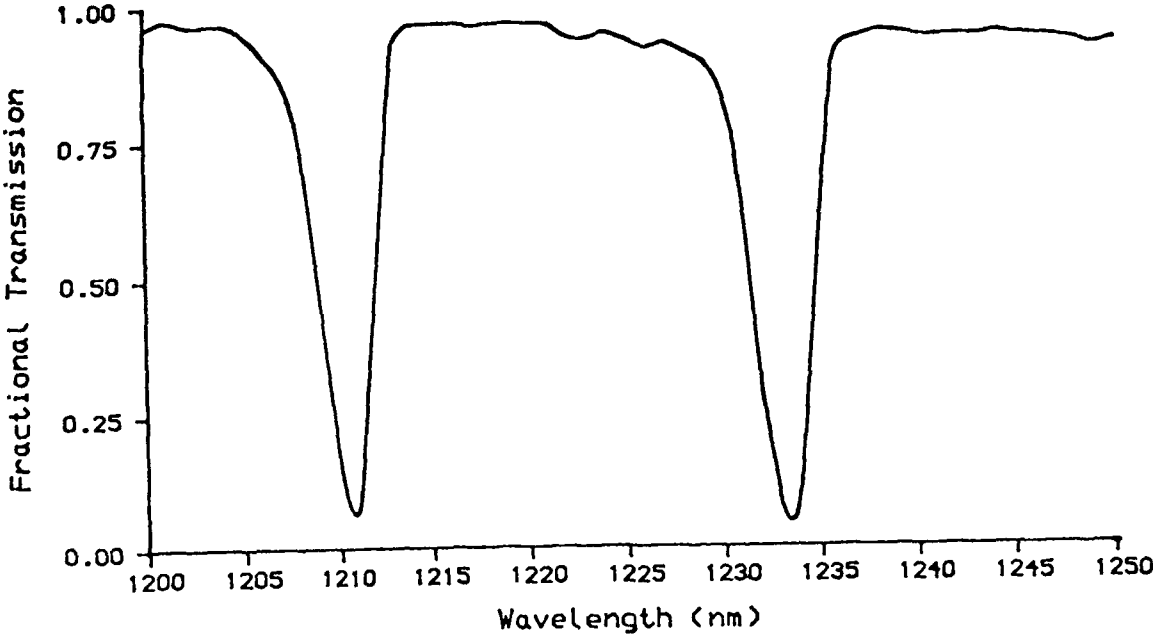

Figure 5: Fractional Transmission of Fibre Block Coupled to Overlay Guide.

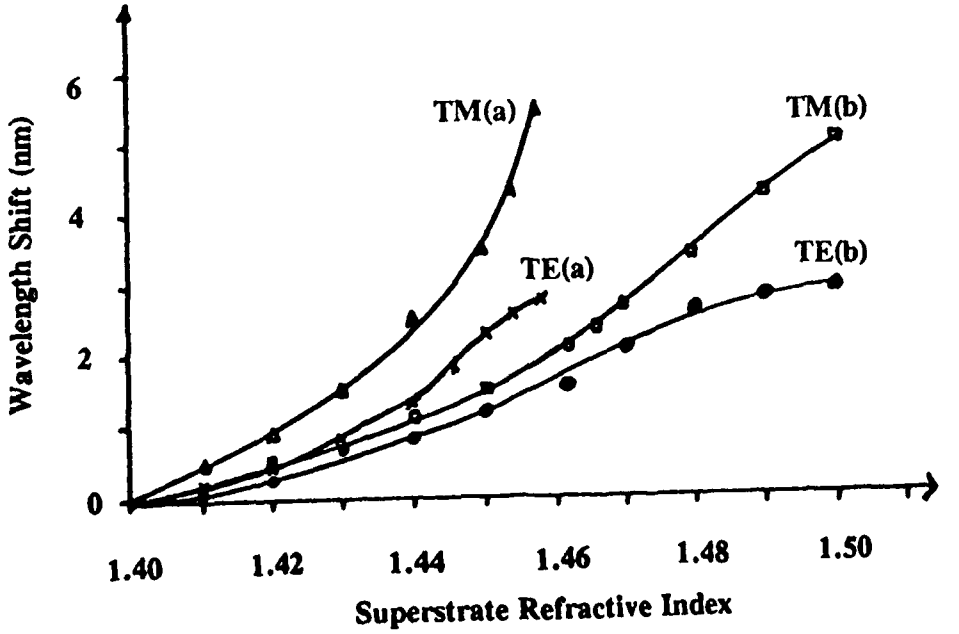

Figure 6: Wavelength Tuning Characteristics of Polished Fibre Block with High Index Glass Overlay.
a: Without CaF_2 Superstrate Buffer b: With CaF_2 Superstrate Buffer.

SMART PROCESSING OF COMPOSITE MATERIALS FOR ENHANCED PERFORMANCE AND PROPERTIES.

A. McDonach R. Pethrick and P. Gardiner

Smart Structures Research Institute
University of Strathclyde
204 George Street, Glasgow G1 1XW
Scotland, U.K.

Introduction

There have been a large number of technologies described whose purpose is to aid in the control of composite manufacture. The aim of this paper is to readdress the requirements of composite manufacture to assess which features of the various techniques are best suited to providing improved processing. To start with, we will consider the requirements of quality in manufacture and the hidden costs associated with incorrect processing. This will allow us to rank the aspects of processing which it would be attractive to improve. Following this, we will consider a range of monitoring processes and their ability to deliver on these improvements and at what cost in terms of expense and complexity. Monitoring processes considered include fibre-optic (Optical) methods, dielectrometry and ultrasonic methods.

A Definition of Cure.

The cure process is the reaction of a multifunctional monomer (liquid) to produce a three dimensional network(solid). During this process, there are a number of stages. Firstly, the reactions lead to a doubling of the average molecular weight and a small increase the viscosity. This continues until 65% - 85% of the monomer has been converted into polymer chains where it is considered that the three dimensional network has begun to form. After gelation, a stable three dimensional network is formed however, it is still mobile, and further reaction is required to complete the process and this leads to a vitrified matrix structure. The complete process is usually only achieved by elevating the temperature and carrying out a post cure process. Figure 1 illustrates the time dependent aspects of these steps in relation to temperature.

There are a number of reasons as to why it would be appropriate to have increased knowledge of the cure process during the manufacture of composites. It is important to clarify the processing implications associated with these stages in the cure process.

Gelation-

This is the point at which the resin has developed its full viscoelastic properties. It is important that the material has been able to flow to its desired location before this point. In the case of Resin Transfer Moulding, the point at which gelation occurs should be reached as soon as possible after the mould has been filled.

Vitrification-

This needs to be determined to ensure that the material is sufficiently mechanically stable to be taken from the moulding. The structure will be defined physically but may not have developed fully the desired mechanical properties.

Post Cure-

The completion of the reaction often will require that the sample be post cured. The process involves raising the incompletely cured network to an elevated temperature and this allows further reaction to occur and also allows the already formed network structure to realign itself to achieve a minimum energy form. This process allows the unreacted ends of the polymer chains to be incorporated into the matrix and this will improve the mechanical properties of the matrix.

The chemistry of crosslinking at high levels of conversion leads to micro stresses being generated which will produce a driving force for structural reorganisation. One of the physical processes that occurs during post cure is a change in the density, and as is often the case this leads to densification, which in turn leads to significant changes in the modulus, extension to break and impact strength of the material. Practically, the post cure process is critical for the development of the required ultimate properties. However, if this process is continued too far, it can lead to network degradation and a reversal of the curing process. The changes which occur during the latter stages of cure present a critical test of any non destructive evaluation method[1] and are rarely discussed in the literature on the topic of cure monitoring. Densification or the reverse process can be measured by determination of the thickness variation of samples, but it will be evident at a molecular level in terms of the amplitude of a relaxation process; dipolar, optical, magnetic or mechanical.

The reactions are very slow and, currently, the only effective method of determining what is occurring is by using test coupons to monitor the progress of the reactions. The methods which are suitable are infrared absorption, Differential Scanning Calorimetry and mechanical measurements of the coupons properties. Further work is required to characterise the material changes in terms of a densification as a result of crosslinking and as a result of changes in the size and distribution of voids.

During this cycle, the viscosity of the mixture increases as the molecular weight increases. However, in the final

stages of the cure process following vitrification, the viscosity ceases to change and consequently, this and related parameters may only be used to monitor the process prior to vitrification and prior to achieving the full mechanical properties.

Important Features for the Manufacturer.

One of the applications for cure monitoring is for accurately predicting the gelation and vitrification stages. This allows the processor to reduce the cycle times to a minimum and it also makes it possible to adapt the cycle to changes in the quality and condition of the input materials. Essentially, the aim is to reduce the skill needed to achieve the efficient operation of the moulding system.

Cure monitoring systems can be applied during the process set-up phases so as to reduce the time needed to optimise the processing conditions for a particular component configuration. The main production cycle may then proceed without the use of a sensor system assuming there is consistency of the input materials. Alternatively, and if possible, a sensor system can be used during production and this should imply that there will be less rejects during processing due to incomplete processing or overheating as a result of variations in the input materials. The suggestion has been made[2] that at present, process operators reduce temperatures and extend cycle times so as to create a more robust system however, this has an obvious effect on the cost of production .

A second demand made on monitoring systems is in the area of post manufacturing quality assurance. For secondary components (non load bearing or not safety critical) used within the aerospace industry, manufacturers follow a certified process using materials that have been stored under controlled conditions and within specified age limits. Following manufacture, the quality assurance process is completed by ultrasonic scanning to detect delaminations and voids. Complete cure of these components is assured by following standard procedures, determined by process temperature profiles, and by using standard input materials of the required quality. It is also the case that, in the majority, these components are mostly of thin and uniform cross section which presents less of a problem in obtaining a broad set of optimum conditions.

For primary components (safety critical items) further post processing quality assurance tests are required. The purpose here is to verify that the manufacturer has achieved the specified mechanical properties set down for the component by the designer. These tests, frequently mechanical, can be time consuming and expensive as they must be applied to every component. Also, they are not viewed as wholly reliable since they are applied to test coupons usually taken from the edge of the component and may not represent the condition of material from the main body of the component. Processing difficulties are more likely with these components since they can contain areas of variable cross section and usually, they will have sections whose thickness is much greater than that of secondary components. An added cost in the this cycle is the time delay associated with verifying the proper manufacturing cycle with a particular batch before proceeding with the next batch. Mechanical testing of individual components can take some time and this can create a bottle neck in the production cycle around testing which adds to the overall cost of processing.

Taken together, these requirements have created an interest in techniques which can follow accurately the progress of the cure reaction described in the previous sections and provide a signature for the various stages involved. A single approach which provided a high contrast low noise output, which was available at a low cost (both in terms of fixed and variable costs) and which did not compromise the mechanical properties (strength, toughness and fatigue life) of the component would be ideal. However, the reality is that the final choice is likely to be much more of a compromise between these area.

Sensing Techniques

The changes that follow from network formation and vitrification are associated with a number of molecular changes and it is these molecular properties that allow the various monitoring techniques to provide a signal which points to cure progress.

Electrical

In the case of electrical properties, the initial mixture will be fairly conductive and hence a reduction in the conductivity can be correlated with the formation of the three dimensional structure and hence the gelation - vitrification process. A related electrical measurement is that of the dipolar relaxation. Initially, the dipoles are very mobile but, as the reaction proceeds, new dipoles are produced or the existing dipoles are slowed down by the increasing molecular weight of the polymerising entities. Correlations have been proposed for the relationship between the dipolar process and viscosity[3] however, there is no fundamental reason why the dipolar process should always be correlated with macro-viscosity[4], but it is possible, using empirical relationships, to use this method to indicate the vitrification and gelation points for a material.

Optical

During the reaction, the nature of the atoms forming the material may change slightly; there may be emission of water in some cases; but in a material such as an epoxy resin, the atomic constituents will remain constant with only the bonding changing as a result of cure. Initially, there will be little change in the density of atoms but as the gelation phase proceeds the necessity to form bonds will result in a decrease in the atomic density. In the case of refractive index, this parameter is a measure of the atom density per unit volume of the material and consequently can be used as a measure of progress during this phase of cure.

Changes in the dielectric properties of the resin during cure at optical frequencies may be monitored via the refractive index of the resin. Zimmerman et al [5] (as well as Abramowitz) have demonstrated a novel system which uses sections of fibre manufactured from the resin material coupled to fibre guides. Since the resin has a higher refractive index when cured the resin fibre starts of as a guide and but reduces in guiding efficiency as the cure proceeds. A problem with this approach is encountered when the graphite fibres touch the resin guide. This results in scattering from the resin guide which can add to the losses due to cure. It is not clear that such added losses can be referenced out. The technique loses sensitivity as the cure proceeds and therefore is not useful in accurately determining the process endpoint but does provide information on the earlier stages in the cure cycle.

Alternative optical parameters include the measurement of shifts in infrared absorption bands which are a result of the changes in the constituents as the reaction proceeds.[6] These display maximum sensitivity in the initial stages of the reaction and sensitivity decreases as the reaction proceeds to the vitrification step. It is possible to use specific absorption such as that created by the epoxy ring at 904 cm^{-1} as a direct indication of the degree of reaction. This allows residuals to a level of 5% to be monitored giving some sensitivity in the post vitrification phase.

Fluorescence techniques have been described which provide a signal that changes in response to the viscosity changes associated with cure[7,8]. This approach utilises the viscosity dependent fluorescence of probe molecules dispersed within the matrix material. During cure, the motions of the probe molecules become progressively more inhibited by the increasing viscosity of the polymer matrix material. In some instances the monomer material itself can be used as the probe molecule (although the behaviour is attributed to an unidentified impurity within the monomer). The probe fibre, which provides both the excitation radiation and collects the fluorescence signal is 0.2 mm in diameter. Its efficient operation is dependant on the ability to collect the signal from the end of the fibre. With this type of arrangement it is unlikely that it will be possible to reduce the size of the probe fibre (down to 0.08mm or 0.03mm) unless there can be an increase or amplification of the fluorescence signal.

A similar probe technique is possible using the Raman signal from the curing matrix material[9]. Care has to be used so as to avoid swamping the Raman signal with the fluorescence signal described above. This is possible by proper choice of the wavelength of the probe radiation. Special methods have to be employed to improve the signal to noise ratio of these methods.

Acoustic

Ultrasound propagation in a liquid medium will be controlled by the viscosity, thermal conductivity and relaxation properties. In most curing polymer systems the increase in attenuation and velocity observed during the initial stages have been correlated with an increase in the modulus of the material and the coincidence in terms of time and frequency of segmental relaxation. The use of Ultrasonic technology is therefore able to identify vitrification as the point at which the absorption becomes a maximum (1MHz) this will usually occur before cessation of motion. The attenuation will then drop to a low level consistent with the material becoming a glass and the velocity will rise and approach an asymtotic value coinciding with the bulk modulus.

Acoustic waveguides have shown a remarkable sensitivity to the level of cure of the surrounding material. In this approach, a metal wire is used as an acoustic channel through the component being manufactured. As cure proceeds the losses from the guide increase dramatically (by a factor of 10^4) as the acoustic radiation becomes less efficiently contained by the hardening resin. The waveguide's efficiency is determined by the impedence mismatch between the guide material and the surrounding material and essentially monitors changes in the density and sound velocity in the surounding material.

The size of such wires has until now been 0.5mm diameter[11]. A reduction of this diameter to around 0.125mm is planned. It is not clear at present that the diameter could be reduced any further without increasing system losses beyond an acceptable level. Other workers[9] using this technique have reported that more repeatable results are obtained when using time of flight measurements with acoustic waveguides. This perhaps reflects the requirement for a suitable referencing technique when using amplitude dependant measurement techniques.

Macro or Micro Viscosity

An important issue when using the sensor data to predict the viscosity changes relates to the issue of macro or micro effects. In the case of dielectric measurements, the signature is very sensitive to the microscopic viscosity. However, in practise, the macroscopic viscosity of even the uncured composite can be several orders of magnitude higher as a consequence of the carbon fibre filler material. Whilst it is true to say that the cure profile can be followed by the dielectric properties, the viscosities which are in practise operative maybe 2 or 3 orders of magnitude different from the micro-viscosities interpolated from the dielectric data. It is important that the contribution from the carbon fibre filler and the influence of the packing configuration are correctly incorporated into the optimisation of the cure process. The dielectric method is ideal for monitoring the microscopic viscosity and its relation to the curing of the resin but may not reflect the observed changes in the macroscopic viscosity which will influence the final form of the structure. This implies that some care must be employed when correlating the sensor outputs and the macro-viscosity features of the cure process[3]. This condition is relevant to the majority of the sensor techniques described above.

Influence of embedded Sensors on Mechanical Properties

Whilst dielectric techniques can provide a signatures related to the cure process, there is concern over the influence of

the sensor (5mm x 5mm x 0.5mm), and its connections, on the integrity of the part under manufacture. Especially, in those circumstances where the sensor must be placed within the component. This is not a problem if the sensor is located in the mould but here it must be accepted that the sensor is only providing information about the cure progress at the component surface. Of course, embedded sensors may be used during the set up phase, when individual process cycles are being optimised prior to full production. However, this still leaves the question of the need for post-manufacture mechanical testing in the case of primary components as described above. These doubts are a serious limitation on the use of such sensors in on-line monitoring of process parameters or indeed in post manufacture quality assurance.

Both acoustic waveguide and optical fibre probes do offer the possibility of a much reduced cross section (0.125mm x 0.125mm x 10mm) with connections of a similar diameter. Further, fibres with diameters of 0.08mm (including protective coating) have been demonstrated and work is in progress on fibre diameters down to 0.03mm. Evaluations of the influence of such structures on the integrity of components is underway. Preliminary indications are that, for uniaxial tension, fibre diameters of 0.08 mm or less (and where the fibre runs parallel to the reinforcing fibres) do not produce significant stress concentration[12] factors and that they do not contribute significantly to the tensile failure of the component. Such indications give the hope that for the appropriate fibre it should be possible to include sensors within the body of the component which do not degrade the performance of the component during its lifetime.

Extension of the Cure Sensor to In service Monitoring

A number of the techniques described above have also been used to monitor the in-service life of the component. For example, the optical fluorescence signal is also dependant on other features such as water content and or aging processes within the matrix material. This is a significant feature since it enhances the usefulness of the embedded sensor network and provides a potential payback throughout the life of the component.

Other methods which provide such a double application include the use of optical fibres (normally used as strain sensors) as acoustic receivers. Measures[13] has described such a network in which optical sensors configured as Michelson interferometers can be used both during the cure process and during the components life. During the cure, the sensitivity of the sensors to an external acoustic signal changes as the cure proceeds. During the component life, the fibre interferometer acts as a strain gauge. Such a system fits in with the quality assurance procedures described for secondary components and as such could provide important information about the level of cure for primary components.

Conclusions

Electrical, optical and acoustic techniques can provide signatures which can be interpreted as signalling the onset of gelation and vitrification. However, we have highlighted the difference between micro and macro features of viscosity implying that some care must be used in the direct interpretation of these signatures. A proper choice can only be made after considering which stage of the process cycle is of interest and whether the sensor output is likely to be well correlated with the features of interest.

If the measurements are only to be used during the set up phase of the process then questions related to intrusiveness are less important. However, if the measurements are to continue into the production phase then it will be important to minimise the size of sensor elements and their connections. This also applies to the extension to in-service monitoring. Optical sensors have an advantage in this situation because of their small size and their applicability to both manufacturing and in-service use has been demonstrated.

For the question of the post manufacturing quality assurance, the issues raised by macro versus micro viscosity are more important. For the post cure phase it is not clear that the important changes in mechanical properties are likely to show a high correlation with changes at a micro level. It is to be expected that there will be a densification with the post cure process however further work is required to characterise these micro-changes and identify which sensing technique would be appropriate for their detection. Hence, future research on sensors for signalling these changes should consider the range associated with each technique and how this correlates with the macro mechanical properties.

1. "Investigation of Cure in Epoxy Resins: Ultrasonic and Thermally Stimulated Current Measurements", Bunton, L.G., Daly, J. H., Maxwell, I. D. and Pethrick, R. A., Journal of Applied Polymer Science, Vol 27, 4283-4294 (1982).

2. "Quality Assurance in the Processing of Thermosets", Michaeli, W., Burkhardt, G. and Stoger, M., pp 10-12 Kuntstoffe German Plastics 81 (1991) 11.

3. "FDMES Sensing for Continous On-Line Monitioring and Control of Cure". D. E. Kranbuehl, RAPRA Conference 1991.

4. Menges, G., Burkhardt, G. and Stoger, M., "Profits and Problems of Correlation Measurements with Dielectric and Mechanical Cure Monitoring Methods. SAMPE, Basel, Switzerland, 1990.

5. "Composite Cure Monitoring Using Optical Fiber Sensors", B. Zimmerman, M. DeVries and R. Claus. p177 Proc of the conference on Optical Fiber Sensor-Based Smart Materials and Structures, (editor R. O. Claus)

6. "Fourier Transform Infrared (FTIR) Fibre Optic Monitoring of Composites during Cure in an Autoclave", Druy, M.A., Elandjian, L. and Stevenson, W.A.. pp150 SPIE Vol 1170 Fibre Optic Smart Structures and Skins II Boston (1989).

7. "In-service Characterisation of Composite Matices with an embedded Fluorescence Optrode Sensor", Schwab, S. D. and Levy, R. L., pp230 Spie Voil 1170 Fibre Optic Smart Structures and Skins II, Boston (1989).

8. "Luminescent Organometallic Complexes as Visible probes in the Isothermal Curing of Epoxy Resins", Kotch, T. G., Lees, A. J., Fuerniss, S. J. and Papathomas, K. I. Chem. Mater., Vol 4, No 3, 1992, 675-683.

9. "In Situ Fourier Transform Raman Studies of Thermally and Photochemically Induced Curing Reactions", Walton, J. R. and Williams, K.P.J., pp339-345, Vibrational Spectroscopy, I (1991). Elsevier Science Publishers B.V. Amsterdam.

10. "Acoustic Waveguide Embedded Sensors for Submarine Structures". R.T. Harrold and Z.N. Sanjana. p201 AMAS Conference November 4-8 1991, Alexandria, Virgina.

11. "In-Situ Acoustical and Optical Waveguide Sensors", O'Keefe, C.V., Djordjevic, B.B. and Ranganathan, B.N. pp391-394, 1st European Conf. on Smart Structures and Materials, Glasgow 1992.

12. "Micro-Mechanics of Sensor-Host Interactions In Fiber-Optic Sensors Embedded in Laminated 'Smart' Composites", Dasqupta, A., Sirkis, J. and Wan, Y. pp47-48. AMAS Conference November 4-8 1991, Alexandria, Virgina.

13. "Fibre-Optic Interferometric Sensors for Ultrasonic NDE of Composite Materials", Liu, K and Measures, R.M.,pp150-151, AMAS Conference November 4-8 1991, Alexandria, Virgina.

SMART STRUCTURES AT AASTRA CORPORATION

D.R. Uffen, H. Scholaert, G. Schmid
Aastra Corporation
1685 Flint Rd.
Downsview, M3J 2W8
Canada

1. Summary

Aastra Advanced Ceramics is a major manufacturer of piezoelectric ceramic materials. Aastra Aerospace is involved in the development of smart structures technology based on these materials. Piezoelectric ceramics as actuators offer high mechanical stiffness, large output stress, and good linearity. As strain sensors, piezoceramics offer very high sensitivity. Initial research into the use of externally-bonded or embedded piezoceramic strain sensors and actuators has lead to the development of in-line sensor-actuator systems for use in truss-type smart structures. The target applications for these units are large flexible space structures, but the technology is applicable to earth-based truss structures as well. Similarly, Aastra is investigating the use of piezoelectric materials for the active damping of aircraft structures, with the goal of reducing structure-borne cabin noise with minimum additional weight. This paper presents the development of Aastra's piezoceramic research activities and an overview of present work in the field of smart structures.

2. Introduction

There has been significant interest lately in the use of smart structures for space applications based on distributed, discrete strain sensors and actuators. A typical objective of this application is the minimization of structural dynamic deformations in large space structures (LSS) such as Space Based Radar (SBR) and Space Station Freedom Remote Manipulator System (SSRMS).

'Smart structures' is a term often used to describe a structure with either built-in deformation assessment and control, or built-in health monitoring. Occasionally included is the concept of distributed processing capability, so that the structure is functionally self-contained. The interest at Aastra Corporation is in smart structures with deformation control in the form of active damping.

3. Mechanical Stability Study of SBR

In 1988 Aastra Aerospace completed a mechanical stability study of space- and corporate- fed Space Based Radar configurations for the Canadian Department of National Defence (DND) (Ref. 1). The mechanical stability of the generic corporate-fed configuration was very good. Due to the stiffness of its structure and its symmetry, the firing of station-keeping thrusters was found not to excite any of the flexible modes. A structural dynamic analysis of the space-fed configuration revealed that extensive deformation of the array would occur, as illustrated in Figure 1. The resulting effect on the radar beam, determined through a full planar array radar simulation of over 100,000 elements is shown in Fig. 2. These results prompted a review of potential shape sensing and compensation technologies.

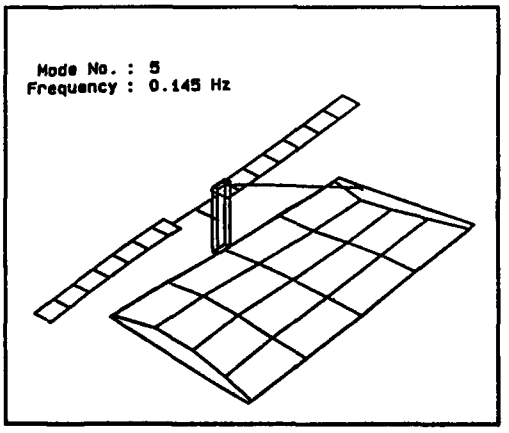

Figure 1: Space Fed SBR

It was from this mechanical stability study that Aastra's research activities in active vibration damping evolved.

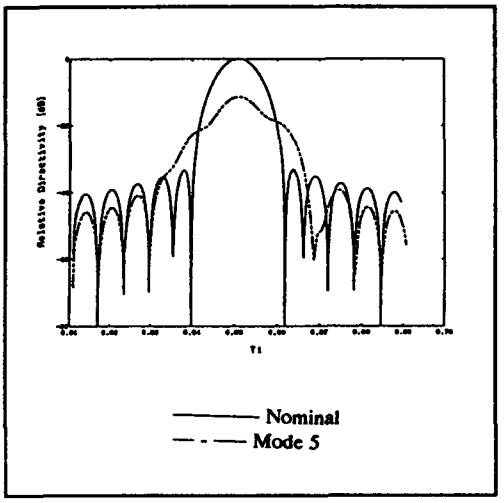

Figure 2:Beam integrity

4. Actuator technologies

In 1989 a study was made of state-of-the-art actuator technologies, including electrostrictive, shape-memory alloys, thermal actuators and piezoelectric systems.

Several actuator concepts based on lead zirconate titanate (PZT) ceramics were investigated. These included discrete bulk elements, thin films and polymer matrix composites. A comparison of the various concepts was made in order to establish the most feasible for further development.

Piezoelectric polymer materials, such as polyvinylidene fluoride (PVDF), offer lower density, and greater flexibility than piezoceramics. Their use as distributed actuators for vibration control has been demonstrated by others (Ref. 2). The suitability of PVDF for embedment in composite structures is limited by its low Curie temperature. Since PVDF loses its piezoelectric properties above about 100°C, it cannot be used in composites requiring high temperature processing. Since high process temperatures are common to most aerospace composites, piezoelectric polymers have found limited application.

Thermal actuators were found to be unsuitable for space structures as the low coefficient of thermal expansion of most composites is incompatible with the design requirements of good thermal actuators. Electro-rheological fluids are equally incompatible as the method results in weaker structures and potential problems with fabrication and sealing.

The study suggested that shape memory alloys and piezoceramic actuators were best suited for active vibration control of space structures. Although the shape-memory actuators provide more force and better performance for low frequency/large amplitude applications the PZT actuators had higher band-widths and consumed significantly less power. In addition there is a potential difficulty with adequate heat dissipation for shape-memory alloys.

Of the PZT-based material concepts, the bulk PZT actuators and thin film concepts demonstrated sufficient adaptability to smart structures to warrant additional research.

5. Sensor systems

A study of external and embedded shape and vibration sensing technologies, for application in LSS, was performed concurrently with the above actuator technology review. Technologies considered included optical systems, radio frequency (RF) measurements, inertial and strain measurements, as well as embedded fibre-optic and piezoelectric sensor systems.

The Spatial High-Accuracy Position-Encoding Sensor (SHAPES) under development at the time at JPL was determined as the most suitable external sensor application as it was the only system with a built-in capacity for measuring target position in three dimensions simultaneously.

Embedded fibre-optics are particularly attractive sensing devices due to their immunity to electromagnetic interference, ruggedness, compatibility with composite material structures and large data transmission bandwidth. Twin-core and elliptical core two-mode sensors are the most attractive of these methods, in terms of resolution, data rate and simplicity.

Piezoelectric sensors have also been successfully embedded in structural composites. They are generally simpler than fibre-optic sensors and fit in well in control systems that have piezoelectric actuators. Piezoceramic/polymer composites are easier to embed than bulk ceramics due to their better flexibility and the compatibility of the polymer with the laminate resin.

6. Active damping simulation on SBR

Based on the results of the above reviews a preliminary study was conducted to determine the effectiveness of active vibration suppression of a space-fed SBR configuration. Using MSC/NASTRAN and Aastra's in-house structural dynamics software, a modal model of the spacecraft was developed. The modal deformations caused by the firing of attitude control thrusters were calculated. Open and closed loop responses to slewing-induced disturbances were compared. For the closed loop case, simple pole placement with rate feedback was used to move selected modes to correspond to a desired percentage of critical damping. The piezoelectric control forces required were evaluated.

The piezoelectric elements used for active control were assumed to be embedded in pairs in elements of the spacecraft structure, with each pair constituting an actuator. Ref. 3 describes a model for embedded actuators of this type. It was assumed that each piezoelectric element was perfectly bonded to the structure. This implies that the elements impart an equal and opposite concentrated moment each end, as shown in Figure 3. The appropriate actuator locations were selected according to the modal force the actuators at each location could generate.

When an active control system was simulated for the roll manoeuvre, it was found that, if the structural modes could be damped to 40% of critical damping, the effects on the radar beam damped out within 20 seconds of completing the slew manoeuvre. This compared very well with a time of over 11 minutes required for the case without active control.

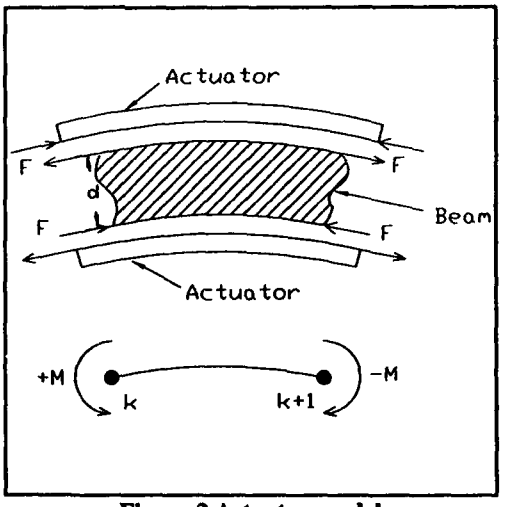

Figure 3:Actuator model

Calculation of the required control forces showed that they could be supplied by a piezoelectric actuator being developed by Aastra.

The encouraging results of the piezoelectric actuators suggested that a feed position sensing system, that would normally be required on a space fed SBR configuration to assure beam pointing accuracy, could possibly be eliminated.

7. Prototype piezoceramic actuators

Aastra Aerospace hence proceeded with the development of a smart structure prototype based on piezoceramic active elements.

The first prototype consisted of a rectangular glass-fibre tube with aluminum end plates. The end inertia of the beam could be varied to control the natural frequency of oscillation. The sensor-actuator elements were thickness-poled wafers, approximately 40 mm by 14 mm by 0.3 mm thick, manufactured from a proprietary PZT composition from Aastra Advanced Ceramics. The wafers were bonded near the root of the beam, with one being used as a sensor and two pairs on opposite sides of the beam being used as actuators. The beam is illustrated in Figure 4. The natural frequency of oscillation of the beam is approximately 9.3 Hz.

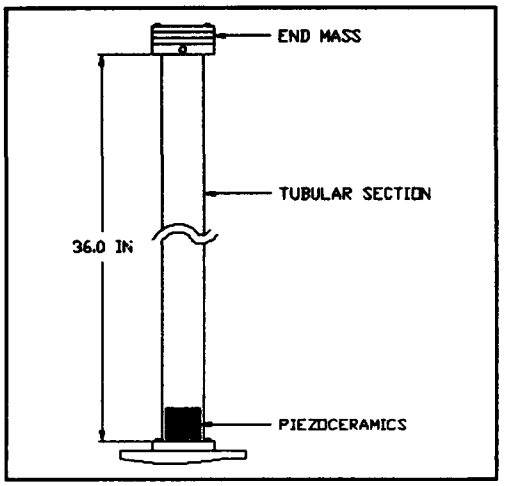

Figure 4: Tubular demonstration

The second prototype consisted of a flat plate of unidirectional carbon-fibre composite, approximately 50 mm wide, 0.8 mm thick and 350 mm long, with an arrangement of ceramic elements similar to that of the tubular beam. The beam configuration is illustrated in Figure 5. The natural frequency of oscillation of the beam was approximately 9.8 Hz.

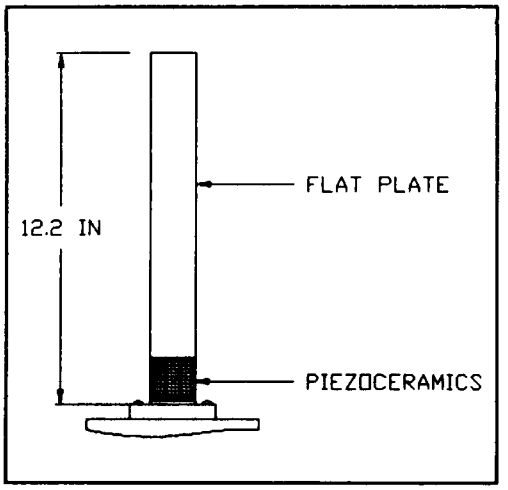

Figure 5: Flat beam demonstration

The feedback circuit consisted of a band-pass filter, a pre-amplifier, a phase shifter, and a high-voltage amplifier.

The pre-amplifier was a simple non-inverting op-amp circuit. The phase shifter circuit was essentially a gain-compensated RC filter. The gain and phase were set by specific resistor values contained in a plug-in connector. This allowed the circuit parameters to be tailored to each specific demonstration beam. The general set up procedure was to adjust the phase to define the bounds of instability. Then choosing a setting in the middle of the stable region, the gain would be increased until either instability occurred or until clipping of the high voltage amplifier became troublesome.

The high-voltage amplifier was a monopolar FET device, with stability provided by an op-amp driven feedback loop. A second pre-amplifier was used to drive an analog-to-digital converter in a personal computer. A Fast Fourier transform of the input data was performed and a decaying exponential fitted to the maxima of the decaying sinusoidal signal.

Figures 6 through 9 display typical results for the damping in the beams. Both beams showed an increase in damping ratio on the order of a factor of 6 or 7. The results were heavily dependant on the settings chosen for the gain and phase change in the feedback circuit.

Clipping in the high voltage amplifier is evidenced, in the case of the tubular beam, by the change in the decay rate with falling amplitude. An almost linear decay is seen in the region where the amplifier clips, followed by the normal exponential decay once the amplifier de-saturated.

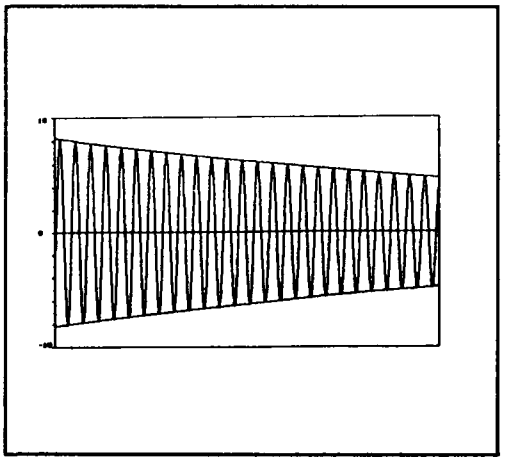

Figure 6: Tubular Beam - Free Vibration

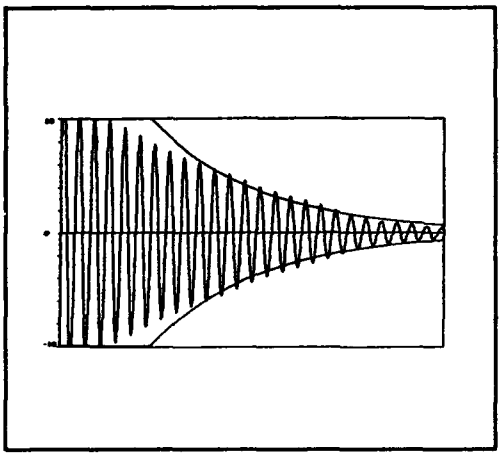

Figure 7: Tubular Beam - Actively Damped

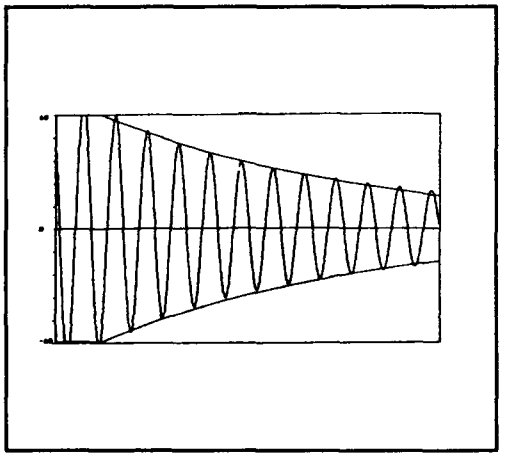

Figure 8: Flat Beam - Free Vibration

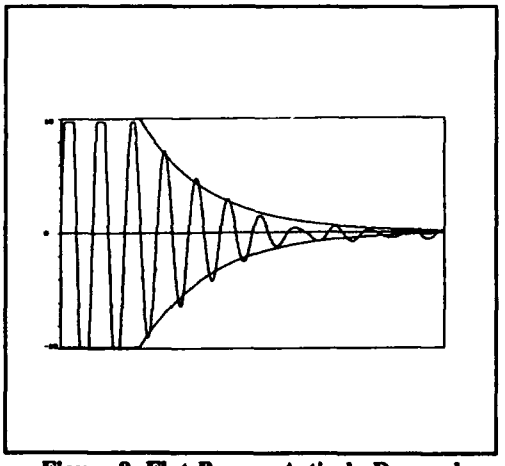

Figure 9: Flat Beam - Actively Damped

The flat beam results show a definite upward frequency shift during decay, from 9.8 Hz to 11.6 Hz. At the same time there is a decrease in decay rate. This represents a change in mode shape, with the highly damped section near the root of the cantilever becoming less significant as the vibration decays, effectively shortening the beam.

The increases in damping ratio with active damping displayed by the beam prototypes were significant, though somewhat modest. This was primarily due to limitations in the feedback circuitry. Further, the ceramic elements used were off-the-shelf wafers of a proprietary Aastra composition with a relatively low coupling-modulus product. Wafers of other Aastra materials were not readily available.

It was noted that the actuators were bonded to the surface of the beam, and that the strain energy was shared between the actuator and the beam itself. A significant increase in damping could be achieved if the beam segment under the actuator were removed, so that all of the load path could pass through the actuators.

8. In-line Sensor/Actuator system (SAS)

In order to address the concerns raised during testing of the two beam prototypes, Aastra proceeded with the development of an in-line actuator design. The active elements would be spliced into the structure rather than being bonded or embedded on the surface. This is particularly simple in the case of a truss made of tubular elements, where the active modules would be constructed in a manner similar to the tube connectors.

To this end Aastra designed, developed and characterized a prototype in-line sensor/actuator system (SAS) for the active damping of truss structures. This work formed Phase I of a smart structures development project funded by the Canadian Space Agency (CSA) and DND. The geometry and performance specifications for the device were based on the anticipated requirements of a large space structure. Among the potential LSS applications considered were:

- Space Station Freedom Remote Manipulator System (SSRMS)
- Space-Based Radar(Space-fed, and parabolic Reflector designs)
- Space Station Freedom Main Truss
- Space Crane Manipulator

These applications were reviewed to determine the general performance requirements each would place on smart structures implementation. The SSRMS and Space Crane were selected for more detailed study.

The Spar Aerospace SSRMS is similar to, but larger than, the Canadarm used on the Space Shuttle. The flexibility of the manipulator places severe performance restrictions on the system, since the arm must be moved slowly to avoid the build-up of large oscillations. Thus it would appear that SSRMS is a good candidate for active damping. However, information provided by Spar indicates that the majority (80%) of the overall flexibility of the arm is caused by the joints, rather than by the bending of the tubular booms. Dynamic modelling by Aastra showed that even a factor of 100 improvement in boom damping would not significantly improve overall damping unless the joints represented less than 40% of the overall flexibility.

The NASA-Langley Space Crane manipulator concept (Mikulas 1988) is a 95m by 5m hinged truss that would be used for in-orbit assembly of large structures. A complete Space Station Mobile Servicing System, with associated SSRMS, would be used as an end effector. The use of linear actuators rather than rotary joints ensures that the flexibility will be dominated by the truss elements. Thus active damping of the truss tubes could be used to significantly reduce the time to manoeuvre and assemble components. For this reason, Space Crane was chosen as the target application for the program.

A structural model of a space crane was developed which was similar to, but stiffer than, the NASA-Langley concept. The specifications for payload mass and capture velocities, etc., were taken to be the same as those for SSRMS. The frequency of the empty boom was found to be ≈ 1 Hz, and with an arbitrary baseline damping ratio of 0.3%, the time to half amplitude was 36 s. The frequency dropped to 0.12 Hz with a maximum payload mass of 128,000 kg (shuttle orbiter), with a time to half amplitude of 2800 s.

8.1 Design of SAS unit

The Aastra SAS unit envisaged for the Space Crane involves packaging a sensor and actuator within a standard truss element, while retaining the same mechanical interface hardware. A tubular piezoceramic actuator assembly would be spliced into the truss element load path. The length change of the truss element would be used as the feedback parameter. Optical ranging would be used as the feedback parameter. This sensing method would be used to provide sufficient sensitivity, given the small strain levels expected. SAS components would be placed in the corners of the truss near the root of the arm and at the joints. The concept is illustrated in Figure 10.

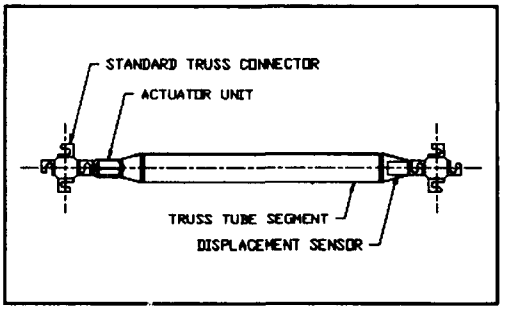

Figure 10: Aastra SAS unit

In order to evaluate the SAS concept, a scaled prototype unit was designed and fabricated, as illustrated in Figure 11. The actuator element is a bonded assembly of stacked piezoceramic wafers. The selected stack dimensions were 22.6 mm diameter with a 3.3 mm wall thickness, and a length of 38 mm. The individual wafers in the stack were 0.76 mm thick.

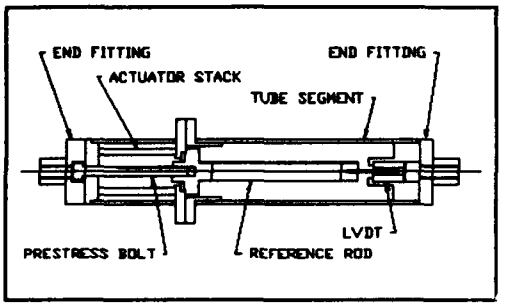

Figure 11: Scaled SAS unit

Debonding was avoided using a conical washer and prestress bolt. A linear variable differential transformer (LVDT) was used to measure the truss tube length changes. A simple analog circuit combining a band-pass filter, phase shifter, and high voltage amplifier was used for feedback.

A preliminary applications test structure was built to simulate the dynamics of a complete truss. It is a 3.05 m cantilevered beam, consisting of a 88.9 mm diameter aluminum tube, attached to a single truss bay at the root. The SAS units are inserted into the truss bay to provide damping, as illustrated in Figure 12.

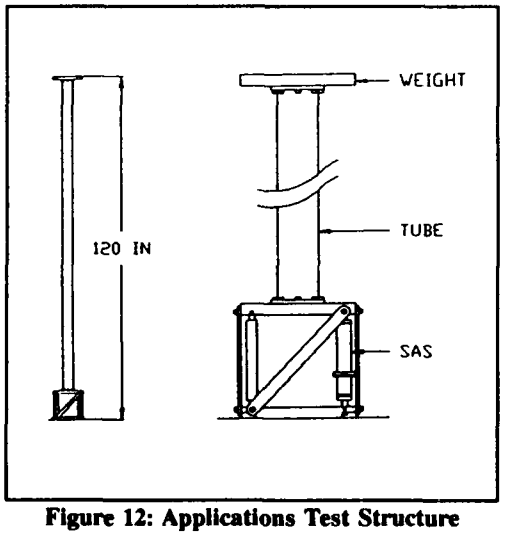

Figure 12: Applications Test Structure

The natural frequency of the beam was 4.8 Hz with a measured damping level of 0.18%. Using a maximum ±360V to drive the actuator, a single SAS unit increased the damping to 5.1%. This represents an improvement in damping by a factor of 29. Figure 13 illustrates the natural damping overlayed with a typical damped decay. The gain was limited by an instability in the feedback electronics which caused the amplifier to saturate alternately to the positive and negative supply voltages. The instability developed because of the high-pass filter used to remove the DC component of the LVDT sensor output. Eliminating this filter would require the sensor to be re-zeroed periodically to account for thermal drift.

The performance of the SAS unit illustrated that the use of a high signal-to-noise ratio displacement sensor will be critical since, in LSS, large displacements can result from small strain levels. Sensor thermal stability will also be important, in order to allow a broad frequency response. Additionally the gain selection is complicated by the maximum available amplifier voltage, since non-exponential damping occurs when the amplifier is saturated.

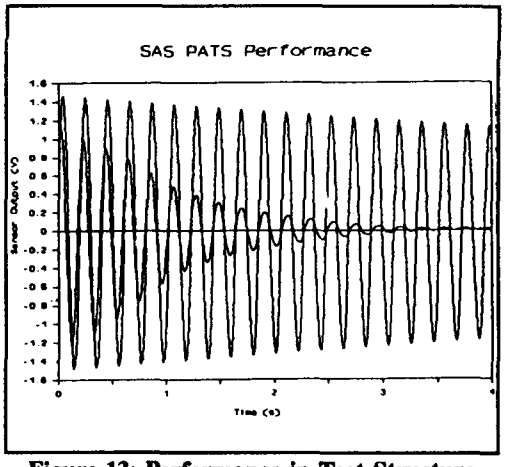

Figure 13: Performance in Test Structure

9. Horizontal truss test model

Aastra is presently involved in the design and construction of a more elaborate test structure, representative of Space Crane. The structure will consist of a horizontally arranged hinged truss, approximately 8 m long, with linear actuator elements. The SAS performance will be measured with the truss fixed in various

geometries, and with the truss moving through a series of predetermined motions. The proposed applications test structure is illustrated in Figure 14. The test structure is not only representative of Space Crane but also of an advanced robotic manipulator, or of a beam steering device for an advanced space-fed radar satellite. Air bearings may also be introduced to support the truss, in order to unload the hinges and minimize friction.

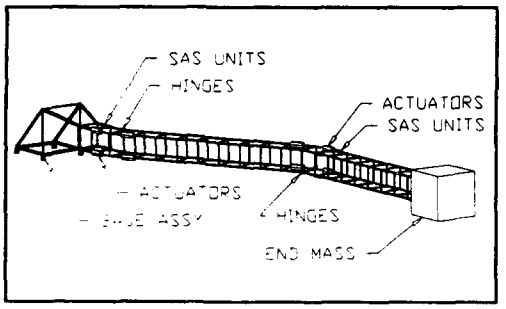

Figure 14: Proposed Test Structure

10. Active damping of aircraft structures

Piezoceramic actuators offer significant possibilities in providing an active noise and vibration control system for aircraft structures. Aastra Aerospace has submitted a proposal, in conjunction with Bombardier/de Havilland, for a first-tier subcontract in support of the joint USA-Canada Integrated Smart Structures (ISmaS) program. This involves the integration of active actuators and processors with advanced composite structures; with special emphasis being placed on embedded/surface actuation, control systems, and systems integration. In general, the active smart structures may be used for flutter control, active control of cabin noise and vibration, alleviation of airframe dynamic loads, and de-icing applications.

11. Future research

Aastra is not limiting its research effort to the implementation of monolithic piezoceramic materials. Laboratory research is currently directed toward the development of smart materials, more specifically advanced ceramic thin films. These films are expected to perform the active damping functions previously discussed. However, they are expected to be more adaptable to a variety of structural designs, while feedback electronics are expected to be virtually eliminated.

12. Acknowledgements

Much of the research presented in this paper has been financially supported by the Canadian Space Agency and the Department of National Defence, Defence Research Establishment Ottawa, Space Based Radar Project Office.

References

1. Aastra Document 3018, "Space Based Radar Mechanical Stability Study-Structural Dynamic Analysis" submitted to the Canadian Department of National Defence, Defence Research Establishment Ottawa (DREO), Jan 1988

2. T. Bailey and J.E. Hubbard, "Distributed Piezoelectric-Polymer Active Vibration Control of a Cantilever Beam", Proceedings, AFWAL Vibration Damping 1984, Long Beach, California, Feb. 27-29, 1984.

3. E.F. Crawley and J. de Luis, "Use of Piezo-Ceramics as Distributed Actuators in Large Space Structures", AIAA Paper No. 85-0626.

FIBER OPTIC SENSING FOR COMPOSITE SMART STRUCTURES

Raymond M. Measures

University of Toronto Institute for Aerospace Studies
4925 Dufferin St., Downsview, Ontario, M3H-5T6, CANADA

SUMMARY

Structurally integrated fiber optic sensors (SIFORS) will form a necessary part of of future Smart Structures and strain sensing will provide valuable information on the use and loading of such structures and also determine the response of the structure to these loads. Strain measurements may be used to check structural integrity and in the case of Smart Adaptive Structure they would provide the deformation information required by the structurally integrated actuation control system. Continuous monitoring of the applied loads could also be used to determine the actual fatigue life of the structure at any point in its operation. In the case of composite materials improved quality control during fabrication may be possible from such a built-in sensing system and this could lead to a more consistent and reliable product. Overall the introduction of an embedded fiber optic strain sensing system to composite structures may enhance confidence in their use and lead to an expansion in there range of application, especially as primary structures in the Aerospace field.

In this paper the types of fiber optic sensor are reviewed and it is shown that the intracore Bragg grating and the intrinsic Fabry-Perot interferometer appear to qualify for continued consideration as the universal sensor for the broad range of potential Smart Structures. The key elements of strain sensing with both types of structurally integrated fiber optic sensor are reviewed and issues such as thermally induced apparent strain are discussed. It is shown that although both sensors now have good methods of demodulation, the Bragg grating sensor has the greatest potential to satisfy the requirements demanded of the ideal sensor for Smart Structures due to the recently developed ratiometric wavelength demodulation system. This system promises the fabrication of a: robust, simple, absolute measurement, low cost multisensor system that could be integrated on to an optoelectronic chip that can form part of the interface to any structure and in essence solve the critical interrconnect problem. Two important questions, however, remain to be addressed: can the intracore Bragg grating sensor perform all of the tasks required, and can Bragg gratings of "sufficient quality" be fabricated in an automated process.

LIST OF SYMBOLS

ε_γ^f fiber strain component in the γ – direction
ε_z host strain in the optical fiber direction
σ_z host stress in the optical fiber direction
E Youngs modulus for the host
ν Poisson's ratio for the optical fiber
$\Delta\phi$ strain induced phase change
S phase-strain sensitivity
L sensor gauge length
S^I interferometric phase-strain sensitivity
k free-space propagation constant
n effective core index of refraction
$P_{\alpha\gamma}$ strain-optic coefficients
P_e effective strain optic coefficient
S^P polarimetric phase-strain sensitivity
n_F fast effective core index of refraction
n_S slow effective core index of refraction
S_α^m two-mode strain sensitivity, α - polarized light
n_α^{01} effective core index of refraction for LP_{01} mode
n_α^{11} effective core index of refraction,even LP_{11} mode
λ_B Bragg wavelength
Λ index modulation periodicity
ε_1 axial strain in the optical fiber
$n_{0,\alpha}$ mean core index of refraction, α - polarized light
P_α^{eff} index weighted strain optic coefficient
$\lambda_{o,\alpha}$ reference Bragg wavelength, α - polarized light
$\Delta\lambda_\alpha$ measurand induced change in Bragg wavelength
S_B Bragg grating wavelength-strain sensitivity
$R(\Delta\phi)$ two beam interferometric response function
V visibility factor
λ wavelength
$\backslash\Delta\lambda_Q\backslash$ quadrature wavelength shift
N quadrature order
Θ Serrodyne induced phase shift
ω_m Serrodyne angular frequency
ϕ_m depth of Serrodyne phase modulation
t time
$F(\lambda)$ linearized filter function
I_F filtered optical signal
I_R reference optical signal
A slope of filter function
$\Delta\lambda$ Gaussian width of Bragg grating signal
λ_0 wavelength for which $F(\lambda) = 0$
ΔT change of temperature
$\Delta\sigma$ thermally induced stress
α_F coefficient of thermal expansion of optical fiber
α_H coefficient of thermal expansion of host
g bonded fiber phase strain coefficient
f free fiber thermal phase strain coeffient
ε_{app} apparent strain
κ apparent strain sensitivity
C_T temperature compensation factor
$\Delta\varepsilon_{stress}$ stress induced strain

1. INTRODUCTION

In the 70's new approaches to complex engineering systems like aircraft were adopted. These assume that each major component contains one or more critical flaws at a level not detected initially. This led to new engineering strategies, such as:

* *Lifetime System Monitoring*
* *Retirement for Cause*
* *Designed-in Inspectability*

The earlier approach of retiring an entire batch of structural components once a potentially critical flaw (crack) was discovered in one component led to an enormous cost. Retirement for Cause involves periodic inspection of each component with expensive and elaborate NDE systems. Once a critical flaw is detected that component is retired. Although this ASIP (Aircraft Structural Integrity Program) program has been successful in preventing loss of aircraft from structural failures, it is expensive and not always accurate, furthermore, it leads to greatly increased downtime and a commencerate increase in life cycle costs. The introduction of components with built-in inspectability should significantly reduce costs, improve maintenance and shorten downtime. In addition, monitoring the loads and deformations of a component on a continuous basis will permit its true fatigue life to be estimated at any time.

The past six years has seen the emergence of a new field of engineering termed "Smart Structures" or "Smart Adaptive Structures." This new multidisciplinary field represents a unique marriage of materials with structurally integrated fiber optic sensors and actuation control systems. Smart Structure principles could radically change the engineering design of structures as diverse as: aircraft and space platforms, marine vehicles and installations and terrestrial structures.

The development of *structurally integrated fiber optic sensors* [SIFORS] represents a necessary first step in the evolution of Smart Structures and will lead to improvements in safety and economics of many diverse industrial products. Structures constructed from materials with resident sensing systems could continuously monitor their internal strain and thermal state. Such measurements could be used monitor the loads imposed on the structure as well as its vibrational response and deformation. In addition strain sensing may be capable of assessing damage and warning of impending weakness in structural integrity. This same strain sensing system might also be capable of improving the quality control of thermoset composite materials during fabrication through cure monitoring and measurement of residual strain. Built-in sensing systems are equally likely to be found in future aircraft as in new bridges. In terms of advanced composite materials the greater confidence instilled by this intrinsic inspectability and the prospects of undertaking cure control with the same sensing system will lead to their increased use as primary structures and could avoid overdesign with its multiplier effects, particularly in the Aerospace Field. This technology should lead to a reduction in maintenance, repair and downtime of future aircraft and could also find broad application in ships, submarines, pressure vessels and bridges (1) [Measures] where composite materials are penetrating.

Fiber optic sensors are: extremely small and light weight, resistant to corrosion and fatigue, immune to electrical interference, safe and practically incapable of initiating fires or explosions, and are compatible with composites. They can serve both as sensors and conduits for the sensory signals and could integrate into future fiber optic systems such as the fly-by-light concept currently under active consideration for the next generation of aircraft. Furthermore, the increasing use of optical fibers for communications will ensure that the cost of this technology will decline with time.
In more advanced Smart Structures the information provided by the built-in sensor system could be used for controlling some aspect of the structure, such as its: stiffness, shape, position, or orientation (2) [Ahmad, et al.]. These systems could be called "Adaptive" (or Reactive) Smart Structures to distiguish them from the simpler "Passive" Smart Structures (3) [Measures]. A more appropriate term for structures that only sense their state might be "Sensory Structures". Smart Structures might eventually be developed that will be capable of adaptive learning and these could be termed "Intelligent Structures". Indeed, if we consider the confluence of the four fields: materials and structures; sensor systems; actuator control systems and neural network systems, we can appreciate that there is the potential for a broad class of structures, **figure 1.** Adaptive Smart Structures, have particular relevance to the Aerospace Field leading to: aircraft with adaptable wings, active noise suppression and space structures that constantly adjust their shape and damp out unwanted vibration.

2. FIBER OPTIC SENSORS AND CRITERIA FOR SMART STRUCTURES

In general we can characterize optical fiber strain sensors as either "distributed" or "localized." Distributed sensors are, in principle, very attractive for they would permit the use of fewer sensors and represent a more effective

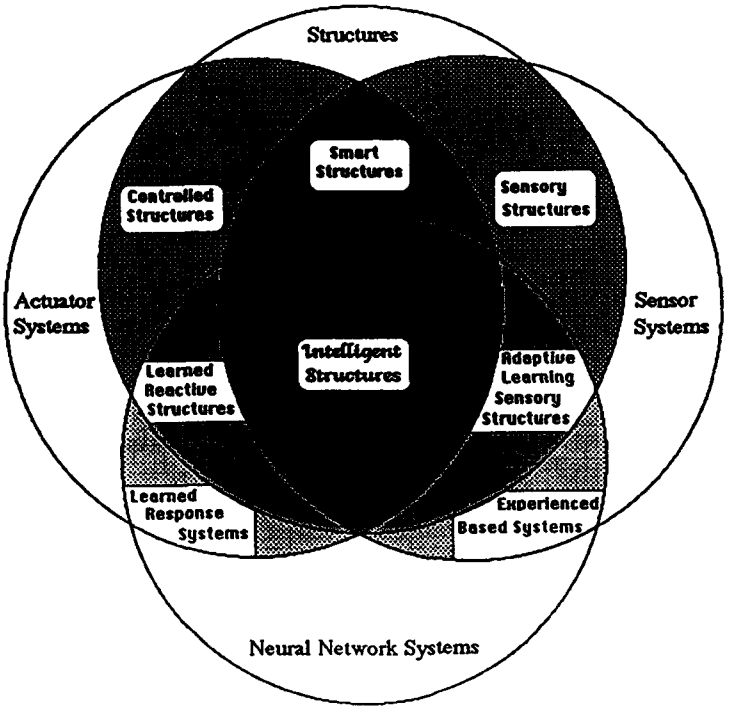

Figure 1. Structures possible by the confluence of four disciplines: materials and structures, sensing systems, actuator control systems, and adaptive learning neural networks, [Measures 1990].

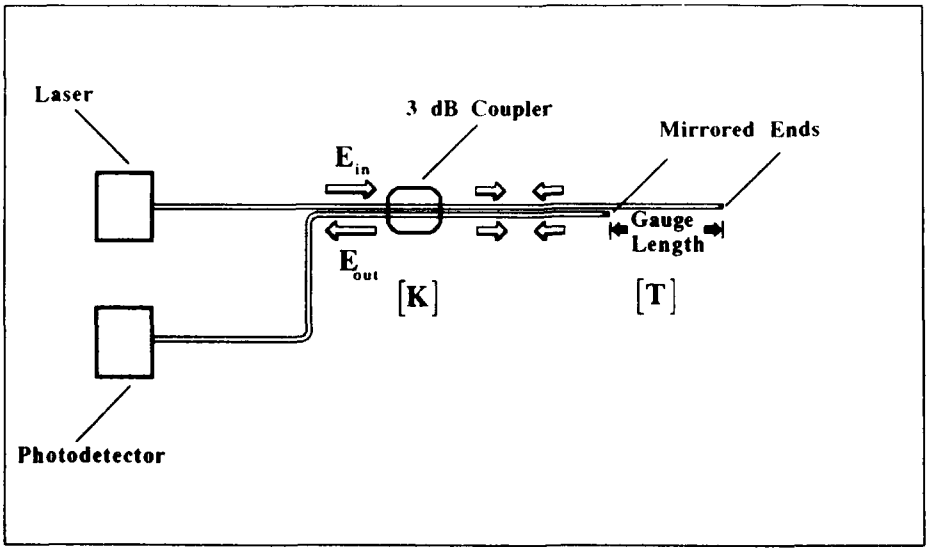

Figure 2. Michelson interferometric fiber optic sensor.

use of the optical fibers, in that *each element* of the optical fiber is used for both *measurement* and *data transmission*. Although, time of flight measurments can be used to map the strain along the length of an optical fiber, this is not practical or economic for aircraft structural components where the real-time spatial resolution should be about 1 cm. Furthermore, the need for high resolution, flexible sensing architecture and graceful degradation is not satisfied with distributed sensors. Often a single break in the optical fiber effectively takes out of commission a large proportion of the sensing capacity. Localized fiber optic sensors determine the *measurand* over a *specific segment* of the optical fiber and are similar in that sense to conventional strain or temperature gauges. Information about the state of the structure is impressed upon the transmitted light by a number of mechanisms. These include interactions that change the: intensity, phase, frequency, polarization, wavelength or modal distribution of the radiation propagating along the optical fiber.

Types of Fiber Optic Sensor

Interferometric fiber optic sensors function by sensing the measurand induced phase change in light propagating along a single mode optical fiber and encompass a large class of sensitive devices. As we shall see later one of the most important requirements for any fiber optic sensor that is to qualify for use with Smart Structures is that it involve a single fiber. Nevertheless, in the past Michelson interferometric fiber optic sensor has been used in the laboratory setting to explore some of the potential applications that might be undertaken with the Fabry-Perot sensor in practical Smart Structures. For example, the Michelson sensor has demonstrated that damage induced acoustic emission could be detected within various composite materials, (4) [Liu et al.) and that cure monitoring of thermoset composites might also be feasible. What made the Michelson fiber optic sensor attractive in the early days was its near identical sensitivity to the Fabry-Perot sensor combined with a much greater ease of fabrication and demodulation. However, its two optical fiber arrangement, **figure 2,** makes it quite unsuitable for Smart Structures due to its: rejection, greater intrusiveness, poor common mode and required phase preservation at the structure's interface. The latter two effects are likely to represent particularly serious problems for practical structures that are invariably subject to high levels of mechanical noise. This sensor is also vulnerable to stress induced birefringence effects along the entire length of the embedded optical fibers, (4) [Liu et al.].

There are four single fiber sensors that are potential Smart Structures candidates: the Fabry-Perot, the two-mode, the polarimetric, and the intracore Bragg grating. The first three can be treated as different forms of two path interferometers. In the Fabry-Perot fiber optic sensor a cavity comprising two mirrors that are parallel to each other and perpendicular to the axis of the optical fiber forms the localized sensing region. A change in the optical path length between the mirrors leads to a shift in the cavity mode frequencies. In this way the reference and sensing optical fiber are one and the same, up to the first mirror that constitutes the start of the sensing region. The Fabry -Perot sensor is normally configured to be single ended, and if built with low reflectivity mirrors will provide a sinusoidal phase strain relationship. Fabry-Perot sensors can be configured as either "intrinsic", **figure 3a** (5) [Lee and Taylor], (6) [Hogg et al.] or "extrinsic", figure 3b (7) [Kruschwitz et al.]. The former has the advantage of being the least perturbative, capable of being used in the form of a strain rosette (8) [Valis et al.], and possibly the more robust. As a consequence of the separation between gauge length and cavity length in the latter, it can be built with long gauge lengths yet work with lasers of modest coherence length, but requires careful calibration. The extrinsic sensor has less transverse coupling and can therefore evaluate more directly the axial component of strain in a host material (9) [Sirkis and Haslach,].

In general, the circular symmetry of optical fibers used to make the sensitive fiber optic interferometric sensors, discussed above, may not be adequate to stabilize the two orthogonal linear polarization eigenmodes. This can lead to polarization-fading and the possibility of cross coupling between the polarization modes. These effects represent a source of noise in interferometric measurements based on small changes (of the order of a few fringes) (10) [Sheem et al]. Although a number of methods have been proposed for aleviating this problem (11) [Kersey et al.], one of the most effective involves the use of polarization maintaining single mode optical fibers. Another method of avoiding polarization fading is to employ a high frequency polarization scrambler. This can be a low cost solution in the case of a network of sensors, however, this gain is at the expense of the interferometic fringe visibility which declines to 0.5.

The most weil developed form of modalmetric sensor is called an "elliptic-core two mode" sensor and involve changes in the transverse spatial mode distribution of light within the optical fiber, (12) [Blake et al.], (13) [Kim et al.], (14) [Murphy et al.], (15) [Lu and Blaha]. In this sensor the lowest order transverse mode {LP01} propagates along the lead-in fiber to the sensing region. Here a section of elliptic core optical fiber that permits

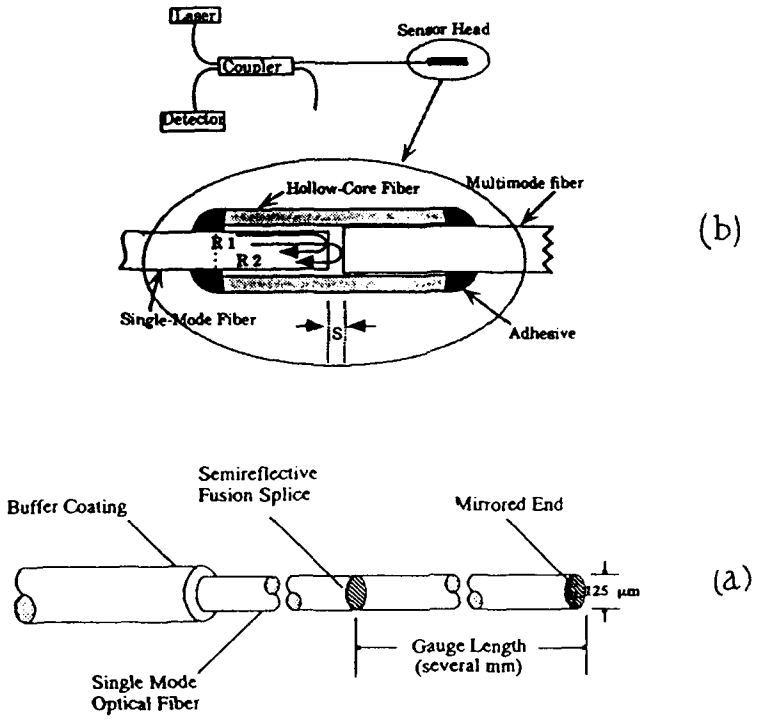

Figure 3. Fabry-Perot fiber optic sensor configurations: (a) Intrinsic [Hogg et al., 1992], and (b) Extrinsic [Kruschwitz et al., 1992].

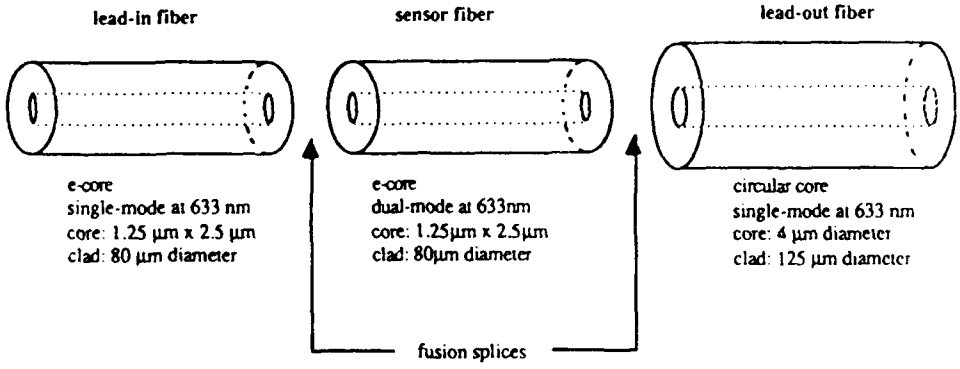

Figure 4. Two mode e-core fiber optic sensor configuration [Murphy et al., 1989].

two transverse {LP_{01} and the even LP_{11}} modes to propagate, at the wavelength for which the lead-in fiber is singled mode, has been fusion spliced with its core slightly offset so that both spatial modes are excited, **figure 4.** A second section of single mode fiber can be fusion spliced to the end of the sensing section or the end of the two-mode (for short) sensing section can be mirrored. Either way the spatial variation in the transverse light distribution is converted into a nonlinear (cosine) relation between the signal and the strain in the host structure, typical of an interferometer.

In a polarimetric sensor changes in the state of polarization of light traveling in a single mode optical fiber are used to determine the strain imposed on the sensor. In order to make the sensor reliable special polarization maintaining optical fiber is used and it is the change in the phase of the two orthogonal polarization eigenmodes of this high-bifringence fiber that is used to evaluate the strain. Localization of the sensor is achieved by rotating the polarization eigenaxes through 45^0 in the sensing section relative to their orientation in the lead in/out sections of optical fiber, **figure 5**, and linearly polarised light is launched into one of the polarization axes of the lead-in optical fiber, (16) [Varnham et al.], (17) [Kersey et al.] and (18) [Hogg et al.], (19) [Bock and Wosinski].

The intracore Bragg grating fiber optic sensor relies on the narrowband reflection from a region of periodic variation in the core index of refraction of a single mode optical fiber. In this sensor the centre (Bragg) wavelength of the reflected signal is linearly dependent upon the product of the scale length of the periodic variation and the mean core index of refraction. Changes in strain or temperature to which the optical fiber is subjected, will consequently shift this Bragg wavelength leading to a wavelength encoded optical measurement, **figure 6**, (20) [Morey et al.].

Criteria and Selection of Fiber Optic Strain Sensor

In order to assess the potential suitability of any fiber optic sensor for undertaking strain measurements in Smart Structures the following criteria can serve as a guide (21) [Turner et al.]. An ideal fiber optic strain sensor for Smart Structures should be:

1. *Intrinsic* in nature for minimum perturbation and stability
2. *Localized,* so it can operate *remotely* with *insensitive leads*
3. Able to respond only to the *strain field* and discern any *change in direction*
4. *Well-behaved* with *reproducible* response
5. *All-fiber* for operational stability
6. Able to provide a *linear response*
7. A *single optical fiber* for minimum perturbation and *common mode rejection*
8. *Single-ended* for ease of installation and connection
9. Sufficiently *sensitive* with adequate *measurement range*
10. *Insensitive* to phase interruption at the structural interface
11. *Nonperturbative* to the structure and *robust* for installation
12. Interrupt immune and capable of *absolute measurement*
13. Amenable to *multiplexing* to form sensing networks within structure
14. *Easily* manufactured and adaptable to *mass production.*

Although there are many fiber optic sensors that have been suggested and used for strain measurements only the: polarimetric {P}, two-mode {TM}, Fabry-Perot {FP} and Bragg grating {BG}, comply with criteria: 1, 2, 4, 5, 7 and 10. These are consequently selected as possible strain sensors and a further down selection is made based on how they comply with the remaining criteria. This can be gauged by reference to **Table I.**

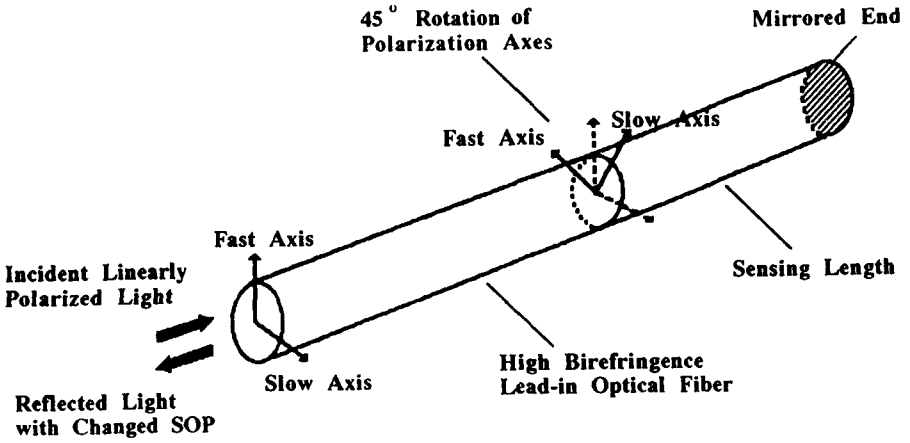

Figure 5. Back-reflective polarimetric fiber optic sensor using a 45 degree rotation of the polarization eigenaxes for localization of sensing segment.

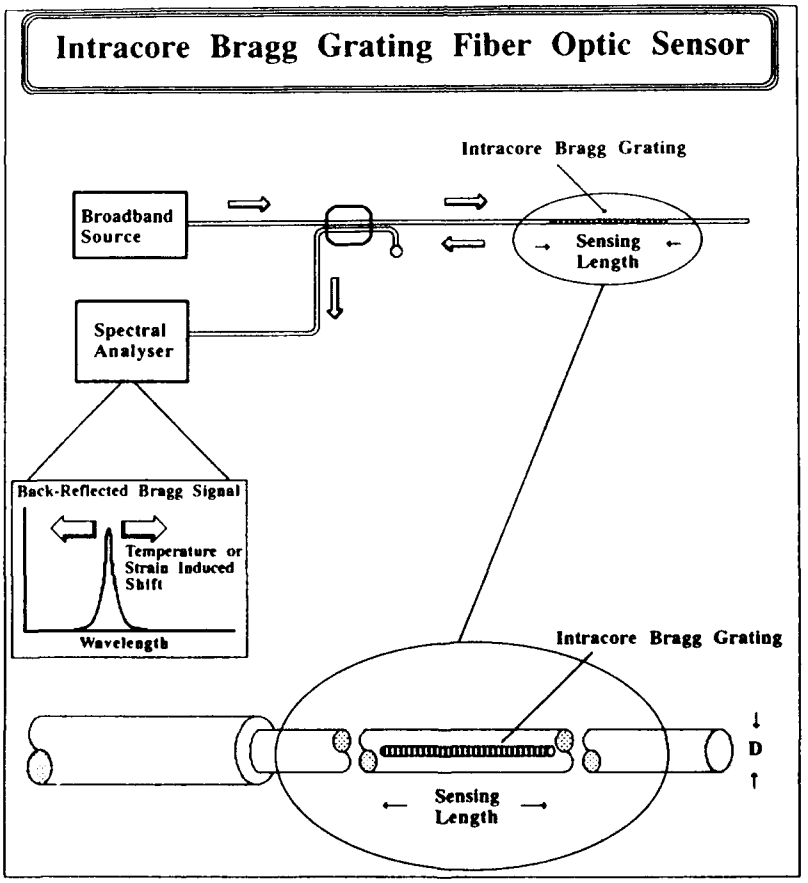

Figure 6. Intracore Bragg grating fiber optic sensor. Also indicated is the backreflected narrow peak Bragg spectrum.

Table I. Comparison of Fiber Optic Sensors

	FP	BG	TM	P
Localized	Y	Y	(1)	(2)
Responds only to strain	(3)	(3)	(3)	(3)
Direction change response	(4)	Y	(4)	(4)
Linear response	(4)	Y	(4)	(4)
Single-ended	Y	Y	(5)	(5)
Adequate sensitivity & range	Y	(6)	(7)	(7)
Absolute measurement	(8)	Y	(8)	(8)
Multiplexing within structure	(9)	Y	(9)	(9)
Potential for mass production	(10)	Y	(10)	(10)

(1) Sensing length is two-mode while lead-in/lead-out optical fibers are single mode.
(2) Polarization eigenaxes is rotated by 45 degrees at start and the sensing length ends in a mirror.
(3) If temperature changes sensor must be able to compensate for thermal apparent strain.
(4) Requires *quadrature* detection and suitable signal demodulation [FiberMetrics Corp.].
(5) Requires a mirror at the end of sensing length.
(6) Limited by demodulation system, but 1 μstrain should be achievable when used as laser sensor
(7) Sensitivity is about 1% that of the FP. This would restrict spatial resolution to many cms.
(8) Requires special demodulation system, so absolute measurement is not available at all times.
(9) Difficult, except for large structures where time division multiplexing can be used.
(10) Requires at the least one fusion splice and therefore some degree of handling.

As we shall see in the next section the high sensitivity of both the intracore Bragg grating and the Fabry-Perot sensor make it possible to use them with short gauge lengths. In order that the cost of implementing Smart Structure technology be kept to a minimum a single type of sensor should be developed that is capable of undertaking all of the requiste measurements. This suggests a sensor with as high a sensitivity as possible so it can be used in the broadest range of applications including: measurement of the internal strain and the detection of anomalies that might indicate the development of a structural weakness; monitoring of the loads applied to a structure and its subsequent deformation; evaluation of the vibration modes and resonant frequencies; cure monitoring and the measurement of residual strain in thermoset composites. The assessment of any degradation in structural integrity is certainly a most desirable capability of any resident strain sensing system. It is expected that if this is to be achieved through the detection of internal strain anomalies that arise when the structure is loaded - very careful strain measurements will have to be undertaken and this is expected to demand a set of highly localized (almost point) sensors of high precision.

This sensor should also be capable of measuring both strain and temperature since infact both will invariably be required for practical Smart Structures due to potential wide temperature excursions. Based on **Table I** and the above considerations the choice probably lies between the intrinsic Fabry-Perot and the intracore Bragg grating sensors. Both the FP and the BG sensors can certainly be used for either strain or temperature measurements and as we shall see later it is expected that strain and temperature will be simultaneously determined with the appropriate sensor design and demodulation.

3. FIBER OPTIC STRAIN SENSOR SENSITIVITY

Fabry-Perot Fiber Optic Strain Sensor Sensitivity

If a uniaxial longitudinal stress σ_z is applied to an isotropic, elastic optical fiber oriented in the z-direction, the resulting strain from first order elastic theory will

be:

$$\varepsilon_\gamma^f = \begin{bmatrix} -\nu\varepsilon_1^f \\ -\nu\varepsilon_1^f \\ \varepsilon_1^f \end{bmatrix} \qquad (1)$$

where we have assumed zero shear strain, (22) [Butter and Hocker]. In the case of a surface adhered or embedded optical fiber sensors, Butter and Hocker made two assumption: (i): $\varepsilon_z = \varepsilon_1^f$, where $\varepsilon_z = \sigma_z/E$ is the strain in the host in the optical fiber direction, and (ii) that no transverse strain fom the host is coupled to the optical fiber so $-\nu\varepsilon_1^f$, is the only component of transverse strain. E is Young's Modulus for the host and ν is Poisson's ratio for fused silica. If we also assume that the optical properties are independent of the polarization state of the light then, in general, the incremental change in the phase suffered by light propagating through the sensing (gauge) length, L, of the optical fiber:

$$\Delta\phi = SL\varepsilon_z \qquad (2)$$

where we have introduced S as the phase-strain sensitivity , (23) [Measures 1993].

For the case of the "interferometric" fiber optic sensor:

$$S^I = kn\{ 1 - n^2 Pe /2 \} \qquad (3)$$

where k is the free-space propagation constant, n is the effective core index of refraction and we have introduced the effective strain optic coefficient :

$$P_e = [P_{12} - \nu (P_{11} + P_{12})] \qquad (4)$$

For an isotropic material there are only two independent strain optic coefficients: P11 and P12, (24) [Jackson and Jones].

For a "polarimetric" sensor the corresponding phase-strain sensitivity is given by the relation:

$$S^P = k (n_F - n_S)[1 - N^2(n_F, n_S)P_e /2] \qquad (5)$$

where n_F and n_S are the respective indices of refraction for the lowest order transverse mode polarized along the "fast" and "slow" polarization eigenaxes of the optical fiber and we have introduced the general relation:

$$N^2(n_a, n_b) = n_a^2 + n_a n_b + n_b^2 \qquad (6)$$

The phase strain sensitivity for the" e-core two mode" sensor can be expressed in the form:

$$S_\alpha^m = k (n_\alpha^{01} - n_\alpha^{11})[1 - N^2(n_\alpha^{01}, n_\alpha^{11})P_e /2] \qquad (7)$$

where n_α^{01} and n_α^{11} represent the respective effective indices of refraction for the LP_{01} and LP_{11}^{even} transverse modes that are linearly polarized in the α - direction and we assume that the strain optic coefficients are essentially independent of the radiation mode. This is a common assumption but one that may have to be examined more closely in future, especially where stress loaded polarization maintaining optical fibers are used.

Recent values of these strain-optic coefficients, P_{11} and P_{12}, have been reported by Bertholds and Dandliker (25), for single mode optical fibers. They indicate that for fibers with a pure silica core and B_2O_3 doped cladding: P_{11} = 0.113 and P_{12}= 0.252 , about 7% lower than for bulk silica. In the case of silica optical fibers (n = 1.458, E = 70 GPa, ν = 0.17) the interferometric phase-strain sensitivity is about 6.5 deg. μstrain^{-1} cm^{-1} [or S = 11.3 rad μstrain-1 m-1] which is close to the value obtained in experiments. For double pass interferometers, like the low finesse Fabry-Perot fiber optic sensor, this figure must be multiplied by two. A comparison of the strain sensitivities for the three kinds of fiber optic strain sensor discussed above is provided in **Table II**. It is quite clear that the Fabry-Perot strain sensor has a much greater strain sensitivity.
For many applications it is important that the strain sensor gauge length is small compared to the scale length over which the strain changes. Some idea of the relative gauge lengths needed to achieve 1 μstrain resolution for the three different types of fiber optic sensor can be obtained from the second row of **Table II** where we have assumed that each sensor has a demodulation system capable of 6.5 degrees of phase shift resolution.

Table II. Strain Sensitivity and Gauge Length Comparison

Strain Sensitivity	Fabry-Perot	Polarimetric	E-Core Two Mode
degrees μstrain^{-1} cm^{-1}	6.5 [Valis..1989]	0.06 [Hogg..1989]	0.02 [Huang..1990]
gauge length for 1 μstrain	1 cm	108 cm	325 cm

Bragg Grating Fiber Optic Strain Sensor Sensitivity

A Bragg grating sensor comprises a segment of optical fiber in which a priodic modulation of the core index of refraction has been formed, (26) [Meltz et al.] (20) [Morey et al.] and (27) [Dunphy et al.], usually by means of exposure to an interference pattern of intense ultraviolet light (at about 245 nm). The optical back-reflected spectrum of such a Bragg grating comprises a very narrow spike (in polarization preserving optical fibers two spikes can be resolved, one for each of the two orthogonal polarization modes). This strong backreflection occurs at the Bragg wavelength, λ_B, which can be related to the effective core index of refraction, n, and the "period" of the index modulation, Λ, by the relation:

$$\lambda_B = 2n\Lambda \qquad (8)$$

Since, this Bragg wavelength will shift with changes in either, n, or, Λ, monitoring the wavelength of this narrow band spectrum will serve to determine the strain or temperature environment to which the optical fiber is subjected. The Bragg grating sensor possesses a number of advantages that make it very attractive for Smart Structures:

-- Linear Response:
the Bragg grating centre wavelength is a linear function of the measurand so there is no direction ambiguity.

--Absolute Measurement:
the Bragg grating centre wavelength determines the measurand value in terms of some reference state.

--Spectral Encoding:
the measurand signal information is spectrally encoded.

--Fiber Optic Strength:
the intracore fiber optic Bragg grating have inherent high strength.

--Multiplexing Potential:
the Bragg grating sensors are readily wavelength multiplexed.

A Taylor expansion of (8) permits us to determine the differential change in the Bragg wavelength, for light linearly polarized in the α– direction, resulting from an applied strain field, (28) [Measures]:

$$\frac{\Delta\lambda_\alpha}{\lambda_{0,\alpha}} = \varepsilon_1 - \frac{n_{0,\alpha}^2}{2}\sum_{\gamma=1}^{6} P_{\alpha\gamma}\varepsilon_\gamma^f \qquad (9)$$

where $P_{\alpha\gamma}$ is the *strain optic tensor*, $\lambda_{0,\alpha}$ represents the reference state Bragg wavelength for light linearly polarized in the α– direction, $n_{0,\alpha}$ is the effective core index of refraction, and ε_γ^f is the *strain tensor* for the optical fiber, comprising three principal and three shear strain components.

In the case of the (22) Butter and Hocker (22) model we can write:

$$\frac{\Delta\lambda_\alpha}{\lambda_{0,\alpha}} = \left[1 - P_\alpha^{eff}\right]\varepsilon_1 \qquad (10)$$

which reveals that the *wavelength-strain sensitivity* of the Bragg grating sensor :

$$S_B = \left[1 - P_\alpha^{eff}\right] \qquad (11)$$

with

$$P_\alpha^{eff} = \frac{n_{0,\alpha}^2}{2}\left[P_{12} - \nu(P_{11} + P_{12})\right] \qquad (12)$$

as the *index weighted strain optic coefficient*.

It should be noted that we have assumed that the bulk value of the strain optic coefficients can be used in all of the above discussion. For polarization preserving optical fiber this is highly questionable. In the case of germanosilicate glass the index weighted strain optic coefficient, equation (12), has the value of 0.22. It should also be noted that in the case of the Bragg grating sensor the strain sensitivity is independent of the length of the Bragg grating. However, the sharpness of the backreflected narrow band spectrum is dependent upon the grating length. One of the most important advantages of this sensor is the direct relation between the Bragg wavelength and the fiber strain which makes absolute measurements of the strain possible. This makes it immune to power interruption (an intentional or unintentional break in the electric power of the system) a weakness of the other kinds of interferometric sensors {in the sense that they normally only determine the incremental strain and require a specialized demodulation system for absolute measurements}.

The *wavelength strain sensitivity* of an intracore Bragg grating formed in Andrew E-type elliptical core fiber and purchased from United Technology Research Centre was measured to be **0.648 pm μstrain^{-1}** for the fast axis and **0.644 pm μstrain^{-1}** for the slow axis when operated at 830 nm (29) [Melle et al.]. A more relevant figure of merit for this kind of sensor is its *strain resolution* and recently, this has been reduced to **8 μstrain**, using a wavelength dependent ratiometric demodulation technique, (30) [Melle et al.]. Morey et al, (31) have determined that the wavelength strain *sensitivity* of a 1.55 μm Bragg grating is: 1.15 pm μstrain^{-1} while its *temperature sensitivity* is 1.3 pm $^{o}C^{-1}$.

Sensor /Host Strain Coupling and Signal Interpretation

For the more general case of a birefringent optical fiber interferometric strain sensor with "short" sensing length embedded within an infinite, isotropic and homogeneous host, the phase increments, $\Delta\phi_2$ and $\Delta\phi_3$, for light linearly polarized in the 2- and 3- directions, respectively, take the form:

$$\Delta\phi_2 = n_2 kL\left[\varepsilon_1^f - \frac{n_2^2}{2}\left\{P_{11}\varepsilon_2^f + P_{12}\left(\varepsilon_1^f + \varepsilon_3^f\right)\right\}\right] \quad (13)$$

and

$$\Delta\phi_3 = n_3 kL\left[\varepsilon_1^f - \frac{n_3^2}{2}\left\{P_{11}\varepsilon_3^f + P_{12}\left(\varepsilon_1^f + \varepsilon_2^f\right)\right\}\right] \quad (14)$$

while equation (9) for the Bragg grating sensor gives rise to normalized wavelength shifts for light linearly polarized in the 2- and 3- directions, respectively, of:

$$\frac{\Delta\lambda_2}{\lambda_{0,2}} = \left[\varepsilon_1^f - \frac{n_2^2}{2}\left\{P_{11}\varepsilon_2^f + P_{12}\left(\varepsilon_1^f + \varepsilon_3^f\right)\right\}\right] \quad (15)$$

and

$$\frac{\Delta\lambda_3}{\lambda_{0,3}} = \left[\varepsilon_1^f - \frac{n_3^2}{2}\left\{P_{11}\varepsilon_3^f + P_{12}\left(\varepsilon_1^f + \varepsilon_2^f\right)\right\}\right] \quad (16)$$

assuming the optical fiber is aligned with the 1-direction of the host principal strains. In equations (13) to (16), ε_α^f, represents the α - component of the optical fiber strain tensor, while it is the host strain tensor that is desired.

The essential simplification made in the Butter and Hocker model were that the strain in the optical fiber in the 1-direction matches that of the host, while zero host strain is coupled to the optical fiber in the 2- and 3- (transverse) directions. Equations (13) to (16) clearly indicate that in the more general case the phase change for the interferometer or the wavelength shift for the Bragg grating sensor observed for each polarization eigenmode of the optical fiber depends on all three principal strain components within the optical fiber and clearly each of these has to be related to the far-field strain in the host. Recently, Sirkis and Haslach (32) extended the Butter and Hocker (22) free-fiber, uniaxial-stress phase-strain model and have shown that their results are closer to those observed in "transverse loading" experiments (33) [Mathews and Sirkis]. Sirkis and Haslach (32) and Mathews and Sirkis (33) indicated that the Butter and Hocker (22) model leads to strain predictions with errors that increase substantially as the stiffness of the optical fiber approaches that of the host.

Recent comparison with experiments (34) [Sirkis and Mathews] suggest that although the theoretical model of Sirkis and Haslach (32) predicts the trend in the variation of phase-strain sensitivity with fiber/host stiffness ratio, the experimental variation is stronger. However, when the optical fiber is collinear with the

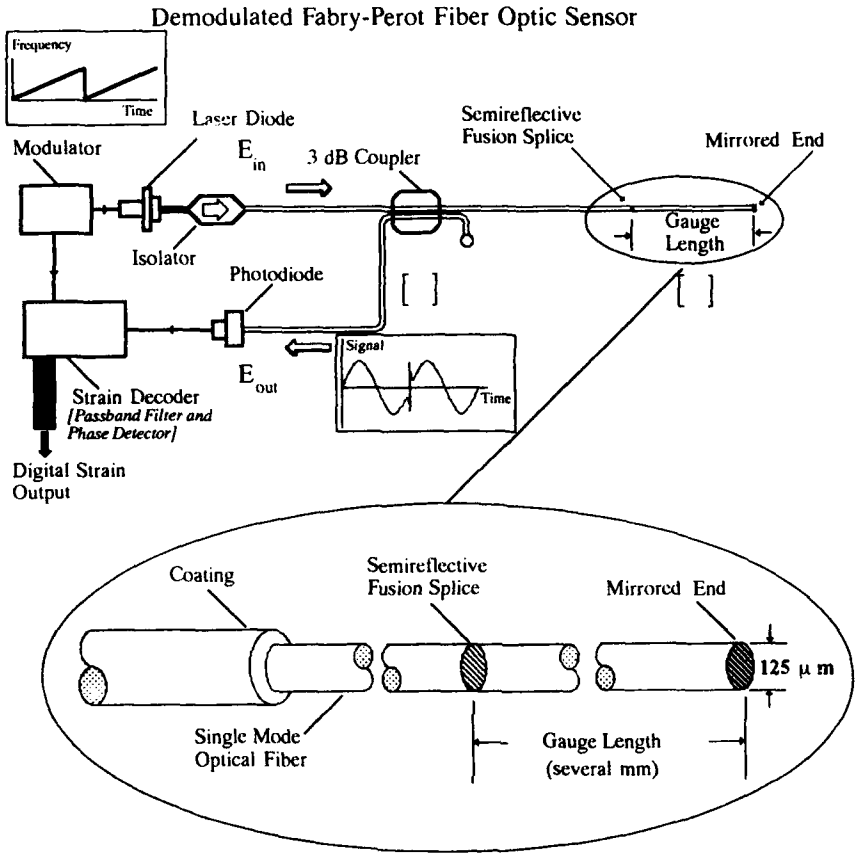

Close up of Fabry-Perot Fiber Optic Sensor

Figure 7. **Pseudo-heterodyne Fabry-Perot interferometric fiber optic sensor demodulation system based on repeated linear frequency ramping of the laser diode and a combination of pass band filtering and phase detection, [Hogg et al., 1991].**

adjacent stiff reinforcing fibers of the host and the loading is in this ply direction the Butter and Hocker model gives reasonable strain predictions. Interestingly, this has often been the configuration used in many experiments. For optical fiber sensors embedded within composites the difference between the theories should not be greater than about 10% , if the *stiffness* of the optical fiber is greater than *ten times* that of the *host matrix*, i.e., $E_f/E_h > 10$. If the stiffness of the optical fiber is not that much greater than that of the host, decoupling the sensing length of the optical fiber from the transverse strains in the host, allows the simpler theory of Butter and Hocker to apply. This appears to be the case for the extrinsic Fabry-Perot sensor, and to a lesser extent the polarization sensor, (35) [Sirkis]. Recently, Valis and Measures (36) have suggested that both the parallel and perpedicular far field stress components within a host can be evaluated by an embedded Fabry-Perot sensor of special design, provided its polarization eigenaxes are suitably aligned with the principal strain axes of the host.

When considering the issue of sensor/host strain coupling there is, however, another factor that must be taken into account. This is the possible presence of an optical fiber coating. Although it may be possible to tailor the properties of this coating to minimize the transverse coupling or greatly reduce stress concentrations in the host adjacent to the optical fiber, Sirkis and Dasgupta (37) have indicated that the sensor's phase-strain sensitivity is not likely to be strongly influenced by the coating. Clearly much work remains to be done to fully understand the fiber/host interactions and as will be alluded to later the presence of a coating maybe important in terms of the sensors performance life (38) [LeBlanc and Measures].

4. STRAIN SENSOR DEMODULATION AND CHARACTERIZATION

Signal Recovery for Interferometric Fiber Optic Sensors

Unlike resistive-foil strain gauges, interferometric fiber optic strain sensors require phase-demodulation, and suffer form interrupt ambiguity (i.e., if the phase-demodulation electronics is interrupted, the new value of the phase becomes nonunique and must be reinitialized). The generic Response Function, $R(\Delta\phi)$, for a two beam interferometer can (24) [Jackson and Jones 1986] be expressed in the form:

$$R(\Delta\phi) = I/I_o = \{1 + V\cos(\Delta\phi)\}/2 \qquad (17)$$

where I - is the photodetector current in the presence of the sensor, I_o - is the photodetector current that would arise directly from the source and $\Delta\phi$ - is the *phase retardation* introduced between the two paths of the interferometer. The *visibility factor, V* (or fringe contrast) is introduced to cover partial coherence situations.

The purpose of *signal recovery* or *demodulation* is to convert the complex optical output from a fiber optic sensor into an electrical signal proportional to the phase retardation . The problem with the fiber optic sensor Response Function is that it is sinusoidal and therefore *multivalued and nonlinear.* Furthermore, the nature of the cosine function leads to: *sign ambiguity* and *signal fading* . The purpose of any signal recovery scheme is to address as many of these short comings as possible. One of the simplest forms of signal recovery is "fringe counting" - this is acceptable for large changes in $\Delta\phi(>> 2\pi)$ but fails to distinguish changes in direction of the measurand. A further problem of the Response Function given by (17) is that it does not provide *interrupt immunity* (i.e., an absolute measurement). Signal recovery techniques should address all five of these issues:

1. *Signal Fading*
2. *Interrupt Immunity*
3. *Sign Ambiguity*
4. *Nonlinearity*
5. *Multivalued Response*

Signal recovery techniques can be broadly classified as: "passive" or "active" and they can involve "heterodyne" or "homodyne" detection (39) [Jackson et al.] and (40) [Liu and Measures]. In heterodyne detection the optical frequencies in the two interferometer arms are unequal, while in homodyne detection there is a common frequency for both arms. True heterodyne signal recovery is unlikely for sensors to be used in smart stuctures as it is somewhat difficult to affect the frequency in one arm (path) of a single fiber sensor.

Switched Dual Wavelength QuadratureTechnique

One of the most elegant methods of overcoming signal fading is to use a system that produces two outputs that have a "phase bias" of $\pi/2$. Such *quadrature* (orthogonal) outputs ensure that one output has maximum sensitivity while the other

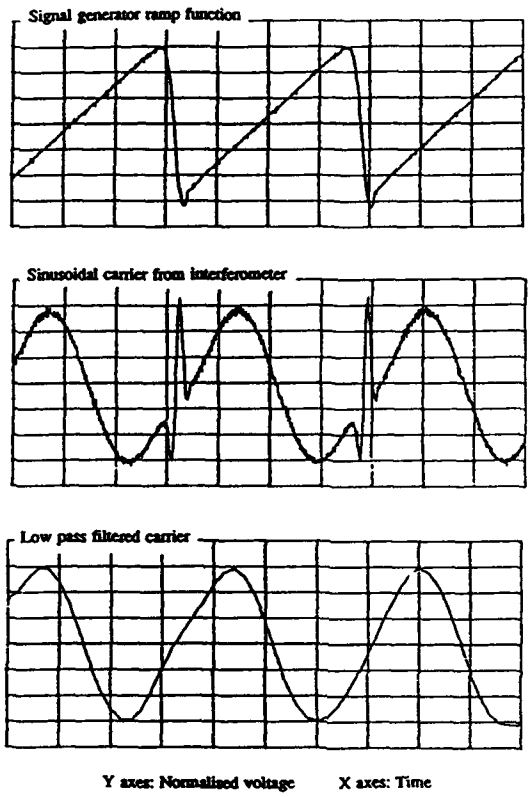

Figure 8. Experimental signals for the pseudo-heterodyne demodulated Fabry-Perot fiber optic sensor. (a) linear saw tooth driver signal to laser diode; (b) resulting Fabry-Perot optical signal; (c) bandpassed filtered signal, [Hogg et al., 1991].

experiences a minimum sensitivity. In the case of the single fiber: polarimetric (41) [Turner et al.], two-mode (42) [Lu and Blaha] and Fabry -Perot (6) [Hogg et al.] sensors, quadrature outputs can be achieved through an active process, such as switching or shifting the laser frequency by some multiple of $\pi/2$ phase shift for the sensor. Such techniques are sometimes referred to as *quadrature phase modulation*. If the laser wavelength is switched between two values corresponding to a $\pi/2$ phase shift, quadrature phase signals are essentially extracted from the sensor. If these are: sampled by orthogonal gating pulses, summed and bandpassed filtered, the resulting sinusoidal signal can be demodulated with a phase sensitive detector (43) [Kersey et al.]. The required *quadrature wavelength shift:*

$$|\Delta\lambda_Q| = \{2N + 1\} \frac{\lambda^2}{4nL} \qquad (18)$$

where N (= 0,1,2....) is termed the *quadrature order*. For small gauge lengths, L<10 mm, the quadrature wavelenght shift falls well within the tuning range of a single longitudinal mode (SLM) laser diode, i.e., $|\Delta\lambda_Q|$ = 0.02 nm. By comparison a quadrature wavelength shift of about 20 nm is required for a polarimetric sensor {birefringence beat length of 1.4 mm, and laser wavelngth of 820 nm} with a gauge length of a few cm (41) [Turner et al.]. This necessitates switching between two separate lasers, and represents a problem in terms of phase control. However, when the sensor was operated with a gauge length of about 1 m, the quadrature wavelength shift reduced to 0.7 nm and the sensor could be operated by switching a single laser between two wavelengths.

Pseudo-Heterodyne Phase Detection

Since variation of the injection current in a semiconductor laser causes a corresponding wavelength change, the laser can directly provide optical phase modulation (44) [Jackson et al.]. This approach is particularly applicable to single lead and single ended sensors, such as the Fabry-Perot interferometric fiber optic sensor. In the case of "Serrodyne" or chirped wavelength modulation of the laser diode the optical frequency is swept over a given range of frequencies. During the linear part of these saw-tooth laser drive signals (of period $2\pi/\omega_m$) a constant rate of phase change is produced in the interferometer by the corresponding shift of frequency. The phase change arising within each period of the saw-tooth waveform is given by the expression:

$$\Theta = [\phi_m \omega_m / 2\pi]t \qquad (19)$$

where ϕ_m represents the *depth of modulation of the phase*. If the peak amplitude of this saw-tooth waveform is adjusted to be 2π (i.e., $\phi_m = 2\pi$) then $\Theta = \omega_m t$ and the normalized signal will be sinusoidal with angular frequency ω_m over this linear ramp part of the saw-tooth modulation. The sudden fall in the modulation frequency at the end of each ramp will give rise to a sinusoidal signal of much higher frequency (in essence a spike). If a suitable bandpass filter is used to remove this fly-back spike then to first approximation the signal is phase modulated with a carrier, ω_m, and we can write the normalized signal in the form:

$$I/I_o = 1/2 \cos\{\omega_m t + \psi\} \qquad (20)$$

where ψ is the sum of the measurand and nonmeasurand induced phase change. Clearly, this "Serrodyne" or chirped wavelength excitation leads to a sinusoidal optical signal onto which is impressed any phase modulation arising from changes in the strain field of the sensor.

A schematic illustration of such a pseudo-heterodyne modulated Fabry-Perot sensor system is presented in **figure 7**, (6) [Hogg et al.]. In this experiment the laser diode injection current was modulated by a linear saw tooth signal with an amplitude corresponding to one fringe. **Figure 8**, displays a representative laser diode driving current waveform and the resulting phase generated optical carrier signal before and after filtering. After detection the carrier signal is fed to a digital/analogue hybrid phase tracker similar to one reported by (45) [Jackson]. This system used a carrier frequency of 31.25 kHz and had an effective strain-bandwidth figure of merit of about 2,200 μstrain Hz cm^{-1} when operated at 850 nm with a gauge length of 1 cm. The theoretical strain resolution of this system is a small fraction of a microstrain and its time response is adequate to cover the normal loading of most practical structures. However, its limited temporal response can pose a serious problem in the event that the structure is exposed to any sudden high rate of loading, such as an impact. Under these conditions the strain sensing system can lose track of the strain.

An improved pseudo-heterodyne Fabry-Perot sensor demodulation system based on sinusoidal modulation of the wavelength of the laser diode and three point phase sampling of the detected optical signal has been developed recently (46) [Mason et al.] and is commercially available. This demodulation system

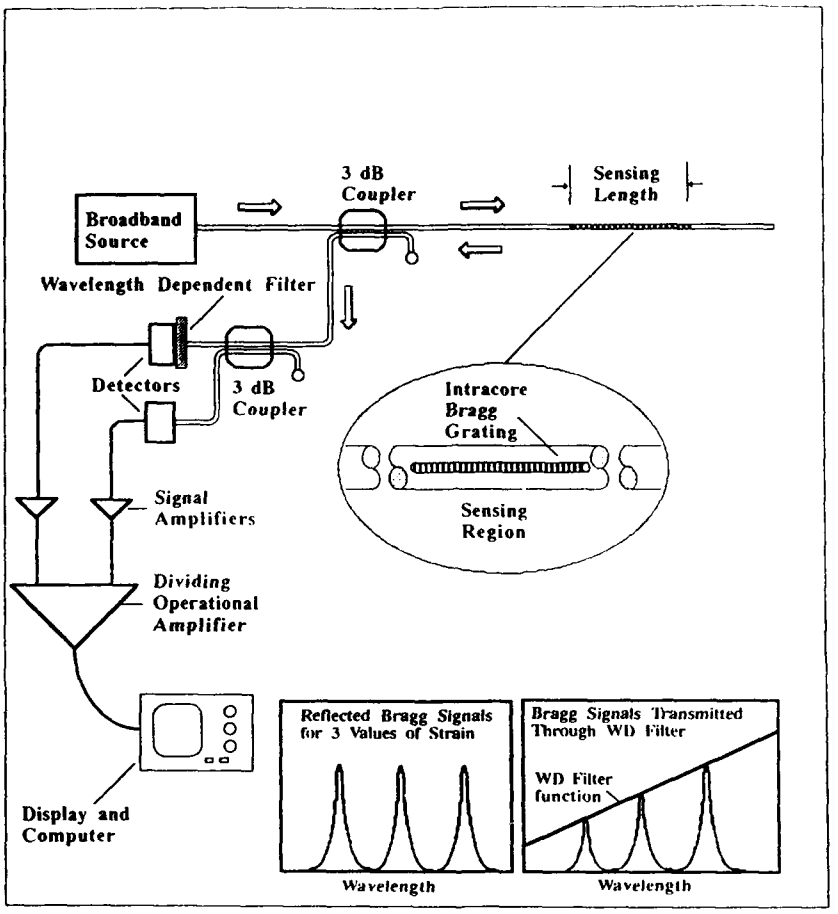

Figure 9. Intracore Bragg grating fiber optic sensor Wavelength Demodulation system. The Bragg wavelength is determined from the ratio of the signals from the two detectors indicated, one receiving its light after passage through the wavelength dependent filter, the other receiving its light directly and serves as a reference. Small insets: bottom left indicates Bragg reflected signals for three values of strain; bottom right reveals how these three signals are affected by transmission through a wavelength dependent linear filter.

provides a strain resolution of a few μstrain with the Fabry -Perot sensor with a 2 cm gauge length and it can operate to a loading rate of 10^5 μstrain sec^{-1} making it suitable for a broad range of strain sensing applications. In principle, it can also be used for demodulating an e-core two-mode fiber optic sensor.

Spectral Encoding/Ratiometric Demodulation

A number of schemes have been devised to determine the wavelength of the narrowband backreflected signals from intracore Bragg grating sensors (31) [Morey et al.] and (47) [Kersey et al.]. However, none of them are as: inexpensive, simple, compact and fast as the elegant spectral ratiometric method of wavelength demodulation, see **figure 9**, demonstrated for the fiber optic intracore Bragg grating sensor by Melle et al.(29). If the narrowband backreflected Bragg peak is modelled as a Gaussian function of spectral width, $\Delta\lambda$, and center wavelength, λ_B, and a linearized filter function of the form:

$$F(\lambda) = A (\lambda - \lambda_0) \qquad (21)$$

assumed, then the ratio of the filtered, I_F, to reference, I_R, optical signals:

$$I_F/I_R = A (\lambda_B - \lambda_0 + \Delta\lambda/\sqrt{\pi}) \qquad (22)$$

where A is the filtering slope and λ_0 is that wavelength for which $F(\lambda)$ is zero. This is clearly a linear function of the back-reflected Bragg wavelength, (29) [Melle et al.]. Fluctuations and variations of the source intensity, connector alignment and coupling losses will not affect the output of this ratiometric detection system, as the system is self-referencing. Amongst the types of filters that can be used in such a system are: coloured glass bandpass filters, narrow band or edge interference filters, dichromic filters, tapered optical fibres or guided wave Bragg gratings.

The strain-sensitivity of this ratiometric wavelength demodulation system is primarily determined by the "slope" of the filter function, while the strain resolution is limited by the signal to noise ratio. Melle et al., (30) have recently demonstrated a strain resolution of better than 10 μstrain with a measurement range of about 3000 μstrain in the case of the intracore Bragg grating sensor. This resolution is limited by the small reflected optical signal and is a direct manifestation of having to use a spectrally broad source {LED or SLD} to cover the wavelength range associated with the potential variation in strain, yet reflecting a very narrow band to obtain a relatively high strain resolution. The need to use this kind of low intensity source represents the primary weakness of this approach and also restrict its multiplexing possibilities through power budget considerations.

Bragg Grating Laser Sensing System

A clever way around this dilema is to use the sensing intracore Bragg grating to tune the wavelength of a laser. Intracore fiber optic Bragg gratings were first employed as an external tuning mirror for an argon ion laser by Hill et al. (48) and later for a semiconductor laser by Dunphy et al., (49). In this arrangement the lasing wavelength is controlled by the measurand determined back-reflected Bragg grating optical signal. Monitoring the lasing wavelength with the spectral ratiometric technique allows direct determination of the measurand, **figure 10**. The advantage of this approach is the greatly improved signal to noise ratio arising from the much larger optical signals. A fiber laser can be used as an alternative to a semiconductor laser and tuning of this kind of laser has already been demonstrated, (50) [Ball and Morey]. Recently, we have continuously tuned an erbium doped optical fiber laser over an interval of about 5 nm by varying the temperature of its intracore Bragg grating, (51) [Alavie et al.].

The real advantage of this intracore Bragg grating laser sensor approach, however, is its potential to be developed into a multisensing system with an electrical/optical structural interface. The concept involves using one intracore Bragg grating sensor to control the wavelength of one semiconductor laser in an array of lasers (52) [Measures et al.]. Indeed, if this wavelength demodulation system were to replace the single detector normally used to stabilize the semiconductor laser output, the resulting sensing system would be extremely simple, compact, robust (with no couplers). For low speed applications a single wavelength ratiometric demodulation system could be used to interrogate each sensor in turn by directing the outputs from all the lasers to it by means of an optical system and exciting each laser in sequence. This spatially multiplexed optical system is schematically portrayed in **figure 11**.

Where high speed, real-time monitoring is required each laser would have its own wavelength ratiometric demodulation system and electronic multiplexing would be used to enable a single output channel from the interface. Either of these systems could handle

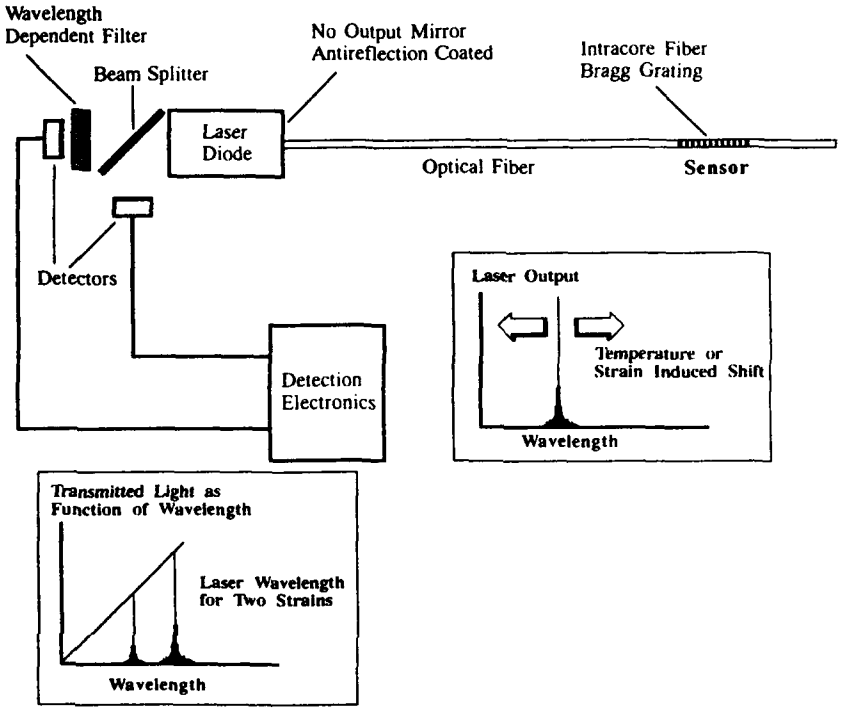

Bragg Grating Semiconductor Laser Sensor with Ratiometric Wavelength Demodulation

Figure 10. Intracore fiber Bragg grating semiconductor laser sensor with ratiometric laser wavelength demodulation, [Measures 1991].

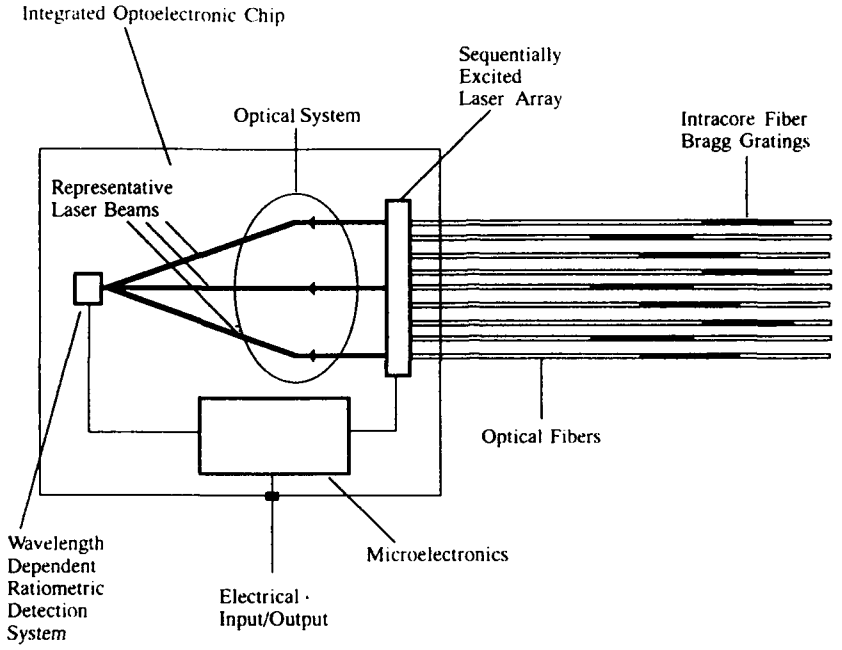

Merits of Multiplexed Multiple Bragg Laser Sensor Array with Single Wavelength Demodulated Detection System

- ***Multiplexing Within Structural Interface***
- ***Many Sensors Processed on Single Optoelectronic Chip***
- ***Optoelectronic Chip within Structural Interface***
- ***Optoelectronic Chip Performs Optical/Electrical Conversion***
- ***Single Electrical Cable with User Friendly Interconnection***

Figure 11. **Schematic of a proposed optoelectronic chip for signal processing of many Bragg grating laser sensors with a single ratiometric laser wavelength demodulation system, [Measures .991].**

many sensors, yet be constructed on an optoeletronic chip that would make it very compact, robust and low cost (in large numbers). This would endow this sensing system with a number of significant advantages over other systems under consideration today, one of the most important being the prospect of a combined sensing and demodulation system small enough to be mounted inside the structural interface (or even embedded within a composite structure) and invoving a single electrical or optical interconnect (52) [Measures et al.]. This could solve many of the critical issues facing the practical implementation of Smart Structure technology and discussed in the next section.

5. CRITICAL ISSUES FOR SMART STRUCTURE STRAIN SENSING

Implementation of Smart Structure technology will require a number of critical issues to be addressed. These are indicated in **figure 12**, and can be divided into micromechanic issues and system architecture issues, (52) [Measures et al.]:

Influence of Embedded Optical Fibers on the Material Properties

If optical fibers are to be embedded within advanced composite materials they must not: compromise the tensile or compressive strength, increase the damage vulnerability or reduce the fatigue life of these materials. Preliminary evidence suggests that the presence of embedded optical fibers has a minimal degradation of composite material properties (53) [Czarnek et al.], (54) [Blagojevic et al.], (55) [Loken], (56) [Roberts and Davidson] providing that the diameter of the optical fiber is less than about 125 μm. Nevertheless, micrographic studies reveal that if the optical fibers are embedded at an angle to the adjacent ply directions, resin cavities are created. Clearly, more definitive research will be needed before optical fibers can be imbedded with confidence within structures intended to have a 20 (plus) year working life.

Sensor/Host Interface and Performance Life

The interfacial shear strength between the optical fiber and the host resin matrix determines the degree of adhesion of the optical fiber within the composite material and thereby the reliability and performance life of embedded fiber optic sensors. It is possible that high stress concentration observed around embedded optical fibers could cause debonding between the optical fiber and the host matrix. This represents a potentially serious concern in terms of sensor performance. Careful consideration will have to be given to the diameter of optical fibers and their type of coating if they are to be embedded within composite structures and function correctly with no performance degradation for the useful life of the structure. The presence of a coating could have a profound influence on this sensor/host interface and could permit the sensor's sensitivity and performance life to be optimized by reducing the high stress concentration in the vicinity of the optical fiber. Sirkis and Dasgupta, (37) have considered the effects of coating size and stiffness, while DiFrancia et al., (57) employed a pull-out test to compare the properties of different polyimide coated optical fibers embedded within neat resins. Pak, (58) has modelled a coated optical fiber embedded within a host composite as a set of cencentric circular inclusions. When optical fibers are embedded collinear with the ply direction no resin eye forms and minimal stress concentration is expected. However, for this configuration a resin cavity is formed at the end of the optical fiber and this could lead to initiation of sensor debonding from the host material. This suggests that it may be prudent to locate the sensing region some distance from the end of an embedded optical fiber intended for extensive use. We are currently investigating the seriousness of this problem and will shortly publish our initial findings, LeBlanc and Measures (38).

Sensing System Architecture and Multiplexing

A sensing system within a practical Smart Structure will have to be fairly robust and degrade gracefully when the structure suffers modest damage. Special coatings, a judicious choice of location and orientation may help to reduce premature fracture of the embedded optical fiber and use of a cellular sensing architecture could minimize the degradation of sensing capability associated with the loss of any particular set of optical fibers. The type of measurement to be undertaken will dictate whether the fiber optic sensors should be localized or distributed, while the nature of the structure will determine if they are multilayered or limited to form a single layer. Optical fiber orientation and placement, especially in an advanced composite material layup, spatial resolution and constraints imposed by the optical fiber finite bend radius are all important factors to be considered. Sensing system damage vulnerability and ease of fabrication represent other considerations to be taken into account.

Multiplexing is the merging of data from several channels into one channel, while demultiplexing is the inverse. The primary parameters used in optical

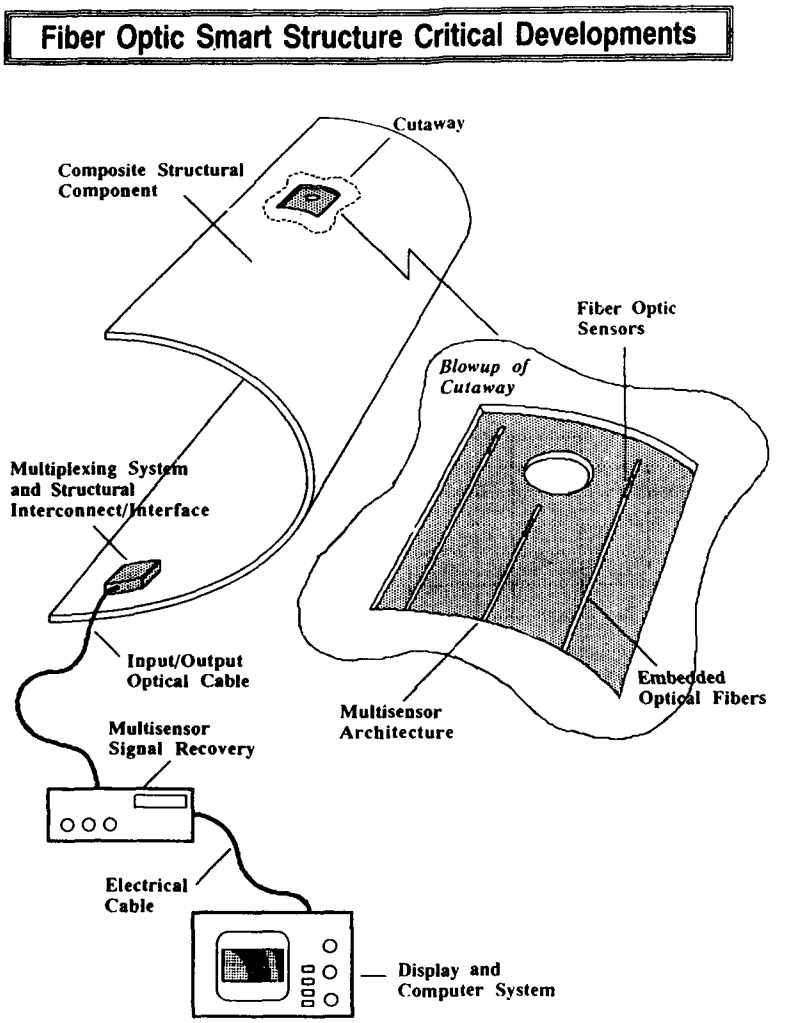

Figure 12. Critical development areas for fiber optic Smart Structures.

multiplexing schemes are: wavelength, time, frequency, phase and space, consequently, there are five
multiplexing techniques. In terms of modest scale structures, such as the section of an aircraft wing, it may not be possible to accomplish multiplexing as part of the structure. An exception based on the intracore Bragg laser sensing system was mentioned earlier (52) [Measures et al.].

Structural Interconnect/Interface
The nature of the structural interconnect problem hinges on whether the input/output is optical or electrical. Current thinking is predicated on optical signals flowing into and out of the structure via the structural interface. In general this interface must have minimal structural perturbation, be easy to fabricate and introduce during fabrication of the structure. If multiplexing is not used each sensor has its own input/output and a ribbon or bundle of optical fibers would have to egress from the structure. The structural interconnect problem would be greatly simplified if each major sensing cell were connected through a single electrical cable to a central computer facility for interpreting the data. The development of a multisensor signal processing optoelectronic chip would simplify the interconnect issue and provide a number of advantages, (52) [Measures et al.].

One of the most important is the great reduction of unit cost when so much of the system is reduced to the form of an optoelectronic chip. This includes: multiplexing, multisensor signal processing and possible conversion to an electrical output. Another important aspect of the structural interconnect is its need to be extremely user friendly. This is particularly true if Smart Structure technology is to be implemented broadly, such as on: aircraft, spaceplatforms, or any other site where someone may have to plug in the system in a hash environment or in an awkward location.

6. THERMALLY INDUCED APPARENT STRAIN

The change in the phase of light propagating along a structurally integrated optical fiber subject to a change in temperature, but no applied force, is another issue that has to be addressed when considering the use of optical fiber sensors for strain measurements in practica l Smart Structures. This is especially so in the Aerospace field, where they are likely to be subjected to considerable temperature excursions. Strain measurements made with optical fiber sensors embedded within such structures would thus be complicated by the appearance of apparent strain due to the appreciable thermal sensitivity of the index of refraction and thermal expansion of the optical fiber and the host, (6) [Hogg et al.] and (53) [Measures].

Thermal Sensitivity and Apparent Strain
In the case of interferometric sensors the incremental change in the phase associated with an incremental change in both the local stress, $\Delta\sigma$, and the temperature, ΔT, is given by (53) [Measures, 1992a]:

$$\Delta\phi = nkL\left[\left\{1 + \frac{1}{n}\left[\frac{\partial n}{\partial \varepsilon}\right]_T\right\}\frac{\Delta\sigma}{E} + \left\{\frac{1}{n}\left[\frac{\partial n}{\partial T}\right]_\sigma + \alpha_F\right\}\Delta T\right] \tag{23}$$

in which E, is Young's Modulus and α_F, and α_F, is the coefficient of thermal expansion for the optical fiber. The 2nd term in (23) corresponds to the *strain-optic effect* and the 3rd term accounts for the *thermooptic effect*. Note that the coefficient of thermal expansion in (23) corresponds to that of the free fiber.

If we introduce the *bonded fiber phase strain coefficient* :

$$g = nkL\left\{1 + \frac{1}{n}\frac{\partial n}{\partial \varepsilon}\right|_T \tag{24}$$

and the *free fiber thermal phase coefficient* :

$$f = nkL\left\{\frac{1}{n}\frac{\partial n}{\partial T} + \alpha_F\right|_\sigma \tag{25}$$

In the case of an optical fiber bonded to a composite host material, under conditions of no applied load other than the incremental stress arising from the difference in the coefficient of thermal expansion between the host material and the optical fiber, we can write:

$$\Delta\sigma = E(\alpha_H - \alpha_F)\Delta T \qquad (26)$$

where α_H, is the *coefficient of thermal expansion* for the host material. Equation (23), would thus indicate that the incremental change in the phase associated with an increase of temperature, ΔT, can be expressed in the form:

$$\Delta\phi = g(\alpha_H - \alpha_F)\Delta T + f\Delta T \qquad (27)$$

If we rewrite (27) in terms of an *apparent strain*, ε_{app}, then we have:

$$\Delta\phi = g\,\varepsilon_{app} \qquad (28)$$

and we see that the apparent strain is given by:

$$\varepsilon_{app} = \left[\frac{f}{g} + \alpha_H - \alpha_F\right]\Delta T \qquad (29)$$

The *apparent strain sensitivity* can thus be defined by the relation:

$$\kappa = \frac{f}{g} + \alpha_H - \alpha_F \qquad (30)$$

A similar analysis undertaken for the intracore Bragg grating sensor leads to comparable results.

For a double pass Fabry-Perot fiber optic sensor, with $\alpha_F \sim 0.5$ [μstrain K^{-1}], representative values of: g; f; and κ, are provided for two types of optical fiber in **Table III**, assuming that the sensor is bonded to an aluminium plate {$\alpha_H = 23.8$ [μstrain K^{-1}] }.

Table III. Strain and Temperature Coefficients for Two Types of Optical Fiber

	York HB 600 [Hogg et al., 1991]	830 nm PANDA [Hogg et al., 1992]
g [deg.μstrain^{-1} cm^{-1}]	13.3	8.2
f [deg. K^{-1} cm^{-1}]	55.0	83.1
κ [μstrain K^{-1}]	27.4	33.4

Temperature Compensated Strain Sensing and Cross Sensitivity

One method of dealing with the appearence of thermal apparent strain is to measure the temperature at the same time as the strain is monitored. This approach is often employed with conventional strain gauges, and is fairly easy to implement for fiber optic strain sensors by introducing a compensating sensor that is exposed to the same temperature, but not the strain, **figure 13**.

For an optical fiber bonded to a host material subject to an incremental change in temperature, ΔT, with no applied load, we saw from equation (26) that the incremental change in the stress:

$$\Delta\sigma = E(\alpha_H - \alpha_F)\Delta T$$

where α_H, is *coefficient of thermal expansion* for host material, and α_F, is *coefficient of thermal expansion* for the optical fiber. The change in phase experienced by two sensors: one bonded to the host, the other free (ie uncoupled to host strain) subject to an incremental change in temperature, ΔT, are:

$$\Delta\phi_{Bonded} = [\,g(\alpha_H - \alpha_F) + f\,]\,\Delta T + g\Delta\varepsilon^{stress} \qquad (31)$$

and

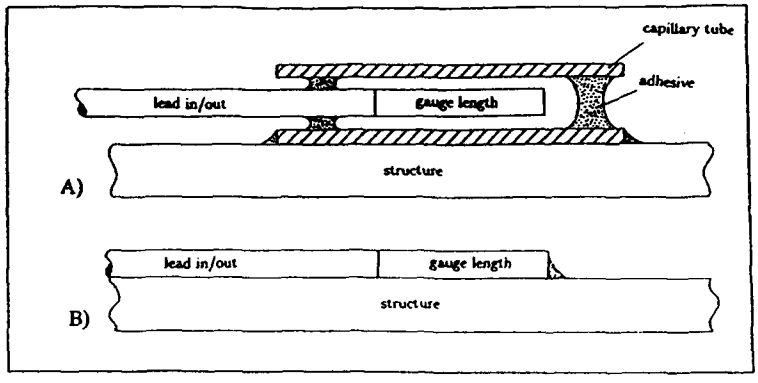

Figure 13. Temperature compensated strain sensing with two surface adhered Fabry-Perot fiber optic sensors. (A) temperature sensor that is supported only at one end so as to be decoupled from any external strain, (B) sensor for measuring both strain and temperature of host.

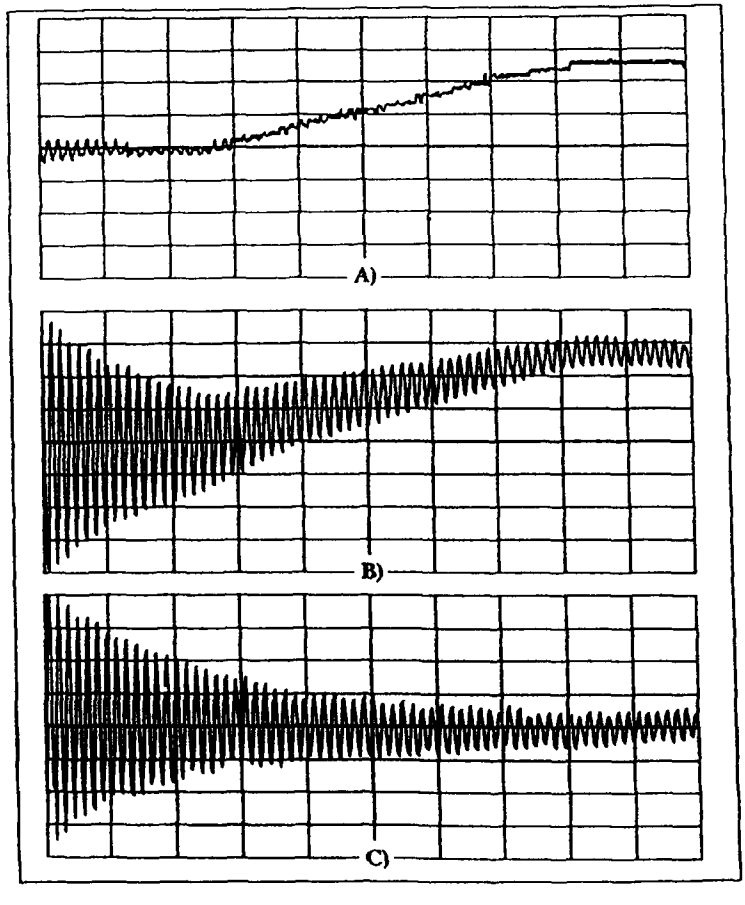

Figure 14. Set of three Fabry-Perot fiber optic sensor temporal outputs from a vibrating cantilever beam subject to a sudden rise of temperature: (A) temperature sensor output; (B) strain and temperature sensor output; (C) strain signal with temperature influence removed, see text.

$$\Delta\phi_{Free} = f\ \Delta T \qquad (32)$$

where $\Delta\varepsilon_{stress}$ represents the stress induced strain to be evaluated.

If we introduce the *Temperature Compensation Factor*:

$$C_T = [\, g\{\alpha_H - \alpha_F\} + f\,]/f \qquad (33)$$

then the "stress induced strain" :

$$\Delta\varepsilon_{stress} = [\, \phi_{Bonded} - C_T\, \phi_{Free}\,]/g \qquad (34)$$

Hogg et al., (54) have determined experimentally that for an 830 nm PANDA optical fiber adhered to aluminium:

C_T = **3.32** and **g** = **8.2** [deg.μstrain-1 cm-1]

They have also demonstrated that this means of temperature compensation permits load induced strain sensing to be undertaken even in the presence of a rapidly varying temperature, **figure 14**, at least in the case of a surface adhered sensor. Note that use of a similar sensor for both the temperature and strain measurement is in keeping with the strategy of using one kind of sensor for all measurements.

In certain situations it may be possible to deconvolute the strain and temperature by making two measurements with the same sensor. For example, Blake et al., (12) [1987] and Huang et al., (55) [1990] suggested that strain and temperature could be simultaneously evaluated by monitoring the LP_{01} and LP_{11} spatial mode interference on the two eigenpolarization axes of an "elliptic-core two-mode sensor." The two polarization modes in a highly birefringent Fabry-Perot fiber optic sensor were used by Farahi et al., (56) to evaluate the strain and the temperature experienced by the sensor when heated. Simultaneous measurements of strain and temperature were also undertaken by Vengsarkar et al., (57) using two wavelength excitation of an e-core two-mode sensor. The sensor performed as a polarimeter when operated at a wavelength greater than the cutoff wavelength and as a two-mode sensor when operated below the cutoff. A resolution of 10 μstrain and 5^0 C was attained when a 28 cm gauge length was employed.

In the case of a polarimetric sensor, Dakin and Wade (58) and Bock and Wolinski, (57), have shown that the use of a 90 degree rotation of the polarization axes can lead to temperature compensation that diminishes the temperature sensitivity of a free fiber optic sensor. In reality, however, it is necessary to bond or embed the sensor and the difference in the thermal expansion coefficients between the optical fiber and the host material is still likely to give rise to an appreciable apparent strain, see the above calculated relative contributions to the apparent strain sensitivity for an optical fiber bonded to aluminium.

In the case of optical fiber sensors embedded within composite material structures the thermal apparent strain can depend quite strongly on the orientation of the optical fiber relative to the reinforcing fibers due to the highly anisotropic properties of these materials. These factors might have contributed to the errors observed in trying to make simultaneous strain and temperature measurements within a heated composite specimen with embedded polarimetric and two mode fiber optic sensors, (59)[Michie et al.]. The relative importance of transverse coupling to these consideration has also to be resolved. Conventional resistive foil strain gauges expected to work over appreciable temperature ranges have to be tailored to the material to which they are adhered. A similar procedure may be required for fiber optic strain sensors and this would necessitate the development of special thermally compensated optical fibers, probably based on suitable doping.

Lastly, the issue of strain and temperature cross sensitivity terms may have to be taken into account. However, Farahi et al., (56) and Vengsarkar et al., (57) have shown that for free optical fibers these terms are negligible unless large strain or temperature excursions are to be considered.

7. STRAIN MEASUREMENT APPLICATIONS

Sensing Strategy for Strain Field Measurements

If a scalar field, like pressure or temperature, is to be mapped a grid of localized line integrated fiber optic sensors can be used in conjunction with an inverse Radon transform. However, a grid of line integrated optical fiber sensors, in general, cannot be used to map a vector or tensor field, such as strain. Exceptions can arise where the field is constrained in such a way that it is not truly two dimensional in nature. Where the field is two dimensional, three independent measurements are required at each point to uniquely specify the field. This can be

Figure 15. Photograph permitting comparison of a conventional foil electrical strain rosette (left side) with that of a fiber optic strain rosette (right side).

accomplished, in certain situations, by using the optical analogue of the conventional resistive foil strain rosette, comprising three small identical high sensitivity fiber optic sensors set at different orientations, **figure 15**, (8) [Valis et al.]. Under these conditions high spatial resolution is important as each sensor must have a gauge length that is small compared to the scale length for the field gradient. This tends to rule out two mode and polarization sensors, except for very large structures, **Table II**.

The structural interface and interrconnect aspects of any particular situation are likely to be key factors that must be taken into account when considering the sensing system architecture. In the case of structural components that have to be inspected, tested, and serviced on a regular basis (like aircraft) an extremely robust and user friendly interface/interconnect system will be required. The multisensing system based on the intracore Bragg grating laser sensor described earlier, **figure 10**, has the potential to be integrated onto an optoelectronic chip, **figure 11**, to form a part of such an structural interface, (52) [Measures et al.] and greatly simplify the interconnect problem.

Basic Strain Measurements

The strain field within a structure represents a primary parameter which can be related to any load applied to the structure and is clearly relevant when considering the response of the structure in terms of its vibration and deformation. We shall see that such measurements are crucial for active control of adaptive structures and that precise measurements of strain may also permit other parameters, such as the degree of cure of a thermoset composite or the extent of delamination damage within a multilaminate composite material structure, to be evaluated.

Simonsen et al., (58) have investigated the strain sensitivity, linearity and reproducibility of fiber optic intracore Bragg grating sensor embedded within glass-fiber reinforced polyester. Their strain resolution was about 100 μstrain, compared to 8 μstrain achieved recently using a passive, ratiometric, wavelength demodulation technique on a reflective Bragg grating sensor, (30) [Melle et al.]. Furthermore, in the case of the ratiometric wavelength demodulation system it was the very low optical signal that limited the strain resolution to 8 μstrain. It is expected that this limit could easily be exceeded by at least an order of magnitude when the ratiometric wavelength demodulation system is used with a intracore Bragg grating laser sensor, (52) [Measures et al.], **figure 10**.

The first fiber optic measurement of strain from the wing of an aircraft have been reported by Murphy et al., (59). They affixed an extrinsic Fabry Perot sensor to the underside of the wing of an F-15 aircraft mounted on a Test Facility at the Wright Patterson Airforce, Base, Ohio. The wing was loaded from zero to 100% load (representative of a fully loaded F-15 at an altitude of about 6000 m performing a 7 g manoeuver) and also cyclically loaded. A comparison of the quadrature phase shifted fiber optic sensor with that of a conventional foil strain gauge during part of the cyclic loading is presented as **figure 16**. The comparison is quite reasonable and although this represents a significant first, the complexity of the dual fiber extrinsic Fabry-Perot sensor head, required for quadrature detection, **figure 17**, leaves much to be desired in terms of a practical, robust and unobtrusive sensor for embedding within composite material structures. For this reason the "intrinsic" fiber optic Fabry-Perot interferometer pioneered by Lee and Taylor (5) constitutes an important advance. We have been able to fabricate Fabry-Perot sensors using a reflective fusion splice based on a metal evaporation technique (8) [Valis et al.]. The advantage of this approach is that it leads to the formation of internal mirrors of high reflectivity which is important from a power budget standpoint. Recently, Lee et al., (60) have demonstrated that internal mirrors of high reflectivity could be fabricated using multilayers of TiO_2 and SiO_2 and that these Fabry-Perots sensors can be embedded in thermoplastics and even cast aluminium.

We have measured the strain sensitivity of embedded intrinsic Fabry-Perot strain gauges and shown that their strain response is linear when embedded within several different composite materials: Kevlar/epoxy; graphite/epoxy and graphite/PEEK and that it is free of hysteresis during load and unload cycles an we have also shown that the strain sensitivity of the Fabry Perot sensor is not a function of its gauge length, (8) [Valis et al.]. We have embedded uniaxial FP sensors in graphite/PEEK and Kevlar/epoxy to assess sensor survival and response. **Table IV**, summarizes the Fabry-Perot fiber optic strain sensor characterization.

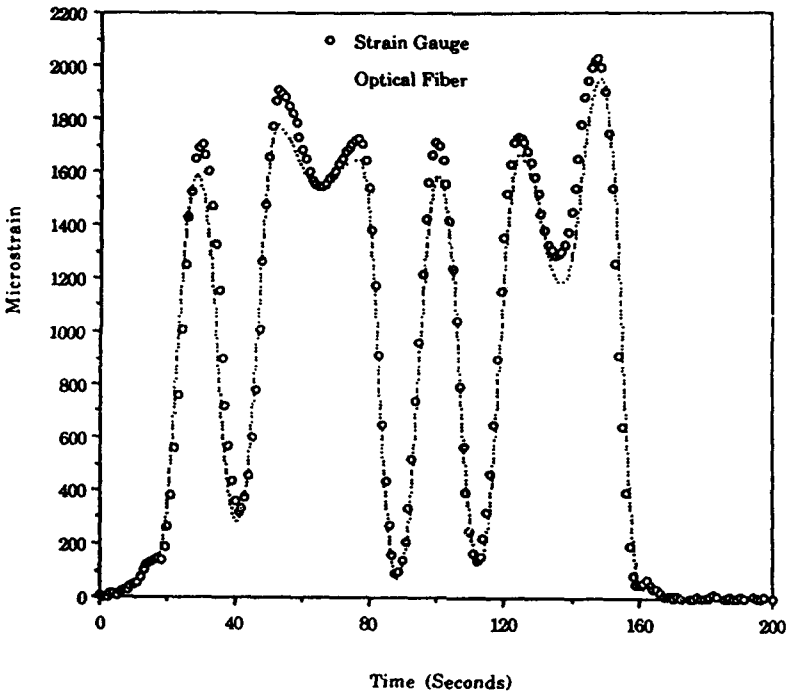

Figure 16. Comparison of the strain measured on the wing of an F-15 aircraft by a conventional foil strain gauge (open circle) and extrinsic Fabry-Perot fiber optic sensor (dot) [Murphy et al., 1991].

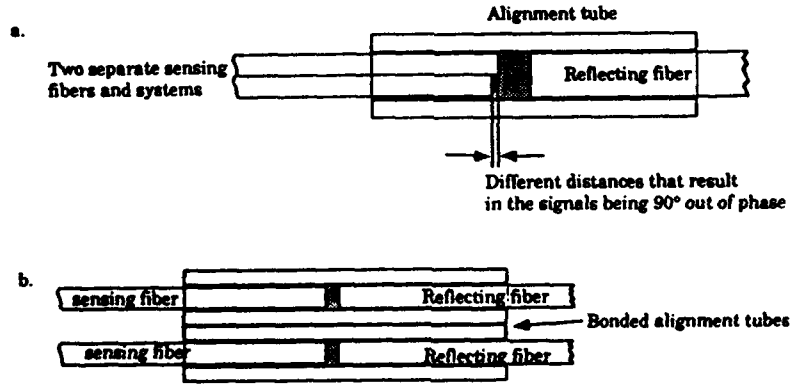

Figure 17. Two quadrative phase shifted sensor condigurations for the extrinsic Fabry-Perot fiber optic sensor, each involves essentially two sensors, with a 90 degree phase shift between them, [Murphy et al., 1991].

Table IV. Fabry-Perot Fiber Optic Strain Gauge Characterization

Typical Gauge Length	3-20	[mm]
Sensor Diameter	125	[μm]
Operating Wavelength	632.8	[nm]
Strain Sensitivity{at 633 nm}	13.3	[deg. μstrain^{-1}cm^{-1}]
Temperature Sensitivity	55.0	[deg.K^{-1} cm^{-1}]
Tensile Strength	2,000	[μstrain]

The performance of these devices indicates that they can match, and probably surpass, the performance of conventional resistive-foil electrical strain gauges eventually. However, unlike the conventional resistive-foil devices, they require phase-demodulation, and suffer from interrupt ambiguity. A demodulation system has been developed recently for the Fabry-Perot sensor that may be suitable from a Smart Structures perspective (46) [Mason et al.] and is commercially available from FiberMetric Corporation.

Unfortunately, the semireflective metal fusion splice represents a source of structural weakness for the Fabry-Perot sensors. It is susceptible to failure in bending and tension at loads significantly less than those of bare fibers. The reason for this weakness is that at present the entire endface of each optical fiber is coated with a metallic film prior to fusion. This approach is unwarrented, as only the core needs to be reflective, and has the effect of preventing complete fusion of the two fibers. Ideally, the cladding regions of the endfaces should be glass-to-glass fused. In order to improve the strength of our FP sensors we have developed a method of creating localized semireflective-mirrors, (8) [Valis et al.].

Where it is necessary to measure the in-plane strain tensor at a point within a structure the fiber optic analogue of a resistive foil strain rosette is required. We were the first to recognize the importance of such a fiber optic strain rosette and to demonstrate its viability based on three Fabry-Perot fiber optic sensors, **figure 18a,** (8) [Valis et al]. Test optical strain rosettes have been constructed and bonded to the surface of an aluminium cantilever beam and embedded within a carbon/PEEK cantilever beam. The laminar strain tensor measured with the embedded fiber optic strain rosette was found to be in good agreement with the results obtained from a surface adhered electrical strain rosette, **figure 18b.** A picture of an illuminated optical strain rosette and a conventional resistive strain rosette is presented as **figure 15.** Recently, we have extended this work to the more general case of an arbitary 3-D strain field, (61) [Liu and Measures].

Measurements Relevant to Aerospace Applications

Although, in the next section we discuss strain measurements under the Aerospace heading it should be borne in mind that many of the measurements are generic in nature and would find broad application to other mobile platforms or stationary structures. A selection of some of the more important measurements for: aircraft; helicopters; space platforms...., includes:

- Vibration frequencies of: flexible space structures, flight control surfaces, propellers...
- Spatial vibration modes of: flexible space structures, flight control surfaces, propellers...
- Thermal deformation of space structures caused by shadows and one sided solar heating.
- Excessive loading, pressures leaks, impacts.....
- Long-term health monitoring including mechanical and thermal load history.
- Internal strain distribution and pressure loads (especially for human occupied structures).
- Onset of internal crack formation (especially for human occupied structures).
- Impact detection and localization.
- Damage assessment (delamination in ACM).
- Corrosion degradation of aircraft and helicopters.
- Oxygen erosion of composite space structures.
- Real time aerodynamic loads for aircraft.
- Shape evaluation for actuation control and monitoring of vibration damping.
- Flap and engine control position monitoring.
- Flutter and noise measurement for active suppression.
- Temperature distribution and anomalous hot spot detection.

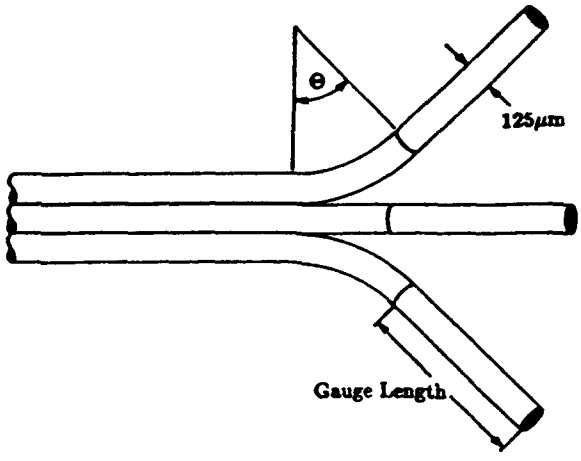

Detail of the FFP fiber-optic strain rosette.

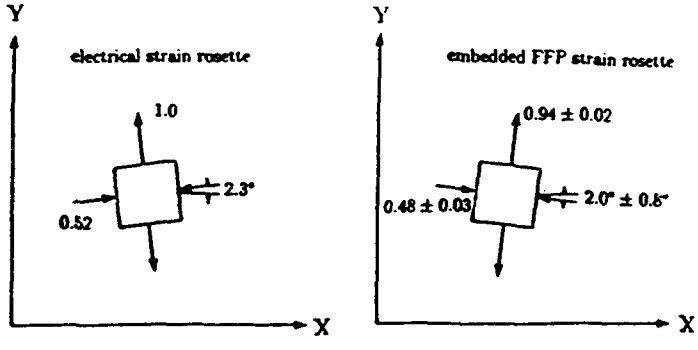

Figure 18. (a) Fiber optic strain rosette based on three Fabry-Perot fiber optic sensors: (b) A comparison of the laminar strain tensor measured by the fiber optic strain rosette embedded within a composite cantilever beam with the results obtained from a surface adhered conventional foil strain rosette, [Valis et al., 1990].

For convenience we can discuss the applications under three headings:

Damage Assessment

Even though, the Michelson sensor is not suitable for practical Smart Structures it has served as a useful demonstrator of what should be possible with Fabry-Perot sensors as their strain sensitivity is comparable. For example, the Michelson fiber optic sensor has verified that acoustic energy released as a result of matrix cracking, fiber breakage or interlamina debonding (delamination) within various composite materials{Kevlar/epoxy and graphite /epoxy} could be it detected by an embedded interferometric fiber optic sensor. In this work, quadrature detection was ensured by a low frequency piezoelectric (PZT) phase modulation feed-back system that also eliminated drifts and slowly varying strains, Liu et al., (4). In these experiments the composite panels were subjected to out-of-plane loading and the high frequency signals from the fiber optic sensor recorded. We have been able to demonstrate that embedded Michelson fiber optic strain gauges can detect acoustic emission associated with the generation of threshold delaminations. However, the complexity of composite materials may frustrate this approach and in the end the use of neural networks may be required to help locate and assess the extent of damage from acoustic emission signals. Furthermore, acoustic wave generated birefringence induced in the embedded optical fibers can prevent the amplitude of the acoustic emission signals from conveying any useful information unless polarization maintaining optical fibers are employed, (4) [Liu et al.]. Recently, Lee et al., (60) have demonstrated that intrinsic Fabry-Perot fiber optic sensors can indeeed detect acoustic waves with frequencies of 0.1 to 8 MHz within cast aluminium and graphite/epoxy composites structural elements.

Another possible method of assessing damage {specifically delamination} within composite material structures is based on vibration analysis, (62) [Marple] and (63) [Alpher]. It is anticipated that an embedded optical fiber strain sensing system might detect: shifts in the frequency and{or}changes in the damping constants of one or more mechanical vibration modes of a structure. This concept is illustrated in **figure 19**. However, initial work (64) [Gao et al.,] suggests that vibration analysis cannot serve as the sole indicator of delamination damage within composite structures although it may well compliment other approaches. Optoacoustic probing and strain anomaly measurements represent two such techniques to be explored.

Composite Material Cure Monitoring

Cure monitoring of thermoset advanced composites with the same embedded sensing system designed for in-service structural monitoring would improve quality control of many composite material structures and thereby represent another very important application for the resident optical strain sensors. Dunphy et al., (27) indicated that an intracore Bragg grating sensor embedded within a 6 layer graphite/epoxy specimen detected the onset of vitrification and survived the high temperature and pressure conditions within the autoclave. Their measurements also appeared to pickup the thermally-induced residual strain as the specimen cooled. In these experiments a second, reference, intracore Bragg grating sensor along the same optical fiber was strain decoupled from the specimen and served to compensate for the temperature changes. However, use of the strain field coupled to the optical fiber may limit the accuracy and relevance of this approach as it samples the resin properties only in the immediate vicinity of the optical fiber.

Sun and Winfree (65) suggested that measurement of spatially averaged bulk moduli should serve as good indicators of the cure state. We have undertaken some initial research to determine if cure monitoring of thermoset advanced composites might be feasible through the use of optoacoustic probing. In this approach the high sensitivity of embedded interferometric fiber optic sensors is used to measure the velocity of acoustic waves averaged over the distance between the launch and sensing sites. This should provide a measurement of the average cure state over a specific region of the structure. If it is desirable to use a purely optical technique then intense laser pulses can be employed to create the probing acoustic waves. A schematic of such a possible laser generated optoacoustic sensing arrangement involving a Fabry-Perot fiber optic sensor and an embedded laser pulse delivery optical fiber is presented in **figure 20**. Preliminary results of the variation in the arrival time for acoustic pulses as a function of cure time for Hysol resin is presented in **figure 21**, (66) [Measures et al.]. The experimental setup is indicated in **figure 22**, where it is seen that the acoustic waves were generated on the surface of the specimen by laser pulses delivered from a Nd-YAG laser through an optical fiber and a Michelson fiber optic sensor was used. These and later results, (67) [Ohn et al.] are quite encouraging and it is expected that autoclave tests should be shortly conducted.

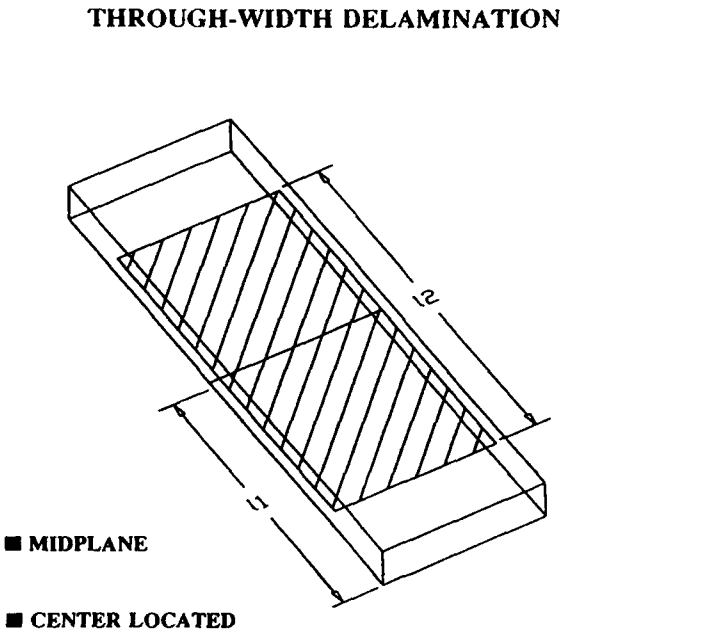

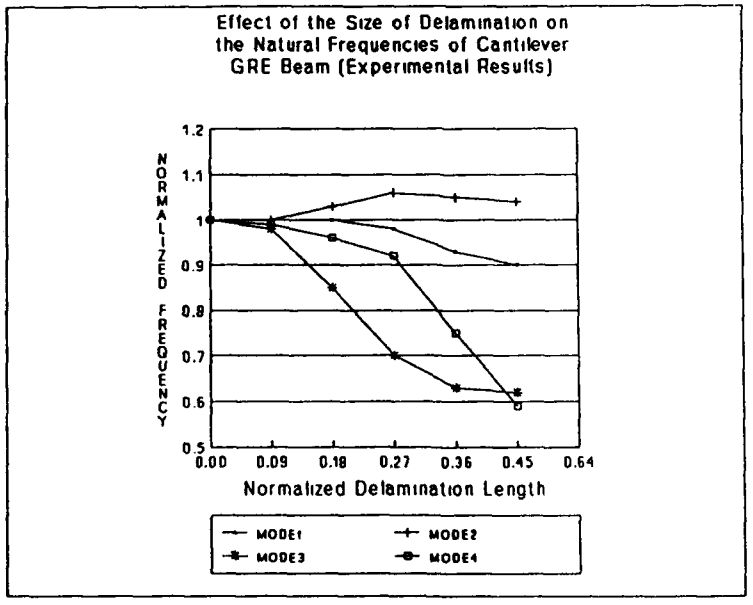

Figure 19. (a) Schematic of composie cantilever beam with full-width delamination. (b) Normalized change in the measured frequency of a composite cantilver beam's first four vibration modes as a function of the normalized (full-width) delamination length.

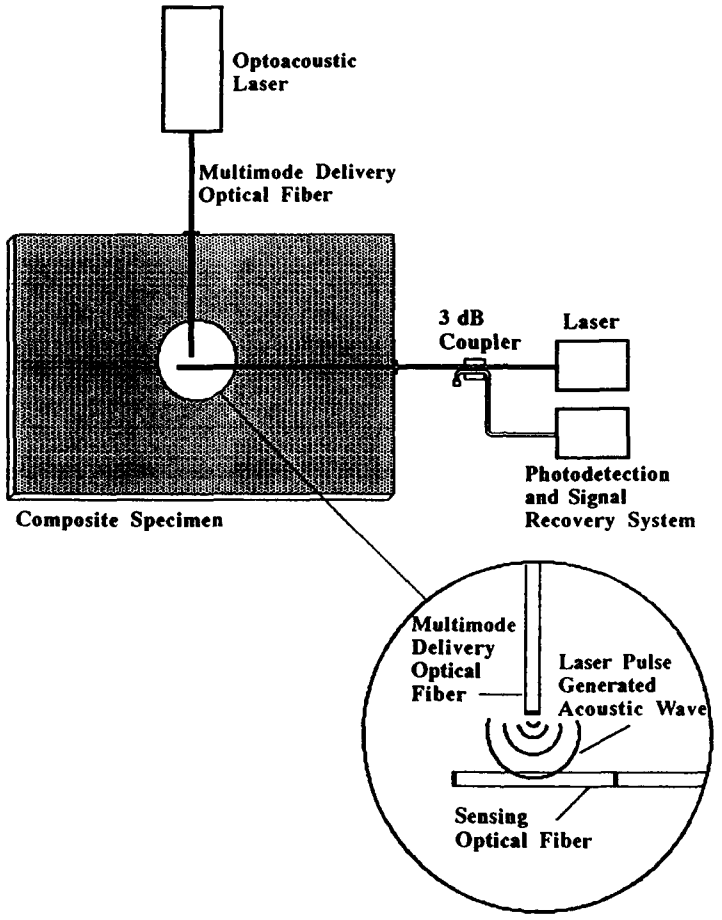

Figure 20. Schematic of a possible optoacoustic experimental arrangement for resin cure monitoring involving an embedded Fabry-Perot fiber optic sensor and a multimode laser pulse delivery optical fiber.

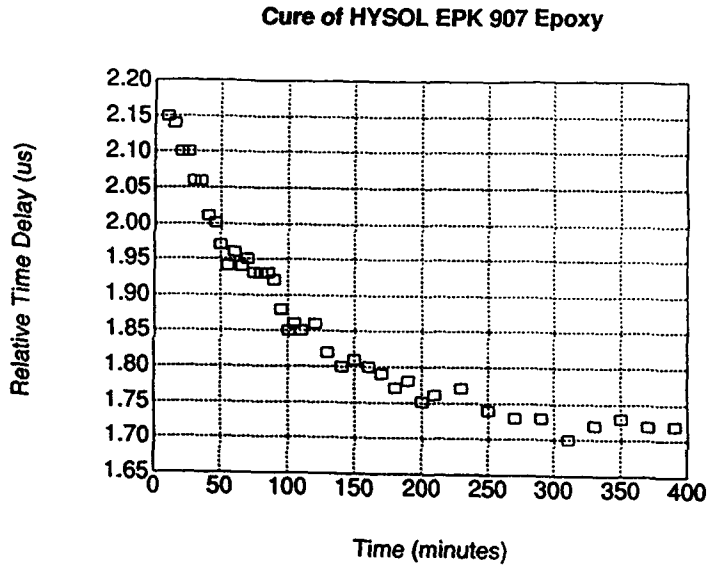

Figure 21. Preliminary results of the variation in the arrival time for optically generated acoustic pulses as a function of cure time for Hysol resin.

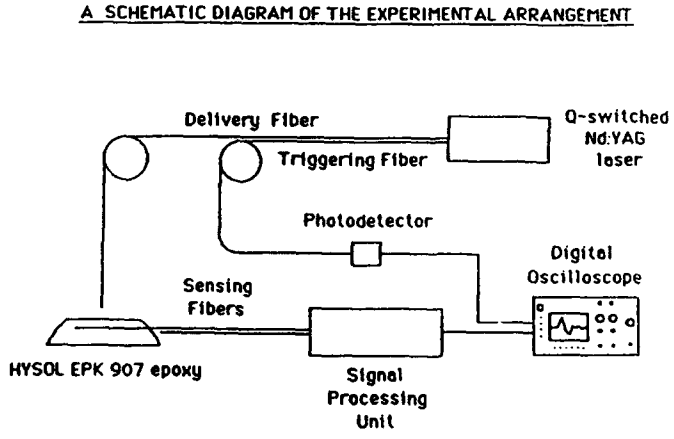

Figure 22. The experimental setup for evaluating change in the arrival time of optically generated acoustic pulses as a function of cure time for Hysol resin

Active Structural Control

In Smart "Adaptive" Structures the information provided by the built-in sensor system is used for controlling some aspect of the structure, such as its: stiffness, shape, position, or orientation. Adaptive (variable-geometry) truss structures possess multiple degrees of freedom that makes them ultradexterous and capable of adopting complex configurations impossible for a conventional, multi-joint, multi-link anthropomorphic manipulator of comparable size and mass. They are superior in terms of: deployment and contraction; minimal storage space; strength-to-mass and stiffness-to-mass; telescopic motions; redundancy of actuator function; and resistance to longitudinal and lateral buckling. "Smartruss" represents a generic smart adaptive structure element, **figure 23**, that could find application in space structures as diverse as the Space Based Radar Satellite and the Space Station Remote Manipulator System and serve as the forerunner of flexible robotic manipulators.

Accurate and fast strain measurements will be required by any resident sensing system to be used for Smart Adaptive Structures. We have developed a dual Fabry-Perot fiber optic strain sensor system to be used with the actuation control system of " Smartruss," (46) [Mason et al.]. Each of the Fabry-Perot strain gauges was formed in SM800 optical fiber and had a phase-strain sensitivity : $S = 1.02$ deg. $\mu strain^{-1}\ mm^{-1}$, (6) [Hogg et al.] at 819 nm. In this dual Fabry-Perot sensor system one modulated laser was used to excite both Fabry-Perot sensors. The back reflected signal from each sensor was directed to its own photodiode and strain decoder electronics, **figure 24**. This system has a linear response and provides a strain resolution of better than 10 μstrain for a 9 mm gauge length. Furthermore, this system can respond to strain changes of 10^5 $\mu strain\ sec^{-1}$, which is important when strain measurements are to be attained against a mechanically noisy background {vibrations and impacts}. An example of the controlled and uncontrolled response to step excitation is presented as **figure 25**.

8. CONCLUDING REMARKS AND FUTURE PROSPECTS

Structurally integrated fiber optic sensors (SIFORS) will form the optical nerves of future Smart Structures and strain sensing will constitute the most important measurement to be undertaken. Strain measurements will provide valuable information on the use and loading of such structures and will also indicate the response of the structure to these loads in terms of shape change and vibration. Strain information would obviously be vital to the structurally integrated actuation control system of any Smart Adaptive Structure. Strain measurements may also be used to detect and assess any damage sustained by the structure and even more crucially ascertain if the structure has suffered an acute or chronic loss of structural integrity. Continuous monitoring of the applied loads could also be used to determine the actual fatigue life of the structure at any point in its operation. In the case of composite materials improved quality control during fabrication may be possible from such a built-in sensing system and this could lead to a more consistent and reliable product. Overall the introduction of an embedded fiber optic strain sensing system to composite structures may enhance confidence in their use and lead to an expansion in there range of application, especially as primary structures in the Aerospace field.

Two types of fiber optic sensor appear to qualify for continued consideration as the universal sensor for the broad range of potential Smart Structures. In principle intracore fiber optic Bragg gratings could be formed during the fiber pulling process by exposure to intense pulses of laser (or other) radiation which makes possible automated fabrication, (68) [Askins et al.] and ensures no loss in the strength of the optical fiber. Furthermore, if they are used to control the wavelength of (fiber or semiconductor) lasers and used with the new ratiometric wavelength demodulation system,(52) [Measures et al.] they can form robust, simple, absolute measurement, low cost multisensor systems with the potential to be integrated on to an optoelectronic chip that can form part of the structural interface and in essence solve the critical interrconnect problem. There are two questions that remain to be proven: first can the intracore Bragg grating sensor perform all of the tasks required, and second can Bragg gratings of "sufficient quality" be fabricated in an automated process. The Fabry-Perot sensor can undertake any measurement likely to be required of an optical strain gauge and a new pseudo-heterodyne demodulation system allows this sensor to be used with high precision. For the Fabry-Perot sensor to be seriously considered for Smart Structures,however, a low cost, fast method of fabrication will have to be developed and one that does not compromise the strength and fatigue life of the optical fiber.

Although the sensing architecture is strongly dependent upon the specific application and the structure to be instrumented it is clear that a sensing cell architecture offers great flexibility and is particularly attractive for complex, multilaminate

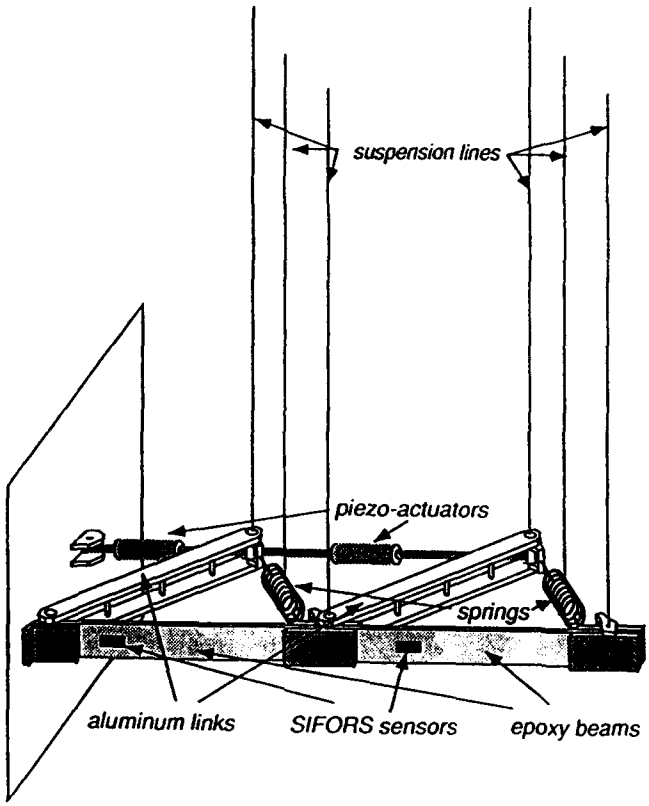

Figure 23. Schematic of "Smartruss," revealing fiber optic sensor and piezoelectric actuator control configuration, {Courtesy of Dynacon Ltd.}. Note in final configuration both Fabry-Perot fiber optic sensors were placed on the left segment of the beam.

Demodulated Dual Fabry-Perot Fiber Optic Sensor

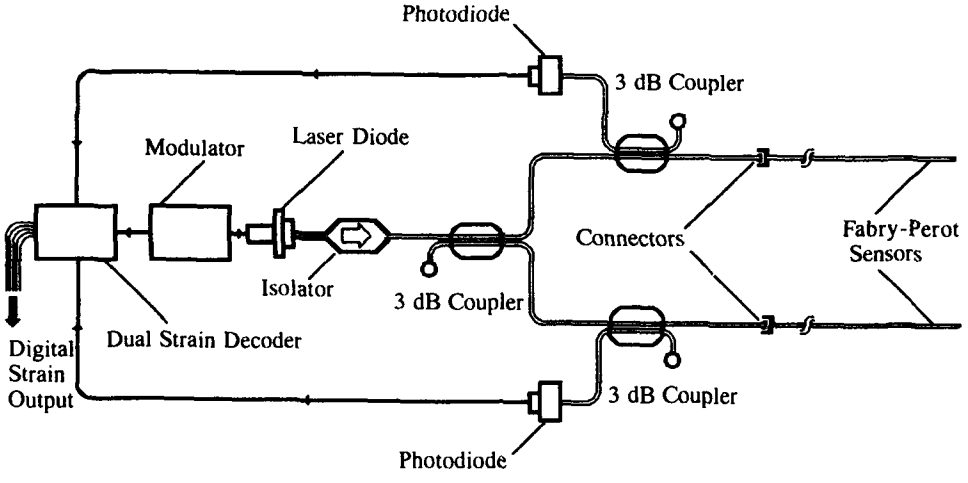

Figure 24. Dual Fabry-Perot fiber optic sensing system used on the Smartruss, {Courtesy of Dynacon Ltd.}.

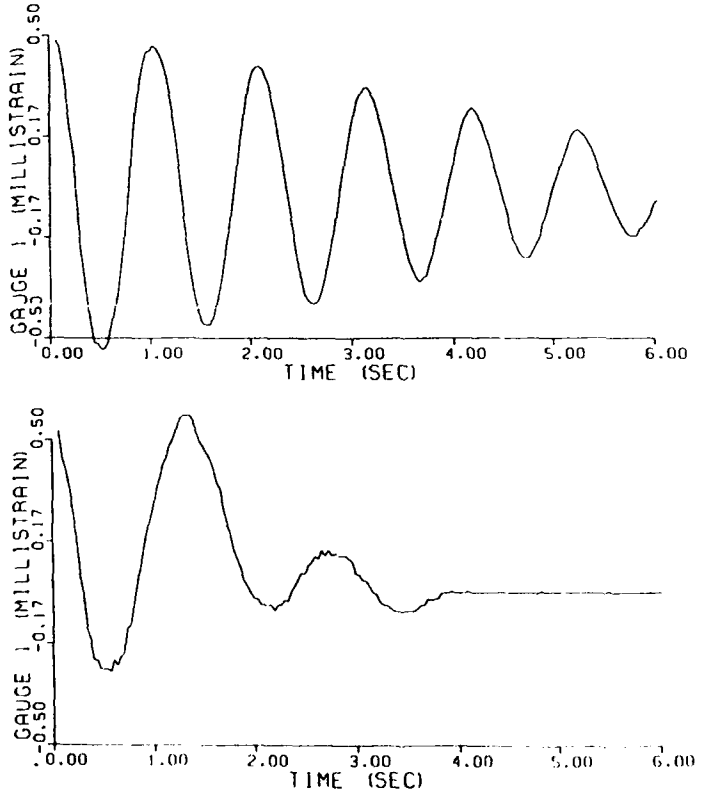

Figure 25. Controlled and uncontrolled response of the Smartruss to impulse excitation.

composite structures. For embedded fiber optic sensors: interpretation of the optical signals in terms of the host strain field; thermal apprent strain; performance lifetime; structural interface and interrconnection, represent serious issues that remain to be addressed.

In the 21st Century Smart Structure technology could lead to a structures that are self monitoring and even self scheduling of their maintenance and repair. This revolution in technology could usher in a "new age of engineering". This era would see the marriage of fiber optic technology and artificial intelligence with material science and structural engineering. Major structures constructed in this period would be constructed with built-in optical neurosystems and active actuation control that would make them more like living entities than the inanimate edifices we are familiar with today. To carry this biological paradigm one step further, it may even be possible to contemplate future structures that have the capacity for limited self repair. Indeed, if we think of the new frontiers for engineering as being in space or underwater, self diagnosis, self control and self healing may not be so much esoteric as vital.

ACKNOWLEDGEMENTS

The work reported from the UTIAS Fiber Optic Smart Structures Laboratory was supported by the Ontario Laser and Lightwave Research Centre, the Natural Science and Engineering Research Council of Canada, The Institute for Space and Terrestrial Science and the Ontario Centre for Materials Research. The author would like to acknowedge the excellent work of : T. Alavie, A. Davis, M. LeBlanc, D Hogg, D. Janzen, K.Liu, B. Mason, S. Melle, M. Ohn, R. Turner and T. Valis, who contributed to the research reported from my group.

REFERENCES

1. Measures, R.M., (1992), "Smart Structures..... A Revolution in Civil Engineering", Keynote Address, ACMBA-1st International Conference, Sherbrook, 9 Oct.

2. Ahmad, A., Crowson, A., Rogers, C. A., and Aizawa, M., (1990), US-Japan Workshop on Smart/Intelligent Materials and Systems, Technomic Publishing.

3. Measures, R.M., (1989), "Smart Structures with Nerves of Glass", Progress in Aerospace Sci. vol. 26, 289-351.

4. (a) Liu, K., Ferguson, S. M., and Measures, R.M., (1989)," Damage Detection in Composites with Embedded Fiber Optic Interferometric Sensors, " SPIE, vol. 1170, Fiber Optic Smart Structures and Skins II, 205-210.

   (b) K. Liu, S. Ferguson, K. McEwen, E. Tapanes, and R.M. Measures, (1990) " Acoustic Emission Detection for Composite Using Embedded Ordinary Single-Mode Fiber Optic Interferometric Sensors," SPIE vol.1370: Fiber Optic Smart Structures and Skins III, 316-323.

5. Lee, C.E., and Taylor, H.F., (1988), "Interferometer Fiber Optic Sensors using Internal Mirrors,"Electron. Lett., vol. 13, 193-194.

6. (a) Hogg, D., Janzen, D., Valis, T.,and Measures, R.M., (1991), "Development of a Fiber Fabry-Perot Strain Gauge", SPIE, vol. 1588, Fiber Optic Smart Structures and Skins IV, 300-307.

   (b) Hogg, D., Janzen, D., Mason, B., T. Valis and R.M. Measures, (1991), "Development of a Fiber Fabry-Perot (FFP) Strain Gauge with High Reflectivity Mirrors", International Symposium on Active Materials & Adaptive Structures, Alexandria,Virginia, 4-8 November.

7. Kruschwitz, B., Claus, R.O., Murphy, A., May, R.G., and Gunther, M.F., (1992) "Optical sment in Composite Materials with Embedded Fiber Optic Sensors," J. Composite Engineering, Vol 2, 573-596.

8. Valis, T., Hogg, D., and Measures, R. M, (1990), "Composite Material Embedded Fiber Optic easures, R.M., (1992), "Far-Field In-Plane Stress Measurement with an Embedded Eigenaxis-Flipped Fiber Fabry-Perot Strain Gauge," In preparation.

9. Sirkis, J.S., and Haslach Jr., H.W., (1990), "Full Phase-Strain Relation for Structurally Embedded Interferometric Optical Fiber Sensors", SPIE, Vol. 1370, Fiber Optic Smart Structures and Skins III, San Jose, 248-259.

10. Sheem, S.K., Giallorenzi, T.G., and Koo, K., (1982), "Optical Techniques to Solve the Signal Fading Problem in Fiber Interferometers", Appl. Optics, vol.21, 4, 689.

11. Kersey, A.D., Dandridge, A., and Tveten, A.B. (1988), "Elimination of Polarization Induced Signal Fading in Interferometric Fiber Sensors Using Input Polarization Control", WCC2-1 -4, Optical Fibre Sensors '88.

12. (a) Blake, J.N., Huang, S.Y., and Kim, B.Y., (1987), "Elliptical Core Two-Mode Fiber Strain Gauge". SPIE vol. 838, Fiber Optic and Laser Sensors V, p.332.

(b) Blake, J.N., Huang, S.Y., Kim, B.Y., and Shaw, H.J., (1987), "Strain Effects on Highly Elliptical Core Two-Mode Fibers:, Opt. Lett. vol. 12, 732.

13. Kim, B.Y., Blake, J.N., Huang, S.Y., and Shaw, H.J., (1987), "Use of Highly Elliptical Core Fibers for Two-Mode Fiber Devices", Opta. Lett. vol. 12, 729-731.

14. Murphy, K.A., Miller, M., Vengsarkar, A.M., Claus, R.O., and Lewis, N.E., (1989), "Embedded Modal Domain Sensors Using Elliptical Core Optical Fibers", SPIE. vol. 1170, 566-573.

15. Lu, Z.J., and Blaha, F.A., (1991), "Application Issues of Fiber Optics in Aircraft Structures", SPIE. vol. 1588, Fiber Optic Smart Structures and Skins IV, 276-281.

16. Varnham, M.P., Barlow, A.J., Payne, D.N., Okamoto, K. (1983), "Polarimetric Strain Gauges Using High Birefringence Fibres", Electron Lett. vol.19, 699-700.

17. Kersey A.D., Corke, M., and Jackson, D.A., (1984), " Linearised Remote Sensing Using a Momode Fibre Polarimetric Sensor", (1984), SPIE vol. 514, Optical Fibre Sensors '84, 247-250.

18. Hogg, D., Turner, R.D., and Measures, R.M., (1989), "Polarimetric Fibre Optic Structural Strain Sensor Characterisation", SPIE vol. 1170, Fiber Optic Smart Structures and Skins 11, Boston, 542-550.

19. Bock, W.J. and Wolinski, T.R., (1990), "Temperature-Compensated Fiber-Optic Strain Sensor Based on Polarization-Rotated Reflection", SPIE vol. 1370, Fiber Optic Smart Structures and Skins III, 189-196.

20. Morey, W.W., Meltz ,G., and Glenn, W.H., (1989), "Fiber Optic Bragg Grating Sensors", SPIE Vol. 1169, Fiber Optic & Laser Sensors VII, 98-107.

21. Turner, R.D., Valis, T., Hogg, W. D., and Measures, R. M., (1990), " Fiber Optic Strain Sensors for 'Smart ' Structures," J. of Intelligent Material Systems and Structures, Vol. 1, 26-49.

22. Butter, C.D., and Hocker, G.P., (1978). "Fiber Optics Strain Gauge", Appl.Opt., Vol 17, 2867-2869.

23. Measures, R.M., (1993), Chapter; "Fiber Optic Strain Sensing, " in 'Fiber Optic Smart Structures,' Editor E. Udd., Wiley & Sons.

24. Jackson, D.A., and Jones, J.D. C. (1986)," Fibre Optic Sensors", Optica Acta, Vol. 33, 1469-1503.

25. Bertholds, A., and Dandliker, R., (1988)."Determination of the Individual Strain-Optic Coefficients in Single-Mode Optical Fibers", J. Lightwave Tech., Vol.6, pp. 17-20.

26 Meltz, G., Morey, W.W. and Glam. W.H. (1989), "Formation of Bragg Grating in Optical Fibers by a Transverse Holographic Method", Opt. Lett., vol. 14, 823-825.

27. Dunphy, J.R., Meltz, G., Lamm, F.P., and Morey, W.W., (1990), "Fiber-Optic Strain Sensor Multi-Function, Distributed Optical Fiber Sensor for Composite Cure and Response Monitoring", SPIE vol. 1370, Fiber Optic Smart Structures and Skins III, 116-118.

28. Measures, R.M., (1992), "Smart Composite Structures with Embedded Sensors", Composites Eng. vol. 2. 597-618.

29. Melle, S.M., Liu, K., and Measures, R.M., (1991),"Strain Sensing Using a Fiber Optic Bragg Grating", SPIE, Vol. 1588, OE/Fibers' 91 - Conference: Fiber Optic Smart Structures and Skins IV, Boston.

30. Melle, S. M., Liu, K., and Measures, R. M., (1992), "A Passive Wavelength Demodulation System for Guided-Wave Bragg Grating Sensors", IEEE Phot.Tech. Lett. vol.4, 516-518.

31. Morey, W.W., Dunphy, J.R., and Meltz, G.,"Multiplexed Fiber Bragg Grating Sensors", Proc. "Distributed and Multiplexed Fiber Optic Sensors", SPIE vol. 1586, pp. 216-224.

32. Sirkis, J.S., and Haslach Jr., H.W., (1990), "Full Phase-Strain Relation for Structurally Embedded Interferometric Optical Fiber Sensors", SPIE, Vol. 1370, Fiber Optic Smart Structures and Skins III, San Jose, 248-259.

33. Mathews, C.T., and Sirkis, J.S., (1990), " The Interaction of Interferometric Optical Fiber Sensors Embedded in a Monolithic Structure, "SPIE, Vol. 1370, Fiber Optic Smart Structures and Skins III, San Jose, 142-153.

34. Sirkis and Mathews, (1992), private communication.

35. Sirkis, J.S., (1991), "A Unified Approach to Phase-Strain-Temperature Models for Smart Structure Interferometric Optical Fiber Sensors", Opt. Engineering.

36. Valis, T., and Measures, R.M., (1992), "Far-Field In-Plane Stress Measurement With An Embedded Eigenaxis-Flipped Fiber Fabry-Perot Strain Gauge", Optical Fiber Sensor-Based Smart Materials and Structures Conference, Blacksburg, Virginia.

37. Sirkis, J.S., and Dasgupta, A., (1990), "Optimal Coatings for Intelligent Stucture Fiber Optic Sensors", SPIE Vol. 1370, Fiber Optic Smart Structures & Skins III, San José, 129-140.

38. LeBlanc, M., and Measures, R.M., (1992), "Impact Damage Assessment in Composite Materials with Embedded Fiber Optic Sensors," J. Composite Engineering, Vol 2, 573-596.

39. Jackson, D.A., Kersey, A.D., Cork, M., and Jones, J.D.C., (1982), "Pseudo-Heterodyne Detection Scheme for Optical Interferometers", Elec. lett., vol.18, 1081-1083.

40. Liu, K., and Measures, R.M., (1992), "Signal Processing Techniques for Localized Interferometric Fiber-Optic Strain Sensors", Accepted for the Journal of Intelligent Material Systems and Structures.

41.. Turner, R.D., Laurin, D.G., and Measures, R. M., (1992), "Localized Dual-Wavelength Fiber-Optic Polarimeter for the Measurement of Structural Strain and Orientation", Appl. Optics. Vo. 31, 2994-3003.

42. Lu, Z.J., and Blaha, F.A., (1989), "A Fiber Optic Strain and Impact Sensor System for Composite Materials", SPIE, vol. 1170, Fiber Optic Smart Structures and Skins II, 239-242.

43. Kersey, A.D., Lewin, A.C., and Jackson, D.A., (1984), "Pseudo-Hetrodyne Detection Scheme for the Gyroscope", Elec. Lett., 20, 368-370.

44. Jackson, D.A., Kersey, A.D., Cork, M., and Jones, J.D.C., (1982), "Pseudo-Heterodyne Detection Scheme for Optical Interferometers", Elec. lett., vol.18, 1081-1083.

45. Jackson, D.A., (1981), "A Prototype Digital Phase Tracker for Fiber Interferometer", J. Phys.E:Sci.Instrum. vol.14, 1274-1278.

46. Mason, B., Hogg, D., and Measures, R. M.(1992), " Fiber Optic Strain Sensing for Smart Adaptive Structures," SPIE vol 1777, 1st European Conference on Smart Structures and Materials, Glasgow, 12-14 May.

47. Kersey. A.D., Berkoff, T.A., and Morey, W.W., (1992), "Fibe-Grating Based Strain Sensor With Phase Sensitivie Detection", Ist. Euop. Conf. On Smart Structures and Materials, Glasgow.

48. Hill, K.O., Fujii, Y., Johnson, D.C., and Kawasaki, B.S., (1978), "Photosensitivity in Optical Fiber Waveguides: Application to Reflection Filter Fabrication", Appl. Phys. Lett., vol. 32, 647-649.

49. Dunphy, J.R., et al., United Technologies Research Centre, (1990), "Development of Optical Fibers with Embedded Gratings for Sensor and Signal Processing Applications", Rome Air Development Centre, RADC-TR-90-280 Final Technical Report.

50. Ball, G.A., and Morey, W.W., (1992), "Continuously Tunable Singe-Mode Erbium Fiber Laser", Opt. Letters. vol. 17, 420-422.

51. Alavie, T., Melle, S., and Measures, R.M., (1992), "Bragg Grating Tuned Fiber Laser and Its Application to Sensing", in preparation.

52. Measures, R.M., Melle, S.M., and Liu, K., (1992), "Wavelength Demodulated Bragg Grating Fiber Optic Sensing Systems for Addressing Smart Structure Critical Issues", Jr. Smart Mater. Struct. vol.1., 36-44.

53. Czarnek, R., Guo, Y.F., Bennett, K.D., and Claus, R.O., (1988), "Interferemetric Measurements of Strain Concentrations Induced by an Optical Fiber Embedded in a Fiber Reinforced Composite", SPIE, Vol 986, Fiber Optic Smart Structures & Skins I, Boston, 43-54.

54. Blagojevic, B., Tsaw,W., McEwen, K., and Measures, R.M., (1989), "The Influence of Embedded Optical Fibers on the Interlamina Fracture Toughness of Composite Materials", Review of Progress in Quantitative NDE, Brunswick, Maine, July 23-28.

55. Loken, D., (1990), "Effect of Fiber Straightness on Fatigue of Aligned Continuous CFRP Composites ", University of Toronto (Chemical Eng.) M.A.Sc Thesis.

56. Roberts, S.S.J., and Davidson, R., (1992), "Short Term Fatigue Behaviour of Composite Materials Containing Embedded Fiber Optic Sensors and Actuators", 1st Europ. Conf. Smart Structures & Materials, Glasgow, Proc., 255-262,

57. DiFrancia, C., Claus, R.O., Hellgeth, J.W., and Ward, T.C., (1991), "Discussion of Pullout Tests of Polyimide-Coated Optical Fibers Embedded in Neat Resin", Proc. Conference on Optical Fiber Sensor-Based Smart Materials and Structures, 70-82, April 3-4, Blacksburg, Virginia.

58. Pak, Y.E., (1992), "Longitudinal Shear Transfer in Fiber Optic Sensors", Smart Mater. Struct. vol. 1, 57-62.

59. Michie, W.C., Culshaw, B., Roberts, S.J., and Davison, R., (1991). "Fibre Optic Technique for the Simultaneous Measurement of Strain and Temperature Variations in Composite Materials, " SPIE, Vol 1588, OE/Fibers' 91 - Conference: Fiber Optic Smart Structures and Skins IV, Boston, September 5-6.

60. (a) Lee, C.E., Gibler, W.N., Atkins, R.A., and Taylor, H.F., (1992), "In-Line Fiber Fabry-Perot Interferometer with High Reflectance Mirrors," To Appear in J. Lightwave Techn.

(b) Lee, C.E., Alcoz, J.J., Yeh, Y., Gibler, W.N., Atkins, R.A., and Taylor, H.F., (1992), "Optical Fiber Fabry-Perot Sensors for Smart Structures", Smart Mater. Struct. vol.1, 123-127.

61. Liu, K., and Measures, R.M., (1992), "Signal Processing Techniques for Localized Interferometric Fiber-Optic Strain Sensors", Accepted for the Journal of Intelligent Material Systems and Structures.

62. Marple, S.L.Jr., (1987), "Digital Spectral Analysis with Applications", Prentice-Hall Signal Processing Series, Englewood Cliffs, New Jersey.

63. Alper, J.M., (1991) "Two-Mode, Elliptical-Core, *Weighted Fiber Sensors for Vibration Analysis*", Proc. Conference on Optical Fiber Sensor-Based Smart Materials and Structures, 102-106, April 3-4, Blacksburg, Virginia.

64. Gao, P., Alavie, A. T., Mason, B. and Measures, R. M., (1992), " Effect of Delamination on the Natural Frequencies of Composite Beam as Measured by Fiber Optic Fabry-Perot Sensors," SPIE vol. 1798, Fiber Optic Smart Structures and Skins V.

65. Sun, K.J., and Winfree, W.P., (1987), "Propagation of Acoustic Waves In a Copper Wire Embedded In a Curing Epoxy", IEEE Ultrasonic Symp.439-442.

66. Measures, R. M. Liu, K. Davis, A. and Ohn, M.(1991), "Composite Cure Monitoring with Embedded Optical Fiber Sensors," SPIE OE/Aerospace Sensing, Conference 1489; Structures Sensing and Control, Orlando, April 1-5.

67. Ohn, M., Davis , A., Liu, K., and Measures, R. M., (1992), "Embedded Fiber Optic Detection of Ultrasound and its Application to Cure Monitoring", Optical Fiber Sensor-Based Smart Materials and Structures Conference, Blacksburg, Virginia, April.

68. Askins, C. G., Tsai, T. E., Williams, G. M., Putman, M.A., Bashkansky, M., and Friebele, E. J. (1992)," Fiber Bragg Reflectors Prepared by a Single Excimer Pulse," Opt. Lett., vol 17, 833-835.

STRAIN MEASUREMENT OF CARBON/EPOXY COMPOSITE WITH FIBRE OPTICS WHITE LIGHT QUASI DISTRIBUTED POLARIMETRIC SENSOR

B. Fornari
ALENIA SPAZIO, Corso Marche 41, 10146 TORINO, ITALY
J.J. Guerin, P. Sansonetti†, M. Lequime
BERTIN, BP 22000, 13791 AIX EN PROVENCE CEDEX 03, FRANCE
G.Romeo
POLITECNICO DI TORINO, Corso D. Abruzzi 24, 10129 TORINO, ITALY

† presently at ALCATEL ALSTHOM Recherche, Route de Nozay 91460 MARCOUSSIS FRANCE

ABSTRACT

We report the results obtained in measuring the static and dynamic strain of carbon/epoxy composites with embedded or bonded fibre optics white light quasi-distributed polarimetric sensor. Linear and accurate measurements were obtained and up to six sensing zones were parallely interrogated along a single optical fibre.

INTRODUCTION

Intrinsic optical fibre sensors where the optical fibre itself is the transducer offer low invasiveness which is of high interest for the monitoring of strain and vibration fields in structures. Such sensors can even be embedded in composite materials such as glass/epoxy or carbon/epoxy in order to give information on their internal health. Ideally, the optical sensor should give a linear, accurate as well as distributed measurement along a single fibre in order to lower the number of optical fibres and therefore help in the sensing network integration in the host material. A quasi distributed polarimetric measurement based on white light interferometry between the two linear polarization modes of a Highly Birefringent (Hi-Bi) fibre was recently reported [1,2]. In this technique, the successive sensing zones are delineated by polarization mode couplers which can be implemented through application of stress [2] or more advantageously through a grating photoinduced in the core of the optical fibre by a KrF laser [3]. The polarimetric signals generated by the polarization mode couplers are then demultiplexed by white light interferometry [4], the phase difference between two successive signals giving the polarimetric phase on the sensing zone comprized between the two corresponding polarization couplers.

We here report results obtained with such a technique on static and dynamic strain measurements in carbon/epoxy composite with either embedded or surface bonded optical fibre. Up to six sensing zones were interrogated in parallel by using a multichannel Michelson receiver [5].

EXPERIMENTS

The sensing system is made of an emission unit, the optical fibre transducer and the multichannel white light interferometric receiver. The emission unit is based on a Hi-Bi pigtailed RCA SuperLuminescent Diode with a centre wavelength of 816 nm. Its output is then polarized by a YORK fibre polarizer. The polarization axes of the Hi-Bi pigtail, the fibre polarizer and the Hi-Bi optical fibre transducer all have the same orientation. These fibres are connected with RADIALL polarization maintaining connectors, whilst one is also used for the input into the white light receiver ; this insures easy connection of the optical fibre transducer to the emission and reception units. The white light receiver first contains an analyzer axes of which are orientated at 45° from those of the optical fibre transducer. The analyzer is followed by a Michelson interferometer possessing a mirror with seven facets of differing thicknesses with a bundle distribution in its aperture, in order to demultiplex up to seven polarimetric signals [5]. These signals are then detected in parallel with an array of seven lenses and by seven photodetectors, and the phase between each of them measured at an Intermediate Frequency generated by a sawtooth displacement of the plane mirror of the Michelson receiver (piezoelectric actuator). This therefore allows the parallel measurement of the polarimetric phases on six sensing zones.

An optical fibre transducer possessing two 27 cm long sensing zones along a stress birefringence Hi-Bi fibre from 3M was first embedded, parallel to the reinforcement, between plies 39 and 40 of a 40 plies, 1100 mm long,

unidirectional carbon/epoxy composite. The specimen was then statically flexured in three point and four point bending configuration. The four point bending test is represented in figure 1.

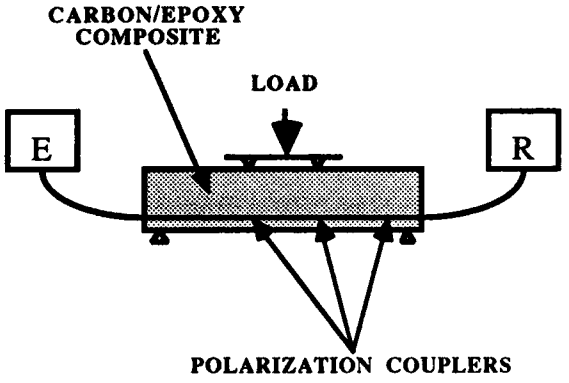

Figure 1 : Scheme of four point bending test on carbon/epoxy composite with embedded optical fibre transducer possessing two sensing zones (E : emission unit, R : white light parallel receiver)

The sensing zone 2 is located at mid sample and is therefore more strained than sensing zone 1 which is adjacent. Classical strain gauges were also surface bonded at the middle of each sensing zone. The distance between the two upper loading points is equal to the sensing zone length. In this way, the local strain values given by the strain gauges are equal to the average strain values given by the optical fibre, apart from a scale factor coming from the fact that the strain gauge is surface bonded whilst the optical fibre is embedded between the plies 39 and 40.

The averaged strain on the two sensing zones obtained through the optical sensor, the local strain given by the strain gauges as well as the theoretical values, all in micro-strain (10^{-6}), are given versus load in Figure 2a when the optical fibre is in extension (the optical fibre is on the bottom side of the composite). Figure 2b represents the same results when the optical fibre is in compression (the optical fibre was this time on the upper side).It can be seen from both figures that the agreement between all these values is excellent which means that the optical fibre sensor gives, in parallel on the two sensing zones, linear and accurate informations. This is true for the optical fibre being either in extension or in compression. No hysteresis was observed for both cases, the loading and unloading curves being the same. Three point bending tests yielded equivalent results.

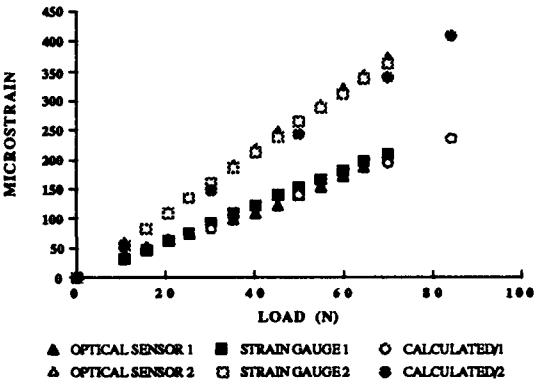

Figure 2a : Average strain on the two sensing zones given by the optical sensor, local strain given by the strain gauges and theoretical strain versus loading during four point bending test; the optical fibre is in extension on the bottom side of the composite

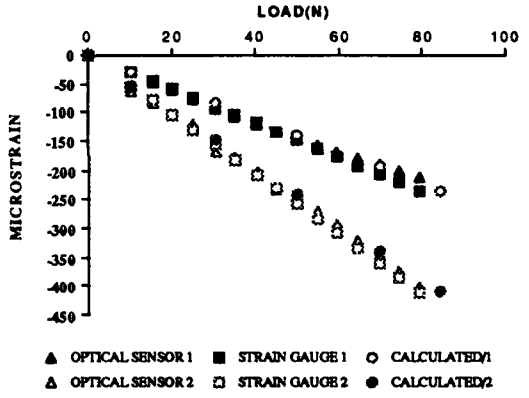

Figure 2b : The legends are the same as those of figure 2a; the optical fibre is in compression on the upper side of the composite.

To characterize the properties of the sensing system on the six sensing zones, a stress birefringence YORK Hi-Bi fibre possessing six 27 cm long sensing zones was bonded on the upper surface of a 1.81 m long carbon/epoxy cantilever. Sensing zone 1 began at the fixed edge of the cantilever whilst sensing zone 6 ended close to its free edge. Therefore, when loaded, the strain level on each sensing zone decreases from sensing zone 1 to sensing zone 6.

This cantilever was suddenly loaded by its own weight by removing its support at the free edge side. The oscillating phases of all sensing zones were measured in parallel from the loading start until the damping was finished. The

resulting AC traces of the analog output proportional to the phases on sensing zones 3 to 6, obtained with a 4-channel parallel tracer, are represented versus time in Figure 3.

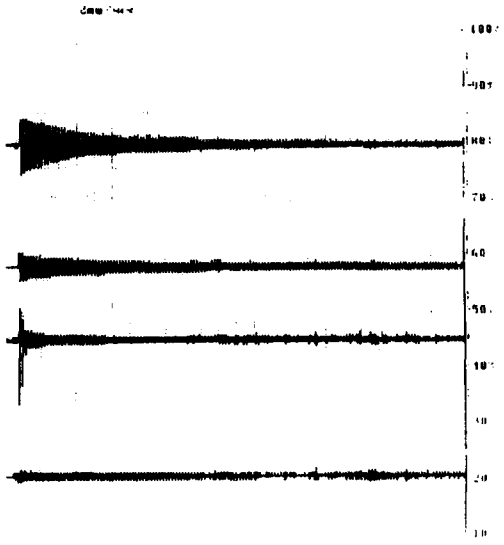

Figure 3 : AC traces of the parallely measured analog outputs proportional to the polarimetric phase on sensing zones 3 to 6 versus time for sudden loading of the cantilever under its own weight

Sensing zones 1 and 2 suffered from 0-2π phase transitions (spikes on sensing zone 5 are also attributed to 0-2π transitions). It is first seen that, as previewed, the measured phase variation decreases when closing to the free edge of the cantilever. The damping is also clearly seen, and the observed oscillation frequency of 2.39 Hz is in good agreement with the value of 2.37 Hz calculated from the mechanical characteristics of the cantilever [6].

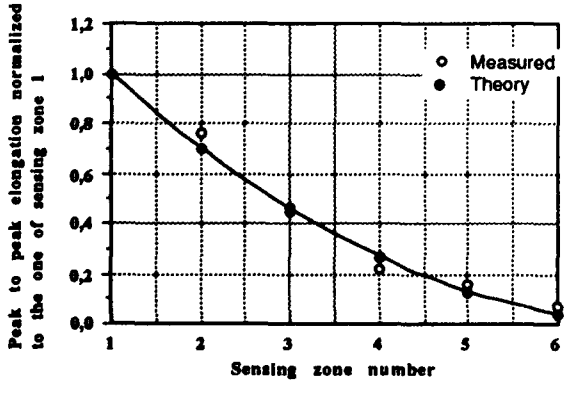

Figure 4 : Peak to peak elongation of the cantilever normalized to the one of sensing zone 1

Figure 4 shows the measured peak to peak elongation values at the beginning of the loading, for each sensing zone, normalized to the one of sensing zone 1 (although 0-2π phase transitions were present on sensing zone 1 and 2 the peak to peak phase excursions were easily extracted). These values are compared to the theoretical curve calculated for the case of a cantilever loaded by its own weight [6]. It is seen that a good agreement is obtained.

CONCLUSION

We have reported results obtained on static and dynamic strain measurement in carbon/epoxy composite with either embedded or bonded white light quasi distributed polarimetric sensor. It was shown that linear and accurate measurements were obtained. To our knowledge, this is the first time that white light quasi- distributed polarimetric sensing allows a real time parallel measurement of static strain on two sensing zones of an embedded optical fibre and of dynamic strain on six sensing zones of a surface bonded optical fibre.

ACKNOWLEDGMENTS

This work was performed under the auspices of an european BRITE-EURAM project n° RI1B-0173-C(CD). Thanks are also due to all partners of this project for fruitful discussions and to P.FERDINAND, J.PLANTEY and J.BENARD from EDF/DER for implementing the source and installing polarization connectors.

REFERENCES

1 TURPIN M., ROJAS D., PUECH C., "Nouveau Concept de Capteurs Répartis Tout Fibre", MESUCORA Conference, PARIS, 1988, pp 33-41.

2 GUSMEROLI V., VAVASSORI P., MARTINELLI M., "A Coherence Multiplexed Quasi Distributed Polarimetric Sensor Suitable for Structural Monitoring", Springer Proceedings in Physics, 44, Optical Fiber Sensors OFS'89 Conference, PARIS, 1989, pp 513-518.

3 GUERIN J.J., MAILLARD J.M., SANSONETTI P., "Polarization mode couplers made by photoinduced gratings for white light quasi distributed polarimetric sensing", OFS'8 Conference, MONTEREY, 1992, pp 288-291.

4 BOSSELMANN T., ULRICH R., "High accuracy position sensing with fibre coupled white light interferometers", OFS'84 Conference, STUTTGART, 1984, pp 361-364.

5 SANSONETTI P., GUERIN J.J., LEQUIME M., DEBRIE J., "Parallel Coherence Receiver for Quasi-Distributed Optical Sensor", Fiber Optic Smart Structures and Skins IV Conference, BOSTON, 1991, SPIE Vol. 1588, pp 143-149.

6 YOUNG W.C., "Roark's Formulas for Stress & Strain', Sixth Edition, McGraw-Hill Book company.

ON THE STABILITY OF SHAPE MEMORY MATERIALS AND THEIR PROPERTIES IN STATIC AND DYNAMIC APPLICATIONS.

J. Beyer
M. Chandrasekaran

University Twente, Department of Mechanical Engineering, Laboratory for Material Science
P.O. Box 217, 7500 AE ENSCHEDE
The Netherlands.

ABSTRACT

Shape memory materials form one group of "smart materials" which are of current interest. The sensing and actuating performance of these shape memory materials have been used in diverse industrial applications. These applications involve either the one-way or two-way effect, pseudoelasticity, recovery forces or damping characteristics of the SM-alloy. Each of these characteristics is associated with its unique response to thermal-mechanical forces. Besides these material parameters, the operating conditions and design parameters have to be taken into account when structures, in which SM elements are incorporated, are to be considered. The processing as well as subsequent operating conditions are relevant to the reproducible (stable) behaviour and life time of the material and are discussed.

1. INTRODUCTION

Smart materials have been defined as those which have the ability to sense and respond in a controlled manner to external or internal stimulus. As component parts these materials can be built into the (smart) structure where they can sense the state of the structure or the environment in which it is operating or effect a change in stiffness, shape, positions or stresses in the structure through the addition of an actuator control loop or even make the structure capable of adaptive learning by adding a control system to interpret the sensor data and react appropriately. Depending on how many of the above characteristics the material possesses it can be classified as passive, reactive or intelligent (1).
Several materials can be considered as smart, like electrorheological fluids, piëzoelectric ceramics, magnetorestrictive materials and shape memory alloys (SMA) (1). A number of SMA, have been developed during the last 20 years of which at present the Cu-Zn-Al, Cu-Ni-Al and Ni-Ti alloys have been commercialized for a variety of applications in both the medical and engineering fields (2, 3, 9). It is just in recent years, though that the application of SMA-elements, and other smart materials, in large composite structures where they can act as active control or load bearing elements (4), has generated interest. Thus in the space industry SMAs are used in release mechanisms, antenna deployment, damping of vibrations during launching and space-grippers. In composite materials for aircraft or space structures they can be used for active strain energy tuning, active modal modification or in biased actuators. Shape memory actuators are used where high forces and large strains are required at relatively low frequencies whereas piezoelectric actuators are used where small strains at high frequencies have to be obtained.
These structural elements have been actively researched in the USA and Japan for four years already while in Europe the response is only recent with the first coordinated effort leading to the 1992 conference in Glasgow (5, 6)
Constitutive equations have been developed for these shape memory alloys, which would help a designer in designing an actuator involving a shape memory element. While this is the first step, very often fine tuning of the responses are required in the structure. The constitutive equations can again be of help here, providing the shape memory element behaves well and reproducibly. But the complex stress-strain-temperature-time relations of the shape memory

alloy can sometimes alter, during processing to incorporate the alloy into a structure or during service, their physical property and transformation characteristics. It is felt that a designer would be better equipped if he/she were aware of these possible changes so that appropriate measures can be taken a priori for a reproducible shape memory behaviour in service. The objective of this paper is to address these issues.

2. SHAPE MEMORY ALLOY CHARACTERISTICS

Shape memory is observed in alloys which exhibit a diffusionless-shear or martensitic transformation. Besides being diffusionless, the transformation is also athermal in character, implying that the amount of volume transformed is dependent only on the temperature and is independent of time at that temperature. The transformation is characterized by the temperatures M_s (martensite start) M_f (martensite finish), A_s (austenite start) and A_f (austenite finish). The change in crystal structure is accompanied by a volume change and a shape change. The difference in crystal symmetry between austenite and martensite causes more than one martensite variant to form within a single austenite grain or crystal. The shape change also leads to accommodation strains in the matrix. The minimization of these accommodation strains, influenced by the presence and direction of stress, is reflected in the shape memory effect which manifests itself in the following way: Plastic deformation of the martensite and subsequent heating to above the A_f temperature will restore the original shape of the alloy. (one-way SME.) Plastic strains up to 8% can be recovered in this way in a typical SMA such as NiTi when the martensite reverts to autenite. In majority of the SM alloys there is also an equilibrium between chemical energy and mechanical energy at any moment during the transformation. The transformation is then referred to as thermoelastic. Nevertheless frictional forces felt by the moving transformation interfaces cause a hysteresis (H) which is generally small in thermoelastic transformation (fig. 1).

In addition, in the specific case of Ni-Ti alloys another transformation called R-phase transformation precedes the martensitic transformation on cooling. This additional transformation also has martensitic characteristics and shape memory effect "though the transformation hysteresis is very small (1.5°C), as is also the shape change.

If the material is deformed at constant temperature above A_f the presence of stress will induce martensite which reverts to austenite on unloading, thereby recovering its original shape. This proces is termed pseudoelasticy and can occur up to a certain temperature beyond which no martensite can be formed by the application of stress (M_D temperature).

If the material is restrained from regaining its original shape high recovery stresses, as much as 700 MPa, can be generated at maximum recoverable strain. This compares to the yield strength of martensite that is typically 80 MPa. Upon transformation to austenite the Youngs modulus increases by a factor of 4 and the yield strength by a factor of 10. These changes in property are also reversible. The change in stiffness influences the damping characteristics of SMA dramatically.

Thermal cycling a shape memory alloy under an applied stress leads to a two-way memory. After a number of cycles a reversible M ← → A macroscopic shape change will be established during subsequent thermal cycling under zero stress. This is known as thermo mechanical two-way memory training. For the development of the two-way memory in NiTi it is essential that the R-phase transformation mentioned earlier is absent. The two-way memory behaviour is dependent on internal stresses and the dislocation substructure resulting from training. This is not only true for the two-way memory but is valid for all properties mentioned and, therefore, one should take care when the material behaviour is described by constitutive equations. Some specific aspects will be addressed and discussed in the following pages.

3. SMA-CHARACTERIZATION

In recent years several approaches have been taken to develop constitutive equations describing the shape memory behaviour of SM-materials (4,-7). Schetky (7) has recently quoted from literature an equation following a free energy minimization method, for a one-dimensional model (4).

$$(\sigma-\sigma_o)=D(\epsilon-\epsilon_o)+\Theta(T-T_o)+\Omega(\zeta-\zeta_o) \qquad (1)$$

where zero subscript refers to the initial condition, σ is the stress, ϵ is the strain, ζ is fraction of martensite, depending on the direction of the transformation and T is the actual temperature. The constants D, Θ and Ω are the Youngs modulus, the thermoelastic tensor and the transformation tensor. In this particular case the fraction of martensite transformed at the actual temperature T is assumed to be a cosine function of $(T-A_s/A_s-A_f)$ for martensite to austenite transformation and $(T-M_f/M_s-M_f)$ where M_f, M_s, A_s, A_f are the specific transformation temperatures. The values of all the terms in the above equation can be determined experimentally.
The transformation temperatures can be determined by electrical resistivity, dilatometry or differential thermal analysis (DSC). The information obtained from these measurements is given in figure 1.

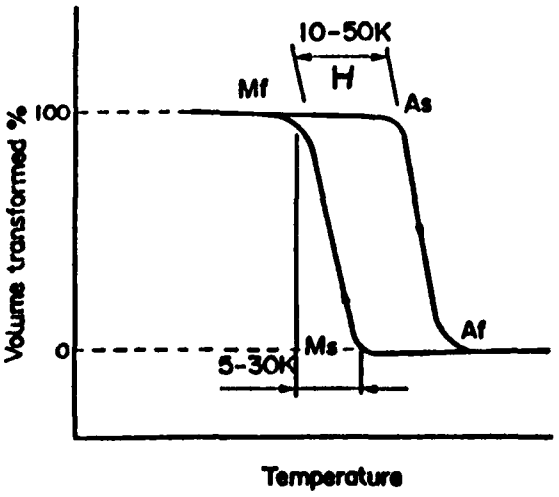

Fig. 1. Schematic representation of the volume transformed to martensite as a function of temperature. Transformation temperatures M_s, M_f, A_s, A_f, are indicated (2).

The transformation temperatures for a given SM-alloy can be influenced by several factors.
Compositional changes such as increasing Ni concentration from 50 to 52 at % in NiTi will dramatically change the transformation temperatures from 60°C down to -100°C whereas alloying with Zr, Au, Pt can raise them to 600°C. The hysteresis can also be influenced by compositional changes. Cu additions narrow down the hysteresis from 30 to 15°C whereas Nb additions widen it to approximately 80°C when no external stress is applied. Soft second phase Nb particles deform irreversibly in contrast to the reversible nature of the martensite deformation from twin boundary motion. This irreversible slip deformation expands the hysteresis of NiTiNb to as much as 120°C. The amount, size and morphology of the particles will also influence the rate at which the transformation takes place (the slope is (M_s-M_f) in figure 1). Besides in Cu base alloys a shift of A_s relative to M_s can be effected for one time due to aging and diffusion which also leads to a stabilization of the martensite. Once recovery is complete martensite can be reformed after which A_s is restored to the original value, provided further aging in martensite is avoided.

Thermo mechanical processing of the alloys generally lowers the transformation temperatures when plastic deformation by cold working is increased and subsequent heat treatment temperature is decreased. Figure 2 illustrates the effect of heat treatment after cold deformation in a binary NiTi-alloy. Annealing at increasing temperatures up to the recrystallization temperature (600°C) will gradually reduce and annihilate the dislocation substructure, thereby restoring the transformation temperatures to the original level.

The influence of stress during temperature cycling (amplitude) is to raise the transformation temperatures some 20-50°C. The redistribution of dislocations allows preferred martensite variants to form easily which will enhance the relative stability of the martensite with respect to autenite. Special types of dislocations, dictated by the applied stress,

are formed additionally during cycling causing the changes in M and A temperatures.

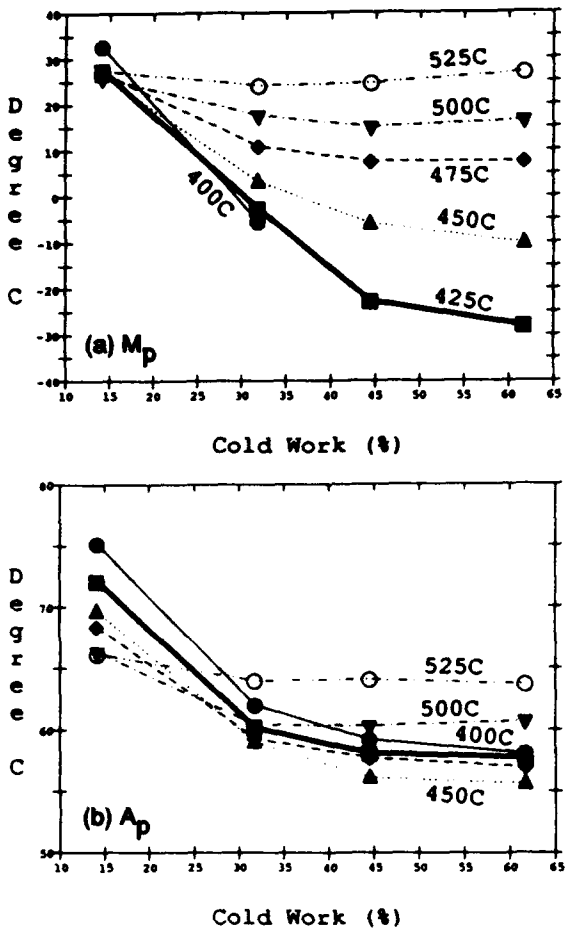

Fig. 2 Effect of heat treatment and cold work on the forward (M) and reverse (A) transformation temperatures (7).

At the same time the hysteresis is reduced as a function of stress at full transformation amplitudes. Partial transformation results in even smaller hysteresis.
Besides these factors, mechanical interface joint effects will also have to be considered when the SM material is used as an actuator element. The mechanical friction of the system will then enhance the hysteresis of the SMA. An increment of cooling is thus needed before the actuator can generate enough force to overcome the frictional forces in the system.

The stress-strain curves at constant temperatures in figures 3 and 4 illustrate the above mentioned stress dependence of the transformation temperature.

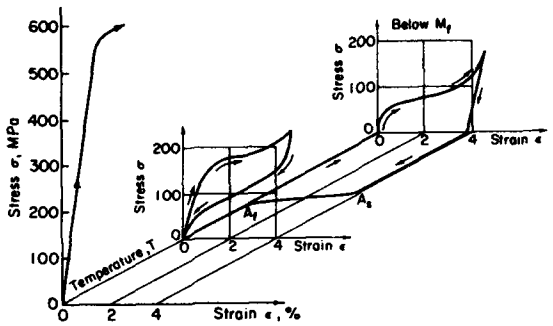

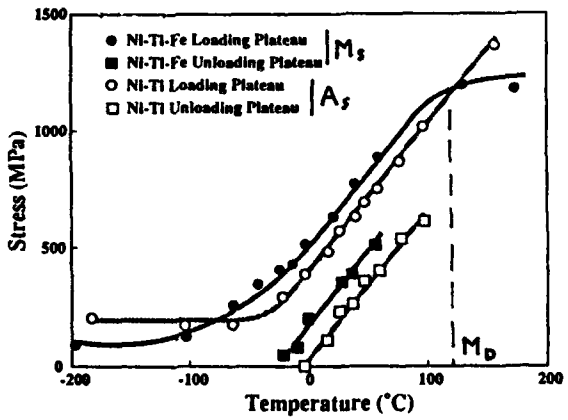

Fig. 3. Stress-strain-temperature relationship of a TiNi alloy (3)
a) stress-strain curves below M_f, above A_f and above M_d, are shown
b) loading/unloading plateau stresses of binary and a ternary NiTi-alloy.

The Youngs modulus D in equation 1 of the fully austenitic (ζ=0) and fully martensitic (ζ=1) conditions can be determined from the fully austenic and fully martensitic stress-strain curves. Thus $\sigma=D_A.\epsilon$ and $\sigma=D_M.\epsilon$. Modulus changes in NiTi by a factor of 4 in going from martensite to austenite. Dynamic modulus measurements as shown in figure 5 illustrate that a pronounced modulus decrease in austenite on cooling occurs before M_s.

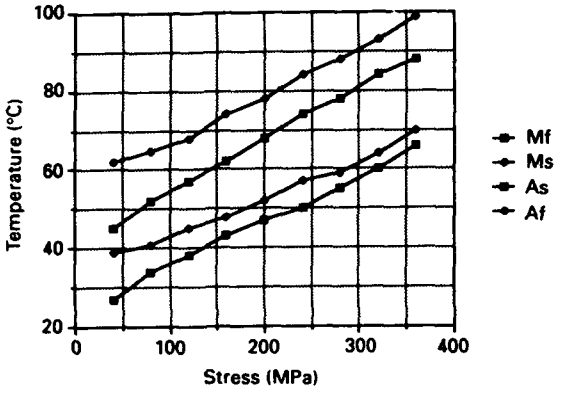

Fig. 4. Dependence of transformation temperatures on stress of a NiTiCu alloy (3).

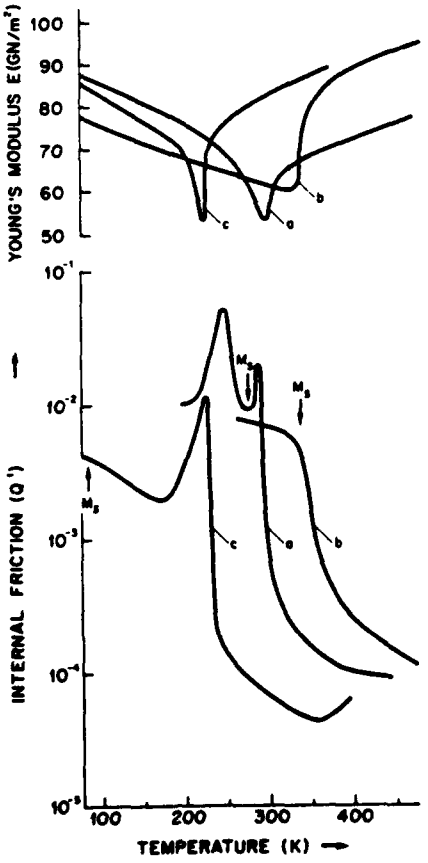

Fig. 5. Young's modulus and internal friction Q^{-1} on cooling for
a) binary NiTi,
b) NiTiCu and
c) NiTiFe (3)

Another complication concerning modulus is the slope of the loading and unloading lines in the stress-strain curves which are not the same. In deformed martensite the unloading line has a non-linear behaviour. For strains exceeding 8% the dislocations introduced can act as pinning points for martensite twin boundaries. When the external stress is removed the dislocations move back to new equilibrium positions and take the twin boundaries with them giving more unloading strain than normal alloys. The unloading strain is dependent on the amount of total deformation strain. Above M_s on cooling the transformation temperature depends linearly on stress given by the Clausius-Clapeyron relation

$$\frac{\partial \sigma}{\partial M_s} = \frac{\Delta H}{T \varepsilon_o}$$

where ΔH is the transformational latent heat and ϵ_o the transformation strain resolved in the direction of the applied stress. The martensite is induced by the applied stress and disappears on unloading at constant temperature. The stress rate, $\partial M_s/\partial \sigma$, of NiTi can vary significantly from one alloy to the other. Values from 2.5 MPa/°C to 15 MPa/°C are observed. In general, lower transformation temperatures have lower stress rates due to lower latent heat of transformation; higher strength alloys show generally higher stress rates (figure 3b).
The recovery strain limit, ϵ_L, can be determined by tensile testing at $T<A_s$. The limit strain of the plateau where $\zeta=1$, is the maximum strain that can be recovered on heating after unloading the specimen. The transformation tensor $\Omega=D_M.\epsilon_L$ when $\zeta=1$.
During loading the martensite will detwin and due to the low symmetry of the martensite lattice a deformation anisotropy will be introduced. In polycrystalline material this anisotropy is obtained by the development of texture during fabrication. Therefore, ϵ_L is dependent on the orientation of the texture relative to the applied stress. In cold rolled NiTi sheet, ϵ_L in the rolling direction can be 8% whereas in the transverse direction ϵ_L is only 3%.

The thermoelastic tensor Θ in equation 1 is determined by the restrained recovery test on heating above the $A_s(o)$ temperature (o is in stress free condition).

$$\Theta = \sigma/(A_s(o)-T).$$

SMAs are particularly used in constrained recovery applications such as fasteners but also when used in composite elements the recovery stress depends on the compliance of the composite, figure 6.

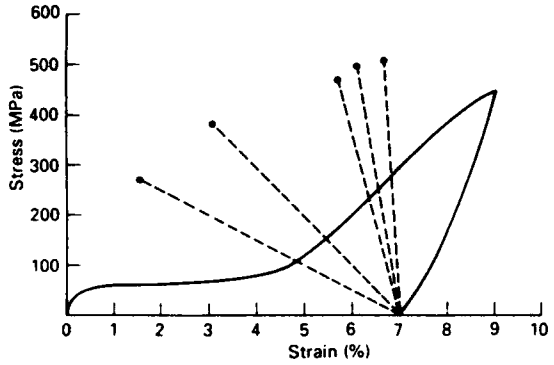

Fig. 6. Restrained recovery of an em bedded NiTi-alloy. Lower compliance of the matrix leads to lower recovery stresses. (3)

In an actual situation, the recovery stress decreases relative to a rigid matrix with $\Delta\sigma = E'\Delta\alpha\Delta T$ where $\Delta E'$ is the system compliance which accounts for the compliance of both the matrix and the SMA. $\Delta\alpha$ takes into account the difference in thermal expansion coefficient of the matrix and SMA. Finally, the recovery stress is also altered by the amount of total strain and the unresolved recovery. The recovery stress decreases as the total strain is increased, while the unresolved recovery is constant.

Damping in SMA-materials is caused by the high concentration of twin boundaries, martensite-martensite interfaces and martensite-austenite interfaces depending on the temperature. These interfaces show a high mobility after an appropriate thermomechanical treatment. The moving interfaces under cyclic loading leads to the interaction of interfaces with dislocations and other lattice defects like vacancies.
The resulting internal friction causes a high damping, which is temperature and stress dependent as indicated by the loss-factor Q^{-1} in figure 7 and figure 5.

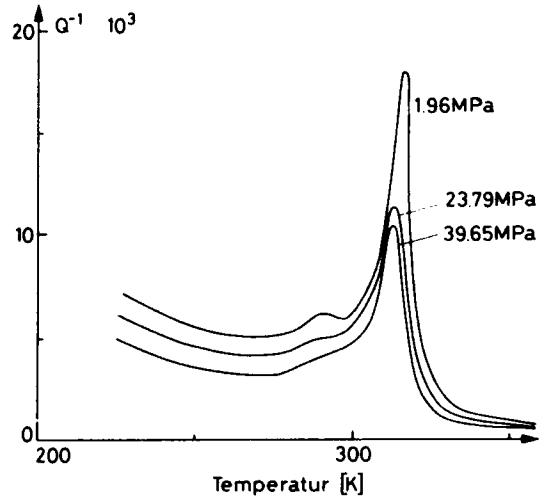

Fig. 7. Damping of NiTi as a function of temperature and variation of preload. (9)

The amplitude of the load cycle changes the damping capacity of the SMA. A high preload will reduce the number of mobile interfaces due to the formation of preferred martensite variants, thereby reducing the damping.

The internal structure responsible for the damping can be influenced by the change in composition and thermomechanical treatments, thus giving the means for optimization of the damping characteristics of the material.

The use of SMA reinforced composites are now being investigated for active modal modification or active strain energy tuning techniques. In these cases additional problems arise which are even more important under these circumstances than in the case of sensors or actuating elements. Overheating the SMA element during the fabrication of the composite can change the microstructure of the material previously optimized for its properties.

The dimensional stability of the SM element is important to assure long life time of the composite. Creep

as a result of thermal cycling under stress is an indication of instability and will increase with increasing number of cycles. Little is known about the effects of uneven variations in the cycling where the heating temperature is in the partial or fully transformed region under variable load conditions. The operating conditions need to be defined accurately in order to be able to optimize the material properties and stabilize it without degradation of the required properties with time.
In composite structures, interfacial problems between SMA and the matrix need additional attention as well as the heat transfer from the SMA to its surroundings during cooling. This response determines the cycling frequency range where the SMA can operate. In composite structures joining and connecting dissimilar elements also need more attention.

4. CONCLUSIONS

Modelling of SM material behaviour and behaviour of composite elements or structures in current use are applicable to a well behaved material whose shape memory characteristics are reproducible with time-temperature during processing and service. While such models are necessary they may not be sufficient in case the material characteristics are changed due to processing conditions or during service. This is quite probable due to the complex stress-strain-time-temperature response of the SM materials owing to concurrent changes in the microstructure or defects in the material. Improvements to the material behaviour and the models can be brought about only if cognizance of the changes to particular conditions are noted and appropriate measures are taken. This approach is particularly important if fine tuning of the material response by controlled changes in composition and microstructure are to be brought about.

5. REFERENCES

1. Newnham, R.E. and Ruschau, G.R., "Smart Electroceramics". J. Am. Ceram. Soc. *74* 3 (1991(pp. 463-480.
2. Van Humbeeck, J., Chandrasekaran, M. and Delaey, L., "Shape memory alloys: materials in action". Endeavour *15* 4 (1991) pp. 148-154.
3. Duerig, T.W., Melton, K.N., Stöckel, D. and Wayman, C.M., "Engineering Aspects of Shape memory alloys", Butterworth-Heinemann, 1990, (ISBN 0-750-61009-3).
4. Rogers, C.A., "Smart Materials, Structures and Mathemetical issues", Technomics, Basel, 1989 (ISBN 87762-682-0).
5. "The concept of Intelligent Materials and guidelines for their R&D promotion". Japanese Science and Technology Agency, Nov. 1989.
6. Proc. of first European Conference on Smart Structures and Materials", Copublished by Institute of Physics Publishing and EOS/SPIE, SPIE Vol. 1777.
7. Liu, C.T., Kunsman, H., Otsuka, K. and Wuttig, M., "Shape memory Materials and Phenomena-Fundamental Aspects and Applications", Mat. Res. Soc., Vol. 246, Symp. Proceedings 1992 (ISBN 1-55899-140-9).
8. Stöckel, D., "Superelastic Nicke-Titanium wires - Raychem Corporation, Menlo Park, CA, USA.
9. Hornbogen, E., Thuman, M., Die martensitische Phasenumwandlung und deren Werkstofftechnische Anwendungen, DGM, 1986 (ISBN 3-88355-096-5).

Smart Polymeric System for Electromechanical Transduction

P. Chiarelli
D. De Rossi
Kayo Umezawa
Centro "E.Piaggio", Faculty of Engineering
University of Pisa,
via Diotisalvi 2, 56126 Pisa, Italy.

SUMMARY

In this paper we briefly review the various mechanisms eliciting electromechanical response, in polymer gels and conducting polymers, which have been exploited to eventually develop electrically driven gel actuators. We also indicate a few approaches we have undertaken to eventually obtain electrochemomechanical system with better performance.

LIST OF SYMBOLS

h	chain end-to-end distance
e	electron charge
k	Boltzman constant
T	temperature °k
do	permanent dipole moment of chain
ε	dielectric constant
εo	vacuum dielectric constant
α	chain polarizability
K	dissociation constant
E	electric field

1 INTRODUCTION

The development of polymeric "muscle like" actuators, as they are perceived today, relies upon the observation that changes in conformation and equilibrium length of constituent macromolecules, induced by physicochemical stimuli, can manifest themselves at macroscopic level in terms of volume and shape changes or force generation in solvent-swollen polymer networks. Starting from the early fifty's water swollen polyelectrolyte gels have been largely investigated as mechanochemical (or, using today terminology, chemomechanical (ref.1)) energy converters (ref.2). Only recently, however, has their potential usefulness as electrically driven actuators been fully realized and substantial research efforts devoted to their implementation (ref.3).

2 ELECTRICAL EFFECTS ON POLYMER GELS

To describe in detail electric field effects on macromolecules is beyond the scope of this paper. Only few arguments of general nature on the subject are reported here in order to provide a frame for classifying and elucidating electrochemomechanical (ECM) phenomena exploited in actuator drive. The most relevant effects caused by electric fields on polyelectrolytes (in solution or as swollen networks) are:

a. orientation of dipolar species;
b. deformation of polarizable species and orientation of induced dipoles;
c. influence on the degree of dissociation of weak acids and bases (Wien effects);
d. motion and redistribution of mobile charged species;
e. electrochemical reaction at interfaces.

These effects may be associated to various modifications and structural readjustments at a molecular level that, in a crosslinked gel, manifest themselves at a macroscopic level owing to existing intermolecular bridges.
The estimation of the orders of magnitude, although under simplistic assumptions, may provide very useful comparative evaluation of ECM working mechanism. These calculations have been performed (ref.4) and can be applied, as a first approximation, to ionized polyacrylamide, poly(acrylic acid)-poly(vinyl alcohol) (PAA-PVA) mixtures and others, currently utilized to develop polymeric actuators (ref.3).

Table 1:

Effect	'E' Dependence	'E'(for 1% change)
a.	$\Delta h/h = E\, m^{1/2}\, do/3kT$	10^3 /Vcm
b.	$\Delta h/h = E^2\, \alpha/3kT$	10^4 /Vcm
c.	$\Delta K/K = e^3 \lvert E \rvert /8\pi\varepsilon\varepsilon o(kT)$	10^4/Vcm

In table 1 orders of magnitude of the electric field on a polyelectrolyte chain are reported with reference to effects of class a.,b.,c., above. From this consideration it appears that significant structiural modification caused by effects of classes a.,b.,c., can be excluded for electric field intensity lower than 10^2 -10^3 V/cm. Electric fields as low as 10 V/cm have been shown, however, to induce large shape and volume changes in polyelectrolyte gels. In these cases electrokinetic and electrodic effects are dominant.

3 ELECTROKINETIC AND ELECTRODIC EFFECTS IN EMC COUPLING

ECM transduction in crosslinked collagen has been induced and the response analyzed in terms of electrokinetic coupling (ref.5).
Modulating the spatial profiles of neutral salt by electric forces causes reversible expansion and contraction in non isoelectric, crosslinked collagen membranes; a phenomenon attributed to changes in Debye length and, hence, in lateral repulsion forces between ionized collagen fibrils (ref.6).
Contraction, and even phase transition, in partially hydrolyzed polyacrylamide gel in contact with platinum electrodes (under a DC potential difference of a few volts) has been observed and the effect ascribed to electrophoretic pressure gradients inducing gel deswelling (ref.7).
Similar effects have been reported by Osada and Hasebe (ref.8) using a water swollen poly(2-acrylamido-2-methyl-1-propanesulfonic acid). The sample's weight was reduced by 30% because of loss of water when a DC electric current density of 7 A/m^2 flowed across the sample for 20 minutes.
The generation of tensile forces in crosslinked membranes made of PAA-PVA has been related to changes in ionization state of the membrane induced by electrochemically generated pH and salt concentration changes at the electrode(ref.9).
To speed up the process of ECM coupling, electrohydrodynamic control of ion flux across a tubular membrane made of ionizable hydrogels separating acid and basic bath has also been used (ref.10).
In addition, alternate bending of ionized gel samples immersed in the aqueous salt solution under an alternating electric field has been reported and analyzed (re.11).
Shinohara and Aizawa (ref.12) used PPy coated platinum electrode to modulate the pH of the nearby solution and observed reversible aggregation and dissolution of microsphere made of a polymethacrylic acid (PMAA) Ca^{++} chelate gel.
Chiarelli et al. (ref.13) prepared a polyelectrolyte gel made of PAA-PVA interpenetrated by PPy through a gas-phase process and demonstrated that the composite material manifests both chemomechanical and electrochemomechanical responses.
Poly(acrylamide-allylamine) and poly(acrylamide-acrylic acid) gels contained some redox compounds (viologen and hydroquinone) have been ionized through electron charge transfer with a metal electrode (ref.14).
Tanaka et al (ref.15) prepared a conducting polymer gel made of poly(3-butylthiophene) crosslinked with dithiophenyl octane and observed reversible swelling-contraction behavior by reversible electrochemical doping by Bu_4NClO_4 dissolved in THF.
Osada et al (ref.16) prepared a charge-transfer complex gel made of poly(N,Ndimethylaminopropylacrylamide) and TCNQ and observed 4 fold faster contraction speed and 8 fold increase in work efficiency compared to conventional hydrogels.

4 DISCUSSION

To design and construct truly viable polymeric "muscle-like" actuators several requirements that are often in conflict with one another should be fulfilled. High force density (>0.1MPa), fast response time (<100 ms) and high efficiency in energy conversion (biological muscle can attain conversion efficiency as high as 45-70%), are actuator characteristics that are thought to be necessary to achieve (ref.3). At present, no electrically driven gel actuators combine all these specifications together.
Conducting polymers (in gel or bulk form) can potentially generate force density as high as 100 MPa (ref.17), but, using present technology, at a relatively slow contraction rate. This class of polymeric actuators, however, is presently being actively investigated (ref.18).
To date no experimental evidence related to the feasibility of electrically triggered, chemically fueled ECM coupling has been reported. Such a system would more closely mimic biological mechanism and would possibly improve the efficiency and power input capacity of the system. Advances in understanding and operating electric control of enzyme activity (ref.19) may provide in the future a way of efficiently coupling electric control with chemomechanical system (ref.18).

5 REFERENCES

1)Osada Y., Adv. Polym. Sci., 87, 1987, pp 1-46.
2)Katchalsky A., Lifson S., Michaeli T. and Zwick H., "Size and shape changes of contractile polymers", Wasserman A. (Ed.), Pergamon press, New York, 1960.
3)De Rossi D., Suzuki M., Osada Y. and Morasso P. in press on J. Intell. Mat. Syst. Structures.
4)Neumann E., In, " Ions in macromolecular and biological system", Everett D.M. and Vincent B. (Eds.), University Park press, Baltimore, 1978.
5)Grodzinsky A. J. and Melcher J.R., IEEE Trans. Biomed. Eng. BME, 23, 1976, pp 421-433.
6)Yannas I.V. and Grodzinsky A.J., J. Mechanochem. Cell Motility, 2, 1973, pp 113-120.
7)Tanaka T. Nishio I., Shao-Tang S. and Ueno-Nishio S., Science, 218, 1982, pp 467-470.
8) Osada Y. and Hasebe M., Chem. Lett., 1985, pp 1285-1288.
9)De Rossi D., Chiarelli P., Buzzigoli G., Domenici C., and Lazzeri L., Trans. Am. Soc. Artif. Int. Organs, XXXII, 1986, pp 157-162.
10)Suzuki M., Proc. 9th Int. Conf. IEEE-EMBS, Philadelphia, Nov., 1990, pp 1-4.
11)Shiga T., Karauchi T., J. Appl. Polym. Sci. 39, 1990, pp 2305-2320.
12)Shinohara H. and Aizawa M., Kobunshi Ronbunshu, 46,11, 1989, pp 703-708.
13)Chiarelli P., Umezawa K. and De Rossi., In "polymer gels: fundamental and biomedical applications", De

Rossi D., Osada Y., Yamauchi A., Kajiwara K. (Eds), Plenum Press, London.
14)Enomoto K., Umemoto S, Okuni N. and Sakai T., Proc. Jap. Society Polym. Sci., 1989, pp 65-66.
15)Tanaka Y., Shiga T., Hirose Y., Okada A. and Karauchi T., Proc. 4th Polymer gel conference, 1991, pp 68.
16)Onishi s., Goung W., Miyano M., Iwabuci T., Kawakami I. and Osada Y., Proc. 4th Polymer gel conference, 1991, pp 69.
17)Baughman R.H. and Shacklette L.W., "Science and applications of conducting polymers", Salaneck W.R. (Ed) et al., Bristol.
18)De Rossi D: Proceedings of 1st International Conference on Intelligent Materials, to be presented.
19)Aizawa M., Yabuki S. and Shinohara H., "Molecular electronics biosensors and biocumputers" Felix T. Hong (Ed), Plenum Press New York, 1989.

Adaptive Structure Design Employing Shape Memory Actuators

Mohan S. Misra, Bernie Carpenter, Brian Maclean
Martin Marietta Astronautics
Denver, Colorado 80127

ABSTRACT

Shape memory alloy wire "tendons" can be used as embedded actuator elements to control the level of facesheet strain in adaptive structural components which utilize sandwich panel construction. As facesheet strain is varied, the degree of curvature and magnitude of tip deflection of a panel section can be controlled. Methods for modeling and conditioning shape memory materials and their subsequent integration into composite structures are described along with related control system and feedback sensor development. Finally, an adaptive antenna application employing "flex-biased" actuation and an attitude control surface based on "antagonistic" actuation are described.

1.0 INTRODUCTION

The performance capabilities of aerospace systems such as control surfaces and adaptive antennas can be greatly enhanced by incorporating advanced structures and material technology into future designs. While significant improvements have been demonstrated using passive design approaches which incorporate efficient airfoil geometries, or low CTE composite materials, acceptable responses might be restricted to narrow operational environments. Innovative concepts are required to expand this environment while providing controllable degrees of freedom. "Adaptive" structures have the ability to sense their own response to environmental and operational stimuli and modify that response in such a way as to optimize structural performance.

Amongst a growing family of "adaptive materials," including piezoceramics, electrostrictors, electro-rheological fluids, paraffin wax, etc., are shape memory alloys (SMA), which utilize a reversible crystalline phase transformation to recover their originally trained shape when heated above a critical transformation temperature range (recoverable strain can be as high as 8%).

The primary intent of this paper is to describe design approaches for adaptive structures, shape memory alloys, composite structure design and control systems development. Two applications on adaptive antennas and a control surface are also described based on this design approach.

2.0 SHAPE MEMORY MATERIAL CHARACTERIZATION

SMAs exhibit an interdependent force-length-temperature (FLT) response to operational cycling with significant property instability early in the life of the actuator element. These characteristics can be accounted for by effective analytic modeling and physical conditioning. This is not only critical for

exploiting the shape memory effect for the conversion of heat to mechanical work but also to optimize actuator performance in specific structural applications with associated control algorithms.

Analytic Modeling -- Insight into behavior of shape memory alloys can be gained by understanding that the existence of each phase in an SMA is dependent upon the combination of free energy available from temperature, stress, and strain. This has lead to the development of a method for predicting the FLT response of SMAs referred to as Non-Equilibrium Thermostatics (NET) which describes the work and heat flow, and the thermodynamic paths of a shape memory actuator element. [1]

NET theory can be used to develop a set of design equations for the actuator elements and coupled to the finite element model of the host structure to provide the necessary mechanical transductance for the level of shape adaptivity needed in the application. Optimization of actuator placement and density is determined by incorporation of NET into finite element model(s) of the structure to meet stress, strain, and fatigue and bandwidth requirements.

Conditioning -- SMAs demonstrate a pseudo-elastic effect (at a temperature above an alloy's characteristic austenitic finish temperature) in which the martensitic phase can be stress induced from otherwise stable austenite. At zero force the wire is fully austenitic with martensite forming as the wire is stretched. Hysteresis is observed during unloading as the austenitic phase is recovered. This behavior, shown in Figure 1, illustrates the cycling instability of as-annealed SMA wire. Hysteresis is reduced on a semi-log basis with increasing number of transformation cycles. This reduction has been noted as the effect of transformational cycling on the nucleation and growth of martensitic plates within the parent grains. Accelerated isothermal "conditioning" [2] of SMA actuator elements can be used to reduce hysteresis and stabilize material property drift, without impacting fatigue life, before NET property characterization and actuator installation.

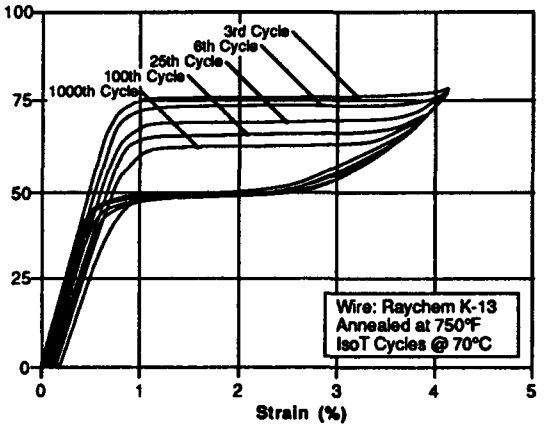

Figure 1 Cyclic Stability of NiTiCu as A Function of Transformation Cycle

Fatigue Response -- Representative cycle to failure data, as a function of transformation strain, is presented in Figure 2. Life spans of 4000 cycles can be expected at 8% strain, increasing by two orders of magnitude at 3% strain. Operational fatigue life is used to establish the allowable operational strain of the actuator elements.

3.0 ADAPTIVE STRUCTURE DESIGN

SMA wire "tendons" can be used as embedded actuator elements to control the level of facesheet strain in adaptive structures which utilize sandwich panel construction. As facesheet strain is varied, the degree of curvature and magnitude of tip deflection can be controlled. This is demonstrated in Figure 3 in terms of a finite element model used to analyze this approach on a representative

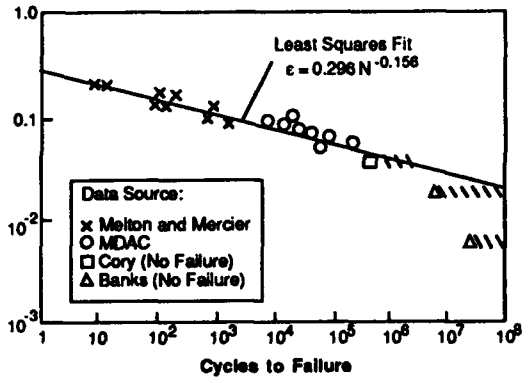

Figure 2 Strain Dependence of Fatigue Life for NiTi Shape Memory Alloys

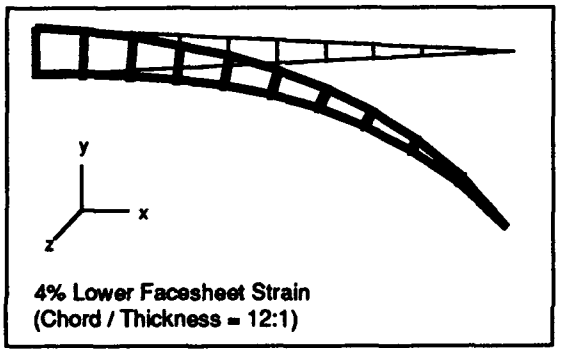

Figure 3 Wing Section of Deformation as a Function of Lower Facesheet Strain

airfoil section (chord to thickness ratio of 12). Tip deflection of 40% cord is predicted for 4% facesheet strain. The relationship between facesheet strain and tip deflection is nearly linear and strictly a function of the chord-to-thickness ratio. Selection of that ratio is driven primarily by the required life span of the adaptive structure and associated fatigue limitations of the SMA actuators.

Winglet Demonstration -- Shape memory alloys are of great interest as an embeddable actuator material for high strain-compliancy structures because of their ability to operate at high stress and strain. A 1" wide by 12" long winglet wedge section, 1" thick at the root, was subsequently fabricated to demonstrate this concept, as seen in Figure 4. This particular design utilizes a 0.125" thick fiberglass epoxy laminate on the underside bonded to an aluminum honeycomb core using epoxy film adhesive. The tip and root sections of the honeycomb were core-filled, prior to bonding, to provide additional bond area at these locations. The top facesheet was fabricated by first producing 0.038" thick films of GE Plastics' LoMod™, an elastomeric thermoplastic material with elastic modulus of 30 ksi and elastic limit of >30%. The sheet was subsequently bonded to the upper side of the honeycomb core using a silicone rubber-based adhesive. Pre-conditioned SMA wires were incorporated in the facesheet. Electrical circuit plates were then fabricated to create three parallel circuits of four wire lengths each to produce a favorable electrical resistance of 2.2Ω. (At 12 volts the wire circuit draws 5.5 amps, producing approximately 66 watts of heating power.)

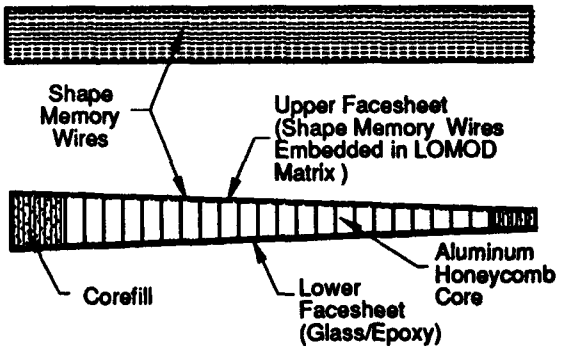

Figure 4 Shape Memory Actuated Wing Section

Another important point to be made regarding the design of the winglet is its ability to balance externally applied loads. With 12 each 0.020" diameter wires contracting with a potential of 65 ksi operational recovery stress (= 245 lbs total contraction force potential),

against a facesheet stiffness of 150 lbs/in, 4% wire recovery corresponds to only 72 lbs of wire tension. This leaves a wire operating margin of 173 lbs. That means that with a lever arm of 12:1, the 1.0" wide winglet is capable of lifting almost 15 lbs at its tip. However, to generate a "balanced" or symmetric force response for externally applied load, i.e. establish the capability to balance loads equally whether applied from above or below, an "antagonistic" control approach can be used. Figure 5 compares the "flex-biased" approach, developed and described above, with an antagonistic approach where a composite laminate is located in the middle of the sandwich panel and active facesheets are bonded to both outer surfaces.

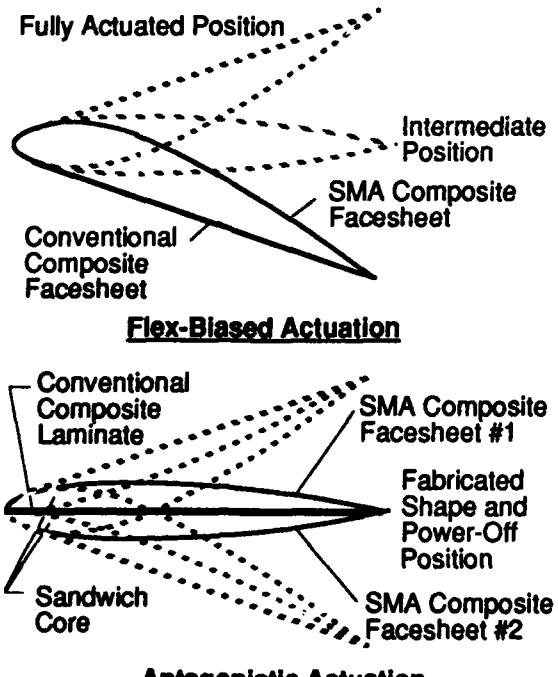

Figure 5 Comparison of Flex-Biased and Antagonistic Actuation Approaches

4.0 CONTROL SYSTEM DEVELOPMENT

The control of deformable panel structures can be accomplished using a closed-loop, displacement sensor feedback approach. A proportional/integral/differential (PID) [3] control law provides the ability to supply electrical power to the SMA wires based on a sensed displacement error. As error is reduced, the integral term takes over and accounts for ambient heat losses while the differential term controls rate of approach to the command set point.

The bandwidth for shape control of an adaptive sandwich panel is dependent on the rate of heat transfer in and out of the SMA wires. This, in turn, is a function of transient effects between the facesheet material and the SMA wires, as well as the rate of cooling of the facesheet to ambient conditions. Bandwidth improves with enhanced cooling of the facesheet but enhanced cooling requires greater power levels to maintain wire temperature for a given command position. The demonstration winglet, for example, can be cycled through most of its range of motion at about 0.1 Hz in air. This bandwidth response can be improved by a factor of 5 to 10 by placing the winglet in water or fast-moving air, albeit with the associated increase in required power to hold any particular position.

5.0 ADAPTIVE ANTENNA APPLICATION

Spacecraft structures with stringent dimensional tolerancing requirements (i.e. large space antenna systems) will require advanced design approaches to meet performance requirements. For example, space-based communication antenna dishes (e.g. 12 GHz range and 2.7 meter diameter)

are presently fabricated with state-of-the-art graphite-epoxy facesheets and honeycomb core but on-orbit thermal loading in geosynchronous orbit causes periodic distortion of approx. 0.20 inches peak-to-peak at the antenna's rim, causing loss of antenna gain. Multiple feedhorns and frequent antenna recalibrations are presently being used to minimize performance loss. Distortion must be limited to < 0.050 inches peak-to-peak to improve performance, however, if the antenna surface can be controlled with rim displacements on the order of 1.00 inch, the ability to steer and distribute gain across the beam footprint will provide substantial additional payoffs over existing systems for this particular example. Other significant applications include sub- or secondary reflectors where the ability to control the surface provides significant improvements in beam quality during steering or feed switching.

Figure 6 shows the fabrication approach for a 60" diameter adaptive antenna reflector test article presently under development. The structure utilizes conventional processing of a composite sandwich panel dish (graphite epoxy reflector and quartz/polycyanate back facesheets). Quartz capillary tubes will be embedded in the back facesheet along preferential radial load paths. After consolidation, an isogrid rib pattern will be machined to establish transverse compliancy and to expose capillary tube ends at the nodes of the pattern. The remaining open core material will provide some support to the reflector facesheet. Shape memory wires will then be conditioned, laced through the tubes, and secured to anchor strips. The strips will maintain wire pre-strain and act as busses for electrical resistance heating of the shape memory alloy. By activating various combinations of the SMA wire segments, the surface of the dish can be controlled.

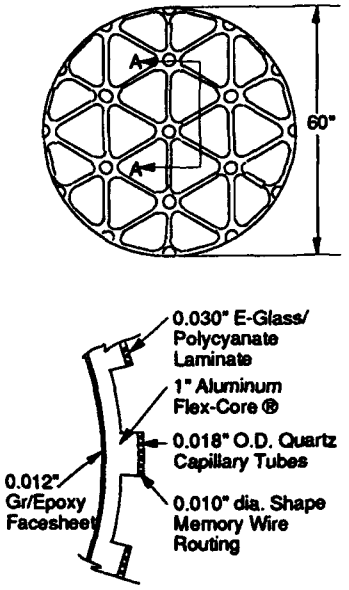

Figure 6 Adaptive Antenna Fabrication Approach

6.0 SUMMARY

Development of adaptive composite structural components using integrated or embedded actuator elements is a relatively new technology area. Prior approaches for deformation and control of surfaces has been limited to other types of actuation such as externally attached ferroelectric devices, voice coil actuators, stepper motors, hydraulic actuators, etc. This paper presents an approach which utilizes shape memory alloy actuator elements embedded in the facesheet(s) of a sandwich panel structure to minimize system weight and complexity, while maximizing thermal transfer to the environment for optimized bandwidth response. This approach eliminates internal lever arms, gears and drives, torsion rods, hydraulics, etc. and minimizes electrical, hydraulic and/or mechanical interconnects over baseline counterpart applications. System performance payoffs are dependent on a specific application, but in many cases this type of approach provides enabling

technology for consideration of first generation adaptive shape-controlled structures.

7.0 REFERENCES

1. J.S. Cory and J. L. McNichols, "Non-Equilibrium Thermostatics", J. Applied Phys., Vol. 58, No. 9, pp 3282-3294, 1985.

2. B.J. Maclean, "Shape Memory Material Actuator", Final Report PL-TR-91-3000, OL-AC Phillips Laboratory, 1990.

3. F.G. Shinskey, Process Control Systems, McGraw Hill, NY, 1988. ISBN 0-07-056903-7.

RECENT DEVELOPMENTS IN PIEZOELECTRIC AND ELECTROSTRICTIVE SENSORS AND ACTUATORS FOR SMART STRUCTURES

L. Eric Cross
Evan Pugh Professor of Electrical Engineering
Materials Research Laboratory
The Pennsylvania State University
University Park, PA 16802-4800 USA

ABSTRACT

Piezoelectricity will be defined phenomenologically and discussed pictorially to underscore the distinction between single crystal piezoelectrics and the poled ceramics which form the basis for most practical sensor and actuator systems. The classical Lead zirconate: lead titanate (PZT) family is the most widely used. Recent advances in the understanding of the conventional morphotropic phase boundary (MPB) compositions will be discussed with particular emphasis upon the nature and the control of fatigue at high strain levels. Phase switching compositions in the lead zirconate stannate titanate PZSnT system exhibit very high switching volume strain, shape memory and controlled induced piezoelectric response.

Electrostrictors in the lead magnesium niobate: lead titanate and lead lanthanum zirconate titanate (PMN:PT and PLZT) families form most interesting spin glass states at lower temperature in which precise reproducible elastic strain may be induced by electric field. In PMN:PT the strain is free from aging and other domain related problems, the thermal expansion is very low and these materials are ideal for very precise actuation. Polarization biased electrostrictors have exceedingly high induced piezoelectric d_{33}, d_{31} and d_h coefficients and can be used as agile transducers in which both the magnitude and phase of the response is under DC field control. Both spin glass and phase switching systems can be tuned in composition to optimize performance at 100°K and provide low power "dial-a-displacement" capability.

Recent advances in the fabrication of highly perfect thin films of PZT type compositions on silicon, by both vapour and liquid phase techniques provides a new high force electromechanical power source for microelectromechanical (MEMS) systems. The current status of the evaluation of electromechanical response in PZT, PMN:PT and PbSnZT thin films on silicon will be briefly reviewed and possible applications in MEMS systems discussed.

1.0 PIEZOELECTRIC CERAMICS

1.1 Phenomenological and Pictorial Descriptions of Piezoelectricity in Crystals

The phenomenological master equation which describes the deformations of an insulating crystal subject to both elastic and electric stress takes the form

$$x_{ij} = s_{ijkl} X_{kl} + d_{mij} E_m + M_{mnij} E_m E_n \quad (1.1)$$

where

x_{ij}	are the components of elastic strain
X_{ij}	the stress components
s_{ijkl}	the elastic compliance tensor
$E_m E_n$	are components of electric field
d_{mij}	the piezoelectric tensor components
M_{mnij}	the electrostriction tensor in field notation

and the Einstein summation convention is assumed.

For crystals in which some components of the d_{mij} tensor are non zero, when $X_{kl} = 0$ the elastic strain is given by

$$x_{ij} = d_{mij} E_m \quad (1.2)$$

which is the equation for the converse piezoelectric effects, relating induced strain directly to the first power of the field, i.e. x_{ij} changes sign with E_m.

In the thermodynamically equivalent direct effect

$$P_m = d_{mij} X_{ij} \qquad (1.3)$$

Clearly 1.2 describes the actuating function of a piezoelectric, changing shape under electric field control Equation 1.3 the sensing function, a change in polarization under stress charges the capacitance of the sensing crystal giving a voltage proportional to the stress applied.

If the d_{mij} constants are zero due to symmetry as for example in a centric crystal, the residual effect is electrostrictive and at zero stress

$$x_{ij} = M_{mnij} E_m E_n .$$

Now the strain is a quadratic function of the applied field.

The thermodynamically converse effect is now given by

$$\eta_{mn} = M_{mnij} X_{ij}$$

i.e. the elastic stress dependence of the dielectric susceptibility.

Pictorially, the piezoelectric effect is illustrated by the two dimensional sketches in fig. 1.1 which models a polar crystal of the perovskite Lead titanate in its single domain ferroelectric form. To simplify the description it is assumed that the polarization resides in the Ti^{4+} ion as in $BaTiO_3$ and the lead ion displacements are neglected. In the base state, the titanium ion is displaced along the 3 directions a distance corresponding to the spontaneous polarization P_3 and the resulting symmetry is tetragonal 4mm.

If a tensile stress σ_3 is now applied in the X_3 direction(fig. 1.1b), the upper and lower oxygen ions pull out the equatorial ions squash in forcing the Ti^{4+} farther away from the cell center and generating an enhancement of P_s by ΔP. Since the displacement are very small $\Delta P \alpha \sigma_3$ and the constant of proportionality d_{33} is positive, i.e. a positive (tensile stress) gives a positive change in ΔP.

For a transverse tensile stress σ_1 however (fig. 1.1c) the equatorial oxygens are pulled out, the Ti^{4+} brought back more towards the center of the cell, giving a negative increment ΔP_3 so that

$$\Delta P_3 = d_{31} \sigma_1$$

and d_{31} must be a negative quality.

Similarly a shear stress σ_5 (σ_{31}) leads to a canting of the Ti^{4+} and a displacement direction normal to P_3 i.e. a ΔP_1 so that fig. 7.1d.

$$\Delta P_1 = d_{15} \tau_5$$

For the point group 4mm clearly the action of the 4 fold axis makes 2 equivalent to 1 so that

$$d_{31} = d_{32} \qquad \text{and} \qquad d_{15} = d_{24}$$

and the complete piezoelectric tensor takes the form

$$\begin{matrix} 0 & 0 & 0 & 0 & d_{15} & 0 \\ 0 & 0 & 0 & d_{15} & 0 & 0 \\ d_{31} & d_{31} & d_{33} & 0 & 0 & 0 \end{matrix}$$

PIEZOELECTRIC COEFFICIENTS

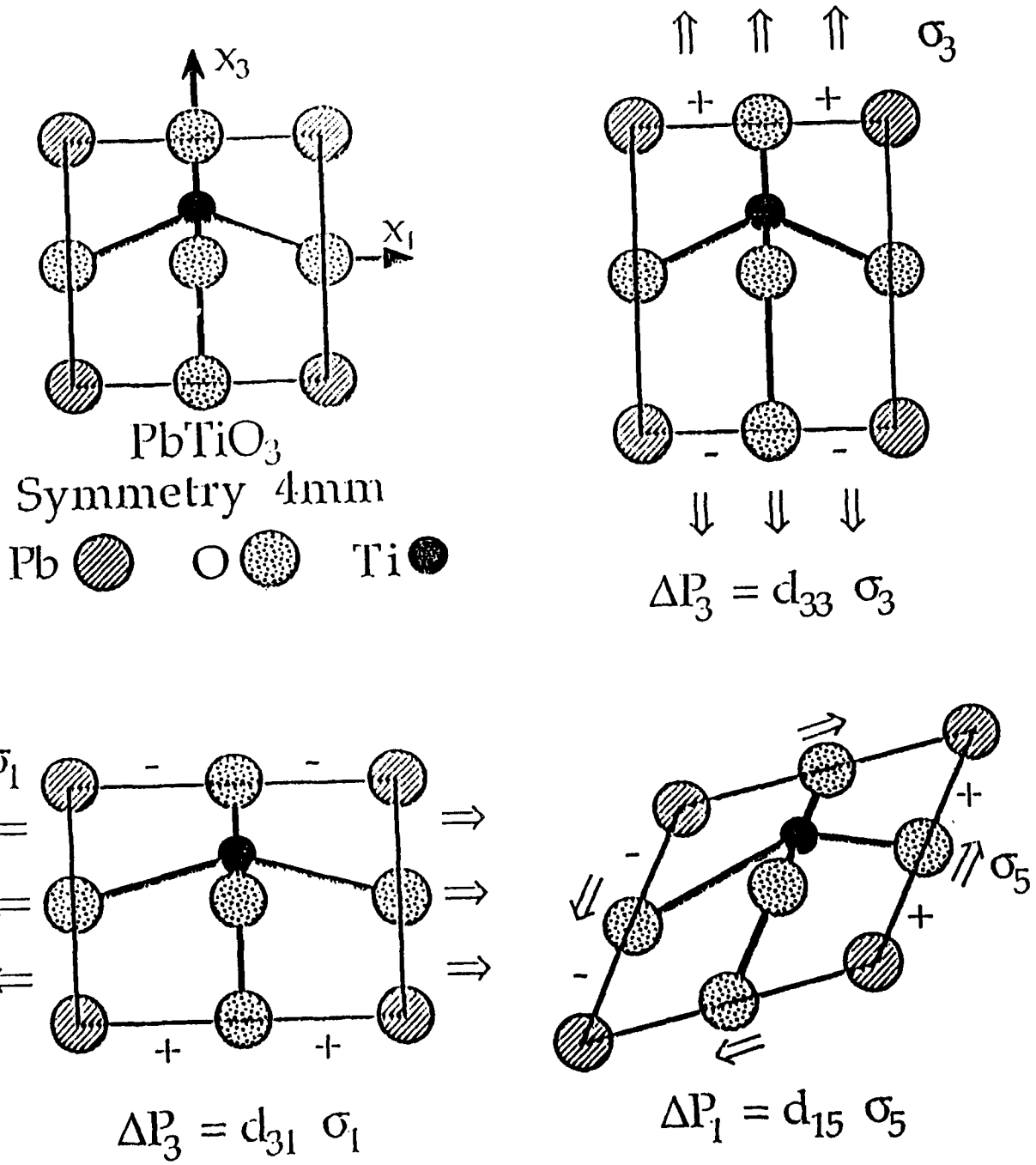

Fig. 1.1 Graphic illustration of the piezoelectric effects in a single domain single crystal of Lead titanate $PbTiO_3$.

1.2 Piezoelectricity in Ceramics

In a randomly axed polycrystal ceramic, even if the grains are polar or ferroelectric as in fig. 1.2 under normal circumstance the random orientation will cancel out any anisotropy engendering a macroscopic center of symmetry which forbids piezoelectricity. For the ferroelectric ceramic however a new anisotropy can be induced since the domain polar vectors can be switched under realizable field. Thus the poling operation which develops a high remanent polarization P_R in the ceramic is essential to destroy the macro center of symmetry taking the material into the texture symmetry group ∞ m. Theoretically it is quite straightforward to derive the possible P_R which may be induced in a ferroelectric ceramic if all domains of a given type may switch under the poling field. In a ferroelectric with only 2 antipolar domain states, only 180° switching would be possible and $\overline{P}_{Rmax} = 0.25\,P_S$. In a tetragonal ferroelectric perovskite there are 6 axial orientation for the domains and $\overline{P}_{Rmax} = .83\,P_S$, and for the rhombohedral case with 8 body diagonal orientations $\overline{P}_{Rmax} = 0.87\,P_S$. Unfortunately the ability to pole in practical ceramics is more restricted, so that a high count of available orientation states becomes essential. This is illustrated for $BaTiO_3$ at room temperature in fig. 1.3 In the single domain single crystal $P_s = 26\ \mu c/cm^2$ (fig. 1.3a). Even in a very large grain ceramic $P_{r\,max} \simeq 8\ \mu c/cm^2$, fig. 1.3b and in a practical fine (1 μ meter grain) ceramic P_r almost vanishes (fig. 1.3c).

1.3 Lead Zirconate Titanate Piezoceramics

The uniquely advantageous feature of the Lead zirconate Lead titanate ferroelectric (phase diagram fig. 1.4) is the almost vertical phase boundary near the 50:50 Zr/Ti composition, the so called morphotropic phase boundary which separates a tetragonal and a rhombohedral ferroelectric phases. All ferroelectric:ferroelectric phase transitions are first order so that the boundary encompasses a finite two phase region where the 6 domain states of the tetragonal variant coexist with the 8 domain states of the rhombohedral. The advantage in terms of polability for ceramics near this composition is compared to other perovskite possibilities in fig. 1.5 showing the clear superiority of the PZT.

The maximum polability for compositions near the MPB is shown clearly in fig. 1.6, and the consequent advantage in piezoelectric constants in fig. 1.7, both taken from the book by Jaffe Cooke and Jaffe.[1]

1.3.1 *Phenomenology of Piezoelectricity in PZTs*

It is clear from the very high dielectric permittivity the Curie point T_c that the instability at the paraelectric:ferroelectric phase transition contributes an intrinsic compliance in the dielectric property which can be manipulated to great practical advantage. For $BaTiO_3$, it is easy to trace this enhanced compliance as excellent single crystals can be grown and by simple poling procedures converted into single domain states. Thus the properties of a single domain can be measured at any temperature or stress of interest and a full Landau:Ginsburg:Devonshire phenomenology developed which will minimic the intrinsic properties of $BaTiO_3$ domains under any set of electric/elastic boundary conditions.[2,3,4]

In the lead zirconate titanate solid solution system however, the situation is significantly more complex. Different composition across the phase field exhibit antiferroelectric, oxygen octahedral tilted, and simple proper ferroelectric phases. An even more important constraint is that in spite of almost 30 years of continuous effort there are still no reputable single crystals available with compositions near to the critical 50/50 Zr/Ti ratio of the MPB and thus no direct measurements of single domain properties. Only compositions close to pure $PbZrO_3$ and pure $PbTiO_3$ have been grown with adequate quality and for other compositions it is necessary to use indirect methods to deduce the thermodynamic constants.

Over some 10 years the ferroelectric group at Penn State has dedicated a continuing effort to formulating an adequate phenomenology. Faculty and students involved have included B. Gadger, A. Amin, H. McKinstry, T. Halemane, M. Haun, G. Rossetti and L. E. Cross and their work is documented in a sequence of papers.[5,6,7,8,9,10,11,12,13] The papers 9–13 provide an excellent summary of the pure PZT work.

In developing the "master equation" for the free energy in terms of the extensive variables, it is necessary to start with a two sub lattice model to encompass the antiferroelectric states, however, since these are confined to compositions very close to Lead zirconate it is advantageous to use linear combination of the sub lattice polarization P_A and P_B in the form

$$P = P_A + P_B \qquad (1.4)$$

$$p = P_A - P_B \qquad (1.5)$$

Thus when $P_A = +P_B$ $P \neq 0$ and represents the effective ferroelectric polarization, and when $P_A = -P_B$ $p \neq 0$ and represents the magnitude of the antipolarization in the antiferroelectric phase. Polarization and antipolarization have the axial components $P_1P_2P_3$ and $p_1p_2p_3$ respectively. The oxygen octahedra have tilt angle θ with components about the axial direction $\theta_1\theta_2\theta_3$. Elastic stress and strain are designated X_{ij} x_{ij}. The full family of coupling variables are delineated in table 7.1 and the resulting equation for the Free Energy in 1.6.

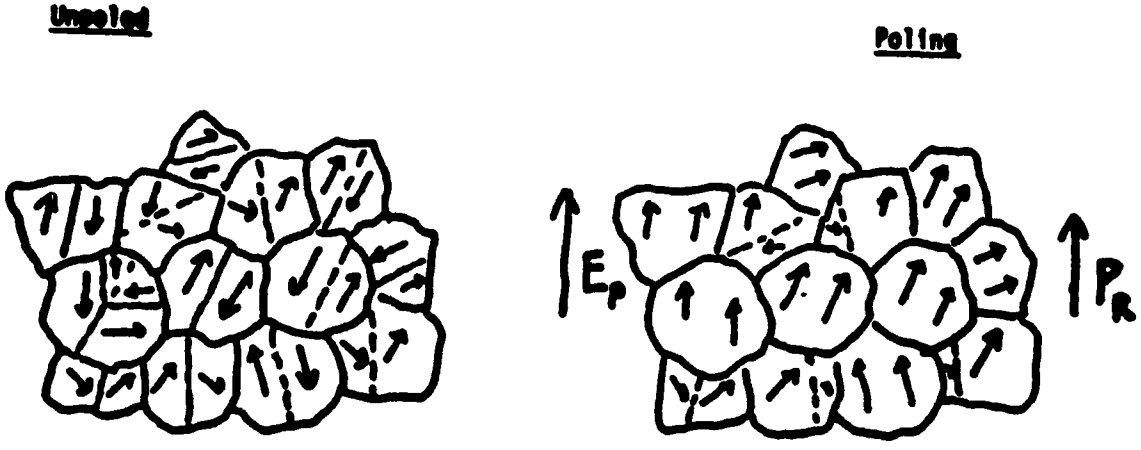

Fig. 1.2 Two dimension schematic of the polarization vectors in unpoled and in poled PZT. In (a) the symmetry is $\infty\infty$ which is centrics and forbids piezoelectricity. In (b) the symmetry is ∞mm which is non centric (polar) and permits piezoelectricity.

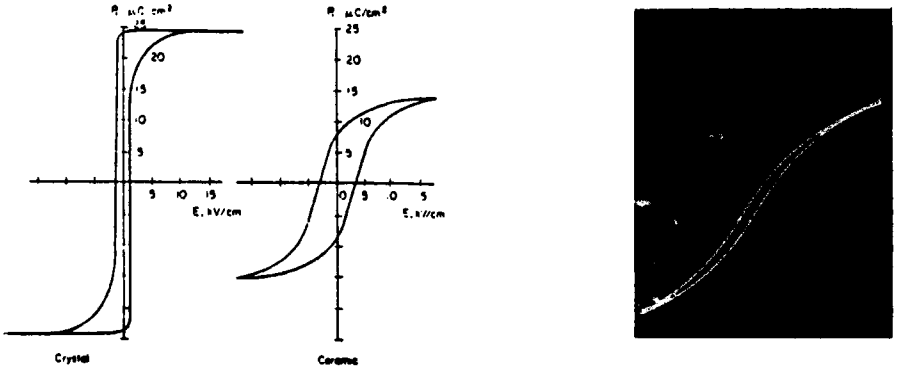

Fig. 1.3 Contrasting polarization hysteresis in (a) single crystal ; (b) ceramic polycrystal ; (c) fine grain ceramic $BaTiO_3$ samples.

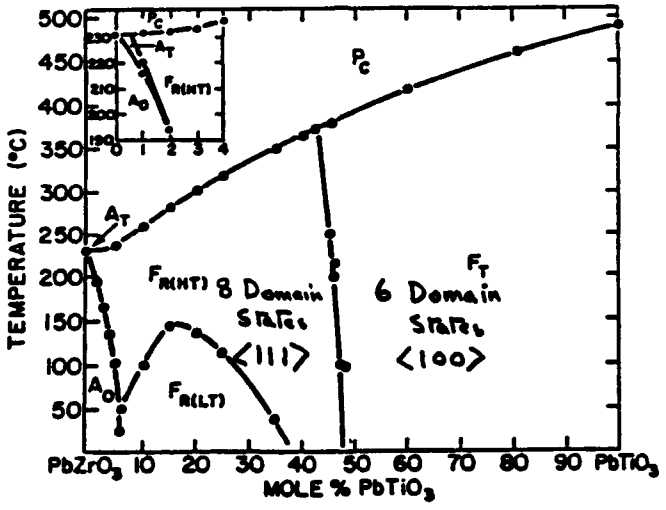

Fig. 1.4. Phase diagram of the Lead zirconate:lead titanate solid solution system, highlighting the important morphotropic phase boundary (MPB).

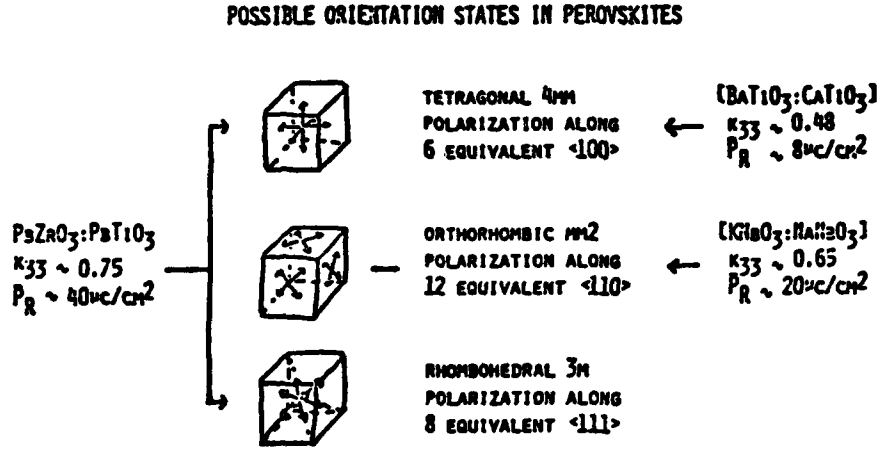

Fig. 1.5 Indicating from examples in different perovskite ceramic compositions the importance of number of equivalent domain states in realizing poling and high piezoelectric activity.

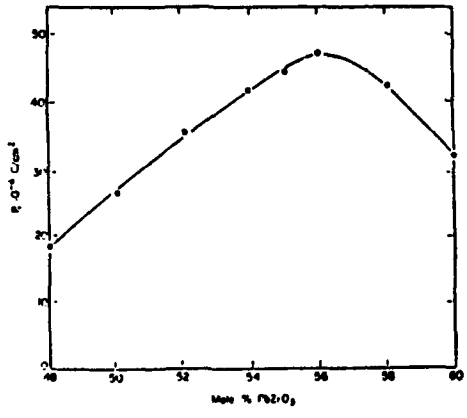

Fig. 1.6 Remanent polization in PZT ceramics of comparable grain size as a function of Zr:Ti ratio.

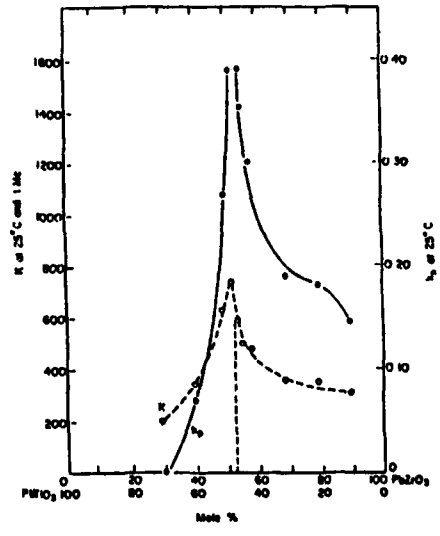

Fig. 1.7 Dielectric and piezoelectric response in poled PZT as a function of Zr:Ti ratio.

TABLE 1.1

Coefficients of the PZT Energy Function

α_i, α_{ij}, α_{ijk}	ferroelectric dielectric stiffness at constant stress
σ_i, σ_{ij}, σ_{ijk}	antiferroelectric dielectric stiffness at constant stress
μ_{ij}	coupling between the ferroelectric and antiferroelectric polarizations
β_i, β_{ij}	octahedral torsion coefficients
γ_{ij}	coupling between the ferroelectric polarization and tilt angle
s_{ij}	elastic compliances at constant polarization
Q_{ij}	electrostrictive coupling between the ferroelectric polarization and stress
Z_{ij}	electrostrictive coupling between the antiferroelectric polarization and stress
R_{ij}	rotostrictive coupling between the tilt angle and stress

$$
\begin{aligned}
\Delta G = {} & \alpha_1[P_1^2 + P_2^2 + P_3^2] + \alpha_{11}[P_1^4 + P_2^4 + P_3^4] \\
& + \alpha_{12}[P_1^2P_2^2 + P_2^2P_3^2 + P_3^2P_1^2] + \alpha_{111}[P_1^6 + P_2^6 + P_3^6] \\
& + \alpha_{112}[P_1^4(P_2^2 + P_3^2) + P_2^4(P_1^2 + P_3^2) + P_3^4(P_1^2 + P_2^2)] \\
& + \alpha_{123}P_1^2P_2^2P_3^2 + \sigma_1[p_1^2 + p_2^2 + p_3^2] + \sigma_{11}[p_1^4 + p_2^4 + p_3^4] \\
& + \sigma_{12}[p_1^2p_2^2 + p_2^2p_3^2 + p_3^2p_1^2] + \sigma_{111}[p_1^6 + p_2^6 + p_3^6] \\
& + \sigma_{112}[p_1^4(p_2^2 + p_3^2) + p_2^4(p_1^2 + p_3^2) + p_3^4(p_1^2 + p_2^2)] \\
& + \sigma_{123}p_1^2p_2^2p_3^2 + \mu_{11}[P_1^2p_1^2 + P_2^2p_2^2 + P_3^2p_3^2] \\
& + \mu_{12}[P_1^2(p_2^2 + p_3^2) + P_2^2(p_1^2 + p_3^2) + P_3^2(p_1^2 + p_2^2)] \\
& + \mu_{44}[P_1P_2p_1p + P_2P_3p_2p_3 + P_3P_1p_3p_1] + \beta_1[\theta_1^2 + \theta_2^2 + \theta_3^2] \\
& + \beta_{11}[\theta_1^4 + \theta_2^4 + \theta_3^4] + \gamma_{11}[P_1^2\theta_1^2 + P_2^2\theta_2^2 + P_3^2\theta_3^2] \\
& + \gamma_{12}[P_1^2(\theta_1^2 + \theta_2^2) + P_2^2(\theta_1^2 + \theta_3^2) + P_3^2(\theta_1^2 + \theta_2^2)] \\
& + \gamma_{44}[P_1P_2\theta_1\theta_2 + P_2P_3\theta_2\theta_3 + P_3P_1\theta_3\theta_1] \\
& - \tfrac{1}{2}S_{11}[X_1^2 + X_2^2 + X_3^2] - S_{12}[X_1X_2 + X_2X_3 + X_3X_1] \\
& - \tfrac{1}{2}S_{44}[X_4^2 + X_5^2 + X_6^2] - Q_{11}[X_1P_1^2 + X_2P_2^2 + X_3P_3^2] \\
& - Q_{12}[X_1(P_2^2 + P_3^2) + X_2(P_1^2 + P_3^2) + X_3(P_1^2 + P_2^2)] \\
& - Q_{44}[X_4P_2P_3 + X_5P_1P_3 + X_6P_1P_2] - Z_{11}[X_1^2p_1 + X_2^2p_2 + X_3^2p_3] \\
& - Z_{12}[X_1(p_2^2 + p_3^2) + X_2(p_1^2 + p_3^2) + X_3(p_1^2 + p_2^2)] \\
& - Z_{44}[X_4p_2p_3 + X_5p_1p_3 + X_6p_1p_2] - R_{11}[X_1\theta_1^2 + X_2\theta_2^2 + X_3\theta_3^2] \\
& - R_{12}[X_1(\theta_2^2 + \theta_3^2) + X_2(\theta_1^2 + \theta_3^2) + X_3(\theta_1^2 + \theta_2^2)] \\
& - R_{44}[X_4\theta_2\theta_3 + X_5\theta_1\theta_3 + X_6\theta_1\theta_2]
\end{aligned}
\tag{1.6}
$$

1.3.2 *Delineation of the Phenomenological Constants*

The initial basic assumption applied was that all temperature dependence was carried in the lowest order stiffness constants α_1 and τ_1 which were made linear functions of temperature. The Curie temperature Tc was taken from the phase diagram and the Curie constant C used measured values taken from high density ceramic samples. The temperature dependence of P_s required to model the higher order α_{ij}, polarization was determined by assuming quadratic electrostriction and measuring the X-ray spontaneous strain in carefully prepared chemically coprecipated powders. The MPB imposes a major constraint upon the α's since it requires that near the 50/50 Zr/Ti composition the tetragonal and rhombohedral phases have similar energies across a very wide temperature range.

Full details of the procedures, and of the most recent families of constants can be found in references 9-13. A tabulation of the room temperature values is given in table 1.2.

1.3.3 *Intrinsic Properties of PZT*

Plots of the free energy vs compositions, using the fitted parameters are given in fig. 1.8 for temperatures of 25°C, 75°C and 125°C. The resulting phase diagram deduced from the crossing points of the phase stability lines for the whole composition temperature field is given in fig. 1.9 and is shown to be in good agreement with the accepted phase diagram.

Indications of the capability to delineate single domain properties are given in fig. 1.10 for the susceptibility as a function of temperature in the PZT 60:40, and in the susceptibility as a function of composition at room temperature, given in fig. 1.11. Examples of the full family of elasto-dielectric properties which can be deduced are given in the original references.

1.4 Extrinsic Contributions to Response in PZT Type Piezoceramics

Even in the best poled PZT ceramic, because of the random orientation and the internal stresses generated by switching the large spontaneous strains during poling, the sample does not come to an ensemble of single domain grains. Thus in considering the polarizability of the ceramic in its ferroelectric phases, we must consider the extrinsic contributions due to changes in the polar domain structure and phase makeup brought about by the field. The type of changes occurring which could contribute to the polarizability are shown schematically in two dimensions in fig. 1.12.

For the piezoelectric response, only extrinsic actions which are shape changing will contribute so that simple 180° domain wall motion does not contribute, and is in fact deleterious to piezo response since it contributes polarization without any shape changes e.g.

$x_3 = Q_{11} P_3^2$ and $\pm P_3$ give rise to identical strains x_3 and x_1

$x_1 = Q_{12} P_3^2$

Non 180° wall motion, that is motion of 90° walls in the tetragonal phase, and motion of 71° and 110° walls in the rhombohedral phases will give rise to shape change, however, the nature of the shape change will depend on the relation between

TABLE 1.2

Values of the coefficients used in the energy function (eq. 7.3) at 25°C, as a function of Zr:Ti ratio.

	Mole Fraction $PbTiO_3$ in PZT										
	0.0	0.1	0.2	0.3	0.4	0.5	0.6	0.7	0.8	0.9	1.0
T_C(°C)	231.5	256.5	300.6	334.4	364.3	392.6	418.4	440.2	459.1	477.1	492.1
C(10^5 °C)	2.027	2.050	2.083	2.153	2.424	4.247	2.664	1.881	1.642	1.547	1.500
Q_{11} (10^{-2} m^4/C^2)	4.620	5.080	5.574	6.175	7.260	9.660	8.116	7.587	8.142	8.504	8.900
Q_{12} (10^{-2} m^4/C^2)	−1.391	−1.540	−1.720	−1.997	−2.708	−4.600	−2.950	−2.480	−2.446	−2.507	−2.600
Q_{44} (10^{-2} m^4/C^2)	4.664	4.900	5.165	5.522	6.293	8.190	6.710	6.356	6.417	6.569	6.750
a_1 (10^5 m/F) at 25 °C	−4.582	−6.376	−7.470	−8.116	−7.904	−4.887	−8.340	−12.47	−14.84	−16.17	−17.08
a_{11} (10^7 m^5/C^2F)	52.35	41.25	31.29	22.30	13.62	4.764	5.614	0.6458	−3.050	−5.845	−7.255
a_{12} (10^8 m^5/C^2F)	−16.71	−4.222	−0.0345	1.688	2.391	1.735	3.233	5.109	6.320	7.063	7.500
ζ (10^8 m^5/C^2F)	−34.42	−0.2897	9.284	11.75	11.26	6.634	10.78	15.52	18.05	19.44	20.32
a_{111} (10^8 m^9/C^4F)	5.932	5.068	4.288	3.560	2.713	1.336	1.859	2.348	2.475	2.518	2.606
a_{112} (10^8 m^9/C^4F)	311.2	34.45	18.14	15.27	12.13	6.128	8.503	10.25	9.684	8.099	6.100
a_{123} (10^8 m^9/C^4F)	−104.1	−8.797	−7.545	−7.052	−5.690	−2.894	−4.063	−5.003	−4.901	−4.359	−3.600
ζ (10^8 m^9/C^4F)	84.41	13.39	4.627	3.176	2.402	1.183	1.596	1.851	1.652	1.256	0.7818

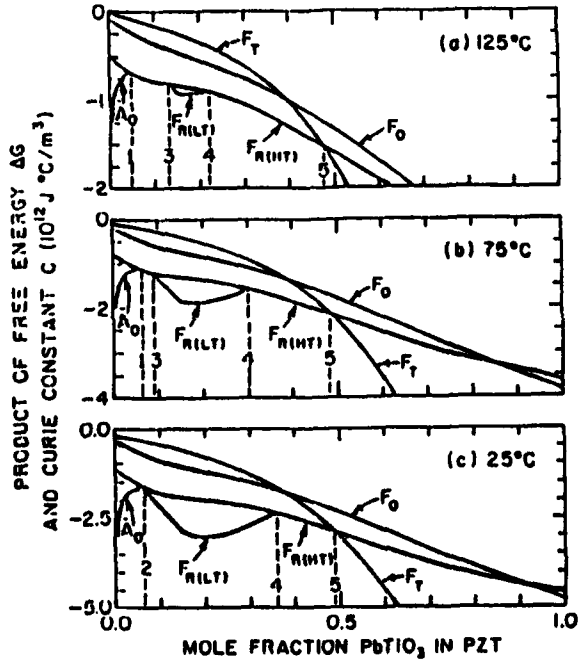

Fig. 1.8 Calculated Free Energy profiles for each realizable phase as a function of Zr:Ti ratio at (a) 25°C, (b) 75°C, (c) 125°C.

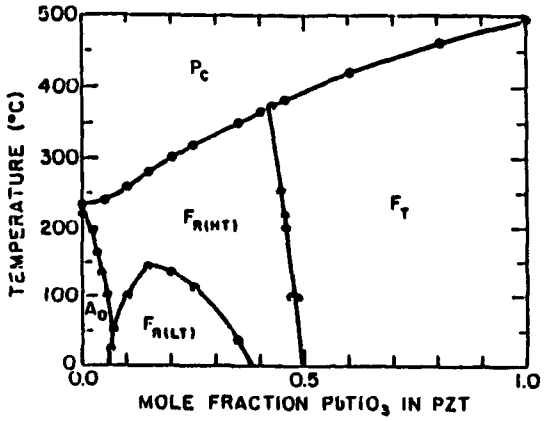

Fig. 1.9 Comparison of calculated and measured phase diagram for PZT.

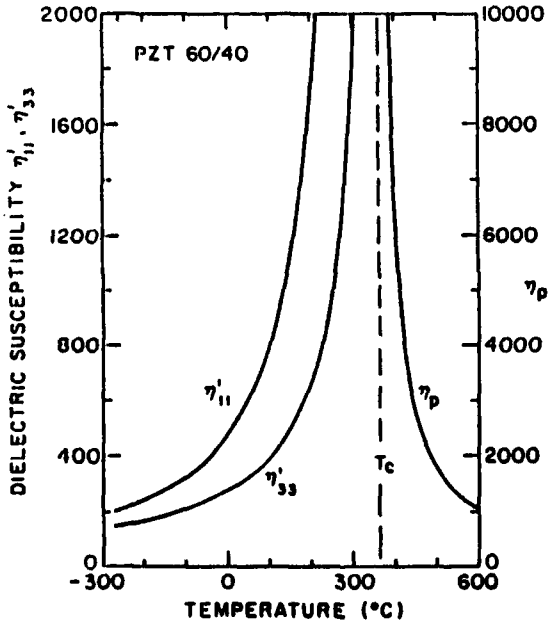

Fig. 1.10 Single domain dielectric susceptibility calculated for a PZT 60:40 composition.

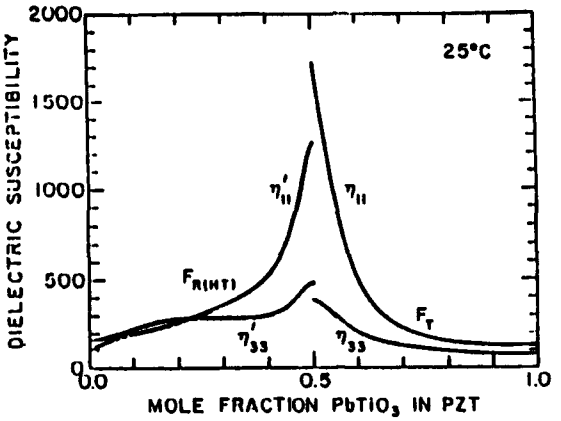

Fig. 1.11 Dielectric susceptibility of single domain states as a function of Zr:Ti ratio.

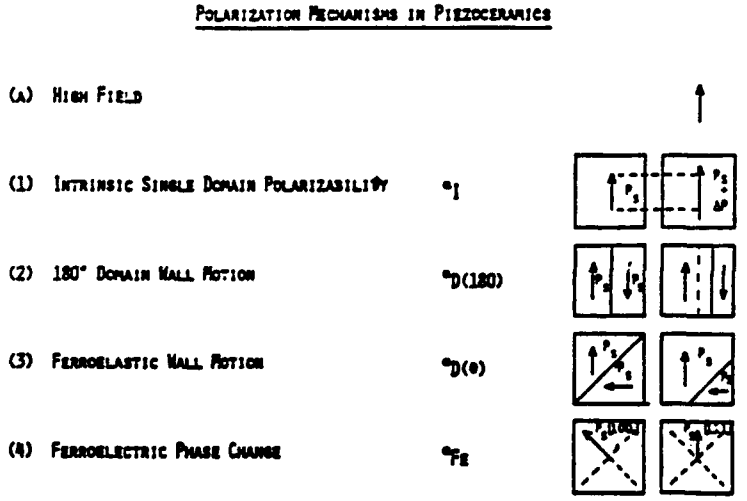

Fig. 1.12 Possible mechanisms which can contribute to the dielectric polarizability in a ferroelectric PZT at the MPB composition.

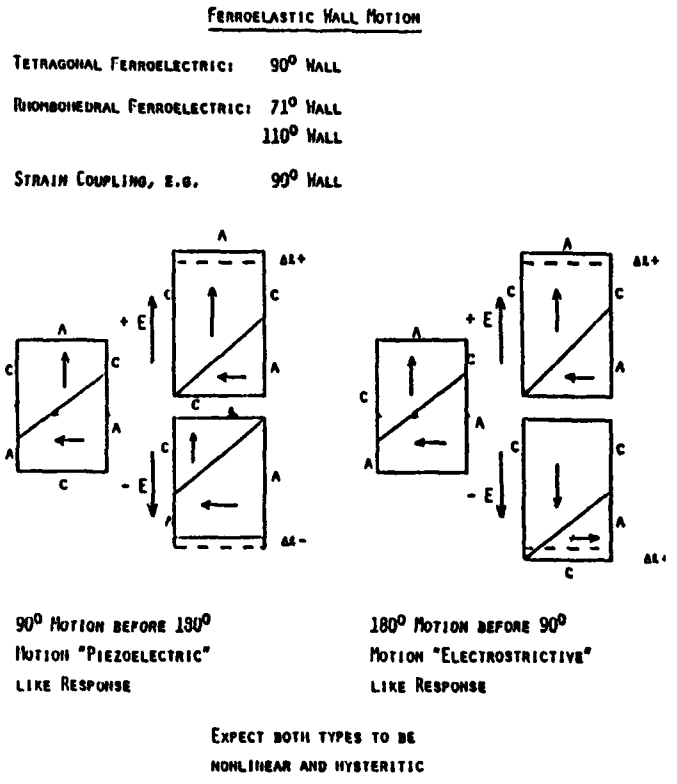

Fig. 1.13 Shape changing effects of 180° pure ferroelectric and ferroelectric:ferroelastic domain wall motion, depicted in schematic two dimensional models.

ferroelectric: ferroelastic wall motion and pure ferroelectric wall motion. From figure 1.13, if 90° motion occurs before 180° motion the effective shape change reverses sign with the field, if however 180° motion precedes 90° wall motion the shape change does not reverse sign with the field and is effectively electrostrictive. A similar situation exists for phase boundary motion (fig. 1.14) where again the relation to pure ferroelectric 180° wall switching is quite critical.

It must be stressed that in all these considerations it is that component of wall motion which is reversible with the field and which persists down to almost zero field which is of importance.

1.4.1 *Control of Extrinsic Contributions to Response*

During the course of many years of empirical development a wide range of low level additives (0-5 mole%) have been found to have a marked influence upon dielectric and piezoelectric properties in PZT compositions. In general, the aliovalent oxides fall into two distinct groups. Electron donor additions where the charge on the cation is larger than that which it replaces in the PZT structure and electron acceptor additives where the charge on the cation is smaller than that of the ion which it replaces (table 7)

The donor additions enhance both dielectric and piezoelectric response at room temperature and under high fields show symmetrical unbiased hysteresis loops with good "squareness" and lower coercivity.[14,15] The acceptor additives in general reduce both dielectric and piezoelectric responses, they give rise to highly asymmetric hysteresis response, larger coercivity and higher electrical and mechanical Q. That the effects of the dopants are mostly upon the extrinsic components of response is expected from their marked influence on the hysteresis and is confirmed by the very low temperature behaviours (fig. 1.15). For the Navy type I to V the compositions range from a strongly donor doping (type V) to a strongly acceptor doping in type III but all are at the same Zr:Ti ratio. It may be noted that the very large difference in weak field permittivity ($\varepsilon \sim 3000 \rightarrow \varepsilon \sim 750$) is completely lost at liquid helium temperature where all extrinsic contributions are frozen out, and that the data agree quite well with the intrinsic permittivity calculated from the average of the single domain values deduced from the thermodynamic theory for that composition and temperature.

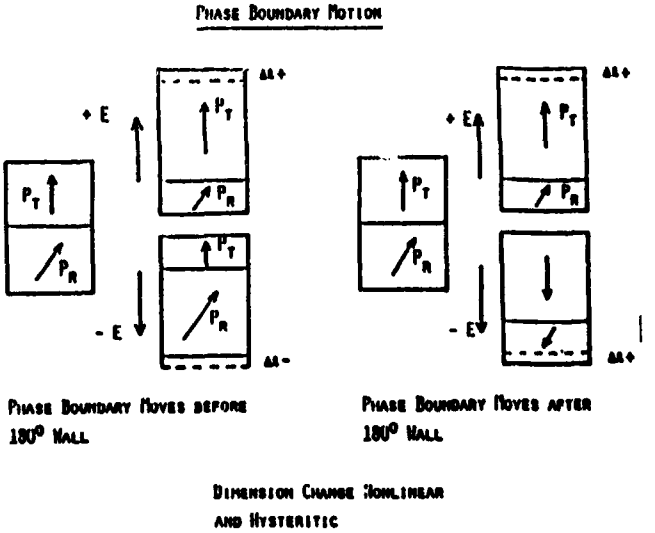

Fig. 1.14 Shape changing effects of 180° pure ferroelectric domain motion and of phase boundary motion in a PZT ferroelectric at a composition near the MPB.

LOWER LEVEL MODIFIERS (0 to 10 MOLE %)

'Donor' Additives	'Acceptor' Additives
Nb_2O_5 or $PbNb_2O_6$	Fe_2O_3
Ta_2O_5 or $PbTa_2O_6$	Al_2O_3
WO_3	Cr_2O_3
Bi_2O_3	MnO_2
Sb_2O_5	MgO
La_2O_3	NiO
Y_3O_6	

Other Low Level Additives:

Na_2O, K_2O, Ga_2O_3, In_2O_3, IrO_2, ThO_2

Fig. 1.15 Common 'dopants' used in 'soft' donor doped and 'hard' 'acceptor' doped PZT compositions.

In the acceptor doped compositions there are very good explanations of how the domain structure (not the wall) is stabilized.[16,17,18] In essence the charged acceptor associates with an oxygen vacancy to produce a slowly mobile defect dipole. The vacancy is the only mobile defect in the perovskite at room temperature and the defect dipole orients by vacancy migration in the dipole field associated with the domain. Thus over time the existing domain structure (poled or unpoled) is stabilized and the walls are "stiffened." Bias phenomena in both poled and unpoled ceramics can be logically explained as can some facets of the aging behaviour and the time dependence of mechanical Q.

For donor doped samples, there are only "hand waving" arguments as to how or why the domain walls should become more mobile and indeed it is not clear whether the effects are from domain walls, phase boundaries, or are defect induced. Much more work is needed to determine the physics of the softening in these materials.

A favorite pastime for empirical development has been the combination of PZTs with relaxor spin glass lead based compositions to produce improved "soft" high permittivity high coupling ceramics (fig. 1.16) and a vast range of compositions has been explored. In general the effect is to lower T_C, raise ε, raise k_t and k_p and d_{33}. The typical ranges of advantage are given in 7.16. Usually the compositions used follow closely along the MPB into these 3 component phase diagrams.

1.5 Electrostrive Actuators

The poled ferroelectric domain structure of the normal piezoelectric PZT provides very useful actuators with field induced strain of order $1 \sim 2.10^{-3}$ at field levels of 10kV/cm. For systems which require a fiducial zero strain position however, aging and deaging of the domain structure under high fields lead to uncomfortable changes of the zero field dimensions which are unacceptable in precise positioning applications.

For the electrostrictor (fig. 1.17) useful strain levels require very high levels of induced polarization i.e. high dielectric permittivity.

In the relaxor ferroelectric spin glass compositions like lead magnesium niobate (PMN), at temperatures above the freezing temperature large levels of polarization can be induced at realizable field levels and high quadratic levels of strain are possible (fig. 1.18). Reproducibility of the strain under cyclic E field is evident in fig. 1.19, and is compared to the "walk off" which

occurs in a PZT8 due to de-aging. Figure 1.20 show that the strain is truely quadratic when referenced to the polarization as would be expected in electrostrictors. It is interesting to note that the Q constants for PMN are essentially temperature independent over the range from 100 to -60°C (fig. 1.21). An unexpected bonus in the relaxors is that the steady accretion of polarization for temperatures below T Burns leads to an expansion term of the form

$$\Delta v \ \alpha(Q_{11} + 2Q_{12})P_{<111>}^2$$

which tends to compensate for the normal thermal contraction. Thus over a range of temperatures near 20°C it is possible to mate PMN:10%PT with ULE glass so that dimension can be controlled electrically but do not drift thermally.

For valence compensated additions the systems studied have included:

$Pb(III_{1/3}{}^{IIb}{}_{2/3})O_3:PbTiO_3:PbZrO_3$.
$Pb(Co_{1/3}{}^{IIb}{}_{2/3})O_3:PbTiO_3:PbZrO_3$.
$Pb(Mn_{1/3}{}^{IIb}{}_{2/3})O_3:PbTiO_3:PbZrO_3$.
$Pb(Cu_{1/3}{}^{IIb}{}_{2/3})O_3:PbTiO_3:PbZrO$.
$Pb(Mn_{1/3}{}^{Ta}{}_{2/3})O_3:PbTiO_3:PbZrO_3$.
$Pb(Zn_{1/3}{}^{IIb}{}_{2/3})O_3:PbTiO_3:PbZrO_3$.
$Pb(III_{1/3}{}^{Fe}{}_{1/3}{}^{IIb}{}_{1/3})O_3:PbTiO_3:PbZrO_3$.

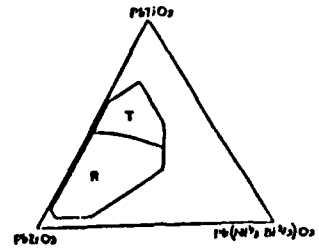

$Pb(Cu_{1/3}{}^{IIb}{}_{2/3})O_3:PbTiO_3$.
$Pb(Cd_{1/3}{}^{IIb}{}_{2/3})O_3:PbTiO_3$.
$Pb(Zn_{1/2}{}^{Te}{}_{1/2})O_3:PbTiO_3$.
$Pb(Mg_{1/2}{}^{Te}{}_{1/2})O_3:PbTiO_3$.

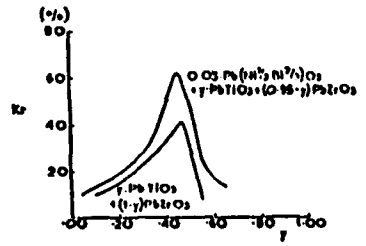

$Pb(Sb_{1/2}{}^{IIb}{}_{1/2})O_3:PbTiO_3:PbZrO_3$.
$Pb(Sn_{1/3}{}^{IIb}{}_{2/3})O_3:PbTiO_3:PbZrO_3$.
$:PbTiO_3$
$:PbZrO_3$
$Pb(IIg_{1/2}W_{1/2})O_3:PbTiO_3:PbZrO_3$.
$Pb(Mn_{1/3}Sb_{2/3})O_3:PbTiO_3:PbZrO_3$.
$Pb(Li_{1/4}{}^{IIb}{}_{3/4})O_3:PbTiO_3:PbZrO_3$.
$Pb(Sb_{1/2}{}^{IIb}{}_{1/2})O_3:PbTiO_3:PbZrO_3$.
$Pb(Fe_{1/2}Sb_{1/2})O_3:PbTiO_3:PbZrO_3$.
$Pb(In_{1/2}{}^{IIb}{}_{1/2})O_3:PbTiO_3:PbZrO_3$.
$Pb(In_{1/2}{}^{IIb}{}_{1/2})O_3:PbZrO_3:PbSnO_3:PbTiO_3$.

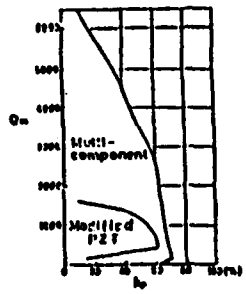

$(Ag_{0.5}Bi_{0.5})TiO_3:PbZrO_3:PbTiO_3$.
$(Ag_{0.5}Bi_{0.5})ZrO_3:PbTiO_3:PbZrO_3$.

Fig. 1.16 Examples of systems using a relaxor additives to PZT.

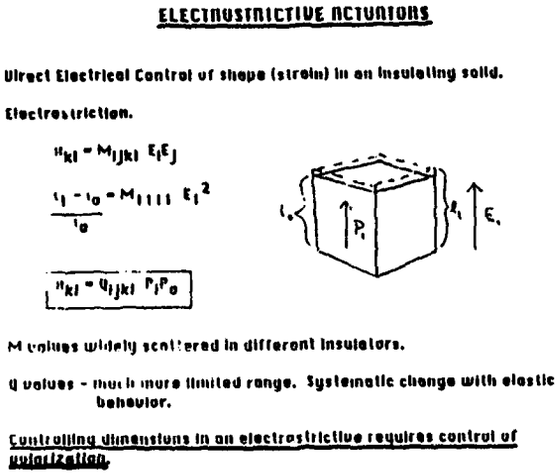

Fig. 1.17 Actuation using the direct electrostrictive effect in a very high K ferroelectric type perovskite.

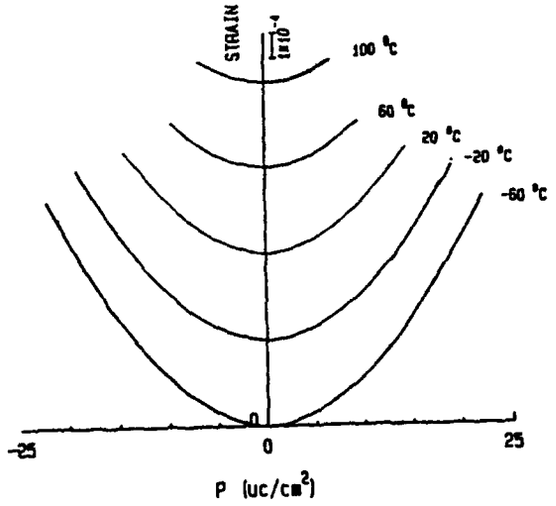

Fig. 1.18 Typical polarization:strain curves in a PMN electrostriction actuator as a function of temperature.

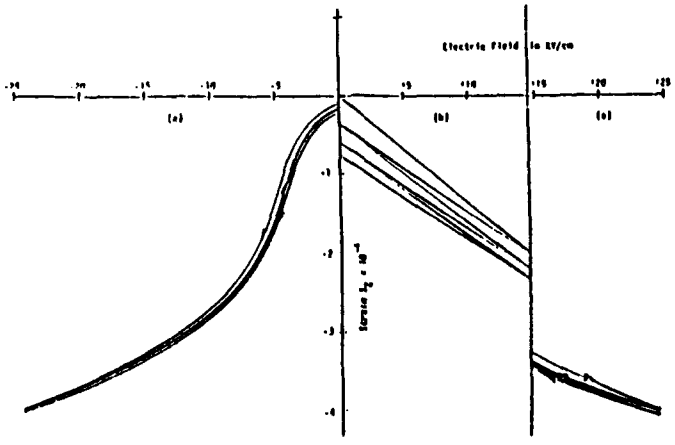

Fig. 1.19 Contrasting the non linear but repeatable strain response in a PMN:PT relaxor with the walk-off in zero field strain which occurs in a PZT 8 formulation.

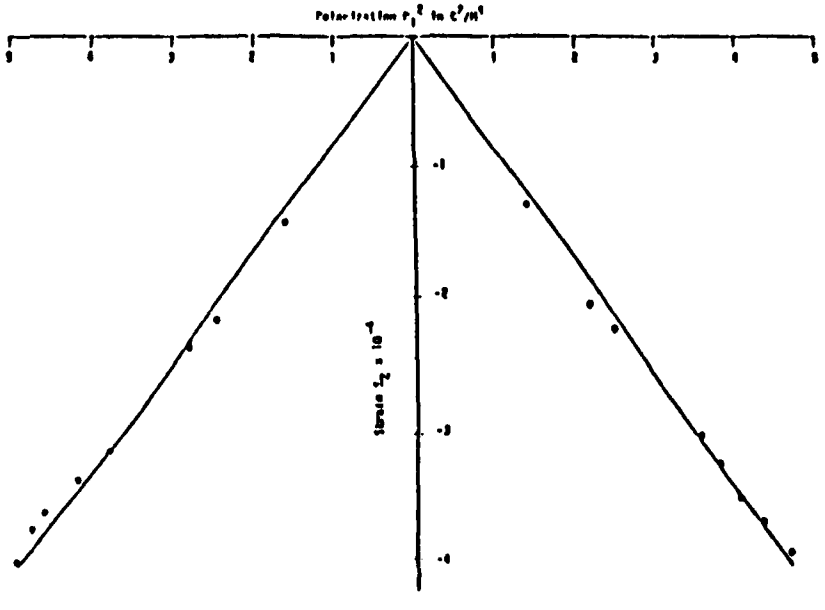

Fig. 1.20 Quadratic electrostrictive response in a PMN:10%PT actuator composition.

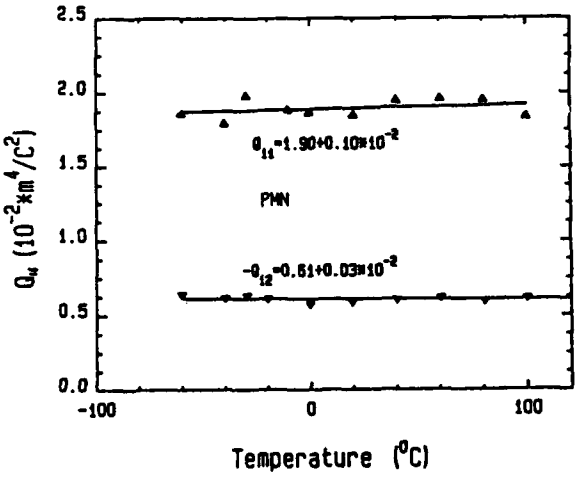

Fig. 1.21 Electrostriction constants Q_{11} and Q_{12} vs temperature in PMN:10% PT.

2.0 PHASE SWITCHING SYSTEMS

2.1 Introduction

Two types of phase switching have been extensively studied. In the PLZT family of relaxor ferroelectrics, compositions can be found which switch from a macroscopically cubic nano-polar state into a strongly polar rhombohedral state. The onset of polarization is accompanied by longitudinal strains up to 0.5% with the highest strains occuring for compositions close to the Morphotropic phase boundary between rhombohedral and tetragonal symmetry macro states.

For certain compositions in the lead lanthanum zirconate stannate titanate family of ceramics compositions can be chosen which are in an antiferroelectric state at room temperature but are very close in free energy to a strongly polar ferroelectric state so that antiferroelectric to ferroelectric switching can be achieved under high electric fields. The switching is accompanied by a major volume expansion in the lattice and the resulting strain can be controllled by controlling the volume fraction switched into the polar state by limiting the charge which flows.

2.2 Micro-Macrodomain Switching in Lead Lanthanum Zirconate Titanate (PLZT) Ceramics

The composition of PLZT explored in this study are identified in the phase diagram of figure 2.1. Composition are believed to conform to the formula $Pb_{1-3x/2}La_x(2r_yTi_2)O_3$, though they are batched with excess lead oxide to promote densification. Following convention the description is simplified to the form 100x/100y/100z so that for example $Pb_{0.88}La_{0.08}(2r_{0.65}Ti_{0.35})O_3$ is described as an 8/65/35 PLZT. For these studied the La_2O_3 was in the range 4-8 mole% and the Zr/Ti ratio was adjusted to keep the composition close to the morphotropic phase boundary between rhombohedral and tetragonal macro symmetries.

Compositions were prepared both by conventional ceramic processing and by uniaxial hot pressing to achieve a range of grain size and of pore structures in the ceramic. For studied of initial dielectric elastic and electrostrive response microstructure and density were not critical. However in fatigue behaviour, that is in the loss of properties on repeated

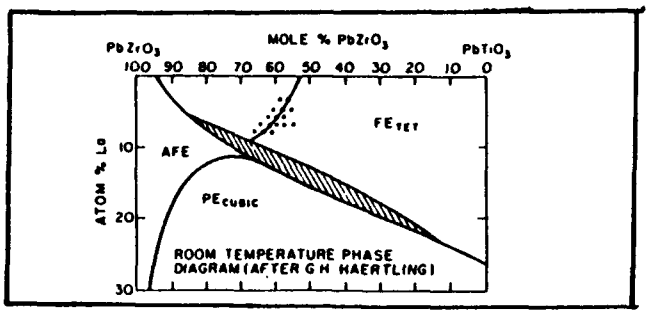

Fig. 2.1 Phase diagram of PLZT system (after Haertling and Land) with the marks at the selected compositions.

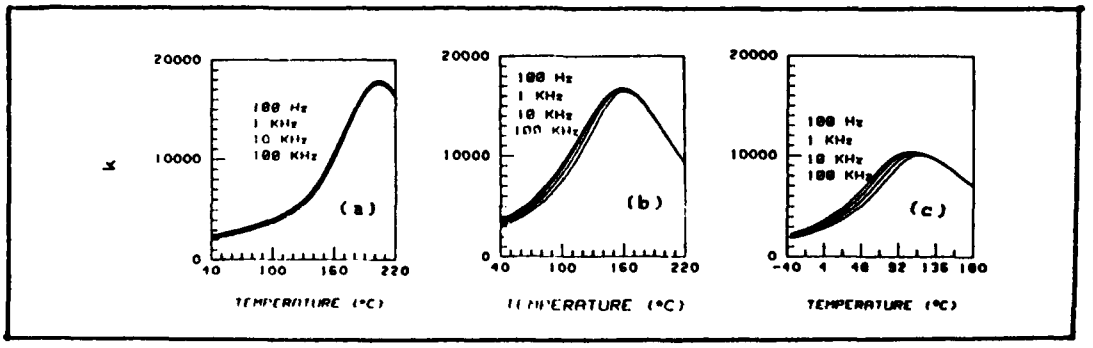

Fig. 2.2 Dielectric constant versus temperature for three MPB ceramic compositions: (a) 6/60/40, (b) 7/62.5/37.5 and (c) 8/65/35).

cycling these parameters were most important. Typical weak field dielectric response as function of temperature is shown in figure 2.2, demonstrating the expected increase in dispersion and relaxor ferroelectric behaviour with increasing La content. High field behaviour for all compositions is hysteretic, figure 2.3a and accompanying longitudinal strains are shown in 2.3b. Parameters of interest for the whole range of compositions are summarized in Table 2.1. Maximum strain achieved in this family was 0.54% and it may be noted that all members can sustain a remanent strain which is under polarization control. Figure 2.4 gives typical values of remanence in a 7/65/35 composition.

Switching studied have shown that switching times of under 1μ sec can be achieved at high fields and that aging of the remanent strain is comparable to aging of the fully poled state.

Cyclic switching between states will be essential for practical actuator use so that studies of property degradation as a function of the number of cycles switched (fatigue) are most important. Initial data on fatigue under repeated cycling were very disappointing typical resonse for a 7/68/32 composition is given in figure 2.5 showing severe fatigue starting at ~10^4 cycles. Several different types of surface treatment modified but did not significantly improve response. Additional experiments have proven however that this premature failure is a surface phenomenon and is traceable to debonding of the gold electrodes used. This field assisted debonding appears associated with traces of organic contamination on the surface and can only be relieved by high temperature annealing immediately before electrode deposition. For a hot pressed 7/65/32 sample subjected to this pre-anneal before electroding, no fatigue at all is evident up to 10^9 cycles with intial and final hysteresis loops superposing exactly and there is no change in strain behaviour (figure 2.6).

In the same composition made by conventional ceramic processing, subjected to the same electrode treatment fatigue is again evident, now however as a volume controlled phenomenon. Other tests in the hot pressed 7/65/35 also show fatigue re-appearing in grain grown material (grain size ~30 μ meters).

For the 8 · 4/65/35 fatigue appears very different. Even in the best hot pressed ceramic fatigue appears associated with internal micro-cracks which are visible in the body of the dielectric and appear to originate at field concentration near the electroded edges .

The reason for this behaviour is not simply the strain level, since 8/65/35 has lower electrostriction than the 7/68/32 composition which shows no evidence of cracking at similar density, grain size and electrode configuration.

The studies to date on these PLZTs suggest that switching fatigue depends upon the complex interplay of anumber of variables including electrode interface properties, microstructure including grain size, density and flaw population and probably also upon the nature of the electro-dielectric interation in the particular composition. It is however most encouraging to have the demonstration that fatigue can be completely eliminated under proper circumstances, even under conditions of full polarization switching.

2.3 Antiferroelectric: Ferroelectric Switching in Modified Lead Zirconate Stannate Titanate Compositions

Studies in the Materials Research Laboratory at Penn State have focused upon antiferroelectric compositions in the family $(Pb_{0.97}La_{0.02})(ZrTiSn)O_3$ in which the Zr:Ti:Sn ratios are adjusted to explore the phase boundary with the ferroelectric rhombohedral form. The compositions studied are tabulated in Table 2.2 and the position in the phase diagram illustrated in figure 2.7. Samples were in all cases preparedby conventional ceramic processing from reagent grade oxides.

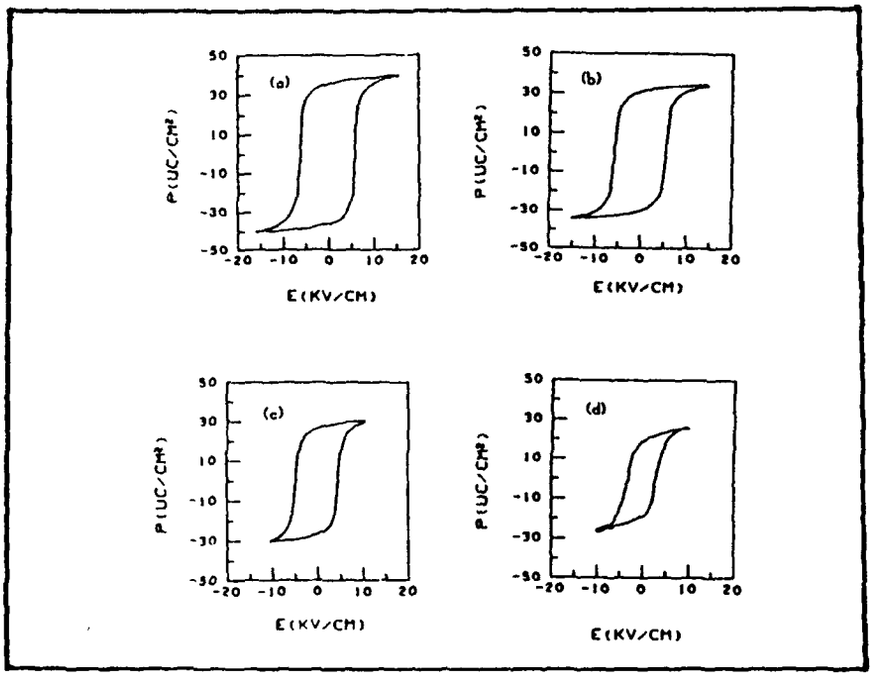

Fig. 2.3a Polarization-electric field hysteresis loops for the MPB compositions: (a) 4/57/43, (b) 6/60/40, (c) 7/62.5 and (d) 8/65/35.

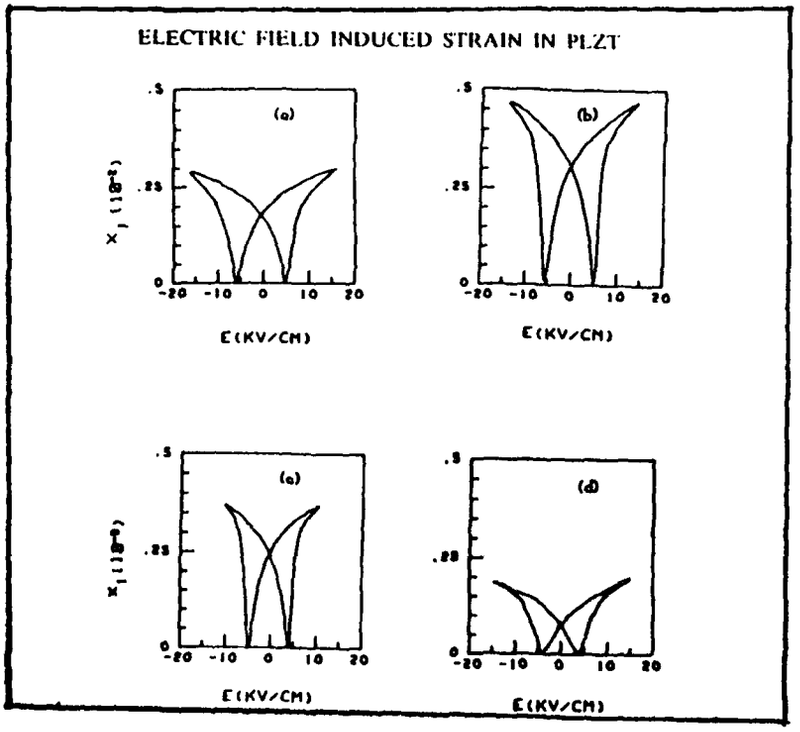

Fig. 2.3b The longitudinal strain-electric field hysteresis loop for the MPB compositions: (a) 4/576/43, (b) 6/60/40, (c) 7/62.5/37.5 and (d) 8/65/35.

TABLE 2.1

Field Induced Strain and Related Dielectric Data

Comp.	T_m (°C)	K_m	K_{25}	Ec (kv/cm)	Pr (uc/cm^2)	x_t (10^{-3})	x_l (10^{-3})	x_r/x_t
8/67/33	99	12000	5500	2.6	21	0.81	2.5	0.1
8/65/35*	106	11350	4600	3.6	20	0.82	2.3	0.32
8/63/37	114	11300	4500	4.7	21	0.76	1.9	0.32
7/65/35	140	15000	3000	4.5	28.4	1	3.1	0.7
7/62.5/37.5*	160	16000	2900	5	27.2	1.2	3.7	0.64
7/60/40	172	17000	3000	6.3	26.2	1.2	3.8	0.4
7/58/42	180	17300	2600	8	22	1.1	3.2	0.39
7/56/44	190	17200	2200	10	22	0.94	2.3	0.4
6/62/38	196	19000	2100	5	31	1.45	4.1	0.58
6/60/40*	204	18000	2000	5.6	29.5	1.35	4.7	0.57
6/58/42				7.45	29	1.32	3.9	0.53
5/60/40	230	19000	1600	6.52	32	0.79	4.2	0.53
5/58.5/41.5*				6.41	34	1.24	4.5	0.59
5/56/44				8.5	32.1	1.6	5.4	0.56
4/57/43*				7.47	35.2	1.26	3.0	0.6
4/55/45				10	29.5	1.21	2.9	0.55

* MPB compositions. x_t: Transverse strain induced at 15 kv/cm, x_l: Longitudinal strain induced at 15 kv/cm, x_r: Transverse remanent strain, T_m: Temp. of dielectric maximum, K_m: Maximum dielectric constant, K_{25}: Dielectric constant at 25°C.

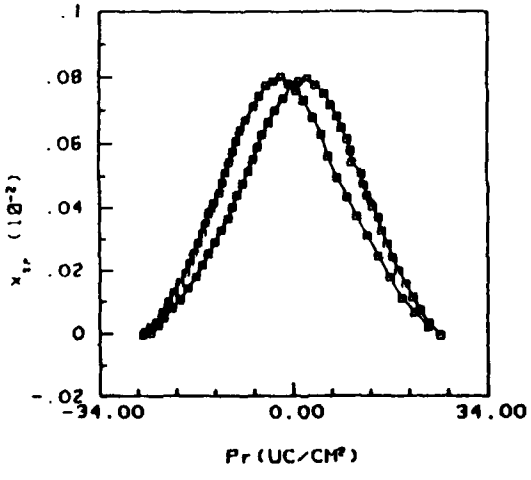

Fig. 2.4 The remanent transverse strain as a function of remanent polarization for PLZT 7.5/65/35 Ceramic.

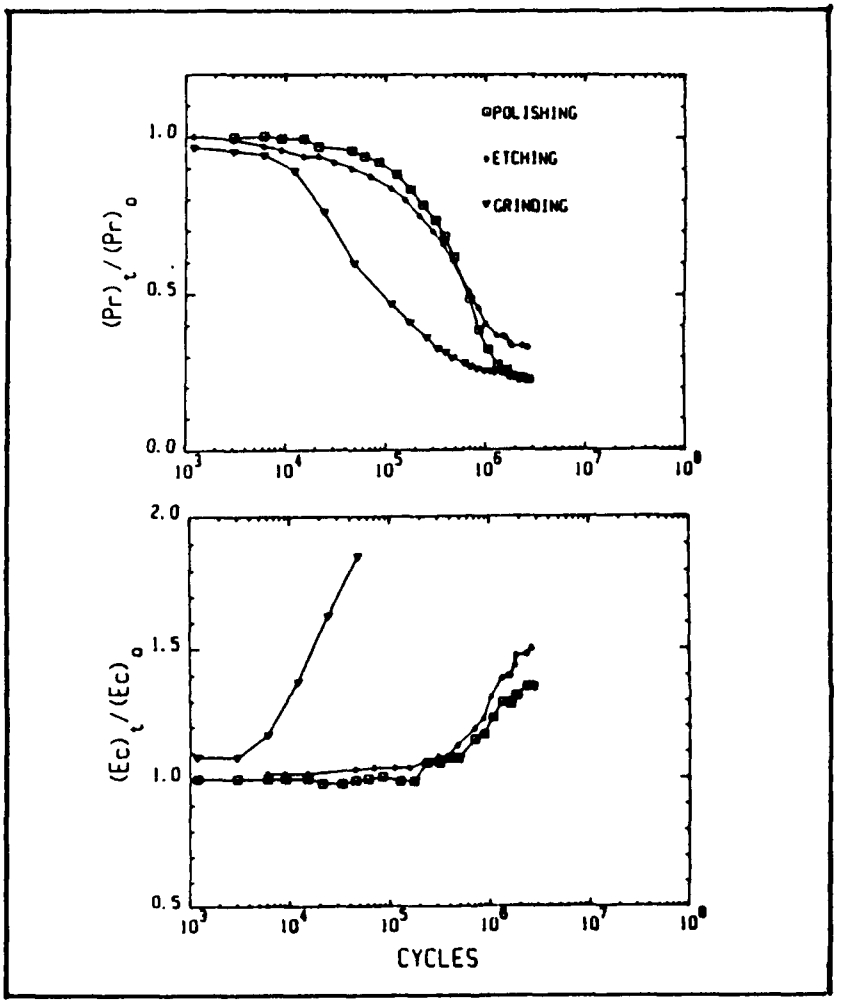

Fig. 2.5 Premature fatigue in a PLZT 7/68/32 showing the effect of different surface treatments, when the gold sputtered electrode is applied after conventional cleaning using organic solvents. The fatigue is associated with field assisted electrode debonding.

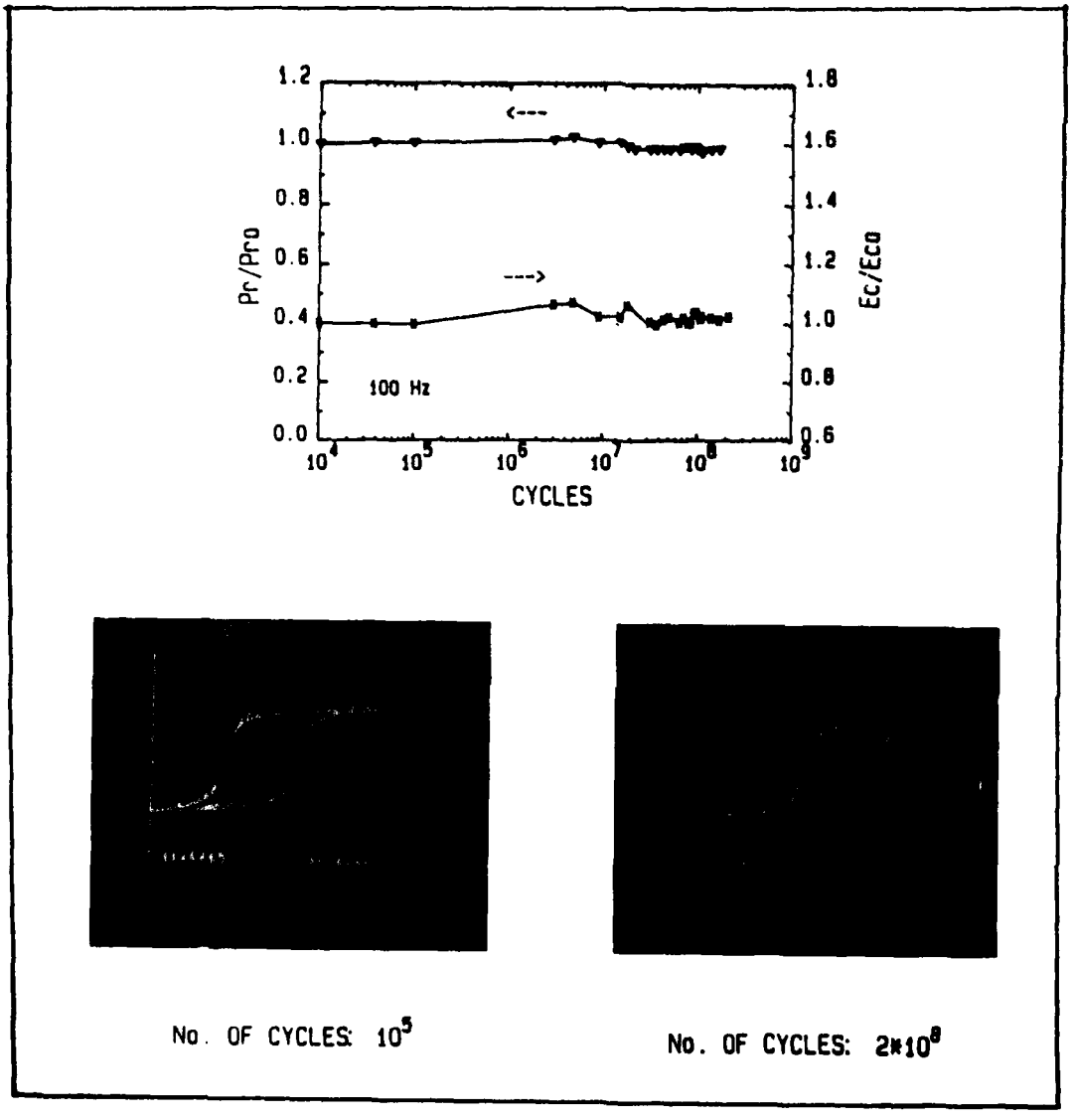

Fig. 2.6 Absence of fatigue in a 7/68/32 PLZT after high temperature surface cleaning. Sputtered gold electrode.

TABLE 2.2

Chemical Compositions and the Reference Numbers

No.	Composition
4	$(Pb_{0.97}La_{0.02})(Zr_{0.66}Ti_{0.09}Sn_{0.25})O_3$
5	$(Pb_{0.97}La_{0.02})(Zr_{0.53}Ti_{0.12}Sn_{0.35})O_3$
6	$(Pb_{0.97}La_{0.02})(Zr_{0.66}Ti_{0.11}Sn_{0.23})O_3$
7	$(Pb_{0.97}La_{0.02})(Zr_{0.66}Ti_{0.105}Sn_{0.235})O_3$
8	$(Pb_{0.97}La_{0.02})(Zr_{0.64}Ti_{0.09}Sn_{0.27})O_3$
9	$(Pb_{0.97}La_{0.02})(Zr_{0.64}Ti_{0.11}Sn_{0.25})O_3$
10	$(Pb_{0.97}La_{0.02})(Zr_{0.62}Ti_{0.11}Sn_{0.27})O_3$
11	$(Pb_{0.97}La_{0.02})(Zr_{0.68}Ti_{0.09}Sn_{0.23})O_3$
12	$(Pb_{0.97}La_{.02})(Zr_{0.60}Ti_{0.10}Sn_{0.30})O_3$
13	$(Pb_{0.97}La_{0.02})(Zr_{0.575}Ti_{0.1125}Sn_{0.1125})O_3$
14	$(Pb_{0.97}La_{0.02})(Zr_{0.55}Ti_{0.10}Sn_{0.35})O_3$

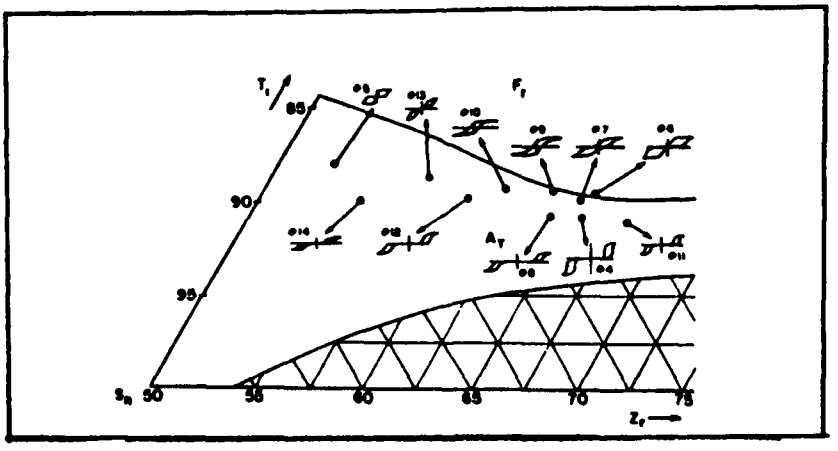

Fig. 2.7 Antiferroelectric tetragonal compositions selected for study and their dielectric hysteresis loops.

Typical hysteresis and longitudinal strain curves taken on sample 4 (Table 2.2) are shown in figure 2.8 and the parameters for all samples studied are summarized in Table 2.3. Evidently maximum strains up to 0.87% are possible in the higher zirconia compositions and fortunately this is combined with a lower switching field.

An important consideration for the practical utility of these materials is the speed with which the field forced phase change can be accomplished both in the forward AF→ F and in the backward F → AF transitions. Pulse field studies have shown that forward switching is fast, figure 2.9 gives data for composition 5 which is quiet typical. Clearly switching can be accomplished in times ~1/3 μ sec at realizable field. Backward switching when the field is simply reduced to zero is slightly longer, and depends on the degree of original forward poling. But even for very high forward fields (figure 2.10) the back switching is accomplished is under 2.5 μ sec. Thus for most types of AF–F actuators the speed will be set by the propagation of the strn wave and not by the polarization process.

Fatigue in the cyclic switching is illustrated for composition 6, the maximum strain material in figure 2.11. In spite of the fact that the ceramic is not near theoretical density the polished sample only shown less than 10% change in switched polarization after $5 \cdot 10^7$ cycles a very encouraging result. However much more work is needed to define and control the fatigue processes in these ceramics.

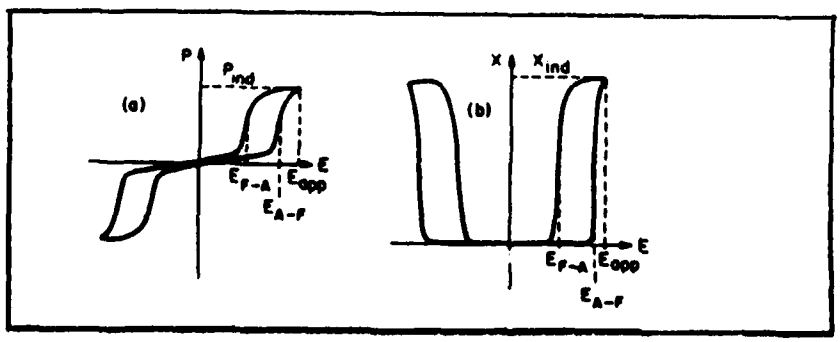

Fig. 2.8 Typical polarization and strain hysteresis loops (composition No. 4) and some illustrated parameters.

TABLE 2.3

Switching Data for Different Compositions

No.	P (uC/cm^2)	E_{A-F} (kV/cm)	E_{app} (kV/cm)	x_1 (ind)
(a)	Group 1 compositions			
5	30	30	35	0.18%
13	28	30	43	0.45%
10	36	28	60	0.5%
9	36	24	60	0.59%
7	36	22	58	0.52%
6	40	21	46	0.87%
(b)	Group 2 compositions			
14	31	44	56	0.35%
12	32	49	59	0.42%
8	30.5	52	68	0.37%
4	43	50	75	0.55%
11	33	45	60	0.45%

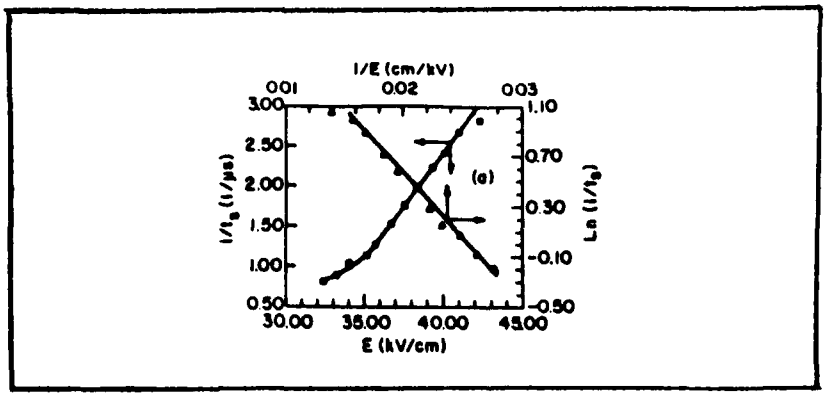

Fig. 2.9 (a) 1/ts (forward switching speed versus E.

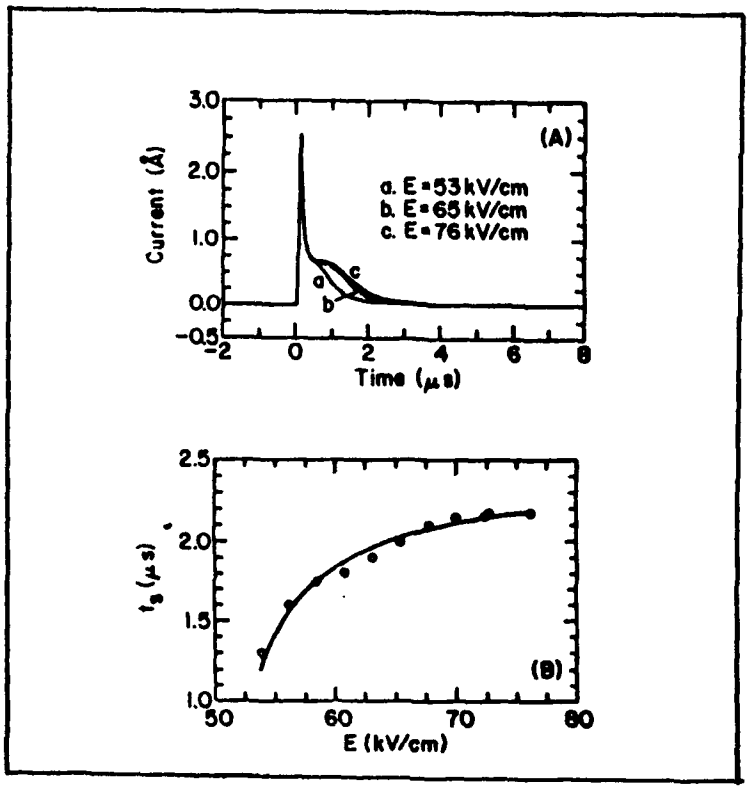

Fig. 2.10 (a) Backward switching current under different dc poling fields and (b) backward switching time as a function of dc poling field for composition No. 4.

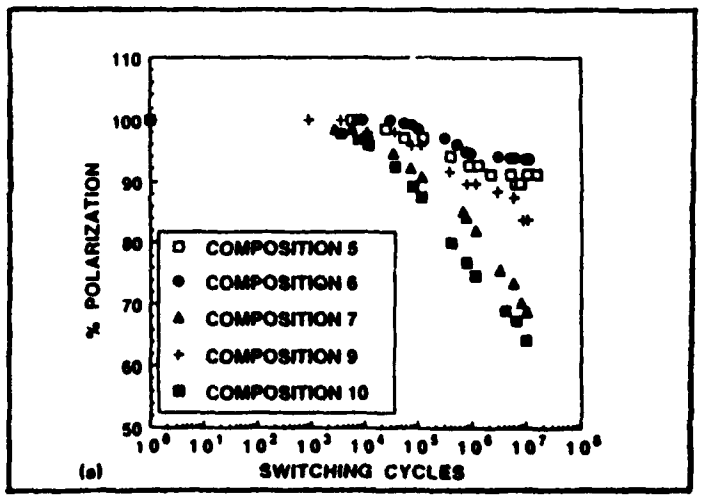

Fig. 2.11 Fatigue in Antiferroelectric Ferroelectric switching for several high strain compositions.

3.0 PIEZOELECTRIC PROPERTIES OF THIN FILMS

In a perovskite structure ferroelectric in its tetragonal ferroelectric phase, symmetry 4mm, the non zero intrinsic piezoelectric constants of the single domain are:

$$d_{31} = d_{32} = 2Q_{12}P_3\varepsilon_{33} \quad (3.1)$$

$$d_{33} = 2Q_{11}P_3\varepsilon_{33} \quad (3.2)$$

$$d_{15} = d_{24} = Q_{33}P_3\varepsilon_{11} \quad (3.3)$$

where the Q_{ij} are the non zero electrostriction constants

P_3 is the spontaneous electric polarization.

ε_{ij} the components of the dielectric tensor.

For a bulk ceramic poled into conical symmetry (Curie group ∞ m) we expect similar relations except that now the $\bar{Q}_{ij}$ are orientation averages, the P_3 is now P_R and ε_{33} is to be measured along the poling direction.

In the thin film it is probable that the Q constants are not significantly changed so that if we can achieve high values of P_R and of ε_{33} we might expect strong piezoelectricity. Initial measurements of the change of film thickness under field, using the Penn State MRL optical ultradilatometer show a clear piezoelectric effect (fig. 9.1). Measuring the slope of a sequence of strain: field curves like figure 3.1 at different DC bias levels a maximum

d_{33} = 217 pC/N (is recorded in figure 3.2).

For an undoped PZT of a similar 52/48 Zr:Ti composition

d_{33} = 223 pC/N .

To measure d_{31}, since the film is firmly bonded to a platinum film on the silicon substrate, it was necessary to use a monomorph bending mode excited in a thin silicon strip. Again the measured deflections yield a value for

d_{31} = -88.7 pC/N (fig. 9.3).

close to the value

d_{31} = -93.5 pC/N

quoted for the 52:48 Zr:Ti undoped composition.

Taking values for the elastic constants s_{11}^E, s_{33}^E, s_{12}^E similar to the bulk ceramic it is then possible to derive the piezoelectric coupling coefficients

K_{33} = 0.49
K_{31} = 0.22
K_p = 0.32.

As a preliminary exercise to explore the utility of the high piezoelectric constants and strong electromechanical coupling for PZT films on silicon we have cooperated with MIT and Lincoln Labs to demonstrate a piezoelectric flexure wave micro-motor.

The concept is shown schematically in fig. 3.4. The silicon wafer is coated with a thick (2 μ meters) silicon oxynitride film, then etched from the back side to define a window 2.5 mm square. Titanium bonded platinum electrode is deposited upon the upper surface and a 4,500 A° 52:48 PZT sol gel film is spun on and processed on the upper surface.

The upper electrode pattern 1 mm in diameter is plated onto the upper surface of the PZT using a photo-resist technique.

To examine the surface flexure wave generated by sine:cosine fields applied to the electrodes a 0.8 mm diameter glass lens was centered on the electrode pattern. With a field of 2 volts applied it was possible to generate stable rotation of the lens at a speed ~ 120 rpm. The experiment was in the nature of a proof of concept, and the system is now being redesigned to better locate the plattern and to improve the electrode geometry and dielectric perfection.

From observation of the acceleration of the glass lens on switching on the fields, we

project that torques of the order 10^{-9} Newton meters are realized even with this very primitive design. Such torques would not be unrealistic, given the high energy density and the strong coupling coefficient of the ferroelectric film.

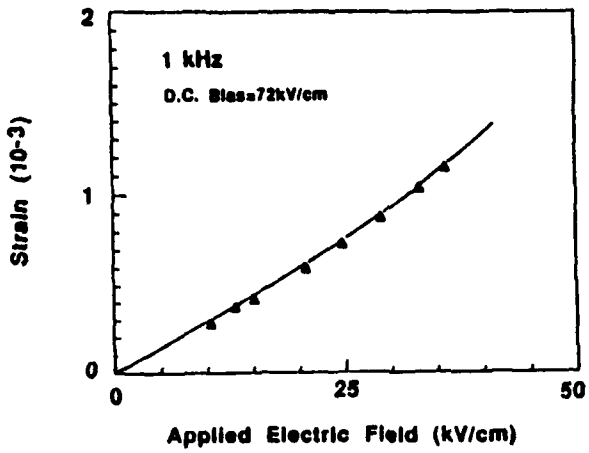

Fig. 3.1 Thickness strain x_3 measured as a function of applied DC field

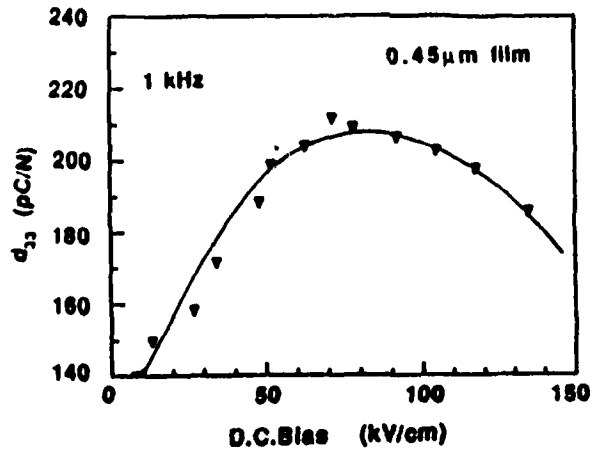

Fig. 3.2 Piezoelectric constant d_{33} as deduced from a sequence of strain:field curves such as 9.1 under different static bias field levels.

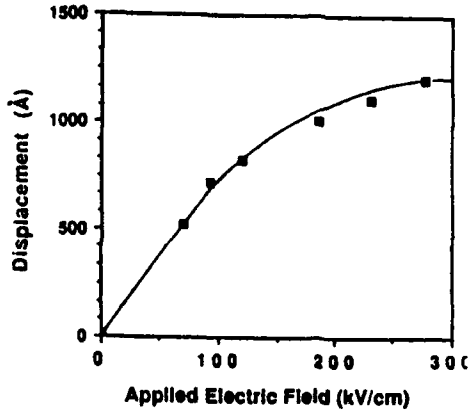

Fig. 3.3 Strain measured from the flexure of a PZT 52/48 thin film monomorph on a silicon substrate.

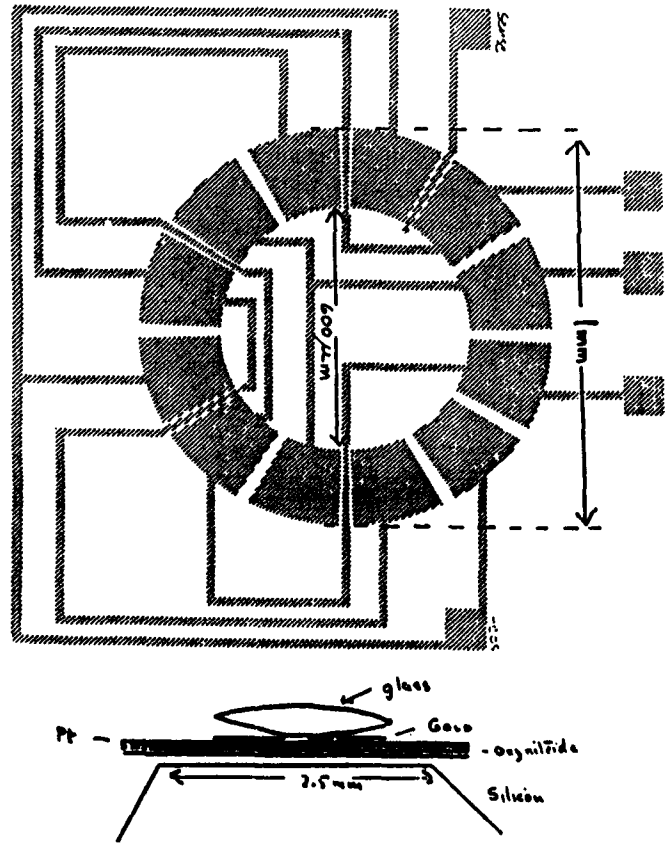

Fig. 3.4 Schematic drawings of the electrode pattern for a PZT thin film micro-motor using a rotating flexure wave generated in a PZT film on a silicon oxy nitride diaphragm. The rotating wave has been demonstrated to rotate a small (0.8 mm) glass lens at ~120 rpm.

REFERENCES

1. B. Jaffe, W. R. Cooke, Jr and H. Jaffee. Piezoelectric Ceramics, Academic Press, London (1971).
2. A. F. Devonshire. Adv. in Physics **3**, 85 (1954).
3. L. E. Cross. Phil. Mag ., Ser. 8 1, 76 (1956).
4. L. E. Cross. J. Phys. Soc. Japan **23**, 77 (1967).
5. A. Amin and L. E. Cross. Ferroelectrics **50**, 237 (1983).
6. T. R. Halemane, M. J. Haun, L. E. Cross and R. E. Newnham. Ferroelectrics **62**, 149 (1985).
7. A. Amin, M. J. Haun, B. Badger, H. McKinstry and L. E. Cross. Ferroelectrics **65**, 107 (1985).
8. M. J. Haun, T. R. Halemane, R. E. Newnham and L. E. Cross. Japan J. Appl. Phys. **24**, 209 (1985).
9. M. J. Haun, E. Furman, S. J. Jang and L. E. Cross. Ferroelectrics **99**, 13 (1989).
10. M. J. Haun, E. Furman, H. A. McKinstry and L. E. Cross. Ferroelectrics **99**, 27 (1989).
11. M. J. Haun, Z. Q. Zhuang, E. Furman, S. J. Jang and L. E. Cross. Ferroelectrics **99**, 45 (1989).
12. M. J. Haun, E. Furman, T. R. Halemane and L. E. Cross. Ferroelectrics **99**, 55 (1989).
13. M. J. Haun, E. Furman, S. J. Jang and L. E. Cross. Ferroelectrics **99**, 55 (1989).
14. R. Gerson, H. Jaffe. J. Phys. Chem. Solids **24**, 979 (1963).
15. R. Gerson. J. Appl. Phys. **31**, 188 (1960).
16. K. Carl and K. H. Hardtl. Ferroelectrics **17**, 472 (1978).
17. D. Dederichs and G. Arlt. Ferroelectrics **68**, 281 (1986).
18. W. Y. Pan, T. R. Shrout and L. E. Cross. J. Mat. Sci. Lett. **8**, 771 (1989).
19. R. E. Newnham, D. P. Skinner and L. E. Cross. Mat. Res. Bull. **13**, 525 (1978).
20. A. A. Shaulov, M. E. Rosar, W. A. Smith and B. M. Singer. Proc. ISAF 86, Leigh University, 8 June 1986, p. 231.
21. T. R. Gururaja, W. A. Schulz, L. E. Cross and R. E. Newnham. Proc. IEEE Ultrasonics Symp., 1984, pg. 523.
22. W. A. Smith. Proc. ISAF 86, p. 249, Lehigh University (8 June 1986).
23. Z. M. Zhang, W. Y. Pan and L. E. Cross. J. Appl. Phys. **63**, 2492 (1988).
24. W. Y. Pan and L. E. Cross. Rev. Sci. Inst. **60** (8), 2701 (1989).

IN-FLIGHT AIRCRAFT STRUCTURE HEALTH MONITORING BASED ON SMART STRUCTURES TECHNOLOGY

by

Chr. Boller and **R. Dilger**
Deutsche Aerospace
Aircraft Division
PO Box 80 11 60
8000 Munich 80
Germany

SUMMARY

Aircraft are known to be highly complex systems requiring an extensive amount of monitoring because of their safety criticality. To reduce direct operating or life cycle cost a lot of effort has been spent on automated monitoring systems. On-board loads monitoring systems for aircraft as well as built in test equipment in avionics systems are already available nowadys. On-board loads monitoring systems do however not monitor damage in-situ and on-board. This still has to be performed on-ground by manual NDT inspection. Smart structures technology is a means which can support development towards automated in-situ monitoring of damage even on-board the aircraft. The paper starts with a brief view on aircraft maintenance cost, describes existing aircraft health and usage monitoring systems as well as NDT procedures and explains how these procedures could be combined to a smart system using smart materials and structures technology. A strategy is proposed how gradual introduction of smart structures technology into structure health monitoring systems can make this new technology beneficial for aircraft operators in short term.

LIST OF ABBREVIATIONS

AE Acoustic Emission
BVID Barely Visible Impact Damage
CFRP Carbon Fibre Reinforced Polymers
ECM Engine Condition Monitoring
NDT Non Destructive Testing
PVDF Polyvinylidene fluoride

1 INTRODUCTION

Aircraft are known to be highly complex systems. They are composed of a variety of electronic, hydraulic and propulsion systems and a light weight/high stiffness structure, that has to withstand severe loading conditions. In addition the whole system is highly safety critical and suffers degradation even when not being in service. Such complex systems require extended maintenance.

Because of safety criticality, most of the maintenance effort is related to monitoring. Only a smaller amount of maintenance effort should be related to repair. Manpower has become a major cost driving force in highly industrialized countries while increased competition like in commercial aircraft business has led to low transport fares and highly sophisticated technology like in military aircraft or space vehicle business requires extended care in functionality and reliability. Possible solutions for minimizing maintenance cost are therefore reliable procedures for automated aircraft health monitoring.

Beside minimization of inspection efforts and cost through aircraft health monitoring, a variety of other requirements and reasons exist which includes:

- preservation of flight safety and improve operational capability
- minimization of aircrafts' availability through on-condition monitoring
- reduction of weight because of better design
- extension of aircrafts' operational life
- simplification of damage detection
- detection, localization and validation of damages such as cracks, delaminations and corrosion resulting from fatigue impacts or mishandling
- improvement of inspectability of composite materials' structures
- saving of fuel
- reduction of pollution.

Monitoring of aircraft structures is nowadays still fully performed on-ground using Non Destructuive Testing (NDT) procedures according to prescribed instructions and after fixed service time intervals. As these fixed intervals have been mainly based on severe flight conditions first attempts have been made to flexibilize these by on-condition monitoring using an aircraft loads monitoring system. Smart materials and structures technology including microelectronics and advanced data processing such as data bases, neural networks, fuzzy logic and artificial intelligence are emerging areas of science which might allow to integrate a NDT-system into an aircraft structure similar to the nervous system in a human body. Fully automated aircraft structure condition monitoring even in-flight would be enabled.

Starting with a brief view on aircraft maintenance cost, this paper will describe existing aircraft health and usage monitoring systems as well as NDT techniques and explain how these could be combined to a smart system using smart materials and structures technology.

2 AIRCRAFT MAINTENANCE COST

Before considering development of an aircraft structure health monitoring system it is advisable to roughly determine the amount of aircraft maintenance cost and the percentage of maintenance cost reduction achieved by that monitoring system. The reduced maintenance cost combined with other pay offs such as reduced fuel consumption, better reliability, less down times or extended operational life will finally define the allowable cost of the monitoring system to be developed.

Although it is quite difficult to obtain representative maintenance cost data an attempt is made within the following to give a rough estimate for at least a corrosion monitoring system and to describe possible pay offs with composite materials monitoring.

Independant of the type of aircraft (commercial or military) monitoring is required for the various types of damage listed below:

o metals

- cracks
- corrosion
- wear

o composites

- cracks
- delaminations (especially resulting from BVID)
- debonding

Common types of damage to both materials is misrepair or lost parts such as rivets and bolts.

Considering metallic structures, corrosion is a type of damage which already starts shortly after initial delivery while fatigue damage occurs mainly after some years in service. Fig. 1 is a general view on how the fleet damage rate develops over the airplane age for commercial aircraft [1] due to corrosion and fatigue. A study recently performed on corrosion maintenance for military aircraft in the USA [2] reports of annual corrosion maintenance cost per aircraft ranging from 3,627 US$ for a T037 up to 352,187 US$ for a B52, the average value for all types of aircraft considered being around 75,000 US$. This includes cost for repair, paint, inspection, wash, material and others. There is no question that improved corrosion prevention is the best way to reduce corrosion maintenance cost. But already a reduction of corrosion cost of simply 10% using a corrosion monitoring system could be of remarkable help. It would not just reduce inspection manpower but also cause less repair, paint and material because of earlier detectiontion of corrosion damage. Life cycle cost for a corrosion monitoring system of 150,000 US$ sounds therefore not unrealistic when considering 20 years flight time.

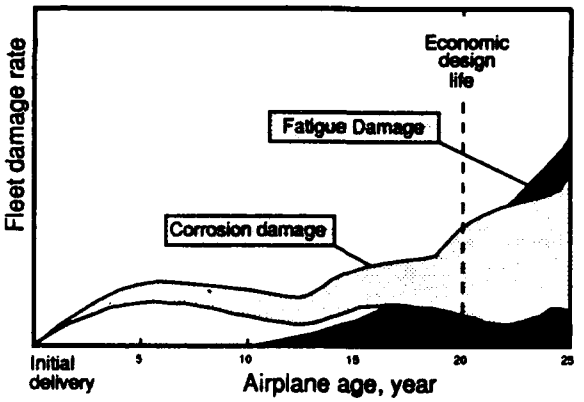

Fig.1 : Observed Fleet Damage Rate [1]

Composite materials have become increasingly applied in military aircraft because of better camouflage, lighter weight, better fatigue behaviour, less degradation by corrosion and the possibility of tailoring strength and stiffness according to structural needs. When compared to metals composites however also possess a number of disadvantages such as less ductility, higher environmental (especially ho/wet) sensibility, less lightning strike resistance and detectability of Foreign Object Damage (FOD). Another major concern which especially airlines have [3] is repair efforts required and operational reliability with composite materials. Their higher repair expenses are mainly caused by workshop and test equipment required for quality control, special requirements for materials storage and the non-standard work procedures.

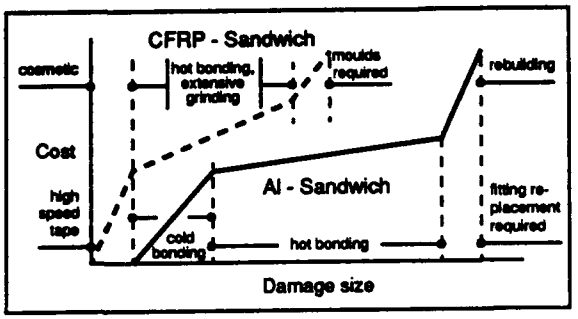

Fig.2 : Comparison of Repair Cost [3]

Damage Size	CFRP	Aluminium
70mm Dia.	2.700,–	500,– in situ
150mm Dia.	3.000,–	2.800,–
Approx. 2 sqm	34.000,–	20.000,–
100 % Restoration	n.a. (Spare part price is 168.000,–)	50.000,–

Assumptions: 1.) Prices in DM
2.) Skin and core damaged
3.) Cost for autoclave charge is 1.300,–
4.) Cost per M/H is 100.– DM
5.) No materials storage and certification cost considered

Fig.3 : Repair Cost Comparison for CF6 Fan Cowl Door [3]

Fig. 2 shows their qualitative view of development of repair cost versus damage size for CFRP and aluminium structures. Fig. 3 gives some values for repair cost of a CF6 fan cowl door. For any size of damage the repair cost for CFRP is always, mainly even significantly higher than for aluminium. These higher repair cost can be remarkably reduced when CFRP becomes much more applied, leading to reduced cost for spare parts, workshop and quality control tools and repair related labour because of standardized procedures. Other pay offs will come from:

- avoiding known design deficiencies
- minimizing the risk of unknown problems encountered
- substituting metal by CFRP only for structural parts with high weight and low maintainability.

A composite structure health monitoring system is therefore a good means to obtain pay offs from the first two aspects mentioned above. It must however be mentioned that allowing damage in a composite structure because of better knowledge of damage behaviour through a structure health monitoring system will cause structural repair cost which has not occured before. Calculation of the allowable price for a health monitoring system for composite structures is therefore influenced by various factors which are difficult to quantify at present.

3 STATE-OF-THE-ART IN AIRCRAFT HEALTH MONITORING

When considering an aircraft from a health and usage monitoring aspect four different areas within the aircraft are of major importance:

- the aircraft structure
- hydraulic systems
- electronics/avionics
- propulsion systems.

For propulsion systems health and usage monitoring are highly advanced. Whole in-flight Engine Condition Monitoring (ECM) systems have been developed and built which are already in use within various aircraft operators' fleets [4,5]. This takes in engine data such as revolutions per minute, vibrations, temperatures, pressures and rate of fuel usage. By immediate data analysis, engine condition can be monitored long before in-flight malfunctions occur, and de-

fects can be traced to a specific module within the engine. ECM has received FAA and JAA approval.

Since the widespread introduction of digital technology, the control and avionics systems of aircraft incorporate varying levels of Built In Test Equipment (BITE) to monitor system behaviour and to provide corrective action in the event of failures.

In-situ monitoring aircraft structures or hydraulic systems is still limited to on-ground monitoring using NDT procedures such as eddy current, ultrasonics, pressurization or simply the naked eye [6].

In-flight monitoring, having gained large interest during the past decades, is performed nowadays by either monitoring strain or flight parameter sequences which are then used to derive a load sequence for the aircraft part considered. A description of this kind of monitoring is given in the following.

Strain Gauge Based Health Monitoring Systems

Initial work with in-flight monitoring was performed bonding strain gauges to well selected areas in the aircraft and measuring strain sequences. On ground, but even with sufficient computer capacity on-board, the strain sequences are then converted to stresses and/or loads allowing a numerical evaluation of fatigue damage using mainly simple damage accumulation rules (e.g. Palmgren-Miner's rule).

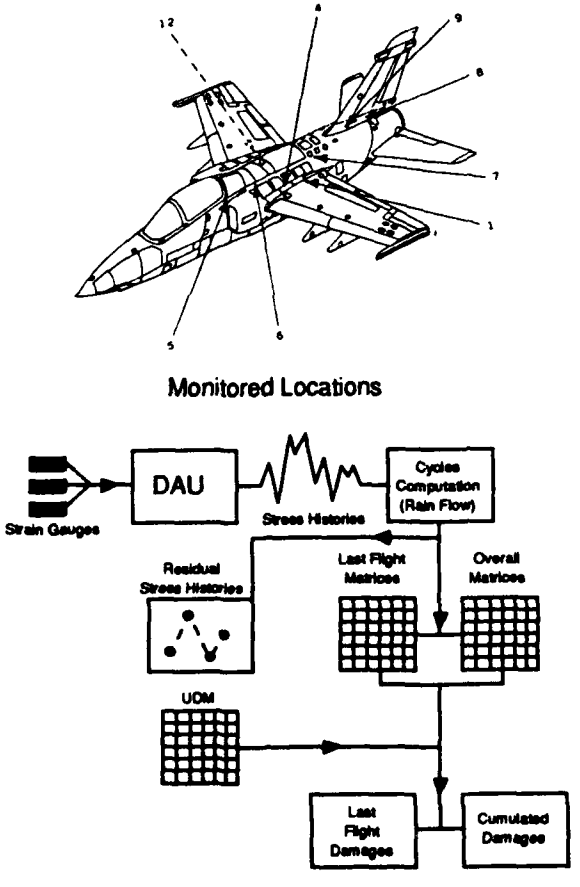

Fig.4: Strain Gauge Based A/C Health Monitoring [8]

This kind of monitoring system has been continuously developed through the past years mainly using better bonding technique, advanced electronics and data processing as well as improved sensors. Various examples are described in [7] where Fig. 4 shows one example for a military aircraft [8]. All strains measured with strain gauges are converted to digital signals and stored in-service in a Data Acquisition Unit (DAU). Within a following step the strain histories are then converted to stress histories and a detailed damage/fatigue life evaluation is performed for the last flight and the overall flight history of the aircraft. This damage/fatigue life evaluation might be performed either in-flight or on-ground.

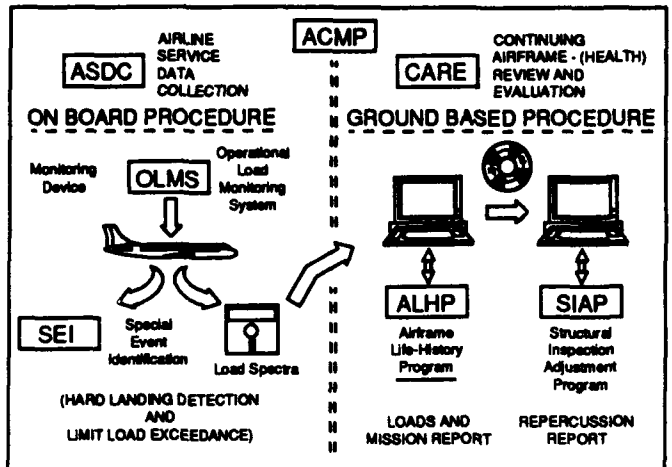

SOURCE	PARAMETER
ADIRU Air Data Inertia Reference Unit	ALT, MN, TAS, AOA, PTCR, ROLR, LATG, VRTG
FMGC Flight Manag. Guid. Computer	GW, CG
PRESS.CONTR. Pressure Control System	PDC (cabin different pressure)
DMC Data Management Computer	RALT
FQIS Fuel Quantity Indication System	FUEL QUANTITIES WING (inner and outer cell)
FCDC Flight Control Data Computer	STAB, AIL, ELEV, RH SPL 1-6
SDAC System Data Analog Converter	RUDD
SFCC Slat Flap Control Computer	SLAT/FLAP
FWC Flight Warning Computer	FLIGHT PHASE
FDIU Flight Data Interface Unit	TIME, DATE, AC-TAIL NUMBER

Fig.5: OLMS, Flight Parameter Based A/C Health Monitoring [9]

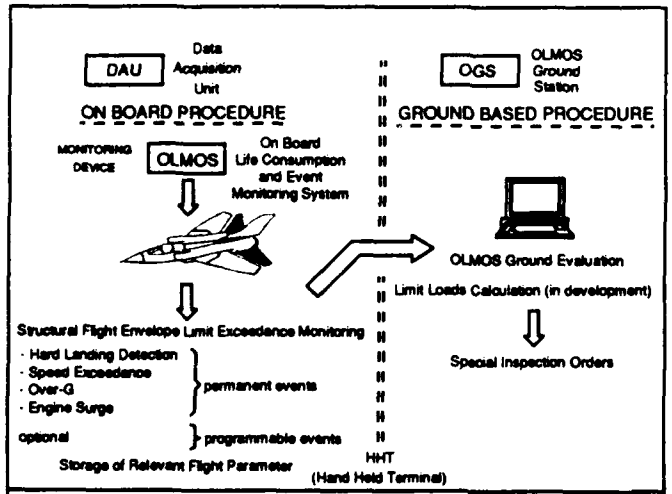

Summary of 'Begleitparameter' Permanent Events
BANK, INCLINATION, HEADING, VX, VY, VZ, Ma, VCAS,
ALPHA, SPOILER, ROLLRATE, RUDDER, L/R, YAWRATE,
PITCHRATE, TAILERON L/R, FLAP/SLAT, WINGSWEEP,
NZ, NY, MASS, EXTAST, HEADING RATE

Fig.6: OLMOS, Flight Parameter Based A/C Health Monitoring

Flight Parameter Based Monitoring Systems

Aircraft operators try to minimize the risk of complexity within an aircraft by avoiding additional sensors. Strain gauges for use of loads monitoring are therefore mainly unliked. Instead sensors already available in the aircraft are used for monitoring the aircraft's load sequence. Early work started by using the g-meter for converting measured gravity accelerations to flight loads. This work was then extended including further flight parameters such as speed, altitude, air data, pressure, fuel quantity, flaps position, etc. for a more precise evaluation of loads. Fig. 5 shows an example of the Operational Loads Monitoring System (OLMS) developed for the Airbus A320 [9] and Fig. 6 the main procedure of the Onboard Life Monitoring System (OLMOS) used for the Tornado military aircraft within the German Tornado fleet [10,11].

Both systems are designed for onboard preprocessing of data, differing between special events (hard landings and limit load exceedances) and the general load spectrum. Even though the accuracy of the load sequence monitored is not fully satisfying at present a lot of improvement has already been gained in the past and further improvement can be ex-

pected from ongoing work. The optimum result obtainable with a flight parameter based system is therefore a load sequence identical to a load sequence measured with strain gauges.

Disadvantages with Loads Monitoring

A loads monitoring system as described before is not able to monitor - or in other words detect - damage. It is only able to evaluate damage by additional use of numerical evaluation procedures. The difference between predicted and detected damage can be quite remarkable. A factor of two is very common in fatigue life prediction [12]. Furthermore structures exhibit large scatter in their damage behaviour. Fig. 7 is a typical example for a fatigue life curve [13]. The scatter in experimentally obtained fatigue lives easily varies by a factor of +/- 2 around the mean value. The two solid lines in Fig. 7 are the result of numerical fatigue life evaluation using different baseline data for the same material. It is obvious that the predicted fatigue life is significantly influenced by the appropriate selection of baseline data. Other factors are known to be the damage accumulation rule or the state of stress (uni-/multiaxial mean stress) applied. It can therefore be concluded that real monitoring of damage would be of great advantage to get more precise and reliable information of structural behaviour.

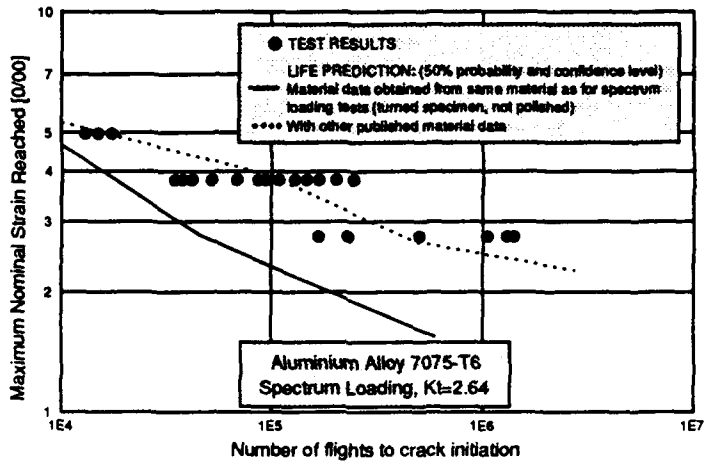

Fig.7: Predicted versus Actual Fatigue Life [13]

The gap between predicted and real damage becomes even larger when considering composite materials. Damage evaluation for these materials is still at an early stage. Monitoring flight loads is hardly of great use to detect damage in composites such as fibre or matrix fracture, delamination or BVID. Composite structures nowadys are designed such that they can withstand all service loading conditions without experiencing damage. They could however be designed much more light weight if damage such as mentioned above could be monitored. This would lead to make better use of composite materials potential without reduction in security.

Another aspect which cannot be covered by loads monitoring are environmental effects such as corrosion in metallic and humidity and temperature effects in composite structures - aspects which are becoming important with the increasing age of aircraft.

As a conclusion, considering safe-life as well as damage tolerant design and taking full advantage of materials' potential is only possible through continuous monitoring of material's condition applying NDT procedures. These NDT procedures must be applied on-board and even in-flight of an aircraft. An NDT system being an integral part of the aircraft will lead to

reduced manpower for inspection and ground times.

4 NDT TECHNOLOGY AS A MEANS FOR ON-CONDITION MONITORING

A variety of NDT procedures is used within on-ground maintenance of aircraft structures nowadys. Apart from visual inspection, use of ultrasonics and eddy current are the procedures generally applied. Procedures such as computer tomography, holography, shearography, thermography, Barkhausen noise or magneto optical eddy current have recently gained more attraction because of improved availability of these techniques. Major applicability and experience gained with these techniques has been with metals. A limited number of them is however also applicable to composite materials. Within the following three procedures able to account for monitoring damage in both, metals and composites will be shortly described.

Acoustic emission (AE) has been successfully used for monitoring discontinuities, fatigue failures, materials behaviour, welds including welding process or stress corrosion cracking in pressure vessels, aerospace and engineering structures. Acoustic emission is the elastic energy being suddenly released when materials undergo deformation. It may be released from propagation of cracks and/or delaminations, friction, leakage or microscopic deformation or transformation. The elastic energy - or better acoustic signal - emitted from the damage is registered as acoustic signal of a frequency in the range between 10 kHz and 1 MHz using a piezoelectric sensor well attached to the structure. Fig. 8a shows a typical example of an AE signal. The signal is then analyzed and classified according to specific features such as amplitude, rise time, decay time, duration, counts, etc. (Fig. 8b). Including time as a parameter allows damage source localization when at least three AE sensors are used. A good compilation of AE fundamentals and applications is given in [14].

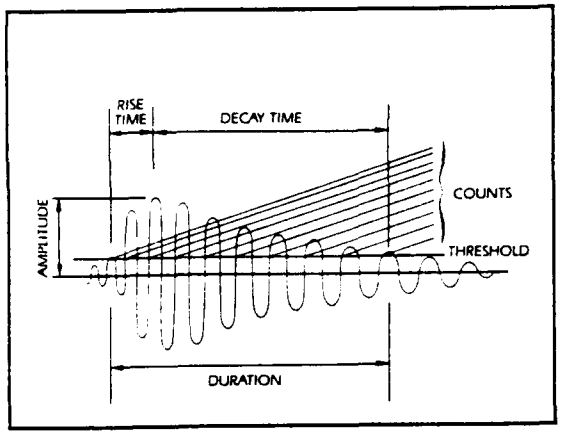

Fig.8a: Definition of simple waveform parameters [14]

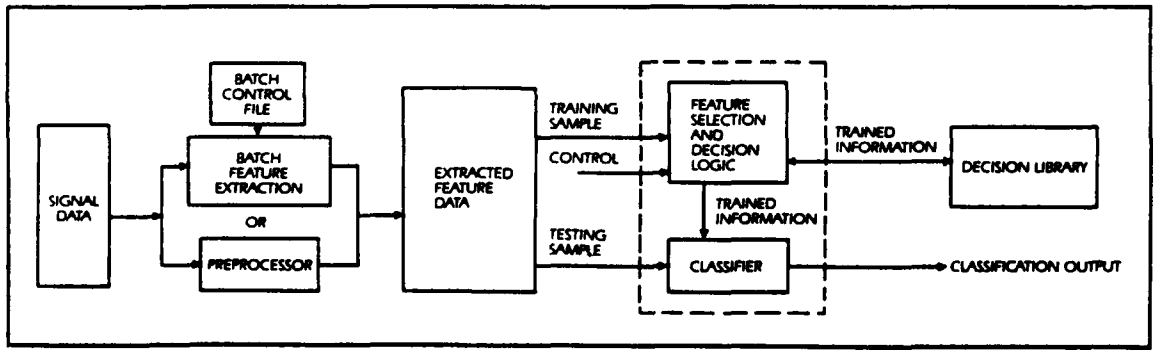

Fig.8b: A classification system for treatment of acoustic emission signals [14]

Various studies have been performed during the past decades using AE for monitoring damage in aircraft structures [15-18]. Some of these studies report of having even applied AE for in-flight monitoring [16,19]. This has however been limited to either monitoring an aircraft structure in a rig test [16] performed on-ground under simulated in-flight conditions or implementing an inertial loading apparatus with a precracked test specimen in a flying aircraft [19].

Other studies have been performed pressurizing the cabin in aircraft fuselages of commercial aircraft to detect fatigue cracks, corrosion, cracked lap joints and cracks around rivets and in forgings and wing splices [18]. The F-111 fighter/bomber aircraft has been tested in a chamber where the aircraft was periodically chilled to -40^{o} C and stressed between +7,3 g and -3,0 g and an AE system was used to locate any sources of structural failure [17]. Techniques were developed to eliminate loading noise and a strategy was set up to identify locations where sensors should be placed to obtain optimized signals. These developments have become feasible since handling, processing and interpretation of data has been improved through better computer technology and new attempts [20].

Acousto-ultrasonics is a technique which has been proved to be even more sensible than acoustic emission [21,22]. Fig. 9 illustrates the principle of this technique. It requires two probes, one of which is used to introduce ultrasonic stress waves into the structure and the other to pick up these stress waves at another position. As soon as the damaged area lies between the two probes the shape of the received acoustic signal changes because of change in material damping characteristics due to the damage (crack, delamination) occured. Acousto-ultrasonics has not been an NDT procedure established with aircraft structures up to now but it shows significant potential for future health monitoring systems.

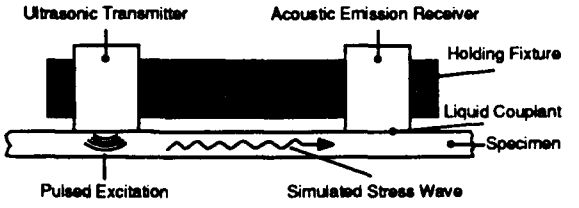

Fig.9: Schematic Diagram of the Acousto-Ultrasonic Technique

Modal analysis is a further NDT procedure which is widely applied for monitoring space structures. It is based on monitoring vibration modes. These vibration modes change when damage occurs. Pandey et al. [23] have shown the applicability of modal analysis for a cracked beam based on numerical (FEM) analysis. Tracy and Pardoen [24] used modal analysis for monitoring damage in a delaminated beam. Fig. 10 shows the change in natural fre-

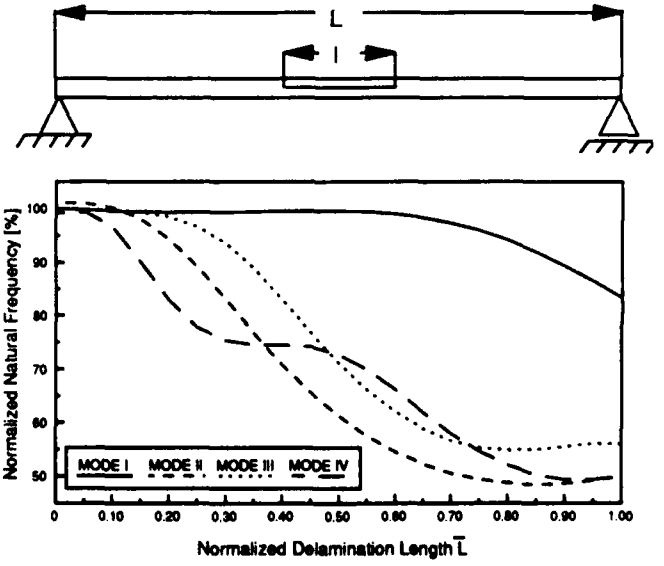

Fig.10 Modal Analysis of a Delaminated Beam [24]

quency versus size of delamination for the first four vibration modes of a midplane delamination centered in the middle of the beam. Mode IV proves to be the most sensible. Delaminations larger than 5 to 10% of structures' longitudinal surface have a significant effect on natural frequency of mode IV. Considering higher modes does not lead to significant higher sensibility in change of natural frequencies resulting from delaminations [25]. The applicability of modal analysis is therefore limited to monitoring larger defects. Hickman et al. [26] have shown on a demonstrator aircraft, that modal analysis could well be used for monitoring damage such as lost rivets or bolts.

Requirements for On-Condition Monitoring.

Future aircraft health and usage monitoring systems to be designed as built-in systems must be able to monitor damage on-condition. Major damage to be detcted includes:

- fatigue and corrosion in metallic structures and
- delaminations, especially BVID, in composite structures

resulting either from material degradation (aging) or mishandling including misrepair.

Damage has to be detected, localized and monitored in accordance with damage tolerance design principles.

On-condition monitoring is closely related to in-flight monitoring. The major criterion for selecting the appropriate NDT procedures is therefore their in-flight applicability. Fig. 11 shows an overview of NDT procedures in respect to applicability for in-flight monitoring, degree of development, degree of monitoring and type of damage monitored.

Monitoring Qualities / Monitoring Technology	In-flight Applicability	Degree of Development	Loads	Damage Identification	Damage Propagation	Fatigue Crack	Impact (BVID)	Delamination	Corrosion
Visual/Boroscope	No	+				+			+
Strain	Yes	+	+			(+)			
Flight Parameters	Yes	+	+			(+)			
Magnetic Particle	No	+		+	+	+			
Eddy Current	No	+		+	+	+	(+)	(+)	
Penetrant	No	+		+	+	+		(+)	
Paintings	No	-		+			+		
Chem. Sensing	Yes	-		+					+
Radiography	No	+		+	+	+	+	+	+
Modal Analysis	Yes	+	+	+	+	+	+	+	?
Acoustic Emission	Yes	+	+	+	+	+	+	+	(+)
Holography	?	-		?	?	?	?	?	?
Ultrasonic	Yes	+		+	+	+	+	+	?
Shearography	?	-		?	?	?	?	?	?
Thermography	No	-		+	+	+	+	+	
Barkhausen Noise	?	-	?	?		?			?
Magneto Opt. Eddy Curr.	No	-		?	?	?			?
Comp. Aid. Tomography	No	-		+	+	+	?	?	?

Fig.11: Technology Selection for Health Monitoring Systems

The following NDT techniques turn out to show in-flight capability:

- strain
- flight parameters
- chemical sensing
- modal analysis
- acoustic emission and
- acousto ultrasonics.

When considering well established NDT procedures which is generally identical to a high degree of development chemical sensing might be excluded from the techniques mentioned before.

In-situ monitoring of damage is a further major criterion for an advanced aircraft health monitoring system which reduces the candidate NDT procedures to modal analysis, acoustic emission and acousto-ultrasonics. These latter procedures are also able to monitor various kinds of damage such as fatigue cracks, BVID, delamination or may be even corrosion. Depending on the kind and size of damage to be monitored these are the NDT procedures proposed to be considered in future health monitoring systems.

Sensor Selection

The three candidate NDT procedures modal analysis, acoustic emission and acousto-ultrasonics are all based on monitoring stress waves. The frequency of these stress waves range from a few Hz in modal analysis to 1 MHz in acoustic emission. Registration of these waves is performed either using an accelerometer (especially with modal analysis) or sensors based on either piezoelectric materials (ceramics or polymers) or optical fibres.

Traditionally acoustic emission and acousto ultrasonics testing has been performed using sensors made of piezoelectric ceramics. These sensors are highly sensitive and either work on a broad band or limited band/resonant basis. The working principle and different kinds of available sensors is well described in [14,27].

Recently work has been published using sensors made of polyvinylidene fluoride (PVDF) for either ultrasonics or acoustic emission application [28,29]. PVDF has a molecular conformation of fluorine atoms opposite to hydrogen atoms along a carbon backbone. Because of the strong electronegativity of fluorine, PVDF molecules possess a large dipole moment leading to piezoelectric properties after processing. PVDF processing includes electrical poling, unidirectional mechanical stretching and thermal treatment. The product obtained is a piezofilm with maximum in-plane displacement sensitivity in the stretched direction as well as some out-of-plane displacement sensitivities. The film can be tailored in its geometrical shape according to specific needs. Its sensitivity is satisfactory when monitoring composite materials. Advantages have to be seen in lower cost, lower mass, higher flexibility, wide-band frequency response and high internal damping.

A lot of development work has been spent in the past years in using fibre optics for health monitoring of engineering and especially aeronautical structures [30]. Major work has been reported in [31]. Optical fibres are mainly based on silicon but may even be made of sapphire when used in an ultra-high temperature environment (<2400^{0} C). To obtain satisfactory reliability of signals measured, optical fibres usually have to be integrated into the material. As this is especially feasible with composite materials, fibre optic sensors have been used in various examples for monitoring the curing process and/or damage induced by impact or overloads. A detailed description of fibre optics technology including its applicability to fibre optic smart structures is given in [32].

Fibre optic sensors have several advantages compared to electronic technology such as lightweight, all passive configurations, low power utilization, immunity to electromagnetic interfe-

rence, high sensibility and bandwidth, compatibility with optical data transmission and processing, long lifetimes and low cost (as long as using silicon fibres). Disadvantages exist with repairability as long as optical fibres have to be integrated into the material and placed according to major occuring stresses and strains to obtain reliable data. Furthermore a lot of effort has to be made to simplify optical signal transmission between or out of structural parts leading mainly in development of smaller, lower cost and less sensible optical signal clutches.

Summarizing the advantages and disadvantages of the three types of sensors leads to the following table:

Type of Sensor	Advantage	Disadvantage
Piezoceramic	Large Experience	Expensive; High Mass; No Flexibility
Piezopolymer	Low Cost; Low Mass; Flexibility; Wide-Band Frequency; High Internal Damping	Limited Experience; Low Temperature Stability
Optical Fibre	Electromagn. Immunity; Compatible to Optical Data Transmission; High Temp. Stability	Repairability; Signal Transfer Clutches; Need for Materials/ Structures Integration

The large effort performed in development of fibre optics technology as well as in improving performance of piezoelectric materials will certainly help to diminish the number of disadvantages mentioned above. It is therefore timely to consider the application and integration of these sensors into smart materials and structures especially under the aspect of structure health monitoring.

5 THE WAY AHEAD WITH SMART STRUCTURES TECHNOLOGY

Smart materials and structures technology has attracted increasing interest within the last ten years. This is mainly due to looking for new areas in materials research and the need for integrating highly developed areas of technology to smart structures or systems.

Smart structures technology is sometimes simply characterized to be the combination of structures or even materials with electronics. Looking at smart structures technology in more detail however leads to the conclusion that much more disciplines are included such as data processing and informatics, sensor technology, NDT, dynamics, chemistry, biomechanics and many others. It is therefore not astonishing when a lot of disciplines use the expression 'smart' for their techniques as soon as they have developed a strong interaction with other disciplines

and have proven that their technique includes at least two of the three elements sensor, controller and actuator mainly used for characterizing smart materials and structures.

Structure health monitoring systems is one of the candidate applications suitable for introducing smart structure technology [33]. In their actual stage structure health monitoring systems consist of sensors and sensor data processing and are limited to monitoring loads and evaluating damage. Technology however exists for in-situ monitoring of damage even though its applicability is still limited to on-ground inspection. Fig. 12 shows on the upper half the sequence of systems interacting during a conventional structure health monitoring process. The lower part of Fig. 12 shows how smart structures technology can help to make a health monitoring system smart.

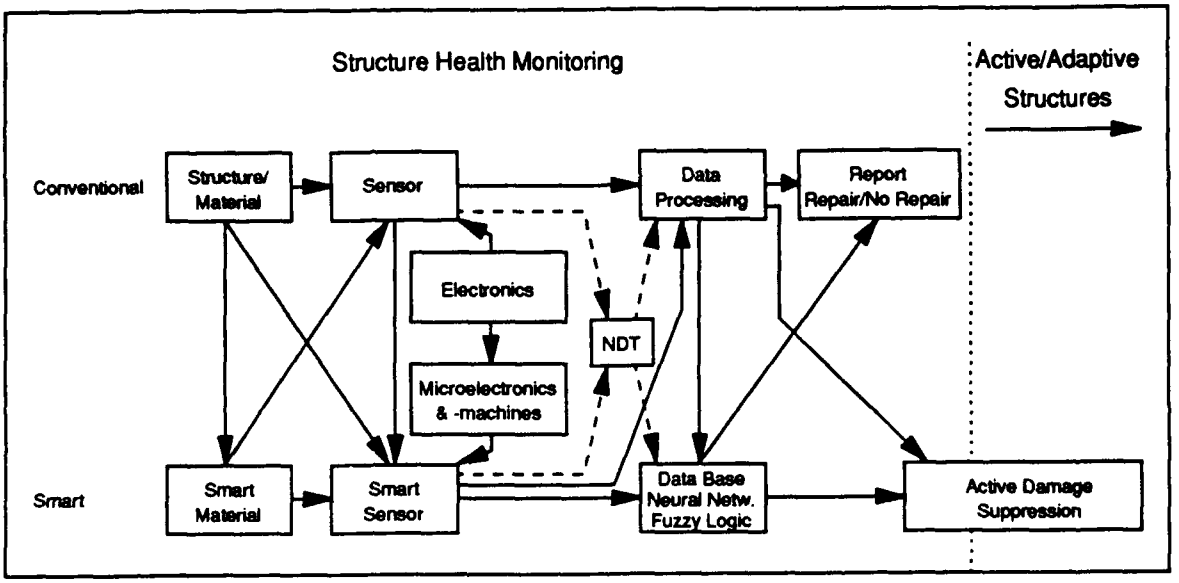

Fig.12: How Structure Health Monitoring Can Get Smarter

Smart health monitoring can be performed by using a smart material for structural components. This might not be the initial step for developing such a system but smart materials with intrinsic functions such as emitting specific noise or influencing magnetic or electric properties as a consequence of occuring damage is a large field worth to be considered. Such ideas have been recently reported in [34].

Another area which can highly contribute to smart systems is electronics and microsystems leading to miniaturized smart sensors with integrated data preprocessing, amplification or filtering capabilities [35].

Data processing or generally informatics is a large area with a high potential of development. Data bases have become very popular and well established for collecting, storing and analysis of very large quantities of data. Use of data bases is especially important when the damaging process is highly difficult to describe. An example is corrosion monitoring in aircraft structures where continuous registration of inspection results can help to predict or better even prevent corrosion. An area where data bases might also be used is pattern recognition.

Another recently emerging area in informatics is neural networks. Neural networks are adaptive information processing systems inspired by brain research. They are conceptually different to programmed computing and are used for sensor signal processing. Fig. 13 shows a schematic description of a neural network. The network is composed of different layers where each layer can contain several nodes. The nodes in the hidden layers represent activating functions while the connections from and to the hidden layers serve for transmission of the signal being either amplified, attenuated or inhibited by a weighting factor. These weighting factors have to be determined by training the neural network. Based on measured sensor signals of an input the network is then capable of identifying the condition of the structure with high probability. Detailed description on neural network technology can be found in [36]. Neural networks are highly useful when thinking of monitoring complex aircraft structures where a correlation between measured sensor signals and structural behaviour mainly turns out to be impossible by standard numerical means.

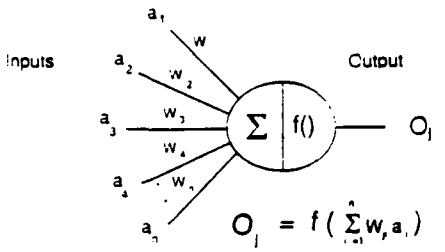

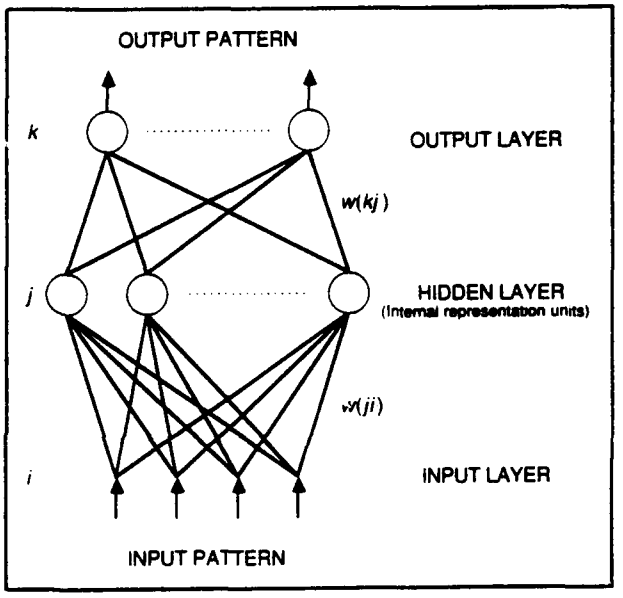

Fig.13: Schematic Description of a Neural Network [36]

A third technology within informatics science useful for smart structures is fuzzy logic. Fuzzy logic is the concept or method to take into account uncertainty and impreciseness in input data in mathematical models. There are three ways how to model this being based on:

a) stochastics as long as the given conditions characterizing the situation do not uniquely determine the result being expected,

b) interval mathematics when it is not exactly known what happened because of lack in in formation,

c) methods to find out the semantic contents of verbally expressed messages (e.g. tall person, low speed, high profit).

More detailed descriptions of fuzzy logic techniques are given in [37,38].

When trying to include fuzzy logic into aircraft health monitoring systems different applications are of interest. One application is to improve the estimation of structural behaviour by making better use of available sensor data. Another application is analysis of inspection reports where verbal notes can be included into an evaluation process (e.g. corrosion monitoring).

An aspect which even gives a smart health monitoring system an active component is active damage suppression. One example could be limiting flight manoeuvers after battle damage in military aircraft. Another example could be changing the geometrical shape of a structural part in the sense of active/adaptive structures to reduce or even stop damage propagation in damaged zones of the structure. A third example could be avoidance of acoustic fatigue by including active elements (e.g. piezoelectric actuators) into structural components.

These various options of making a structure health monitoring system smart including all technology available are certainly difficult to be realized in a short period of time. Some believe a fully smart aircraft structure capable of sensing damage over every square centimeter of its surface will not be available earlier than the year 2040 [39]. The authors'optinion is however that a smart health monitoring system could be delivered earlier on a lower technological but sill highly beneficial level if development would gradually follow a sequence of steps. Starting with a first step which includes decision of applied NDT procedure and sensors and demonstration of feasibility, each of the following steps equals the introduction of one or few of the smart structure technology options mentioned before. An example of such a sequence of steps can be as follows:

Step 1: Decide Kind of Damage to be Monitored

There are two kinds of materials mainly used in aircraft structures - metals and metal or polymer matrix composites. When ranking these kinds of materials in view of smart structures, composite materials should be favourized because of their better capability in integrating sensors or sensor functions and possibly even actuators. The most beneficial damage to be monitored is delaminations and here especially BVID.

Feasibility of such a system should be shown by simply bonding sensors on the surface of aircraft structural components. Electronics and data processing units should be taken "from the shelf" not considering any kind of miniaturisation. Examples being at this stage of development include those reported in [15-20] and a little more advanced in [26].

Step 2: Integration of Sensor Actuator into the Structural Material

There is a number of problems to be solved within this step which includes:

- Repair of Sensors and Actuators

If repairability is not possible low cost sensors/actuators have to be selected allowing to integrate more sensors/actuators into the structure for redundancy.

- Environmental Stability

Sensors/actuators have to withstand the curing process (temperature up to 180^{o} C, pressure up to 7 bar during 10 hours) in polymer matrix composites.

- Interface

It must be ascertained that strains are linearly and preferably fully transfered from the structure/actuator to the sensor/structure. This requires much care on the interface between sensor/actuator and the structure.

- Structural Integrity

It has to be proved that the integrated sensors/actuators do not affect structural integrity in respect of strength. If this occurs possibilities for miniaturisation and/or improved materials of sensors/actuators have to be identified.

Electronics and data processing units should be handled as described for step 1. Various examples in the area of fibre optics can be placed on this step of development where a very interesting example for aircraft applications is given in [30].

Step 3: Miniaturization

This step should include miniaturization of electronics and data processing units as far as possible using microelectronics and micromachines and placing them close to the sensor/actuator. Data preprocessing should be performed close to the sensor using smart sensors. Electrical signals should be converted to optical signals to minimize EMI problems. As a result of this miniaturization and structure-integrated electronics the following requirements should be fulfilled:

- Electronic components, wires, sensors and actuators should not increase structural weight when compared to the original structure.
- The smart health monitoring system should not lead to a reduction in aircraft reliability and lead to reduced inspection cost.
- Structure integrated electronics should consider the problems already mentioned with sensors/actuators under step 2.

Step 4: Use of Advanced Data Processing Techniques

Data bases for structure health monitoring purposes can be used for storing signal patterns resulting from acoustic emission signals, vibration modes, loads, temperatures or any other parameter. These data bases can then be used for pattern recognition purposes.

Neural networks as described above will be applied for monitoring a structural component in real time even with uncomplete data.

Fuzzy logic will be implemented either in a main data processing unit or even in microprocessors close to or integrated into smart sensors.

Summarizing data base, neural networks and fuzzy logic technique can finally lead to an artificial intelligence system ready for use in a smart structure health monitoring system.

Step 5: Second Generation of Miniaturization

This is certainly the most far reaching step. It includes the introduction of smart materials with intrinsic sensor and actuator functions on a molecular basis. It is difficult to mention requirements for or problems with these materials at this stage because development in the area of this kind of materials has just started.

In addition to these steps there are some further aspects to be considered. All smart structure technology applied within these steps has to leave the laboratory stage. It has to be applied to real aeronautical structures with geometrical discontinuities, tested in-flight and qualified for

airworthiness. This requires a significant amount of development work and time. It is therefore advisable to concentrate smart structure health monitoring on components with high inspection cost.

6 CONCLUSION

It is unquestioned that aircraft structure health monitoring is of significant importance in respect of direct operating or life cycle cost. Existing loads monitoring systems are a first step to monitor if aircraft have flown according to their design load-spectra or not. The output of such systems can lead to either shorter or longer inspection intervals.

Actual security factors in aircraft design take into account scatter in materials properties as well as lack in knowledge of damage behaviour, the latter being especially related to composite materials. One of the major objectives with smart health monitoring systems is to improve detection of damage leading to an increase in security factor or in other words allowing to reduce overdesign and saving weight without change in the initial security factor. It therefore seems highly promising to start with developing smart health monitoring systems for composite structures where damage is monitored in-situ and on-board the aircraft. Candidate NDT procedures are modal analysis, acoustic emission and acousto-ultrasonics.

Even though smart structures technology which includes materials science, electronics, microsystems and informatics is still in an early stage of development it is already timely to consider this technology in the field of practical application such as structure health monitoring systems. A gradual (stepwise) change from existing loads monitoring to smart health monitoring systems seems to be the best way for introducing smart structures technology in short term. This can well be achieved by a fruitfull cooperation of people, sciences, organisations and nations being the major driving force for research and development.

REFERENCES

[1] Houlihan G., "Corrosion Control for an Aging Fleet", Sympos. Proc.: Aerospace Corrosion Control, Sawell Publ. Ltd., March 1992, Paper 3

[2] Kinzie R.C., "The Cost of USAF Corrosion Maintenance", Sympos. Proc.: Aerospace Corrosion Control, Sawell Publ. Ltd., March 1992, Paper 8

[3] Thorbeck J., "Economical View on Composite Structures Maintenance", in: Kwakernaak A., van Arkel L. (Eds.)"Advanced Materials: CostEffectiveness, Quality Control, Health and Environment", SAMPE/Elsevier, 1991, pp. 323- 335

[4] Spragg D., Ganguli U., Thamburaj R., Hillel H., Cue R.W., "The Role of Inflight Engine Condition Monitoring on Life Cycle Management of CF-18/F404 Engine Components", AGARD R-770, April 1989, Paper 4

[5] Haberding R., "Schwingungsüberwachung an Turboflugtriebwerken am Beispiel des Airbus A310", VDI-Berichte 568, November 1985, pp. 167-181

[6] Achenbach J.D., Thompson D.O., "Towards Quantitative Non-Destructive Evaluation of Aging Aircraft", in: S.N. Atluri, S.G. Sampath, P. Tong (Eds.), "Structural Integrity of Aging Airplanes", 1991, pp. 1-13

[7] "Fatigue Management", AGARD-CP-506, April 1991
[8] Amabile P., Giacobbe T., "Proposal for the New Fatigue Management System for the AMX", AGARD-CP-506, April 1991, Paper 9
[9] Ladda V., Meyer H.-J., "The Operational Loads Monitoring System OLMS", AGARD-CP-506, April 1991, Paper 15
[10] Bauer W., "Event Monitoring Functions Introduced by the Onboard Life Monitoring System (OLMOS) into a German Aircraft", DFVLR-Mitt. 88-04, September 1987, pp. 131-154
[11] Krauß A., "Betriebslastenermittlung fuer Flugzeugentwurf und -entwicklung", 14. Vortragsveranstaltung DVM-AK Betriebsfestigkeit, 1988
[12] Boller Chr., Heuler P., Seeger T., Buxbaum O., Oppermann H., Köbler H.-G., Schütz D., "Vergleich der Lebensdauervorhersage nach dem Kerbgrundkonzept und dem Nennspannungskonzept", Fachgebiet Werkstoffmechanik, TH Darmstadt, Report FD-5/1983
[13] Simpson D.L. (Ed.), Minutes of 20th ICAF, June 1987, p. 5/23
[14] Miller R.K., McIntire P (Eds.), "Nondestructive Testing Handbook", 2nd. Ed., Vol. 5"Acoustic Emission Testing", 1987, Amer. Soc. for Nondestruct. Testing
[15] Bailey C.D., "Acoustic Emission for In-Flight Monitoring on Aircraft Structures", Matrials Evaluation, Vol. 34, No. 8, 1976, pp. 165-171
[16] Scala C.M., "A Semi-Adaptive Approach to In-Flight Monitoring Using Acoustic Emission", in Proc. of: Review of Progress in Quantitative NDE, San Diego, August 1986, pp. 361-369
[17] Carlyle J.M., "Acoustic Emission Testing the F-111", NDT International, Vol. 22, No. 2, April 1989, pp. 67-73
[18] Fotos C.P., "Acoustic Emission Technique Tests Aircraft Integrity", Aviation Week & Space Technology, August 28, 1989, p. 76
[19] McBride S.L., Pollard M.D., MacPhail, Bowman P.S., Peters D.T., "Acoustic Emission Detection of Crack Presence and Crack Advance During Flight", AGARD-CP-462, October 1989, Paper 16
[20] McBride S., Viner M., Pollard M., "Acoustic Emission Monitoring of a Ground Durability and Damage Tolerance Test", in: Thompson D.O., Chimenti D.E., "Review of Progress in Quantitative Nondestructive Evaluation, Vol.10B", Plenum Press, 1991, pp. 1913-1919
[21] Vary A., Lark R.F.,"Correlations of Fiber Composite Tensile Strength with the Ultrasonic Stress Wave Factor", Journal of Testing and Evaluation, 1979, pp. 185-191
[22] Hillger W., Block J., "Ultraschall- und Schallemissionsprüftechnik zur zerstörungsfreien Schadensanalyse an CFK-Proben", Zeitschr. f. Flugwiss. u. Weltraumforschung 10, 1986, Heft 4, pp. 273-280
[23] Pandey A.K., Biswas M., Samman M.M., "Damage Detection from Changes in Curvature Mode Shapes", Journal of Sound and Vibration, 1991, pp. 321-332
[24] Tracy J.J., Pardoen G.C., "Effect of Delamination on the Natural frequencies of Composite Laminates", J. of Composite Material, Vol. 23, D ecember 1989, pp. 1200-1215
[25] Boller Chr., "Behaviour of Natural Frequencies of Modes I to X in a Delaminated Beam", 1992, unpublished
[26] Hickman G.A., Gerardi J.J., Feng Y., "Application of Smart Structures to Aircraft Health Monitoring", J. of Intell. Mater. Syst. and Struct., Vol. 2, July 1991, pp. 411-430

[27] Becht J., Fischer T., Heide W., "Messtechnische Grundlagen", in: "Schallemission - Grundlagen und Anwendungen einer neuen Pruefmethode", Battelle-Inst. e.V., Frankfurt/M.

[28] Stiffler R., Henneke II E.G., "The Application of Polyvinylidene Fluoride as an Acoustic Emission Transducer for Fibrous Composite Materials", Materials Evaluation, July 1983, pp. 956-960

[29] Brown L.F., Brown R.H., "Permanently Mounted Piezo Film Sensors for Structural Quantitative NDE", in: 1990 Review of Progress in Quantitative NDE, July 1990

[30] Glossop N.D., Dubois S., Tsaw W., LeBlanc M., Lymer J., Measures R.M., Tennyson R.C., "Optical Fiber Damage Detection for an Aircraft Composite Leading Edge", Composites, Vol. 21, 1990, pp. 71-80

[31] Fibre Optic Smart Structures and Skins I-V, SPIE Vol. 986 (1988), SPIE Vol. 1170 (1989), SPIE Vol. 1370 (1990), SPIE Vol. 1588 (1991), SPIE Vol. 1798 (1992)

[32] Udd E. (Ed.), "Fiber Optic Sensors", John Wiley & Sons, New York, 1991

[33] Schmidt W., Boller Chr., "Smart Structures - A Technology for Next Generation Aircraft", This volume

[34] Neelakanta P.S., Subramaniam K., "Controlling the Properties of Electromagnetic Composites", Advanced Materials & Processes 3/92, 1992, pp. 20-25

[35] Schoess J.N., Sullivan C.T., "Conformal Acoustic Waveguide Technology for Smart Aerospace Structures", in: B. Culshaw, P.T. Gardiner, A. McDonach (Eds.), 1st European Conf. on Smart Structures and Materials, Glasgow, 1992, SPIE Vol. 1777, pp. 131-134

[36] Pao Y.H., "Adaptive Pattern Recognition and Neural Networks", Addison-Wesley Publ., Reading Mass., 1989

[37] Bandemer H., Gottwald S., "Einfuehrung in FUZZY-Methoden", 3. Aufl., Akademie-Verlag, Berlin, 1992

[38] Kandel A., "Fuzzy Mathematical Techniques with Applications", Addison-Wesley Publ. Comp., Reading Mass., 1986

[39] Sweetmann B., "Why Composites Wait in the Wings", Interavia Aerospace Review, April 1992, pp. 48-53

STRUCTURAL HEALTH MONITORING USING EMBEDDED FIBRE OPTIC SENSORS

by

Dr P.A. Tutton and **Dr F.M. Underwood**
British Aerospace
Richmond Road
Kingston-upon-Thames
Surrey KT2 5QS
United Kingdom

Abstract

Structural health monitoring on military aircraft is currently carried out via strain gauges attached to the surface of the aircraft structure. A parametric system based exclusively on flight parameters is being developed for use on EFA. Both of these systems monitor the airframe fatigue life.

With the emergence of Smart Structures technology a new method of structural health monitoring is feasible that has perceived advantages over the current technology. This paper describes how fibre optics embedded within a composite laminate can be used to monitor strains within the aircraft structure, and hence its fatigue life. Embedded fibre optics can be used to monitor sustained damage - battle or low velocity impact damage, give a full flight history and, with diagnostic capability, unconditioned maintenance would be available.

1.0 Introduction

Current structural health monitoring on combat aircraft covers fatigue monitoring and flight envelope exceedance monitoring. Generally the monitoring is carried out using a fatigue meter located close to the CG of the aircraft, and analysis carried out after the flight. Newer techniques involve using a strain gauge system, originally with recorded data, but now moving towards 'real time' processing during flight. The aim is to progress towards a fleetwide monitoring system.

In 1978 Butter and Hocker published details of a fibre optic strain gauge [1], which formed the basis of a new measuring technique that has been adopted by a number of engineering disciplines. The research that has been carried out since 1978 shows that 'real time' strain monitoring with fibre optics is feasible, and in addition, fibre optics have been shown to measure strain when embedded in composite laminates. Combining these two factors there is the potential to use embedded fibre optics as a structural health monitoring system.

This paper describes current fatigue monitoring techniques, referencing systems used on Tornado, Harrier and the proposed parametric Structural Health Monitoring (SHM) system for EFA. A review of fibre optic sensors is undertaken, and how these can be used for monitoring the strains within an aircraft structure. Finally the use of fibre optics for damage assessment purposes and inspection techniques is discussed.

2.0 Current Structural Health Monitoring Techniques

Structural health monitoring of aircraft is carried out in order to give the user knowledge of fatigue loadings on the structure, which could lead to an increased service life, or increased safety. This is particularly true for envelope exceedance monitoring.

As mentioned above, the common method of fatigue monitoring is by recording data from a 'g' meter, located near the centre of gravity of the aircraft. This data is analysed on the ground after the flight and the fatigue life and damage calculated at this point. The drawbacks of this system are that only the structure using parameters directly related to vertical 'g' can be monitored. However the system is cost effective and reliable, and with a few exceptions (two particular cases are reviewed in Section 2.1 below), has proved sufficient. With the advances in microprocessors and strain gauges in recent years it has been possible to re-examine fatigue monitoring, and Sections 2.2-2.4 discusses how these advances have led to new types of structural health monitoring on Tornado, Harrier, and the proposed monitoring system for EFA.

2.1 Fatigue Monitoring of Jaguar and Jet Provost

Following the completion of the Jaguar fatigue test, cracks were discovered in the main fin to fuselage attachment frame. The base requirement for the Jaguar had been fulfilled, but subsequently there was a requirement for an extended fatigue life. To achieve this a limited fatigue monitoring exercise was undertaken [2]. Two aircraft were monitored using three strain gauge bridges, true airspeed and altitude. The three gauges were mounted to measure the fin shear and torque, and the fuselage frame end loads at the fin centre spar position. The aircraft was then calibrated (loads and electrical) and returned to the RAF. The data was analysed by BAe and showed the primary fatigue loading was due to atmospheric turbulence at low levels. They also were able to determine a seasonal effect, with highest damage occurring over the winter months. This resulted in more efficient fleet management.

Monitoring of the Jet Provost was carried out using a fatigue meter, flying log and mission profile data. This method proved sufficient for 22 years, when an incident (failure of the fin spar booms and web) occurred which highlighted the need for empennage monitoring [2]. Strain gauge bridges were used to monitor fin and tailplane loading and transducers were used to monitor altitude, airspeed, normal and lateral acceleration. The results showed that actual fin loading was more severe than estimated, and highlighted the need for a more comprehensive fatigue monitoring system.

2.2 Structural Usage Monitoring System (SUMS)

In order to give an improved knowledge of operational fatigue loading and its' effect on the aircraft fatigue life, an extensive fatigue monitoring system was installed on a number of Tornado aircraft [3]. Ten aircraft were allocated from the fleet, six Strike and four trainer aircraft. 67 strain gauge bridges, sampled at 512 samples per second (sps), are used to monitor 18 loading actions, (see Figure 1), as described below :

- o wing bending moment at four stations
- o wing shear at three stations
- o wing torsion at three stations
- o fin and taileron root shear force, bending moment and torsion
- o front and rear fuselage vertical bending moment

The recorded data is analysed by BAe and gives comparisons between fatigue meter data and strain gauges; hot spot strain histories are compared with gauges mounted on the MAFT (main airframe fatigue test); and the damage per flight load given by time-history traces are compared with those calculated from the fatigue meter. This information is used by the customer to improve fleet management of the Tornado.

2.3 Fatigue Monitoring and Computer System (FMCS)

Developed for fleetwide use on the Harrier GR7, it is an updated version of SUMS. There are sixteen bridges that monitor the loads on the wing pick-ups, fuselage, fin, tailplane and wing. Data is sampled at 2000sps and analysed during flight. An example of this is damage, pylon status, position and status of airbrake, flaps, and nozzles. Envelope exceedance is also monitored and raw flight data recorded for operational load measurement.

The cost of development of the system has been high, but lifecycle costs will be reduced significantly by processing the information during the flight and carrying out the necessary life calculations to automatically produce fatigue index values and supplementary information after the flight.

2.4 Parametric System

One of the systems, for use on EFA, is based exclusively on flight parameters to calculate structural loads in real-time and in turn fatigue data (see Figure 2). The damage is monitored at ten locations on the airframe, similar to those mentioned for Tornado and Harrier. In addition to fatigue monitoring, the following are monitored:

- o g and roll rate
- o Altitude cycling monitoring
- o Buffet monitoring
- o Event monitoring

and calculations include determining the total stress at each of the monitoring locations, detection of turning points, envelope monitoring, damage calculations (including cumulative damage from first flight) and the frequency of occurrence matrix.

As can be seen SHM has advanced considerably since the monitoring of the Jaguar and Jet Provost. To replace these systems with a fibre optic sensing system capable of SHM there must be the potential to give equivalent returns.

3.0 Fibre Optic Sensing Techniques

Since Smart Structures has emerged as a technology there has been a considerable amount of discussion concerning the potential of using fibre optics, adaptable materials and conformal arrays to create a stealthy, adaptive, 'thinking' aircraft. This maybe possible in the 21st Century, but there are some shorter term realisable gains, such as using fibre optics embedded within (or surface mounted on) a structure to form a sensing system for damage assessment, strain monitoring and envelope exceedance.

3.1 The Building Blocks

In order to be able to install a structural health monitoring system in an aircraft there are certain building blocks that have to be put in place. This paper will not discuss each one in detail, but will highlight each area in order to give an overview. To cover all aspects the case of a fibre optic sensing system embedded within a composite structure will be taken.

3.1.1 Fibre Optic Sensors

There are currently a number of fibre optic strain sensors that are commercially available and manufactured specifically for use within composite materials. They come from a class of sensor known as interferometers which are extremely sensitive and are therefore ideal for measuring relatively small changes in strain such as those experienced within an aircraft structure. The principal of interferometers is to sense a change in phase within the fibre which is caused by some external perturbation. Common types of interferometers are :

- Mach-Zehnder
- Michelson
- Fabry-Perot
- Bragg Gratings

Other types of fibre optic sensors available are:

- Twin Core, and
- Polarimetric

The majority of these sensors are point sensors, although quasi-distributed sensors can be manufactured by engineering a number of sensors along the same length of fibre optic [4] (see Figure 3). It is assumed that this type of sensor will be used for strain monitoring within a structure,as discussed in Section 3.2 below.

3.1.2 Manufacturing

A number of components have to be taken into account within this section, and they are listed briefly below:

- The laying in of the fibre optic has to be done accurately, especially if the fibre optics are laid down in a pattern to sense directional strain and / or damage. The simplest solution to this

is automation, although this will in turn mean a considerable capital outlay.

- To accurately determine the position (laterally and vertically) of the fibre optics within the laminate sophisticated NDT techniques have to be employed.

- Techniques have to be developed to ensure that the fibre optics withstood the rigours of manufacture because fibre optic breakage would be unacceptable.

3.1.3 Connectors and Multiplexing

For any type of sensing system, be it optical or not, the connection from the laminate to the outside environment has to be examined in great detail. It must be capable of integrating into the laminate without degrading the properties of the structure and in addition it must be capable of withstanding production, test, assembly and finally a service life of thirty years!

Multiplexing or de-multiplexing must consider this possibility - ten fibre optics being brought out of one connector, five sensors per fibre optic, which would mean information from fifty sensors being handled at any one point in time.

3.1.4 Data Processing

There are a number of fields of thought on the types of data processing that will be required for a complete SHM system. There will be a large amount of data output from the sensors, and this could lend itself to neural networking or data transfusion and various computational techniques. It should be pointed that out that current space available within military aircraft is limited and therefore any system chosen should integrate into the architecture already there.

However, with the move from 'fly-by-wire' to 'fly-by-light' systems within future military aircraft, utilising fibre optics as sensors has particular attraction.

3.2 Strain Monitoring

There are certain advantages that are apparent from using fibre optics, namely:

- they can cover a greater area of the structure
- they are not prone to electrical interference
- because they are embedded they are not prone to accidental damage.

The main disadvantage is that it is unlikely that fibre optics will be repairable, and so the design and redundancy aspect has to be examined. In addition, a detailed calibration of a fibre optic sensing system would be

required. Since the constraints of an aircraft production run will only allow a limited number of aircraft to undergo a detailed calibration, the output of the optical gauges should be controllable and subject to minimum scatter.

To implement a SHM system on an aircraft using fibre optics as strain sensors would need a combination of both surface mounted and embedded sensors. At present, composite components such as a wing, are not monitored because of their reduced susceptibility to fatigue damage. Flight loads are monitored, and this is done by attaching strain gauges to the metallic components within a wing (ie spars) because of the inherent problems of gauging composite structures (bonding and strain distribution through composites). Using embedded fibre optics would enable the flight loads to be taken directly from the composite structure, and by covering a greater area more data could be obtained or the loading spectrum at different positions on the structure could be examined.

It would still be necessary to monitor metallic components for fatigue damage, and this could be done by surface mounting fibre optic strain sensors, or using transfer functions to read across from adjoining composite structures.

An example of how fibre optics would be laid into a wing structure to monitor strains can be seen in Figure 4. Sampling rates should be in the region of 550sps, and so the interrogation equipment must be able to handle the amount of data this will create.

3.3 Damage Assessment

Combined with a strain monitoring system, a damage assessment system will take the form of a grid or pattern laid through the laminate. The fibres must be able to sense typical in-service damage levels which could be done two ways - using fibre optics to sense delamination, or using the simple light / no-light approach. Figure 5 shows a possible damage detection system embedded within a taileron structure.

3.4 Unconditioned Maintenance

This refers to a novel inspection technique that would reduce some of the inspection times and highlight problem areas. The idea is to have a 'plug-in' type system linked to a network of fibre optics that would be used on the ground at service intervals, and so reduce the amount of visual inspection required. The system could also highlight areas of damage on the inner surface, that would not be detected otherwise unless a full NDT of the structure was carried out.

4.0 Concluding Remarks

Structural health monitoring has progressed significantly since monitoring of the Jet Provost. The most recently designed systems are capable of monitoring up to sixteen locations, and processing the information in 'real-time' to give the fatigue life of the aircraft, the damage incurred, operational load measurement and envelope exceedance. This all leads to more efficient fleet management and enhanced operational safety.

Fibre optics have the potential to be used to monitor the structure, both for strains and damage, and have a number of advantages over current systems. The ability to cover a greater area will give increased knowledge of the structure, and this can be combined with a comprehensive system to monitor damage so that repairs can be carried out at the earliest opportunity. It is these advantages over the current systems that make the use of fibre optics sensors attractive.

5.0 References

1. C D Butter, G B Hocker, 'Fiber Optic Strain Gauge', Applied Optics, Sept. 1978, Vol 17, No 18.
2. A P Ward, 'Experiences obtained from Service Fatigue Monitoring Exercises', Paper 8, AGARD Operational Loads Data Specialists Meeting, Sienna, Italy, 1984.
3. A P Ward, 'Tornado - Structural Usage Monitoring System', Paper 16, AGARD Operational Loads Data Specialists Meeting, Sienna, Italy, 1984.
4. R M Measures, 'Smart Structures with Nerves of Glass', Progress in Aerospace Sciences, Vol 26, No 4.

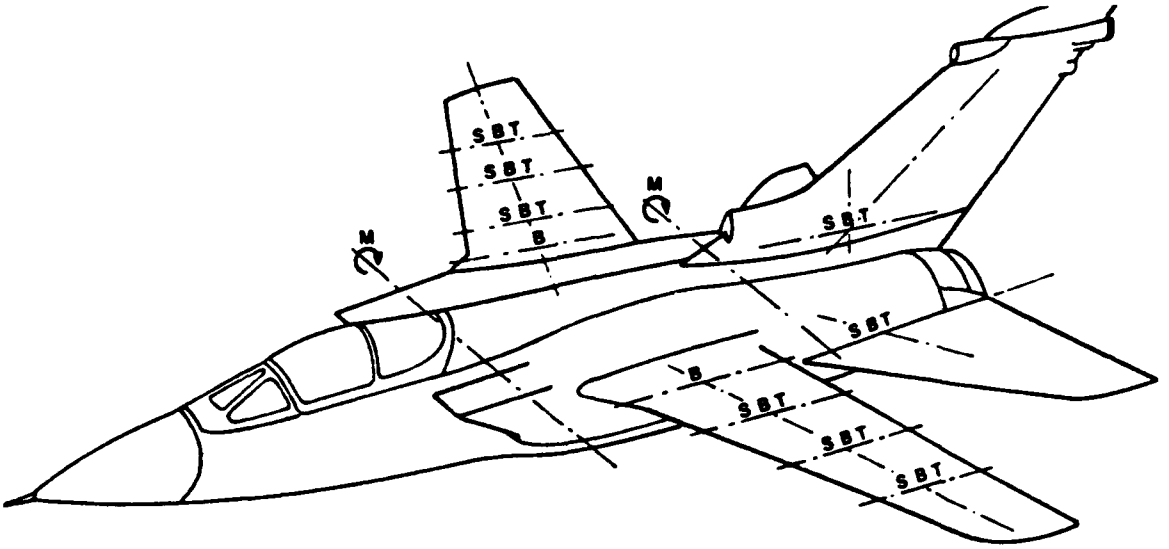

S Shear
B Bending Moment
T Torsion
M Fuselage Vertical Bending

Load Monitoring Stations (3)

Figure 1

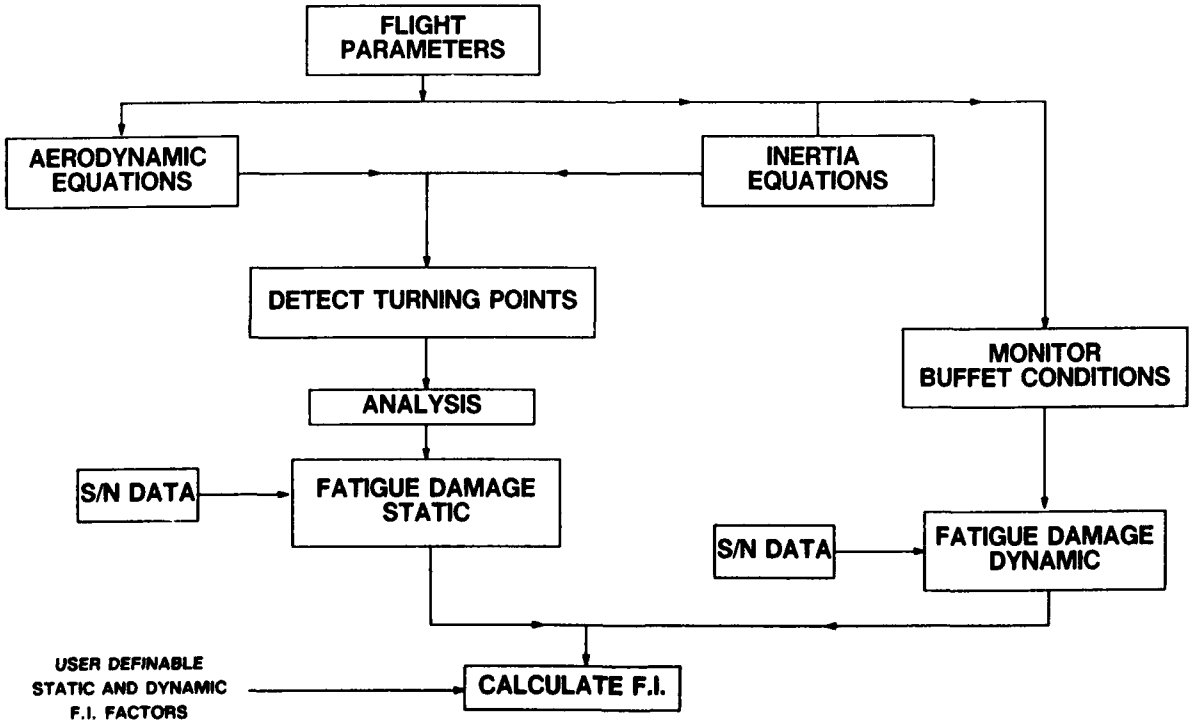

Overview of Parametric System

Figure 2

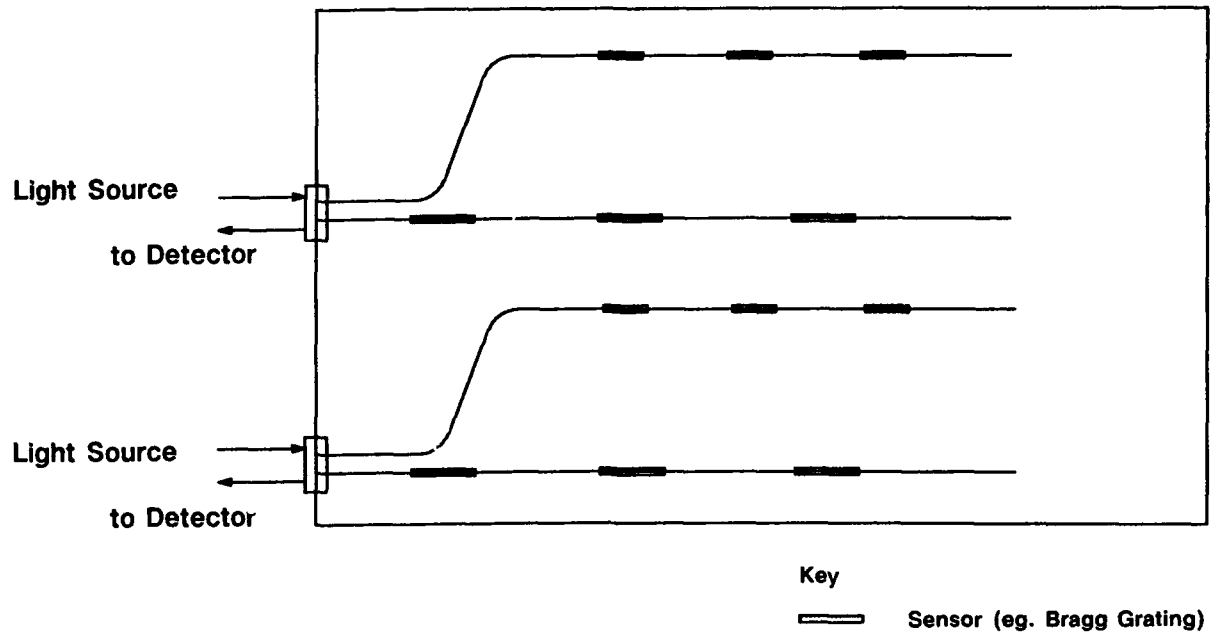

Example of a Quasi-Distributed Sensor System

Figure 3

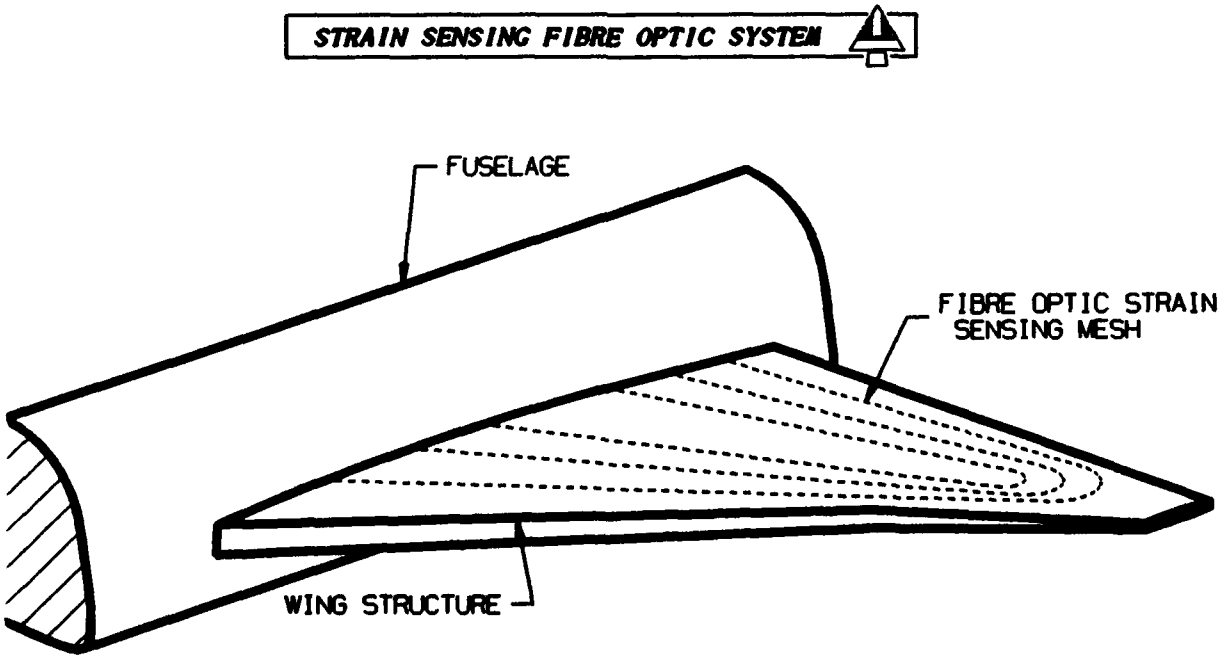

Figure 4

FIBRE OPTIC DAMAGE DETECTION SYSTEM

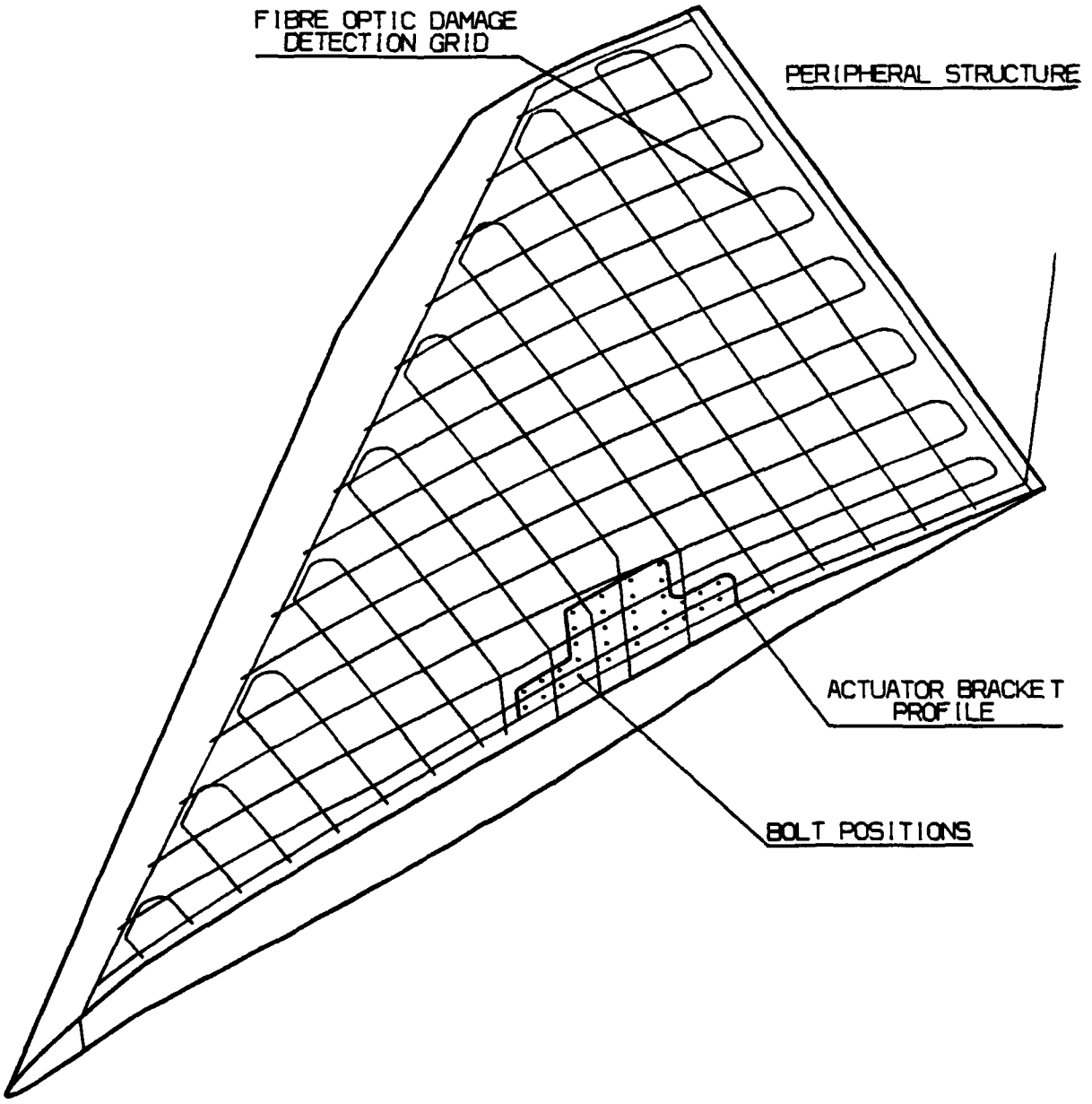

Figure 5

FAULT LOCATION IN STRUCTURES USING NEURAL NETWORKS

by

K. Worden, A.D. Ball and G.R. Tomlinson
Dynamics Research Group
Department of Engineering
University of Manchester
Simon Building, Oxford Road
Manchester M13 9PL
United Kingdom

Abstract

A neural network is trained to report the position of a fault in a framework structure. It is shown that a network trained on data from Finite Element simulation of the structure can successfully locate faults in the framework itself.

Nomenclature

J	:	Network error function
f	:	Node transfer function
w_{ij}	:	*Connection weight from i to j*
x_i	:	Output from node i in a layer
y_i	:	i^{th} desired output
$\hat{y}_i$	:	i^{th} network output
z_i	:	Activation for node i
α	:	Network momentum coefficient
η	:	Network learning coefficient
θ_i	:	Network parameters
δ_i	;	Error at output i

1 Introduction

The problem of fault detection or location on the basis of measured data is essentially one of pattern recognition; data from an undamaged system must be distinguishable from data from a system with a fault. In traditional approaches to pattern recognition, a significant amount of preprocessing may be necessary; appropriate 'features' must be extracted from the raw measured data which allow the separation of data sets into meaningful disjoint classes. Determination of the appropriate features can be regarded as the fundamental problem. Neural networks have recently been established as a powerful aid to pattern recognition, in that they offer the possibility of bypassing the explicit feature extraction by allowing the formation of internal representations of classes within the network when trained on raw measured data [10].

In the area of fault detection and location, pattern recognition techniques have been pursued for some time, many based on the approach of Cawley and Adams [4] who considered the natural

frequencies of a system to be a reliable indicator of fault presence and location; a recent example of this approach is [9]. Only recently have neural networks attracted attention as a possible technique for fault detection. Wu *et al* [13] demonstrate a damage detecting network trained on measured Frequency Response Functions (FRF's) from the system. In both these cases a basic Multi-Layer Perceptron (MLP) network was used with the backpropagation method of training. An interesting approach to signal classification is reported in the work of Barschdorff and Bothe [1] [2], where a self-organising network is used which has much faster convergence properties than backpropagation; the network used shows strong similarities with the Radial Basis Function networks of Chen and Billings [5]. A neural network approach to fault detection via the classification of nonlinear systems is demonstrated in [11] and [12].

The present study is motivated by the work of Kudva *et al* [6] who showed that a neural network can be used to locate and quantify damage in a plate structure, the network was trained on strain data for various locations on the structure obtained from finite-element analysis. In order to facilitate understanding of the network techniques a simpler structure was adopted here. The use of a framework structure allows the problem of fault location to be reduced to a discrete one. The work of Kudva *et al* is extended in that a network trained on Finite Element data is shown to successfully locate faults in an experimental structure.

2 The Multi-Layer Perceptron (MCP)

The neural network paradigm used here is the Multi-Layer Perceptron (MLP). For the sake of completeness, a brief description of the MLP is given here; for a more detailed discussion, the reader is referred to [3] or the seminal work [8].

The MLP is simply a collection of connected processing elements called *nodes* arranged together in layers (Figure 1). A set of signal values pass into the *input layer* nodes, progress forward through the network *hidden layers* and the result finally emerges through the *output layer*. Each node i is connected to each node j in the preceding and following layers through a connection of weight w_{ij}. Signals pass through the node as follows: a weighted sum is performed at i of all the signals x_j from the preceding layer, giving the excitation z_i of the node; this is then passed through a nonlinear *activation function* f to emerge as the output of the node x_i to the next layer i.e.

$$x_{i+1} = f(\sum_j w_{ij} x_i)$$

Various choices for the function f are possible, the one adopted here is the hyperbolic tangent function $f(x) = \tanh(x)$. One node of the network, the *bias* node is special in that it is connected to all other nodes in the hidden and output layers, the output of the bias node is held constant throughout in order to allow constant offsets in the excitations z_i of each node.

The first stage of using a network to model an input-output system is to establish the appropriate values for the connection weights w_{ij}. This is the *training* or *learning* phase. The type of training adopted here is a form of *supervised* learning and makes use of a set of network

inputs for which the desired network outputs are known. At each training step, a set of inputs are passed forward through the network yielding trial outputs which are then compared to the desired outputs. If the comparison error is considered small enough, the weights are not adjusted. If however a significant error is obtained, the error is passed *backwards* through the net and a *training algorithm* uses the error to adjust the connection weights. The algorithm used in this work is the *backpropagation* algorithm which can be summed up briefly as follows. For each presentation of a training set, a measure J of the network error is evaluated where

$$J(t) = \frac{1}{2}\sum_{j=1}^{n^{(l)}}(y_i(t) - \hat{y}_i(t))^2$$

and $n^{(l)}$ is the number of output layer nodes. J is implicitly a function of the network parameters $J = J(\theta_1, \ldots, \theta_n)$ where the θ_i are the connection weights ordered in some way. The integer t labels the presentation order of the training sets After a presentation of a training set, the standard steepest descent algorithm requires an adjustment of the parameters

$$\triangle\theta_i = -\eta\frac{\partial J}{\partial\theta_i} = -\eta\nabla_i J$$

where ∇_i is the gradient operator in the parameter space. The parameter η determines how large a step is made in the direction of steepest descent and therefore how quickly the optimum parameters are obtained. For this reason η is called the learning coefficient. Detailed analysis [11] gives the update rule after the presentation of a training set

$$w_{ij}^{(m)}(t) = w_{ij}^{(m)}(t-1) + \eta\delta_i^{(m)}(t)x_j^{(m-1)}(t)$$

where $\delta_i^{(m)}$ is the error in the output of the i^{th} node in layer m. This error is not known *a priori* but must be constructed from the known errors $\delta_i^{(l)} = y_i - \hat{y}_i$ at the output layer. This is the source of the name backpropagation, the weights must be adjusted layer by layer moving backwards from the output layer.

There is little guidance in the literature as to what the learning coefficient η should be; if it is taken too small, convergence to the correct parameters may take an extremely long time. However, if η is made large, learning is much more rapid but the parameters may diverge or oscillate. One way around this problem is to introduce a *momentum* term into the update rule so that previous updates persist for a while, i.e.

$$\triangle w_{ij}^{(m)}(t) = \eta\delta_i^{(m)}(t)x_j^{(m-1)}(t) + \alpha\triangle w_{ij}^{(m)}(t-1)$$

where α is termed the momentumi coefficient. The effect of this additional term is to damp out high frequency variations in the backpropagated error signal. The variant of the algorithm used for network training throughout this paper makes use of a momentum term.

Once the comparison error is reduced to an acceptable level over the whole training set, the training phase ends and the network is established. The networks used for this study were

designed and trained using the NeuralWorks Professional II package produced by NeuralWare Ltd [7].

3 The Framework Structure

The experimental structure (Figure 2), was an essentially two-dimensional cantilever latticework, mounted rigidly to a support at one end with its major axis horizontal and minor axis vertical, and measuring approximately 1m x 0.25m. The lattice was comprised in total of nineteen members, arranged into four equally-sized cross-braced square bays. Each member was made from 1" x 1/4" aluminium strip, and all joints were overlapped and pinned with shanked silver steel bolts in reamed holes. The overlapping of members was arranged to minimise the third dimension of the structure, and spacers were used where necessary.

Strain gauges were attached axially at mid-span to both sides of all the horizontal and vertical members, totalling twenty-four gauges in all. Arrangement was made for the readings from gauges on opposite sides of the same member to be averaged to eliminate the effects of bending and twisting in the third (horizontal) dimension.

The structure was loaded via a stirrup hanger and weight pan which could be attached to any of the eight pin joints. Throughout the experimental procedure, a pre-load of 5kg was applied to the lower of the two pin joints most distant from the support.

With all cross members in place, three loads of 10, 20 and 30kg were applied consecutively to each of the eight pin joints. For each load case, the averaged reading (in microstrains) from each strain gauge pair was recorded (twelve readings in all). This resulted in a reference data set describing the strains in the structure with all cross members intact. The measurement procedure was then repeated for the twenty-four load cases with each of the cross members removed in turn, resulting in a further eight data sets describing the strains in the structure with a differing cross member removed. In all cases, the readings from the strain gauges were adjusted to give zero for the preloaded structure before the application of the loads.

4 Finite Element Data

A Finite Element (FE) simulation of the framework was established using the package LUSAS. Removal of a member was simulated by giving a very low Young's modulus for that member i.e. a value of 1 Nmm^{-2} was used compared to 70000 Nmm^{-2} for the 'intact' members. A UNIX shell script was used to automate the running of the LUSAS program for all the required fault conditions and load cases. For each fault condition, a 'background' strain pattern was obtained for the framework subjected only to the preload. These background strains were then removed from each of the data sets in order to model the fact that the experimental strain gauges were set to read zero in the preloaded configuration.

A comparison between the measured strains and those predicted by the FE model showed excellent agreement as to the relative sizes of the strains within each pattern of 12 strains. However, there occurred a slight mismatch between the overall scales of the experimental and

FE data. This was attributed to inadequate temperature compensation.

When the neural network is trained, the set of strain measurements for a given load case and fault condition are presented to the input layer. In any neural network application it is necessary to scale the data; if a hyperbolic tangent transfer function is used, the whole training data set for a given input node is usually mapped onto the interval $[-1, 1]$. This means that the scale mismatch described above between the measured and FE data is unimportant, scale information is discarded. With this in mind, a measured strain pattern together with the corresponding FE prediction is presented in Figure 3; the patterns have been adjusted so that the maximum strain in a given pattern is unity. The agreement between the strain patterns is quite good. This instils a certain amount of confidence in the strategy adopted here which is to train the network on FE generated data and apply the resulting structure to the experimental data.

5 The Location Network

The first problem in any network application is to establish the correct network structure. In this case, the input data are the sets of twelve measured strains; this fixes the number of units in the input layer. The outputs of the network were required to signal which member was missing. For this reason, eight outputs were used, each corresponding to a possible missing member. Outputs 1 to 8 were chosen to represent members 9 to 16 respectively (Figure 2). With this configuration, the network was trained to produce a unit response at the output corresponding to the missing member when presented with the appropriate set of strains, and zero at all other outputs. The numbers of hidden layers and nodes in each layer are not fixed by the problem. Very little guidance is available on how to establish the optimum dimensions for neural networks; a trial and error approach is usually adopted. In this case, preliminary trials showed that excellent results could be obtained if three hidden layers were used with twelve, twelve and eight nodes respectively (Figure 4).

6 Results

The preliminary study mentioned in the previous section used FE simulation data for the framework *without* preload. The training data constituted 192 sets of 12 strains. (8 fault conditions $\times$ 8 load positions $\times$ 3 load intensities). During training the strain sets were presented in random order to the network. It was judged that the network had acheived an acceptably small error after approximately 50000 presentations. Time-varying learning and momentum coefficients were chosen, i.e. for the connections to the first hidden layer, the initial values were 0.5 and 0.6 respectively to give fast learning in the early phase of learning; these values fell to 0.1 and 0.2 towards the end of training to allow 'fine-tuning' of the parameters. Similar values were used for the other layers.

To test the network the training sets were presented and the resulting outputs were plotted as in Figure 5. This figure requires some explanation. The input patterns are presented in order so that the patterns corresponding to the removal of member 9 appear first, followed by those

generated by the removal of member 10 etc. Each subgraph of Figure 5 shows the response of a given output node to the presentation of this ordered array of the training sets. As output 1 is required to signal the removal of member 9, the desired response should be unity over the first 24 points of the graph and zero elsewhere, as indicated by the solid line in the first subgraph of Figure 4. The dotted line shows the actual response of the network which is in good correspondence with the desired results. Similarly, output 2 should be unity over points 25 to 48 which label the presentation of those data sets obtained when member 10 was missing, and so on.

The network is used in the following way: when a strain pattern is presented, the highest of the outputs is taken to signal the fault condition i.e. if output 6 is highest, it is assumed that member 14 is missing. Another simple measure of the network accuracy is provided by the *location matrix* which is defined as follows. The average response of each output $i = 1, \ldots, 8$ is taken when all strain patterns corresponding to a given fault condition $j = 1, \ldots, 8$ are presented in the order described above. For each fault, the set of averages is scaled so that the largest is unity and the numbers are entered into the j^{th} row of the matrix. It is clear that a perfectly trained network will produce in this way the unit matrix. Table 1 shows the location matrix for the network described above. The zero elements of the matrix are shown as dashes to improve the clarity of the results.

Member removed	Output node							
	1	2	3	4	5	6	7	8
9	1.0	-	-	-	-	-	-	-
10	-	1.0	-	-	-	0.1	-	0.1
11	-	-	1.0	0.1	-	-	0.2	0.1
12	-	-	0.1	1.0	-0.1	0.1	0.1	0.5
13	-	-	-	-	1.0	-	-	-
14	-	0.1	0.1	-0.1	-	1.0	-	0.1
15	-	-	0.2	0.1	-	-	1.0	-
16	-0.1	-	0.1	0.5	-0.1	-	0.1	1.0

Table 1: Location matrix for Finite Element data - no preload.

An unambiguous diagnosis of the fault location is obtained throughout. Note that there are high values off the diagonal in rows 4 and 8. This is because the corresponding members are those furthest from the support. These members experience the smallest measured strains and their removal affects the framework least; as a result the network has more difficulty establishing that these members are missing.

The network structure was then trained on the FE simulation data with the preload added and subsequently compensated for. This data is supposed to represent the experiment. The resulting location matrix is given in Table 2 and a graphical comparison between the ideal and network outputs is given in Figure 6. As one might expect, the results are very similar to those obtained for the framework without preload.

Member removed	Output node							
	1	2	3	4	5	6	7	8
9	1.0	-	-	-	-0.1	-	-	-
10	-	1.0	-	-	-	0.1	-	-
11	-	-	1.0	0.1	-	-	0.3	0.1
12	-	-	0.1	1.0	-	-	0.1	0.6
13	-0.1	-	-	-	1.0	-	-	-
14	-	0.2	-	-	-	1.0	-	-0.1
15	-	-	0.3	0.1	-	-	1.0	-
16	-	-	0.1	0.5	-	-0.1	0.1	1.0

Table 2: Location matrix for FE data - network trained on noise-free data.

Having established the diagnostic network, the validation exercise is repeated using the *experimental* data. The results are given in Table 3 and Figure 7. In six out of the eight cases, the network correctly reports which member is missing.

Member removed	Output node							
	1	2	3	4	5	6	7	8
9	1.0	-	-	-	-0.1	-	-	-
10	1.0	0.4	-	0.1	-0.1	0.2	-	0.1
11	0.2	-	1.0	0.2	-	0.6	0.4	0.1
12	0.1	0.1	0.2	1.0	-	0.6	0.5	0.4
13	-0.1	-0.1	0.4	0.3	1.0	-	0.6	0.2
14	0.4	-0.1	0.1	-	-	1.0	0.1	-0.1
15	0.8	0.1	-	0.2	-0.1	0.5	1.0	0.1
16	1.0	0.1	-	0.5	-0.2	0.5	0.1	0.3

Table 3: Location matrix for experiment data - network trained on noise-free data.

One of the reasons for the misclassifications is that the network has been trained on ideal noise-free data. The experimental data however, is corrupted by noise. One source of uncertainty in the experimental data sets is caused by the sensitivity of the strain gauges to variation in temperature. Some compensation for this effect is made by using a reference strain gauge. Another source of error is the digitisation of the analogue strains. The output of the instrumentation is quantised in units of one microstrain; as some of the measured strains are of the order of microstrains this effect is serious. In order to avoid the problem of noise corruption, the network was trained to signal the fault location even when presented with corrupted strain data. 100 copies of each strain pattern were generated, each with a noise pattern of rms 1.0 microstrain superimposed. After training the network gave the results shown in Table 4 and Figure 8 when presented with the noise-free FE data.

Member removed	Output node							
	1	2	3	4	5	6	7	8
9	1.0	-	-	-	-0.1	-	-	-
10	-	1.0	-	-	-	-0.1	0.1	-
11	-	0.1	1.0	0.2	-	0.1	0.2	0.2
12	-	0.1	0.3	1.0	-	-	0.2	0.5
13	-0.1	-	-	-	1.0	-	-	-
14	-	-0.1	0.1	-	-	1.0	0.1	-
15	-	0.1	0.2	0.1	-	0.1	1.0	0.2
16	-	0.1	0.2	0.5	-	0.1	0.2	1.0

Table 4: Location matrix for FE data - network trained on noisy data.

The results are almost identical to those obtained from the network trained on noise-free data. However, when the experimental data was presented to the network, the results (Table 5 and Figure 9) show an improvement.

Member removed	Output node							
	1	2	3	4	5	6	7	8
9	1.0	-	-	0.1	-0.1	-	-	-
10	0.1	1.0	-	0.1	-	-	0.1	0.1
11	0.3	-0.2	1.0	0.5	-0.1	0.8	-	0.3
12	0.3	-	0.1	1.0	-0.1	0.3	0.1	0.2
13	-0.1	-	-	0.2	1.0	-	-	-
14	0.4	-0.1	-	0.1	-0.1	1.0	-	-
15	0.3	-	0.1	0.3	-0.1	0.2	1.0	0.2
16	1.0	-	0.2	0.3	-0.1	0.2	0.2	0.3

Table 5: Location matrix for experimental data - network trained on noisy data.

A correct diagnosis is obtained in seven out of eight cases. This shows clearly that the networks must be trained to disregard small disturbances in the strain patterns due to measurement noise.

The difficulty in identifying the removal of members 12 and 16 has been attributed to the fact that they experience small strains throughout the experiment. This is purely due to the fact that the gauge readings are zeroed after the application of the preload. If the zero level is fixed *before* preloading, the average strain levels in members 12 and 16 is increased. If the arguments above are correct, a better diagnosis will be obtained if the background strains due to the preload are allowed to remain. In order to test this, strain patterns were generated with the preload pattern superimposed. The network was trained and tested on this (clean) data and gave the results shown in Table 6 and Figure 10. The results are considerably better than those in Table 2 and Figure 6. This forces the conclusion that a carefully applied preload can be a considerable advantage in using this method.

Member removed	Output node							
	1	2	3	4	5	6	7	8
9	1.0	-	-	-	-	-	-	-
10	-	1.0	-	-	-	-	-	-
11	-	-	1.0	-	-	-	-	-
12	-	-	-	1.0	-	-	-	-
13	-	-	-	-	1.0	-	-	-
14	-	-	-	-0.1	-	1.0	-	-
15	-	-	-	-	-	-	1.0	-
16	-	-	-	-0.1	-	-	-	1.0

Table 6: Location matrix for FE data - with preload.

7 Conclusions

It is demonstrated that a neural network can successfully locate faults in an experimental structure when trained on FE simulation data. It is also shown that the network must be trained to recognise noise-corrupted data to avoid misclassification of distorted patterns. Finally, it is suggested that the application of preloads to the experimental structure (and of course to the FE simulation on which the network is trained) could improve the diagnostic ability of the network.

Acknowledgements

Thanks are due to Dr. Jan Wright for providing the FE analysis template. The help of Dr. Andy Burrows proved invaluable for the transformation of data between various formats. Finally, the authors are very grateful to Dave Earl and Jonathan Beer who performed the tedious task of acquiring the experimental data. This work is supported wholely by Brite/Euram - The European Community Research and Development Programme on Manufacturing Technologies and Advanced Materials.

References

[1] Barschdorff (D.) & Bothe (A.) 1991 *Noise and Vibration Worldwide* **22** pp.11-19. Signal classification using a new self-organising and fast converging neural network.

[2] Barschdorff (D.) & Bothe (A.) 1991 *Proceedings of Fourth International Conference on Neural Networks and Their Applications* pp.241-251. Adaptive condensed nearest neighbour network for pattern classification.

[3] Billings (S.A.), Jamaluddin (H.B.) & Chen (S.) 1991 *Mechanical Systems and Signal Processing* **5** pp.233-255. A comparison of the backpropagation and recursive prediction error algorithms for training neural networks.

[4] Cawley (P.) & Adams (R.D.) 1979 *Journal of Strain Analysis* **14** pp.49-57. The location of defects in structures from measurements of natural frequencies.

[5] Chen (S.), Billings (S.A.) & Grant (P.M.) 1990 *International Journal of Control* **51** pp.1191-1214. Non-linear system identification using neural networks.

[6] Kudva (J.), Munir (N.) & Tan (P.W.) 1992 *Smart Materials and Structures* **1** pp.108-112. Damage detection in smart structures using neural networks and finite-element analysis.

[7] NeuralWorks Professional II Manuals. 1990 *(i) Neural Computing, (ii) Using Nworks - An Extended Tutorial, (iii) Reference Guide.* NeuralWare Inc.

[8] Rumelhart (D.E.) & McClelland (J.L.) 1988 *Parallel Distributed Processing: Explorations in the Microstructure of Cognition (Two Volumes).* MIT press.

[9] Samman (M.M.), Biswas (M.) & Pandey (A.K.) 1991 *Journal of Analytical and Experimental Modal Analysis* **6** pp.35-44. Employing pattern recognition for detecting cracks in a bridge model.

[10] Schalkoff (R.) 1992 *Pattern Recognition - Statistical, Structural and Neural Approaches.* John Wiley & Sons.

[11] Worden (K.) & Tomlinson (G.R.) 1992 *Submitted to Mechanical Systems and Signal Processing.* Modelling and classification of nonlinear systems using neural networks.

[12] Worden (K.), Tomlinson (G.R.) Lim (W.) & Sauer (G.) 1992 *Submitted to Mechanical Systems and Signal Processing.* Fault detection in an experimental system using neural networks.

[13] Wu (X.), Ghaboussi (J.) & Garrett (J.H.) 1992 *Computers and Structures* **42** pp.649-659. Use of neural networks in detection of structural damage.

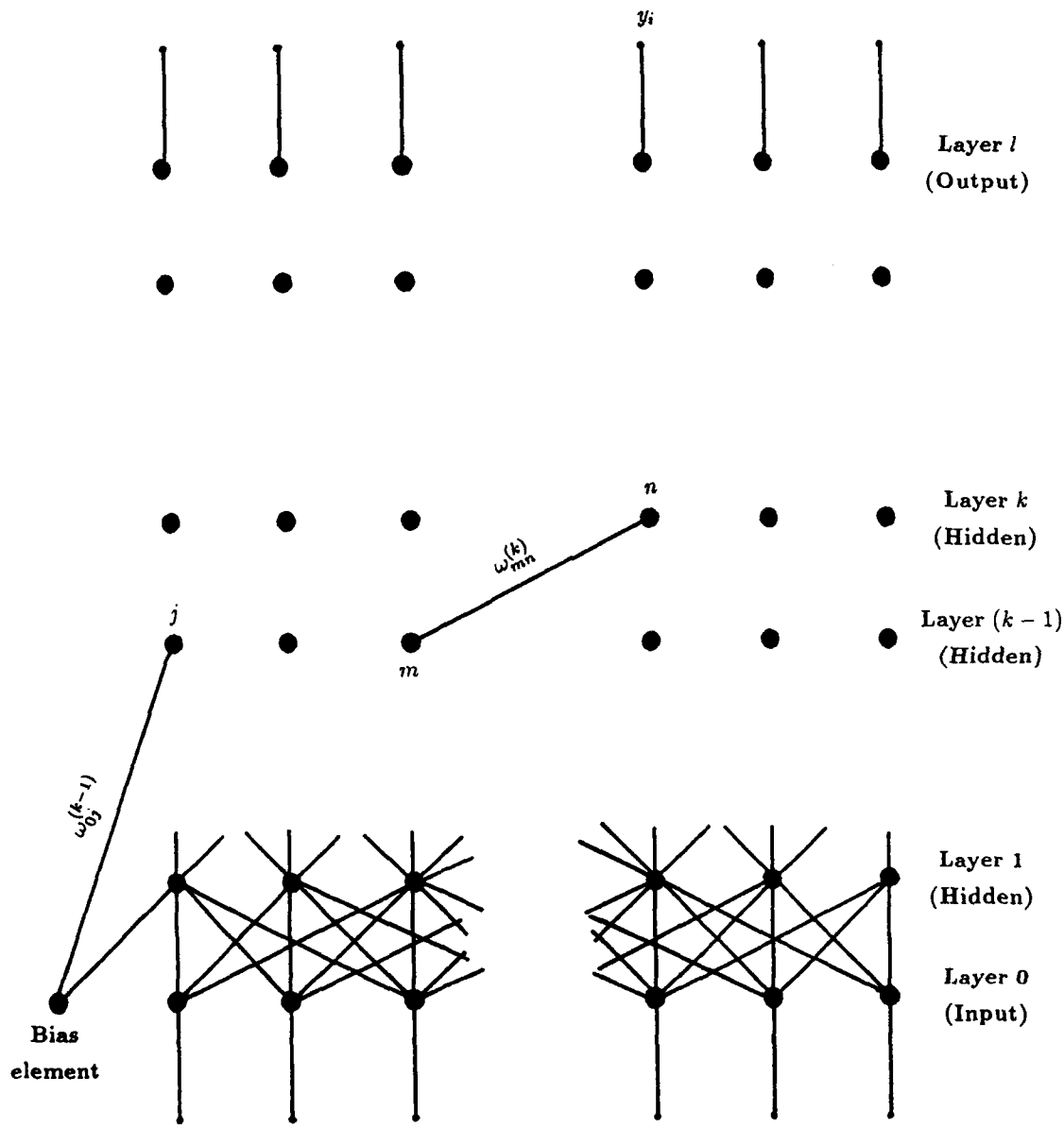

Figure 1. Multi-Layer Perceptron.

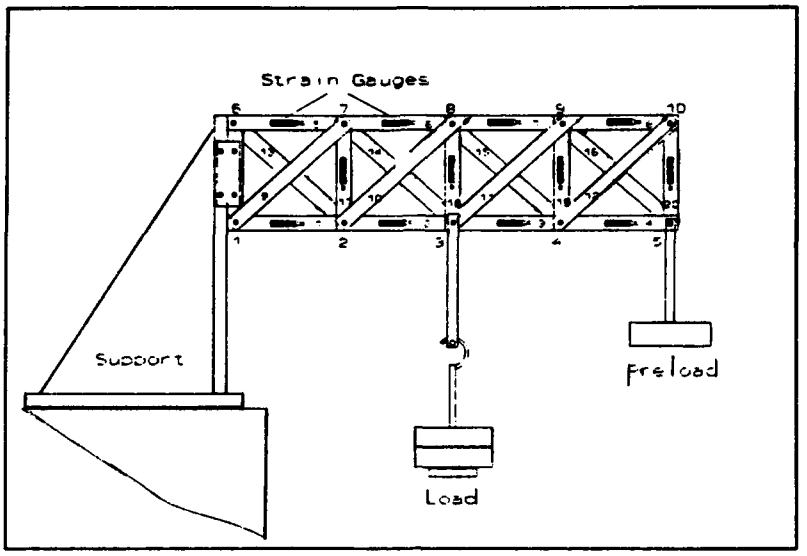

Figure 2. Experimental framework.

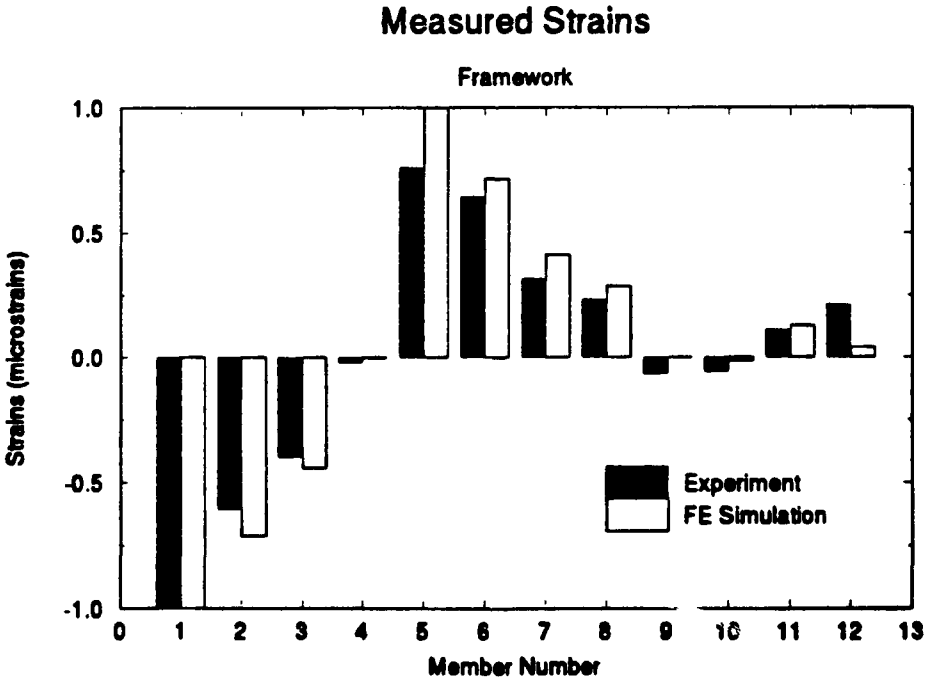

Figure 3. Comparison between experimental and FE stress patterns.

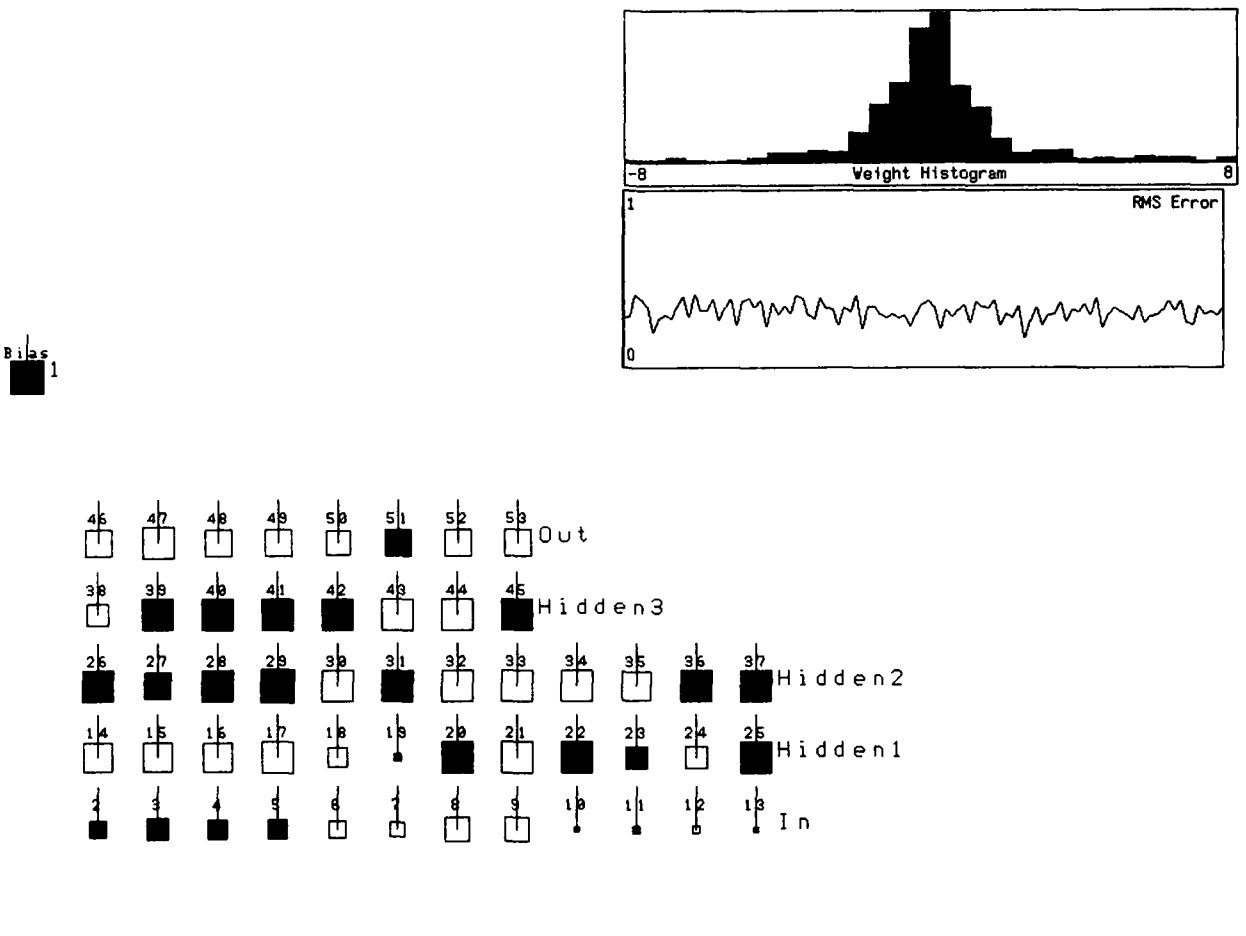

Figure 4. Location Network.

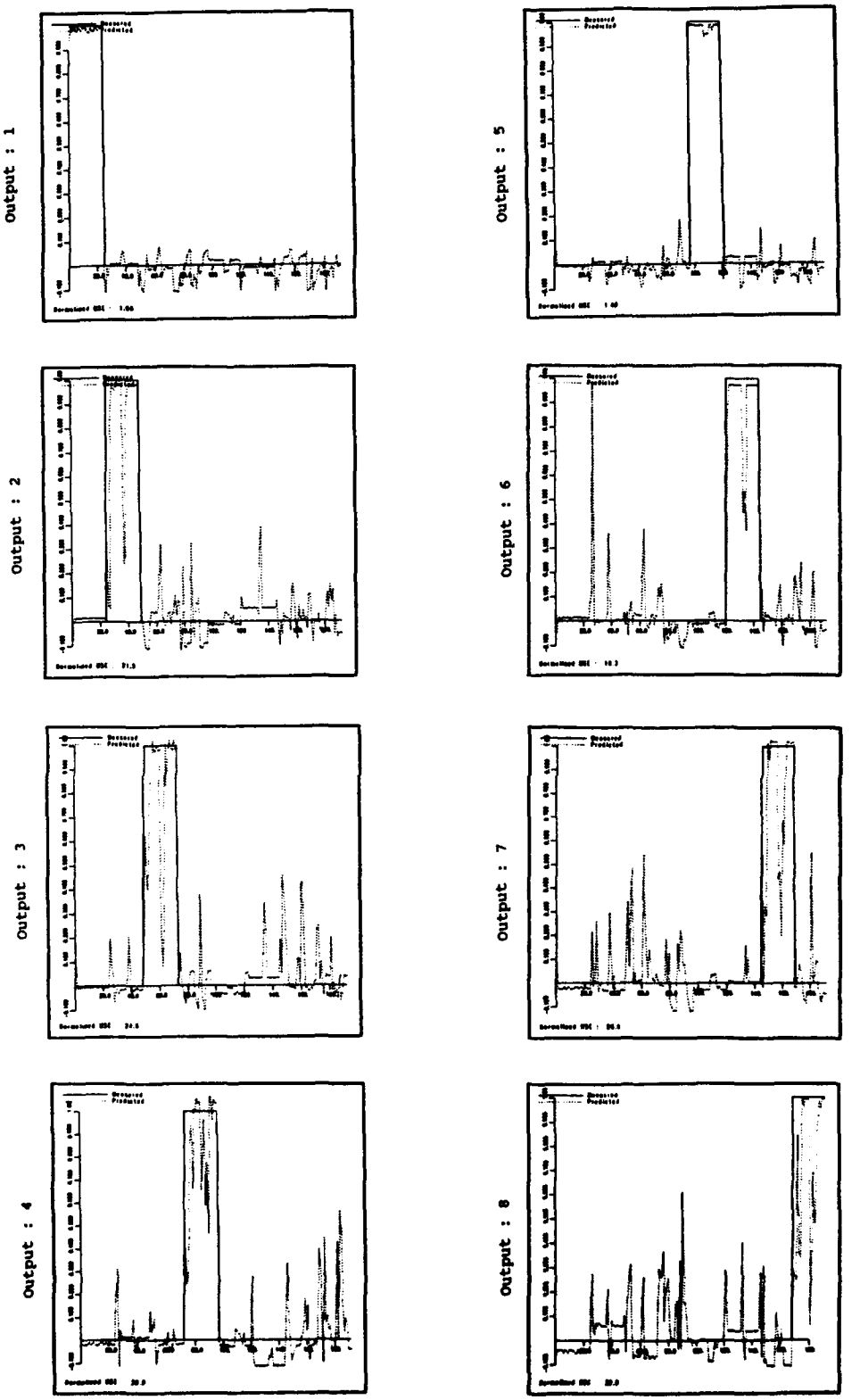

Figure 5. Desired and predicted outputs for FE data from network trained on noise-free FE data. No preload.

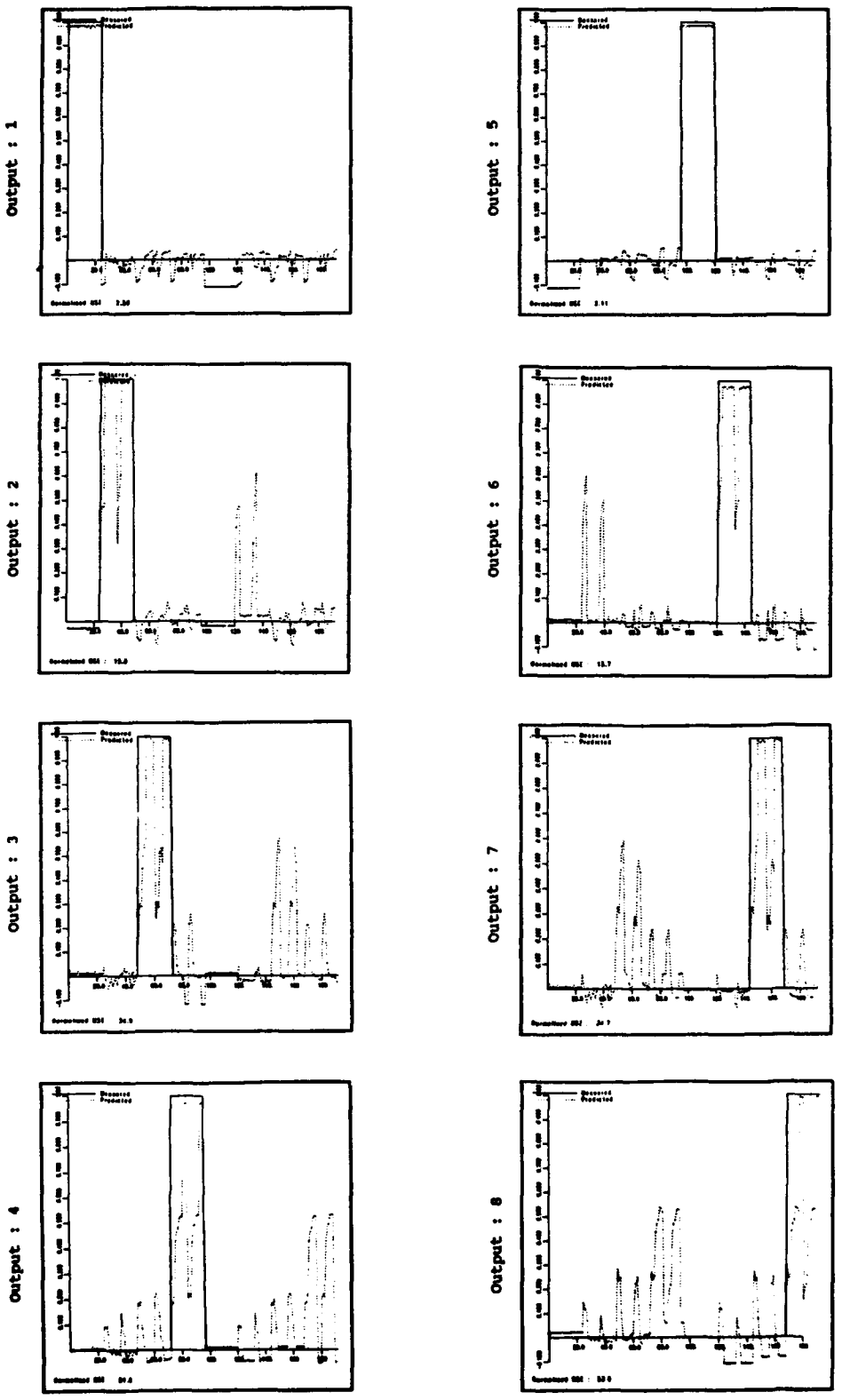

Figure 6. Desired and predicted outputs for FE data from network trained on noise-free FE data.

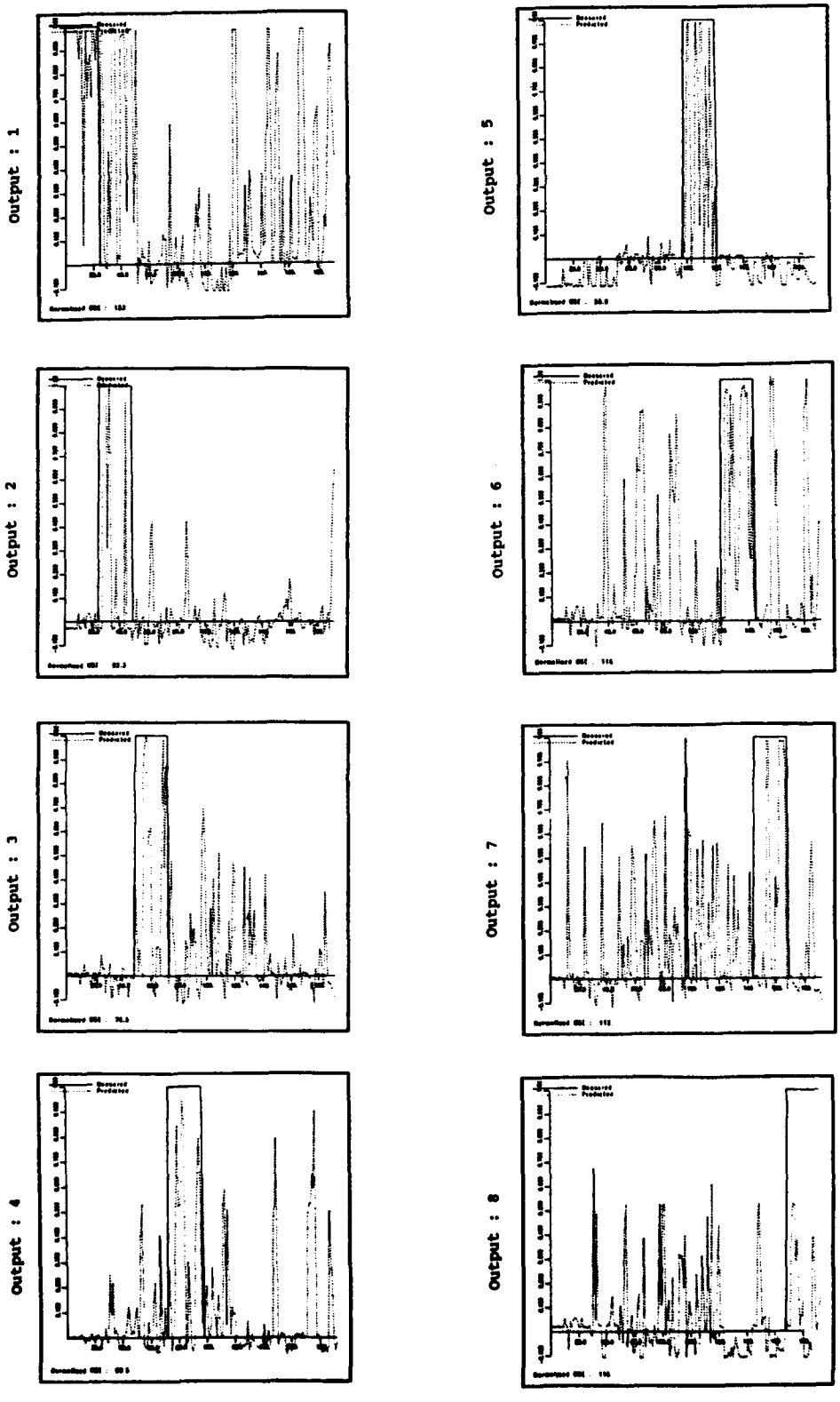

Figure 7. Desired and predicted outputs for experimental data from network trained on noise-free FE data.

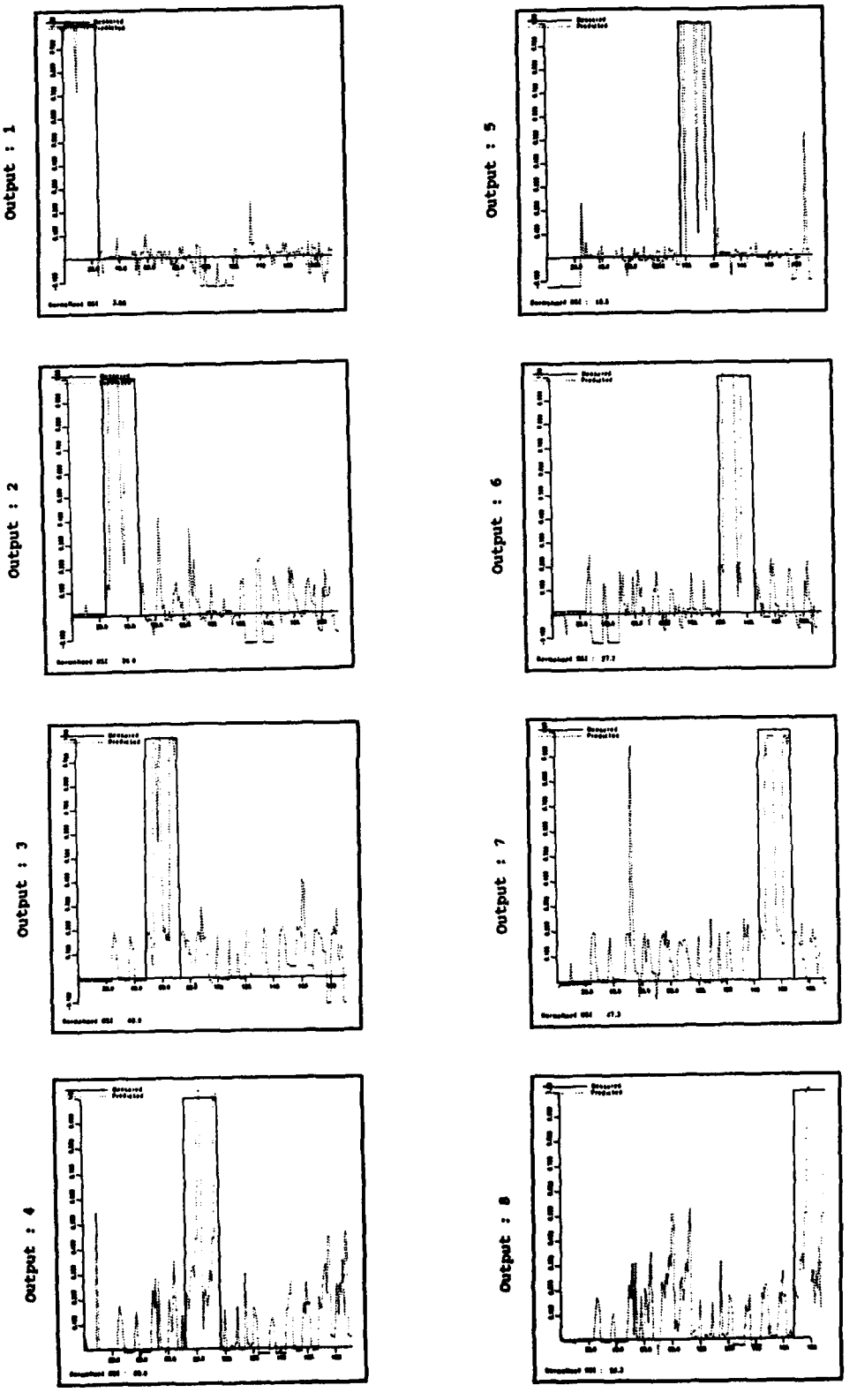

Figure 8. Desired and predicted outputs for FE data from network trained on noise-corrupted FE data.

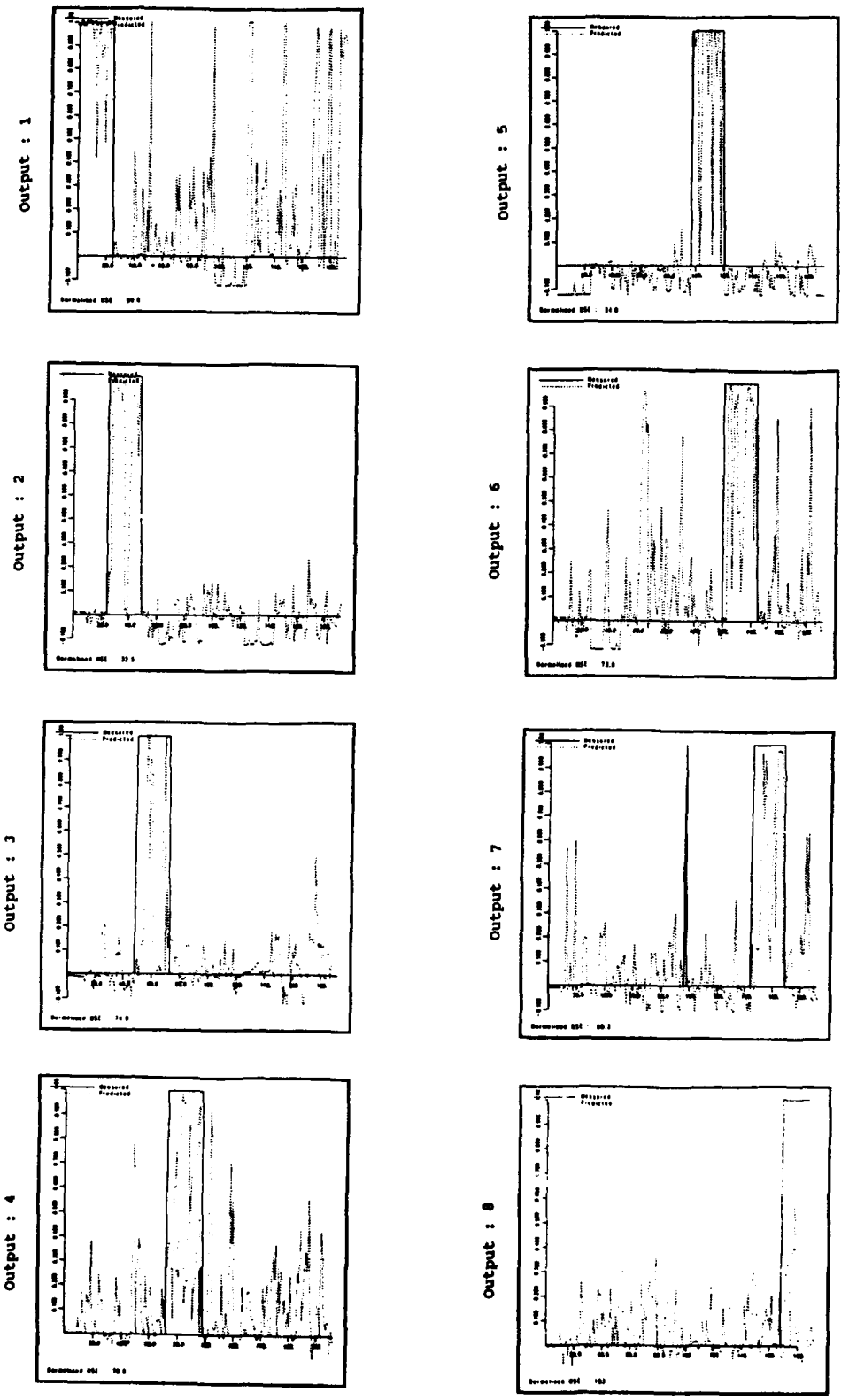

Figure 9. Desired and predicted outputs for experimental data from network trained on noise-corrupted FE data.

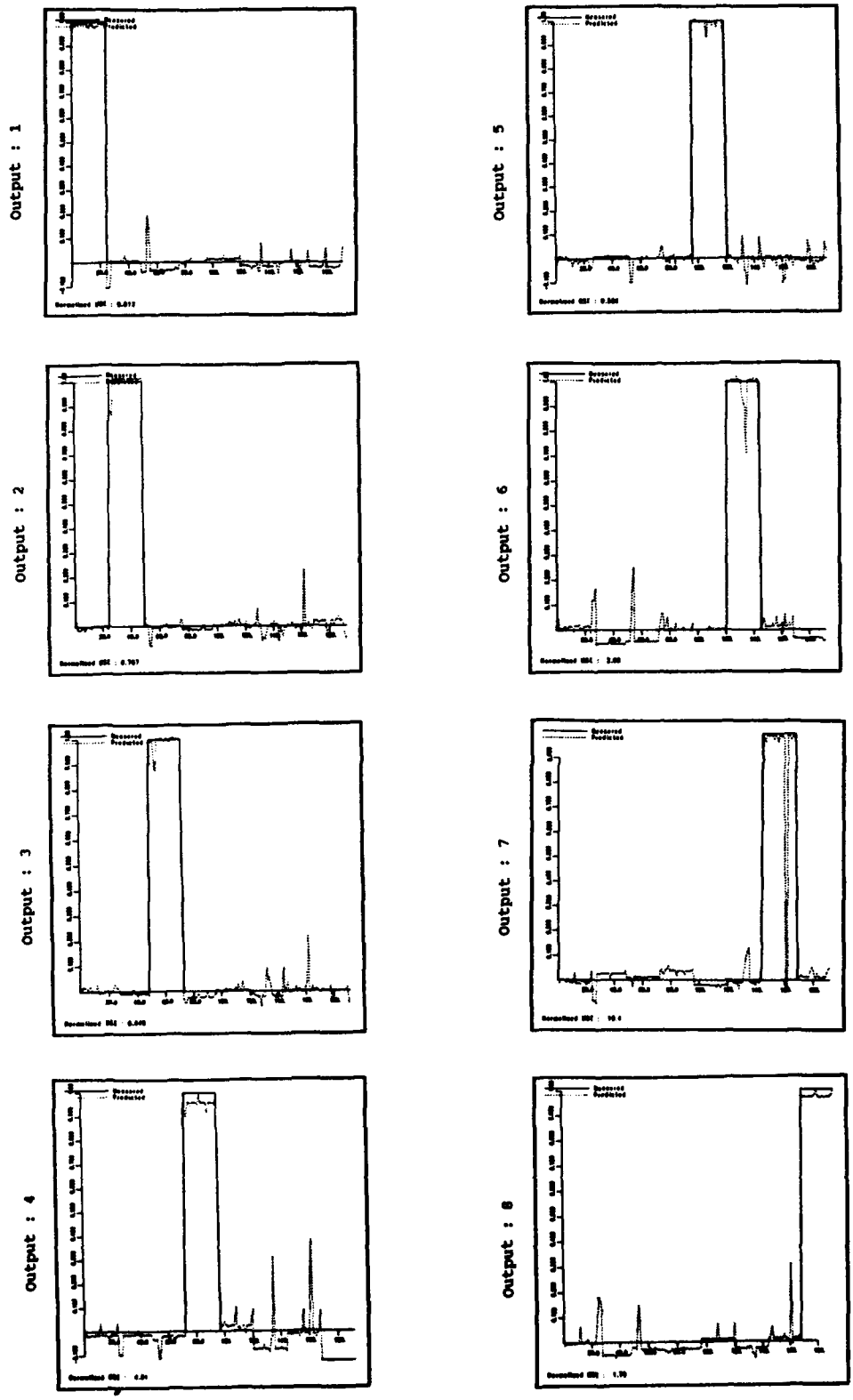

Figure 10. Desired and predicted outputs for FE data from network trained on noise-free FE data. Framework preloaded.

FACTORS AFFECTING THE EMBEDDING OF OPTICAL FIBRE SENSORS IN ADVANCED COMPOSITE STRUCTURES

by

N.C. Eaton and **M.J. Curran**
Westland Aerospace Ltd
Cowes
Isle of Wight
United Kingdom

J.P. Dakin and **H. Geiger**
Optoelectronics Research Centre
University of Southampton
Southampton SO9 5NH
United Kingdom

1. INTRODUCTION

Composite materials offer tremendous benefits for engineering applications and are now specified for use in several safety critical structures. However, despite extensive materials research and development, they do have a number of areas where their behaviour is still not fully understood.

This is particularly so with the more complex mechanical parameters in larger structures. Current structural design attempts to allow for these unknowns by over-designing, extensive testing and frequent inspection.

Embedded optical fibre sensors offer the potential to monitor many of these parameters, and are additionally of a similar physical and mechanical nature to the reinforcement fibres used in advanced composites.

Westland Aerospace have been involved in the development of fibre sensors for composite monitoring for over five years, and pioneered the application of embedded fibre sensors in thermoplastic composites during earlier joint research projects with the United Technologies Research Centre.[1]

Previous programmes have shown that research and development into both optical fibre sensors and materials is a key to the success of "smart structures" technologies.

The BRITE sponsored Optical Sensing Techniques in Composites (OSTIC) programme represents the largest European research programme to date. Similar research is underway at several centres worldwide, mainly in the USA and Canada.

It was decided to set up a joint sensors/materials project under the UK Government supported LINK Structural Composites collaborative research programme. The project will be performed by Westland Aerospace and the Optical Fibre Sensors Group at the UK Optoelectronics Research Centre.

This paper addresses factors relating to the development and application of optical fibre strain sensors for the monitoring of composite structures, and in particular the factors relating to the embedding of these optical fibres in composite laminates.

2. APPLICATIONS OF FIBRE SENSORS IN SMART STRUCTURES

2.1 Advantages of Fibre Sensors

Embedded fibre optic sensors offer the potential to measure several parameters in their host material, such as dynamically varying strain and temperature. In addition, they are immune to corrosion, lightning strike, and electro-magnetic interference.

Fibre sensors are particularly attractive for structural monitoring since they offer both point and distributed sensing. Since the fibre transmits the measurement signal, multiplexed point sensing can be easily realized.

The optical fibre contains both the sensing and the telemetry system without the need for any mechanical discontinuities, which would occur with electrical sensors and their connections. Thus the fibre sensor should give a more reliable sensing system and is compatible with the adoption of optical fibre based data transmis sion links in modern aircraft.

In the longer term it will be possible to actively control the shape or properties of the composite by means of embedded actuators, which can be monitored and hence controlled by the same sensing system.

2.2 Structural Health Monitoring

Composite materials are currently used in critical structure applications where they may be simultaneously subjected to extremes of temperature and high levels of mechanical loading.

The long term reliability of composites in such environments is uncertain. There is therefore a need to monitor the integrity under such conditions. **Continuous monitoring** will allow inspection or replacement scheduling to be based on a true record of loading history and structure performance (rather than simply on the basis of a pre-determined life

which must be conservative to cater for worst-case scenarios). Safety will also benefit, since structural damage will be detected immediately even in inaccessible areas. Continuous monitoring will also offer enhanced design efficiency since information on structure performance in service can be applied in the design of future structures.

A structural monitoring system should have the ability to memorise the strain field distributions resulting from normal structure performance, and be able to recognise potentially dangerous uncharacteristic behaviour. It also should be capable of determining the natural frequency of the structure, which are known to be related to structural health. Fibre optic sensors have been shown to be capable of accurate measurement of at least the first three natural frequencies of composite structures.[1]

2.3 Integrated Sensor/Actuator Packages

It is envisaged that embedded fibre sensors could be used with integral actuating capabilities. Such a sensor/actuator package is presented in Figure 1.[2] The package features an optical fibre strain sensor with an electro-strictive coating. Due to the fast response time, this can operate in separate modes:-

1) actuator
2) sensor
3) time shared sensor/actuator.

In the actuator mode, a control voltage applied across the coating will produce strain in the optical fibre and in the surrounding host composite. By combining several actuators we could control the behaviour of the host structure.

In the sensor mode, loads applied to the structure produce an electrical signal which can be used to calibrate the optical fibre sensor.

In the time share mode, the coating is used both as a sensor and an actuator in the following way: an electrical control signal is applied to the coating so as to produce in it a mechanical strain which will depend on the stiffness of host material local to the sensor/actuator, and this strain is monitored with the fibre sensor. The control voltage is now switched off and the relaxation of the host structure is monitored with the fibre sensor.

We are thus able to monitor or control static and dynamic mechanical properties, both of the host material local to the fibre/actuator package and of the host structure.

2.4 Process Monitoring

Reliable processing of composite materials and bonding of cured laminates relies on the precise measurement of process critical parameters such as pressure and temperature.

The trend towards increasing use of co-curing of components, together with increasing component size and complexity, can cause difficulties in maintaining consistency in process parameters.

Embedded fibre sensors, integrated prior to processing, may provide valuable potential for measurements in the following areas;

1) Pressure
2) Temperature
3) Cure state
4) Residual strain.

3. FACTORS AFFECTING EMBEDDING

3.1 General Discussion

Many practical issues relating to the embedding of optical fibres need to be resolved before the commercial application of smart structures can become feasible. Introduction of the optical fibre sensor into the manufacturing cycle of the composite structure presents a considerable technological challenge, since current manufacturing processes are generally incompatible with fragile optical fibres. Ideally, the embedding of optical fibres would be accomplished with only minor changes to such processes.

The large number of sensors required, together with the complexity of associated sensing optics and signal processing electronics, are likely to represent significant cost increases in the near term. It is important therefore to examine the embedding process to minimise the fabrication costs.

The successful embedding of optical fibres into engineering structures requires the solution of several practical difficulties. The key areas requiring attention are:

1) development of specialised optical fibres and coatings for embedding,
2) development of methods for handling the fragile optical fibre,
3) development of a reliable method of connecting the embedded optical fibre to the external monitoring system.

3.2 Special Optical Fibres and Coatings

Optical fibres suitable for embedding as sensors in composite materials present very different requirements to those for communications fibres. The range of optical fibres which have been specially developed for sensing purposes are very limited, and there are presently no fibres developed specially for monitoring in composite materials which are commercially available. We therefore intend in our programme to develop and manufacture fibres specifically for this purpose.

The fibre construction must satisfy the following requirements:

1) Small diameter. Embedded sensor fibre diameter should be optimised so as to produce minimum perturbation to the very small (approx. 10 micron diameter) composite material reinforcement fibres.
2) Robustness. The fibre must possess adequate handling properties, and be capable of surviving the high pressures and temperatures encountered in composite materials processing, and should be resistant to abrasion from the composite reinforcement fibres.
3) Mechanical property compatibility. Mechanical design of the coating, to ensure efficient performance of the sensor as a strain transducer, and to prevent the sensor fibre behaving as a significant strain concentration within the composite, is required.
4) Environmental compatibility. The sensor fibre must be inert with respect to the resin used in the composite,
5) Buffering from microbends. Microbending of an embedded sensor fibre occurs when either bare or coated fibres are embedded in woven reinforcement composite materials. Tiny microbends increase the optical attenuation and can introduce

mechanical strain in the optical fibre. They must therefore be minimised by suitable coatings.

Buffering of the embedded fibre against microbending loss may require the use of coatings with a degree of lateral compliance.

6) Adhesion promotion. Strong and robust bonding between the embedded sensor fibre and the host composite is essential if the embedded fibre is to perform as a reliable transducer without weakening the host material.

Since the range of properties of the optical fibres themselves is generally limited, it is anticipated that multiple coatings could be required.

Figure 2 shows a generic fibre sensor/coating package. The optical fibre is afforded environmental protection by a primary coating. A secondary coating is present to optimise mechanical coupling and promote adhesion between the fibre sensor and the composite.

3.3 Embedding Methods

A primary concern is in the handling of the fragile optical fibres during lamination of the composite. A method allowing production of an insert layer of optical fibre/composite material is required. This layer can then be laminated with other layers in the normal production process.

Figure 3 shows a new method for introducing optical fibres into pre-preg laminates.[3] The method involves the following stages:

1) The optical fibres are laid into grooves in a non-stick pattern tool.
2) Resin of the same type as that used in the composite pre-preg is applied as a film. A controlled amount is applied to maintain the resin/fibre ratio of the composite.
3) The resin is cured to the same state as the resin in the host pre-preg.
4) Pre-preg ply #1 (ie one of the pre-preg plies used next to the fibre sensor in the laminate) is pressed onto the optical fibre in the resin film and the two are withdrawn leaving the optical fibre/resin film now held in place by the tackiness of the partially cured resin.
5) Pre-preg ply #2 (ie the other pre-preg ply used next to the fibre sensor in the laminate) is pressed onto the optical fibre/resin film so as to sandwich the optical fibre/resin film between the two plies of pre-preg.
6) A protective backing film is applied to the sandwich, allowing it to be handled and stored.

The above method has the following advantages;

1) The fibre sensor/pre-preg sandwich is robust and easy to handle, with the fragile optical fibre afforded protection by the pre-preg when sandwiched.
2) Testing of the optical fibre in the fibre sensor/pre-preg package can be performed prior to final laminating to minimise the chance of embedding a damaged optical fibre.
3) The fibre sensor/pre-preg sandwich is easily integrated into the structure manufacturing cycle, as it may be treated almost as any other ply of pre-preg, and hence does not slow the laminating sequence significantly.
4) The sandwich can be bulk manufactured to reduce cost. Generalised forms, such as tapes, could be used in many different structures.
5) The method is suited to automated production. Automated placement of optical fibres as a separate operation would be much more difficult to achieve during typical lamination operations.

3.4 Connecting The Fibre Sensor

Development of a reliable method of connecting the embedded fibre to external fibre links is particularly critical. Such a method should be;

1) consistent with the manufacturing processes of composite structure, such as autoclave moulding and edge trimming,
2) environmentally insensitive, ie should not be affected by vibration, temperature fluctuation, moisture ingress, etc,
3) low cost and repairable.

Many types of fibre sensor require the use of monomode optical fibre which have core diameters of typically less than 10 microns. Clearly, achieving reliable connection between two fibres (ie end alignment) with such small dimensions presents practical difficulties in an industrial environment.

3.5 Possible Deleterious Effects of Embedded Fibre

Researchers have generally agreed that optical fibres tend to produce only minimal perturbation to reinforcing fibres when embedded parallel to them, but a large disturbance may result when the optical fibre is embedded across the direction of the reinforcement fibres.[4,5,6] The non-parallel alignment results in a greater distortion of the reinforcement fibres and a large resin-rich region, both of which may be detrimental to the strength of the laminate.

Several groups of researchers have performed mechanical test programmes in which composite testpieces containing optical fibres have been tested in a number of configurations. Conflicting results have been obtained, with the effects of embedding ranging from relatively insignificant to severe.[7] Further investigation may yet reveal other problems, such as reduced fatigue performance or inferior failure behaviour. Therefore, it is essential that any detrimental effects on the mechanical properties of the host composite material are fully quantified.

4. DETAILS OF THE CURRENT PROJECT

4.1 Background to the Project

As mentioned in the introduction, a three year research project has been set up as part of the U.K government supported LINK Structural Composites Programme. This project between Westland Aerospace Ltd and the University of Southampton's Optoelectronics Research Centre is being undertaken in response to the perceived need for smart structures research and development within the civil aerospace industry.

Under the LINK scheme, collaborative research projects benefit from shared expertise. Technological developments in advanced materials and optical fibre sensors are undoubtably a key to advancement in smart structures, and the joint programme is designed to stimulate progress in both of these areas.

Within the two broad disciplines several other activities arise. Figure 4 illustrates the range of these activities. These activities are addressed in detail in the following paragraphs.

4.2 Fibre Sensors for Composite Material Monitoring

4.2.1 Basic Principles

In order to sense a parameter affecting the composite, it must produce a measurable effect on the properties of the fibre (*modulation*). Modulation of the optical path length is (in contrast to modulation of the intensity) convenient to use since delays in the optical signal are not influenced by changes of the optical attenuation in the system.

Optical delays may be interrogated using either:

1) an interferometric sensor, or
2) optical time domain reflectometry (OTDR).

An interferometric sensor is very sensitive to changes in the order of the wavelength of light (ca 1μm) or less, but can suffer from ambiguity when measuring larger changes, unless considerable care is taken to provide complex phase referencing schemes. It hence lends itself to local strain measurement in short lengths of fibre, using the remainder of the fibre for signal transmission only.

Conventional OTDR systems measure the optical propagation delays to and from reflective points in a fibre. They can interrogate long lengths of fibre (kilometres) for inhomogeneities (ie reflective points), but can typically only discern such points with centimetre resolution. Monitoring the difference between the time delays from each of the inhomogeneities allows the measurement of averaged strain between these inhomogeneities.

4.2.2 Proposed Optical Fibre Sensor

Our measurement philosophy attempts to combine the "best of both worlds" to achieve a very efficient sensor system. We propose to construct an enhanced OTDR system to track the position of inhomogeneities along the length of a fibre, and to use the inhomogeneities themselves as local strain sensors (Fig 5).

To achieve the first aim, we have designed a novel OTDR system intended to improve the spatial resolution of current OTDR systems. Our enhanced OTDR will monitor the location of inhomogeneities in the fibre. Bragg gratings are an appropriate form of inhomogeneity as they provide suitable reflective points for OTDR monitoring.

In addition each grating also provides a discrete-point sensing capability since they respond to local strain by changing their reflected wavelength.[8] In this manner they act as an interferometric sensor which can be interrogated unambiguously.

By using both the time delay of the reflections from the gratings and the reflected wavelength of the gratings, a system can be developed which provides information on both line-averaged and local strain (Fig 5). When multiple gratings are incorporated in one fibre a multiplexed sensor system can be produced. Such a configuration greatly reduces the number of fibres needed to interrogate a given structure.

In general, the response of a fibre to temperature variation is of the same order of magnitude as the response to strain. Therefore considerable effort will be directed into providing temperature compensation to realize a practical system capable of operation over an extended temperature range.

One of the most promising approaches is a system having different responses to strain and temperature, thereby allowing independent measurement of the two responses.

Work is well under way on our enhanced OTDR system and we are looking forward to publishing further details of the basic concepts and the first results on the strain response in the near future.

4.3 Mechanical Modelling of Sensors in Composites

Preliminary analytical studies of the micromechanics of optical fibres embedded in composites have attempted to predict the complex interaction between the embedded optical fibre sensor and the host material.[9,10,11] To date however, many of these models have considered only the simplest case conditions and have generally been applied only to interferometric type sensors. Developments are needed which will predict strain fields within the optical fibre itself and which may be applied to more general conditions of structural loading and environmental effects. Such models will prove indispensable in deriving more precise and useful measurement data from the optical signals, and in establishing optimum coatings etc. for the embedded sensors.

One of the sensor systems which we are developing will employ Bragg gratings, which can be produced with lengths of the order of 1 mm. Hence we can effectively model the embedded fibre sensor as a point sensor. Much of the analytical micromechanical modelling reported to date has concerned standard interferometric type optical fibre sensors, and will require some adaption to apply it to Bragg type sensors.

Micromechanic modelling will be used to provide information on the optimum diameter and mechanical properties of embedded fibres and their coatings. Models will be based on observations of embedded fibres and will include, for example, regions of resin richness. Models will predict the concentration of strain in the fibre, in its fibre coating and in the host composite. These will allow an optimised fibre/coating, compatible with the composite matrix to be selected (ie one producing minimum strain concentration).

Finite element techniques have been applied to the problem of micromechanical modelling of embedded optical fibres in composites. Such approaches have been shown to yield useful information on the intensity and distribution of strain fields. Within the scope of the present project it is intended to make further use of such techniques to predict strain levels and states in embedded fibres, and to aid in the optimisation of fibre sensor coatings.

4.4 Mechanical Tests of Composites with Embedded Sensors

As mentioned earlier, it is important to assess the effects of the presence of an embedded optical fibre on the mechanical properties of the host laminate, and to establish the long term service durability of fibre coatings. The two main reasons for this are:-

1) The usefulness of embedded fibre sensors in long term structure health monitoring is lost if the sensor package fails prematurely.
2) The advantages of the embedded sensor are dubious if its presence compromises the performance of the host structure.

Previous research has shown that the nature and dimensions of the embedded optical fibre and its coating are significant in determining the effect on the mechanical properties of the host material.[12,13] It is proposed to investigate this aspect

further to ensure that the optical fibre and its coating are optimised to produce minimal degradation of the host laminate properties. The optimisation will involve designing the embedded fibre for optimum performance as a mechanical strain transducer, whilst ensuring the long term survival of the fibre sensor and composite.

Longitudinal compressive testing is likely to be sensitive to the presence of an embedded optical fibre since bridging of the optical fibre by the reinforcement fibres represents an approximation to a pre-buckled condition.[14] Interlaminar shear testing is also envisaged to be a sensitive test as the combination of fibre bridging and a resin rich zone will tend to aggravate laminate de-lamination in the presence of applied shear strain. Both tests will be part of this programme.

It is also proposed to perform fatigue assessment studies in which the service environment is simulated as closely as possible.

A number of material characterisation methods are intended to be used to study in detail the effect of embedded optical fibres on both the mechanical properties and the quality of the host composite materials. Figure 6 lists the main classes of tests proposed within the scope of the current project.Non-destructive Tests (*NDT*) of Composites with Embedded SensorsAs mentioned before, defects arising from the embedding of optical fibres in laminates have been shown to include resin-rich regions and distortion of reinforcement fibres. One method of assessing the extent of these is by micrographic examination of polished sections of laminate, but clearly alternative, non-destructive techniques need to be developed.

Typical aerospace techniques include ultrasonic scanning and X-ray imaging. The applicability of both of these techniques will be investigated. However, preliminary studies have indicated that the small size of the optical fibre will in some cases restrict the applicability of such techniques.

5. PRELIMINARY FINDINGS

This section describes our results achieved so far. Some of the earlier results were achieved before the LINK programme.

5.1 Embedding trials with thermoset materials

Embedding of optical fibres in thermoset pre-preg material was investigated. The composite was in this case processed by the autoclave moulding technique.

5.1.1 Method of manufacture and test

Embedding of optical fibres in thermoset pre-preg material (ie reinforcement fabric pre-impregnated with resin) was investigated. The composite was in this case processed by the autoclave moulding technique.

125 μm diameter multimode optical fibre was stripped of its protective coatings and cleaned. Various narrow bore tubes, as detailed below, were used to protect the fragile optical fibre at the points of exit from the test-panels. Approximately 10 cm of optical fibre was embedded in each case, with 9 cms unprotected and with the protective tube extending approximately 1 cm into the panel.

The test panels were fabricated from 8 plies of a carbon fibre reinforced pre-preg material (NARMCO® R5250-T300 Bismaleimide thermoset resin/ 3K 5-Harness satin woven fabric). The cure cycle for this material involve curing at 175°C (350°F) under a pressure of 586 kPa (85 p.s.i) for 6 hours. This material was used because the higher than typical cure pressure, and the longer than typical cure periods associated with it, were reasoned to provide a more demanding test of the effectiveness and durability. Optical loss measurements were performed (i) before application of vacuum consolidation pressure, (ii) after application of vacuum consolidation pressure, and (iii) after curing of the composite.

5.1.2 Results of trial panel manufacture tests

The results of our embedding tests, in terms of the optical attenuation during curing, are shown below. Loss measurements were made using flying leads fitted with temporary mechanical splices. The losses were measured relative to unstrained sensor fibre, connected via leads to source and detector. This was measured before embedding in the composite to provide the zero loss reference level in column 1 in table below.

Protective tube	Loss before consolidation (dB)	Loss after consolidation (dB)	Loss after cure (dB)
Polyimide			
140/160 μm ID/OD	0	0.09	0.50
Silicone			
250/2250 μm ID/OD	0	0.07	0.43
PTFE			
140-250 μm ID/OD	0	0.07	0.43
Stainless Steel			
200/400 μm ID/OD	0	0.15	0.87

5.1.3 Summary

In each case, relatively small increases in optical attenuation were suffered as a result of consolidation and curing of the host laminate. The increase can in each case be attributed to increased microbend attenuation. Optical fibre fracture would be expected to produce larger losses. From this we conclude that protection of the fragile optical fibre at the laminate exit may be afforded by means of a close fitting polymer or metal tube. Further investigations will attempt to confirm that failure has not occurred, for example by using short distance resolution OTDR to examine for reflections from breaks. The OTDR will also help to locate the origin of microbend induced losses.

5.2 Embedding trials with advanced thermoplastic materials

Embedding of optical fibres in advanced thermoplastic composite materials was investigated.

A twin-core fibre sensor, with an external diameter of 125 μm, was embedded in carbon fibre reinforced thermoplastic material (ICI APC2 PEEK/AS4). The composite material was moulded into a tube (Figure 7). The tube was manufactured by laying the pre-preg onto a rigid mandrel and subsequently consolidating using an inflatable diaphragm process.

A reinforcement fibre orientation of +30°,-30°,0°,0°,-30°,+30°, was used, where the 0° direction is that of the tube length axis. The fibre optic sensor was placed in 0° direction between the two 0° reinforcement fibre plies with a layer of pure PEEK film either side to give further protection. The assembly was transferred to a split female cavity tool (Figure 8) which was placed between the platens of a 500 ton electrically heated press. The tool was heated to

380°C and internal pressure was increased in increments of 1 bar up to a maximum of 14 bar. After dwelling for 15 minutes, the press was cooled to room temperature and the tube removed. The internal diaphragm was removed by acid digestion.

Early attempts invariably resulted in fracture of the embedded fibre at the point of exit from the composite laminate. The following three approaches were adopted with the aim of overcoming this problem:

1) The tube was moulded with no end support for the emerging optical fibres, which were simply run directly along the mandrel and through holes drilled in the tool end plates. Moulding resulted in fracture of the embedded fibre at the point of exit from the laminate.

2) Support tape, 3 plies thick (ie the thickness of the laminate between the fibre sensor and the diaphragm) was wrapped around the diaphragm between the pre-preg and the mould tool ends to provide a smooth even thickness over the transition area. This was then overwrapped with tape to form a cushion for the emerging optical fibres. The ends of the emerging optical fibre were wrapped around the mandrel ends and secured. Moulding again resulted in fracture of the fibre sensor at the point of exit from the laminate.

3) A very small bore stiff tube was slipped over the fibre sensor, penetrating approximately 1 mm into the laminate. The tube was subsequently removed after moulding. A successful moulding operation resulted which did not cause optical fibre fracture.

5.3 Securing of Fibre Sensor Connectors

Bare optical fibre, terminated with modified FC type connectors, was moulded into a test laminates to demonstrate the feasibility of this technique.

Molex FC connectors were modified for embedding by removing the threaded securing sleeve, leaving only the ceramic ferrule and the plastic body of the connector. The connector was further modified by turning the plastic body down to a diameter of only 2.5 mm. A PTFE block was machined to accept the connector and was designed to restrict the outward flow of resin from the pre-preg during consolidation. Bare 125 µm optical fibre was terminated with the modified connectors and embedded between plies 8 and 9 of a 16 ply BMS 8-79 type woven glass/epoxy pre-preg material. An optical attenuation measurement was made. The test panel was cured at 125°C under a pressure of 293 kPa for two hours.

The cured laminate was examined visually and appeared to be of reasonable quality. The connectors appeared to have been slightly displaced and some resin had flowed into the PTFE block and adhered to the connectors. Optical loss measurement confirmed only a slight increase in attenuation of 3 dB which was probably due to increased microbend attenuation, confirming that the optical fibre had survived the embedding process. Investigations of the effect of the connector on the host material are underway. Further research will attempt to develop improved connectors with reduced overall diameters.

5.4 NDT Investigation of Fibre Sensor Embedding

Experiments were designed to study the effectiveness of aerospace type NDT techniques in assessing the effect of an embedded optical fibre on the host material.

5.4.1 Effect of varying embedded fibre diameter

Rings of optical fibre (of various types and diameters) were manufactured by fusion splicing the ends of short lengths of fibre together. The rings were laid down as concentric circles in a 25 cm square laminate between plies 4 and 5 of 10 plies of BMS 8-79 3K 5-Harness satin woven, glass reinforced epoxy pre-preg.

Three fibres were embedded

1) a 125 µm outer diameter (*OD*) bare glass fibre,

2) a 200 µm OD bare glass fibre and

3) a 125 µm glass fibre with a 900 µm OD acrylate coating.

The panel was cured and investigated using "C" type ultrasonic scanning (Figure 9).

Only the 900 µm OD fibre was clearly visible in this preliminary investigation. Optimisation of the various ultrasonic NDT parameters may allow detection of the smaller fibres. However these and other results suggest that the problem of resolving inclusions of dimensions typical of bare optical fibres will require development of special NDT techniques. It is possible that detection of the embedded fibre is made more difficult by the fact that the host laminate already consists mainly of glass fibre, and hence the ultrasonic attenuation properties are similar.

5.4.2 Detection of embedded fibres in carbon reinforced laminates

In another experiment, 20 metres of 125/250 micron diameter (fibre/polymer coating) was embedded in a 16 ply (R52-50/T300-3K 5-Harness satin woven carbon reinforced Bismaleimide) pre-preg laminate, approximately 80 x 130 cm. Approximately 10 metres were embedded between plies 4 and 5, and the remaining 10 metres embedded between plies 11 and 12. The fibre was laid into the panel so as to follow a serpentine pattern. A single piece of fibre was used, with a short length of 1 mm diameter silicone tube used to protect the fibre in the region where the fibre entered and exited the laminate and in the connecting region. The laminate was cured and examined by ultrasonic C scanning shown in Figure 10.

The embedded fibre can be seen quite clearly as a green line against a pink background. The effect of the fibre is to increase the ultrasonic attenuation by 1 dB above the background. The white regions represent the regions where the protective silicone tube extends into the laminate. These regions show markedly higher attenuations, and are significantly larger than the tube diameter. The top region of the panel shows increased attenuation, which is due to porosity resulting from a manufacturing defect (the bag seal failed early on during cure, and the laminate was simply re-bagged and the cure process continued).

We are proposing to investigate other techniques, such as ultrasonic "A" scan and conventional and advanced forms of X ray such as X ray tomography.

5.5 Investigation of Microbending Attenuation of Embedded Sensor

A 60 cm circular loop of bare 50/125 µm optical fibre was embedded in the mid plane of an 8 ply (R5250 3K 5HS woven carbon fibre reinforced Bismaleimide) laminate. The emerging ends of the fibre sensor were sleeved in silicone tube for protection. The fibre ends were terminated previous to embedding to facilitate measurements of optical loss.

Loss measurements were made;

1) Prior to embedding with no mechanical pressure on fibre 0 dB,
2) after embedding 0 dB,
3) after applying vacuum consolidation pressure to the laminate 0.02 dB,
after curing the laminate 3.20 dB.

Embedded bare 125 μm optical fibre apparently does not suffer from increased microbend attenuation even when the laminate experiences applied pressures of 1 bar. Curing of the laminate occurs under applied pressures equivalent to about 5 bar. At these higher pressures the fibre sensor apparently suffers from increased microbend attenuation. This microbending is presumably retained in the cured laminate. The increased loss of 3.18 dB over a length of 60 cm of embedded fibre will not be significant for measurement, but could indicate a risk of later strain corrosion of the fibre sensor.

Further investigations will attempt to discern whether the increased loss occurs at the point of exit of the embedded fibre from the laminate or in the sensor fibre.

5.6 Summary

Investigations into aspects of fibre sensor embedding have revealed that:

1) Exiting the fibre through narrow diameter tubes, of either polyimide, silicone or steel, affords sufficient protection of the fibre to allow bare optical fibres to survive typical (pre-preg/bag moulding) composite processing environments.
2) Moulding of connectors into laminates can be accomplished without damaging the fragile fibre sensor.
3) Ultrasonic "C" type scanning techniques are not completely effective for locating optical fibres of the dimensions typically used for embedded sensors.
4) Micro-bend attenuation of fibre sensors in typical woven fibre composites is an issue which requires further investigation. However preliminary investigations have revealed this effect may not be particularly severe, at least for moderate sensor lengths of the order of 1 metre.

6. CONCLUSION

Past experience and extensive recent literature searching has allowed us to establish clearly the technological areas of smart structures requiring detailed further development. We have therefore set up a three year collaborative research and development project which will further our expertise in;

1) Fibre optic sensors and sensor signal processing,
2) Materials and manufacturing of smart structures.

We aim to develop novel multiplexed Bragg grating type sensors capable of multiple independent discrete measurements of strain and temperature. We will also develop materials and manufacturing techniques, and generate design information, consistent with advanced composite structures. During the project we aim to explore the use of embedded fibre sensors in the monitoring of advanced materials and structures manufacturing.

The project will culminate in the manufacture of a demonstrator component. Extensive materials and processes related research and development, performed during the project, is intended to allow the demonstrator to be both technically and industrially relevant.

REFERENCES AND NOTES

1.Eaton N C, Maidment C T, "The Development of Intelligent Structures", *European Space Agency ESTEC Contract no 8521/89/NL/TB*, 1991

2.patent pending

3.patent pending

4.Jensen D W, Pascual J, August J A, "Performance of graphite/bismaleimide laminates with embedded optical fibres, Part I & II", *Smart Materials and Structures*, vol 1, 1992, pp 31-45

5.Roberts S S, Davidson R, *Fibre Optic Smart Structures and Skins IV*, SPIE vol 1588, 1991

6.Measures R M et al, *Applied Optics*, vol 28, 1989, p 2631

7.see notes 5,6

8.Meltz G et al "Formation of Bragg gratings in optical fibers by a transverse holographic method", *Optics Letters* vol 14, no 15, 1989, pp 823-825

9.Davidson R, Roberts S S, "Finite element analysis of composite laminates containing transversely embedded optical fibre sensors", *First European Conf on Smart Structures and Materials*, SPIE Vol 1777, 1992, pp 115-123

10.Sirkis J, *Smart Structures and Skins IV*, SPIE Vol 1588, 1991

11.Pak Y E, "Longitudinal shear transfer in fibre optic sensors", *Smart Materials and Structures*, vol 1, 1992, pp 57-63

12.Roberts S S, Davidson R, *Fibre Optic Smart Structures and Skins IV*, SPIE vol 1588, 1991

13.Vengsarkar A M et al, *Fibre Optic Smart Structures and Skins IV*, SPIE vol 1588, 1991

14.Jensen D W, Pascual J, August J A, "Performance of graphite/bismaleimide laminates with embedded optical fibres, Part I & II", *Smart Materials and Structures*, vol 1, 1992, pp 31-45

- CALIBRATION OF SENSORS
- STRUCTURE CHARACTERISATION

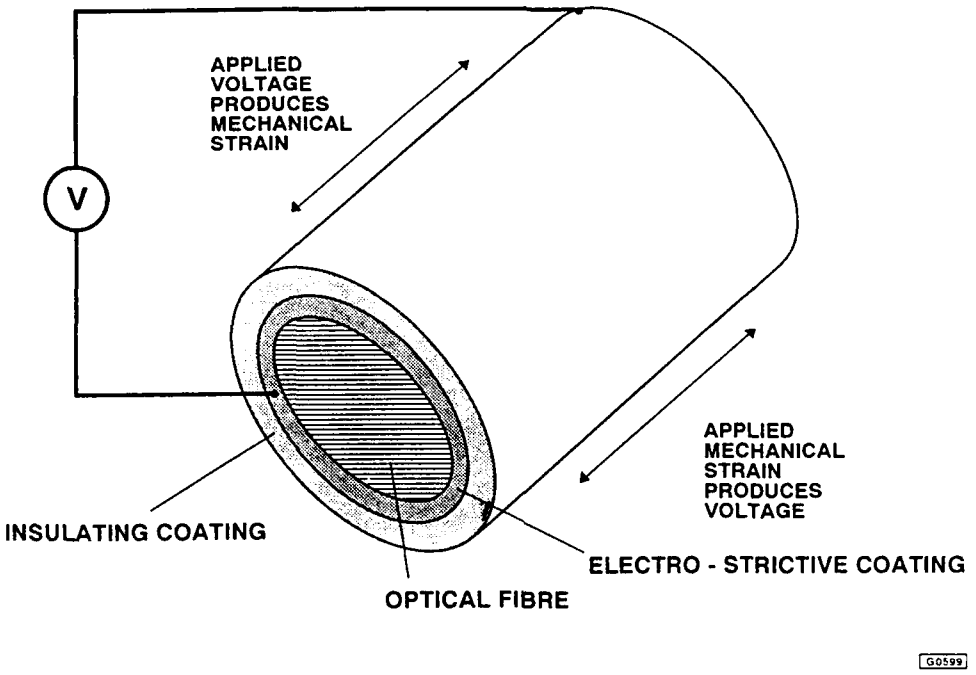

FIGURE 1a - INTEGRATED SENSOR/ACTUATOR PACKAGE

DAMAGE / DEFECT DETECTION - COMBINATION OF OPTICAL FIBRE SENSING AND 'ACTIVE' FIBRE COATINGS PROVIDE MEANS FOR INTERROGATING MATERIAL AND STRUCTURE HEALTH

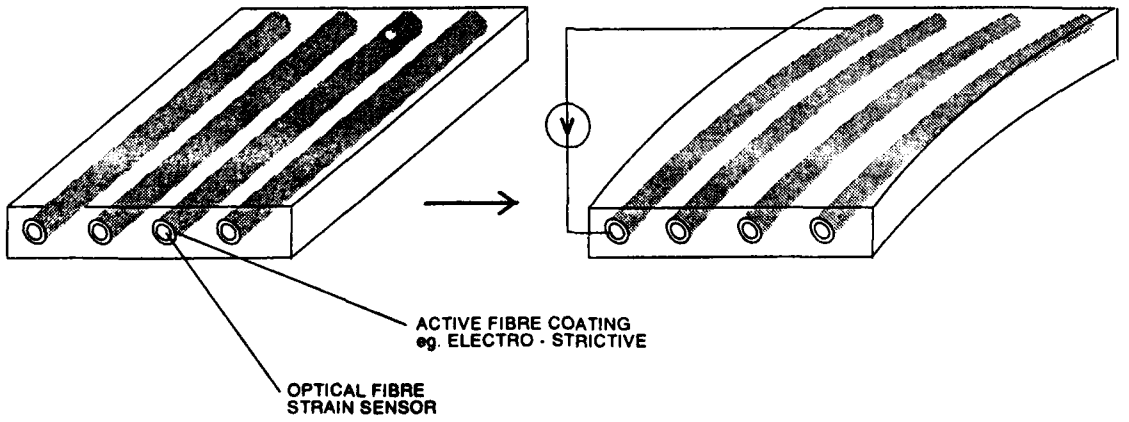

ARRAY OF COMBINED SENSOR / ACTUATOR PACKAGES MONITOR MATERIALS MECHANICAL RESPONSE

STRUCTURE IS DRIVEN BY ACTIVE ELEMENT, AND MODE SHAPES AND FREQUENCIES DETERMINED BY SENSOR ELEMENTS

FIGURE 1b - HEALTH MONITORING BY FIBRE SENSOR/ACTUATOR PACKAGES

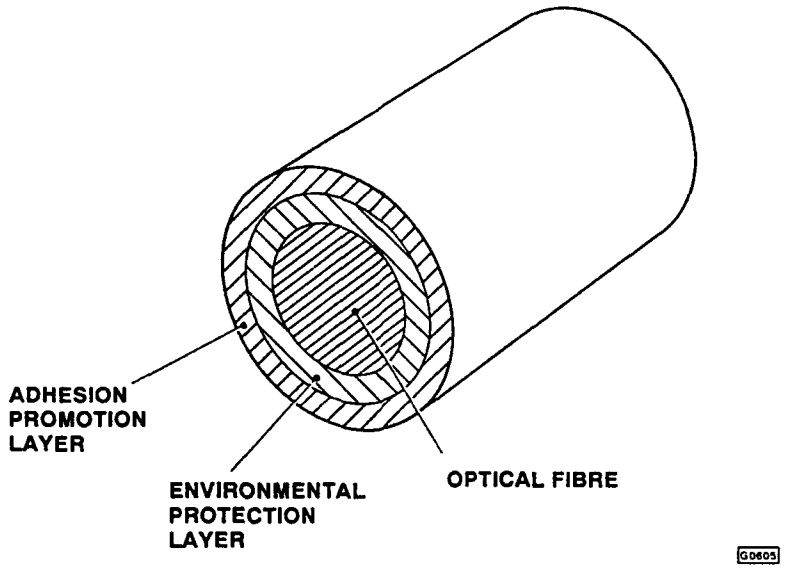

FIGURE 2 - GENERIC SENSOR/COATING PACKAGE

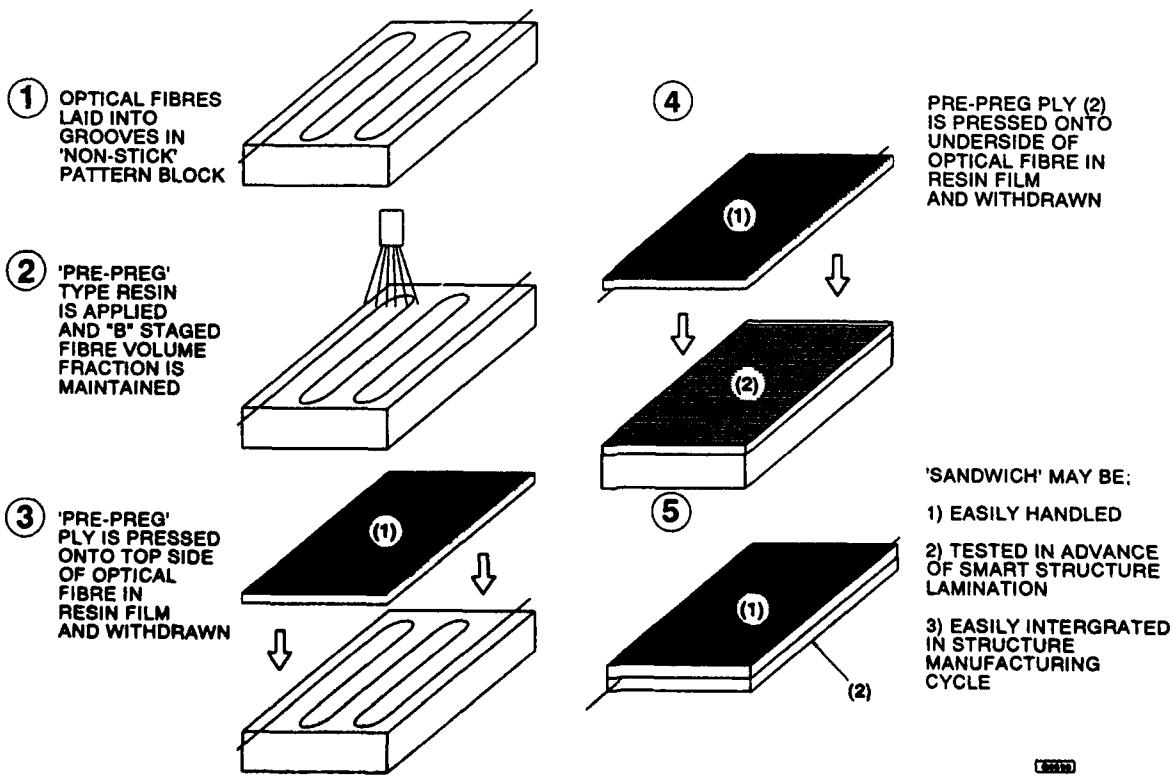

FIGURE 3 - EMBEDDING METHOD

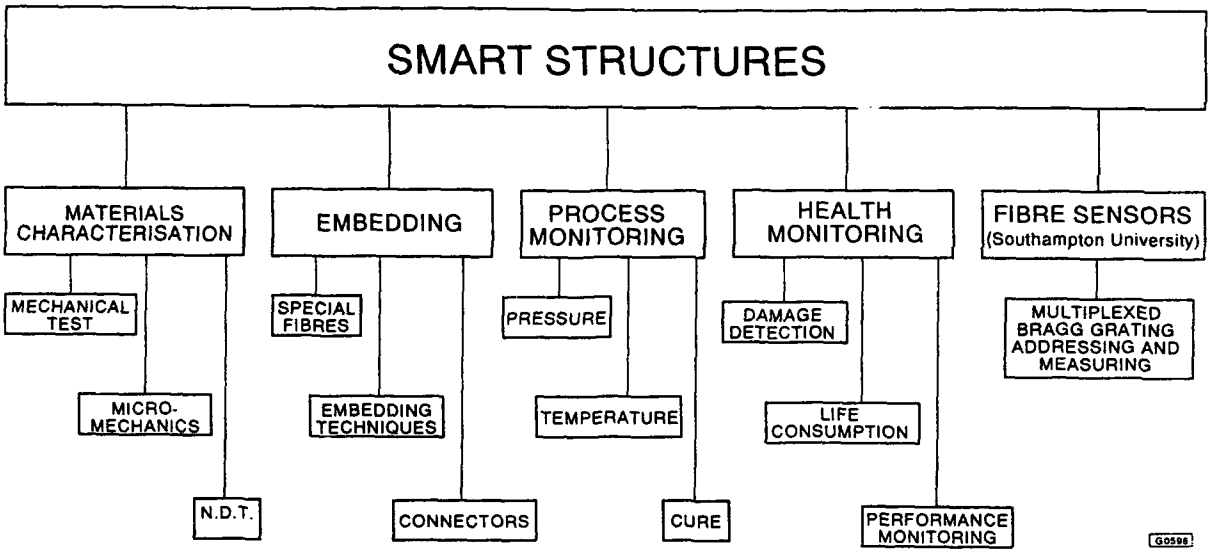

FIGURE 4 - SMART STRUCTURES RESEARCH ACTIVITIES

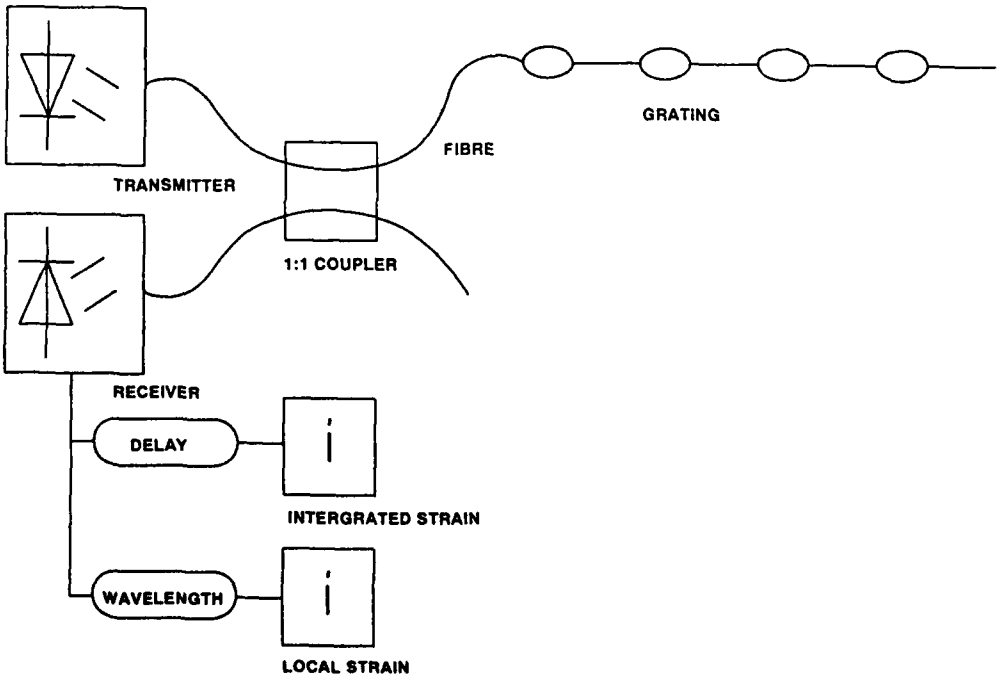

FIGURE 5 - PROPOSED FIBRE SENSOR SYSTEM

1. MECHANICAL TEST	- TENSION - COMPRESSION - INTER LAMINAR SHEAR - FATIGUE ASSESSMENT
2. NON-DESTRUCTIVE TEST	- ULTRASONIC "A" AND "C" SCAN - X-RAY - TRANSMISSION - X-RAY - BACK SCATTER AND TOMOGRAPHY
3. MICRO-MECHANICAL MODELLING	- STRESS FIELDS IN OPTICAL FIBRES - STRESS FIELDS IN HOST LAMINATES

G0587

FIGURE 6 - PROPOSED MATERIALS CHARACTERISATION PROGRAMME

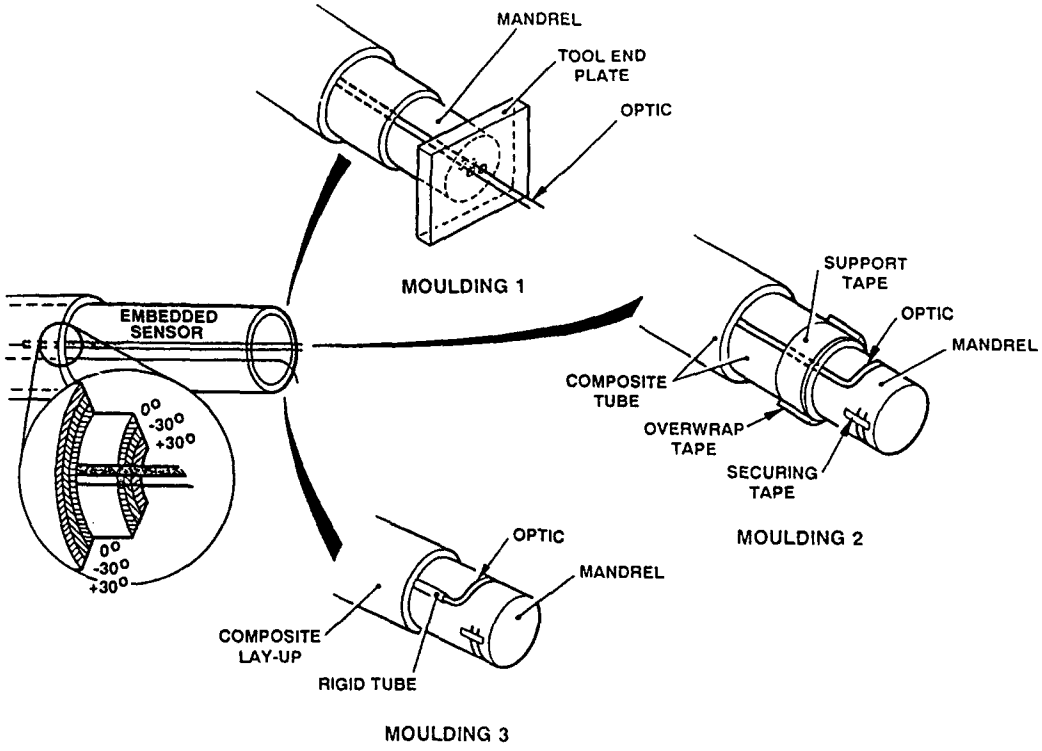

FIGURE 7 - SCHEMATIC OF THREE MOULDING APPROACHES

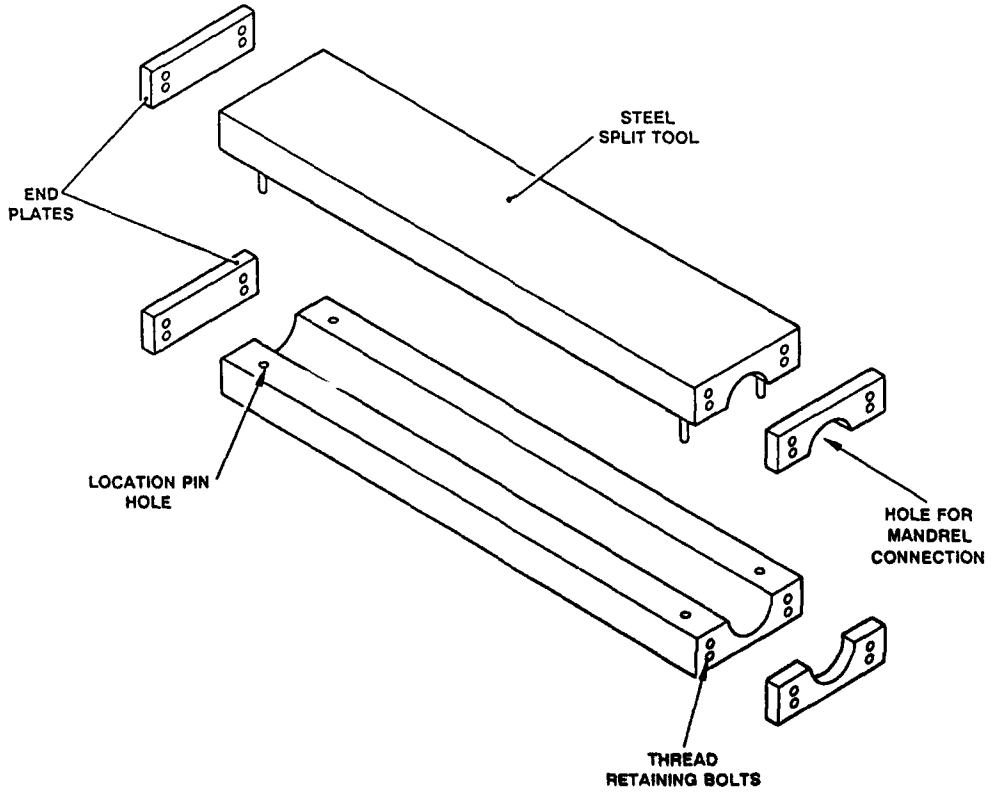

FIGURE 8 - MOULDING TOOL

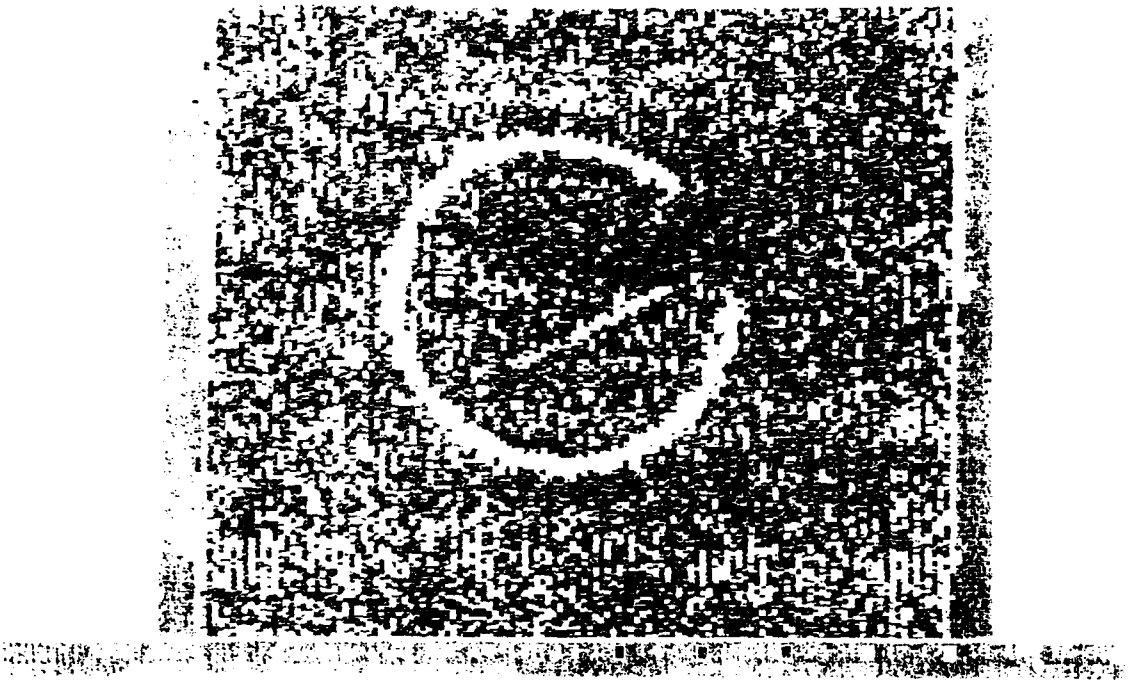

FIGURE 9 - 'C' SCAN INVESTIGATION - OPTICAL FIBRES IN GLASS PANEL

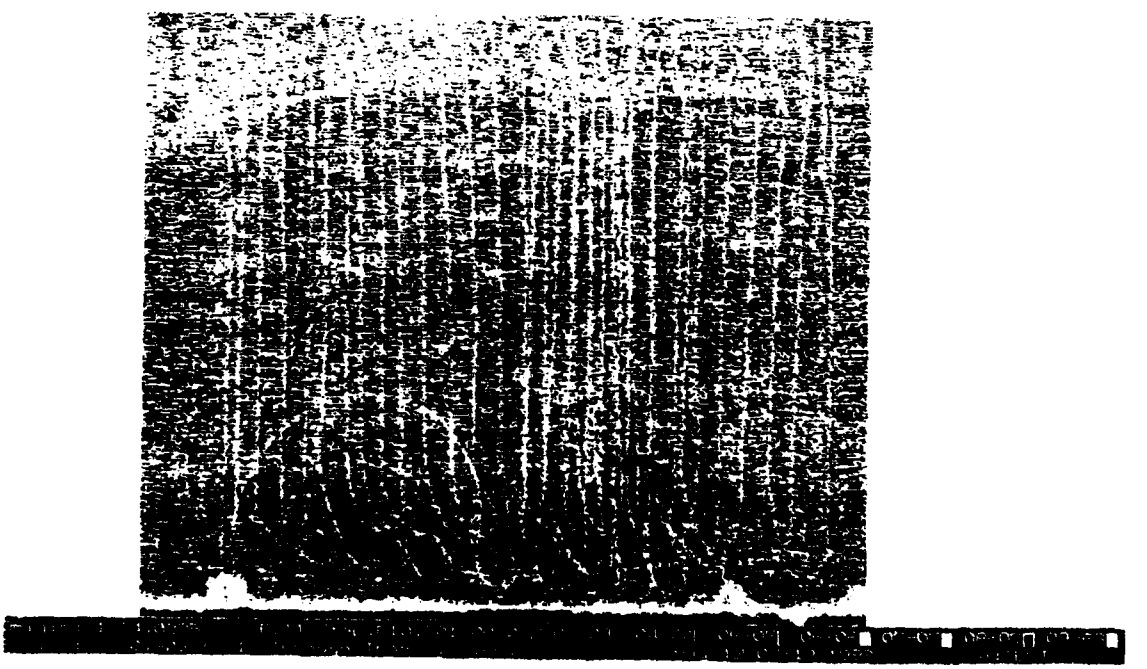

FIGURE 10 - 'C' SCAN INVESTIGATION - OPTICAL FIBRES IN CARBON PANEL

Fiber-Optic Sensor Systems for Measuring Strain and the Detection of Acoustic Emissions in Smart Structures

F.A. Blaha, Canadian Marconi Company
S.L. McBride, Acoustic Emission Monitoring Services Inc.
2442 Trenton Avenue
Montreal, Quebec, Canada H3P 1Y9

SUMMARY

This paper outlines the requirements of a fiber-optic strain sensor system for aircraft smart structures, and reports on an experimental system developed by Canadian Marconi Company for this application. Fiber-optic strain sensors have been mounted on an aircraft undergoing full-scale durability and damage tolerance tests, the results of which are presented. Tests were also carried out to verify the response of fiber-optic sensors to acoustic impulse signals. Input signals, similar to the ones encountered in damaged materials under stress, were used to evaluate the response of the sensor to bulk, surface and plate waves. This was done in order to assess the performance of fiber-optic sensors employed in the acoustic detection of damage in materials.

1. INTRODUCTION

Smart structures will provide a reliable and cost-effective means of aircraft structural health monitoring, and will drastically alter currently implemented Aircraft Structural Integrity Programs (ASIPs).[1] Structural maintenance and repair will be performed as needed, and not as dictated by life expectancy models which derive their input from individual aircraft usage tracking and scheduled non-destructive tests.[2]

With the advent of smart structures, structural health will be monitored while the aircraft is in use. Near-real-time, on-board signal processors will provide a measure of the flight-worthiness of the aircraft structure and, if necessary, alert the pilot and recommend restrictions to the flight profile. Indications of required repairs will be available to ground and maintenance personnel.

Two complementary concepts are being developed for structural health monitoring, based on the evaluation of changes to stress fields and of stress waves, respectively. The first involves the measurement of absolute strain, and the second the detection of acoustic emissions under loaded conditions in order to detect any damage to the structure.

It has been clearly demonstrated recently that acoustic emission can be a powerful tool for the location and identification of fatigue cracks in aerospace structures.[3,4] In these and other acoustic emission tests, the sensors used to detect the acoustic emissions were piezoelectric elements attached to the surface of the structure. The output voltage is preamplified before transmission via coaxial cable to the data acquisition and analysis instrumentation.

Several significant advantages of fiber-optic sensors over electrical sensors will permit the realization of smart structures. These include insensitivity to electromagnetic interference to provide low-noise data transmission; small size and embeddability; ease of implementing sensor arrays; and high measurement sensitivity.

2. FIBER-OPTIC SENSORS

A variety of fiber-optic sensor concepts have been investigated for the measurement of a multitude of parameters and diverse applications. Table 1 provides an overview of the characteristics required for the application to health monitoring in smart aircraft structures.

The requirements of Table 1 considerably reduce the number of fiber-optic sensors suitable for this specific application. Four very promising candidates are evaluated in Table 2.

3. FIBER-OPTIC STRAIN SENSING

All the sensors in Table 2 exhibit the periodic transfer function typical of interferometric sensors. For measuring the optical path difference (OPD) of interferometric sensors -- a requirement for absolute strain measurements -- concepts have been developed employing low-coherence (white light interferometry) or modulated highly coherent sources.[5,6,7]

CMC has implemented a strain sensing system utilizing interferometric sensors based on the two-mode concept.[5] Figure 1 is a basic block diagram of the system. Its signal source comprises two GaAs diode lasers which are on/off-toggled for sequential operation in low and high coherence modes. Thus, the signal source provides four different outputs for one measurement cycle of a sensor. The system employs a number of time-shared sensors.

The wavelengths of the two lasers have been selected for quadrature operation with respect to the sensor transfer function. Ratiometric measurements of the outputs of a reference and a strain sensor are performed. An analytical reduction of these measurements eliminates the influence of variations in transmission losses (L), laser power (P), wavelength (λ), and detection preamplifier gain (G_p).

The reduced ratiometric measurement quantities are:

$$V_1 = \frac{V_{L1S} / V_{LED1S}}{V_{L1R} / V_{LED1R}}$$

$$V_2 = \frac{V_{L2S} / V_{LED2S}}{V_{L2R} / V_{LED2R}}$$

Subscripts 1 and 2 in the equations refer to measurements made with lasers 1 or 2 respectively. V_{L1S} and V_{L1R} are the sensing and reference outputs when the system is powered with laser diode 1 in the high coherence mode. V_{LED1S} and V_{LED1R} are the same outputs with laser diode 1 in the low coherence mode.

Two corresponding strain equations can be set up:

$$S_1 = 1/a_1 \{ \cos^{-1} [1/\alpha_1 (V_1/G_1 - 1)] - \phi_1 \}$$

$$S_2 = 1/a_2 \{ \cos^{-1} [1/\alpha_2 (V_2/G_2 - 1)] - \phi_2 \}$$

Four parameters must be known in order to solve each equation: the imbalance (a) and initial phase angle (ϕ) of the strain sensor, fringe visibility (α), and effective system gain (G). These parameters, which are evaluated by performing a least square fit, are assumed to be constant over a reasonable period of time.

The system has been used on an aircraft undergoing fatigue tests. Data have been logged and evaluated from four fiber sensors and two conventional strain gauges, surface-mounted in proximity as shown in Figure 2. Various test cycles of the aircraft have been tracked. Figure 3 shows the experimental development model (EDM) of the system together with the portable PC employed for data collection evaluation and display of strain data.

Figures 4 and 5 indicate the resultant strain measurements performed by one sensor during specific test cycles. Figure 6 shows a plot of the relative strain derived from measurement data of a conventional strain gauge and a fiber sensor mounted close by. The plot indicates that test data from the two sensors are in close agreement.

The tests also provide an indication of sensor reliability. Sensor performance was monitored over a period of approximately one month, during which the aircraft underwent many high-G manoeuvres.

4. FIBER OPTIC ACOUSTIC EMISSION SENSING

During the past 20 years, acoustic emission has been applied successfully for the detection of numerous material degradation and failure problems. The results of these applications are catalogued in Drouillard's bibliography of acoustic emission.[8,9] McBride and Maclachlan[10,11,12] and McBride et al[3,4] have investigated the application of acoustic emission to aerospace structures. It has been shown that continuous acoustic emission monitoring can reliably detect fatigue cracks in complex structures such as a full-scale fatigue test specimen[4], and that the technique can be used during flight.[3] Figure 7 shows the instrumentation with piezoelectric sensors which are currently being used, with typical test results shown in Figure 8. Figure 9 shows the results of McBride et al[4], with a comparison of acoustic emission location and actual fatigue cracks as determined by conventional NDI.

In order to assess the performance of fiber-optic sensors for the detection of acoustic signals, a Fabry-Perot sensing element was bonded to the flat surface of an aluminum cylinder 23 cm in diameter and 16 cm in length. A piezoelectric sensor, with a reasonably flat frequency response in the range 0.1 to 1.5 MHz, was also acoustically coupled to the same surface, close to the Fabry-Perot sensor element. The use of the large aluminum cylinder permits the sensors to detect acoustic pulses from an acoustic source injected on the same surface of the sensors, without overlap with reflected pulses from the cylinder boundaries.

The acoustic emission simulation source used is the fracture of a 0.5-mm Pentel lead. This produces a broadband (0 - 1.5-MHz) acoustic pulse which is about an order of magnitude larger than pulses associated with damage in materials. Figure 10 shows a comparison of resulting signals detected by the piezoelectric sensor and a 5-mm gauge-length Fabry-Perot sensor. The important feature is the relatively large amplitude pulse which occurs in both cases, showing clearly that the simulated acoustic emission source is readily detectable by the Fabry-Perot sensor.

Figure 11 shows the directional dependence of the Fabry-Perot sensor. Here, the simulated acoustic emission source was applied at various angles to the optical fiber. The directivity increased with longer gauge lengths. This result was expected, since the acoustic length is on the order of 1 cm for the recorded frequency range.

6. CONCLUSION

Although a number of practical problems need to be resolved, the strain test results demonstrate the feasibility of using fiber-optic systems for sensing absolute strain in an aircraft environment. Further work is required to resolve the strain vector and to distinguish between load- and temperature-induced strains.

From the results, it is also clear that it is possible to detect acoustic emission signals using the Fabry-Perot fiber-optic interferometer.[13] More detailed data will be required for the quantitative definition of the dynamic range and signal-to-noise ratio of this device, compared to those obtained for the high-output piezoelectric sensors currently used for acoustic emission sensing. Further, the stability of the fiber-optic sensor system must be improved before it can become a practical method for continuous acoustic emission monitoring.

7. ACKNOWLEDGEMENTS

The authors would like to thank the members of CMC's Opto-Electronics group; in particular, Jun Lu, François Séguin and Kexin Liu for performing measurements, and Eric Johnstone and Martin Houde for their systems work. Support from the Canadian Department of Defence and Canadair, and helpful discussions with Bob Hastings and the DAS-ENG 6 staff, especially Pierre Beaudet and Mirko Zgela, are gratefully acknowledged.

8. REFERENCES

1. Zgela, M.B. and Madley, W.B., "Durability and damage tolerance testing and fatigue life management: A CF18 experience", Fatigue Management, AGARD CP506, Bath, England, pp.10.1-16, April 1991.

2. Sendeckyi, G.P. and Paul, C.A., "Some smart structures concepts", Fiber Optic Smart Structures and Skins II, SPIE Vol.1170, pp.2-10, 1989.

3. McBride, S.L. et al, "Acoustic emission detection of crack presence and crack advance during flight", AGARD CP.462, Ref.16, pp.1-5, 1990.

4. McBride, S.L. et al, "Acoustic emission monitoring of aging aircraft structures", Review of Progress in Quantitative Nondestructive Evaluation, Vol.11, pp.2275-82, 1992.

5. Lu, Z.J. and Blaha, F.A., "A Fiber optic strain and impact sensor system for composite materials", Fiber Optic Smart Structures and Skins II, SPIE Vol.1170, pp.239-248, 1989.

6. Gusmeroli, V. and Martinelli, M., "Absolute measurements by low coherence source", OFS-China, 1991.

7. Uttam, D. et al., "Close loop interferometric remote optical fiber sensor", Fiber Optic and Laser Sensors, SPIE Vol.412, pp.256-257.

8. Drouillard, T.F., "Acoustic Emission, A Bibliography with Abstracts", Plenum Data Company, New York, 1979.

9. Drouillard, T.F., "Bibliography update", Journal of Acoustic Emission (JAC), 1992.

10. McBride, S.L. and Maclachlan, J.W., "In-flight acoustic monitoring of a wing attachment component", JAC vol. 1, pp.223-8, 1982.

11. McBride, S.L. and Maclachlan, J.W., "Effect of crack presence on in-flight airframe noises in a wing attachment component", JAC vol. 1, pp.229-35, 1982.

12. McBride, S.L. and Maclachlan, J.W., "Acoustic emission due to crack growth, crack face rubbing and structural noise in the CC-130 Hercules aircraft", JAC vol. 3, pp.1-10, 1984.

13. Liu, K. et al., "Damage detection in composites with embedded fiber optic interferometric sensors", Fiber Optic Smart Structures and Skins II, SPIE Vol.1170, pp.205-210, 1989.

TABLE 1 - SENSOR REQUIREMENTS FOR AIRCRAFT SMART STRUCTURES

REQUIREMENT	REASON FOR REQUIREMENT
Intrinsic	Ease of surface mounting. Embedding of sensors without structural degradation.
Size	Gauge length typically 1 cm, diameter 80 μm.
Absolute Strain Measurement	Strain measurements referenced to the sensor under zero strain. Sensor reference must be retained with sensor disconnected.
Large dynamic range	Strain sensor requires a minimum dynamic range of 30 db. A typical strain measurement range is -2000 to 5000 μE.
High sensitivity	Acoustic emission sensing with the application of strain sensors requires a measurement sensitivity in the nE region.
Multiplexing	Multiplexing of sensors is an essential requirement in order to implement sensor arrays and maintain a low number of feed fibers and composite structure ingress points.
Temperature compensation	Discrimination between mechanical and temperature induced strain components.
Longitudinal strain measurement	Measurement of the strain vector.
EM interference immunity	Essential for implementing extensive fiber-optic sensor arrays on an aircraft.
SM transmission fiber	Ease and economy of interconnect. System performance must not deteriorate with the insertion of a large number of connectors in the transmission line.
High reliability	MTBF of embedded fiber sensor >20 years. Graceful degradation of the sensor performance.
High-yield manufacturing process	Cost-competitiveness of fiber sensor with conventional strain gauge.

TABLE 2 - CANDIDATE FIBER-OPTIC SENSORS FOR APPLICATION IN AIRCRAFT SMART STRUCTURES

CONCEPT	ADVANTAGE	DISADVANTAGE
Two-mode	Low production cost	Not suitable for acoustic emission sensing. Difficult to manufacture with consistent performance characteristics.
Polarimetric	Low production cost	Unsuitable for acoustic emission sensing.
Fabry-Perot	High sensitivity	Complex fabrication process. Uncertain reliability.
Fiber Grating	Low system complexity	Applicability to acoustic emission sensing has yet to be determined. Fabrication process unsatisfactory.

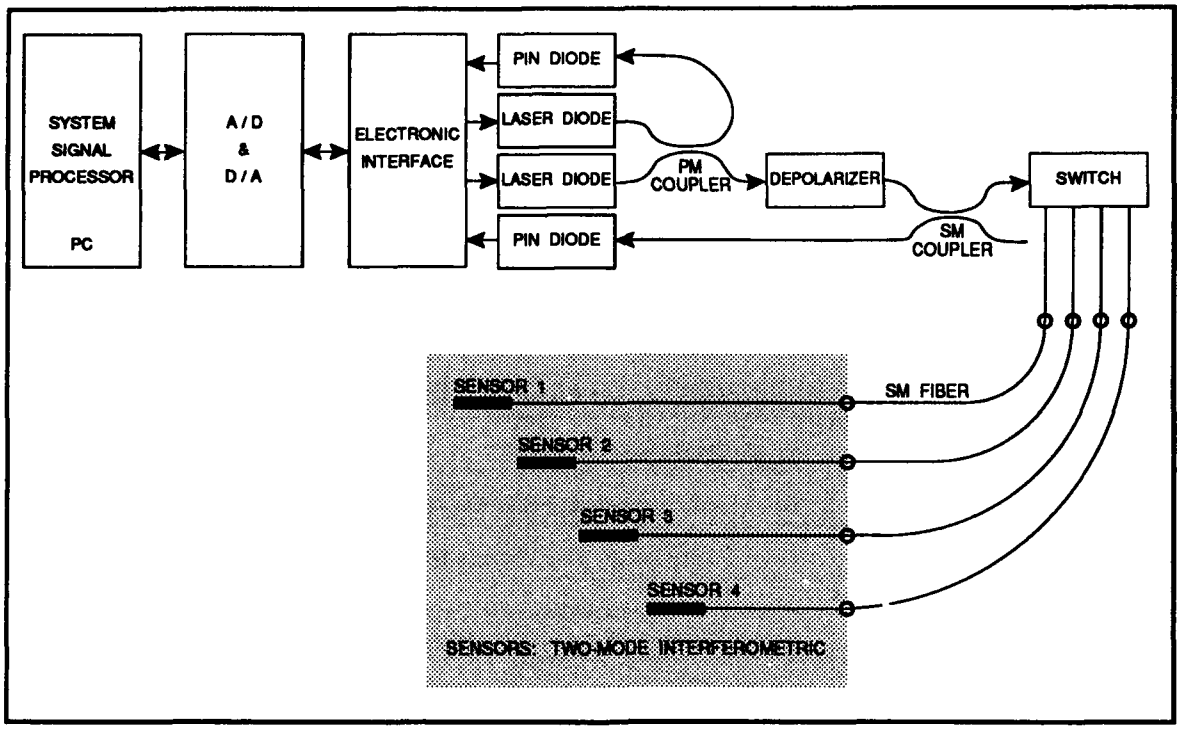

FIGURE 1 - BLOCK DIAGRAM OF THE FIBER OPTIC STRAIN SENSOR SYSTEM

FIGURE 2 - AIRCRAFT FATIGUE TESTS:
PHOTOGRAPH OF SURFACE-BONDED FIBER AND RESISTIVE STRAIN GAUGES

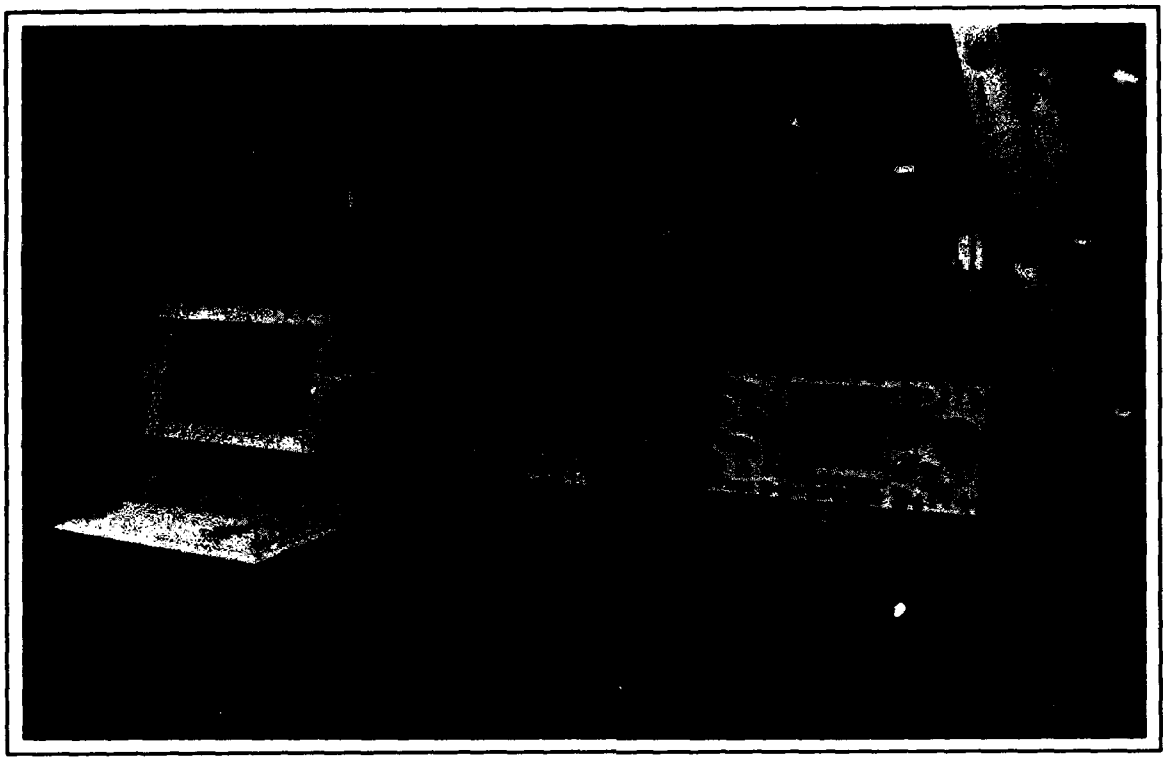

FIGURE 3 - AIRCRAFT FATIGUE TESTS:
PHOTOGRAPH OF FIBER-OPTIC SENSOR SYSTEM AND SUPPORT EQUIPMENT

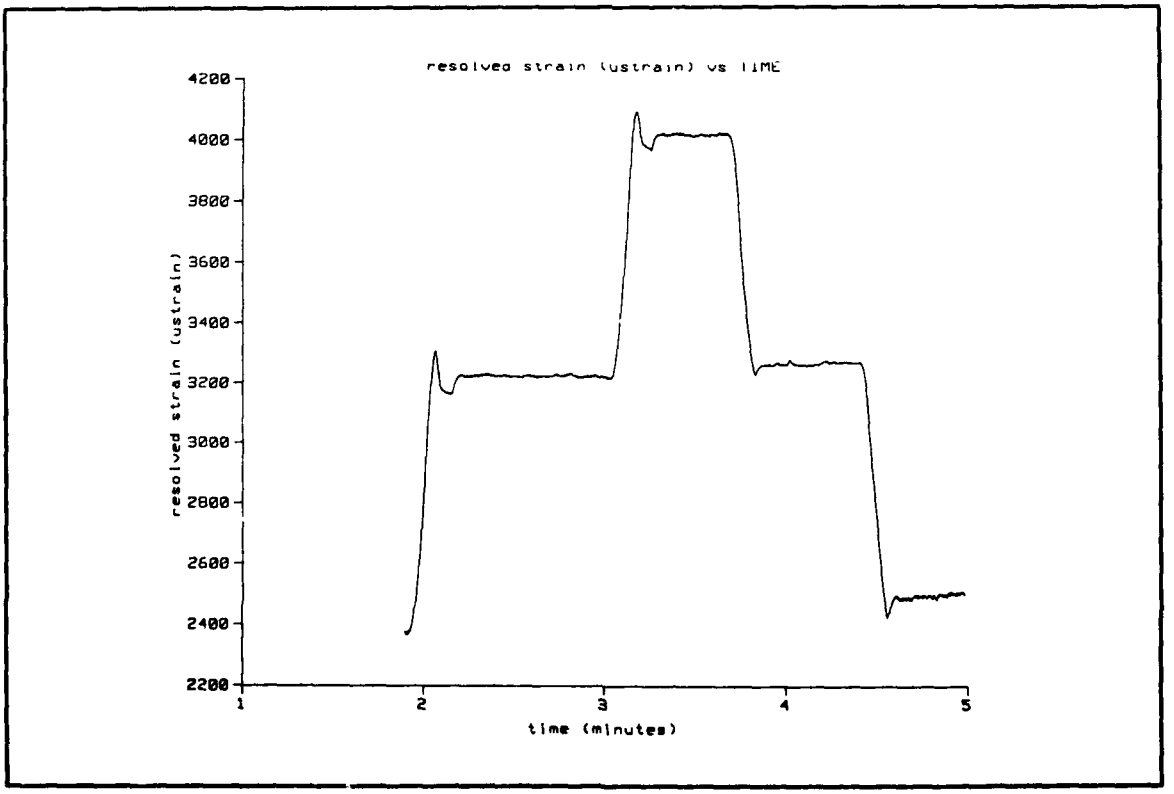

FIGURE 4 - AIRCRAFT FATIGUE TESTS:
STRAIN MEASUREMENT WITH FIBER-OPTIC SENSOR DURING ONE TEST CYCLE

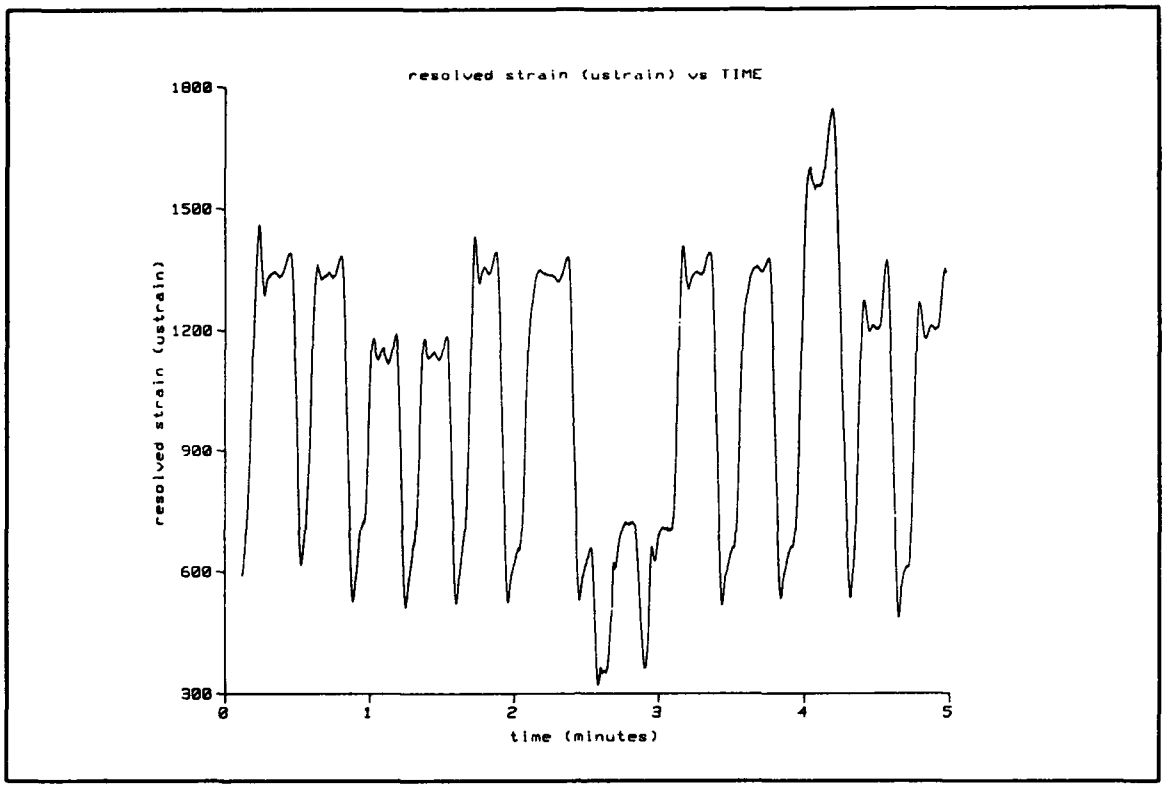

FIGURE 5 - AIRCRAFT FATIGUE TESTS:
STRAIN MEASUREMENT WITH FIBER-OPTIC SENSOR DURING ONE TEST CYCLE

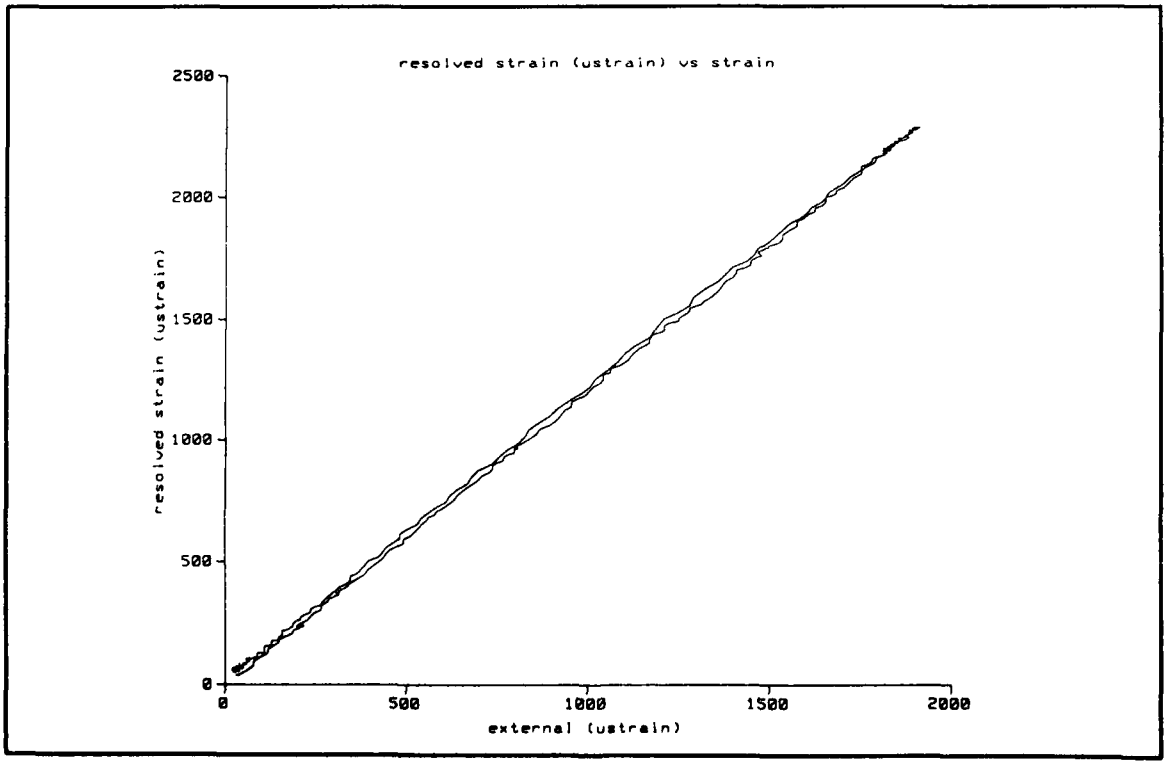

FIGURE 6 - PLOT OF RELATIVE STRAIN BETWEEN FIBER-OPTIC SENSOR
AND RESISTIVE STRAIN GAUGE DURING ONE TEST CYCLE

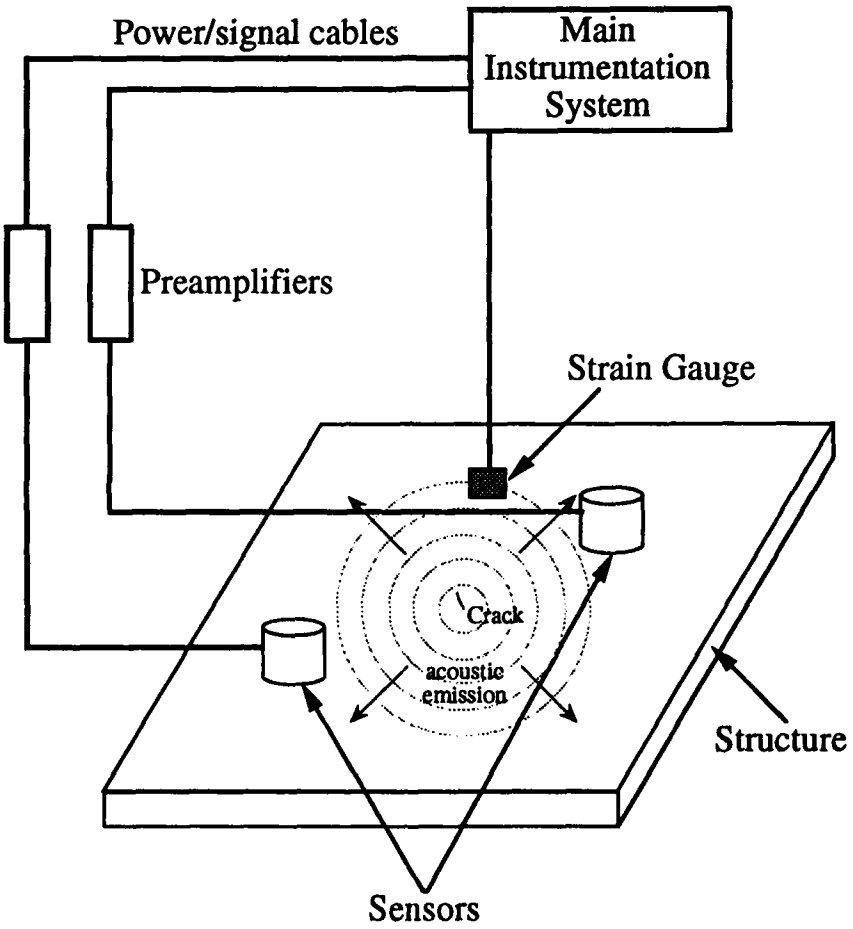

FIGURE 7 - INSTRUMENTATION EMPLOYING PIEZOELECTRIC GAUGES TYPICALLY USED FOR ACOUSTIC EMISSION SENSING AND THE LOCATION OF DEFECTS

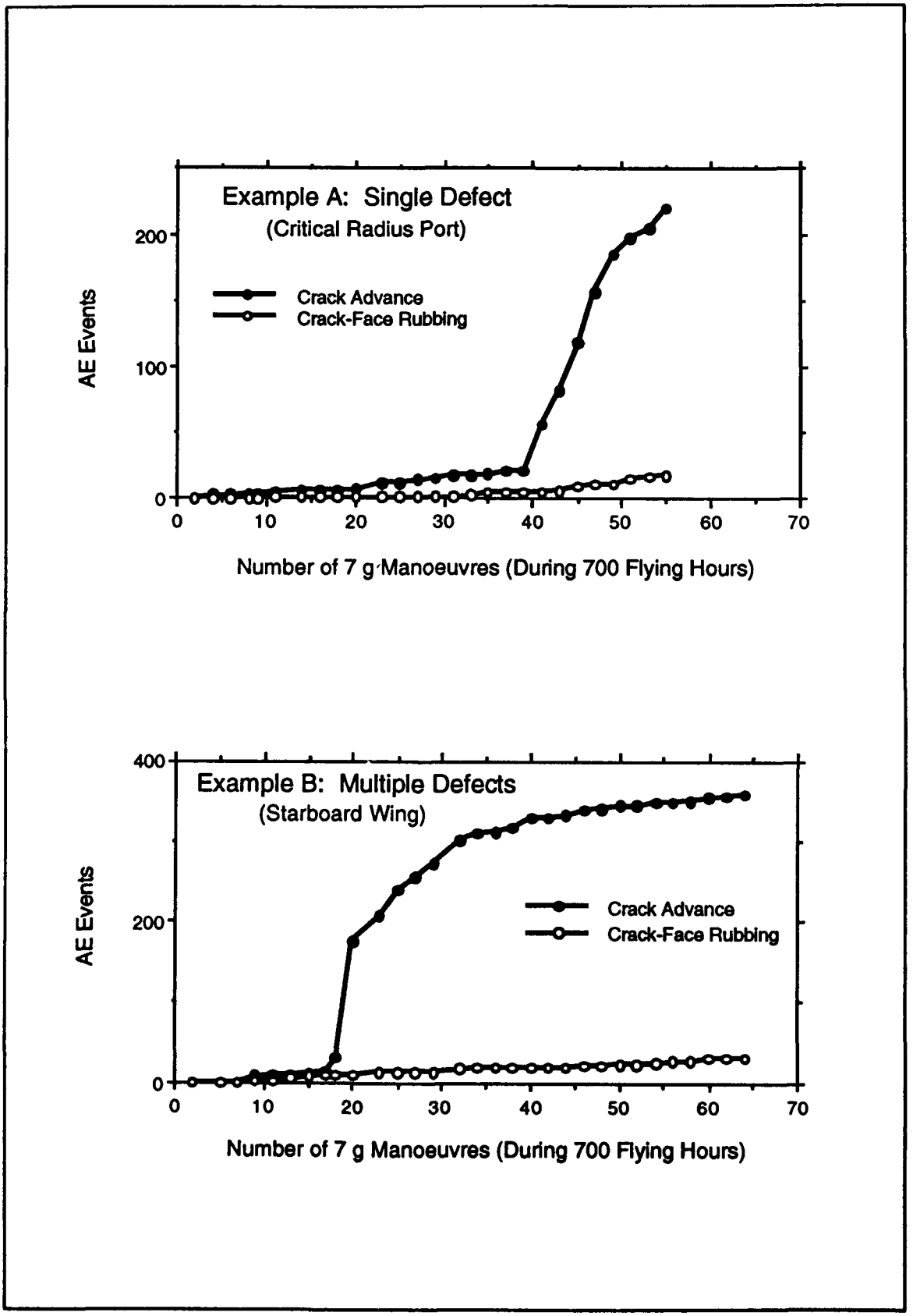

FIGURE 8 - ACOUSTIC EMISSION HISTORY OF CRACK GROWTH FROM (A) A SINGLE DEFECT, AND (B) A CLUSTER OF DEFECTS

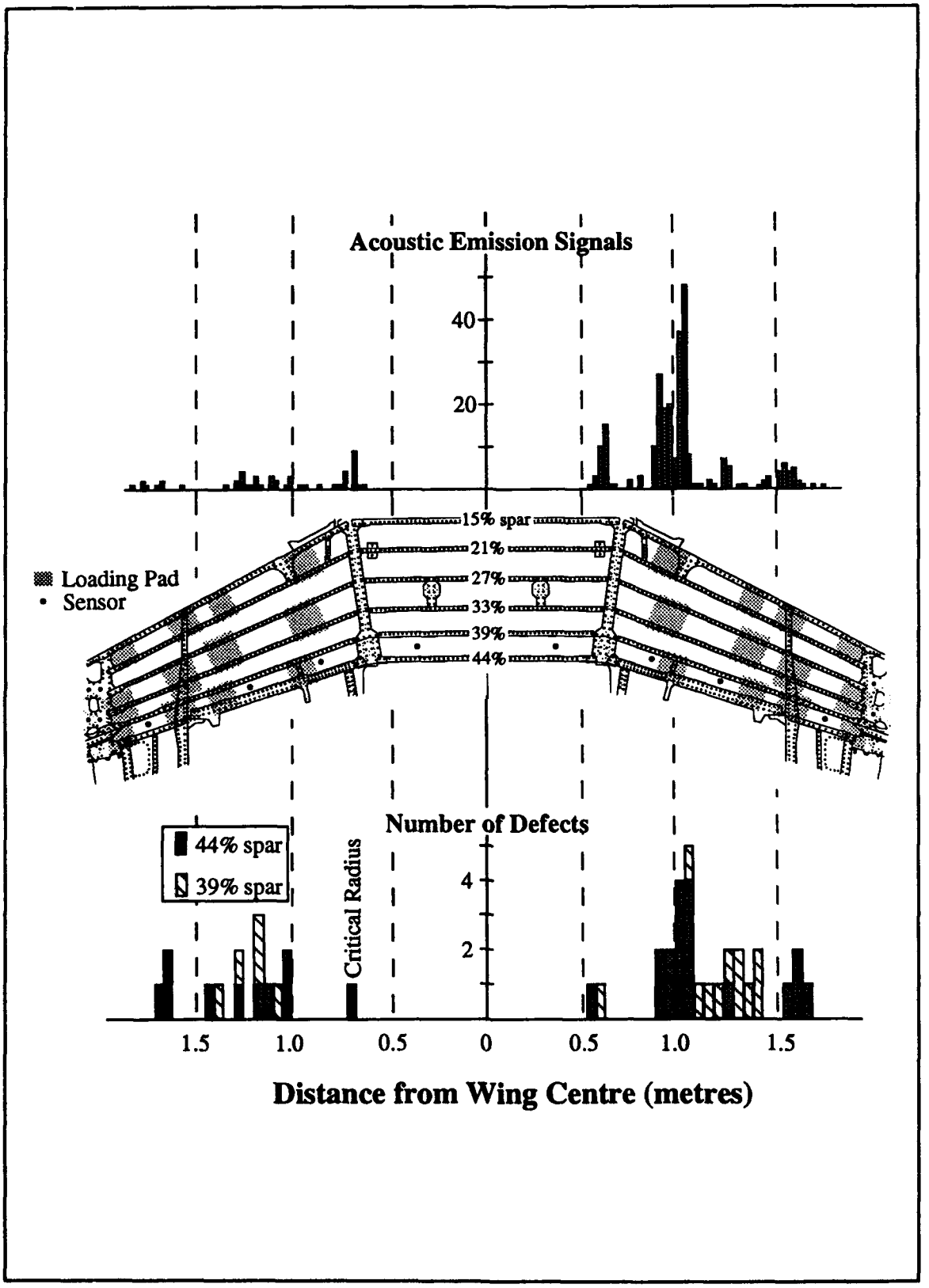

FIGURE 9 - SCHEMATIC OF MONITORED WING SECTION, INDICATING LOADING PADS AND SENSOR LOCATIONS, AND HISTOGRAMS OF DETECTED ACOUSTIC EMISSIONS AND FATIGUE CRACKS CONFIRMED BY ROTATING-COIL EDDY CURRENT MEASUREMENTS AFTER REMOVAL OF ALL FASTENERS IN THE 39% AND 44% SPARS

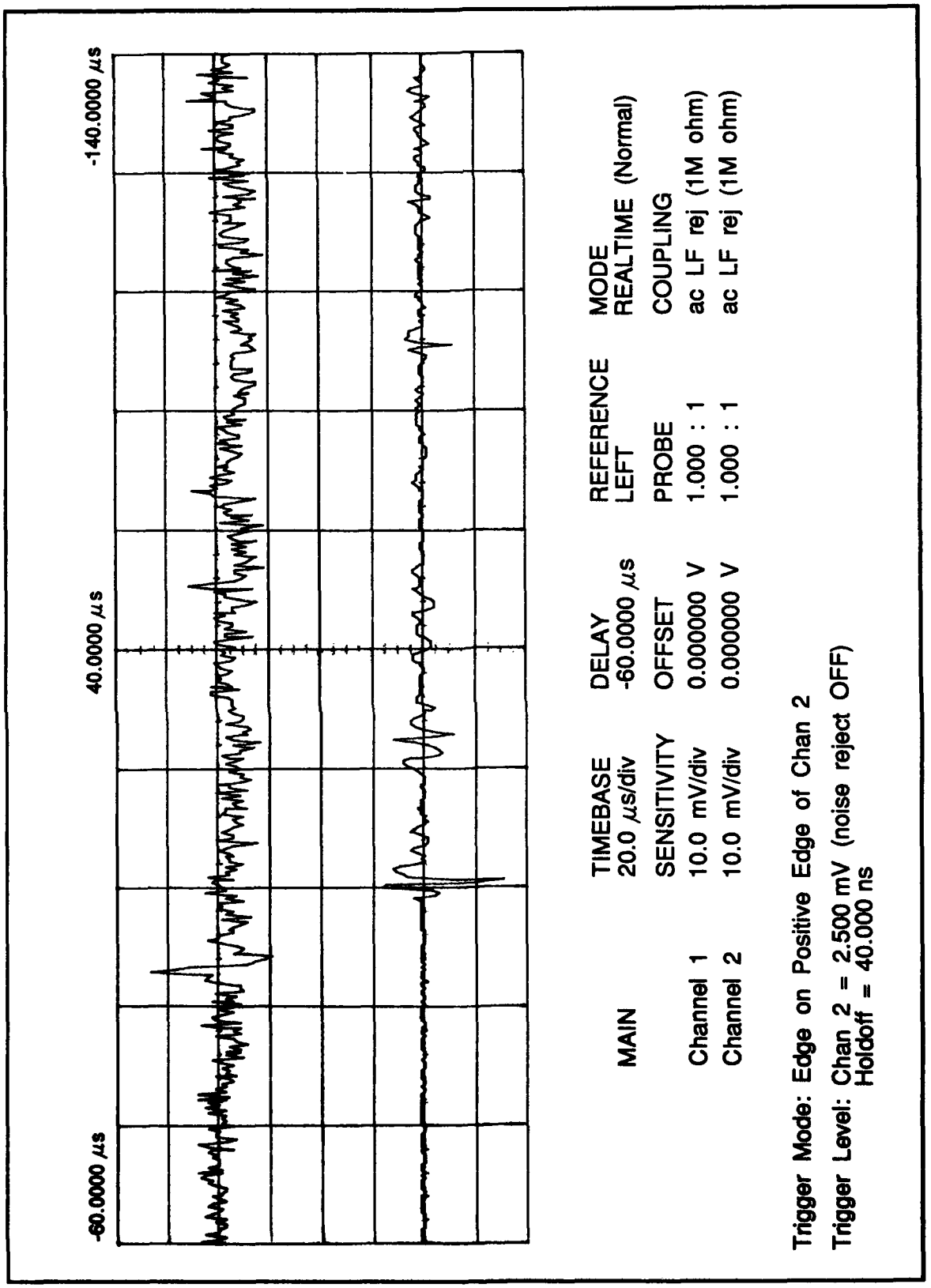

FIGURE 10 - ACOUSTIC EMISSION SIGNAL DETECTED WITH FABRY-PEROT SENSOR (TOP) AND PIEZOELECTRIC SENSOR (BOTTOM)

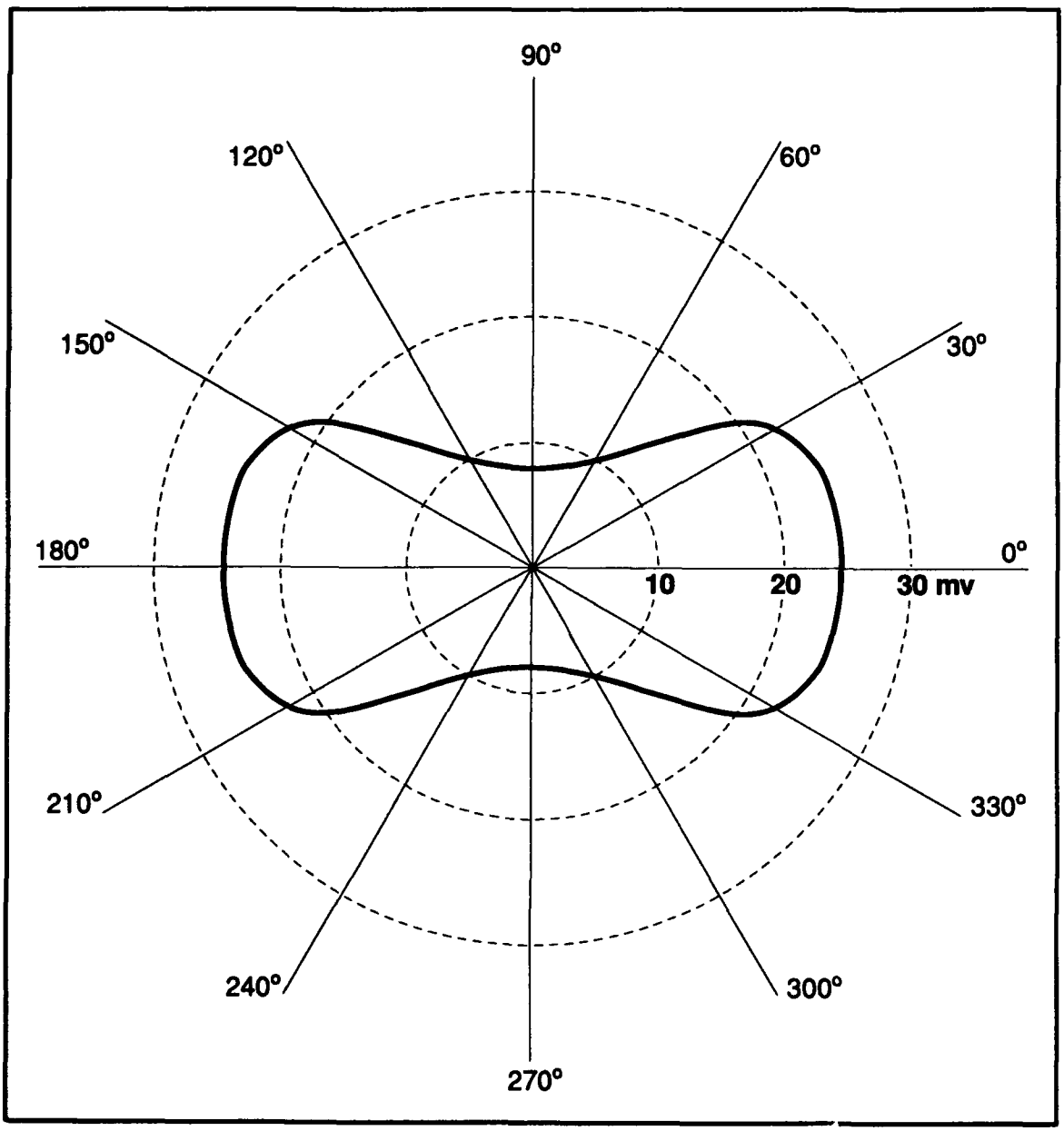

FIGURE 11 - DIRECTIONAL SENSITIVITY OF A FABRY-PEROT SENSOR WITH A 5-*mm* GAUGE LENGTH

Adaptive Algorithms for use with Digital Filters in Vibration Control

R. Wimmel

German Aerospace Research Establishment (DLR), Institute of Aeroelasticity
Bunsenstrasse 10, D-3400 Göttingen, Germany

ABSTRACT

Digital filters can easily be used to alter signal flows. As long as the desired transfer function of the filter is causal, a great variety of responses is made possible by appropriate choice of filter coefficients. To make use of this property in vibration control, algorithms should automatically change the filter coefficients to meet any given objective. This paper describes a class of adaptive algorithms which search the gradient of a given performance function. In order to illustrate the requirements of adaptive structures, such as structurally conformed design, the feed-forward control environment serves as an example for applying these algorithms.

1. INTRODUCTION

The design and development of technical structural systems are necessarily based on the proper knowledge of

- a desired profile of objective functions,
- the corresponding external loads,
- the resulting structural responses.

At the end of the development process, the structural system must naturally comply with all of the requirements set within this conditional frame. Two industrial problems arise:

1. The objective functions often conflict with each other (e.g. weight minimization ⇔ safety and stability).
2. The relevant objective functions should stay optimized despite the presence of external loads.

In cases of unforeseen changes or when it is impossible to control these objective functions, the objective behavior very often exceeds realistic structural limits. Therefore, it seems to be inappropriate that technical structural systems avoid adaptability, particularly when adaptive dynamics are ever present in living nature.

The employment of active control technology as a kind of troubleshooting generally introduces some penalties, e.g. additional weight, increased maintenance costs, etc. However, these problems can be eliminated if

- new kinds of integrated, multifunctional sensors and actuators working as components lying in the load path and
- adaptive controllers consisting of digital filters which are adaptive in that they react to external influences as well as to changes within the structure itself

are developed in a simultaneous design process. For a description of this design method as well as possible applications, see Breitbach [1].

Digital filters possess powerful properties because of their adaptability. They allow for real-time operation if programmed on high-speed digital signal processors. The development of such rapid processors must be considered a decisive step towards a breakthrough in adaptive structures.

This paper describes how digital filters can be used for

- vibration control of adaptive structures with integrated actuators and sensors and
- vibration isolation of different vibrating structural systems connected through multifunctional interfaces

if they are combined with adaptive algorithms.

2. DESIGNING DIGITAL FILTERS

The transfer function of any kind of digital filter can generally be written as

$$H(z) = \frac{A(z)}{1 - B(z)} \tag{1}$$

$$\text{with } A(z) = \sum_{j=0}^{N} a_j z^{-j}, \quad B(z) = \sum_{j=1}^{N} b_j z^{-j},$$

where the a's and b's form a set of coefficients of the IIR filter $H(z)$ [2].

The transfer function of a structural system can likewise be described mathematically as a ratio of polynomials. Consequently, the transformation of the excitation signal into the structural response signal through the structure's dynamics is simply a signal filtering action from the signal processing point of view.

This allows proven representations from structural dynamics to be adopted in order to give digital filter systems a design which is in conformance with the structure.

A first example may illustrate the principle: A measurement could, for instance, result in impulse response samples which could be used to design the structure's digital filter representation for simulations. If the fact is taken into account that the z-transform of a sampled impulse response is an FIR filter with a set of coefficients equal to the impulse response samples, the simplest thing to do is design an FIR filter, i.e. $B(z) = 0$ in Eq. (1).

2.1 Digital Filters for System Identification

The modal representation seems to offer the best possible means of finding a filter system representation applicable in system identification environments (see Figure 1). In order to configure the filter in a way identical to the modal configuration of the transfer function of the structure to be identified, it is decom-

posed into a set of parallel modal subfilters. The block diagram of such a modal filter is shown in Figure 2.

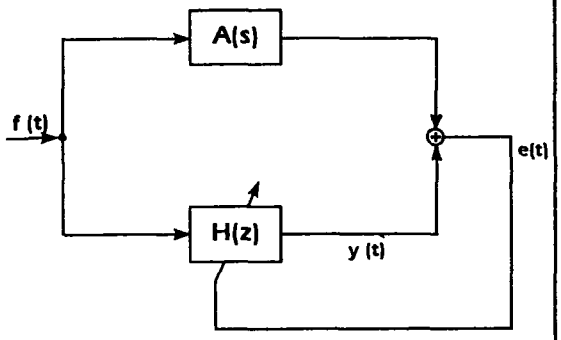

Fig. 1: Signal flow in system identification.
H(z): digital time-varying transfer matrix of the adaptive filter system. *A(s)*: behavior of the continuous structural system, e.g. given by the accelerance matrix. The AD- and DA-converters are not explicitly carried out.

$$A(s) = \sum_{i=1}^{m} A_i(s) \quad \text{(modal formulation)}$$

assuming m modes $A_i(s)$

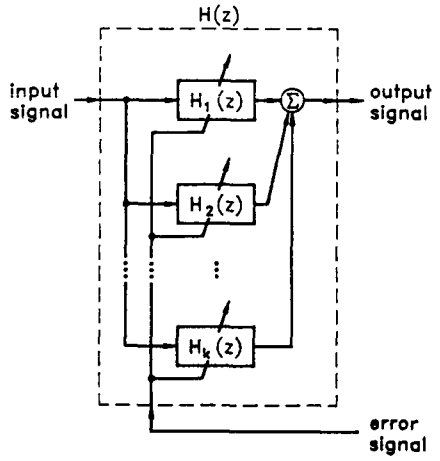

$$H(z) = \sum_{i=1}^{k} H_i(z) \quad \text{(parallel form)}$$

assuming k filter modules $H_i(z)$

Fig. 2: Block diagram of a modal filter

If an accelerance function has to be identified, the single mode can be described as

$$A_{ikl}(s) = \frac{s^2}{K_i + D_i s + M_i s^2}\, \varphi_{ik}\, \varphi_{il} \qquad (2)$$

or

$$A_{ikl}(s) = \left(\frac{1}{M_i} + \frac{r_i}{s - s_i} + \frac{r_i^*}{s - s_i^*} \right) \varphi_{ik}\, \varphi_{il} \quad , \qquad (3)$$

where K_i, D_i and M_i are the i-th elements of the corresponding modal matrices of stiffness, damping, and mass, respectively; r_i, r_i^* and s_i, s_i^* are the complex conjugate pairs of the residues and the poles, respectively; φ_{ik} and φ_{il} are elements of the i-th eigenvector; and k and l represent two measuring points.

Different kinds of subfilters with structural conformity can be chosen. Their transfer functions can be of second order:

$$H_{ikl}(s) = \frac{a_{ikl}\left(1 - 2z^{-1} + z^{-2}\right)}{1 + b_{1,i}z^{-1} + b_{2,i}z^{-2}} \qquad (4)$$

(a_{ikl}, $b_{1,i}$ and $b_{2,i}$ are the real coefficients, see Melcher and Wimmel [3]) or can be divided into a sum of two complex first-order sections and one real multiplication:

$$H_{ikl} = c_{ikl} + \frac{a_{ikl}}{1 - b_i z^{-1}} + \frac{a_{ikl}^*}{1 - b_i^* z^{-1}} \qquad (5)$$

(c_{ikl} is the real coefficient, a_{ikl} and b_i are the complex coefficients).

To overcome the computational costs due to the complex algorithm of the latter, an optimized new filter type called the MX filter (see Melcher [4]) has been developed. This filter has a cross-coupled structure with real coefficients and its transfer function is equal to Eq. (3), except for a time delay.

These examples from system identification show how important it is to find solutions for a filter design in conformance with the structure. Due to the direct relation of the filter coefficients to the modal data, the filter systems are predestined to act as digital representations of the structure in simulation, system identification, and structural control.

2.2 Digital Filters for Feed-Forward Control

Figure 3 shows the signal flow for a basic feed-forward controller. The primary signal path is depicted as $P(s)$. A secondary or control path contains the transfer function $S(s)$. A sensor measures the sum of both signals as an error signal. It vanishes if the control filter $H(z)$ is adapted to

$$H(z) \approx -\frac{P(s)}{S(s)} \qquad (6)$$

An optimized filter which conforms to the controlled structure as well as to the feed-forward environment is still a topic of research, but in order to maintain stability a parallel structure with second-order subsections might be effective. Since the feed-forward controller contains system identification elements as shown in [5], filter types such as in Eqs. (4) and (5) should also be applied in this environment.

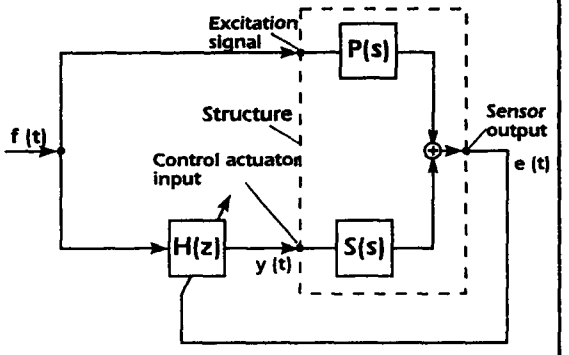

Fig. 3: Typical set-up of an adaptive feed-forward controller: the structural response (represented by the transfer function $P(s)$) due to a given excitation signal can be altered by a multifunctional control actuator and an adaptive control filter $H(z)$.
$S(s)$: secondary (control) path.
The AD- and DA-converters are not explicitly carried out.

New filter systems must be developed for different types of structures, e.g. those with

- local concentrated dampers,
- nonlinearities,
- anisotropies,
- boundary conditions,

or for special measurement conditions, e.g.

- noise in the signal path,
- limited equipment,
- drift,
- transient phenomena,

and other application tasks, e.g.

- inverse modeling,
- prediction,
- feedback phenomena,
- acoustic control,
- echo canceling,
- wave propagation control.

These filter systems should use as much a priori knowledge as possible from related disciplines such as

- structural mechanics,
- structural dynamics,
- acoustics.

So far, general design rules have been described for digital filters. Different applicational tasks demand specialized filter structures which are all different manifestations of the underlying rational function Eq. (1). The following deals with adaptive algorithms which enable the digital filters to not only alter the signal flow, but also to adaptively control the vibrational behavior of structures.

3. ADAPTIVE ALGORITHMS

If a digital filter system is configured as described above, then the adaptation algorithm is clearly dictated by the filter structure. A more common question is: what kind of performance function should underlie the algorithm? A commonly used function with good properties is the mean square error.

To take advantage of this function, one must first measure or define a signal which indicates the misadjustment of the adaptive system. In a system identification application the response of a structural system is measured, e.g. using displacement sensors and accelerometers. An error signal is then obtained by comparing (through subtraction) the actual filter output to the sampled response signal.

In control applications a transducer can often be located precisely at the point where the vibration should vanish in order to directly measure the error signal. Two problems arise, i.e.:

- The performance function may have several minima of which only the global minimum relates to an optimal set of filter coefficients.
- A fast and stable adaptive algorithm is required to find a minimum.

3.1 Mean Square Error as a Performance Function

The mean square error function $\psi(n)$ appropriate for a given structural system depends on the chosen filter structure as well as the task of the filter. For Feed Forward Control and System Identification, the function is:

$$\psi_{FF}(n) = \frac{1}{2\pi j} \oint \Phi_{xx} |P(z) + S(z)H(z)|^2 \frac{dz}{z} \qquad (7)$$

and

$$\psi_{SI}(n) = \frac{1}{2\pi j} \oint \Phi_{xx} |A(z) - H(z)|^2 \frac{dz}{z} \qquad (8)$$

respectively.

The path of integration is the unit circle. Φ_{xx} is the auto power spectrum of the signal $x(n)$ and can be assumed to be 1 for white noise.

The transfer functions $P(z)$, $S(z)$ and $A(z)$ could be determined according to any mathematical model of the structure.

Since $\psi(n)$ is a function of $H(z)$ and therefore of the coefficients of $H(z)$ at time step n, it can be seen why $\psi(n)$ also depends on the filter structure as stated above.

Examples illustrating contour plots of the performance function in compliance with Eq. (7) for filter structures like Eq. (4) and Eq. (5) are given in [3] and [6], respectively. It should also be mentioned that the performance function is quadratic with regard to the transversal coefficients of $H(z)$. This makes any F.R version highly interesting and particularly simple for any adaptive algorithm (see Widrow and Stearns [2]). The computation of the performance surface of complex or high-order filter structures as well as a theory for avoiding local minima are goals for further research. Much knowledge can be drawn from a study of the shape of the performance surface:

- areas where it is flat or steep,
- areas around the global minimum where no local minima exist,
- changes occurring because of parameter variations.

This knowledge can be helpful when designing algorithms that adaptively find the minimum of the mean square error function.

If the strong real-time condition in vibration control is considered, the choice of possible adaptation methods is restricted. Clearly, off-line computation should be avoided, and any analytical method of computing the minimum of the error function will not cater for changing operational conditions and, therefore, contradicts the basic idea of adaptability.

Among gradient search algorithms meeting these conditions, the class of LMS algorithms will be described as a solution with low computational costs and ease of implementation.

3.2 The Class of LMS Algorithms

One popular way to find a minimum of the performance function is to follow the gradient. The equation describing the steepest descent can generally be formulated as

$$\mathbf{W}(n+1) = \mathbf{W}(n) - \mu \cdot \nabla\psi(n) \quad , \tag{9}$$

where $\mathbf{W}(n)$ is the coefficient vector at time step n, μ is the diagonal matrix of convergence parameters, and $\nabla\psi(n)$ is the gradient vector of the performance function $\psi(n)$ relating to the coefficients W_i.

The idea behind LMS-type algorithms is to take the squared error $e^2(n)$ itself as an estimate of its expectation $\psi(n)$. For the gradient of the squared error,

$$\nabla e^2(n) = e(n)\,\nabla e(n) \tag{10}$$

is obtained.

In order to find a clear formulation, the computation of the gradient is described here in the z-domain, *although the algorithm itself works in the time domain.* The equations governing feed-forward control and system identification in the z-domain are

$$\begin{aligned} E_{FF}(z) &= X(z)\,(P(z) + S(z)H(z)) \\ \text{and} \quad E_{SI}(z) &= X(z)\,(A(z) - H(z)) \quad , \end{aligned} \tag{11}$$

respectively. $E(z)$ and $X(z)$ are the z-transforms of the error and input signals. It should be noted that $P(z)$, $S(z)$ and $D(z)$ are formal representations of the actual transfer functions $P(s)$, $S(s)$ and $D(s)$. The gradient with respect to the coefficients of $H(z)$ is

$$\begin{aligned} \nabla E_{FF}(z) &= X(z)S(z)\nabla H(z) \\ \nabla E_{SI}(z) &= X(z)(-\nabla H(z)) \end{aligned} \tag{12}$$

Two results can be recognized from Eqs. (12):

1. If the signal path contains any transfer function besides $H(z)$ (i.e. $S(z)$ in the case of feed-forward control), this must be considered in the gradient computation. An example that considers $S(z)$ is the filtered-x algorithm (see Widrow and Stearns [2]).
   This result demonstrates the dependence of the algorithms on the filter task or control environment.
2. The problem of computing the gradient of the squared error is reduced to that of finding the gradient of the filter's transfer function, which is dependent on the filter structure.

The following will give some examples for determining the filter gradient.

The ∇H-Module

As mentioned above, $\nabla H(z)$ relates to the filter structure. Therefore, it will first be derived for the IIR filter as defined in Eq. (1):

$$\begin{aligned} \frac{\partial H}{\partial a_j} &= \frac{1}{1 - B(z)}\, z^{-j} \\ \frac{\partial H}{\partial b_j} &= \frac{1}{1 - B(z)}\, H(z) \cdot z^{-j} \end{aligned} \tag{13}$$

or in vector notation

$$\nabla H = \frac{1}{1 - B(z)} \begin{bmatrix} z^0 \\ \cdot \\ \cdot \\ \cdot \\ z^{-N} \\ H(z) \cdot z^{-1} \\ \cdot \\ \cdot \\ \cdot \\ H(z) \cdot z^{-N} \end{bmatrix} , \tag{14}$$

which is simply a filtering of the U-vector (i.e. the filter's input and output values) through the filter's recursive part $1 / (1 - B(z))$.

Reduction to an FIR filter yields

$$\nabla H = \begin{bmatrix} z^0 \\ \cdot \\ \cdot \\ \cdot \\ z^{-N} \end{bmatrix} , \tag{15}$$

demonstrating the extreme simplicity of the FIR-LMS as a multiplication of the error and input signals to compute $\nabla e^2(n)$.

A derivation for a parallel-type IIR filter has been given in [5], resulting in a ∇H_i for each second order section:

$$\nabla H_i(z) = \frac{1}{1 - B_i(z)} \begin{bmatrix} z^0 \\ z^{-1} \\ z^{-2} \\ H_i(z)z^{-1} \\ H_i(z)z^{-2} \end{bmatrix} . \tag{16}$$

In the same way, the ∇H-modules for other specialized filter systems like the MX filter can also be found.

It should be realized that the algorithms described here represent only one class of possible algorithms. For the sake of stability, other considerations can be made.

Implementation

In order to obtain the most effective and rapid algorithms, several methods of implementation into a software code have been made. A discussion of several approaches for the parallel recursive LMS algorithm can be found in [7]. Possible simplifications as well as extensions, e.g. time and performance-dependent convergence parameters or frequency representations, are not dealt with in this paper.

However, another problem should be mentioned, which arises from the first result of Eq. (12): the complete transfer function of the signal path containing the adaptive filter $H(z)$ (or short: the control path) is required to compute $\nabla e^2(n)$. Since the control path transfer function contains analog and structural parts, it has to be modelled digitally by system identification. A block diagram depicting this is presented in Figure 4. It appears that the algorithm loses part of its adaptability unless the system identification unit works parallel to the control unit. Sommerfeld and Tichy [8] introduced a solution that simultaneously performs a system identification task. A solution is especially necessary if structural properties are changing.

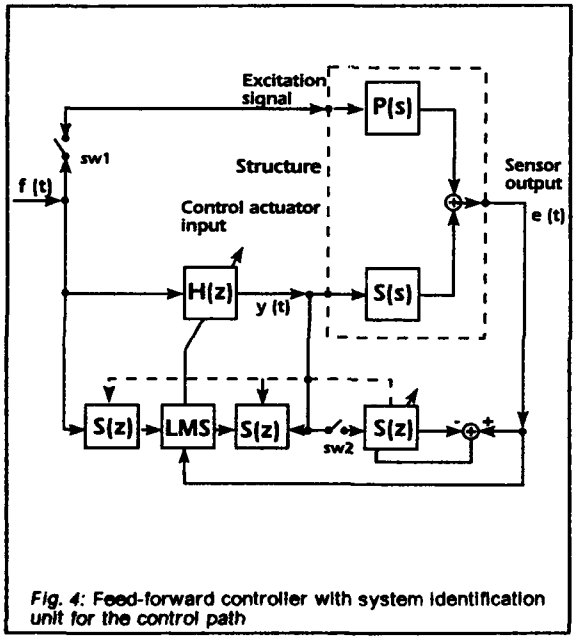

Fig. 4: Feed-forward controller with system identification unit for the control path

CONCLUDING REMARKS

It has been shown that digital filters perform appropriately for system vibration control if they are

- designed in conformance with the structure and the control task and are
- combined with an adaptive algorithm which must be optimized due to the filter structure and the control environment.

Since there is at least one class of algorithms that is able to meet these requirements, adaptive filtering can be seen as a breakthrough in adaptive structures technology. The immense number of applications of this technology should influence the search for new optimized filter types and adaptive algorithms as well as suitable performance functions.

REFERENCES

[1] E. Breitbach. Research Status on Adaptive Structures in Europe. *Proc. of the 2nd Joint Japan/US Conference on Adaptive Structures*, Nagoya, Japan, Nov. 12-14, 1991, Technomic Publishing Co., Lancaster, USA (1991).

[2] Widrow, B. and Stearns, S.D. *Adaptive Signal Processing*. Prentice Hall, Inc., Englewood Cliffs, New Jersey, USA (1985).

[3] Melcher, J. and Wimmel, R. Modern Adaptive Real-Time Controllers for Actively Reacting Flexible Structures. *Journal of Intelligent Material Systems and Structures*, 2,3 (1991).

[4] Melcher, J. Adaptive On-Line System Identification of Aerospace Structures Using MX Filters. *Proc. of the IFAC Symposium on Automatic Control in Aerospace*, Ottobrunn/Munich, Germany, September 7-11 (1992).

[5] Wimmel, R. Adaptive Digital Filters for Modal Control of Adaptive Structures. *Proc. of the Int'l Forum on Aeroelasticity and Structural Dynamics Combined with a One-Day Workshop on Smart Material Systems and Structures*, Aachen, Germany, June 3-6, 1991, DGLR Bericht 91-09, Paper No. 91-139, pp. 8-12 (1991).

[6] Melcher, J. Synthesis of Optimized Adaptive Digital Filters for System Identification and Vibration Control. *Proc. of the Int'l Forum on Aeroelasticity and Structural Dynamics Combined with a One-Day Workshop on Smart Material Systems and Structures*, Aachen, Germany, June 3-6, 1991, DGLR Bericht 91-09, Paper No. 91-145, pp. 56-64 (1991).

[7] Wimmel, R. and Melcher, J. Application of Recursive Adaptive Algorithms for System Identification and Vibration Control. *Journal of Intelligent Material Systems and Structures*, 3,3 (1992).

[8] Sommerfeld, S.D. and Tichy, J. Adaptive Control of a Two-Stage Vibration Isolation Mount. *Journal of the Acoustical Society of America*, 88, 2, August (1990).

Structural Analysis and Optimization of Adaptive Structures by use of the Finite Element Method

R. Lammering

German Aerospace Research Establishment (DLR), Institute of Aeroelasticity
Bunsenstrasse 10, D-3400 Göttingen, Germany

ABSTRACT

New finite elements which allow for the analysis and optimization of adaptive structures are presented. In the first part of this paper two finite elements accounting for integrated piezo-electric devices are formulated: a shell element for the analysis of shallow shell structures with piezo-electric polymers bonded to the surfaces and a truss element with an integrated piezo-electric ceramic. Test cases are presented to illustrate the potential of the finite elements. The shell element is used to compute the vibration excitation of a thin plate as well as the vibration control of a cantilever beam. The truss element is applied to the problem of optimal actuator placement in adaptive truss structures. For the solution of this problem, objective functions for the minimization of the control effort and the spillover energy are formulated. The second part of this paper is concerned with the finite element analysis of the behavior of shape memory alloys. A non-linear one-dimensional finite truss element and a non-linear beam element are used for the analysis of a composite beam with embedded shape memory alloy wires, of which the temperature is varied in order to tune the eigenfrequencies.

1. INTRODUCTION

The increasing demands on the performance of structural systems for mechanical and civil engineering applications as well as the necessity of lightweight constructions require a new class of structural systems, so-called smart, adaptive or intelligent structures. These structures are characterized by integrated actuators and sensors that are interconnected by adaptive real-time controllers. Among others, the most promising canditate materials for sensor/actuator applications in adaptive structures are piezo-electric and magnetostrictive materials as well as shape memory alloys. The high degree of integration of these materials into the structure results in multifunctional components with sensor, actuator and load bearing capabilities. Adaptive structures overcome the shortcomings of conventional passive structures because they independently react against both environmental influences as well as changes in the structure itself. Therefore, they allow for

- vibration suppression,
- shape control, and
- alignment precision control.

Due to their high performance and efficiency, adaptive structures offer additionally vast advantages, for instance:

- low energy consumption and, consequently, environmental benefits,
- noise reduction and, because of this, e.g. better working conditions,
- delay of fatigue and, therefore, reduction of maintenance and extension of life,
- lightweight construction and, consequently, conservation of raw materials.

Current work and technology assessment studies give the highly interdisciplinary and system-oriented adaptive structures technology a promising forecast for future applications in a wide range of industrial areas. In aerospace engineering, for instance, possible applications for fixed wing aircrafts are (cf. Breitbach [1]):

- attenuation of dynamic loads by means of an active wing-fuselage interface or an active wing-engine pylon,
- flutter suppression and vibration reduction by means of adaptive stiffness tuning and adaptive control of the wing camber.

The vibrations of helicopters can be reduced by:

- adaptive blade roots with embedded multifunctional actuators,
- blades with adaptive twist angles by means of distributed actuator material (Individual Blade Control, cf. Nitzsche and Breitbach [2]).

Automobiles are also heavily affected by noise and vibrations from different sources, such as the motor, road roughness, road-tire contact, wind and the exhaust system. The adaptive structures technology offers solutions such as

- vibration and noise control by actively controlled motor suspension systems,
- attenuation of noise radiation by actively controlling the vibrations of the roof sheet and the splash board, and
- noise and vibration control by means of the adaptively controlled suspension system.

In order to be able to effectively design, evaluate and select adaptive structures before their construction, in any particular application it is necessary to precisely understand their static and dynamic mechanical behavior. For this purpose methods for the analysis and optimization of smart structures are currently being developed. The main technical objectives for the mathematical modeling of adaptive structures are outlined as follows:

- the development of constitutive equations of smart materials and their implementation into software codes, e.g. finite element codes,
- the formulation of mathematical models for multifunctional components, and
- the development of optimization algorithms in order to compute the most efficient sensor and actuator positions.

It is emphasized that the constitutive equations of all the abovementioned smart materials have to take into account coupling effects: either an electro-mechanical, a thermo-mechanical or a magneto-mechanical coupling. These coupling effects must also be considered in the development of mathematical models of multifunctional actuators and sensors, e.g. finite elements

for plates and shells with piezo-electric polymers bonded to the surfaces.

This paper is concerned with the finite element analysis of smart structures and is divided into two parts: the first one considers piezo-electric materials and the second one shape memory alloys. The first part starts with the derivation of the electrical and mechanical balance equations and their coupled weak form. Two finite elements are derived from this formulation: a shell element taking into account piezo-electric polymers bonded to the upper and lower surfaces of shell structures and a truss element with an integrated piezo-electric ceramic. The shell element is used for the analyses of two problems: vibration excitation of a thin plate and vibration control of a cantilever beam. The problem of optimal actuator placement is solved for the case of adaptive truss structures by use of the piezo-electric truss element. The optimal placement strategy is based on the Independent Modal Space Control and finite element computations of the eigenvectors that consist of displacements and electric potentials.

In the second part of this paper the physical basis of shape memory behavior is outlined, and the implementation of a general one-dimensional constitutive equation, proposed by Brinson [3], into a non-linear finite element code is presented. This finite element is applied to the example of a clamped composite beam with integrated shape memory alloy wires, of which the temperature is varied in order to tune the eigenfrequencies.

2. FINITE ELEMENT ANALYSIS OF STRUCTURES WITH INTEGRATED PIEZO-ELECTRIC DEVICES

Since piezo-electric materials can be used for actuator as well as for sensor applications, they are very attractive in smart structures technology. Piezo-electric materials are able to exert large forces when an electric field is applied. This feature is used in the design of actuators. On the other hand, mechanical stresses cause an electric field and make piezo-electric materials well-suited for sensor applications. Moreover, these materials offer the following advantages: wide frequency range, high resolution in positioning applications, extremely short reaction times, low energy loss factor, and vacuum ability.

Piezo-electric devices for sensing/actuating purposes are commercially available in the following forms:

- stacked piezo-electric ceramics,
- thin plates of piezo-electric ceramics, and
- thin foils of piezo-electric polymers.

The stacked forms of piezo-electric ceramics are constructed in order to enlarge the displacements of piezo-electric actuators. They are prestressed in order to avoid tension forces under working conditions. Due to their geometry, piezo-stacks are well-suited for truss applications. They replace either an entire member or a part of it. Thin plates of piezo-electric ceramics as well as foils of piezo-electric polymers are preferably used as layers bonded to surfaces of plates and shells. The influence of the very thin adhesive layers is neglected in the structural analysis calculations. Unlike piezo-electric ceramics, piezo-electric polymers offer the advantage that they are not brittle and, therefore, can work under tension.

The following part of this section presents a linear finite element formulation which allows for the analysis of shell structures with piezo-electric layers bonded to the surfaces and of truss structures with piezo-electric members replacing conventional ones.

2.1 Continuum Formulation of the Piezo-Electric Equations

Balance laws

The balance laws serve as the starting point for the variational formulation of the governing equations. The mechanical balance is given by the conservation of momentum

$$\mathrm{Div}\,\mathbf{S} + \rho\,\mathbf{b} = \rho\,\frac{\partial^2 \mathbf{u}}{\partial t^2}\ . \tag{1}$$

Here, $\mathbf{S}$ denotes the symmetric stress tensor, $\mathbf{u}$ the displacement vector, ρ the material density, $\rho\,\partial^2\mathbf{u}/\partial t^2$ the inertial forces per unit volume, and $\rho\mathbf{b}$ the body forces per unit volume.

The electrical balance expressed by use of the electric displacement vector $\mathbf{D}$ is written for an insulating material as

$$\mathrm{Div}\,\mathbf{D} = 0\ . \tag{2}$$

Variational formulation

The equivalent coupled weak formulation of Eqs. (1) and (2) is very useful from a numerical point of view because it serves as the basis for the subsequent finite element formulation.

Introducing the vector function

$$\mathbf{p} = \{\,\mathbf{u},\,\Phi\,\}^T \tag{3}$$

(which is composed of the displacement vector $\mathbf{u}$ and the electric potential Φ), as well as its variation

$$\delta\mathbf{p} = \{\,\delta\mathbf{u},\,\delta\Phi\,\}^T \tag{4}$$

(which contains the virtual displacement vector $\delta\mathbf{u}$ and the virtual electric potential $\delta\Phi$ as test functions), Eqs. (1) and (2) are combined into the coupled piezo-electric functional G in the configuration Ψ

$$\begin{aligned} G(\Psi, \mathbf{p}, \delta\mathbf{p}) = &\int_B \left(\mathrm{Div}\,\mathbf{S} + \rho\,\mathbf{b} - \rho\,\frac{\partial^2\mathbf{u}}{\partial t^2}\right)\cdot\delta\mathbf{u}\,dV \\ &+ \int_B \mathrm{Div}\,\mathbf{D}\,\delta\Phi\,dV = 0\ . \end{aligned} \tag{5}$$

Here, V denotes the volume of the body B under consideration. The configuration Ψ has been introduced especially in view of the non-linear formulation in Section 3. Using the transformations

$$\begin{aligned} \mathrm{Div}\,\mathbf{S}\cdot\delta\mathbf{u} &= \mathrm{Div}\,(\mathbf{S}\cdot\delta\mathbf{u}) - \mathbf{S} : \mathrm{Grad}\,\delta\mathbf{u} \\ \mathrm{Div}\,\mathbf{D}\ \delta\Phi &= \mathrm{Div}\,(\mathbf{D}\,\delta\Phi) - \mathbf{D}\cdot\mathrm{Grad}\,\delta\Phi\ , \end{aligned} \tag{6}$$

Cauchy's theorem

$$\mathbf{S}\cdot\mathbf{n} = \bar{\mathbf{t}}\ , \tag{7}$$

for the definition of the traction vector $\bar{\mathbf{t}}$ by use of the unit normal vector $\mathbf{n}$ and Green's formula, Eq. (5) results in (cf. Naillon, Coursant and Besnier [4]):

$$\begin{aligned} G(\Psi, \mathbf{p}, \delta\mathbf{p}) = &\int_B \left[\mathrm{Grad}\,\delta\mathbf{u} : \mathbf{S} - \delta\mathbf{u}\cdot\rho\left(\mathbf{b} - \frac{\partial^2\mathbf{u}}{\partial t^2}\right)\right] dV \\ &- \int_{\partial B} \delta\mathbf{u}\cdot\bar{\mathbf{t}}\,dA + \int_B \mathrm{Grad}\,\delta\Phi\cdot\mathbf{D}\,dV \\ &- \int_{\partial B} \delta\Phi\,(\mathbf{D}\cdot\mathbf{n})\,dA = 0\ . \end{aligned} \tag{8}$$

Here, A denotes the surface ∂B of the body B. Because of the symmetry of the stress tensor $\mathbf{S}$, the virtual work of the stress is rewritten as

$$\text{Grad}\,\delta\mathbf{u} : \mathbf{S} = \frac{1}{2}\left(\text{Grad}\,\delta\mathbf{u} + \text{Grad}^T\delta\mathbf{u}\right) : \mathbf{S} = \delta\mathbf{E}_m : \mathbf{S}\ , \tag{9}$$

where $\delta\mathbf{E}_m$ is the variation of the linear Green-Lagrangian strain tensor.

Constitutive equations

The linear constitutive equations expressing the coupling between the elastic field and the electric field can be written as

$$\begin{aligned}\mathbf{S} &= \mathbf{C} : \mathbf{E}_m - \mathbf{e} \cdot \mathbf{E}_{el} \\ \mathbf{D} &= \mathbf{e}^T : \mathbf{E}_m + \varepsilon \cdot \mathbf{E}_{el}\ .\end{aligned} \tag{10}$$

In Eq. (10) the 4^{th} order elasticity tensor $\mathbf{C}$ is used in the same way as in Hooke's law. Its constants are evaluated at a constant electric field $\mathbf{E}_{el}$. The electric part of Eq. (10) is formulated by use of the 2^{nd} order dielectric tensor ε, evaluated at constant mechanical strain $\mathbf{E}_m$. The coupling between both equations is given by the 3^{rd} order piezo-electric tensor $\mathbf{e}$. From Eq. (10) it can be seen that an applied electric field as well as a mechanical deformation of the piezo-electric structure result in electric displacements and mechanical stresses. The pyroelectric effect is not taken into account, i.e. the temperature variation is assumed to be negligible.

The electric field $\mathbf{E}_{el}$ is related to the electric potential Φ by

$$\mathbf{E}_{el} = -\,\text{Grad}\,\Phi\ . \tag{11}$$

The basic equation for the finite element formulation

The final expression of the weak problem is obtained by combining the variational formulation Eq. (8) and the constitutive equations (10), taking into account Eqs. (9) and (11):

$$\begin{aligned} G(\Psi, \mathbf{p}, \delta\mathbf{p}) &= \int_B \left[\delta\mathbf{E}_m : \mathbf{C} : \mathbf{E}_m - \delta\mathbf{u} \cdot \rho\left(\mathbf{b} - \frac{\partial^2\mathbf{u}}{\partial t^2}\right)\right] dV \\ &- \int_{\partial B} \delta\mathbf{u} \cdot \bar{\mathbf{t}}\, dA - \int_B \text{Grad}\,\delta\Phi \cdot \varepsilon \cdot \text{Grad}\,\Phi\, dV \\ &- \int_{\partial B} (\mathbf{D} \cdot \mathbf{n})\,\delta\Phi\, dA + \int_B \delta\mathbf{E}_m : \mathbf{e} \cdot \text{Grad}\,\Phi\, dV \\ &+ \int_B \text{Grad}\,\delta\Phi \cdot \mathbf{e}^T : \mathbf{E}_m dV = 0\ . \end{aligned} \tag{12}$$

Note that Eq. (12) is linear in the electric potential Φ and in the displacements $\mathbf{u}$ due to the restriction to the linear Green-Lagrangian strain tensor.

2.2 Finite Element Formulation

Based on Eq. (12), the extension of conventional finite element formulations to problems of piezo-electricity is considered. A shell element for shallow shell structures with piezo-electric polymers bonded to the surfaces as well as a truss element with an incorporated piezo-electric ceramic are presented. These elements are depicted in Fig. 1.

The finite shell element is based on the isoparametric formulation, originally proposed by Wagner [5] (see also Wagner, Wriggers, Stein [6]) and extended for the calculation of composite material shell structures by Lammering [7]. This composite material formulation is used for the integration of the piezo-electric polymers. The shell element is obtained from the shear elastic version of shell theory. From a numerical point of view, it is advantageous to include the shear deformations, because only C^0-continuity is required for the finite element shape functions. In order to avoid shear locking, a reduced integration of the shear terms in the element stiffness matrix is carried out.

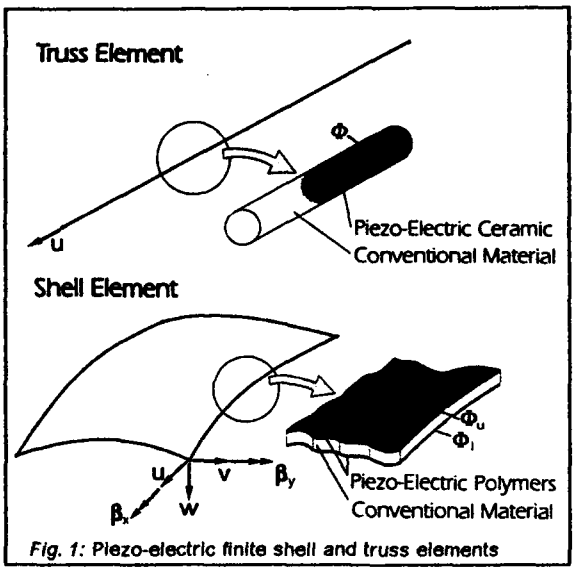

Fig. 1: Piezo-electric finite shell and truss elements

The finite truss element is based on a standard formulation which is extended to account for incorporated piezo-electric devices (cf. Lammering, Jia, Rogers [9]).

Within a single finite element $\Omega_{(e)}$ the vector $\mathbf{p}$ is approximated by

$$\mathbf{p}^h = \begin{bmatrix}\mathbf{u}^h \\ \Phi^h\end{bmatrix} = \begin{bmatrix}\mathbf{N}_m & \mathbf{0} \\ \mathbf{0} & \mathbf{N}_{el}\end{bmatrix}\begin{bmatrix}\mathbf{u}_{(e)} \\ \Phi_{(e)}\end{bmatrix}\ , \tag{13}$$

where $\mathbf{N}_m$ and $\mathbf{N}_{el}$ contain the shape functions for the approximation of the displacement field $\mathbf{u}^h$ and the electric potential field Φ^h, respectively. In the case of piezo-electric shell elements, the mechanical part $\mathbf{u}_{(e)i}$ of the generalized nodal displacement vector $\{\mathbf{u}_{(e)i}, \Phi_{(e)i}\}^T$ at node i consists of the displacements u, v and w and the rotations β_x and β_y; the electrical part $\Phi_{(e)i}$ is composed of the potentials Φ_u and Φ_l at the upper and lower surfaces, respectively (cf. Lammering [8]):

$$\begin{aligned}\mathbf{p}_i &= \{\mathbf{u}_{(e)i}, \Phi_{(e)i}\}^T \\ &= \{u_i, v_i, w_i, \beta_{xi}, \beta_{yi}, \Phi_{ui}, \Phi_{li}\}^T\ .\end{aligned} \tag{14}$$

In the case of piezo-electric truss elements, the mechanical part $\mathbf{u}_{(e)i}$ at node i is given by its single nodal degree of freedom, the axial displacement u_i. The electrical part $\Phi_{(e)}$ is not defined as a nodal quantity but as a degree of freedom in the interior of the element, see Lammering, Jia, Rogers [9]. Thus, for the two-noded truss element in Fig. 1 the generalized displacement vector of the element reads

$$\mathbf{p} = \{\mathbf{u}_{(e)}, \Phi_{(e)}\}^T = \{u_1, u_2, \Phi\}^T\ . \tag{15}$$

The variation $\delta\mathbf{p}$ of the state variable vector $\mathbf{p}$ is calculated in an analogous way to Eq. (13):

$$\delta\mathbf{p}^h = \begin{bmatrix}\delta\mathbf{u}^h \\ \delta\Phi^h\end{bmatrix} = \begin{bmatrix}\mathbf{N}_m & \mathbf{0} \\ \mathbf{0} & \mathbf{N}_{el}\end{bmatrix}\begin{bmatrix}\delta\mathbf{u}_{(e)} \\ \delta\Phi_{(e)}\end{bmatrix}\ , \tag{16}$$

where $\delta(.)$ denotes the variation of $(.)$.

By use of of the matrices $\mathbf{B}_m$ and $\mathbf{B}_{el}$ consisting of the derivatives of the shape functions, the Green-Lagrangian strain tensor as well as the electric field are obtained:

$$\begin{bmatrix} \mathbf{E}_m^h \\ \mathbf{E}_{el}^h \end{bmatrix} = \begin{bmatrix} \mathbf{B}_m & \mathbf{0} \\ \mathbf{0} & \mathbf{B}_{el} \end{bmatrix} \begin{bmatrix} \mathbf{u}_{(e)} \\ \Phi_{(e)} \end{bmatrix} . \tag{17}$$

The corresponding variations read

$$\begin{bmatrix} \delta\mathbf{E}_m^h \\ \delta\mathbf{E}_{el}^h \end{bmatrix} = \begin{bmatrix} \mathbf{B}_m & \mathbf{0} \\ \mathbf{0} & \mathbf{B}_{el} \end{bmatrix} \begin{bmatrix} \delta\mathbf{u}_{(e)} \\ \delta\Phi_{(e)} \end{bmatrix} . \tag{18}$$

With these equations the semidiscrete approximation of the weak form in Eq. (12) yields

$$\begin{aligned} &G(\Psi, \mathbf{p}, \delta\mathbf{p}) = \\ &\bigcup_{e=1}^{n_e} \left\{ \begin{bmatrix} \delta\mathbf{u}_{(e)}^T \\ \delta\Phi_{(e)}^T \end{bmatrix} \begin{bmatrix} \int_{\Omega_{(e)}} \mathbf{B}_m^T \mathbf{C}\, \mathbf{B}_m d\Omega & \int_{\Omega_{(e)}} \mathbf{B}_m^T \mathbf{e}\, \mathbf{B}_{el} d\Omega \\ \int_{\Omega_{(e)}} \mathbf{B}_{el}^T \mathbf{e}^T \mathbf{B}_m d\Omega & -\int_{\Omega_{(e)}} \mathbf{B}_{el}^T \varepsilon\, \mathbf{B}_{el} d\Omega \end{bmatrix} \begin{bmatrix} \mathbf{u}_{(e)} \\ \Phi_{(e)} \end{bmatrix} \right. \\ &+ \begin{bmatrix} \delta\mathbf{u}_{(e)}^T \\ \delta\Phi_{(e)}^T \end{bmatrix} \begin{bmatrix} \int_{\Omega_{(e)}} \rho\, \mathbf{N}_m^T \mathbf{N}_m\, d\Omega & \mathbf{0} \\ \mathbf{0} & \mathbf{0} \end{bmatrix} \begin{bmatrix} \partial^2 \mathbf{u}_{(e)} / \partial t^2 \\ \Phi_{(e)} \end{bmatrix} \\ &\left. - \begin{bmatrix} \delta\mathbf{u}_{(e)}^T \\ \delta\Phi_{(e)}^T \end{bmatrix} \begin{bmatrix} \int_{\Omega_{(e)}} \mathbf{N}_m^T \rho\, \mathbf{b}\, d\Omega + \int_{\partial\Omega_{(e)}} \mathbf{N}_m^T \bar{\mathbf{t}}\, d(\partial\Omega) \\ \int_{\partial\Omega_{(e)}} \mathbf{N}_{el}^T (\mathbf{D} \cdot \mathbf{n})\, d(\partial\Omega) \end{bmatrix} \right\} = 0 , \end{aligned} \tag{19}$$

which is observed to be in form a standard finite element formulation with an extended nodal displacement vector. In Eq. (19), Ω denotes the volume of the finite element, $\partial\Omega$ its surface, and n_e the total number of finite elements. The first expression on the right-hand side represents the stiffness matrix, the second the mass matrix, and the third one the vector of applied forces. Thus, the corresponding matrix notation reads

$$\mathbf{K}\,\mathbf{p} + \mathbf{M}\,\ddot{\mathbf{p}} = \mathbf{F} , \tag{20}$$

where $\mathbf{K}$ is the stiffness matrix, $\mathbf{M}$ the mass matrix, $\mathbf{F}$ the vector of applied forces, $\mathbf{p}$ the generalized displacement vector (consisting of the nodal displacements and the electric potential), and $\ddot{\mathbf{p}}$ the corresponding acceleration vector.

2.3 The Constitutive Equations for Shell and Truss Structures

Since the transverse normal stresses are neglected in the calculation of shells structures, the three-dimensional constitutive equations have to be adapted to the plane stress state.

Furthermore, it has to be considered that from a structural mechanical viewpoint a structure with piezo-electric materials on its upper and lower surfaces is a laminated composite. Therefore, the elasticity matrix $\mathbf{C}$ in Eq. (10) is formulated in the same way as in classical lamination theory (cf. Jones [10]).

The electric part of the constitutive equations (10) is adjusted to thin layers of piezo-electric materials by taking into account that the electric field vector is perpendicular to the surface of the layer. This means that a scalar equation is sufficient for the calculation of the electric field in each layer. A comprehensive description of the constitutive equation, considering the abovementioned characteristics of a shell structure with piezo-electric layers, is given by Lammering [8].

In the case of a truss member with an integrated piezo-electric ceramic, the strain state and the electric field are one-dimensional and the tensors $\mathbf{E}_m$ and $\mathbf{E}_{el}$ reduce to scalar quantities. For this reason the constitutive equations (10) are simplified and become two scalar equations. Lammering, Jia and Rogers [9] give a detailed derivation of the stiffness matrix presented in Eq. (19) for the special case of a truss member with an integrated piezo-electric ceramic.

2.4 Applications of the Finite Shell Element

The general purpose Finite Element Analysis Program (FEAP) originally developed by Taylor (Zienkiewicz and Taylor [11]) was chosen for incorporation of the new finite elements.

In this section two numerical examples are presented: the vibration excitation of a thin plate and the vibration control of a cantilever beam. Both examples require a time integration algorithm which is achieved by the standard Newmark Method. The displacement increments are calculated by

$$\begin{aligned} &\left(\frac{1}{\alpha\,\Delta t^2}\mathbf{M} + \mathbf{K}\right)\Delta\mathbf{p} = \mathbf{F}_{n+1} \\ &\qquad + \mathbf{M}\left\{\left(\frac{1}{2\alpha} - 1\right)\ddot{\mathbf{p}}_n + \frac{1}{\alpha\,\Delta t}\dot{\mathbf{p}}_n\right\} - \mathbf{K}\,\mathbf{p}_n . \end{aligned} \tag{21}$$

The subscripts n and $n+1$ indicate the time step, α is an integration parameter which is chosen as 0.25, and Δt is the time increment.

Vibration excitation of a thin plate

In this numerical experiment a simply supported rectangular plate is excited by use of rectangular PVDF-polymer patches bonded to the upper and lower surfaces. The geometry and material data are given in Fig. 2. Dimitriadis, Fuller and Rogers [12] present an analytical solution of this problem using Fourier series expansions.

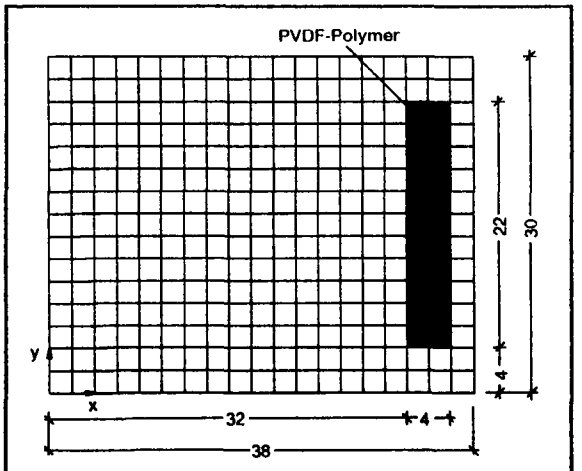

Material properties

PVDF-Polymer

Young's modulus	negligible
dielectric permittivity	$4.40 \cdot 10^{-2}$ C/m²
dielectric cefficient	$1.06 \cdot 10^{10}$ F/m

Steel

Young's modulus	$2.07 \cdot 10^{11}$ N/m²
Poisson's ratio	0.292
Loading	≤ ± 1000 V
Thickness	0.159 cm

Fig. 2: Simply supported rectangular plate (dimensions in cm), discretization and material properties

The excitation frequency $\Omega = 600$ *rad/s* is between the resonant frequencies $\omega_1 = 437.4$ *rad/s* and

$\omega_s = 941.3$ *rad/s*. In Fig. 3 the displacement distribution along the line $y = 0.15$ *m* is shown. It is apparent from Fig. 3 that there is a node close to the actuator boundary. The results of the finite element analysis and the Fourier series expansion agree well.

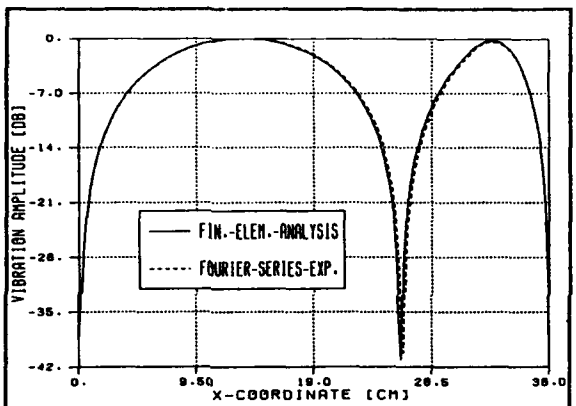

Fig. 3: Displacement distribution at the excitation frequency $\Omega = 600$ *rad/s*

Vibration control of a cantilever beam

In this example the piezo-electric polymers are used to damp out the vibrations of a cantilever beam. For this purpose, a control law has to be formulated. The second or direct method of Lyapunov is used to form the basis for the design of an optimal controller (Ogata [13], Banks [14], Bailey and Hubbard [15]). Lyapunov's theorem is applied to the semidiscrete equation of motion (20). An appropriate Lyapunov function is given by

$$V = \mathbf{p}^T \mathbf{K}\, \mathbf{p} + \dot{\mathbf{p}}^T \mathbf{M}\, \dot{\mathbf{p}} \ , \qquad (22)$$

which is proportional to the energy of the system. Asymptotic stability is achieved when

$$\frac{dV}{dt} = \dot{V} = \dot{\mathbf{p}}^T \mathbf{F} + \mathbf{F}^T \dot{\mathbf{p}} < 0 \qquad (23)$$

holds true. This means that the controller has to work in such a way that the applied voltage produces stress resultants opposing the velocity of the system.

It can be seen that the vector of applied forces on the right-hand side of Eq. (21) has to be taken at time $t = t_{n+1}$. However, at the beginning of the time step the control forces are unknown. Therefore, an iteration procedure is started within the time step. In this example the control forces are calculated by use of the velocity vector in order to ensure that $\dot{V} < 0$ holds true, cf. Eq. (23). From the numerical investigations it has been observed that a small variation of the control forces does not affect the velocity very much and that only a few iterations are necessary to get equilibrium when the method of direct iteration is applied. The initial value of the control force is taken from the preceding time step.

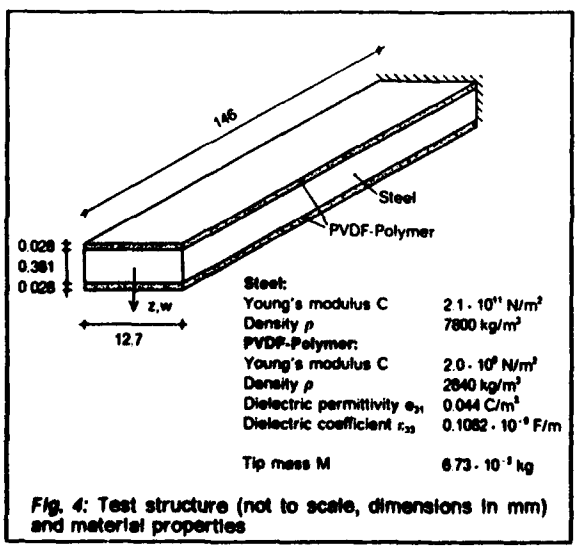

Fig. 4: Test structure (not to scale, dimensions in mm) and material properties

The geometry and the material data of the beam under consideration are taken from the study of Bailey and Hubbard [15] and are given in Fig. 4. Ten finite elements are used for the discretization of the beam. The test procedure is to hold the tip of the beam at 0.005 *m* displacement, release it, and observe the vibrations. In the case of the controlled beam, the voltage is constant over the entire length, and the lower and upper piezo-electric layers are charged differently in the sign. In the numerical investigations, the maximum voltage of 50*V* is much lower than the breakdown voltage of the PVDF-polymer, which is beyond 1000*V*. The magnitude is chosen to be directly proportional to the negative tip velocity.

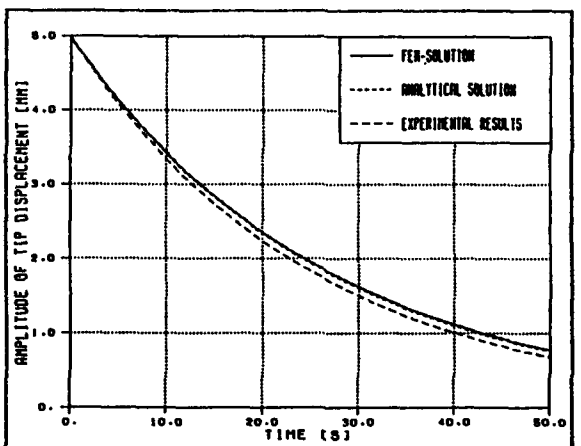

Fig. 5: Tip displacement decay envelope

The results for the controlled beam are shown in Fig. 5, where the tip displacement decay envelope is depicted. The agreement between the analytical solution and the finite element results is very good. The numerical and analytical solutions can be compared with the experimental results presented by Bailey and Hubbard [15]. Eliminating the influence of the structural damping in their study, the damping effect due to the control forces is calculated as $d_{cf} = 6.5 \cdot 10^{-4} Ns/m$. On the other hand, the finite element computations result in a damping coefficient $d_{fem} = 6.14 \cdot 10^{-4} Ns/m$. The data taken from the experimental investigation, also depicted in Fig. 5, agree satisfactorily with the numerical results.

2.5 Optimal Placement of Actuators in Adaptive Truss Structures

In this section a brief derivation of the objective function for the optimization of the actuator locations is given. A more comprehensive description is given by Lammering, Jia and Rogers [9].

Independent Modal Space Control

The starting point in the derivation of the optimization algorithm is the semidiscrete equation of motion (20). Using $\mathbf{p} = \Phi\, \mathbf{q}$ ($\mathbf{q}$: vector of modal coordinates, Φ: modal shape matrix), a modal space representation with uncoupled equations of motion is obtained:

$$\mathbf{m}\,\ddot{\mathbf{q}} + \mathbf{k}\,\mathbf{q} = \mathbf{\Phi}^T\mathbf{F}$$
$$\ddot{\mathbf{q}} + \mathbf{m}^{-1}\mathbf{k}\,\mathbf{q} = \mathbf{f}\ . \tag{24}$$

Here, $\mathbf{m} = \mathbf{\Phi}^T\mathbf{M}\,\mathbf{\Phi}$ denotes the modal mass matrix, $\mathbf{f} = \mathbf{m}^{-1}\mathbf{\Phi}^T\mathbf{F}$ the modal force vector, and $\mathbf{k} = \mathbf{\Phi}^T\mathbf{K}\,\mathbf{\Phi}$ the modal stiffness matrix. A state space representation of the k-th equation reads

$$\dot{\mathbf{u}}_k = \mathbf{A}_k\mathbf{u}_k + \mathbf{w}_k\ , \tag{25}$$

defining $\mathbf{A}_k$, $\mathbf{u}_k$ and $\mathbf{w}_k$ by use of the k-th eigenfrequency $\omega_k = \sqrt{(k_k/m_k)}$

$$\mathbf{u}_k = [q_k\ ,\ \dot{q}_k/\omega_k]^T$$
$$\mathbf{A}_k = \begin{bmatrix} 0 & \omega_k \\ -\omega_k & 0 \end{bmatrix} \tag{26}$$
$$\mathbf{w}_k = [0\ ,\ f_k/\omega_k]^T.$$

The optimal control problem is observed to be the sum of n second order optimal control problems given by the quadratic cost function

$$J = \sum_{k=1}^{n} J_k = \sum_{k=1}^{n} \int_0^{t_f} (\mathbf{u}_k^T\mathbf{Q}_k\mathbf{u}_k + \mathbf{w}_k^T\mathbf{R}_k\mathbf{w}_k)\,dt \rightarrow \min\ , \tag{27}$$

where n is the number of eigenmodes under consideration, t_f is the final time, and $\mathbf{R}_k$ and $\mathbf{Q}_k$ represent weighting matrices. Each modal cost function J_k is minimized independently, resulting in

$$\mathbf{w}_k = -\mathbf{R}_k^{-1}\mathbf{K}_k\mathbf{u}_k\ , \tag{28}$$

where the symmetric matrix $\mathbf{K}_k$ is the steady state solution of the Riccati equation $\mathbf{0} = -\mathbf{K}_k\mathbf{A}_k - \mathbf{A}_k^T\mathbf{K}_k - \mathbf{Q}_k + \mathbf{K}_k\mathbf{R}_k^{-1}\mathbf{K}_k$. Introducing the elements of $\mathbf{K}_k$, e.g. given by Meirovitch and Baruh [16], the control force of the k-th mode is calculated as

$$f_k = \omega_k\left(\omega_k - \sqrt{\omega_k^2 + r_k^*}\right)q_k - \left[\sqrt{2\omega_k\left(-\omega_k + \sqrt{\omega_k^2 + r_k^*}\right) + r_k^*}\right]\dot{q}_k\ , \tag{29}$$

where $r_k^* = r_k/\omega_k^2$. Eq. (28) shows that the actuator location does not affect the magnitude of the modal control forces f_k. However, there are various ways to generate f_k from the nodal forces F, because the control effort depends on the actuator location.

Actuator placement optimization

Introducing the control forces f_k, the controlled vibration is described by

$$\ddot{q}_k + h_k\,\dot{q}_k + g_k\,q_k = 0\ ,\quad k = 1,2,\ldots n\ , \tag{30}$$

where h_k and g_k are constants depending on ω_k and r_k^*. The motion of the controlled structure depends solely on the initial conditions. Therefore, the modal control forces and, consequently, the physical control forces are considered to be random variables, and a suitable objective function is the mean value calculated from the square of the vector of physical control forces

$$E(\mathbf{F}^T\mathbf{F}) \rightarrow \min\ . \tag{31}$$

The definition of the nodal control forces is taken to express f by F:

$$\mathbf{f} = \mathbf{B}\,\mathbf{F}\ , \tag{32}$$

where the modal participation matrix B is defined as $\mathbf{B} = \mathbf{m}^{-1}\mathbf{\Phi}^T$. A unique solution for the physical control forces F can only be calculated if B is a square matrix. In this case the number of actuators is equal to the number of controlled modes. The advantage of the coupled piezo-electric formulation is that the modal forces can be expressed directly by electric quantities, because the electric potentials are included in $\mathbf{\Phi}$, and consequently in B, and the point charges are contained in F. If B is a square matrix, F is calculated by

$$\mathbf{F} = \mathbf{B}^{-1}\mathbf{f}\ . \tag{33}$$

An inverse matrix $\mathbf{B}^{-1}$ exists if the system is controllable. Using the pseudoinverse of B, Lindberg and Longman [17] as well as Jia [18] developed techniques that avoid the stringent requirement for the number of controlled modes to be equal to the number of actuators.

Assuming that the modal control forces are uncorrelated with each other, uniformly distributed, and within the range from $[-b, +b]$, the density function p is $p(f_i) = 1/(2b)^m$, where m denotes the number of modes to be controlled. The objective function now becomes

$$E(\mathbf{F}^T\mathbf{F}) = \int_{f_m}\ldots\int_{f_2}\int_{f_1}\mathbf{f}^T\mathbf{B}^{-T}\mathbf{B}^{-1}\mathbf{f}\,\frac{1}{(2b)^m}\,df_1\,df_2\ldots df_m = \frac{b^2}{3}\,\mathrm{tr}\,(\mathbf{B}^{-T}\mathbf{B}^{-1}) \rightarrow \min\ . \tag{34}$$

Since the constant $b^2/3$ does not affect the minimization process, the objective function finally reads

$$z_1 = \mathrm{tr}\,(\mathbf{B}^{-T}\mathbf{B}^{-1}) \rightarrow \min\ . \tag{35}$$

In order to minimize the spillover energy, the modal forces $\mathbf{f}_s$ of the modes beyond the m controlled modes are considered. They are related to the physical control forces F via the modal participation matrix $\mathbf{B}_s$ analogously defined to B:

$$\mathbf{f}_s = \mathbf{B}_s\,\mathbf{F}\ . \tag{36}$$

A suitable objective function is the mean value of the vector $\mathbf{f}_s$

$$E\{\mathbf{f}_s^T\mathbf{f}_s\} = E\{\mathbf{f}^T(\mathbf{B}_s\mathbf{B}^{-1})^T(\mathbf{B}_s\mathbf{B}^{-1})\mathbf{f}\} \rightarrow \min\ , \tag{37}$$

resulting after an analogous calculation of the mean value as before in

$$z_2 = \mathrm{tr}\,(\mathbf{B}_s\mathbf{B}^{-1})^T(\mathbf{B}_s\mathbf{B}^{-1}) \rightarrow \min\ . \tag{38}$$

A multicriteria optimization problem has to be solved in order to make a compromise between the objective functions in Eqs. (35) and (38). Solution strategies are described e.g. by Osyczka [19].

Optimal actuator placement by use of the piezo-electric finite truss element

The truss structure under consideration, its support, and the numbers of the elements are depicted in Fig. 6; the material properties are as follows: Young's modulus $C = 2.1 \cdot 10^{11}\ \mathrm{N/m^2}$, cross section area $A = 5.0 \cdot 10^{-6}\ \mathrm{m^2}$, mass density $\rho = 7800\ \mathrm{kg/m^{-3}}$, piezo-electric coefficient $e = 0.044\ \mathrm{C/m^2}$, dielectric coefficient $\varepsilon = 0.1062 \cdot 10^{-9}\ \mathrm{F/m}$. The active part of the truss member is located in the center and it is assumed that it takes one third of the member length. The optimal actuator position for minimum control effort of the 1st and 2nd bending modes as well as for minimum spillover energy into the 3rd and 4th bending modes are presented in Fig. 6. This figure shows that the minimization of the objective function z_1, minimization of the control effort, is obtained when the actuators are located at the truss elements 1, whereas the minimum of the objective function z_2, minimization of the spillover energy, is achieved at the truss elements 2. Furthermore, it can be seen that there are compromise solutions, such as 3, 4 and 5.

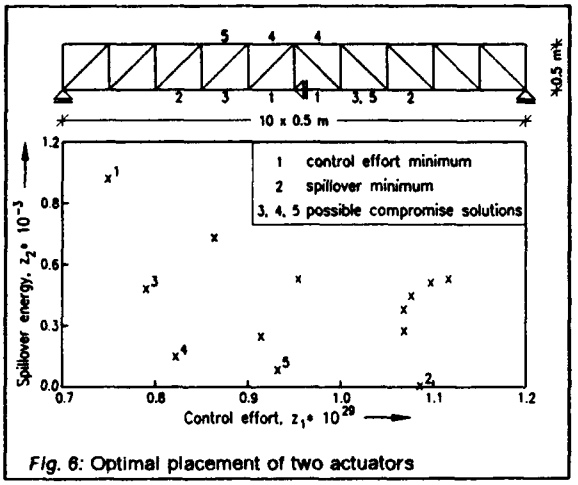

Fig. 6: Optimal placement of two actuators

3. FINITE ELEMENT ANALYSIS OF STRUCTURES WITH EMBEDDED SHAPE MEMORY ALLOY WIRES

In contrast to piezo-electric materials, the use of shape memory alloys in smart structures is based on stress- and temperature-induced phase transformations which can cause forces and/or displacements. Since the material properties of shape memory alloys are sensitive to the composition, a particular alloy with specific properties can be tailored for each individual application. An optimal design can be determined by systematic variation of the material properties in the finite element analysis.

The remarkable features of shape memory alloys that make them especially suitable for active elements in actuators are their capacity for high forces, high displacement reliability with temperature control, and the potential to create compact powerful actuators. Moreover, in contrast to piezo-electric or magnetostrictive materials, shape memory alloys offer the advantage that they can exert large repeatable displacements at zero or constant load. Additionally, since shape memory alloys are mainly manufactured as wires, their integration into smart structures differ from the other abovementioned actuator/sensor materials. A promising method that is currently being investigated is to embed the wires into a composite structure.

In the following, the mechanical behavior and the associated metallurgical phenomena are outlined, and a constitutive equation based on the work of Brinson [3] is presented. Since shape memory alloys exhibit large recoverable strains (on the order of 10%) and due to the highly non-linear constitutive equation, a finite element formulation is presented, which takes into account geometric and material non-linearities.

3.1 Phenomenological Behavior of Shape Memory Alloys

Shape memory alloys exhibit a strong temperature-dependent stress-strain material behavior. At low temperatures an apparent plastic deformation follows the elastic deformation, and a large residual strain can be left after unloading (see Fig. 7a), which can be completely recovered by heating the specimen. This phenomenon is called the shape memory effect. At high temperatures a shape memory alloy specimen also exhibits an apparent plastic deformation after the elastic deformation. However, this is fully recovered during unloading in a hysteresis loop (Fig. 7b). This non-linear elastic behavior is called pseudoelasticity. Furthermore, there are temperature ranges in which only partial pseudoelastic recovery takes place (Fig. 7c). The residual strain after unloading vanishes when the specimen is heated.

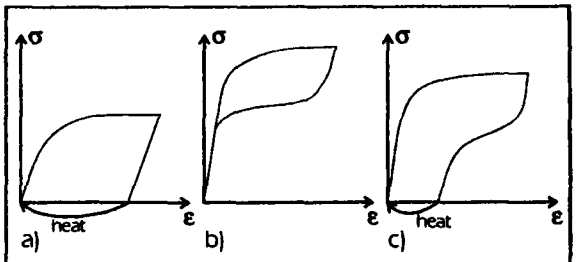

Fig. 7: Schematic of stress-strain curves of shape memory alloy mechanical behavior. The non-linear loading portion of the curves represents detwinning of martensite variants or transformation of austenite to martensite. In b) and c) the non-linear portion upon unloading is due to the inverse transformation to austenite. a) $T < A_s$, beginning with 100% twinned martensite. b) $T > A_f$, beginning with 100% austenite. c) $A_s < T < A_f$, beginning with 100% Austenite.

The physical reason for the complex thermo-mechanical behavior of shape memory alloys is caused by a phase transformation. At high temperatures the stress-free shape memory material is in the austenite phase. During the cooling process the crystal structure undergoes a transformation into the martensite phase. This stress-free state is characterized by multiple martensite variants, each consisting of twin related martensites.

In the stress free state a shape memory alloy material can be considered to have four transition temperatures: Martensite Finish M_f, Martensite Start M_s, Austenite Start A_s and Austenite Finish A_f. This paper is restricted to materials with transition temperatures graded as $M_f < M_s < A_s < A_f$. The transformation regions are given by the respective start and finish temperatures. In the temperature range $M_s < T < A_s$ no phase changes take place and both martensite and austenite can coexist.

When unidirectional stress is applied to a shape memory alloy wire in the martensite phase, there is a critical value, dependent on the temperature, at which the martensite variants begin a detwinning process, resulting in a single variant of martensite. Additionally, when a shape memory alloy in the austenite phase is loaded, a transformation into the martensite phase (which also consists of a single variant) is observed. These detwinning processes cause the apparently plastic deformations in the stress-strain curves. Fig. 8 shows that it depends on the temperature whether this stress induced variant of martensite is stable or not

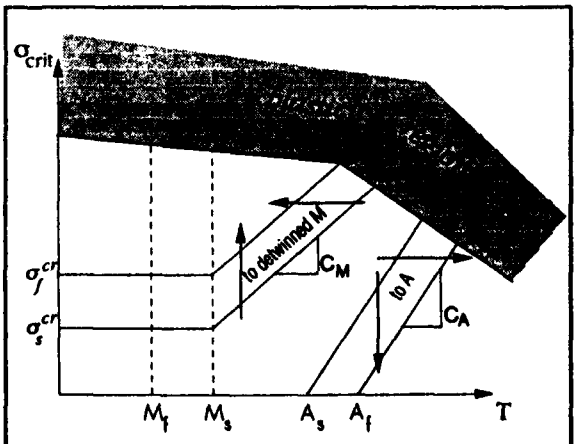

Fig. 8: Critical stresses for transformation or martensite twin conversion as function of temperature. Plasticity region indicated.

during unloading. If the temperature is above A_f, austenite is rebuilt during unloading and the stress-strain curve exhibits the characteristic hysteresis loop. At temperatures below A_s, the detwinned variant of martensite is also stable in a stress-free state. Therefore, a large residual strain remains after unloading, but it can be recovered by heating the material above A_f.

3.2 Constitutive Equations for Shape Memory Alloys

The constitutive equation presented by Brinson [3] is used for the subsequent finite element implementation. This constitutive description is derived on a thermomechanical basis, has a relatively simple mathematical expression, and includes only quantifiable engineering variables and material parameters in its expression. This one-dimensional constitutive law is given in the following form:

$$S - S_o = D(\xi)E - D(\xi_o)E_o + \Omega(\xi)\xi_s - \Omega(\xi_o)\xi_{so} + \Theta(T - T_o), \quad (39)$$

where S is the second Piola-Kirchhoff stress, T is the temperature, and ξ is an internal variable representing the stage of transformation. The function D denotes the modulus of the shape memory alloy material, Ω is considered the transformation tensor, and Θ is related to the thermal coefficient of expansion. The subscript 0 indicates the initial state or the initial conditions. The martensite fraction is additively decomposed into a stress-induced part, ξ_s, and a temperature-induced part, ξ_T,

$$\xi = \xi_s + \xi_T \,. \quad (40)$$

Experiments have shown that the modulus in the austenite phase is about three times larger than in the martensite phase. A linear dependancy of the modulus on the martensite fraction is assumed

$$D(\xi) = D_a + \xi (D_m - D_a), \quad (41)$$

where D_a is the austenite modulus and D_m is the modulus when the material is in the martensite phase (twinned or detwinned). It has been shown by Brinson [3] that the transformation tensor is related to the modulus function by

$$\Omega(\xi) = -E_L D(\xi), \quad (42)$$

where E_L is the maximum residual strain of a shape memory alloy and a material constant.

In addition to the constitutive law (39), evolution equations for the temperature and stress-induced martensite fractions are necessary to complete the set of governing equations for the shape memory alloy behavior. An empirically-based cosine model to represent the martensite fraction as a function of stress and temperature during transformation has been developed by Liang and Rogers [20]. In order to be compatible with Eqs. (39) and (40) and to capture shape memory alloy behavior at all temperatures Brinson [3] modified these equations. The evolution of ξ_T and ξ_s is described by different equations for conversion to detwinned martensite and for conversion to austenite. Moreover, there are different equations for conversion to detwinned martensite below and above M_s. These equations are not repeated here for brevity's sake.

3.3 Non-Linear Finite Element Formulation

For the numerical study of shape memory alloy behavior, the mechanical part of the variational formulation Eq. (8) serves as the starting point. However, since shape memory alloys exhibit large strains, it is essential to extend this linear formulation to the non-linear case by introducing the non-linear Green-Lagrange strain tensor

$$\mathbf{E} = \frac{1}{2}\left(\mathrm{Grad}\,\mathbf{u} + \mathrm{Grad}^T\mathbf{u} + \mathrm{Grad}^T\mathbf{u}\cdot\mathrm{Grad}\,\mathbf{u}\right). \quad (43)$$

Its variation, which replaces the variation of the displacement gradient, is calculated as

$$\delta\mathbf{E} = \frac{1}{2}\left(\mathrm{Grad}\,\delta\mathbf{u} + \mathrm{Grad}^T\delta\mathbf{u} + \mathrm{Grad}^T\delta\mathbf{u}\cdot\mathrm{Grad}\,\mathbf{u} + \mathrm{Grad}^T\mathbf{u}\cdot\mathrm{Grad}\,\delta\mathbf{u}\right). \quad (44)$$

Now, the weak form of the balance of momentum can be written in the reference configuration by

$$G(\Psi, \delta\mathbf{u}) = \int_B \left[\delta\mathbf{E} : \mathbf{S} - \delta\mathbf{u}\cdot\rho\left(\mathbf{b} - \frac{\partial^2\mathbf{u}}{\partial t^2}\right)\right] dV - \int_{\partial B} \delta\mathbf{u}\cdot\bar{\mathbf{t}}\, dA \quad (45)$$

An iterative solution technique based on Newton's method is used in order to solve this equation and to preserve the quadratic rate of convergence. Newton's method makes use of the expansion of the non-linear equation into a Taylor series at the location of a given approximation. The procedure for linearizing the equations of continuum mechanics is comprehensively described by Marsden and Hughes [21] and Hughes and Pister [22].

At a known configuration $\bar{\Psi}$, the linearization of the non-linear function $G(\bar{\Psi}, \delta\mathbf{u})$ is given by

$$G(\Psi, \delta\mathbf{u}) = G(\bar{\Psi}, \delta\mathbf{u}) + \mathbf{D}\{G(\bar{\Psi}, \delta\mathbf{u})\}\cdot\mathbf{u}\,, \quad (46)$$

where $G(\Psi, \delta\mathbf{u})$ is the value of the non-linear function in the unknown configuration Ψ and $\mathbf{D}\{G(\bar{\Psi}, \delta\mathbf{u})\}\cdot\mathbf{u}$ is the derivative of G at the configuration $\bar{\Psi}$ in the direction of u. It is obtained by

$$\mathbf{D}\{G(\bar{\Psi}, \delta\mathbf{u})\}\cdot\mathbf{u} = \frac{\partial G(\bar{\Psi}, \delta u)}{\partial\Psi}\cdot\mathbf{u} = \frac{d}{d\varepsilon}\{G(\bar{\Psi} + \varepsilon\mathbf{u}, \delta\mathbf{u})\}\,|_{\varepsilon=0}\,. \quad (47)$$

Rigorous linearization of the weak form of the momentum balance equation results in (Wriggers [23]):

$$G(\Psi, \delta\mathbf{u}) = G(\bar{\Psi}, \delta\mathbf{u}) + \int_B \mathrm{Grad}\,\mathbf{u} : \mathbf{S} : \mathrm{Grad}\,\delta\mathbf{u}\, dV + \int_B \mathbf{F}(\bar{\Psi}, \delta\mathbf{u})[\mathbf{D}\{\mathbf{S}(\bar{\Psi})\}\cdot\mathbf{u}]\cdot\mathrm{Grad}\,\delta\mathbf{u}\, dV\,. \quad (48)$$

Here, F denotes the deformation gradient and S is the second Piola-Kirchhoff stress tensor. The linearization of S is calculated in the next section with respect to the constitutive equations of shape memory alloys. In a finite element formulation, the first integral expression of Eq. (48) results in the initial stress matrix, the second includes the linear stiffness matrix and the initial displacement matrix. Newton's algorithm is obtained when Eq. (46) is set to zero and the deformation increment is calculated by

$$DG(\bar{\Psi}, \delta\mathbf{u})\cdot\mathbf{u} = -G(\bar{\Psi}, \delta\mathbf{u})\,. \quad (49)$$

Linearization of the constitutive equation

The linearization procedure given by Eqs. (47) is now applied to the constitutive equation (39) in order to calculate the term $\mathbf{D}\{\mathbf{S}(\bar{\Psi})\}\cdot\mathbf{u}$ in Eq. (48). One obtains

$$\mathbf{D}\{\mathbf{S}(\bar{\Psi})\}\cdot\mathbf{u} = \frac{d}{d\varepsilon}\{D(\xi(\bar{\Psi} + \varepsilon\mathbf{u}))\,E(\bar{\Psi} + \varepsilon\mathbf{u}) + \Omega(\xi(\bar{\Psi} + \varepsilon\mathbf{u}))\,\xi_s(\bar{\Psi} + \varepsilon\mathbf{u})\}\,|_{\varepsilon=0} = \frac{d}{d\varepsilon}\{D(\xi(\bar{\Psi} + \varepsilon\mathbf{u})) [\,E(\bar{\Psi} + \varepsilon\mathbf{u}) - E_L\,\xi_s(\bar{\Psi} + \varepsilon\mathbf{u})]\}\,|_{\varepsilon=0}\,. \quad (50)$$

Note that the configuration-independent quantities have been left out in this equation because they vanish in the linearization procedure. The calculations which have to be carried out are straightforward and are presented by Brinson and Lammering [24]. Finally, the linearized second Piola-Kirchhoff stress reads

$$\mathbf{D}\{\mathbf{S}(\overline{\Psi})\} \cdot \mathbf{u} = H\,\overline{D}\,\overline{\mathbf{F}}^T \mathrm{Grad}\,\mathbf{u}\,. \qquad (51)$$

The overbar is introduced for the representation of a value at the known configuration $\overline{\Psi}$. H is a variable depending on material properties, the temperature, and the stress. Moreover, in the calculations of H it must be distinguished whether the material deforms elastically or converts to detwinned martensite or to austenite. In the case of purely elastic deformations, H is equal to 1. Furthermore, in Eq. (50) $\overline{D}$ is the modulus, and the deformation gradient $\overline{\mathbf{F}}$ as well as the displacement gradient Grad $\mathbf{u}$ are defined as vector quantities

$$\overline{\mathbf{F}} = \begin{Bmatrix} 1+\overline{u}_{,x} \\ \overline{v}_{,x} \\ \overline{w}_{,x} \end{Bmatrix}, \quad \mathrm{Grad}\,\mathbf{u} = \begin{Bmatrix} u_{,x} \\ v_{,x} \\ w_{,x} \end{Bmatrix}. \qquad (52)$$

Here, u, v and w denote the displacements in the x, y and z direction, respectively, and the subscript ,x indicates differentiation with respect to x.

Eqs. (48) and (51) are combined and cast into a notation appropriate to form the non-linear element stiffness matrix $\mathbf{K}^e$ for truss elements of shape memory alloy

$$\mathbf{K}^e = H\,\overline{D}\,A\int_l \mathbf{B}^T\mathbf{F}\,\mathbf{F}^T\mathbf{B}\,dx + \overline{S}\,A\int_l \mathbf{B}^T\mathbf{B}\,dx\,, \qquad (53)$$

where A and l are the cross-sectional area and the length of the truss member, respectively. $\mathbf{B}$ denotes a matrix that contains shape function derivatives and is well-known for truss applications from finite element textbooks. Note that the formulation in this equation differs from the standard finite element formulation for non-linear truss members only by the H-factor. It should be emphasized that this H-factor preserves quadratic convergence in a solution algorithm based on Newton's method and that Eq. (53) represents the exact tangent stiffness modulus of the underlying problem.

3.4 Active Frequency Tuning of a Composite Strip

Although the use of shape memory alloys is limited by the low frequency (maximum 2 Hz) at which they can be run, shape memory alloys can be used in many dynamic applications. One possibility currently being researched is structures with embedded wires of shape memory material, activated by an electric current to vary the temperature. Active frequency tuning of this type can be used, for example to avoid resonances. An investigation of this particular application of shape memory alloys is demonstrated by the finite element procedure in the following example.

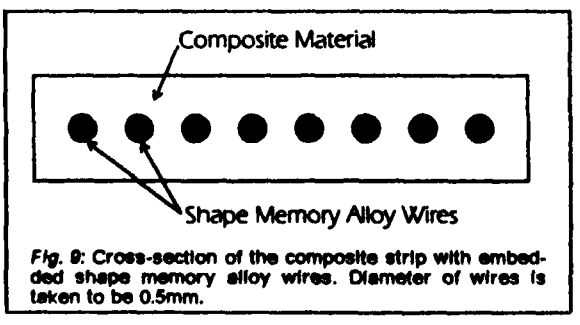

Fig. 9: Cross-section of the composite strip with embedded shape memory alloy wires. Diameter of wires is taken to be 0.5mm.

Material properties of the shape memory alloy	
Moduli	$D_a = 67 \cdot 10^3\ MPa$ $D_m = 26.3 \cdot 10^3\ MPa$ $\Theta = 0.55\ MPa/^0C$
Density	$\rho = 6448.1\ kg/m^3$
Transformation Temperatures (cf. Fig. 8)	$M_f = 9\,^0C$ $M_s = 18.4\,^0C$ $A_s = 34.5\,^0C$ $A_f = 49.0\,^0C$
Transformation Constants (cf. Fig. 8)	$C_M = 8\ MPa/^0C$ $C_A = 13.4\ MPa/^0C$ $\sigma_s^{cr} = 100\ MPa$ $\sigma_f^{cr} = 170\ MPa$
Maximum Residual Strain	$\varepsilon_L = 0.067$
Material properties for the fiber-reinforced composite strip	
Tension Stiffness	$DA = 3.050 \cdot 10^{-5}\ N$
Bending Stiffness	$DI = 2.074\ Nm^2$
Mass per Length	$\mu = 3.5 \cdot 10^{-2}\ kg/m$
Thermal Coef. of Expansion	$\alpha = 1.2 \cdot 10^{-6}\ 1/^0C$

Table 1: Material properties used in the active frequency tuning example.

Fig. 9 shows a fiber-reinforced composite strip with eight embedded shape memory alloy wires. The material properties of the composite strip are given in Table 1. The structure with a total length of 1 m is clamped at both ends. The initial conditions are 0.5% residual strain of the shape memory alloy wires, no prestress, and temperature $T_0 = 20°C$. From these values the stress-induced and temperature-induced martensite fractions are calculated as $\xi_{s0} = 0.075$ and $\xi_{T0} = 0$, respectively.

In the numerical experiment the first two eigenfrequencies of this structure are calculated as a function of temperature. The results are presented in Fig. 10. When the structure is heated, there is a slight decrease in the eigenfrequencies until the temperature reaches 35°C. In the range from 35°C to 75°C there is a strong increase in the eigenfrequencies, after which they slowly decrease again when the temperature exceeds 75°C. When the structure is cooled, a hysteresis loop of the eigenfrequencies vs. temperature is observed. Note that the frequency at the end of the cooling cycle does not return to the pre-loading levels; this is due to the fact that because of the high stress obtained during heating, upon cooling the material first encounters the state at which that stress level and the T_0 would produce a strain of 0.5% in the shape memory alloy. Since the specimen is heated again from here, one obtains

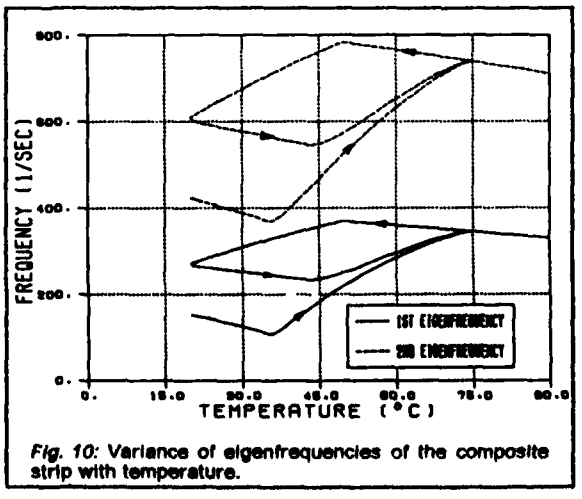

Fig. 10: Variance of eigenfrequencies of the composite strip with temperature.

the closed hysteresis cycle. To obtain the original values of the frequencies, the material must be unclamped and the residual stress removed from the shape memory alloy wires.

Since the material is restrained as the transformation to austenite occurs due to heating, and the shape memory alloy would recover the residual strain if unrestrained, extremely large internal stresses are incurred. As the eigenfrequencies depend strongly on the axial force of this structural system and the stress due to heating raises primarily within the temperature range from 35°C to 75°C (the region of martensite to austenite transformation), the change of the eigenfrequencies reflects this behavior. The slight decrease of the eigenfrequencies with increasing temperaure from 20°C to 35°C and above 75°C is explained by the compression force exerted by the composite strip (due to the constraint of normal thermal expansion) and cannot be compensated for by the shape memory alloy wires outside the transformation region. The hysteresis loop seen upon cooling is due to the transformation of the shape memory material to martensite. These results for the change in the eigenfrequencies of a fiber-reinforced composite strip with embedded shape memory alloy wires agree well qualitatively with experimental results on a similar system studied by Mooi [25]. Direct comparison of numerical results is not possible due to the lack of detailed information on the material properties in the experiment.

The numerical results were obtained by discretization of the structural system by both shape memory alloy truss finite elements and non-linear beam elements. Linking the corresponding nodes has the effect that the stiffness and mass matrices of the shape memory alloy truss elements and the composite beam elements are added. Note that in this technique only the composite strip contributes to the bending stiffness of the system and that the axial force of both the composite strip and the shape memory alloy wires are accounted for.

4. CONCLUDING REMARKS

In this paper new finite elements that allow for the analysis and optimization of smart structures have been presented. In the numerical examples it has been shown that the finite element method must be considered an effective tool for the investigation of the static and dynamic mechanical behavior of smart structures. Moreover, the optimization of the actuator location has been solved by algorithms which are also based on finite element formulations. Therefore, the finite element method is considered to be well-suited for the effective design and evaluation of smart structures before their construction.

Future developments in this area focus on an increasing sophistication of the presented techniques and their expansion to related problems in the smart structures technology. The location of piezo-electric polymers bonded as patches for sensing/actuating purposes onto plates and shells is an important problem. Furthermore, the finite element analysis of structures with embedded shape memory alloy wires could benefit from the addition of heat transfer effects in order to consider a wider variety of applications. Another very important issue is the incorporation of general control algorithms into the finite element code. This would be a decisive step forward in the numerical simulation of the behavior of smart structures.

REFERENCES

[1] E. Breitbach. Research Status on Adaptive Structures in Europe. *2nd Joint Japan/US Conference on Adaptive Structures*, Nagoya, Japan, Nov. 12-14, Technomic Publishing Co., Lancaster (1991).

[2] F. Nitzsche and E. Breitbach. A Study on the Feasibility of Using Adaptive Structures in the Attenuation of Vibration Characteristics of Rotary Wings. *33rd Structures, Structural Dynamics and Materials Conference*, Dallas, April 13-15 (1992).

[3] L. C. Brinson. Constitutive Behavior of Shape Memory Alloys: one dimensional thermomechanical derivation with non-constant material functions and redefined martensite internal variable. Accepted for publication in *Journal of Intelligent Material Systems and Structures* (1992), to appear April 1993.

[4] M. Naillon, R. H. Coursant and F. Besnier. Analysis of Piezoelectric Structures by a Finite Element Method. *Acta Electronica* **25**, 341-362 (1983).

[5] W. Wagner. Eine geometrisch nichtlineare Theorie schubelastischer Schalen mit Anwendung auf Finite-Element-Berechnungen von Durchschlag- und Kontaktproblemen. *Techn. Rep. No. 85/2, Inst. f. Baumechanik, University of Hannover, Germany* (1985).

[6] W. Wagner, P. Wriggers and E. Stein. A Shear Elastic Shell Theory and Finite Shell Element Post-Buckling Analysis Including Contact. In: I. Szabo (ed.) EUROMECH 200, 381-404 (1985).

[7] R. Lammering. Structural Analysis and Optimization of a Propfan-Blade by Use of the Finite Element Method. *Engineering Computations* **7**, 327-337 (1990).

[8] R. Lammering. The Application of a Finite Shell Element for Composites Containing Piezo-Electric Polymers in Vibration Control. *Computers & Structures* **41**, 1101-1109 (1991).

[9] R. Lammering, J. Jia and C. A. Rogers. Optimal Placement of Piezo-Electric Actuators in Adaptive Truss Structures. Submitted for publication in *Journal of Sound and Vibration* (1991).

[10] R. M. Jones. *Mechanics of Composite Materials*. McGraw-Hill, New York (1975).

[11] O. C. Zienkiewicz and R. L. Taylor. *The Finite Element Method*. London: McGraw Hill Book Company, Fourth Edition (1989).

[12] E. K. Dimitriadis, C. R. Fuller and C. A. Rogers. Piezoelectric Actuators for Distributed Noise and Vibration Excitation of Thin Plates. *Proceedings of ASME Failure Prevention and Reliability Conference*, Montreal, 223-233 (1989).

[13] K. Ogata. *Modern Control Engineering*. Prentice Hall, Inc., Englewood Cliffs (1970).

[14] S. P. Banks. *Control Systems Engineering*. Prentice Hall, Inc., Englewood Cliffs (1986).

[15] T. Bailey and J. E. Hubbard. Distributed Piezoelectric Polymer Active Vibration Control of a Cantilever Beam. *J. of Guidance and Control* **8**, 605-611 (1985).

[16] L. Meirovitch and H. Baruh. Control of Self-Adjoint Distributed-Parameter Systems. *Journal of Guidance and Control* **5**, 60-66 (1982).

[17] R. E. Lindberg and R. W. Longman. On the Number and Placement of Actuators for Independent Modal Space Control. *Journal of Guidance and Control* **7**, 215-221 (1984).

[18] J. Jia. Optimization of Piezoelectric Actuator Systems for Vibration Control of Flexible Structures. *Ph. D. Thesis, Virginia Polytechnic Institute and State University* (1990).

[19] A. Osyczka. *Multicriterion Optimization in Engineering*. Chichester: Ellis Horwood Limited (1984).

[20] C. Liang and C. A. Rogers. One-Dimensional Thermomechanical Constitutive Relations for Shape Memory Materials. *Journal of Intelligent Material Systems and Structures* 1, 207-234 (1990).

[21] J. E. Marsden and T. J. R. Hughes. *Mathematical Foundations of Elasticity*. Prentice Hall, Englewood Cliffs (1983).

[22] T. J. R. Hughes and K. S. Pister. Consistent Linearization in Mechanics of Solids and Structures. *Computers & Structures* 8, 391-397 (1978).

[23] P. Wriggers. Konsistente Linearisierungen in der Kontinuumsmechanik und ihre Anwendung auf die Finite-Element-Methode. *Techn. Rep. No. 88/4, Inst. f. Baumechanik, University of Hannover, Germany* (1988).

[24] L. C. Brinson and R. Lammering. Finite Element Analysis of the Behavior of Shape Memory Alloys and their Applications. Submitted for publication in *International Journal of Solids and Structures* (1992).

[25] H. G. Mooi. Active Control of Structural Parameters of a Composite Strip Using Embedded Shape Memory Alloy Wires. *Thesis, University of Twente, The Netherlands, and Deutsche Forschungsanstalt für Luft- und Raumfahrt, Göttingen, Germany* (1992).

FIBER-OPTIC INTERFEROMETRIC STRAIN GAUGE FOR SMART STRUCTURES APPLICATIONS: FIRST FLIGHT TESTS

N. Fürstenau, D.D. Janzen, W. Schmidt
German Aerospace Research Establishment (DLR)
Institute for Flight Guidance
Flughafen, D-3300 Braunschweig, Germany

SUMMARY

Initial flight tests of a fiber-optic strain gauge (OSG) based on a double-polarization Michelson interferometer with incremental readout via fringe counting have been performed. The passive quadrature demodulation technique allows for balanced interferometer arms, exhibiting partial self temperature compensation. A bent reference (R) arm approach for the sake of isolation of the R-arm from the strain to be measured was tested for the first time. The sensor was surface adhered on a carbon fiber reinforced plastic plate which, in turn, was screwed to the main wing spar of a Cessna C207A aircraft. Strain was measured under different flight conditions and compared to the readout of a conventional resistive strain gauge (ESG). Good agreement with the theoretical predictions as well as with the readout of the ESG was observed for short term (of the order of minutes) quasistatic strain measurements deapit large vibration induced noise. The Fourier spectra of the time series exhibited also good agreement between ESG and OSG with respect to the dynamical response up to at least 250 Hz. The measurement range and stability of the present experimental setup is limited by polarization instabilities which partly are due to anisotropic transverse stress effects at the adhered fiber sections. Longer term dc strain measurements require carefully controlled isotropic adhesion conditions and miniaturized optomechanical components with improved mechanical stability.

1. INTRODUCTION

A large number of fiber-optic interferometric and polarimetric strain gauge concepts have been investigated during recent years (e.g. [1,2,3,4]). They appear to be particularly well suited for embedment into 'smart' structures made of composite materials. However, very little experience exists up to now with respect to their practical applicability under real world conditions. Recently, Murphy et al [5] reported on ground tests of an optical fiber extrinsic Fabry-Perot sensor fixed near the wing root of an F15 aircraft, under simulated flight conditions with static and dynamic load. In this paper we report for the first time, to our knowledge, in-flight optical strain measurements on the main wing spar of a CESSNA C207A aircraft under various load conditions. The fringe counting readout of a double-polarization Michelson interferometer with balanced interferometer arms (OSG) [4], as registered by an up-down counter, is compared to the strain indicated by a conventional resistive strain gauge (ESG). The measured strain is related to aircraft speed, as indicated by a differential pressure sensor, and to vertical acceleration, measured using a servo accelerometer. Temperature compensation of the ESG requires a second gauge which is isolated from the strain to be measured. The advantage of the interferometric sensor with balanced arms is its inherent partial temperature self compensation [6].

2. EXPERIMENTAL SETUP

Fig. 1 shows a schematic of the interferometric sensor element. The linearly polarized wave from a 1 mW HeNe laser (L) passes an optical isolator, and is guided to the interferometer via 3 m of cabled polarization maintaining fiber, after coupling into the fiber by means of a GRIN lens fiber coupler (O). It is connected via an NTT-FC single mode connector (FC) to the input arm of a 3 dB directional coupler. Two equal length coupler arms with silvered end faces serve as reference (R) and sensing (S) arms of the interferometer. They are adhered to the surface of a thin carbon-fiber composite plate (CFRP) of rectangular cross section (thickness $2h$ = 1 mm, width = 10 mm) near to a conventional resistive strain gauge (Hottinger Baldwin Meßtechnik, type 6/120LY61), as sketched in fig. 2. For the sake of temperature compensation a second electrical strain gauge is fixed on the CFRP plate outside the strained region. Together, the ESGs represent one half of a Wheatstone bridge. The fiber jacket is removed from both the R and S arms of the interferometer. The lengths of the fixed sections of R and S arms are $L_S = L_R = 49 \pm 0.5$ mm. In order to reduce birefringence variations under loading of the plate, initially only the end points of the fibers were adhered to the surface (using Hottinger two component strain gauge glue, type X60). Because first measurements showed that the S arm was strained only after applying some prestress to the sample, a longer section $L_{SA} = 36$ mm was covered by the glue before starting the flight tests. The corresponding adhesive covered length of the R arm is $L_{RA} = 3.5$ mm. The sensitive length is then obtained as $L_S - L_{RA} = 46 \pm 0.5$ mm.

For the sake of isolating the reference arm from the strain transferred to the CFRP plate by the aircraft structure, the R arm is bent before it is fixed to the plate. The mirrored end faces of the arms are separated by 2.5 mm. Fiber sqeezers (PA) at the R arm and the output fiber serve as photoelastic polarization adjusters, and are used for initial adjustment of the offset phase difference Φ_H - Φ_V. A polarizing beam splitter (PB) splits the collimated (G = GRIN lens) output wave into two orthogonally polarized interference signals (horizontal H, vertical V) with different phase offsets (Φ_H, Φ_V). The light is then focused by GRIN lenses into (SMA) connectorized cabled 100/140 μm multimode output fibers (MF) which in turn are connected to PIN photodiodes (PD). The H and V signals are fed into an up-down counter (16 bit, 10 MHz) after passing through an electronic readout unit (RE) for symmetrizing and automatic intensity-offset control. Counting pulses are produced at the zero crossings of both the V and H signals after offset subtraction, yielding an incremental strain resolution of 0.07 μm. For the present tests the 1 MHz bandwidth of the readout unit was reduced to 3 kHz in order to filter out small high frequency vibrations. These would produce problems in the correct up-down counting if the offset phase difference became small. The simultaneous polarimetric signal [4] (offset phase difference Φ_H-Φ_V) was not registered in these experiments because this would require a careful adjustment of the birefringent axes of the interferometer fibers with respect to the H, V axes, which was not possible during the flight tests due to birefringence instabilities (see below).

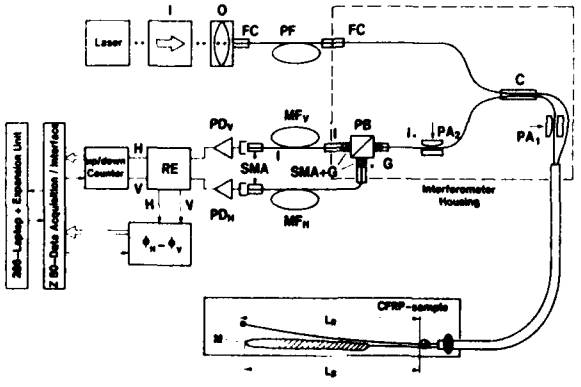

Figure 1: Schematic of interferometric strain gauge with CFRP plate, readout electronics and data acquisition. For details see text.

A plastic housing encloses the optical components of the interferometer. Between the housing and the CFRP sample, the interferometer arms are protected by means of a silicone tube. The housing is permanently glued to the CFRP sample at the end point of the strained section. At the same point a screw fixes the plate to the

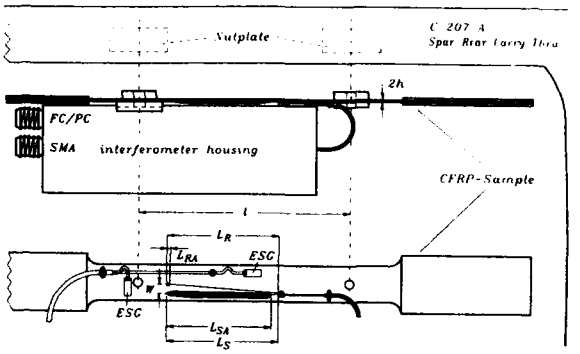

Figure 2: CFRP sample with surface adhered fiber optic and electrical strain gauges. The fixing positions at main spar are indicated.

main wing spar of the C207A. The length of the strained plate section (l = 94.5 mm) is defined by the distance between this and a second screw as indicated in fig. 2.

An elevated part on the spar in between the two screws made it necessary to put spacers between the spar and the CFRP plate. For this purpose, and in order to distribute the stress evenly over the width of the plate, Aluminum pieces of the same width are glued over the screw-hole sections. Under flight conditions the sensor carrying plate is pre-stressed by the lifting force acting on the wings, because the sensor is installed on the ground. Preliminary tests with the ESG showed the pre-strain to be about 200 $\mu\varepsilon$. This can be seen in fig. 5 of the following section.

The electrical strain gauge (120 Ω, length = 6 mm, gauge factor k = 2.01) is connected to a 5 kHz-carrier frequency strain gauge amplifier (Hottinger Baldwin Meestechnik, model M50) with 500 Hz bandwidth. OSG and ESG strain gauge data are related to aircraft speed and vertical acceleration (with respect to the wing plane), measured by means of a differential pressure sensor (Rosemount model 1221F2VL, sensitivity 1.451 V/1000 Pa) and a servo accelerometer (Systron Donner model 4310, sensitivity 1.504 V/g) respectively.

Data is acquired using a single board unit (Modular4, Sorcus Computer Company) containing a Z80 processor with 64 kB RAM, 16 channel A/D-converter with 8 ms conversion time, 3 10 MHz up-down counters, and 5 8-bit digital I/O ports. The data acquisition board is plugged into the expansion unit of a COMPAQ SLT286 Laptop which is used for controlling the Z80 and storing the data on a hard or floppy disc for off-line data evaluation. During flight, sampling rates were chosen between 10 and 500 Hz with data files between 2 sec and 2 minutes long.

The OSG readout electronics with He-Ne laser, the strain gauge bridge amplifier, and the data acquisition unit are mounted in a flight-test rack which is fixed to the aircraft seat rails via shock mounts. The Δp-sensor and the accelerometer (with sensitive axis up) are mounted to the side of the rack.

3. THEORY

The theory of the double-polarization interferometer has been described in detail in previous papers [4,7,8]. The following includes only a brief summary of those details which are of relevance for the discussion of the results.

The two orthogonally polarized (horizontal H, vertical V) interference signals are described by

$$(1)\quad P_{H,V} = \frac{P_o T_{H,V}}{4(1+\mu_{H,V})}\,(1+\mu_{H,V}\cos(\Delta\Phi + \Phi_{H,V}))\,,$$

where P_0 = input power, T = interferometer transmissivity, μ = fringe contrast, and $\Phi_{H,V}$ = phase offset due to path imbalance and fiber birefringence. The offset phase difference $\Delta\Phi_{HV} = \Phi_H - \Phi_V$ can be adjusted, using the elasto-optic polarization adjusters, such that the H and V signals are in quadrature [4]. The gauge factor relating the measurand induced phase difference, $\Delta\Phi$, to the fiber strain is given by [9] $G = \Delta\Phi/\Delta L = \Delta\Phi/\varepsilon/L$ (ε = relative strain $\Delta L/L$, L = length of sensitive fiber section of sensing arm S). The value for G is obtained as [4] G = 1.318 deg/$\mu\varepsilon$/mm = 3.66 2πrad/μm. Counting half fringes of both quadrature signals (π/2-phase shift increments) yields a strain resolution of G^{-1} = 0.0683 μm/count ($\pm$ 0.0001) or G = 14.6 $\pm$ 0.1 counts/μm. The error is due to the uncertainties in the elasto-optic constants [10].

It has been shown in [4] that significant variation of fiber birefringence is produced under external load of the CFRP plate, if the fiber is covered by the adhesive. This gives rise to a variation of the phase offset difference, $\Delta\Phi_{HV} = \Phi_H - \Phi_V$. In order to maintain the unambiguity of the fringe counting procedure, the variation from quadrature must not exceed $\pi/2$. In [4] an estimate of the birefringence induced offset phase variation is given for the case of plate bending under a central load. The birefringence variation in this case is due to shear stress induced transverse force acting on the adhesive covered fiber sections. Instead of plate bending, in the flight tests, axial stress is transferred to the plate along its long (x) axis. Therefore, in this case, anisotropic cross contraction of the plate and the adhesive under axial strain is assumed, in order to estimate the stress transverse to the fiber axis (y-direction, orthogonal to plate surface). Elementary theory of elasticity yields for the y-stress σ_y

$$(2)\quad \sigma_y = -\,E_{adh}\,\nu_{adh}\,\varepsilon_x\,,$$

where ε_x = strain in x direction, ν_{adh} = Poisson contraction ratio and E_{adh} = Youngs modulus of the adhesive. Preliminary flight tests with a conventional resistive strain gauge yielded typical strain variations of the order of ε_x = 100 $\mu\varepsilon$. Multiplying σ_y with the fiber cross section D_f = 125 μm yields an estimate of the transverse line force f acting on the adhesive embedded fiber section: $f = \sigma_y\, D_f$ = 0.41 N/cm. By using (2) and introducing the expression for f into the equation for the transverse force induced birefringence as given by [11] we obtain, for the birefringence variation of the adhesive embedded fiber section on the strained plate:

$$(3)\quad \beta_f = \frac{8\, C_s\, \nu_{adh}\, E_{adh}}{\pi\, E_{fiber}}\,\varepsilon_x\,.$$

With the elastooptic coefficient [11] C_s = -1.6 μm^{-1}, Young's moduli of adhesive and fiber respectively E_{adh} = 1.3 10^{10} Pa, E_{fiber} = 6.5 10^{10} Pa, and the (estimated) Poisson constant ν_{adh} = 0.25, we get β_f = 0.2 rad/cm. In [8] it is shown that the birefringence induced offset phase variation, in general, exhibits a complicated periodic dependence on β_f. For the sake of getting an impression of the order of magnitude of the effect, we treat the special case of the birefringent axes aligned with the H-V axes of the polarizing beam splitter. In this case a linear dependence of $\Delta\Phi_{HV}$ on β_f is expected [4]

$$(4)\quad \Delta\Phi_{HV} = 2\,\beta_f\,L_A\,,$$

yielding an offset phase difference variation of 1.2 rad with L_A = 3 cm. In contrast to [4], in the present experiments the angle between the birefringent (f,s) and the H,V axes is arbitrary. Thus, in general, a periodic dependence is expected instead of the linear one of equation (4), and this should reduce the maximum $\Delta\Phi_{HV}$-variation. Our estimate of the load induced birefringence variation shows that under flight conditions we operate at the critical limit for unambiguous fringe counting, particularly if there are additional uncontrolled sources of β-variation (see next section).

4. EXPERIMENTAL RESULTS AND DISCUSSION

Six one-hour flight tests were performed, under varying flight conditions. Flight altitudes were generally between 5500 and 7500 feet, depending on where the smoothest air was to be found. The flight profiles chosen for the production of wing loading were: i) stepwise increases and decreases of airspeed, between 60 and 120 knots, with different flap positions (0 to 30 degrees = no flaps to full flaps), ii) alternating, roughly parabolic flight path with accelerations between 0 and +2g, iii) up to 60 degree bank angle left and right turns, and iv) fast alternating left and right partial rolls (to about 70 degrees from horizontal in each direction). Ground tests with manual wing loading at different engine idle speeds (1000 to 2000 rpm), as well as with the engine off, yield additional

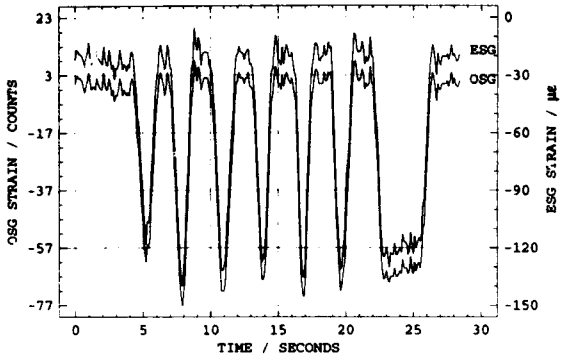

Figure 3: ESG and OSG time series from ground test of manual wing loading with aircraft engine off.

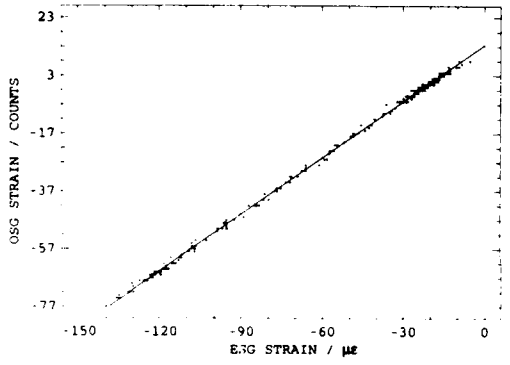

Figure 4: OSG vs ESG for data shown in figure 3. Solid line shows least-squares fit.

information on the response of the sensor under conditions of reduced environmental disturbance. Sampling frequencies were usually between 10 and 30 Hz, and acquisition times were usually from one to several minutes for a single data file. Several runs of 2 to 5 seconds with 200 to 500 Hz sampling rate provide data for comparisons of the higher frequency dynamic responses of the OSG and ESG. The OSG up-down counter was reset before each run.

Figure 3 shows time series plots from a ground test performed outside of the hangar (in an unsteady wind) with the engine switched off. The wing tip was manually lifted and allowed to return slowly to its rest position, repeatedly. The noise in the quasi-static section near 25 seconds is a result of shaking arms trying to hold the wing up, while the effect of the unsteady wind can be seen in this section and in the near zero strain sections. Figure 4 shows the same data, in the form OSG versus ESG data, along with the least-squares-fit line produced by a linear regression analysis. The sensitivity of the OSG is seen from the regression slope to be 1.28 ± 0.01 °/με·mm (= 14.2 ± 0.1 counts/μm), which is about 3 % lower than the predicted value, probably due to incomplete isolation of the reference arm from the strain. Naturally, these sensitivity values are only valid in the case of applied tension. Compression would cause fiber buckling, since the fibers are not fastened to the sample over their entire lengths. In flight, however, due to the effective strain bias mentioned earlier, compression can not occur unless negative accelerations are experienced.

As an example of the flight test data, fig. 5 shows the responses of ESG, OSG and accelerometer to a series of 5 acceleration cycles between roughly 0g and +2g (normal to the wing) over a period of 35 seconds. Again, the correlations are obvious. Figure 6 shows a plot of the strain data from fig. 5, in the form OSG versus ESG data, including a least-squares-fit line. The slope of this line indicates a strain sensitivity of 1.26 ± 0.01 °/με·mm which differs by 1.5 % from the ground test result, and by 4.5 % from the theoretically predicted value.

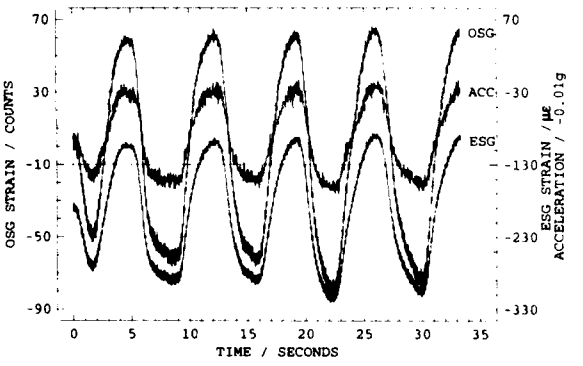

Figure 5: OSG (left ordinate), ESG, and accelerometer data (both right ordinate) from alternating acceleration flight.

If variations in the relative birefringence of the interferometer arms cause the relative phase between the two polarization components to vary from quadrature by some value approaching 90 degrees (in either direction), unambiguous fringe counting becomes impossible. This effect can produce arbitrary offsets in the data between intervals of normal operation. As mentioned in the theory section, the primary birefringence variation is due to the fact that, for these experiments, most of the sensing arm was covered by glue. Environmental disturbances such as small temperature changes (which always accompany altitude changes), and mechanical disturbances to insufficiently protected parts of the interferometer (air drafts were common in the aircraft cabin) could also cause the

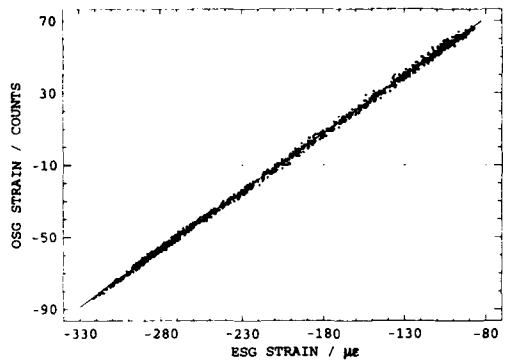

Figure 6: OSG vs ESG for data shown in fig. 5. Solid line shows least-squares fit.

manual readjustment of the interferometer polarization controllers is necessary before normal operation can resume. Reduction of the length of the sensing region, or careful isotropic bonding of the sensing fiber to the sample would help greatly in reducing birefringence drift. After recovery of tracking, the incremental strain sensitivity is not changed, but an arbitrary offset is introduced. Several short term lock-losses occurred during the acquisition of the data shown in figures 5 and 6. This partly accounts for the scatter in the data about the best-fit-line, and for the difference of this slope from that produced in the ground test.

Figure 7 shows the spectra produced by fast Fourier transforms of the data from a 5 second 200 Hz acquisition during normal steady flight. FFTs of both OSG and ESG data are shown. The peak-to-peak amplitude of the vibrational noise on the time series plots is approximately 10 $\mu\varepsilon$. The majority of the prominent spectral peaks corresponds to subharmonics and harmonics of the engine rotation rate. The exception is the peak at 75.2 Hz, which appears strongly in the differential pressure sensor output, while the engine speed peaks do not. This implies some sort of aerodynamic pressure variation producing a vibration experienced by the strain gauges. Regardless, the spectra agree very well, indicating that, at least for small amplitude vibrations, the dynamic response of the OSG extends up to at least the upper frequency limit for this spectrum, which is 100 Hz. In fact, sampling rates up to 500 Hz were used for some tests, and also produced matching OSG and ESG spectra, showing that the small-strain-signal bandwidth of the OSG is at least 250 Hz.

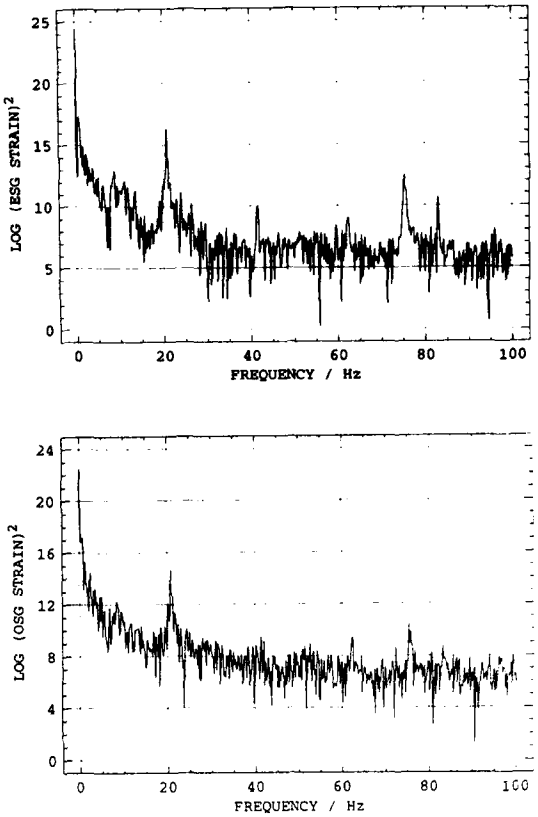

Figure 7: FFTs of 5 sec 200 Hz acquisition during steady normal flight (engine speed = 2500 rpm = 41.7 Hz). Lower spectrum: OSG output, upper spectrum: ESG output.

5. CONCLUSION

For the first time to our knowledge, in flight strain measurements on an aircraft wing structure using a fiber optic interferometric strain gauge have been performed. A double-polarization Michelson interferometer with balanced interferometer arms, surface adhered to a thin CFRP plate was used as the sensing element. Passive quadrature demodulation of two phase shifted interference signals allow for unambiguous fringe counting. In contrast to electrical strain gauges the optical one is partially self temperature compensated. The reference arm is isolated from the sensing arm by fixing it in a bend at the two end points. The stability of the present optical setup proves sufficient for continuous readout over time periods of the order of minutes under flight conditions. As expected from previous laboratory experiments, stress fields transverse to the fiber axis, arising at the adhesive embedded sections of the surface adhered fibers, limit the unambiguous readout due to significant birefringence variations under external load. Improved photoelastic polarization adjusters are under construction in order to improve the temperature stability

of the polarization. The data taken during single runs of up to some minutes exhibit reasonable agreement between theoretical and experimentally determined sensitivity. The latter is determined by taking an electrical strain gauge as a reference. In the case of embedded fibers with anisotropic transverse stress fields the critical sensing length for maintaining unambiguous readout is determined by the maximum transverse stress producing fiber birefringence. Special care should be taken in maintaining isotropic transverse stress conditions with surface adhered fibers.

6. ACKNOWLEDGEMENT

We would like to express our thanks to the pilots H.-J. Berns and S. Seydel for their support during the preparations and their cooperation during the tests. Construction of the test rack under narrow time constrictions in accordance with the severe safety regulations would not have been possible without the help of R. Zick and D. Laschinski. We are indebted to N. Vermeulen for setup of the interferometer and to H. Naumann and D. Albrecht for construction of the readout electronics and the electrical aircraft-to-test-rack interface. We would also like to thank H.C. Goetting for supplying the CFRP samples and support during initial tests at the CFRP test lab.

7. REFERENCES

[1] T. Valis, E. Tapanes and R.M. Measures *Localized Fiber-Optic Strain Sensors Embedded in Composite Material,* SPIE Proc. vol. 1170 (1989) pp 495-504

[2] S.R. Waite , R.P. Tatam and A. Jackson, *Use of optical fibre for damage and strain detection in composite materials*, Composites **19** (1988) pp 435-442

[3] Z.J. Lu, F.A. Blaha, *A two-mode fiber optic strain sensor system for smart structures and skins*, SPIE Proc. vol. 1370 (1990) paper 17

[4] N. Fürstenau, W. Schmidt, H.-C. Goetting *Simultaneous interferometric and polarimetric strain measurements on composites using a fiber-optic strain gauge,* Applied Optics 31 (1992) pp 2987-2993

[5] K.A. Murphy, M.F. Gunther, A.M. Vengsarkar, R.O. Claus, *Fabry-Perot fiber-optic sensors in full scale fatigue testing on an F-15 aircraft,* Appl. Opt. 31 (1992) 431-433

[6] N. Fürstenau , W. Schmidt and H.-C. Goetting, *Simultaneous interferometric and polarimetric strain measurements on composites employing a fiber optic strain gauge*, Proc. Conf. on Optical Fiber Sensor-Based Smart Materials and Structures ed. R. O. Claus (Lancaster: Technomic) (1991) pp 29-39

[7] S.K. Sheem, T.G. Giallorenzi, K. Koo, "Optical Techniques to Solve the Signal Fading Problem", Appl. Optics 21 (1982) 689-693

[8] N. Fürstenau, "Performance of the double-polarization method in interferometric digital force sensing by fiber tension bending", in: 'Polarization Considerations in Optical Systems', SPIE-Proc. vol. 891 (1988) 209-214

[9] C.D. Butter, G.B. Hocker, *Fiber-optics strain gauge,* Appl. Optics 17 (1978) pp 2867-2869

[10] A. Bertholds, R. Dändliker *Determination of the Individual Strain-Optic Coefficients in Single-Mode optical Fibers,* IEEE J. Lightwave Techn. 6 (88) 17-20

[11] S.C. Rashleigh *Origins and Control of Polarization Effects in Single-Mode Fibers*, J. Lightwave Technology LT-1 (1983) 312

THE IMPACT OF ACTIVE CONTROLS TECHNOLOGY ON THE STRUCTURAL INTEGRITY OF AERONAUTICAL VEHICLES

Thomas E. Noll
NASA Langley Research Center
Mail Stop 243
Hampton, VA 23681
United States

Edward Austin, US Army Aviation Research and Technology Activity, United States
Shawn Donley, Naval Air Development Center, United States
George Graham, National Defence HQ, Canada
Terry Harris, Wright Laboratory, United States
Ian Kaynes, Defence Research Agency, United Kingdom
Ben Lee, Institute for Aerospace Research, Canada
James Sparrow, Aeronautical Research Laboratory, Australia

1. SUMMARY

This paper summarizes the findings of an investigation conducted under the auspices of The Technical Cooperation Program (TTCP) to assess the impact of active controls technology on the structural integrity of aeronautical vehicles and to evaluate the present state-of-the-art for predicting loads caused by a flight-control system modification and the resulting change in the fatigue life of the flight vehicle. Important points concerning structural technology considerations implicit in applying active controls technology in new aircraft are summarized. These points are well founded and based upon information received from within the aerospace industry and government laboratories, acquired by sponsoring workshops which brought together experts from contributing and interacting technical disciplines, and obtained by conducting a case study to independently assess the state of the technology. The paper concludes that communication between technical disciplines is absolutely essential in the design of future high performance aircraft.

2. INTRODUCTION

The Technical Cooperation Program (TTCP) was formed to provide a mechanism for government organizations within Australia, Canada, New Zealand, the United Kingdom, and the United States to conduct cooperative research projects. The goal of TTCP is to identify areas of common interest and gaps in existing research and development (R&D) programs, provide recommendations for initiating new R&D activities, and to perform collaborative studies. TTCP is composed of Subgroups that are responsible for broad areas of research where there is sufficient interest among the member countries for initiating collaborative activities. Within the Subgroup structure, Technical Panels are formed to review and establish cooperative programs within the technical realm of the Subgroup and Action Groups are formed to investigate specific issues. Subgroup H, which has the responsibility for aeronautics technology, established Action Group HAG-6 to examine and assess the potential of recent and projected advances in active controls technology (ACT) for producing significant adverse effects on the structural integrity of fixed-wing aeronautical vehicles.

To accomplish these objectives three courses of action were pursued by HAG-6: review related activities within the government and industrial laboratories of the participating countries; sponsor workshops to bring together scientists and engineers who are actively involved in the analysis, design, test, qualification, and operation of aircraft; and perform an independent analysis to evaluate present state-of-the-art methodologies involved in the integration of the technical disciplines of structures, structural dynamics, aerodynamics, and active controls. For the analysis task, the F/A-18 aircraft served as the case study. HAG-6 completed the investigation and prepared a final report[1] for Subgroup H in October 1989. An executive summary of the report[2] was also prepared and distributed to government laboratories and to the aerospace industry within the participating countries in March 1990. The purpose of this paper is to provide an assessment of the state-of-the-art analytical capabilities, design methodologies, and qualification practices, and to highlight other related interdisciplinary issues.

3. STATEMENT OF PROBLEM

3.1 Structural Integrity/Fatigue Tests

Structural integrity is a prime concern during the development of flight vehicles. The structural design and fatigue testing of the aircraft is predicated on an assumed usage spectrum and on a related set of loads, based initially on analysis, and subsequently on wind-tunnel data. During the D&V (Demonstration and Validation) phase of the aircraft development process, a prototype is built and flown to obtain loads data for the flight conditions assumed to make up the fatigue load spectrum. Since operational aircraft may very well differ from the prototype, an EMD (Engineering and Manufacturing Development) phase is required to build a group of test

aircraft intended to be representative of the vehicles to be obtained during the production phase of the acquisition cycle. Flight tests accomplished during EMD are required to identify the critical points in the sky for structural design so that 100% design limit load maneuvers can be flown to measure loads and to verify structural design adequacy. The measured flight data are used to obtain the true loads for the selected flight conditions based on the design usage spectrum, and later when sufficient fleet hours have been acquired, to define a more representative set of flight conditions and a more accurate lifetime load spectrum. The load spectrum can now be compared with the design analysis and fatigue test results to adjust the design lifetime of the operational fleet.

3.2 Digital Flight Controls Technology

The introduction of digital fly-by-wire aircraft into the inventory has required the designers and the users to better understand the critical role played by digital controllers and ACT. One of the significant advantages of digital flight control system (DFCS) technology is the ability of the manufacturer to improve aircraft performance after the aerodynamic and structural designs are complete. This is accomplished through software changes, a task which can be very excruciating when the requirements for reverification and re-evaluation of software under formal configuration control must be included.

During the design of an aircraft with a DFCS, it is reasonable to expect the DFCS to evolve, through software modifications, as the aircraft progresses from the E&V phase to the EMD phase. This evolution may even continue for years after an aircraft has gone into production. It is also reasonable to anticipate that some DFCS changes may have subtle, and sometimes severe, adverse affects on the structural dynamics (aeroservoelasticity) and structural integrity (fatigue) characteristics of the aircraft. Therefore, it is expected that ACT may bring both advantages and disadvantages; for example, while ACT may be used to reduce undesirably large structural loads at one position on the wing, the improvement may be offset by increased loads at other locations. The original problem may not be solved, but merely shifted from one part of the structure to another or from one technical discipline to another.

DFCS can also be used to limit the flight envelope of the aircraft. This is referred to as "carefree piloting". It is expected that "carefree piloting" will lead inevitably to an increase of severity of the aircraft flight spectrum as pilots more aggressively complete maneuvers at the envelope boundary relying on the g-limiter to keep the vehicle safe. It is expected that interpretation of the fatigue test in terms of operational experience with a significantly more severe load spectrum will be very difficult.

3.3 Problem Statement

The problem statement is then, "How can we assure that the design and modification of an active control system has been properly evaluated such that system impacts on structural integrity, particularly, negative impacts can be assessed?"

4. CASE STUDY INVESTIGATION

Answering this question requires a thorough understanding of the structural integrity, structural dynamics, aerodynamic, and active controls technical disciplines, and the methodologies for integrating these disciplines. An analytical study was undertaken to independently evaluate the capability of modern, linear analytical methods to predict the change in wing loads resulting from a change in a DFCS. For this study the ISAC (Interaction of Structures, Aerodynamics, and Controls) code[3] and the FLEX-SIM code[4] were used. Since the F/A-18 (figure 1) is a relatively new high performance aircraft with a DFCS, it was selected as the case study.

4.1 F/A-18 Background Information

For background information, the F/A-18 fatigue test was initiated in 1979 using the approach described earlier in this paper. After a few hundred hours of testing the F.S. 453 carry-through bulkhead failed and a new bulkhead had to be fitted onto the test article. Later, other problems were encountered which lead to the conclusion that significant portions of the fuselage structure were not adequately designed. As a result, a new center fuselage section was fitted into this test article. By the time the fatigue test was ready to resume, sufficient flight testing of the aircraft with the DFCS modified to include a load alleviation system had been completed and loads data measured. The fatigue test was resumed using a new loads spectrum based on the lower wing loads caused by the load alleviation system. The completed fatigue test ultimately demonstrated four lifetimes on the forward fuselage and wings, nearly four lifetimes on the aft fuselage, and over two and one-half lifetimes on the replaced center fuselage. Military design specifications require that only two lifetimes be demonstrated during the test.

In terms of the F/A-18 flight control system, the DFCS[5] has four redundant computers working in parallel. Programmable read-only memory (PROM) holds the operational flight program which consists of the run-time executive, control laws, redundancy management, and built-in-test functions. Redundant electrohydraulic servoactuators and analog sensors provide two-fail-operate control capability. There are 10 independent primary control surfaces consisting of (in pairs) stabilators, rudders, ailerons, leading-edge flaps (LEF), and trailing-edge flaps (TEF). The LEF and TEF deflection and command limits are scheduled as functions of angle-of-attack, dynamic pressure, and Mach number. These schedules are designed to minimize drag during cruise, to improve high angle-of-attack characteristics, to improve spin departure resistance, and to provide flap load alleviation at elevated load factors.

As is typical for any modern DFCS software, the F/A-18 operational flight software went through experimental

evolutionary changes during the full-scale flight testing phase. One of the objectives of the DFCS experiments was to develop a production load alleviation system to reduce wing bending moments. Two successive PROMs involved in the load alleviation system development, PROM V4.3.1.3 and PROM V4.3.2, are studied herein. The basic LEF and TEF position schedules of the F/A-18 are a function of angle-of-attack, airspeed, and Mach number, and they are identical for both DFCS PROMs. However, the PROM V4.3.2 configuration included additional LEF and TEF position increments which were a function of Mach, altitude, and incremental load factor. These increments were an initial attempt to define a load alleviation system. PROMs V4.3.1.3 and V4.3.2 also incorporated a special development feature called the "Fixed Flap Mode". In this mode the pilot could select a particular LEF and TEF position, overriding the scheduled positions. Another difference between PROMs V4.3.1.3 and V4.3.2 is the way dynamic pressure and Mach limits were imposed on the flap schedules. In the PROM V4.3.1.3 system, these limits stopped flap scheduling and set the flap position to zero, and were placed after the command generated by the "Fixed Flap Mode". Thus, the effect of scheduled flap position on wing bending moment above these dynamic pressure and Mach limits could not be investigated. The PROM V4.3.2 configuration placed these limits before the command from the "Fixed Flap Mode". Thus, the "Fixed Flap Mode" command overrode the limit command.

4.2 Flight Test Data

The F/A-18 flights involving the load alleviation system PROMs described above are identified as Flight 164 (PROM V4.3.1.3 implemented) and Flight 167 (PROM V4.3.2 implemented). Flight data, which included pitch stick force, normal load factor at the aircraft center of gravity (Nz), average stabilator position, average LEF position, average TEF position, and wing-root bending moment (WRBM), were obtained for identical maneuvers (7.5 g symmetric pull-up at Mach 0.85, 2000 feet altitude). Figures 2 and 3 show plots of these measured parameters versus time for the two flights. Figure 4 shows the variation of WRBM as a function of Nz.

Flight 164 incorporated the PROM V4.3.1.3 DFCS with the "Fixed Flap Mode". The data in figure 2 shows the LEF at approximately 9 degrees down throughout the maneuver. If the DFCS were in its normal mode, the LEF would have been at about 1 degree down or less during 1 g flight and would have scheduled during the maneuver. In a similar manner, the TEF is at about 0.25 degrees and also does not schedule during the maneuver in the data of figure 2. The data for Flight 167 (figure 3) show the LEF and the TEF scheduling during the maneuver. The data from figures 2 and 3 clearly show that the WRBM is lower with the flap setting used during Flight 164 than that obtained with the baseline load alleviation system used during Flight 167.

During the early stages of the flight test program, comparisons of this type served as the impetus for continuing further studies to obtain a production load alleviation system. The load alleviation development process of adjusting the LEF and the TEF via the "Fixed Flap Mode", flying the maneuver, and measuring the wing bending moments was repeated many times. A set of data that gave wing bending moment as a function of flap position, Mach number, Nz, angle-of-attack, etc., was obtained. Based on this data a flap schedule that minimized wing bending moment was developed. This flap schedule was implemented in a later 6.0 DFCS configuration for flight test evaluation and ultimately in the production 8.3 DFCS configuration.

4.3 ISAC Analyses

Symmetric analyses were performed to obtain information to compare with the data measured during symmetric flight test maneuvers. For this study, the plunge and pitch rigid-body modes and the first 10 symmetric flexible aircraft modes were used to develop the half-aircraft equations of motion. Modal load coefficients were determined by applying the mode shapes to the finite element structural beam model as unit displacement fields. The internal loads consisted of the six stress resultants: two bending moments; one torsion moment; two shears; and one axial force. The coefficients were combined with time histories of the modal coordinates to produce time histories of the internal loads. The doublet lattice method[6] was used to calculate the subsonic steady and unsteady aerodynamics. For the aerodynamic analysis the aircraft was represented as a series of flat plates (figure 5) with the wing, stabilator, and fuselage being coplanar, while the vertical tail was positioned at the correct dihedral. The DFCS was modeled using the appropriate sensors, actuators, and control laws.

The ISAC predictions of aircraft response and load time histories for the DFCS tested on Flight 164 (PROM V4.3.1.3) are presented as solid lines in figure 2, and for the DFCS tested on Flight 167 (PROM V4.3.2), as solid lines in figure 3. The calculated and measured control surface deflections show reasonable agreement; the comparison of normal load factor shows similar trends, but the magnitudes differ by as much as 36 percent for the PROM V4.3.1.3 setting and 40 percent for the PROM V4.3.2 setting. Figure 4 provides comparisons between measured and calculated values of WRBM as a function of normal load factor for both flights. The calculated curves have lower slopes than do the corresponding measured values and differences of about 30 percent for both DFCS PROM configurations. Both the calculated and measured results show an increase in the WRBM for a given normal load factor following the modification to the DFCS.

4.4 FLEX-SIM Analyses

An analysis of the F/A-18 aircraft was also conducted using a group of computer codes linked by a system known as FLEX-SIM. Identical modal data were used in

this analysis as were used by ISAC to develop the equations of motion. A steady-state panel method was employed to represent the full aircraft modeled as a flat plate of equivalent planform. For the dynamic forces associated with the elastic modes an unsteady aerodynamics program by Davies[7] was used independently for the wing and tail. The steady and unsteady aerodynamics were then combined and utilized to formulate the equations of motion. The prediction of loads on the lifting surfaces was accomplished using both the modal displacement method described earlier and the modal acceleration method described by Bisplinghoff and Ashley[8]. For the latter method the load is evaluated as the direct summation of externally applied forces plus the aerodynamic forces resulting from the motion minus the inertia loads due to motion in both the rigid aircraft and elastic mode freedoms.

The predicted responses and loads on the F/A-18 with the PROM V4.3.1.3 DFCS (Flight 164) are compared in figure 6. It is seen that the predicted normal load factor closely follows the flight-test values except for a slight reduction in the later stages of the maneuver, building up to a 20 percent deficit. In addition, there is a 27 percent difference in the magnitude of the stabilator deflection. The two versions of bending moment show the modal displacement prediction to be lower than the modal acceleration curve, which itself is about 30 percent too small as compared to flight data. The predicted responses and loads on the F/A-18 with the PROM V4.3.2 DFCS (Flight 167) are compared in figure 7. For normal load factor the simulation gives a peak which is 18 percent less than the observed increment. The corresponding deficits for the peak control surface deflection differences were 30 percent for the stabilator, 12 percent for the LEF, and 11 percent for the TEF. The bending moments predicted by both methods show a greater reduction from the measured data; the modal acceleration method again has a peak value 30 percent less than the flight data. Normalizing the bending moment by reference to the normal load factor gives a traditional and useful parameter for wing root loads in symmetric motion. Calculating the ratio of incremental bending moment to incremental normal load factor for the measured data on Flight 164 gives a mean value of 87.9×10^4 in-lb/g whereas the modal acceleration method gives 80.6×10^4 in-lb/g. The effect of the load alleviation control law changes on Flight 167 are to modify these values to 95.1×10^4 in-lb/g measured and 83.8×10^4 in-lb/g predicted. The flight data show an 8.3 percent increase in loads due to the modification while the calculations gave a 3.9 percent increase.

5. ASSESSMENT OF NEEDS

Based on the results of the case study and other HAG-6 investigations and workshops, an assessment of needs was established; these needs are summarized below.

5.1 Interaction of Disciplines

The application of structural optimization for the minimization of weight quite often results in lower elastic mode frequencies. ACT is being utilized with an ever-increasing bandwidth of operation. As a consequence, there is a strong tendency for structural dynamics and the active control systems to interact. The potentially destabilizing effect of the sensors feeding back structural mode dynamics becomes more significant as the designer's confidence grows, allowing even further increases in control gains. ACT greatly extends the freedom to configure a vehicle. If full advantage is to be gained from this flexibility, the aerodynamic, structures, and controls disciplines must work together as an integrated team during conceptual and preliminary design phases.

The segregation of technical disciplines as related to this study, unfortunately, is continuing. This appears to be due, at least in part, to the differences in the nature of the disciplines and the grouping of specialists into work units that combine aeroelasticity and controls but do not include structural integrity or fatigue. The deterministic nature of aeroservoelasticity makes it accessible and relevant during the design/testing phase of aircraft production. On the other hand, fatigue is probabilistic in nature and is perceived as being more pertinent to the mature phase of aircraft operation. In order to be prepared for the future, the integration of certain disciplines is a necessity for the analysis and design of high performance vehicles. For this reason, the communication gaps between various technical disciplines need to be eliminated, particularly between the areas of ACT and structural integrity (fatigue).

The integration of disciplines for effective ACT studies is partly a matter of developing mathematical techniques and applying these procedures in a broader field. It also involves a management problem. The traditional compartmentalized approaches to design must be fundamentally changed to allow the relevant specialists to work closely together without encountering the barriers established between the offices of the separate disciplines.

There is, furthermore, a need to rapidly and completely monitor structural loads at all stages of the aircraft development process and to have these loads readily assessed as the control systems are being designed or enhanced. As a result of ACT expanding the flight envelope, many more critical loading cases arise than ever occurred for passively controlled aircraft.

5.2 Analytical Requirements

With respect to the effects of control functions on structural integrity and fatigue life, the critical technical disciplines are currently segregated. Because dissimilar mathematical models are used, controls/dynamics analysts have no incentive or common basis to communicate with fatigue and fracture experts. At the present time, one of the more significant payoffs associated with an aircraft having a DFCS results from the ability to perform rapid and "relatively inexpensive" modifications to the system

as an alternative solution to structural changes in the aircraft. It is recognized that more substantial benefits could be gained by the optimization of the DFCS during the design phase of the aircraft rather than in response to deficiencies demonstrated during flight or fatigue testing. Early consideration of ACT requires the integration of technologies, thus emphasizing the need for multidisciplinary analysis and design codes.

Fatigue in aircraft structures most commonly results from localized high stresses at joints as a result of the stress concentration of the rivets, bolts, or pins. Accurate calculation of the value of the localized stress in all fatigue critical areas is beyond the capability of present finite element methods. This is of particular concern since a 10 percent difference in stress may lead to a factor of about 2 in fatigue life. There is, therefore, much to be gained by improving analytical techniques to provide more accurate predictions of flight loads and resultant localized stresses.

At present the only practical method of determining the fatigue life of an aircraft is by means of a full-scale fatigue test with loading representative of operational conditions. The difficulty of ensuring that the loading is representative, coupled with the ease with which the role and loading of the modern aircraft can be changed by reprogramming the DFCS, means that a realistic assessment of the fatigue life of the aircraft cannot be completed until after the aircraft has spent some years undergoing test and evaluation. After the aircraft is produced and changes to the DFCS occur for one reason or another, the resulting loads should be lower, thus guaranteeing an increase in the fatigue life.

Design optimization including fatigue life for aircraft incorporating a DFCS will remain a difficult, if not impractical, proposition for some time. The statistical nature of fatigue and the strong dependence upon detailed stress magnitudes ensure this assessment. At the present time there appears to be no prospect of changing the situation.

The accuracy in the prediction of steady and unsteady aerodynamic loads at subsonic, transonic, and supersonic speeds is insufficient to define the loads for structural integrity and fatigue life evaluations. In addition, present methods are unable to predict load changes with respect to a change in an active control system to the degree of accuracy necessary to quantify the effect on fatigue life. Thus, more precise tools are needed in the loads prediction area. Especially important for fighter aircraft is the need for an improved method to determine the dynamic response of structures under the influence of separated flow and subjected to random aerodynamic loading. An example is vertical fin buffeting due to a leading edge extension vortex. Furthermore, unsteady aerodynamic loads resulting from control surface deflections are not accurately predicted, especially for novel types of control surfaces, for spoilers, or when large deflections are involved. Hinge moment is a notably difficult quantity to predict and is critical for defining the required control system capabilities.

5.3 Design Requirements

Aircraft performance is a major parameter considered during selection of a new aircraft. The selection process is generally dominated by the views of the aircraft pilots. In addition, it may be relevant that the time scale for any deficiencies in the aircraft to appear be a consideration of the selection team. Operational inadequacies are apparent soon after the aircraft becomes operational, but fatigue problems may not be revealed until the aircraft has been in service for a number of years. In other words, the design process needs to be reassessed with an eye towards including more fatigue considerations in the early stages.

Since design requirements are largely founded on satisfactory experience with previous generations of aircraft, the incorporation of ACT may represent such a large deviation from the past that a number of underlying assumptions become questionable. Examples on transport aircraft include the maneuver and gust load design requirements. The maneuver case demands the structure withstand a specific symmetric pull-up normal acceleration, and the gust case specifies a certain gust velocity. These values together are based on combined gust and maneuver data collected on aircraft very different from current and future transports, and are a representation of an idealized loading environment that would have been equivalent to the observed real life data on early aircraft. There is no guarantee that this equivalence holds after changes in such factors as size, speed, geometry, and the use of ACT. Moreover, modern structural design capability and the application of ACT load alleviation allows the strength of the structure to be tuned very closely to just meet the requirements, whereas earlier generations of transports carried a certain excess weight (and hence strength) because it was not possible at that time to control the design process so closely.

Modern gust load alleviation (GLA) systems are designed principally to moderate the effects of large gusts, thereby eliminating the danger of stress overloads. These systems generally have a threshold beyond which the GLA becomes activated. This threshold is necessary to prevent possible actuator and control-rod fatigue resulting from the small but frequent gust load occurrences. While the small gusts are not important from the point of view of overload, they may make a significant contribution to wing-root fatigue. This contribution may be amplified by the removal of the high gust loads (by the GLA system) that may actually be beneficial to fatigue life through crack growth retardation effects of occasional high loads.

Another problem associated with the interpretation of load alleviation is the relative safety implied by the excess margin from design load to ultimate load. This margin covers many unknowns and variabilities in all parts of the requirements and loading predictions. An apparent

degradation of safety arises when a load alleviation system is effective up to design limit load but saturates before reaching the ultimate load. With the system saturated, the loading gradient reverts to that of a passive aircraft, and the ultimate load is reached for a smaller increment of input gust or maneuver and hence, a smaller proportion of the design load than for an aircraft without ACT. More consideration should be given to the philosophy behind the application of these safety factors to aircraft with ACT.

5.4 Data Requirements

Regarding wind-tunnel testing, model programs are continually needed to calibrate analytical and design codes and to further investigate unusual flow phenomena and the subsequent loads on flight vehicle structures. Pressure fluctuations from flow separations are especially difficult to predict, but can be measured during wind-tunnel tests using rigid models. These measurements provide the driving force in aeroelastic response investigations. The motion-induced unsteady loads, which are important to dynamic response and flutter predictions, are strongly coupled to the separated flow. Currently there is no practical theoretical method to predict unsteady loads associated with separated flow.

Another consideration is the lack of available gust data. There have been a number of turbulence measurement investigations that involved fully-instrumented research aircraft and poorly-instrumented commercial aircraft. Collection of gust data on operational aircraft is the only way to obtain realistic samples of rare severe events that are comparable to the design gust severity. Advances in digital data collection and recording now permit the possibility of measuring turbulence or maneuver response data on operational aircraft, thereby providing a valuable and much needed database. For combat aircraft current turbulence models are sufficiently accurate for ride control studies. However, there are still some unanswered questions concerning the amplitude of turbulence to be encountered, especially as terrain following systems allow the aircraft to fly lower than ever before.

5.5 Design Philosophy

ACT has been used to improve aircraft performance in a rigid-body sense for many years. In the last 20 years significant advancements and applications in ACT towards the control of elastic modes have become quite evident. More recently the analog FCS has been replaced by digital systems. The DFCS offers many advantages over an analog system. These advantages include the capability to implement sophisticated control laws and redundancy-management methodologies, and cheaper and repeatable performance. However, as a result of some of these advantages, there has been a rapid growth in the application of DFCS/ACT highlighting the need for an assessment of the impact on aircraft design philosophy. Initially these benefits were largely seen in the ability to improve or rectify deficiencies in the aircraft structural or flight performance by changes in the DFCS rather than by more expensive structural changes. The logical extension back into the initial design phase of the aircraft suggests the need for reassessment of some of the traditional views regarding aircraft design. Some of the conservatism adopted in earlier military aircraft design philosophies may be in danger of erosion due to competing economic pressures.

The recent advent of DFCS in aircraft has opened the way for a major change in aircraft design philosophy incorporating ACT. The DFCS offers versatility at reasonable cost compared to the earlier analog systems. Increased application of ACT as a result of the benefits offered by the DFCS may be seen in each of the three main phases of the aircraft life. During the initial design ACT confers an advantage by way of reduction in required structural strength in such applications as gust and maneuver load alleviation. Following aircraft production DFCS/ACT offers new opportunities to overcome aircraft performance deficiencies that appear during flight testing or structural weaknesses that may become apparent during fatigue or other structural integrity testing. After the aircraft enters service, the search for increased performance, the desire for a change in role for the aircraft, or the need to overcome fatigue problems may all be aided by the application of ACT.

It is not unusual for the load spectra of military aircraft fleets (and some civil fleets) to change significantly over the life of the aircraft. For a fighter aircraft this can be as a result of increased pilot familiarization with the aircraft capability, development of new flying techniques or maneuvers, or a change in the role of the aircraft. The last reason may result from the tendency, particularly in recent times, for an aircraft to be required to undertake dual roles such as air combat and ground attack, or from development of new stores/weapons/roles in addition to those available when the aircraft entered service. The DFCS/ACT in modern aircraft will exacerbate this trend towards more severe flight spectra. In particular, the ability to provide carefree piloting by appropriate programming of the DFCS enables development of flying techniques that may have a high potential for aircraft overstress. It is expected that removing the need for the pilot to maintain a safety margin will lead inevitably to an increase of severity of the aircraft flight spectrum. Squadron pilots will most likely complete maneuvers at the envelope boundary more aggressively relying on the g-limiter to keep the vehicle safe. Furthermore, the inability to overstress the aircraft has emphasized the need to reassess the reasons behind the choice of aircraft limit load. Traditionally, there has been a factor (usually 1.5) relating service limit load and proof load. This factor has been assumed to take account of the probability of accidental overstress, variability of the mechanical properties of the aircraft materials and uncertainties in the calculation of flight loads, and the structural strength of the aircraft. The relative magnitudes of the contributions (to the factor of 1.5) are difficult to estimate. It would, therefore, be inadvisable to reduce the present safety factor

because of the introduction of the g-limiter, even if the overstress prevention system could not be overridden.

5.6 Design Rectification

The DFCS/ACT can be modified more readily during the flight-test phase than the structure could be changed after construction. This flexibility may be used to enhance handling or performance, usually to overcome deficiencies discovered during the tests, but carries structural implications. If gross changes to control surface utilization are made after the fatigue test has been completed, it becomes almost impossible to interpret the test results in terms of the new configuration. The static strength test could also be reduced in applicability. Another problem of ACT changes during the flight-test program is that structural load clearance must be repeated for the modified system. Given the characteristics of ACT for expanding the range of conditions for which critical loads may be encountered, this implies a considerable validation exercise.

Despite the recent advances in the capability to predict aeroservoelastic characteristics, there remains the possibility of instabilities caused by structural feedback to the control system. Checking for these requires lengthy ground tests of the complete aircraft. If a problem is encountered, then a costly rectification program may be required. Changes to the filter configuration in the control system or repositioning of ACT sensors will need to be evaluated and retested before the program can continue. Consequent changes to structural loads will also need to be checked.

5.7 Operational Considerations

The presence of an active control system can have a substantial influence on how a pilot flies his aircraft, which, in turn, can cause the true loading spectrum to diverge from that originally estimated by the designers. For example, after an automatic g-limiter was installed on an aircraft the number of acceleration exceedances at any given g-level per flight hour increased dramatically. As another example, an airline pilot who is flying with a nonfunctioning GLA system might be compelled to yield a wider berth to thunderstorms to avoid turbulence. For any given active control function the designer needs to assess not only how its addition will enhance performance but also how this addition will change the pilot's operational behavior. This involves a need for additional communication between the designers and operational personnel.

Another area of concern is that the performance of an ACT system must be maintained throughout the life of the aircraft. If the required performance and reliability that were predicted at the design stage are to be achieved, then the system must remain fully serviceable. Minimum dispatch conditions must be observed on every flight to ensure that the full probabilistic performance is followed and failure modes are analyzed for any undesirable departure from predictions. The actuators and controls are likely to require greater care and attention than on earlier aircraft, and the control freeplay may become particularly important. A large value of freeplay may degrade performance of the active system, decrease flutter stability, or introduce oscillatory loadings.

6. CONCLUSIONS

The conclusions resulting from this investigation are summarized as follows:

1) The capability to improve aircraft performance and/or to redistribute aerodynamic loads by reprogramming a DFCS is expected to be exploited when flight or fatigue testing reveals deficiencies from design specifications. As a result, the interpretation of the full-scale fatigue tests will become quite difficult.

2) The opportunity to optimize aircraft control systems for maximum performance throughout the flight envelope increases the number of flight conditions for which critical load cases may arise, thus increasing the task of structural clearance.

3) The potential for a DFCS to adversely affect aircraft fatigue is not being adequately considered or investigated by the aircraft manufacturers and users. In addition, there is very little ongoing research in the combined fields of structural dynamics, structural integrity, active controls, and aerodynamics. This lack of activity has caused solved control or acroelastic problems to reappear in the form of fatigue problems.

4) State-of-the-art analytical tools used in the case study were inadequate for predicting the absolute levels of loads on aircraft with active controls. Therefore, it was not possible to calculate stresses at critical locations with sufficient precision to make accurate predictions of aircraft fatigue life. The possibility of incorporating fatigue life as a parameter in any approach to aircraft design optimization is, therefore, precluded unless significant advancements in load prediction capability are first obtained.

5) The computer codes used in the case study were capable of calculating the change in load resulting from the change in the DFCS. Predictions corroborated the increase in the WRBM as experienced in flight. Therefore, it is possible to predict increments in loads thus permitting a quantitative assessment of the impact of DFCS changes on fatigue life.

6) The knowledge and understanding of the loads on transport aircraft, especially aircraft with GLA systems, is not well established. The same concern exists for military aircraft with other active control concepts. In particular, the lack of modern data on gusts is of concern. This is true for both the smaller magnitude gusts responsible for most fatigue damage and for severe gusts.

7. RECOMMENDATIONS

This paper highlighted the integration issues related to structural dynamics, aerodynamics, active controls, and structural integrity and provided evidence that suggests very little interaction between researchers in these fields. Since multidisciplinary cooperation will be a necessary step towards improving the designs and reducing the life-cycle costs of new aircraft, research activities dealing with multidisciplinary integration should be more aggressively pursued. Since increased interaction is needed between experts in these disciplines to narrow the gaps in knowledge and communication throughout the aerospace industry, continued workshops which stress the interaction and integration of key technical disciplines are recommended. Studies to develop and apply multidisciplinary technology and the exchange of key technical experts from different disciplines are also recommended to develop a common basis of terminology, equations, and tools.

The following are examples of specific technical disciplines requiring serious consideration for integration: 1) linear and nonlinear, steady and unsteady aerodynamic codes; 2) aerodynamic correction factor methodologies; 3) structural finite element modeling; 4) fatigue life prediction; 5) structural optimization; and 6) active control system modeling. As always, further activity is required in the areas of wind-tunnel testing for code validation, ground and flight testing for verification of multidisciplinary concepts, and flight measurement of gust and maneuver data and detailed analysis of operational usage data for improving structural integrity design methodologies.

8. REFERENCES

1. "Structural Integrity of Aeronautical Vehicles - Impact of Active Control Technology," TTCP Subgroup H HAG-6 Final Report, October 1989.

2. "Structural Integrity of Aeronautical Vehicles - Impact of Active Control Technology," TTCP Subgroup H HAG-6 Executive Summary, March 1990.

3. Peele, E. L. and Adams, W. M., "A Digital Program for Calculating the Interaction Between Flexible Structures, Unsteady Aerodynamics and Active Controls," NASA TM-80040, January 1979.

4. Winter, J. S., Corbin, M. J., and Murphy, L. M., "Description of TSIM2: A Software Package for Computer Aided Design of Flight-Control Systems," RAE Technical Report 83007, 1983.

5. McDonnell Douglas Engineering Memorandum 338-5141, Revision A, 24 November 1980.

6. Giesing, J., Kalman, T., and Rodden, W., "Subsonic Unsteady Aerodynamics for General Configurations, Part I, Direct Application of the Nonplanar Doublet-Lattice Method," AFFDL-TR-71-5 Volume I, November 1971.

7. Davies, D. E., "Theoretical Determination of Subsonic Oscillatory Airforce Coefficients," RAE Technical Report 76059, 1976.

8. Bisplinghoff, R. L.; and Ashley, H.: "Principles of Aeroelasticity," John Wiley, 1962.

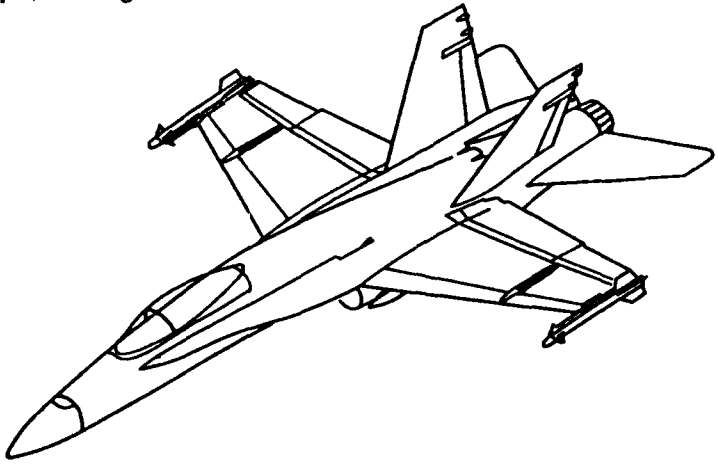

Fig.1.- Schematic of F/A-18 aircraft.

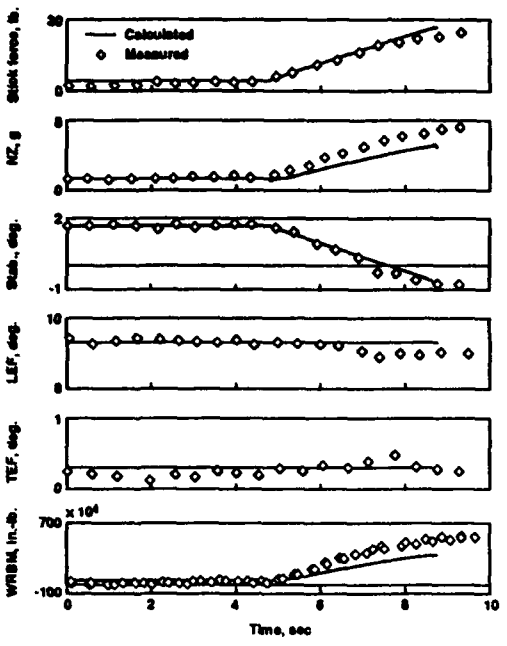

Fig. 2.- Comparison of measured and ISAC-calculated data for Flight 164, PROM V4.3.1.3.

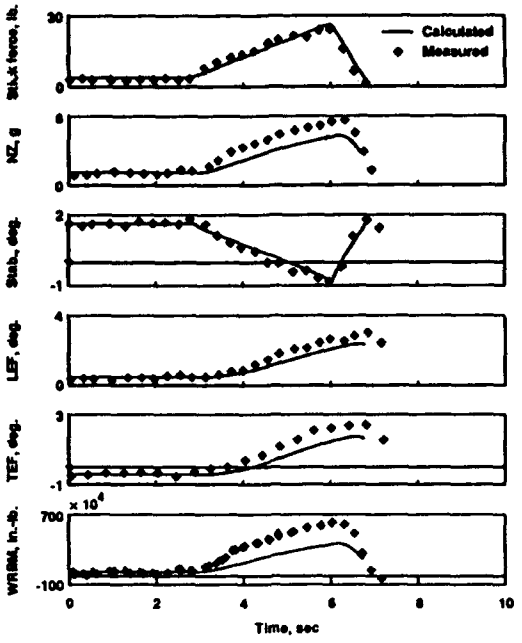

Fig. 3.- Comparison of measured and ISAC-calculated data for Flight 167, PROM V4.3.2.

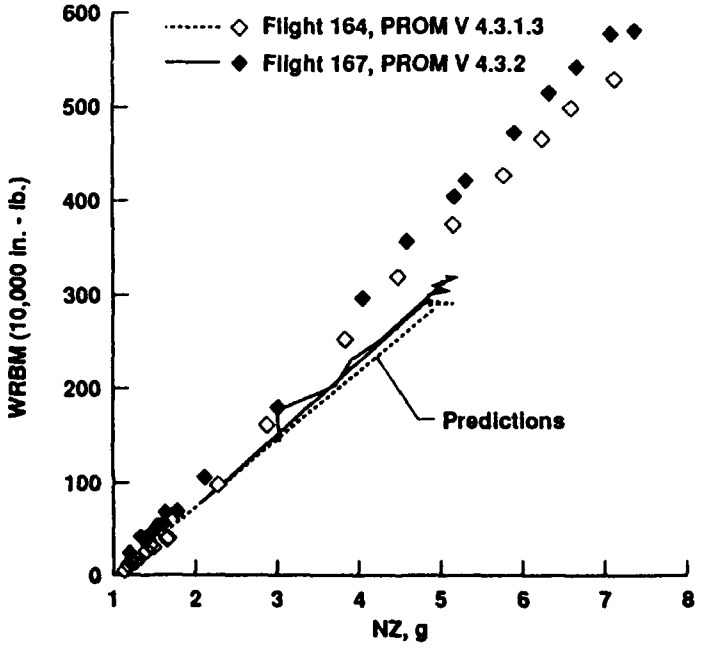

Fig. 4.- Comparison of measured and ISAC-calculated bending moment per g.

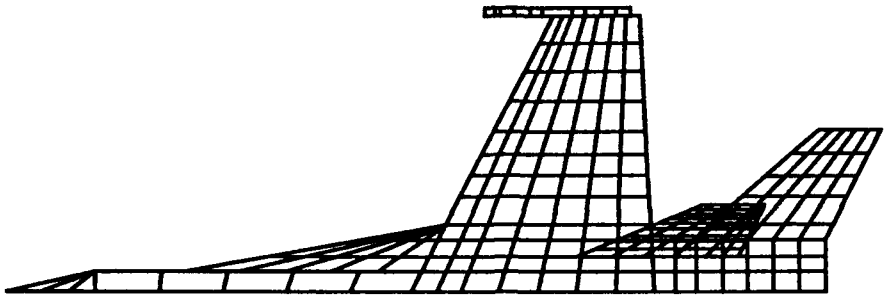

Fig. 5.- Aerodynamic box pattern.

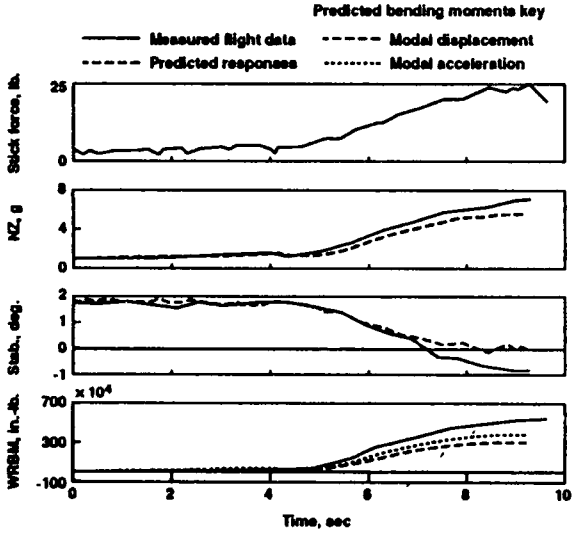

Fig. 6.- Comparison of measured and FLEX-SIM-calculated data for Flight 164, PROM, V4.3.1.3.

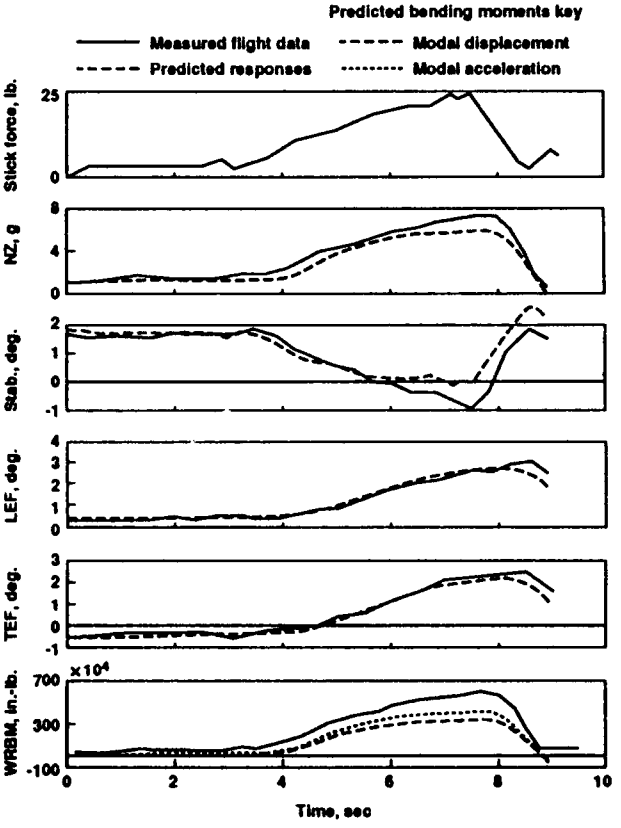

Fig. 7.- Comparison of measured and FLEX-SIM-calculated data for Flight 167, PROM, V4.3.2.

On Possible Applications of Smart Structures to Control of Space Systems

Work performed with the contribution of :
Ministero della Ricerca Scientifica e Tecnologica, Universita' di Roma, Italia
Alenia Spa, Roma, Italia
Istituto Studi e Applicazioni Scienze Aeronautiche Spaziali (I.S.Aer.S) Forli, Italia
Financial Support by Università di Roma, Grant No. 293/62

F.Betti[1] ,P.Gasbarri[1] ,P.Gaudenzi [1] ,F.Persiani [2] ,G.M.Saggiani[3] ,P.Santini [1]

Abstract

The general equations for a multi-body space system with internal control forces are written. Single body,or 'local' ,equations of motion are written and then they are transformed into global equations, associated with a sufficient number of 'internal' equations describing the relative motions of the various parts of the system. In such a transformation, quantities of twc orders of magnitude arise: the first group is associated with the Earth's equatorial radius, and the second group is associated with a characteristic length of the spacecraft. The two groups are separated in order to avoid round-off errors. Furthermore, a law of control associated with deformations of the connections between the elements of the system is introduced, in such a way that efficient control of instability phenomena may be possible. Numerical examples complete the work.

1 Introduction

Dynamic behaviour of a multi-body space system has received much attention in recent years. The great interest associated with the relevant analysis arises from the large number of possible applications to systems such as space stations, satellites with several flexible appendages, scientific instrumentation in orbit,etc.

From a merely dynamic point of view, the problem can be solved by considering the motion of each of the bodies as subjected to the Earth's gravitational field and to the forces exerted by the members connecting the bodies. A sufficient number of equations is thus obtained; it is however very difficult to treat them numerically since the internal forces are associated with the relative displacements between the bodies: the latter are in general small fractions of the length of the connections which, in turn, are small fractions of the Earth's equatorial radius (EER). Now, since the inertial coordinates of the bodies are of the order of EER, the task of obtaining internal forces from inertial coordinates is almost an impossible one, and the problem must be reformulated in such a way that the lengths of (or, better, the relative displacements in) the connections appear directly in the system.

Furthermore, it is known that bodies in orbit may suffer from problems of dynamic instability especially associated with rotational motions. Therefore several methods for

[1]Dipartimento Aerospaziale Università di Roma "La Sapienza" Via Eudossiana 18 - 00184 Rome, Italy
[2]Dipartimento delle Costruzioni Meccaniche Nucleari ed Aeronautiche Università di Bologna, Italy
[3]I.S.Aer.S. Forli

stabilization were deviced in the past, since the beginning of space era, and they need not to be recalled here. In a multi-body system, the single bodies which, on account of their geometry, position and attitude, might be unstable if isolated, can be stabilized through the stiffness of the connecting members, or vice-versa.

A step ahead is made if the connections are 'intelligent', so as to provide forces (but especially moments) depending on the relative rotations and displacements, capable of counteracting destabilizing effects.

The aim of this paper is to present some possibilities that can be helpful in solving the problem. Control moments and forces are obtained through piezo-electric devices which give actions proportional to the relative rotations and displacements and to their time-derivatives. This can be considered only as a possibility, since a deeper investigation should be conducted in order to ascertain whether such a possibility is viable or not from a technological point of view. The main aim, however, is not so much vibrations suppression, but essentially rigid motion instability suppression, as one can see from the numerical results contained in the paper.

2 General Equations for a Multi-body System

(a) The general layout of multi-body space system is described in Fig.1. Here we have a three-dimensional array of bodies, (*i*) each of them associated with a mass matrix and with a stiffness matrix, (*ii*) in general constituting a three-dimensional system, (*iii*) each of them connected to all the others by means of elastic or inelastic connections. In this paper, however, we will confine ourselves to a dynamic analysis for a simplified system, since the aim of the paper itself is to show possible applications of intelligent structures to control of such a system. We will describe our system as follows (see Fig.2):

(*i*) The N bodies B_j $(j = 1,...,N)$ are rigid;

(*ii*) Each of them is connected with one central body B_0 only, Fig.2;

(*iii*) the system is disposed on a two dimensional array;

(*iv*) the connections $\mathcal{T}_i$ between each of the N-bodies and B_0 consist of elements wich provide structural and control forces, depending upon the relative displacements, according to a prescribed rule.

(b) Let us write the translational equations of the system. For the *j.th* body we have:

$$M_j \frac{d^2 \mathrm{P}_j}{dt^2} = -\nu M_j \frac{\mathrm{P}_j}{D_j^3} + \mathrm{R}_j; \qquad (j = 1,...N)$$

$$M_0 \frac{d^2 \mathrm{P}_0}{dt^2} = -\nu M_0 \frac{\mathrm{P}_0}{D_0^3} - \sum_{j=1}^{N} \mathrm{R}_j \qquad (1)$$

where:

- P_j $(j = 0,...N)$ is the vector in the inertial space describing the position of the c.g. of B_j;
- ν = Earth's gravitational constant = $g_e R_e^2$;
- $D_j = |\dot{\mathrm{P}}_j|$, $(j = 0,\ldots,N)$;
- R_e = equatorial radius; g_e = gravity acceleration at R_e;
- R_j = reaction exerted by $\mathcal{T}_j$ on B_j, $(j = 1,\ldots,N)$;
- t = time;
- M_j = mass of the *j.th* body, $(j = 0,\ldots,N)$.

Theoretically, once the law of dependency of the R_j's from the relative displacements of the system is known, Eqs.(1), associated with the proper initial conditions, constitute a complete set which can be integrated numerically. The situation is not sc clear, however, since, in Eqs.(1), the R_j's, as said, must be computed from the relative displacements, which, in turn, depend on the P_j's which are of the order of magnitude of Earth equatorial radius (Fig.3).

In this paper R_j is the sum of structural reactions and of control forces. The former are expressed through the well known relationships connecting end-forces and end-moments with end-displacements and end-rotations in a beam-rod, f.i. The latter are associated with the control law as imposed to the system, see Art.4. This operation is practically very difficult to perform, on account of the high round-off errors associated with it, so big that they would destroy any possible result. So we must transform Eqs.(1).

(c) First of all, let us make Eqs.(1) nondimensional. For this purpose, we set:

$$P_j = p_j R_e; \quad t = \tau T; \quad T^2 = R_e^3/\nu = R_e/g_e$$

$$\epsilon_j = M_j/M; \quad (j = 0, \ldots, N); \quad M = \textit{total mass}$$

By summing up all Eqs.(1) we obtain the equation describing the motion of the instantaneous c.g. (which moves with respect to the system during the motion):

$$\frac{d^2 p_c}{d\tau^2} = -\sum_{j=0}^{N} \frac{p_j}{d_j^3}\epsilon_j \tag{2}$$

where:

$$p_c = \sum_{j=0}^{N} \epsilon_j p_j \tag{3}$$

and:

$$d_j = \frac{D_j}{R_e}; \quad (j = 0, \ldots, N) \tag{4}$$

It should be noted that the terms appearing in (2) are of the order of R_e^0.

Now we set:

$$\lambda q_j = (p_j - p_0); \qquad (j = 1, \ldots, N) \tag{5}$$

with $\lambda = l/R_e$, where l is a typical dimension of the system (e.g., the mean length of the connections).

Thus, from Eqs. (1) we have:

$$\lambda \frac{d^2 q_j}{d\tau^2} = -\left(\frac{p_j}{d_j^3} - \frac{p_0}{d_0^3}\right) + \left[\frac{R_j}{\epsilon_j} + \sum_{k=1}^{N} \frac{R_k}{\epsilon_0}\right] \frac{1}{M g_e} \tag{6}$$

Very simple algebra provides (App.A):

$$\lambda \frac{d^2 q_j}{d\tau^2} = -\lambda \left[I - 3\frac{p_0}{d_0}\frac{p_{0T}}{d_0}\right] \frac{q_j}{d_j^3} + \left[\frac{R_j}{\epsilon_j} + \sum_{k=1}^{N} \frac{R_k}{\epsilon_0}\right] \frac{1}{M g_e} \tag{7}$$

$$(I = \textit{unit matrix})$$

The reaction R_j appearing in (7) can be written in the form

$$R_j = (EA)_j r_j \tag{8}$$

The expressions for the nondimensional vectors r_j are found in App.B.

Let now:

$$(EA)_j = \omega_j^2 M_j L_j \tag{9}$$

so the quantity ω_j has the dimension and the meaning of a frequency (exactly, it is the axial frequency of the system consisting of a mass M_j and of stiffness $(EA)_j/L_j$). So Eq.(7) reads now:

$$\frac{d^2\mathrm{q}_j}{d\tau^2} = -\left[\mathrm{I} - 3\frac{\mathrm{p}_0}{d_0}\frac{\mathrm{p}_{0_T}}{d_0}\right]\frac{\mathrm{q}_j}{d_j^3} + \left[\sigma_j^2\mathrm{r}_j + \sum_{k=1}^{N}\frac{\sigma_k^2\epsilon_k\mathrm{r}_k}{\epsilon_0}\right]\frac{1}{\lambda}; \quad (j = 1,...N) \tag{10}$$

where $\sigma_k^2 = \omega_k^2 L_k/g_e$

The purpose of eliminating λ from the equation of motion has now been reached. As a matter of fact, λ is still appearing in the last term of Eq.(10): this is associated with the ratio of two different time scales (orbital and structural frequencies). Another version of Eq.(10) can be obtained by introducing a new nondimensional time $\theta = \tau/\sqrt{\lambda}$: in this case, as it is easy to see, the gravitational term (the first in r.h.s) becomes small as λ is decreasing, and the remaining two are of the same order of magnitude.

In other words,Eq.(10) is that of a space system, to which some elasticity is added: the other version would be an elastic system to which some 'space' is added.

(d) At this point it is also convenient to re-write Eq.(2) in a slightly different form. From Eqs.(5) and (3), we obtain:

$$\mathrm{p}_j = \mathrm{p}_c + \lambda\mathrm{q}_j^*; \quad (j = 0,\ldots,N) \tag{11}$$

where:

$$\mathrm{q}_j^* = \mathrm{q}_j - \sum_{k=1}^{N}\mathrm{q}_k\epsilon_k; \quad (j = 0,\ldots,N) \tag{12}$$

We write furthermore:

$$\frac{1}{d_j^3} = \frac{1}{d_c^3} + \frac{\lambda\zeta_j}{d_c^3} \tag{13}$$

where, from simple algebra, (App. A), we obtain:

$$\zeta_j = -\frac{2\mathrm{y}_{cT}\mathrm{q}_j^* + \lambda\mathrm{q}_{jT}^*\mathrm{q}_j^*}{d_j^2}\frac{d_j^2 + d_j d_c + d_c^2}{d_j(d_j + d_c)} \tag{14}$$

So Eq.(2) can be written in the quasi-keplerian form:

$$\frac{d^2\mathrm{p}_c}{d\tau^2} = -\frac{\mathrm{p}_c}{d_c^3} + \lambda\mathrm{H} \tag{15}$$

where the vector H is written:

$$\mathrm{H} = -\sum_{j=0}^{N}\frac{\zeta_j}{d_j^3}\mathrm{p}_j\epsilon_j \tag{16}$$

(e) The general equations of the problem are Eqs.(10)(15), containing the $N + 1$ unknown vectors p_c,y_j; $(j = 1,\ldots,N)$, with the relevant initial conditions.

3 Transformed Equations

(a) Eqs.(10) and the degrees of fredom (dof) associated with them are not adequate for the purpose of our analysis: therefore we shall now reformulate the problem in terms of new variables and new dof, and, consequently, of new equations of equilibrium.

Fig.4 represents the pair B_0B_j in the undeformed position, in an arbitrarily oriented reference system. Here L_{j*} denotes the length of the connection $\mathcal{T}_j$, and $L_{j*}\xi_{j0}$, $L_{j*}\xi_{j1}$ the lengths clearly defined in Fig.4; furthermore η_j is the angle between the principal axes of B_0, say $\mathcal{P}_0$, and the principal axes of B_j, say $\mathcal{P}_j$.

Fig.5 represents the pair (B_0, B_j) in the inertial space, and in the deformed position. Here we define $\mathcal{P}_R$, the intrinsic system at Q_0, the center of mass of B_0, and the angle $\beta \equiv (\mathcal{P}_R, \mathcal{P}_0)$: so the angle $(\mathcal{P}_0, \mathcal{P}_{in})$ (where $\mathcal{P}_{in}$ is the inertial reference system) is $(\beta + \omega_0)$, with $\omega_0 \equiv$ true anomaly at Q_0.

Consider now B_j; if the connection were rigid, the angular position of $\mathcal{P}_j$ would be $\beta + \omega_0 + \eta_j$; on account of the flexibility of the system, there is an additional displacement δ_j of the attachment. Finally, there is a rotation ϕ_j of $\mathcal{P}_j$ around Q_j, the center of mass of B_j.

So the angle of $\mathcal{T}_j$ (the connection), with the horizontal inertial axis will be:

$$\nu_j = \beta + \omega_0 + \eta_j + \psi_j$$

where $\psi_j = \delta_j / L_j$, if L_j is the distance Q_0Q_j.

Now we can represent the vector q_j, previously introduced, as:

$$\mathrm{q}_j \equiv [L_j \cos\nu_j; L_j \sin\nu_j] \tag{17}$$

with:

$$L_j = L_{j*}(1 + \xi_{j0} + \xi_{j1} + a_j)$$

where a_j is the unit elongation in $\mathcal{T}_j$.

Substitution into Eqs.(10) and algebraic manipulations lead finally to the equations:

$$\begin{cases} a_j'' = & (1 + \xi_{j0} + \xi_{j1}, \left(\nu'^2 - \frac{1}{d_j^3} - \frac{3}{d_j^3}\cos^2(\nu_j - \omega_0)\right) + \frac{1}{\lambda} r_{ja} \\ \nu_j'' = & -\frac{2a_j'}{(1+\xi_{j0}+\xi_{j1})} - \frac{3}{d_j^3}\sin(\nu_j - \alpha_j)\cos(\nu_j - \alpha_j) + \frac{1}{\lambda} r_{jt} \end{cases} \tag{18}$$

$$(j = 1, \ldots, N)$$

The expressions for the nondimensional forces r_{ja} and r_{jt} are given in Appendix B.

(b) If the bodies have finite dimensions, as it is always the case, we must also write the rotational equations for each of them. For the *k.th* body we have:

$$J_k \frac{d^2\nu_k}{dt^2} = G_k + C_k - (EA)_k r_{kt} L_{k*} \xi_{k1} l; \; ; \quad (k = 1, \ldots, N) \tag{19}$$

Here G_k is the gravitational torque expressed by:

$$G_k = -3\nu \frac{J_{kz} - J_{kx}}{D_j^3} \sin\zeta_k \cos\zeta_k; \quad (k = 1, \ldots, N) \tag{20}$$

where (i) ζ_k is the angle formed by the principal x-axis of B_k with the local vertical $\equiv \nu_k - \omega_k$; (ii) J_{xk}, J_{zk} are the principal inertial axes of B_k, expressed through nondimensional quantities as:

$$\begin{cases} J_{kx} = \epsilon_k M L_{k*}^2 \rho_{kx}^2 l^2 \\ J_{kz} = \epsilon_k M L_{k*}^2 \rho_{kz}^2 l^2 \end{cases} \tag{21}$$

Furthermore we can express the torque C_k exerted on B_k by $\mathcal{T}_k$ as:

$$C_k = (EA)_k L_{k*} m_k l \tag{22}$$

So the final formulation for Eqs.19 is:

$$\frac{d^2\nu_k}{d\tau^2} = -\frac{3\sin\zeta_k\cos\zeta_k}{d_k^3}\frac{\rho_{zk}^2 - \rho_{kx}^2}{\rho_{xk}^2 + \rho_{kz}^2} + \frac{\lambda\sigma^2(1/L_{k*})}{\rho_{kx}^2 + \rho_{kz}^2}(m_k - \xi_{ki} r_{kt}); \quad k = 1, \ldots, N \tag{23}$$

As said before, it is understood that m_k and r_{kt} will also include controls.

(c) Instead of writing a specific rotational equation for the body B_0, it is convenient to stipulate conservation of the sum of total angular momentum and of the gravitational torques acting on the center of mass of the complete system because in this way internal reactions do not appear. We obtain the following rather lengthy expression

$$\begin{aligned} &\sum_{i=1}^{N}\sum_{j=1}^{N} \epsilon_i\epsilon_j L_j \left[(L_J'' - L_j\nu_j'^2)\cos(\nu_i - \nu_j) + (L_i\nu_i'' + 2\nu_i' L_i')\cos(\nu_i - \nu_j)\right] + \\ &+ \sum_{k=0}^{N} \epsilon_k \left[(\rho_{kx}^2 + \rho_{kz}^2) + L_k^2\right]\nu_k'' + \sum_{k=0}^{N} \epsilon_k(\rho_{kx}^2 - \rho_{kz}^2)\frac{\sin\zeta_k\cos\zeta_k}{d_k^3} + \\ &+ \sum_{k=0}^{N} \frac{\epsilon_k\zeta_k}{d_c^3}(z_c f_{kx}^* - x_c f_{kz}^*) = 0 \end{aligned} \tag{24}$$

(d) To summarize, the system is ruled by Eqs.(15),(18),(23),(24); there is no difficulty in writing it in the normal form:

$$V' = F(V;\tau) \tag{25}$$

(where V is full state vector of the dof and their first derivaties) with the relevant initial conditions, prescribing the value of V for $\tau = 0$.

4 Preliminary Investigation on Control

For systems such as the one described in the previous sections of this paper, the problem of the control of the dynamic response is a formidable task to be performed. In fact, the governing equations for the multibody system are coupled and fully non linear. Instabilities may occur due to interactions between the elastic and rigid body motion also for motions that are stable in the rigid body configuration, or vice-versa.

In order to design an appropriate control, accurate performance specifications should be given. Here we merely confine our study to a very simple preliminary approach, assuming that our performance specifications is just to drive the system to a reference configurations or to perform a limited amplitude motion. Recent advances in intelligent materials and structures can be exploited in order to actually exert control actions. From this viewpoint, flexible links between the ancillary bodies and the central one might consist, f.i., of an intelligent structure such as an adaptive truss. In such a structure, an active module capable of producing a bending moment or an axial force to the bodies to which it is connected can be designed by means of active members such as shown in Fig.6. In order to design a control system able to take advantage

of this technology the control must be designed by using only moments and/or forces applicated to each body. A system of sensors which is capable to detect the rotations and the rate of rotations of each body is also assumed to be available. Thus, we will assume, in the following, to have control laws of the type:

$$r_j = \alpha_{j0} Q_j + \alpha_{j1} Q'_j \tag{26}$$

$$m_j = \beta_{j0} Q_j + \beta_{j1} Q'_j \tag{27}$$

where the constants (or matrices) α_j,β_j must be determinated throughout the use of a system like the one described in Fig.6, and Q_j is the quantity (or the quantities) to be controlled.

5 Numerical Examples

(A) In the first group of examples we consider two mass pionts connected in one of the following four modes:

(i) no connection at all

(ii) connection by means of a cable

(iii) connection by means of rod

(iv) connection by means of a smart cable.

For all cases we have the following initial conditions:

(a) for the body B_0 we have initial conditions corresponding to a circular orbit of radius $r_0 = 1.1 R_e$, at true anomaly ω_{i0};

(b) for the body B_j we have initial conditions corresponding to perigee$= 1.079 R_e$, and eccentricity 0.04. The value of ω_{i0} is chosen in such a way that, when the bodies are free, they collide at the intersection (corresponding to true anomaly$= \pi/3$). Here we have $\epsilon_0 = \epsilon_1 = 0.5$.

Fig.8 provides the orbits of the two masses for the case (i) (note that, for reasons associated with graphics difficulties, the scales on the two axes are not the same). Fig.9 represents the ratio L/L_0 (L = actual distance between the two bodies; L_0 = initial distance) vs. nondimensional time τ. The same results are shown in Fig.10 for several orbits after collision. It is clear that we assume that the collision has no effect on the subsequent motion. For the case under (ii) we have similar results plotted in Figs.11 and 12. As far as Fig.12 is concerned we must note that, on account of the reduced sampling, the distance seems not to be able to reach the zero-values, as it actually does. Then, we had to adjust curve in the vicinity of the first zero-value.

For the case *(iii)* we first consider a rod having an axial frequency of $1 Hz$. The trajectories are shown in Fig.13, and the relative unit displacement in Fig. 14. We note that the nondimensional time plotted here is $\tau' = \tau \sqrt{R_e/g_e}(2\pi f)\sqrt{\epsilon_0 \epsilon_1}$, and the time interval represented is just a small fraction of the orbital period. This case corresponds to a very large ratio *structural frequency/orbital frequency*, and for this reason, gravity terms are comparably very small, so the quantity represented in Fig.14 is practically the same as in the free vibration of the rod. The situation is different if we consider much weaker structures, as in the case of Fig.15, corresponding to a frequency of $1/1000$ Hz, close to the orbital frequency. Obviously such low values of the structural frequencies are unrealistic.

Finally Fig.16 and Fig.17, describe the case (iv), in which the masses are connected by the means of a smart cable; here we assume $\alpha_{j0} = k\omega_j$, $\beta_{j0} = \beta_{j1} = \alpha_{j1} = 0$, where

ω_j is the frequency of the rod having the same axial stiffness of the cable in tension, and k is a factor so that the stiffness is k^2 smaller when we pass from the active cable phases ($L/L_0 > 1$) to the unactive phases.

The reaction is provided here through smart materials (piezoelectric, shape memory alloys) which are capable of exciting axial forces. Obviously, the ratio of the amplitudes in the two phases is a function of k. It should be noted that in the above described motion, attitude is uncontrolled.

(B) In the second group of examples, we have, see Fig.18, a central body B_0 consisting of two equal masses connected by a rigid bar, the other body, B_1, is constituited by a mass attached to a rigid bar, hinged at the point C_0 to the central body. This configuration can be seen as a first draft of a space station (B_0), with a targeting appendage (B_1).

We may use the general equations of the text setting the slenderness of the bar $S_1 = 0$. The inertial radius of the central body is assumed to be ten times larger then the one of the appendage: $\rho_{x0} = 5$, $\rho_{x1} = 0.5$ and $\rho_{z0} = \rho_{z1} = 0$ while the dimensionless masses are $\epsilon_0 = \epsilon_1 = 0.5$.

The initial conditions for C_0 are: $r_i = 1.1\,R_e$, $\omega_i = 0$, $\nu_{i0} = 0.1$rad, $\nu_{i1} = \nu_{i0} + \pi/2$. The initial velocity is choosen in such a way that the point C_0 would describe an elliptic orbit of perigee$\equiv r_i$ and eccentricity$\equiv 0.02$ if it were a point-mass.

The initial configuration of the system is choosen in such a way that while the central body is in a stable position, the appendage is in an unstable one, so that in the absence of any control action it experiences large rotation with respect to the central body. This situation is shown in Fig.19, where the time history of the attitude of the two bodies with respect to the vertical in C_0 ($\nu_0 - \omega_0$ and $\nu_1 - \omega_0$) is plotted. Note that while B_0 undergoes small rotations in the neighbourhood of the stable position ($\nu_{0i} > (\nu_0 - \omega_0) > -\nu_{0i}$); B_1 rotates in the range $3\pi/2 > (\nu_1 - \omega_0) > \pi/2$. Fig.20 represents the time history of the relative angle between the two bodies referred to the initial one: $(\nu_1 - \nu_0) - (\nu_1 - \nu_0)_i$. Fig.21 shows the trajectory that the point C_0 describe in an inertial frame of reference, whose origin coincide with the position $\tilde{C}_0$ on the keplerian orbit that the hinge would describe, based on the initial conditions, if it were a point-mass.

To stabilize the body B_1 an internal control moment is exerhted at the hinge. We assume for the control moment the law of Eq.(27) with $Q_1 = (\nu_1 - \nu_0) - (\nu_1 - \nu_0)_i$, and $\beta_{10} = 100$, $\beta_{11} = 1$. Fig.22 shows the time history of the angles $(\nu_j - \omega_0)$ for the two bodies when the aforementioned control law is applied. Comparison with Fig.19 shows the ability of the proposed control law in stabilizing the motion of the appendage. The relative rotation of the two bodies referred to their initial angle $(\nu_1 - \nu_0) - (\nu_1 - \nu_0)_i$, is plotted in Fig.23.

In both Figs.22 and 23 the periodic variation of the amplitudes is associated with the orbital period; in fact the gravitational torque act on the system as a periodic forcing action whose period is equal to the orbital period. Fig.24 shows the trajectory of the point C_0 in the inertial reference frame with the origin in $\tilde{C}_0$.

A Appendix A

In Eq.(6), let :

$$\mathrm{T}_j = \frac{\mathrm{p}_j}{d_j^3} - \frac{\mathrm{p}_0}{d_0^3} = \frac{\mathrm{p}_0 + \lambda \mathrm{q}_j}{d_j^3} - \frac{\mathrm{p}_j}{d_0^3} = \lambda \frac{\mathrm{q}_j}{d_j^3} + \mathrm{p}_0 \left[\frac{1}{d_j^3} - \frac{1}{d_0^3} \right] \tag{28}$$

But: $d_j^2 = \mathrm{p}_{j_T} \mathrm{p}_j = \mathrm{p}_{0_T} \mathrm{p}_0 + 2\lambda \mathrm{p}_{0_T} \mathrm{q}_j$ if quantities of the order of λ^2 are neglected. So now:

$$\mathrm{T}_j = \lambda \frac{\mathrm{q}_j}{d_j^3} + \frac{\mathrm{p}_0}{d_0} \frac{-2\lambda \mathrm{p}_{0_T} \mathrm{q}_j}{d_0} \frac{1 + (d_j/d_0) + (d_j/d_0)^2}{1 + d_0/d_j} \frac{1}{d_j^3} \tag{29}$$

The last factor of Eq.(29) is equal to 3/2, apart from small quantities of the order of λ. So we have:

$$T_j = \lambda \left[I - 3\frac{p_0}{d_0}\frac{p_{0T}}{d_0} \right] \frac{q_j}{d_j^3} \tag{30}$$

where I = *unit matrix*.

B Appendix B

For a beam, with the positive signes as indicated in Fig.7, we have the following relationships between end-quantities:

$$\begin{aligned}
M_0 &= \frac{EI}{L}\left[-6\frac{w_1 - w_0}{L} - 4\theta_0 - 2\theta_1\right] \\
M_1 &= \frac{EI}{L}\left[-6\frac{w_1 - w_0}{L} + 2\theta_0 + 4\theta_1\right] \\
V_0 &= \frac{EI}{L}\left[-12\frac{w_1 - w_0}{L} + 6\theta_0 + 6\theta_1\right] \\
V_1 &= V_0 \\
N_0 &= \frac{EA}{L}(u_1 - u_0) \\
N_1 &= N_0
\end{aligned}$$

for the *j.th* we have:

$$\begin{aligned}
m_{0j} &= \frac{M_0}{(EA)_j L_{j*}} = S^2\left[6(\psi_j - \phi_j\xi_{j1} - 2\phi_j\right] \\
m_{1j} &= \frac{M_1}{(EA)_j L_{j*}} = S^2\left[-6(\psi_j - \phi_j\xi_{j1} + 4\phi_j\right] \\
v_{0j} &= \frac{V_0}{(EA)_j} = S^2\left[-12(\psi_j - \phi_j\xi_{j1} + 6\phi_j\right] \\
v_{1j} &= v_0 \\
n_{0j} &= \frac{N_0}{(EA)_j} = a_j \\
n_{1j} &= n_0
\end{aligned}$$

where S = slenderness ratio for $\mathcal{T}_j$.

By considering the orientations taken as positive, we will have:

$$\begin{aligned}
r_{mj} &= -6(\psi_j - \phi_j\xi_{j1} + 4\phi_j) \\
r_{tj} &= -12(\psi_j - \phi_j\xi_{j1} + 4\phi_j) \\
r_{aj} &= -a_j
\end{aligned}$$

From r_{mj},r_{tj},r_{aj}, the forces r_j in the inertial system can be easily computed.

References

[1] P.SANTINI, "Stability of flexible spacecraft", Acta Astronautica, Vol.3, pp.685-713, 1976.

[2] B.K.WADA, J.L.FANSON, F.F.CRAWLEY, "Adaptive structures". In B.K.Wada editor adaptive structures, pp.1-8,New York 1989,ASME

[3] P.SANTINI "On Some Stabilty Problems In Spaceflight Mechanics". Paper presented at the Seminar Mathematical Methods In Aerospace Problems,Erice, Italy 1991

[4] P.SANTINI, P.GASBARRI, R.BENEDETTI, "Motion of A Satellite In An Elliptic Orbit". Published on Complexity in Physics and Thechnology, Ed. M.Garrido Lisbona,1992.

[5] GUPTA,N.K., LYONS,M.G., AUBURN,J-N., MARGULIES,G., "Modelling, Control and System Identification Methods for Flexible Structures", *AGARDograph*, No.260, 1981.

[6] CRAWLEY,E.F., DE LUIS,J., "Use of Piezoelettric Actuators as Elements of Intelligent Structures", *AIAA Journal*, 1987, Vol.25, No.10, pp.221-230.

[7] ROGERS,C.A. , "Intelligent Material Systems - The Dawn of a New Material Age", 1992.

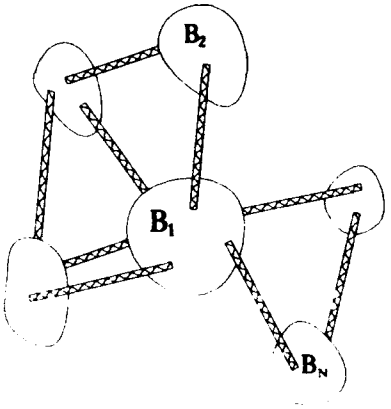

Figure 1: General layout of multi-body space system

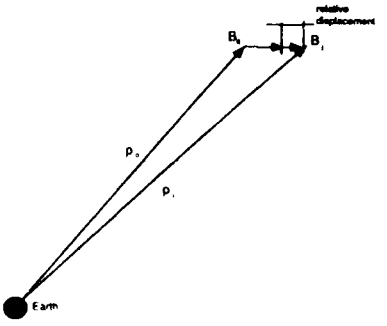

Figure 3: Order of magnitude of geometrical parameters

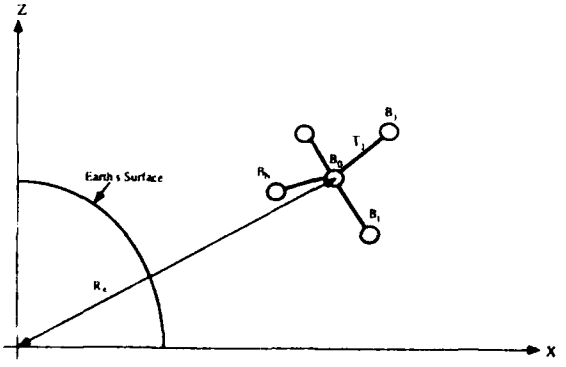

Figure 2: Multibody system investigated in the paper

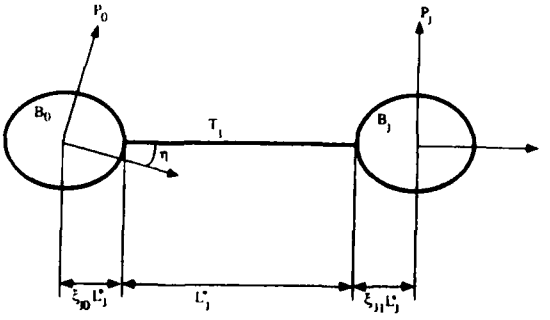

Figure 4: Representation of the generic pair B_0 and B_j in the undeformed position

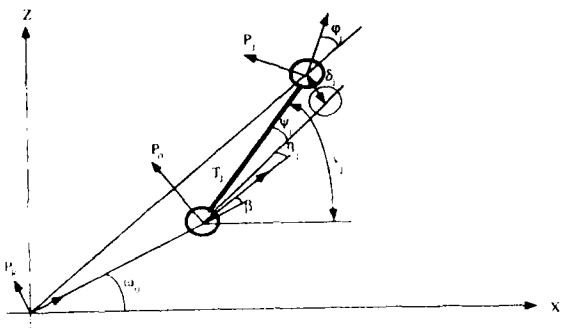

Figure 5: Definition of angles of rotation for the pair B_0 and B_j in the deformed position

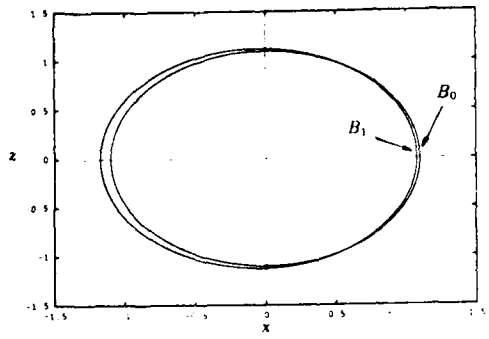

Figure 8: Trajectories of the unconnected masses: $m_0 = m_1, \lambda = 2/100$, intial distance $= 1.2 \cdot 10^5 m$, (a) circular orbit: $r_0 = 1.1Re$, $\omega_0 = 0.036rad$, (b) elliptic orbit: $perigee = 1.079Re$, $\omega_1 = 0.rad$

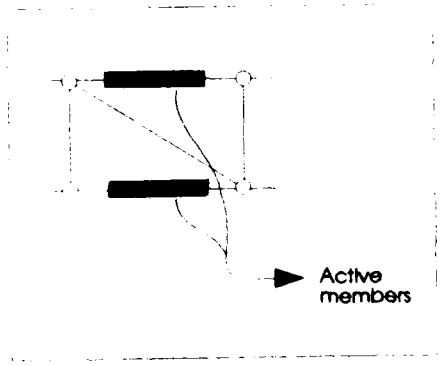

Figure 6: Example of an active module

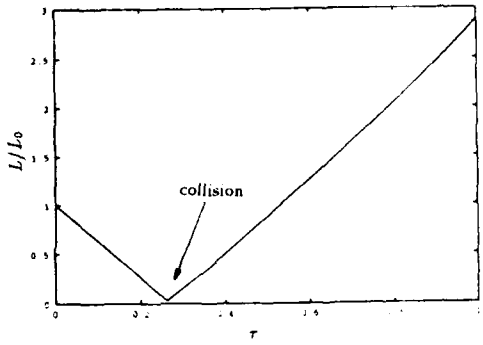

Figure 9: Same initial conditions as Fig.8, unconnected masses. Time history of the dimensionless distance between the masses.

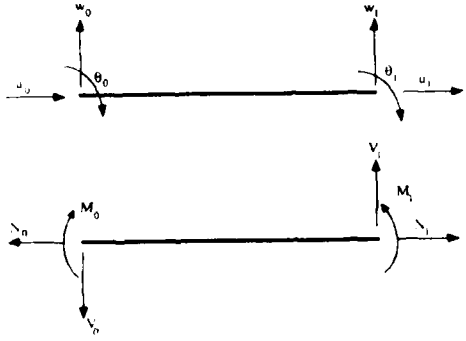

Figure 7: Conventions on the positive signes for the end-quantities in the connections.

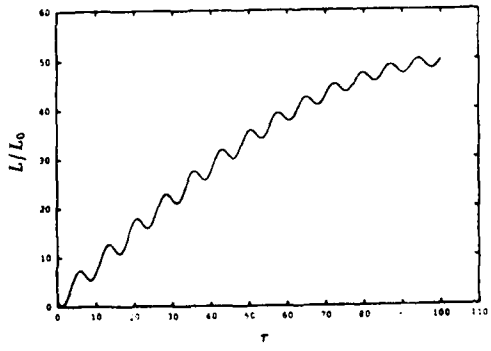

Figure 10: Same as Fig.9 for several orbits.

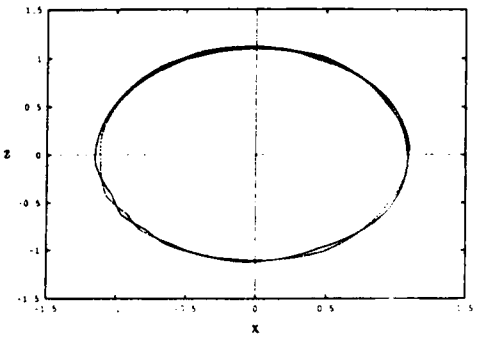

Figure 11: Same initial conditions as Fig.8, masses connected by a cable. Trajectories of the two masses.

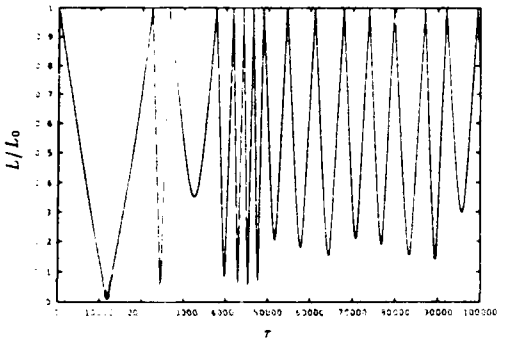

Figure 12: Same initial conditions as Fig.8, masses connected by a cable. Time history of the dimensionless distance between the masses.

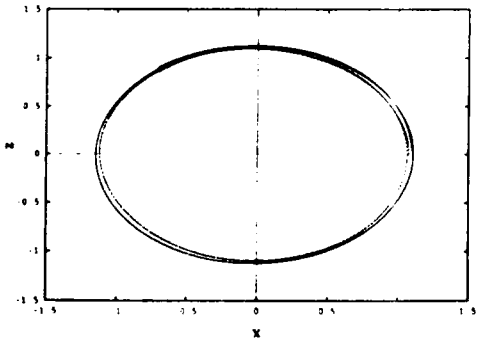

Figure 13: Same initial conditions as Fig.8, masses connected by a rod. Trajectories of the two masses.

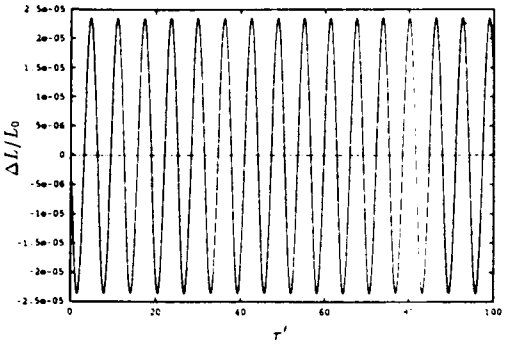

Figure 14: Same initial conditions as Fig.8, masses connected by a rod. Time history of the unit displacements $\Delta L/L_0$. Natural frequency=$1Hz$

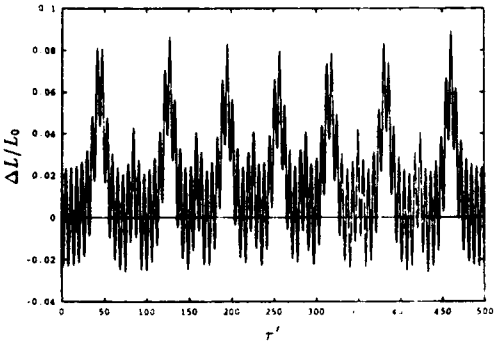

Figure 15: Same initial conditions as Fig.8, masses connected by a rod. Time history of the unit displacements $\Delta L/L_0$. Natural frequency=$1/1000Hz$

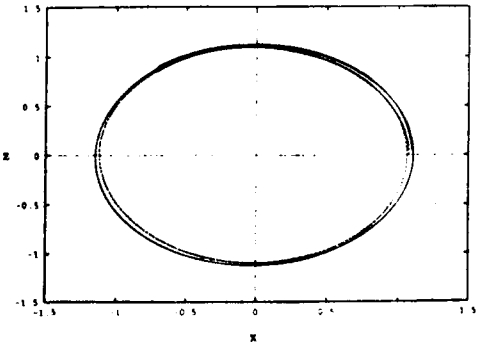

Figure 16: Same initial conditions as Fig.8, masses connected by the smart cable (k =1/10). Trajectories of the two masses.

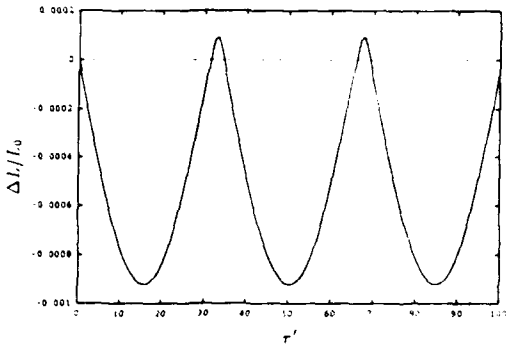

Figure 17: Same initial conditions as Fig.8, masses connected by the smart cable. Time history of the relative displacement $\Delta L/L_0$

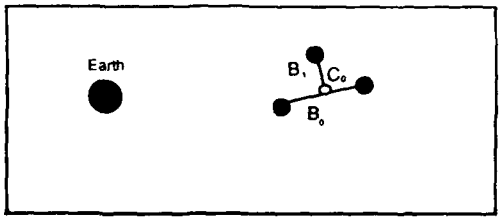

Figure 18: Initial configuration and velocity of the two bodies system

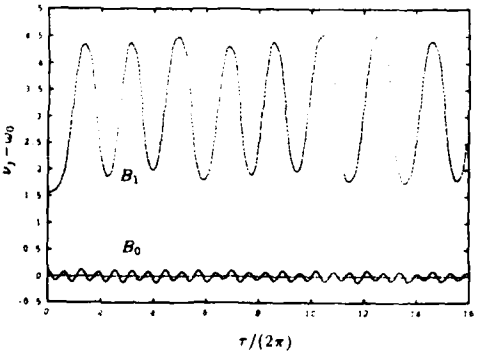

Figure 19: Attidude of the two bodies with respect to the hinge local vertical (no control)

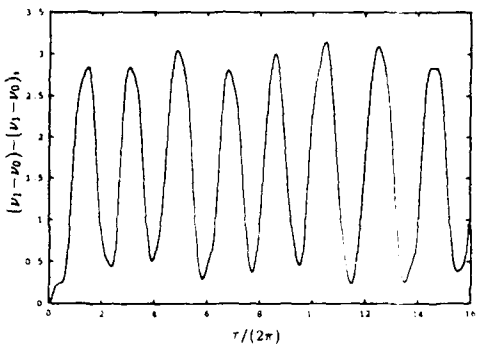

Figure 20: Relative rotation of the two bodies referred to their initial angle (no control)

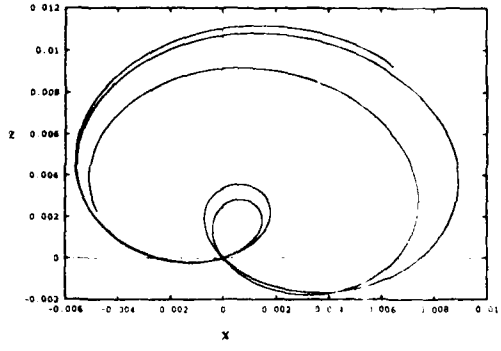

Figure 21: Trajectory of the hinge as seen from the keplerian orbit (no control)

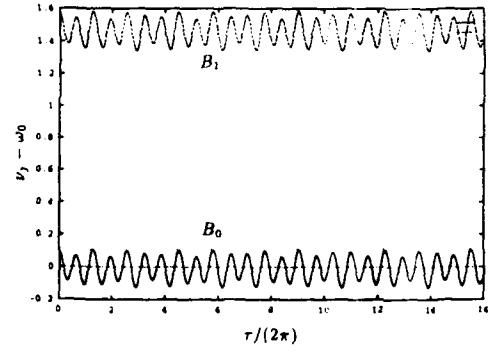

Figure 22: Attidude of the two bodies with respect to the hinge local vertical (with control)

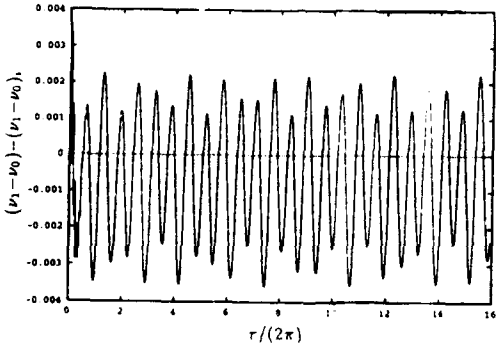

Figure 23: Relative rotation of the two bodies referred to their initial angle (with control)

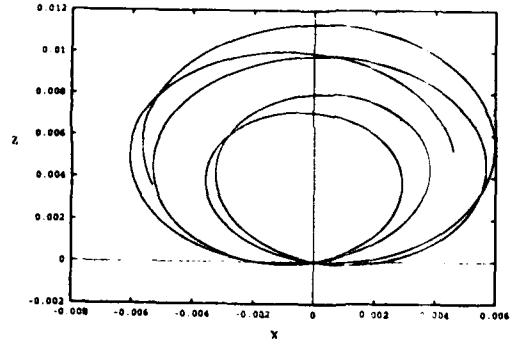

Figure 24: Trajectory of the hinge as seen from the keplerian orbit (with control)

AIRCRAFT SMART STRUCTURES RESEARCH IN THE USAF WRIGHT LABORATORY

Lt. Gregory S. Agnes* **and Capt. Kevin Silva****
Structures Division, Wright Laboratory

1. SUMMARY

For several years, the Air Force Wright Laboratory has been investigating smart structures technologies. Smart structures incorporate active materials into structural components. Active materials either sense their environment or change in response to an external stimulus or both, and also should be able to carry loads. A smart structure is thus capable of sensing and/or reacting to its environment. Smart structures research at Wright Laboratory has mainly concentrated on aircraft sensory structures and multi-functional structures, such as integrated antennae (i.e., smart skins). Several major programs have been initiated to apply and demonstrate these technologies. Recently, the ability of active materials (piezoceramics, for example) to control aircraft structures for improved performance and longevity, has received attention as well. In this paper, the smart structures technologies are categorized as sensory, active, or multi-functional. The current state of the art for each area, and programs aimed at exploiting smart technologies for aircraft applications, are described. Gaps in the current technology are identified.

2. INTRODUCTION

The incorporation of active materials into airframe structure will improve performance and reduce life cycle cost. The active materials can serve as sensors, structural actuators, or elements that both sense and react. Smart systems are being developed that incorporate these elements into the airframe, and integrate them into advanced neural networks and expert systems. The following discussion of anticipated payoffs should explain the reasons for the interest in this technology.

Smart structures technologies blur the lines between the currently very distinct functional disciplines in aircraft design and manufacture of structure, actuators, control systems, and sensors. The integration of active sensing and actuating elements into load bearing structure is the focus of this paper. The specific categories of smart structures that are addressed are sensory structures; multi-functional structures, or structures that integrate historically non-structures-related functions (load-bearing antennae functioning as stressed skin, for example); and active structures. For each category, the current state of the art is discussed, followed by the potential areas where smart structures technologies can improve airframe capabilities. Potential applications and current research efforts are also presented.

3. SENSORY STRUCTURES

Weight is a key factor in the design of high performance aircraft, whether the measure of performance is payload, range, or sustained maneuver load level. Weight reduction and safety assurance usually drive contradictory design goals: a margin of structural safety adds unusable strength and weight. To obtain a reasonable level of performance while ensuring flight safety, the US Air Force conducts an Aircraft Structural Integrity Program that provides design and operational inspection guidelines. These guidelines rely on the predictable accumulation of structural damage in response to measurable flight environments, to detect and repair flaws before they become catastrophic. The margin of safety ensures that the damage accumulates at a slow enough rate to not become catastrophic between inspections, and allows for inaccuracies in load and environment predictions. The weight penalty paid for flight safety represents untapped performance potential. Real-time structural integrity monitoring capability would allow the pilot full use of the airframe, with any dangerous level of damage accumulation immediately known, and without performance degradation from excess weight. Thus the incorporation of sensors for real-time health monitoring will allow higher performance for a given airframe weight, or lower weight for a given level of performance.

While development costs of a sensory structure will be more than for conventional structure, life cycle costs will be reduced. Real-time health monitoring will prevent loss of aircraft due to unanticipated rates of damage accumulation between inspection and maintenance cycles. Maintenance actions will be more efficient when a smart system alerts technicians to potential damage areas and conditions. Parts which are currently retired based on having been exposed to an analytical lifetime of structural loading will not have to be discarded until they exhibit threshold levels of damage accumulation, if integrated into a structural integrity health monitoring system. These sources of savings must offset the expense of the added complexity of building and maintaining a smart structure, to ensure a net benefit.

* Structural Dynamics Branch, WL/FIBGC, WPAFB OH 45433, USA, TEL:(513)255.5236x408, FAX: (513) 255-6684

** Advanced Composites ADPO, WL/FIBAC, WPAFB OH 45433, USA, TEL:(513)255-6639, FAX: (513)255-3740

The integration of sensors and associated signal and data processing electronics into structural elements produces sensory structures. Typically, such structures are investigated for their ability to monitor their own structural integrity. Additional system engineering would also permit incorporation of sensory structures into guidance and control systems, as a farther term goal.

3.1 Current State of the Art

To allow improved structural efficiency without compromising flight safety, military aircraft incorporate fatigue life tracking systems. Initially, these systems used counting accelerometers, to track load exceedences for later structural fatigue analysis. The data gathered is appropriate for metal structures that suffer fatigue damage from the numerous low stress cycles. This method requires accurate structural analysis to correctly predict remaining life, leading to constant checking and updating the structural model to increase fidelity and correlation with actual responses and damage. The application of strain gages to collect in-flight data solved problems in translating load levels to material stresses and strains, by allowing direct measurement of structural response to the flight environment. Such data is also more appropriate for composite structures, since they are less sensitive than metal structures to the accumulation of low stress level cycles, but are instead sensitive to the occasional high strain events.[1] This and the fact that composite structures are designed to strain criteria, makes direct strain sensing desirable. This data is collected in flight and stored on the aircraft, and later reduced and analyzed on the ground, to track structural life. Maintenance organization engineering and analysis departments note that the lag time between flight data acquisition and subsequent data reduction is typically several months, during which time the aircraft continues to fly with predicted but unverified structural integrity.

3.2 Potential Smart Structures Technologies

Advanced sensing and data processing technologies provide the capability for real-time structurally integrated health monitoring. Strain and acceleration sensor alternatives to accelerometers and foil strain gages have been developed. The undesirable weight added by foil strain gages and associated electronics, the fragility of leads, and the weight of accelerometers and associated electronics are seen as areas for improvement. The ability of optical fibers to accurately measure local and distributed strain fields is now well known, as is their utility in acoustic and temperature sensing. Acoustic emissions sensors are useful for detecting events, but other techniques must also be used to determine the condition of the structure. Piezoelectric elements can be used as sensors, actuators, or both. The low ultimate strain capability of piezoceramics (about 2000 microstrain[2]) limits their utility in structural embedment applications designed for strain levels of 4000 - 6000 microstrain, where other sensor types would be used. The built-up nature of composite structures, and the dimensions of some sensors (optical fiber diameter is on the order of the thickness of one ply of reinforced resin) makes sensor embedment an option. This offers protection to the sensor, but creates signal ingress/egress challenges.

The Wright Laboratory demonstrated the ability of an optical fiber strain sensor employing time domain reflectometry to track strain on a F-15 fighter wing undergoing fatigue test. A resolution of ± 40 microstrain was measured, but this system required up to two seconds to acquire a data point. The acquisition time depended on system signal-to-noise ratio and pulse repetition rate. This would be accurate enough for monitoring the health of a structure designed to 4000 microstrain, but speed probably would have to be increased to support real-time monitoring in flight, or short duration high strain cycles might be missed.

Current logical technology developments offers alternatives to the technique of storing flight data for later ground analysis. Automating the structural health monitoring function will enable higher performance if tied into the flight control system, and also will reduce the occasional structural failure and loss of aircraft due to unexpected flaw growth during the lag time between data collection and reduction. Current efforts are applying expert-based systems and artificial neural networks (ANNs) to evaluate damage events and structural condition. Expert systems rely on learning both healthy and degraded structural acoustic, strain, optical, temperature, or other responses, to forcing inputs. Anomalous response can be either identified as specific damage, or if not identifiable, can flag the pilot to reduce flight load severity, and alert the maintenance technician to investigate. ANNs are being investigated for processing the multitude of sensor outputs to deduce structural condition. Test aircraft are already instrumented with more strain gages than can be recorded for later analysis, so advanced data handling methods are needed even with current sensing technology. The number of sensing channels envisioned for even a near term health monitored structure will overwhelm fighter-aircraft-sized modern computer processors, unless some interpretation is automated. The weighting and voting activities implemented in ANNs will reduce an unwieldy number of sensor inputs to a manageable number of structural response signals for structural integrity evaluation in real time. Wright Laboratory research has noted a strong sensitivity to minor variations in ANN interconnections and nesting of nodes, though, significantly affecting system convergence at the threshold of damage detection and requiring serious attention when laying out a network.[3] In addition, the

capability of ANNs to infer possible damage, in response to new inputs it has not been trained specifically to recognize, is important for detecting and notifying the pilot or maintenance technician about probable trouble when unanticipated damage occurs.

3.3 Applications/Current Research Efforts

Wright Laboratory has investigated several of the aspects of a smart health monitoring composite structure, including the fiber optic strain sensing and ANN studies discussed in the previous paragraphs. Under the ongoing Smart Structures Concept Requirements Definition effort, a conceptual design for a smart structure system is being defined, and the technology requirements for the system will be investigated. This program is also funded in part by the US Navy, and will culminate with a laboratory demonstration structure to verify the feasibility of the selected concept. Wright Laboratory is planning to initiate several smart health monitoring system applications developments, as will be discussed in the next section. The operational capability of one expert-based smart system concept has been proven in flight on a de Havilland turboprop wing.[4] In this research, key features of the signal from piezoelectric sensors were stored instead of the actual sensor output, to reduce data storage and throughput requirements. The system was trained to recognize modal response to structural deviations consisting of loosened screws (to simulate missing rivets or a crack), which mostly affected the higher dynamic modes (17th and greater). The system then correctly located and identified this induced "damage" in flight, and also demonstrated the ability to measure ice buildup. It was noted, however, that since the response deviation was greatest at the higher modes, and the flight-induced ambient excitation was at lower modes, the structure had to be actively interrogated at the high modes to identify the damage. System optimization at modes correlating to ambient excitations would eliminate the need for periodic interrogation and allowing uninterrupted health monitoring.

The Wright Laboratory is initiating the Smart Metallic Structures program in the summer of 1992, to develop a system capable of real-time health monitoring of metal aircraft structure. The motivation for implementing such a system is the compounding effects of increasing average age of military aircraft, and the increasing severity of flight environments to which they are subjected. An AIAA study group concluded that aircraft equipped with automatic G-limiters and gust load alleviation systems spend a higher proportion of their flying time at load levels near maximums, than the same airframes without such systems.[5] Upgrading the flight control systems of current fighter aircraft appears to therefore accelerate fatigue damage propagation, and points to the need for a retrofittable health monitoring capability. The desire to develop more structurally efficient airframes capable of sustained higher performance leads to the need for on-board health monitoring for future aircraft. Another motivation is to shorten the lag time between data acquisition and fatigue life assessment, as noted in the beginning of this section.

The monitoring system developed under the Smart Metallic Structures program will be compatible with the US Air Force Aircraft Structural Integrity Program (ASIP). A key task under ASIP is force management, requiring loads/environment spectra survey and individual aircraft tracking. Instead of predicting flaw growth based on environmental monitoring, the smart system will be capable of conducting real-time non-destructive evaluation. Since the system will reside with an airframe, it is inherently capable of tracking individual aircraft, and could even be configured, depending on the system's electrical architecture, to track individual components on the airframe to allow a part's structural history to travel with it if part changeout occurs.

A wide variety of sensor and logical technologies is being considered for this system. Various gages may be employed in areas of known cracking, to sense crack propagation locally or over large regions. Since the sudden energy release of crack propagation in metal usually produces acoustic waves, acoustic emission and ultrasonic sensors may be useful for detecting damage events in unexpected locations. Strain sensors, from typical foil gages to experimental optical fibers, are included in most system concepts since they directly measure a structural disturbance related to fatigue. Electrical techniques may be useful, especially in detecting corrosion. The signal conditioning and handling from a large array of sensors presents a problem that will require development of an expert system to process in near-real-time. While an expert system also may be trained to notice off-nominal conditions and thus infer damage, interpretation of the conditioned data to locate and identify damage probably will be best accomplished with an artificial neural network. The degree of distribution or centralization of the smart system will be determined by the available power, need for individual part tracking, weight considerations of the different architectures, and speed and sensitivity of operation. These are some of the considerations to be addressed in the early phases of the Smart Metallic Structures program.

The program will progress through a full-scale hardware demonstration. The selected logical technologies and their supporting sensor technologies will be developed through test coupons, structural elements and subassemblies, supporting the system design effort. A full-scale component with integrated structural integrity

monitoring system will be built and tested around 1996 in both static and fatigue environments. Load sensing and damage initiation and tracking will be conducted with the smart system through the test. Valuable information will be gained through identification of near- and far-term applications, and issues raised in the system performance tests. Operational capability is desirable for this first attempt at a smart metallic structure system, but is not required for program success. Identification of implementation and application issues will provide valuable input for future smart system developments.

Composite structures present some different challenges, so another major program is focusing on health monitoring of nonmetallic aircraft structures. Composites exhibit a greater variety of failure modes, complicating the issue of determining the nature of damage. Laminated composites can suffer delamination, fiber breakage, and matrix cracking; even transverse cracking does not typically propagate as cleanly as in metals. Composite materials also possess a wider range of electrical characteristics than metals, complicating any electric-based detection schemes. Their directional structural characteristics lead to non-uniform energy propagation at various layers through the thickness, further clouding efforts to locate damage. A joint US/Canada effort is scheduled to begin in the fall of 1992 to pull together the array of technologies that have been shown in early research to address these issues. The Integrated Smart Structures Technology program will focus on demonstrating the payoff of real-time health monitored, active, and adaptive, electrically integrated composite structures.

Because of their built-up construction, laminated (or other forms of) composite structures lend themselves readily to sensor/actuator integration. Wright Laboratory is one of many research organizations assessing the structural implications of integrating sensing and active components into laminated composites. The Integrated Smart Structures Technology program will address several issues in developing the health monitored smart system. One of the first issues is the selection of embedding versus attaching the sensors. Embedment reduces structural strength and component accessibility, and requires close attention to the makeup of any cladding on the sensor elements and transmission lines to control the laminate properties. Attachment leaves the elements exposed to damage. Sensing accuracy also may be degraded, since composite structure's strain response varies through the thickness, possibly making it desirable for some configurations to locate the sensors on the neutral axis. Coupon-level research will lead to selection of the physical configuration of the integrated smart composite structure system to fabricate and demonstrate.

The signal processing and data interpretation issues for the Integrated Smart Structures Technology smart composite structure system are the same as for the Smart Metallic Structure system mentioned previously. The architecture of the logical system will be designed based on desired level of hardware tracking (aircraft or major assembly), power availability, system speed and sensitivity, and the quantity and type of sensors employed.

After developing and selecting the sensing technologies and logical architecture for an integrated composite smart health-monitoring structure, a smart system will be designed, built and ground tested around 1996 in the Integrated Smart Structures Technology program. The demonstration article will be representative of a full-scale aircraft structural assembly, to demonstrate and validate the potential capabilities. The developed system will actively track load levels and damage progression through static and fatigue testing of the structural article. Analysis will predict the cost payoffs in the maintenance and inspection areas, and performance payoffs through full use of the structural load capability of the integrated health monitored part. By applying this technology to new airframe design, the ultimate payoff will be obtained through reduction of overdesign, saving material costs and weight.

3.4 Technology Gaps/Shortfalls

The current state of the art in sensory structures has several shortcomings. Research has noted that acoustic energy propagates nonuniformly in nonisotropic materials, complicating the determination of location of a damage event through acoustic monitoring. The precision of acoustic sensing schemes in composite structures will therefore require characterization of propagation velocities for the range of layups the structure will be made of. The effects of holes, joints, and repairs on propagation characteristics also must be characterized and predictable, to enable design of composite hardware employing acoustic sensing.

Wright Laboratory is conducting extensive material coupon testing to assess sensor embedment effects. Other studies have measured reduction in compression strength due to sensor embedment, for the worst orientation (perpendicular to load and adjacent to longitudinal fiber plies), of up to 70%.[6] This result would seem to be due to the load-bearing longitudinal fibers bending around a transverse optical fiber, creating a prebuckled site. Aligning the optical fibers with the reinforcement fibers and load direction in compression loaded regions reduces the loss of strength to a reasonable 15%. Knockdowns in tensile strength are much less, not exceeding 10%,[7] since instability is not the determining factor. In addition to determining the structural effects of sensor integration, researchers also must establish design rules for educating structural

designers on proper sensor integration techniques, and develop analytical tools, to make sensor embedment a valid design option along with attachment and non-contact sensing methods.

The lower strength and stiffness of optical fibers compared to structural reinforcing fibers reduces overall structural efficiency when they are integrated into structures. Exploiting the sensing capabilities of structurally capable fibers and materials, as well as increasing the structural properties of current sensing devices, would minimize the structural degradation due to sensor integration.

Operational smart systems must be developed to have a higher degree of robustness than current laboratory demonstrations, to recover functionally after inevitable power interrupts, and enable calibration and correction of periodic drifts. This will require that the sensing techniques employed have some absolute or reference capability, and are not completely relative.

While the metallic damage mechanisms of cracking and corrosion are readily distinguishable by various sensing methods, the determination of damage nature in composite structures is not well understood. Sensor techniques for detecting the occurrence of damage cannot distinguish between fiber and matrix cracking, which will affect determination of residual strength. Accurate isolation and measurement of damage effects are fundamental to health monitoring structures.

4. MULTI-FUNCTIONAL STRUCTURE

Most current smart structures research involves the combination of airframe functions, blurring the distinction between the structural, health monitoring, and control actuation disciplines. The Wright Laboratory is also investigating a new area: multi-functional structures, or the incorporation of historically non-structure-related functions into aircraft structure, with the goal of reduced weight and volume. Development of true multi-functional structures presents significant challenges to structural designers, since some features being considered for integration will involve combining very different engineering disciplines.

4.1 Current State of the Art

The modern airplane structure is an aerodynamically shaped framework for mounting navigation and flight control systems, propulsion systems, and other support systems. Typically, the structure accounts for about 30% of the total vehicle weight, with mounted and installed systems accounting for the other 70%. No attempt is made to combine structural supports for different systems, with each electronic box comprising a separate, stand-alone component, sometimes even including its own environmental conditioning.

4.2 Potential Smart Structures Technologies

Any technology which exploits a structural characteristic, to allow combination of functions, may be considered for development. Of particular interest is electrical tailorability of structural materials and miniaturization. the specific technologies that will be combined will depend upon the specific applications, which are varied.

4.3 Applications/Current Research Efforts

A few of the multi-functional structures the US Air Force is currently working to develop are actively filtered transparencies, and conformal antennae. Materials with controllable response to specific wavelengths of light are desirable as variable filter media in aircraft canopies. The capability to model the molecular structure and response of such materials is the first step in designing such smart canopies. Liquid crystal molecular dynamics have been successfully simulated at Wright Laboratory,[8] with the intention eventually to engineer the molecular structure of filter materials with target thresholds and response bands. Several sources have also experimented with mounting flat, thin antenna elements on the outer surface of aircraft to minimize aerodynamic impact, but the rest of the transmission system has been conventional. At the USAF Rome Laboratory, investigators are designing a complete system, including transmit/receive modules and signal processors, which would be installable in the door panel of a large aircraft (a Lockheed L-1011 airliner).[9] The stressed skin is treated as a radome, though, and does not assist in transmission other than to pass energy. While conformal antennae are often portrayed as first generation multi-functional structures, they are really not structural beyond aerodynamic pressure loads, but are an admittedly tough advanced packaging project.

The Wright Laboratory is initiating a research and advanced development effort in late 1992 to integrate avionics elements into airframe structure. The goal of this program is to integrate a load bearing antenna into a structural panel, to demonstrate aerodynamic, packaging volume, weight, and signal transmission advantages over a nonstructural mounted radio antenna. The investigators intend to select an antenna configuration with operating parameters that will benefit from a shallow, flat design, so that its function can be optimized in the conformal application, instead of forcing a design into a shape far from its optimal configuration. The electrical materials used for the antenna also will have to be structurally capable, fatigue resistant, and electrically stable at structural load levels. In addition, the electrical properties of the smart skin and the surrounding structural materials will have to be controlled for high transmission quality. Structural design techniques for ensuring durability, and system

design techniques for producing high quality electrical transmission, will be simultaneously applied so that efficiency and high performance in both areas is obtained. The system design will include all associated signal generating, power, transmission control, and thermal management hardware. The design developed will be built and tested around 1996, to demonstrate the performance payoffs.

4.4 Technology Gaps/Shortfalls

The most obvious drawback to the integration of structural members with other active components is the resulting supportability of this complex package. Access for troubleshooting and part replacement must be considered early in concept development, since the maintenance concept will be practically fixed from then on.

Vulnerability to handling and combat damage is another significant consideration in integrating functions with structures, especially outer skin structures exposed to ground activity. Maintenance-induced damage is a tough requirement on composite structures in general, and the induced damage may be much more serious, and difficult and expensive to repair, when the structure performs many functions and must be functionally restored as well as structurally repaired.

5. ACTIVE STRUCTURE

Since active structures can both carry structural loads and respond to external commands, they must be composed, at least in part, of active materials which exhibit strain in response to an external command signal. This command can be an electrical signal (piezoelectric, electro-restrictive), a magnetic field (magneto-restrictive) or a temperature change (shape memory alloys). The use of active materials allows traditional aircraft structure to control system behavior and improve performance.

5.1 Current State of the Art

In current use there are no systems which use active structures technology as defined in the previous section. Active structural control has, however, solved a variety of problems. Active mirror mounts were used to control vibrations in the Airborne Laser Laboratory,[10] an active decoupler pylon was utilized to increase the flutter margins on an F-16 aircraft,[11] and the Mission Adaptive Wing Program modified an F-111 wing to demonstrate the increase in performance the ability to change wing camber in flight could provide.[12] The hydraulic or pneumatic systems used do not meet the active structures definition above since the active elements are separate from the load carrying structures. Additionally, the systems require an external pumping system to operate that is heavy and requires a large internal volume. In all, systems exist now which utilize active control to increase aircraft performance; however, these systems are weight and internal volume inefficient. The use of active structures technologies will allow these and other performance enhancements to be utilized while maintaining more usable internal volume and lower aircraft weight.

5.2 Potential Smart Structures Technologies

Active structures technology relies on the use of active materials to enhance the performance of aircraft systems. Any active structure will be limited by the performance characteristics of these materials. An essential part of active structures research must therefore be materials research. At the same time, applications research must devise systems requirements and demonstrate scaleable performance to develop materials specifications. Applications not feasible today due to materials limitations can, then, focus materials research to achieve performance improvements tomorrow. Novel materials, both improvements on those discussed below and those undiscovered today, will therefore become available over the next decade.

Many classes of active materials currently exist today and may be differentiated by linearity, frequency, bandwidth, temperature, and power requirements. Note that research into using active materials as composite fibers is ongoing so many of these materials may also be embedded into composite plies and laminated into structures.[13]

The first class of materials, shape memory alloys display a phase change at a specific temperature. Current flowing through the SMA material raises the temperature and causes a contraction of the material returning to the pre-deformation state. They must then be cooled to allow them to deform again. The stiffness and geometry of a structure containing shape memory alloys are dependant on temperature. The effect on the structure is inherently non-linear in nature. Cooling rates limits SMA the actuation frequency bandwidth to less than a few Hz.

The next class of materials, linear electro-mechanical, possess a nearly linear relationship between electrical charge or field and mechanical stress or strain. Piezoelectric materials, such as G1195, are examples of this class. Application of an electric field causes the material to strain allowing structural actuation. Some hysteresis in the strain-voltage relationship may be observed. Actuation is possible over a large frequency range from DC to several kHz although creep effects limit DC performance. The materials are temperature independent over this frequency range if temperatures are below their Curie temperature (~360^{o}F for G1195) above which they loose their electro-mechanical coupling. The power required to actuate piezoelectric materials is generally low.

The third class of materials, non-linear electro-mechanical, includes piezoelectric materials with significant hysteresis effects as well as electro- and magneto-restrictors. Electro-/magneto-restrictors strain when placed into an electric or magnetic field. The relationship is nonlinear in nature (*i.e.*, strain $\propto$ {field}^{2} for electrostictors) causing the actuation to be a non-linear phenomenon. Frequency range, temperature, and power requirements are the similar to linear electro-mechanical materials.

Utilizing active materials, active structural control has been demonstrated, mostly on beams and plates. Too many researchers have demonstrated active vibration control, acoustical emission suppression, and actuation of aerodynamic control surfaces on simple structures to review here. Demonstration and validation of this technology to aircraft typical structures has not yet been accomplished.

5.3 Applications

Incorporating active materials into aircraft structures will allow designers new flexibility with which to increase aircraft performance. These performance enhancements will allow future aircraft systems to outperform their adversaries and better accomplish their mission. Potential applications for active structures span many disciplines including aerodynamics, propulsion, aeroelastics, vibration, and acoustics. Several example applications in each of these fields will be discussed. These examples are no means exhaustive but instead attempt to span smart structures applications envisioned for aircraft systems. Since active aircraft structures research is still at the basic level, performance requirements and design studies for most of these applications have not yet been performed. Actuation requirements for some await materials developments, others could be built today with focused technology development. The purpose of this discussion is to present various applications and briefly discuss known requirements and encourage others to pursue further investigation. The ideas presented are a synthesis of many discussions with various colleagues at Wright Laboratory. Researchers here are currently exploring a few of these applications but a discussion of their efforts will be left to the next section.

Aerodynamic applications for active structures technologies require changing structural contours of the aircraft to influence the airflow. One possible application would be to change airfoil shape to optimize performance at varying airspeeds particularly in the transonic region. Studies[14] have shown that only small changes in airfoil shape can result in significant drag reduction. This application is similar to the Mission Adaptive Wing. Actuation requirements are for quasi-static control therefore shape memory alloys may prove best for this application.

Another possible aerodynamic application is the control of unsteady aerodynamics seen in either high angle of attack flight or in turbulent boundary layers. This application would require local changes in the airfoil skin that would interact with the unsteady airflow, reduce drag, and increase performance. Other than the need for high frequency control, applications requirements are unknown at the present time.

Another set of aerodynamic applications are in propulsion. Active flow field control could be used to keep combustion optimal in future engine designs. Active materials could also be utilized in thrust vectoring nozzles to provide higher frequency control capability and lighter weight. Materials developments will have to proceed these applications due to the high temperatures found in aircraft engines. The externals of engines, however, have lower temperatures, on the order of 300-400^{o}F, and suffer from many vibration problems particularly in the region of turbine rotor frequencies (30-100 Hz). Active damping of the external components could provide life cycle cost savings for propulsion systems.

Solution of the engine externals vibration environment would be similar to other structural dynamics applications in vibration, acoustics and aeroelasticity. The high vibratory environment of aircraft systems presents a range of challenges to the designer. Possible applications would include active isolation of stores, equipment, sensors, or pods; skin panel fatigue life extension; tail buffeting reduction; active landing gear; and gun-fire vibration reduction. These and other vibration applications vary in frequency, bandwidth, temperature and control authority requirements. Solutions could involve active isolation, damping, control, or any combination of the three. Studies of these applications are needed to identify and pursue those which are both feasible and have a high payoff potential.

The second subset of structural dynamics applications are aeroelastic. Coupling between the aerodynamic flow and structural dynamics can result in flutter. Active structures may be able to attack this problem from both directions: aerodynamic and structural. Novel control surfaces or active wing twisting may be possible. In the near term, active structures can improve on the decoupler pylon, designed and tested in the early 1980s, which demonstrated the use of an active pylon to minimize store/wing flutter. Direct active flutter control through wing twisting will require an increase in the control authority currently available from piezoceramics or an increase in the bandwidth of shape memory alloys. Gust load alleviation, which would require actuation schemes similar to flutter control but less authority and does not involve aircraft instabilities,

may be a nearer term application. Finally, active isolation of aeroservoelastic instrumentation may improve the performance of current flight control systems by decoupling the gyros from the elastic aircraft vibration modes.

Acoustics applications comprise the last subset of structural dynamics applications. Two areas which have been demonstrated are cabin noise reduction and cavity resonance problems. Cabin noise can be reduced for either the passengers or pilots of aircraft, especially propeller driven aircraft. This can be accomplished by either changing the fuselage frequency response to decrease resonance or active noise cancellation using loudspeakers. For the pilot, active headsets are also possible and available currently for home use as well. Finally, cavity resonance for internal carriage of weapons with release at varying airspeeds may require active spoiler control.

In summation, a wide array of aircraft applications for active structures technology exist; albeit at the conceptual stage. Further study in this area is therefore required.

5.4 Current Research Efforts

The USAF Flight Dynamics Directorate of Wright Laboratory is beginning research into the application of active structures technology. Currently, the Structural Dynamics Branch is investigating the uses of piezoelectric materials as actuators. The current effort is aimed at exploring different actuation schemes on simple test articles (beams and plates) and developing modelling and design techniques. Concurrently, investigation into vibration isolation requirements for targeting pods and wing/store interaction is underway. Following the requirements definition phase, a preliminary test article will be designed and fabricated. Research into vibration attenuation will then proceed with a series of modifications to this test article adding complexity at each stage. The goal is to demonstrate, in the laboratory the use of active structures technology for a realistic aircraft system.

The Advanced Composite Structures Group of the Flight Dynamics Directorate is also considering active structures technology in its Integrated Smart Structures Technology program, which is primarily focused on structural health monitoring. The active system development will probably be a separate component from the demonstration component for the smart health monitored structure. While this does not achieve maximum integration, it is an appropriate approach at this time, considering the immaturity of applications of both technologies. Each application will have to be developed further before development of a fully integrated smart sensory/active full scale structure would be justified. As resources permit, an active full scale structure may be developed for fabrication and test. The function of this active structure will be determined after assessing the technology maturity and payoff potential of proposed systems, which may be aimed at controlling twin tails during buffeting from radical maneuvers, vibration attenuation in jet engine support structure, efficient flight control surface actuation, and battle damage mitigation.

In other sections of the Flight Dynamics Directorate, research is in its infancy. No formal investigations are currently underway however interest has been expressed by both the Aeromechanics Division, Flight Control Division and the Aeroelasticity Group who wish to look at control of unsteady aerodynamics at high angles of attack. Additionally, the Aeroelasticity Group is investigating the use of active flutter control using active structures technology. No further information is available at this time.

5.5 Technology Gaps/Shortfalls

In general, research at Wright Laboratory on Active Structures Technology is at a much earlier stage than that of Sensory or Multifunctional Structures. It is still possible to identify some technology gaps that must be conquered before active structures technology will be ready for transition to Air Force systems. These may be discussed in three general groupings: systems integration, signal processing/control algorithms, and materials.

Systems integration of active structures technology poses many challenges. First, technology payoffs must be quantified and requirements established. Then realistic demonstrations of this technology on small scale test articles must be conducted and requirements for materials and signal processing/control algorithms determined. Only when this technology is demonstrated on realistic test articles will more advanced flight worthy testing be possible.

Aircraft systems pose a challenging set of control problems. They are non-linear, time varying systems; hence, system identification and active control must be adaptive in nature. Nonlinear adaptive controllers, like neural networks, will be required to field reliable systems. Real-time digital computing will need to be miniaturized and have its bandwidth increased. Advancements in the fields of nonlinear, adaptive control will need to address many issues which can only be specified by aircraft structural researchers. Multidisciplinary collaboration will thus be needed.

Materials improvement and quantification will also be needed before flight worthy structures can be built. Actuation power improvements will be needed to realize some of the greatest benefits, such as active flutter control. Fatigue life characterization for piezoelectric

materials is sketchy at best. Additionally, their weight and linearity need to be improved. Finally, reliable constitutive relations have to be characterized and incorporated into modelling tools for aircraft designers.

6. SUMMARY

The USAF Wright Laboratory Structures Division is focused on improving the performance, affordability and safety of current and advanced airframes. Smart structures technologies have been recognized as offering the potential for advancements across the board. The result of Wright Laboratory's smart structure research and demonstration programs will be full-scale verification of the performance and cost benefits of real-time health monitoring of metallic and non-metallic airframe structures, active and adaptive composite structures, and avionics-integrated composite skins, backed up by extensive structural properties testing. These efforts will contribute substantially to defining the concept for a first generation smart vehicle airframe.

[1]Whitehead, R.S., Kinslow, R.W., and Deo, R.B., "Composite Wing Fuselage Program," AFWAL-TR-88-3098, Feb 89.

[2]Bowden, M.L., Nolet, S.C., and Fanucci, J.P., "An Introduction of Materials and Automated Production Methods for Smart Structures," AL-TR-89-030, Aug 89.

[3]Mazzu, J.M., Caglayan, A.K., and Allen, S.M., "A Hybrid Neural Network Knowledge Base System for Intelligent Structural Monitoring," WL-TR-91-3110, Feb 92.

[4]Hickman, G.A., Gerardi, J.J., and Feng, Y., "Application of Smart structure to Aircraft Health Monitoring," Journal of Intelligent Material Systems and Structures, Vol, 2, No. 3, Jul 91, pp. 411-430.

[5]"Impact of Active Controls Technology on Structural Integrity," Technology Cooperation Program Action Subgroup HAG-6, AIAA-91-0988.

[6]Jensen, D.W., Pascual, J., and August, J.A., "Performance of Graphite Bismaleimide Laminates With Embedded Optical Fibers. Part II: Uniaxial Compression," Smart Materials and Structures, Vol. 1, No. 1, Mar 92, pp. 31-35.

[7]Jensen, D.W., Pascual, J., and August, J.A., "Performance of Graphite Bismaleimide Laminates With Embedded Optical Fibers. Part I: Uniaxial Tension," Smart Materials and Structures, Vol. 1, No. 1, Mar 92, pp. 24-30.

[8]Gerardi, T.G., Pachter, R., Crane, R.L., and Adams, W.W., "Smart Materials Research in the USAF Wright Laboratory," Proceedings of the First European Conference on Smart Structures and Materials, 12-14 May 92, ed. Culshaw, B., Gardiner, P.T., and McDonach, A.

[9]Lee, K.M., Chu, R.S., and Liu, S.C., "A Study of Performance Monitoring/Fault Isolation and Correction Systems for Smart Skins Program," Interim Report RL-TR-91-226, contract F19628-89-C-0110, DTIC #AD-B160 204, Sep 91.

[10]Marzwell, N.I., Katz, E., Givant, F.R., Landis, C.E., and Sack, L.J., "Advanced Benchless Laser Structural Model," DTIC #AD-B075 874, Jan 83.

[11]Reed, W.H. III, Foughner, J.T. Jr., and Runyan, H.L. Jr., "Decoupler Pylon: A Simple, Effective Wing Store Flutter Suppressor," Journal of Aircraft, Vol. 17, No. 3, Article No. 79-0791R.

[12]Hall, J.M., "Executive Summary: AFTI/F-111 Mission Adaptive Wing," Final Report, WRDC TR 89-3083, Sep 89.

[13]Darrah, S.D., Batha, H.D., Damjanovic, D., and Cross, L.E., "Large Area Piezoelectric/Polymer Composites," Proceedings of the ADPA/AIAA/ASME/SPIE Conference on Active Materials and Adaptive Structures, 4-8 Nov 91, ed. Knowles, G.

[14]Austin, F., Knowles, G.J., Jung, W.G., Tung, C.C., and Sheedy, E.M., "Adaptive /Conformal Wing Design for Future Aircraft," Proceedings of the First European Conference on Smart Structures and Materials, 12-14 May 92, ed. Culshaw, B., Gardiner, P.T., and McDonach, A., pp. 387-390.

ADVANCES IN ADAPTIVE STRUCTURES AT JET PROPULSION LABORATORY

by

Ben K. Wada and **John A. Garba**
Applied Mechanics Technologies Section
Jet Propulsion Laboratory
California Institute of Technology
MS 157-507
4800 Oak Grove Drive
Pasadena, CA 91109-8099
United States

Abstract

Future proposed NASA missions with the need for large deployable or erectable precision structures will require solutions to many technical problems. The Jet Propulsion Laboratory (JPL) is developing new technologies in Adaptive Structures to meet these challenges. This paper describes the technology requirements, approaches to meet the requirements using Adaptive Structures, and the recent JPL research results in Adaptive Structures.

Introduction

Future proposed NASA missions with characteristics similar to the Large Deployable Reflector (LDR) shown in Figure 1 and the Optical Interferometer shown in Figure 2 will require large precision structures. The dimensions of the structure are 20-50 meters with precision requirements from a few microns to sub-microns. Research is primarily on truss type structures because they must either be deployed or assembled in space due to the size constraints of the future launch vehicle shrouds. Some important technology challenges for the structure are:

- o to improve the reliability of its deployment/assembly in space,
- o to validate the structural system by ground tests,
- o to meet the precision structural requirements during its 20-30 year lifetime, and
- o to add redundancy to the mechanical system.

These challenges are partially a result of recent flight experiences such as (1) thermally distorted solar array that significantly changed the mode frequency on the Solar Array Flight Experiment (SAFE), (2) large disturbances from release of thermally induced strain energy in the solar array on Hubble Telescope, (3) low resonant frequency of the antenna boom near its zero strain position resulting in large nutation rotation on Ulysses, and (4) partially deployed high gain antenna on Galileo.

JPL is developing technologies to meet the challenges of future NASA missions, including those related to Adaptive Structures [1,2]. Adaptive Structures are systems whose geometric and physical structural characteristics can be beneficially modified to meet mission requirements either through remote commands or automatically in response to internal or external stimulations [3,4]. The use of Adaptive Structures for deployment/construction in space is in [5], for ground test validation is in [6], for meeting precision requirements is in [7,8], and for addition of redundancy is in the various references. Two international meetings on Adaptive Structures [9,10] were successful, the Third International Conference on Adaptive Structures will be in Nov. 1992, and the following meeting will be in Europe, Nov. 1993.

Background

Joints necessary to allow the motion of fixed length members in deployable structures may be incompatible with large precision structures. Upon deployment, the existence of small gaps in the joints will lead to large errors in the shape of the structure and will result in a non-linear structure. The structure will be difficult to adjust statically and actively control because of the random type frequency responses when subjected to a sinusoidal input. In indeterminate structural systems, small member length changes can develop large internal forces within the structural system during its deployment. The large internal

forces are often the cause of unsuccessful deployments. The design must limit the internal force within the structure at any location to an adjustable force level to allow completion of the deployment. After successful deployment, the design must provide for the elimination of joint gaps. One approach is to preload the joints to adjustable levels of force necessary to assure a linear structure.

New technologies are necessary to meet the initial on-orbit alignment requirements and to maintain the alignment in the face of onboard disturbances and environmental effects, such as temperature variations. Presently very little information exists about the behavior of materials and structures in this very low strain and deflection regime. There are several major technology challenges in meeting these stringent dimensional requirements. The structure must have the capability for on-orbit adjustments to provide the prescribed shape and maintain that shape. Also it must have the provisions to quasi-statically correct for dimensional changes due to temperature or space effects of materials. Onboard disturbances, such as reaction wheels and tape recorders, create undesirable jitter. Structural control must be provided to stabilize the system dynamically by adding structural damping, isolating the source, isolating the critical instruments or most likely, all the above.

Another technology issue in the development of large precision structures is the qualification of the structural system for flight, that is the type of ground testing required to assure that the system will meet the on-orbit functional requirements. Historically, structures have been verified by extensive ground testing before project management would commit to launch. The size of the structural systems required for future missions and the gravitational and atmospheric effects will make it difficult, if no impossible, to test these systems on the ground to validate their service configuration. To meet these stringent accuracy requirements and then to validate these requirements by ground testing require new approaches.

The design that incorporates the above capabilities must include redundant features to allow for a reliable system. This report describes the conceptual, theoretical and experimental research in progress at JPL related to Adaptive

Figure 1. Large Deployable Reflector (Artist's Concept)

Structures to address the above requirements.

Static or Shape Control

A requirement is to control statically large precision space system by eliminating nonlinearities due to loose structural joints, by correcting for tolerance buildup in construction, and by providing adjustments to counteract the effect of material degradation, creep, or slowly varying distortions due to temperature changes. Initially, the possible magnitude and distribution of the deviation from the desired position and the magnitude and location of the joint gaps must be established. This information is necessary to select and locate the actuators and sensors [11,12,13] in optimal positions. The structure must be linearized by preloading the structure by the actuators. An important issue in static or shape control is the determination of the shape of the deformed structure. The determination of the static shape is difficult and may require an onboard metrology system. Possibly the observations using the precision structures as a science experiment may establish the static deviations from the ideal shape. A method of using internal displacement sensors to measure

length changes in selected truss members to estimate structural deformations is in [14]. Knowing the deviation, the actuators provide the required adjustments for the critical points of the system. For telescope systems, adjustments of the supporting structure, described above is but one step in achieving the required precision. Another application of shape control is the deformation of the reflector surfaces to improve the optical quality of the image. A deformable panel concept for the correction of long wavelength errors for lightweight space telescope mirrors exists [15,16], developed as part of NASA's Precision Segmented Reflector (PSR) program. The goal of the PSR panel development task is to develop highly accurate, lightweight reflector panels [17,18]. The panels consist of a curved sandwich construction of graphite reinforced polymer laminated facesheets and a honeycomb core.

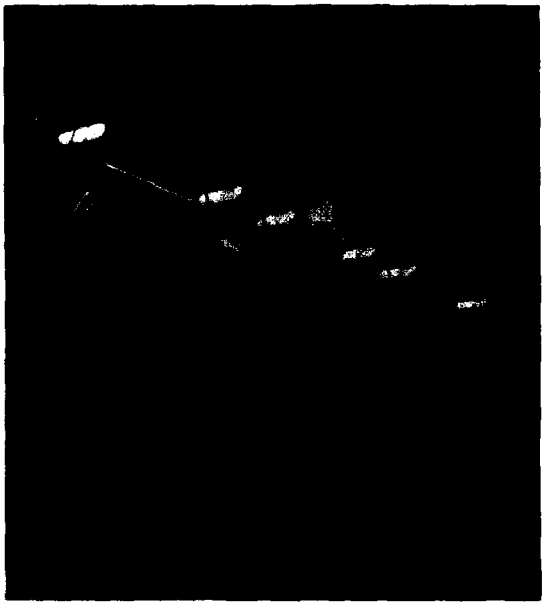

Figure 2 Optical Interferometer

The deformable panel concept uses piezoelectric ceramic actuator elements on the back facesheet of the mirror as actuators. These actuators apply forces in the plane of the back facesheet to deform the reflector surface without a backup structure. The weight of the total active system is only a small fraction of the weight of the mirror itself. The optimization of the actuator locations and the required voltage distribution to obtain a particular correction pattern was a result of extensive analyses. Tests on one meter hexagonal flat panel and a one-half meter hexagonal panel with a radius of curvature of 7.6 meters resulted in a change in focal length of up to 3 cm. The one-half meter test specimen is in Figure 3. These tests also corrected for astigmatism and coma [19].

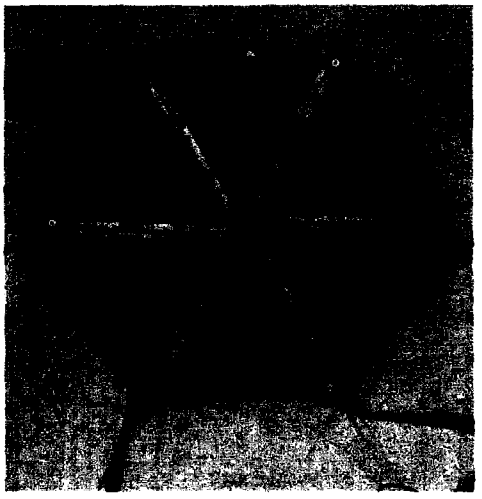

Figure 3. Deformable Composite Mirror Showing Piezoelectric Actuators Installed on Back Surface [19]

Vibration Control

The development of new methodology for the suppression of undesirable dynamic responses will play a very important role in the design of high precision space systems. Adaptive Structure concepts, primary candidates for new vibration suppression methodology, are in development at JPL as part of two focused technology programs. Both are cooperative programs with the NASA Langley Research Center (LaRC) and sponsored by NASA's Office of Aeronautics and Space Technology (OAST). One objective of the Controls Structures Interaction (CSI) program is to integrate the structure and control system [20]. Activities at JPL focus on the development of concepts, integrated design methodology, and ground test methodology including the development of passive and active structural members. Applications to space interferometry are the focus of the CSI program. Figure 4 defines the CSI goal for jitter suppression for a typical space interferometer. The objectives of the PSR program, on the other hand, are to develop

enabling technologies for large, lightweight segmented reflector systems for space. One goal of PSR is to introduce vibration suppression [21] in the backup truss structure. Current research in vibration suppression at JPL can be broadly grouped into four major activities: design and application of passive and active damping devices, development of an active isolation system, development of strategies for vibration suppression, and experimental verification.

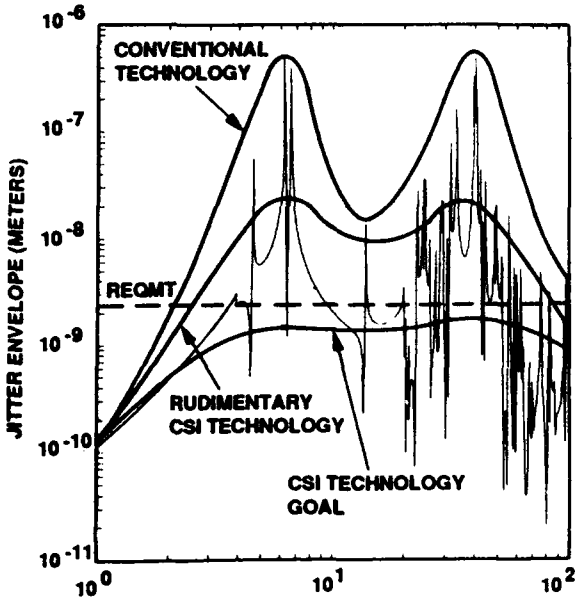

Figure 4. CSI Goal - Jitter Suppression for Space Interferometer [20]

Passive and Active Damping Devices

Two basic devices under development are, passive dampers and active structural members. Precision structures are inherently very lightly damped. During the design of control systems for Adaptive Structures, the addition of passive damping appreciably enhanced the performance. Two concepts for enhancing the system structural damping to date are passive dampers and active members. The first of these concepts uses viscoelastic materials in a parallel load path [22]. For a simple cantilever truss structure, one viscoelastic damper element, placed at a location of maximum strain energy, increased the modal damping by a factor of five for the first normal mode. Four elements produced modal damping values by a factor of 7 higher than the undamped structure in the first mode alone. Viscoelastic dampers will be further evaluated at JPL using the PSR test bed structure. An alternative method of introducing damping is through viscous damping elements. The particular device chosen for evaluation is the D-Strut designed and manufactured by Honeywell/Sperry. The D-Strut is an outgrowth of a space qualified viscous fluid damper designed for use on the Hubble Space Telescope to isolate the telescope from vibrations of the reaction wheel assembly. This device employs a silicon fluid and operates in the micron level displacement regime [23]. In a typical application on a space truss, the damper is in series with the inner of two concentric tubes which form the truss member. The test results will be discussed in a following section. A second generation D-Strut damping unit jointly designed by JPL and Honeywell/Sperry and manufactured by Honeywell/Sperry is currently in use. The performance of these units will be evaluated at JPL using multiple locations in a truss structure. A key aspect in the development of active structures is the incorporation of sensors and actuators into the structural system. Two types of active members are currently under development at JPL. The first of these, called the "mighty worm" combines precise large static position adjustment with dynamic response control. It uses a piezoelectric element with clamping provisions at both ends for static adjustment. When the active member is inactivate, the external loads by passes the piezoelectric actuator. A second active member designed and fabricated by JPL [24,25] is only for vibration control or static deformation for a short period. It functions as both a structural member and as an actuator. The design is such that either of two actuator motors can be used. One is a Lead Zirconite Titanate (PZT) ceramic, the other Lead Magnesium Niobate (PMN). The actuator with the PZT motor is capable of driving a maximum force of 500 Newtons and a maximum member displacement of 63 microns with a maximum operating voltage of 1000 volts. The corresponding data for the PMN actuator are, 455 Newtons, 39 microns and 300 volts, respectively. The PMN motor showed much better hysteretic properties but suffered from temperature sensitivity. The active member has essentially "zero stiction". Typically the residual displacement in the member is between 1-10 nanometers. An eddy current sensors with an accuracy of approximately 2 nanometers, measures the relative displacement across the actuator. Another actuator design [21] includes a

low voltage PZT motor capable of driving a maximum force of 635 Newtons and a maximum member displacement of 45 microns with a maximum operating voltage of 150 volts. The next generation actuators are currently being developed at JPL.

A schematic and a photograph of an actuator is in Figure 5.

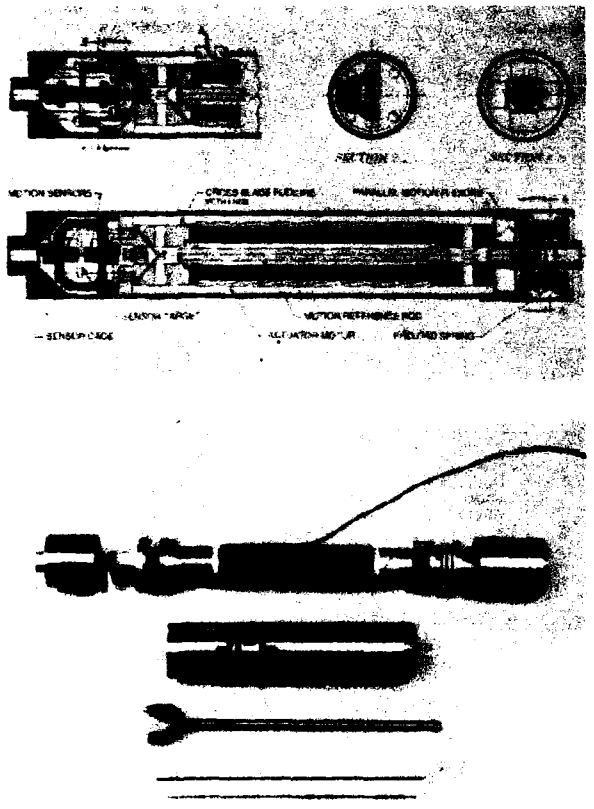

Figure 5. Second Generation Active Member [24]

Disturbance Isolation

A six degree of freedom active vibration isolation system has been designed and fabricated. This system employs six active members to provide local vibration isolation from an onboard disturbance source, such as a reaction wheel assembly. The design objective has been to provide a system that is statically stiff, providing effective dynamic isolation over a prescribed frequency range. Analytical studies for the implementation of a system are progressing [26]. Plans are to run an experimental demonstration of the system on a flexible test bed.

Strategies for Vibration Suppression

The requirements of future astronomical instruments such as telescopes and optical interferometers are so stringent that a multi-layered approach to vibration suppression will be required. The approach under test at JPL combines disturbance isolation, active and passive structural vibration suppression, and active optical pathlength compensation. The most promising means for providing effective structural vibration suppression is through the application of Adaptive Structure technology. An effective strategy requires the distribution of passive and active structural elements throughout the structure in an optimal manner. Experience has shown that engineering judgement does not suffice if the system is complex. The problem is one of combinatorial optimization for which the solution becomes intractable as the problem size increases. The simulated annealing technique successfully provided a near optimum solution [27,28]. Two strategies were pursued in the incorporation of active structural members into an adaptive system. One introduces active damping by using collocated feedback to the active members [29,30,31]. The other scheme achieves global stabilization by non-collocated feedback control [32,33]. In the implementation of the global control algorithm, the finite element model, although test verified by extensive modal testing, was not accurate enough for non-collocated control. As a result, a multi-input multi-output state space model using single-input multi-output frequency response measurements [33] was necessary for non-collocated control. Both the collocated and non-collocated feedback control strategies are in Figure 6 and the results are in the following section.

Experiments in Vibration Suppression

Experimental studies have been invaluable for uncovering research directions in the development of Adaptive Structures. Although ground tests comprise most of the experiments to date, some flight data in a reduced gravity test environment aboard an aircraft exists.

Extensive ground testing proved the application of passive and active damping concepts in vibration suppression. It is linear down to a displacement of 20 nanometers. Upon characterizing the individual units, testing the system with the

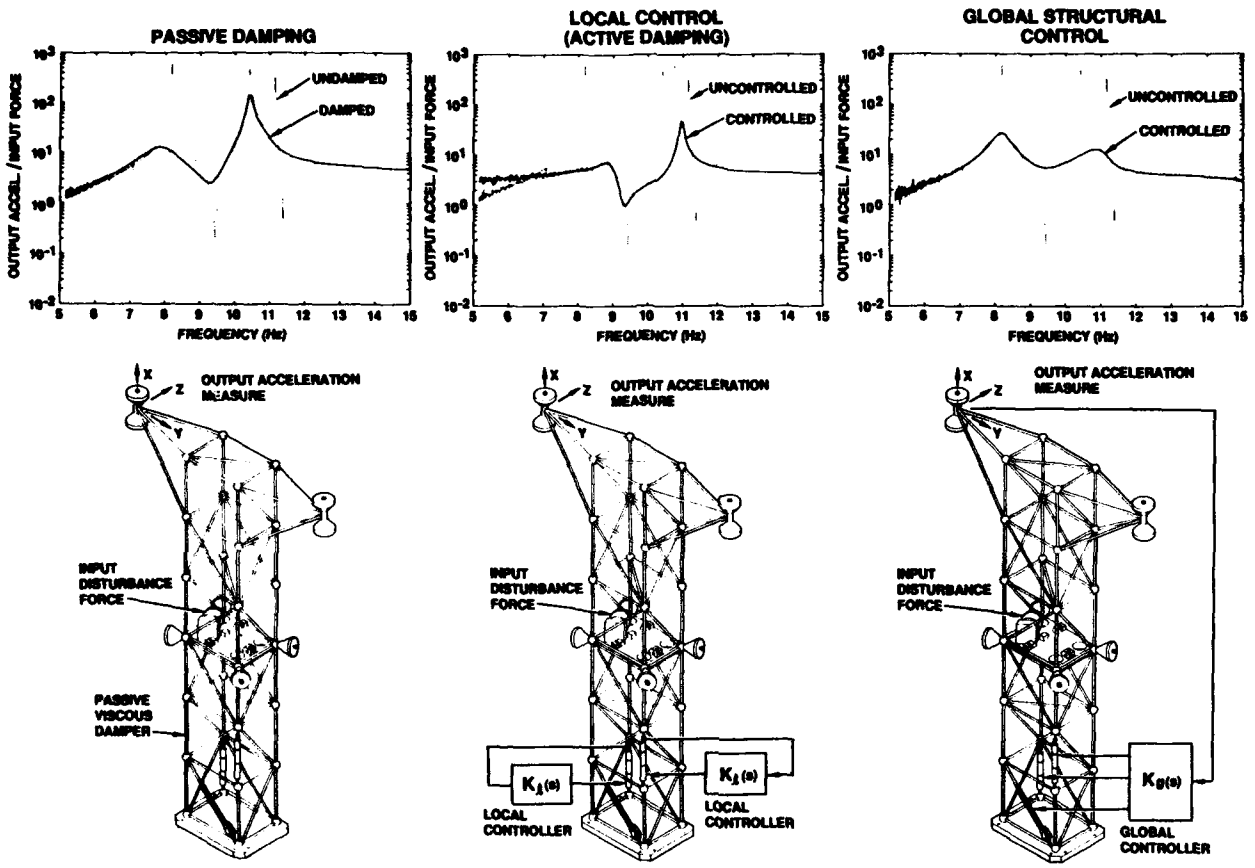

Figure 6. Vibration Suppression Studies [20]

D-Strut in the JPL Precision Truss (CSI Phase 0 Test Bed), Figure 6, validated the D-Strut. The plot labeled "Passive Damping" in this figure shows the effectiveness of only one such damper

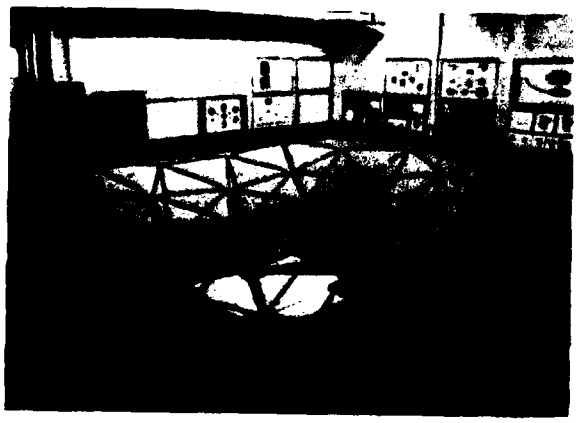

Figure 7. Precision Segmented Reflector

on the transfer function. Active members in the CSI Phase 0 Test Bed helped show the merits of several strategies for vibration suppression. It is important that the impedance of the activemembers matches the impedance of the surrounding structure. Both for the demonstration of the local and global control strategies, the actuators were the two active members at the base of the structure, as shown in Figure 6. The disturbance source is at the center bay and the control points are the concentrated masses at the upper two outriggers. Experimental results using two active members with local controllers are in the plot labeled "Local Control," Figure 6. Global control with the non-collocated sensors and actuators, stabilized the vibration in three degrees of freedom at one outrigger. Experimental results of a control system are in Figure 6, labeled "Global Structural Control".

The PSR test bed shown as Figure 7 is a truss structure for defining an accurate two

dimensional surface in space in contrast to CSI. The vibration suppression results [21] are in Figure 8.

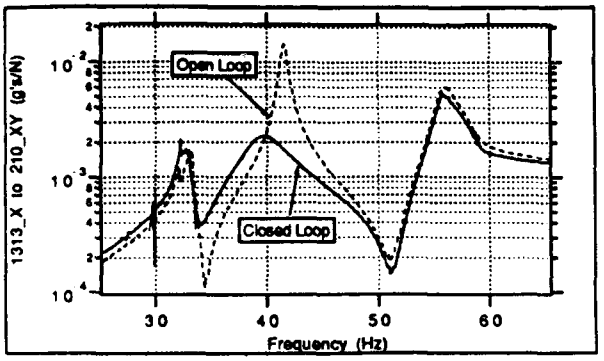

Figure 8. Vibration Suppression Results on the Precision Segmented Reflector [21]

A new, larger and dynamically more complex CSI Phase B Test Bed shown as Figure 9 is currently operational. Several layers of control to show the advantages of integrating optical pathlength control, structural control, and vibration isolation was proven on this test bed. Methods will be investigated to combine passive damping augmentation, local control, and global control. The test setup will contain up to 5 passive members and up to 8 active members. Various combinations of these members will be evaluated to confirm the results of the studies to optimize the passive and active member mix and the member locations [34]. Pathlength control to 10 nanometers was achieved. The development of the six degree of freedom isolation device will continued. Recall that the ultimate goal of the CSI program is to suppress the optical pathlength jitter down to one nanometer over a frequency range of 1 to 100 Hz, Figure 4. JPL is building the next generation CSI test bed, the Phase I Test Bed. Both the CSI Phase 0 and Phase B Test Beds are attached at its base to the ground. The Phase I Test Bed, Figure 10, is a free floating structure designed to validate structural control, disturbance isolation and optics motion compensation with rigid body attitude control and precision optical pointing systems.

The application of Adaptive Structure technology was successful in a flight experiment conducted jointly by the U.S. Air Force Flight Dynamics Laboratory and JPL [35]. The reduced gravity test environment for a 10-20 second period occurred when the KC-135 aircraft flew a parabolic trajectory. Two active members were

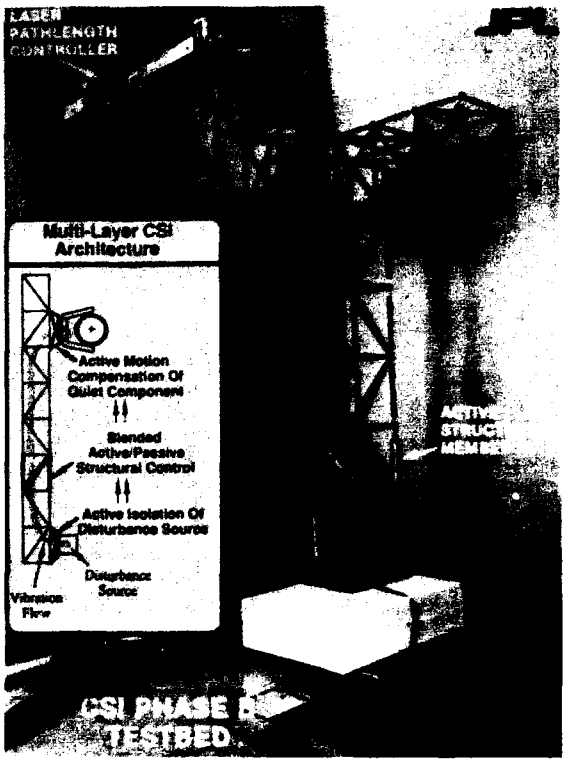

Figure 9. CSI Phase B Test Bed

incorporated into a 12 meter truss structure. The control consisted of collocated force and velocity feedback. An impact force provided the excitation during the 20 second reduced gravity window. Figure 11 shows the open loop and closed loop frequency response functions measured by an accelerometer at the tip of the structure. The experiment demonstrated that effective local controllers can be designed without the precise knowledge of the dynamics of the system. Designing for redundancy is feasible since the failure of one actuator reduces the level of active damping. In future designs, spare actuators in the design can be used if other actuators fail.

Adaptable Deployable Concepts

The application of active members in the development of an adaptive deployable structure concept [5] is currently under study at JPL. The configuration chosen for the focus mission is a deployable tetrahedral truss for a 3.8 meter diameter reflector, Figure 12. The objective of this study is to develop a structural concept

Figure 10. CSI Phase I Test Bed

withactive members to (1) assist in the deployment of the structure, (2) provide preload capability to eliminate non-linearities inherent in the deployable joints, (3) provide static adjustments to maintain a high accuracy backup structure for the reflector panels, and (4) provide the capability of attenuating vibration to within prescribed levels. One approach to improve deployment reliability is to include into the deployable structure an active member that lengthens under tensile loads and contracts under compressive loads. The control of the magnitude of the internal forces during the deployment is through control settings of the threshold force to extend or contract the active member. The non-linearities in the structure due to joint gaps can be eliminated by preloading the members of the indeterminate structure in its deployed position. Then the structure is statically and dynamically adapted. The goal is to minimize the number and type of active members to meet the above objectives [12]. A multi-criteria optimization scheme maximizes the satisfaction of the objectives.

Ground Test Validation

Adaptive Structure concepts provide much needed relief for the qualification process of large high

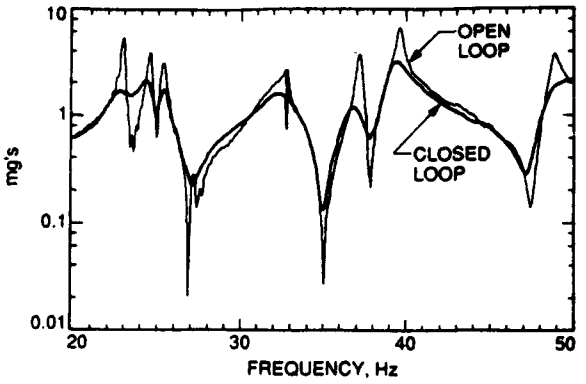

Figure 11. Comparison of Open-Loop and Closed Loop Frequency Response Functions Measured in Reduced Gravity Flight Experiment [35]

precision structures [7]. Advanced structural concepts, required to meet future mission requirements, will not be adopted by project managers unless these concepts can be qualified to meet on-orbit functional requirements by ground testing and analysis. Traditionally, on past programs a strong emphasis has been on testing since analyses often did not adequately represent the hardware. Current approaches for the verification of on-orbit characteristics by testing consist of the simulation of the boundary conditions of the structure and a demonstration of the system performance. Future large precision systems cannot be adequately ground tested using current technology primarily because of gravity. Even with advances in computational capabilities, ground validation tests will be required. The incorporation of Adaptive Structures allows a change in the ground validation test approach. The objective will now be to establish the upper and lower limits of the structural parameters and characteristics. Adaptability in the structure will then be provided by design, assuring that sufficient fidelity in the actuators exists to meet the accuracy requirements and the desired performance requirements are within the range of the ground test. Using this approach, the ground test requirements for large very accurate complex structural systems can be relaxed by several orders of magnitude. During the 20-30 year life of the structure, the structure adapts to changes caused by long term space affects on the stability of the structure.

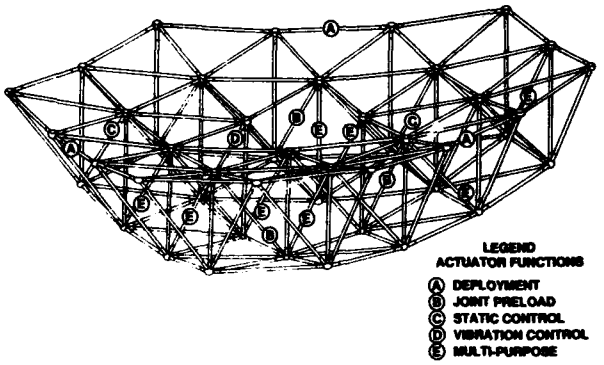

Figure 12. Adaptive Deployable Concept

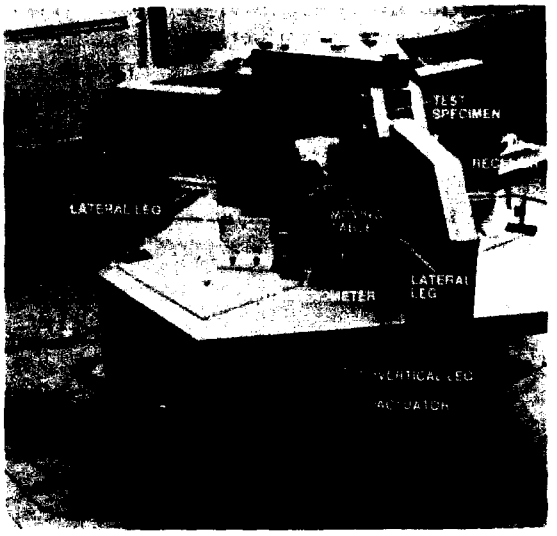

Figure 13. Microdynamic Tester [41]

System Identification

Since Adaptive Structures will change configuration and characteristics frequently if not continuously, on-orbit identification of structural parameters will be required to establish the required adaptation and to optimize the control of the system. The inherent instrumentation embedded into the structure, such as active members and their associated displacement sensors provide an excellent capability for performing on-orbit tests for the identification of parameters.

JPL is using active structural members as excitation sources for an on-orbit modal test, both analytically and experimentally [36,37,38,39]. A distinct advantage of using active members as excitation sources is that transfer functions required for control purposes can be identified directly. Experiments using a rigidly supported ground test bed have shown that the modal parameters obtained using active members as excitation sources have produced modal parameters with equal or better accuracy than those obtained by a conventional modal test. Also the change in structural damping or stiffness of an Adaptive Structure can be established by activating various combinations of active members while using others as an excitation force.

Microdynamics Tester

Adaptive Structures will be operating in the micron or even down to the nanometer regime. Of particular concern is the behavior of structural joints and passive and active energy devices when subjected to very small forces or displacements. A JPL developed test machine can apply forces in millinewtons and measure displacements in nanometers up to 50 Hz, Figure 13. The tester has a moving table supported by six flexure legs. The legs contain piezoelectric actuators to allow changes in length up to 200 microns. These actuators allow axial loads and moments to be generated at the test specimen. Laser interferometry measures the displacements between the ground and the table. The results of using tester on several joint designs and the D-Strut damper are in [40,41].

In-Space Assembly

Adaptive Structures will play an important role in in-space assembly. During the assembly of structures in space, a highly probable situation is the distance between the attachment nodes differs from the fixed length of the structure to be assembled. The discrepancies can be attributable to fabrication/assembly deviations, thermal conditions, space effects, and many other sources. In these situations, a large force capacity mechanism is necessary to force compatibility for the assembly of the indeterminate structure. To simplify the assembly task and improve its reliability, active members to control internal forces during assembly are desirable. Active members are similar to those described for adaptive deployables. Space cranes are another good example of the application of various aspects of Adaptive Structures. Variable length active members strategically placed in the structure, such as in the batten members of an octahedral module, can produce the changes in geometry

required for the operation of the crane. These members statically position and dynamically control the crane. Studies have shown that the application of Adaptive Structure concepts to space crane design results in a more compact stowage volume compared to conventional multi-link manipulators. Adaptive concepts also aid in the deployment and retraction, high dexterity motion, and bracing operations [42].

Cost

The cost associated with Adaptive Structures is offset by relaxation of other requirements. The effort to develop, design, test, and control materials for a precision passive system for the 20-30 years space operation can be significantly relaxed. Additionally a reduction in analysis cost to predict the static performance and the ground validation costs associated with validation of a passive system exists.

Summary

The development of adaptive structural systems has received appreciable attention over the last few years. It is becoming more evident that the stringent accuracy requirements of NASA's future missions cannot be met without the implementation of some adaptive methods in structural design. This reports summarizes the research in Adaptive Structures at JPL. The potential of active structural systems in meeting some requirements for future missions is shown. The emphasis of the research is on the experimental demonstration of concepts. To date very little data exists on the effect of the on-orbit environment on the active members. Very little information on the flight worthiness of the active systems used in the ground experiments for applications in space exists. A consistent methodology for qualifying large flexible adaptive structural systems needs to be developed. Although significant progress exists towards proving the applicability of adaptive structural systems, the requirement is for much more research, development, and proof of concept before such systems are integrated on future missions.

Acknowledgement

The research described in this paper was carried out by the Jet Propulsion Laboratory, California Institute of Technology, under contract with the National Aeronautics and Space Administration, sponsored by the Office of Aeronautics and Space Technology, Code R.

References

1. Wada, B.K., "Adaptive Structures; An Overview," Journal of Spacecraft and Rockets, Vol. 27, No. 3, May-June 1990, pp. 330-337.

2. Garba, J.A., Wada, B.K., and Fanson, J.L., "Advances in Adaptive Structures Technology for Space Exploration," International Symposium on the Potential of the Universe Exploration for New Technologies Development, Toulouse, France, October 24-25, 1991.

3. Wada, B.K., Fanson, J.L., and Crawley, E.F., "Adaptive Structures," Journal of Intelligent Material Systems and Structures, Vol. 1, No. 2, April 1990, pp. 157-174.

4. Wada. B.K., Fanson, J.L., and Crawley, E.F., "Adaptive Structures," Mechanical Engineering, Vol. 112, No. 11, November 1990, pp. 41-46.

5. Wada, B.K. and Utku, S., "Adaptive Structure for Deployment/Construction of Structures in Space," AIAA-92-2339, Proceedings of the 33rd AIAA Structures, Structural Dynamics, and Materials Conference, Dallas, TX, April 13-15, 1992.

6. Wada, B.K., Garba, J.A., and Fanson, J.L., "Ground Test Validation for Precision Structures," Proceedings of the International Conference on Spacecraft Structures and Mechanical Testing sponsored by the European Space Agency, ESTEC, Noordwijk, The Netherlands, April 24-26, 1991.

7. Garba, J.A., Wada, B.K., and Fanson, J.L., "Adaptive Structures for Precision Controlled Large Space Systems," Proceedings of the International Conference on Spacecraft Structures and Mechanical Testing sponsored by the European Space Agency, ESTEC, Noordwijk, The Netherlands, April 24-26, 1991.

8. Fanson, J.L., Anderson, E.H., and Rapp, D., "Active Structures for Use in Precision Control of Large Optical Systems," Optical Engineering, Vol. 29, No. 11, November 1990, pp. 1320-1327.

9. Wada, B.K., Fanson, J.L., and Miura, K., Editors, First Joint US/Japan Conference on Adaptive Structures, Technomic Publishing Company, Inc., Lancaster, PA, May 1991.

10. Matsuzaki, Y. and Wada, B.K., Editor, Second Joint Japan/US Conference on Adaptive Structures, Technomic Publishing Company, Inc., Lancaster, PA, May 1992.

11. Das, S.K., Utku, S, Chen, G.S., and Wada, B.K., "Optimal Actuator Placement in Adaptive Precision Trusses," Chapter in Intelligent Structural Systems, Editor, Tzou, H.S. and Anderson, G.L., Kluwer Academic Publishers, 1992.

12. Baycan, C.M., Utku, S., Das, S.K., and Wada, B.K., "Optimal Actuator Placement in Adaptive Precision Trusses," AIAA-92-2344, Proceeding of the 33rd AIAA Structures, Structural Dynamics and Materials Conference, Dallas, TX, April 13-15, 1992.

13. Julihal, P. Utku, S., and Wada, B.K., "Optimal Location of Actuator for Prestressing Adaptive Trusses with Buckling Considerations," AIAA-92-2343, Proceedings of the 33rd AIAA Structures, Structural Dynamics and Materials, Dallas, TX, April 13-15, 1992.

14. Kuwao, F., Chen, G.S. and Wada, B.K., "Quasi-Static Shape Estimation and Control of Adaptive Truss Structures Using Internal Displacement Sensors," Second Joint Japan/US Conference on Adaptive Structures, Nagoya, Japan, Nov. 12-14, 1992.

15. Kuo, C.P. and Wada, B.K., "Composite Deformable Panel," Proceedings of the SPIE 34th Annual International Symposium, Active Telescope Systems, Orlando, FL, March 28-31, 1989. Volume 1114, pp. 495-505.

16. Chen, G.S., Kuo, C.P., and Wada, B.K., "Adaptive Structures for Precision Segmented Optical Systems," Proceedings of the 1989 ASME Winter Annual Meeting, San Francisco, CA, December 10-15, 1989. ASME Publication Adaptive Structures, AD-Volume 15, pp. 103-118.

17. Freeland, R.E. and Johnston, R.D., "Structural Composite Mirror Technology Development for Submillimeter Space Telescopes," Paper No. IAF-91-317 presented at the 42nd Congress of the International Astronautical Federation, Montreal, Canada, October 7-11, 1991.

18. Helms, R.G., Porter, C.P., Kuo, C.P., and Tsuyuki, G., "Development and Testing of Lightweight Composite Reflector Panels," SPIE Paper No. 1532-09 presented at the SPIE 36th Annual International Symposium on Optical and Optoelectronic Applied Science and Engineering, San Diego, CA, July 21-26, 1991.

19. Kuo, C.P., "A Deformable Mirror Concept for Adaptive Optics in Space," SPIE Paper No. 1542-37 presented at the SPIE 36th Annual International Symposium on Optical and Optoelectronic Applied Science and Engineering, San Diego, CA, July 21-26, 1991.

20. Newsom, J.R., Layman, W.E., Waites, H.B., and Hayduk, R.J., "The NASA Controls-Structures Interaction Technology Program," Paper No. IAF-90-290 presented at the 41st Congress of the International Astronautical Federation, Dresden, Germany, October 6-12, 1990.

21. Umland, J.W. and Chen, G.S., "Active Member Vibration Control for a 4 Meter Primary Reflector Support Structure," 33rd AIAA Structures, Structural Dynamics and Materials, Dallas, TX, April 13-15, 1992.

22. Chen, G.S. and Wada, B.K., "Passive Damping for Space Truss Structures," AIAA Paper No. 88-2469. Proceedings of the 29th AIAA Structures, Structural Dynamics and Materials Conference, Williamsburg, VA, April 18-20, 1988, pp. 1742-1749.

23. Wilson, J.F. and Davis, L.P., "Viscous Damped Space Structure for Reduced Jitter," Proceedings of the 58th Shock and Vibration Symposium, Huntsville, AL, October 13-15, 1987, NASA Conference Publication 2488, pp. 233-243.

24. Anderson, E.H., Moore, D.M., Fanson, J.L., and Ealey, M.A., "Development of an Active Member Using Piezoelectric and Electrostrictive Actuation for Control of Precision Structures," AIAA Paper No. 90-1085. Proceedings of the 31st AIAA Structures, Structural Dynamics and Materials Conference, Long Beach, CA, April 2-4, 1990, pp. 2221-2233.

25. Anderson, E.H., Moore, D.M., Fanson, J.L., and Ealey, M.A., "Development of an Active Truss Element for Control of Precision Structures," Optical Engineering, Vol. 29, No.11, November 1990, pp. 1333-1341.

26. Lurie, B.J., Fanson J.L., and Laskin, R.A., "Active Suspensions for Vibration Isolation," AIAA Paper No. 91-1232. Proceedings of the 32nd AIAA Structures, Structural Dynamics and Materials Conference , Baltimore, MD, April 8-10, 1991, pp. 2256-2260.

27. Salama, M., Bruno, R., Chen, G.S., and Garba, J.A., "Optimal Placements of Excitations and Sensors by Simulated Annealing," paper presented at the Second NASA/Air Force Symposium on Recent Experiences in Multidisciplinary Analysis and Optimization, Hampton, VA, September 1988.

28. Chen, G.S., Bruno, R.J., and Salama, M., "Optimal Placement of Active/Passive Members in Truss Structures using Simulated Annealing," paper accepted for publication in the AIAA Journal, 1991.

29. Chen, G.S., Lurie, B.J., and Wada, B.K., "Experimental Studies of Adaptive Structures for Precision Performance," AIAA Paper No. 89-1327. Proceedings of the 30th AIAA Structures, Structural Dynamics and Materials Conference, Mobile, AL, April 3-5, 1989, pp. 1462-1472.

30. Fanson, J.L., Blackwood, G.H., and Chu, C.C., "Active Member Control of Precision Structures," AIAA Paper No. 89-1329. Proceedings of the 30th AIAA Structures, Structural Dynamics and Materials Conference, Mobile, AL, April 3-5, 1989.

31. Chen, G.S. and Lurie, B.J., "Bridge Feedback for Active Damping Augmentation," AIAA Paper No. 90-1243. Proceedings of the 1990 AIAA Dynamics Specialist Conference, Long Beach, CA, April 6-8, 1990. pp. 502-510.

32. Fanson, J.L., Chu, C.C., Smith, R.S., and Anderson, E.H., "Active Member Control of a Precision Structure with an H Performance Objective," AIAA Paper No. 90-1224. Proceedings of the 1990 AIAA Dynamics Specialist Conference, Long Beach, CA, April 5-6, 1990, pp. 322-333.

33. Chu, C.C., Smith, R.S., and Fanson J.L., "Robust Control of an Active Precision Truss Structure," paper presented at the 1990 American Control Conference, San Diego, CA, May 23-25, 1990.

34. O'Neal, M., Eldred, D., Liu, D., and Redding, D., "Experimental Verification of Nanometer Level Optical Pathlength Control on a Flexible Structure," AAS Paper No. 91-052, presented at the 14th Annual American Astronautical Society Guidance and Control Conference, Keystone, CO, February 2-6, 1991.

35. Lawrence, C.R., Lurie, B.J., Chen, G.S., and Swanson, A.D., "Active Member Vibration Control Experiment in a KC-135 Reduced Gravity Environment," paper presented at the First U.S./Japan Conference on Adaptive Structures, Maui, HI, November 13-15, 1990.

36. Chen, J.C. and Fanson, J.L., "System Identification Test Using Active Members," AIAA Paper No. 89-1290. Proceedings of the 30th AIAA Structures, Structural Dynamics and Materials Conference, Mobile, AL, April 3-5, 1989, pp. 1154-1163.

37. Chen, J.C. and Fanson, J.L., "On-Orbit Vibration Testing for Space Structures," Acta Astronautica, Vol. 21, No. 6/7, 1990, pp. 457-466.

38. Kuo, C.P., Chen, G.S., Pham, P., and Wada, B.K., "On-Orbit System Identification Using Active Members," AIAA Paper No. 90-1129. Proceedings of the 31st AIAA Structure, Structural Dynamics and Materials Conference, Long Beach, CA, April 2-4, 1990, pp. 2306-2316.

39. Fanson, J.L., O'Brien, J.F., Chu, C.C., Lurie B.J., and Smith, R.S., "System Identification and Control of the JPL Active Structure," AIAA Paper No. 91-1231, presented at the 32nd AIAA Structures, Structural Dynamics and Materials Conference, Baltimore, MD, April 8-10, 1991.

40. Anderson, E., Trubert, M., Fanson, J.L., and Davis, P., "Testing and Application of a Viscous Passive Damper for Use in Precision Truss Structures," AIAA Paper No. 91-0996. Proceedings of the 32nd AIAA Structures, Structural Dynamics and Materials Conference, Baltimore, MD, April 8-10, 1991, pp. 2795-2807.

41. Glaser, R.J., "A Microdynamic Version of the Tensile Test Machine," AIAA Paper No. 91-1082. Proceedings of the 32nd AIAA Structures, Structural Dynamics and Materials Conference, Baltimore, MD, April 8-10, 1991, pp. 1305-1313.

42. Chen, G.S. and Wada, B.K., "On an Adaptive Truss Manipulator Space Crane Concept," paper presented at the First U.S./Japan Conference on Adaptive Structures, Maui, HI, November 13-15, 1990.

ACTIVE LANDING GEAR CONTROL FOR IMPROVED RIDE QUALITY DURING GROUND ROLL

Tyrone Catt, David Cowling†, Alan Shepherd
Stirling Dynamics Ltd
42 Priory Avenue
Bristol BS9 4BZ
United Kingdom

1. SUMMARY

Active control of an aircraft landing gear can give improved passenger ride quality during take-off and landing. The active control system studied here uses feedback from airframe mounted sensors to modify rigid body and structural response. The system is based primarily on modifying the damping characteristics in the nose gear oleo. This is achieved by reducing the damping orifice area, with active control of the area about this new datum value. In addition, the benefits of a fully active nose gear using a separate supply of high pressure hydraulic fluid are evaluated.

Significant benefits are demonstrated with the active damping control system compared with the basic landing gear. Responses to general runway roughness and discrete runway bumps are considered. The active damping control system is shown to be effective in reducing peak and r.m.s. passenger normal accelerations at all fuselage stations, particularly nose and tail. Good improvement can be obtained from active damping control of the nose gear, with no modification to the main gear. The first fuselage bending mode response can be reduced by active damping control. The benefits from the fully active system are marginal, considering the additional system complication. These effects are illustrated for a typical transport aircraft configuration.

2. INTRODUCTION

An aircraft landing gear must be designed to meet various requirements over all ground-based operating conditions. It must be capable of absorbing the impact of a severe landing case as well as the response to uneven runway surfaces during taxiing, take-off and landing roll-out, which determines the ride quality on the ground experienced by the passengers.

An actively controlled landing gear system can be used to reduce the transmission of forces into the airframe from general ground contact. The operation of such a system also has the potential to reduce the whole aircraft rigid-body and structural vibration motions transmitted into the passenger cabin due to ground contact, giving improved ride quality on the ground. This concept also holds out the possibility that structural design cases associated with ground contact can be significantly alleviated. Furthermore, a reduction in the fatigue loads on the ground may be achievable using an active landing gear system.

The study described here is of an active landing gear system for passenger ride quality improvement in a commercial transport aircraft. The objective of the study is to investigate an active landing gear control scheme that can provide some improvement in ride quality along the passenger cabin as determined by fuselage normal accelerations during take-off and landing roll out. The direct forces transmitted through the legs from runway surface irregularities influence the whole aircraft rigid body response and the response in the airframe vibration modes. By actively controlling the nose and main gear oleos it is possible to influence the direct runway forces transmitted to the airframe as well as the induced motions from rigid body and structural mode excitations.

Various aspects of the dynamic performance of the system in response to typical random and discrete runway profiles are addressed. The results reported are restricted to active control of the nose gear only, since results indicate that this has the most potential for ride quality improvement in this case. Realistic hardware assumptions are applied to the landing gear design and mathematical models. Two types of system are considered:

(i) Active damping control, where the oleo damping orifice area is modulated in a closed loop feedback control system. This active control of damping effectively varies the oleo characteristics in proportion to a suitable response parameter, such as acceleration of a point on the fuselage. The weight and power required by an active damping control system will be small, and this could be a practical active landing gear control scheme for reasonable ride quality performance benefits.

(ii) Fully active oleo control, where direct force control of the oleo is applied by introducing additional hydraulic flow, effectively using the oleo as an actuator (References 1 and 2). Active damping control can be included in a fully active system. The main drawback to this scheme is that very large hydraulic flows may be required to achieve the desired performance improvements, particularly for the main gear.

The active control requirements for ride quality during take-off and landing roll out conflict with the requirements of the landing impact case. In a practical active landing gear system a scheme must be devised to switch the system on after touchdown. The practical aspects of these two requirements need to be studied to assess how best to satisfy both objectives.

The longitudinal rigid body mode of the aircraft on the ground is the primary contributor to normal accelerations along the fuselage, and this is likely to be at a frequency below 1 Hz. For a large aircraft the first airframe vibration modes that influence the fuselage normal accelerations of interest for perceived ride quality are generally in the range from 1 Hz to 10 Hz. The sensitivity range of the human body to vertical acceleration is maximum between 2 and 6 Hz, with roll off below and above this range, based on a representative criterion such as that in Reference 3. In this study passenger vertical acceleration is used as the basis for defining the active system performance, and the rigid body motion response is the mode that is most amenable in achieving ride quality improvements.

The passenger accelerations at the important structural mode frequencies result primarily from the fundamental fuselage vertical bending mode. Whole aircraft structural vibration modes are used to evaluate fuselage accelerations. For the aircraft studied here the lowest frequency mode significantly affecting fuselage bending is at 3.6 Hz, and the capability of the active landing gear system in reducing the response in this mode is included in the system performance assessment.

3. METHODS OF ANALYSIS

The analysis methods have been developed for a landing gear dynamics software package funded by British Aerospace (Airbus) Limited. This software package incorporates the necessary theoretical modelling and analysis methods for aircraft landing gear, with particular relevance to commercial transport aircraft. It is used as the basis for this study, with several modifications for the active landing gear application.

Landing gear dynamics are significantly nonlinear, so most of the results are generated by time domain analysis using

† D. Cowling also Department of Aerospace Engineering, University of Bristol, UK.

numerical integration. Response to random runway excitation is calculated in the time domain and power spectral densities (PSDs) of the response outputs are derived by Fast Fourier Transform. By running long enough time responses and applying data smoothing the resulting spectra give the primary modal responses. These are used to give good indication of ride quality improvements from the active landing gear system, showing how it is distributed with frequency. Response r.m.s. values are obtained both from the time histories and from integrating the spectra with respect to frequency, depending on the particular requirement. The latter method is applied to selected frequency bands to evaluate the contributions from individual modes.

The software package used for the active landing gear studies is described in Reference 4. It is organized as a series of individual modules that correspond to the components and sub-systems of an aircraft and landing gear. The user is able to build up a comprehensive model by specifying the parameters associated with particular sub-systems and then linking them together. Once the model has been constructed in this way, time response simulations representative of various different situations can be accomplished. By choosing the correct standard of model the following scenarios can be simulated:

- Drop tests for a single landing gear leg.
- Dynamometer tests.
- Whole aircraft touchdowns.
- Whole aircraft braking tests including braking and anti-skid.
- Take-off, including rotation, minimum unstick speed, lateral control, minimum ground control speed, etc..
- Steering rig tests.
- Whole aircraft steering manoeuvres.

The aircraft and landing gear model used in this study has been constructed from the standard modules included in the package without any additional programming. Nevertheless, the software package has been modified for this study to include the feedback control of the landing gear and to provide the outputs of normal acceleration along the fuselage.

4. AIRCRAFT MODEL

The aircraft model used for this study is of a typical commercial transport configuration, such as that shown in Figure 1, with a conventional nose gear and main gear arrangement. The mathematical model of the aircraft used for these studies has three longitudinal rigid body degrees of freedom, plus three airframe flexible vibration modes. The aircraft model is linear, including the rigid aircraft aerodynamics adjusted for ground effect. The simulation is initialized at a set speed and all the dynamic equations are automatically trimmed prior to the start of a run.

The landing gear model has the oleos represented in considerable detail. All mechanical, hydraulic and pneumatic characteristics of the complete system are accounted for, including the relevant nonlinear characteristics such as stiction/friction, travel limits, etc., and tyres. Figure 2 is a schematic diagram of the nose and main gear oleo arrangement, showing the actuator that varies the damping orifice area between the oleo segments. A control valve is shown in the figure for application in the fully active system.

The transition time delays are properly represented as the nose gear tyres and the individual tyres of the main gear pass over each point on the spatially defined runway profile. The model is capable of inputting individual runway profiles to each of the landing gears, but for this study a single profile is applied at all tyres, i.e. it is assumed that there is no lateral variation of the runway profile. The tyre motion over the runway profile is calculated using a "stylus" model for the tyre radius, which ignores the actual geometry of tyre indentations due to the surface profile.

A range of output parameters is provided from the aircraft model. For this study the normal accelerations at a set of six points distributed along the fuselage are used, plus rigid aircraft motion parameters. Also available are airframe loads and landing gear loads, but the effect of the active landing gear system on these is not assessed. The locations of the fuselage points for normal acceleration outputs are shown in Figure 1. For feedback sensor placement any of the six locations can be selected.

5. RUNWAY MODEL

For the assessment of ride quality the runway model must be capable of representing both random profile distributions and discrete bumps. In each case the profile is stored in a data array with uniform distance between data points and linear interpolation between adjacent points. The data points are the vertical heights of the local runway surface relative to a reference datum. The spacing of the points is sufficient to give an accurate representation of the runway profile.

A random runway surface is generated from a sequence of random numbers with Gaussian probability distribution. This is transformed by Fast Fourier Transform to the frequency domain and filtered to conform to the required runway PSD. The runway spectrum used for this study is that described in Reference 5 for a paved runway and is shown in Figure 3. Superimposed on this ideal PSD is the PSD of the random runway surface generated from the white noise source. Different random profiles can be generated if required, but for the assessment of an active ride control system the same profile has been used for all cases. This is particularly necessary for assessment of peak responses.

The discrete bump model assumed is also taken from Reference 5. The geometric parameters for the single and double bumps considered here are given in Figure 4.

6. SYSTEM DESCRIPTION

The landing gear system configurations considered in the results are:

- The basic aircraft system, with the damping orifice sized for the landing impact case, with no active control.
- A switched damping orifice system in which the nose gear damping orifice area is reduced to a smaller fixed value once the initial landing is complete.
- A nose gear with active damping control in which a reduced damping orifice area is modulated in a feedback control system.
- A fully active nose gear with both active damping control and direct control of the oleo pressure from an external hydraulic supply.

In determining the correct strategy for control of the landing gear, studies of simplified representations are necessary to gain a fundamental insight into the behaviour of actively controlled landing gear. However, to restrict the volume of results presented here only those derived from time response simulations of the full nonlinear aircraft model during ground roll are presented.

6.1 Basic Landing Gear System

The basic nose and main landing gears have static load vs. deflection characteristics as shown in Figure 5. The variation along the stroke is dominated by the oleo gas curve, which has low stiffness at full extension, increasing to maximum as the oleo approaches bottom. To this characteristic must be added the flexibility of the tyres. Stiction and friction forces are important in determining the oleo dynamics, particularly for small forcing amplitudes.

The basic landing gear system uses a passive damping method in both the nose and main gear oleos. Damping is provided by hydraulic fluid flow through an orifice in the oleo between two separate fluid chambers. Each of the basic aircraft oleos has a shaped metering pin passing through the damping orifices to tailor the damping characteristic with stroke. In the nose gear oleo different damping is provided in compression and recoil by a unidirectional flow device. The oleo damping orifice area for the basic aircraft is sized for the

landing impact case. Typical variations of damping coefficient with stroke using this method are shown for nose and main gears in Figure 6.

6.2 Active Damping Control

The proposed active damping control system is designed as a modification of the basic system described above. It dispenses with the metering pin, replacing it with a position controlled servo to provide modulation of the damping orifice area. A block diagram showing the active damping control scheme is given in Figure 7. A damping curve similar to Figure 6 for the basic landing gear cannot be drawn explicitly, because the damping is determined actively, varying with response parameters rather than simply the oleo position.

The control algorithm provides a modulation of the damping orifice size about a datum area to determine the damping characteristic. Limits are set on the minimum and maximum orifice openings. The approach adopted to develop the control law is to modulate the damping force such that it minimises the force acting on the aircraft as a result of irregularities in the runway surface. The controller is arranged to modulate the orifice area proportional to an airframe motion feedback.

Since the damping force opposes the oleo closure velocity the feedback to the damping modulation will be a nonlinear function. For a given sign of aircraft feedback motion the change in damping due to the modulation must act in the same direction. Thus when the oleo closure velocity reverses the sign of the feedback must be reversed. This switching with the sign of the oleo closure velocity is shown in the block diagram of Figure 7. The direction of the switching shown takes account of the sign conventions for the motions.

The model utilises the oleo closure velocity as described above to determine the switching logic for the control law. An alternative to velocity is to use a pressure sensor to sense the pressure difference across the orifice. The orifice area control actuator is modelled as a second order lag, with an allowance for other lags that may be present from digital processing, feedback filters, etc., in a practical system.

6.3 Fully Active System

For the nose gear system the active damping control function and the fully active system can operate in parallel, as shown in the block diagram of Figure 7. The fully active system uses an aircraft response parameter, e.g. fuselage acceleration, as the primary input to drive a flow control valve porting high pressure fluid to the oleo. The schematic diagram of Figure 2 shows how the service flow from the valve is supplied to the lower oleo section, with the hydraulic supply and return connections. The valve is controlled in a position feedback loop and is assumed to be actuated by a separate servo system. It is a single acting system, the return motion being effected by the oleo gas pressure. The oleo itself is effectively an actuator in this configuration.

No assumptions are made about the source of the hydraulic pressure. The valve flow is modelled to be sensitive to the pressure difference across the ports, so that the flow reflects the load being carried by the oleo. A supply pressure of 3000 psi has been used and this is assumed independent of demand. A second order lag is specified to represent the dynamic lag of the valve motion, with an allowance for additional lag due to feedback processes.

7. RESULTS

7.1 Basic Aircraft Response

Figure 8 illustrates the behaviour of the aircraft rolling at 70 ms^{-1} over a runway with the spectrum shown in Figure 3. The rigid body heave and pitching motions of the aircraft are seen to be strongly coupled, and have low damping for this example of a large commercial transport aircraft. The nose landing gear reacts to these motions, whereas the main landing gear is seen to be held by stiction, and only moves a small amount following breakout from this condition. This leads naturally to the idea that improved ride quality may be achieved by using an active control system on the nose gear only. This is confirmed by preliminary results, so the results given here focus on nose gear active control without further consideration of use of the main gear.

Figure 8 also shows the normal accelerations at the six stations along the fuselage shown in Figure 1. These again contain strong evidence of the rigid body pitching and heaving motions as well as the higher frequency structural modes. The relative amplitude of the structural mode response varies along the fuselage. To quantify the merits of the various possible active landing gear systems it is necessary to use spectral analysis and the r.m.s. values of the relevant response parameters. Figure 9 shows the basic aircraft nose acceleration PSD, in comparison with cases with modified damping orifice areas discussed below.

These plots are shown on both logarithmic scales and linear scales. The logarithmic plots are useful in showing more clearly the response of all the modes for the full frequency range. The linear plots identify the individual modes of interest more specifically, and since the r.m.s. is the square root of the area under the PSD plot, this highlights the contribution to the r.m.s. made by each mode. The linear scale plots are limited to 5 Hz, which is sufficient to show the important response peaks for passenger ride quality. The rigid body peak at 0.9 Hz dominates the PSD and is well separated from the 3.6 Hz structural mode peak, which contributes very little to the r.m.s. response. The interpretation of this is covered in more detail below in discussion of the effect of reducing the nose gear oleo damping orifice area.

7.2 Switched Damping Orifice Areas

Since the rigid body mode dominates the response and has low damping, one possible method of improving the system is to reduce the nose gear oleo damping orifice area to increase the damping force. The damping orifice area used in the basic system is fixed by the landing impact requirements and therefore cannot be changed for all phases of runway contact. However, it is possible to switch the damping orifice area to a lower value once the landing impact is complete. Figure 9 shows the PSDs of the normal acceleration at the aircraft nose position for 70 ms^{-1} ground speed with two reduced damping orifice areas in comparison with the basic aircraft case, which is shown in the time response of Figure 8. The two reduced orifice areas show progressively improved PSD values for the rigid body mode at about 0.9 Hz. However, although the rigid body response is reduced the flexible mode at about 3.6 Hz is increased.

Figure 10 draws further attention to the contribution to the r.m.s made by each individual mode by plotting the accumulative r.m.s. with frequency. This is the square root of the integral of the PSD curve of Figure 9 with frequency, showing the build up of the r.m.s. as the frequency range being considered is increased from zero. These curves asymptotically approach the true r.m.s. value as frequency increases, with further slight contributions from the higher frequencies beyond the range shown. The first sharp rise in the curves is due to the rigid body mode and this decreases as the orifice area is reduced. The second rise is due to the first flexible mode and this grows as orifice area is reduced. The size of each rise is compared in Figure 11, where the r.m.s contributions of the rigid and flexible modes are calculated individually and plotted along with the total r.m.s. value as the damping orifice area is progressively reduced. It is evident that whilst the rigid mode response is considerably improved by reducing the orifice area the total r.m.s. is not significantly changed, because the contribution made by the flexible modes is increased.

Since the human body response is sensitive over the frequency range of both the rigid body response and the first fuselage flexible mode the passenger comfort will not show significant improvement and there may also be an increase in structural fatigue by simply reducing the damping orifice area. Thus it is necessary to introduce additional system features which are capable of modulating the nose gear characteristics dependent on the structural response.

7.3 Active Damping Control

The primary reduction in rigid body response has been achieved by reducing the oleo damping orifice area, but this has produced an amplification of the response in the first fuselage structural mode. Now active control of oleo damping is investigated to assess the potential for reducing the structural mode response while maintaining the improvement to the rigid mode.

First the feedback of aircraft pitch rate is considered. Figure 12 shows the PSD plots of normal acceleration at the fuselage nose for pitch rate feedback applied to orifice area modulation. In this case the orifice datum area is 100 mm^2 and the ground speed is 70 ms^{-1}. As the feedback gain is increased the PSD of the structural mode reduces as required, whilst the rigid mode PSD increases. Clearly this feedback will only provide limited modification of the system response. The reason for this is that linking the damping coefficient to the pitch rate has a similar effect to changing the orifice area, since damping force is related to pitch rate for a constant area orifice.

Another candidate parameter for feedback for the active damping control scheme is pitch acceleration. This would ensure that as the forcing of the pitching motion increases, the damping force would increase to oppose it. Figure 13 shows the PSD plot for a system with pitch acceleration feedback, again for a ground speed of 70 ms^{-1}. The effect is seen to be similar to pitch rate feedback, but with a rather lower increase in the PSD of the rigid body mode. Both pitch rate and pitch acceleration feedbacks are not pursued further in the results.

A more satisfactory feedback parameter is the normal acceleration sensed by a fuselage mounted accelerometer. This provides a direct feedback of the response which is to be attenuated. The location of the accelerometer can be chosen to give best performance for control of both the rigid body and structural mode response, although for the results given here the accelerometer is assumed to be located at the nose gear station. Figure 14 shows the PSD of the nose normal acceleration response, for a ground speed of 70 ms^{-1}. In this case the result is that the PSD of the rigid body mode is not significantly affected, but the PSD of the flexible mode is reduced almost to the level of the basic aircraft response case. This result gives a good system performance in terms of improved ride quality at the nose and is used in further evaluation and development in later sections.

7.4 Fully Active System

So far a good result for ride quality improvement has been obtained with reduced orifice area and active damping control of the nose gear. A further improvement to the structural mode PSD may be achieved by incorporating normal acceleration feedback into a fully active system, based on the additional high pressure hydraulic flow supply described in Section 6.3 and shown in Figure 2. The best result obtained in this evaluation of the fully active nose gear is given in Figure 15, which shows that some improvement is possible to both the rigid body and fuselage flexible mode PSDs. The flexible mode response is now back down to the level of the basic aircraft case of Figure 9. To achieve this result requires a system which is significantly more complex than the active damping control system discussed earlier. The additional improvement from the fully active system is marginal and it is therefore taken no further. Subsequent results presented here are restricted to examining the performance of the active damping control system in more detail.

7.5 Active Damping Overall Performance

Figure 14 shows the PSD of the fuselage nose normal acceleration for two feedback gain values. In Figure 16 this result is used to produce plots of accumulative r.m.s., starting from zero frequency, to highlight the improvement in the flexible mode response from the active damping control system. The first sharp rise in the r.m.s. value is from the rigid body response and the second rise is from the first fuselage flexible mode. The contribution of the flexible mode to the r.m.s. value is much reduced when the active damping control system is operating, compared to the system with only damping orifice area reduction. The individual contributions of the two modes are plotted in Figure 17 for varying feedback gain. There are higher frequency modes in the mathematical model that contribute a small amount to the accumulative r.m.s., and for convenience this amount is included with the flexible mode curve. Figure 17 shows that increasing the gain progressively reduces the total r.m.s. value. Most of this improvement is achieved with a feedback gain of 1000 mm^2/g. Nevertheless, it will be seen later that when the response to runway bumps is considered, higher gain values continue to give improvement to the peak responses, so a gain value of 2500 mm^2/g is selected and this has been used for all subsequent results presented here.

So far the results have focused on the PSD responses of fuselage nose normal acceleration during a 70 ms^{-1} ground speed. Now the degree of the ride quality improvement along the length of the passenger cabin from the active damping control system is assessed at the same speed. Figure 18 shows the PSDs of the normal acceleration for the six fuselage stations of Figure 1. The basic aircraft case is shown on all plots for comparison. The response in the rigid body mode is most significant at the fuselage nose and tail due to the aircraft pitching motion, with a minimum in the middle stations just aft of the main landing gear location. The fuselage flexible bending mode shows the same effect, with no visible response in the centre fuselage on these plot scales, as would be expected. The active damping control system reduces the rigid mode response at the nose and tail, with less reduction in the centre stations. The flexible mode response is slightly greater than the basic aircraft case, as in Figure 14.

The PSD results of Figure 18 can be used to generate plots of r.m.s variation along the fuselage for the 70 ms^{-1} ground speed. This is shown in Figure 19, with similar results for another five ground speed cases, from 20 to 85 ms^{-1}. These are all computed in the time domain as described in Section 3 and from these responses Figure 19 is produced, showing the peak normal acceleration responses along the fuselage encountered in the time histories. This form of presentation of the data gives a good summary of the overall performance of the active damping control system, as distributed along the passenger cabin. The maximum peaks and r.m.s. values occur at the fuselage extremities, with and without the active damping control system operating, although the distribution is flatter with the system than without. In some cases, mainly at rear fuselage stations, the peak and r.m.s. values are amplified, and further evaluation of these is required.

The same information contained in Figure 19 can be re-plotted to produce Figure 20, showing the variation with speed of the peak and r.m.s. responses at each fuselage station. This form of presentation shows that the system not only reduces the r.m.s. and peak responses, but also reduces their variation with speed.

7.6 Runway Bump Response Cases

Although passenger ride quality is assessed here by normal acceleration PSD response and r.m.s value it is desirable that the system should improve the response to individual runway bumps of various shapes. Figure 21 shows summary plots of the reduction in peak normal accelerations as the feedback gain is increased for the double bump of Figure 4, traversed at 70 ms^{-1}. The effect at six fuselage stations is shown. The reduction of the peak response continues with increasing gain, and a gain value of about 2500 mm^2/g can be used. Higher gains than this have a tendency to saturate the orifice area modulation system and are therefore undesirable.

Example time histories are shown in Figures 22 and 23. Figure 22 shows the basic system with the nose gear oleo damping orifice sized for the landing impact case traversing the double bump at 70 ms^{-1}. The rigid body motions are excited as expected and exhibit low damping as before. When the active damping control system is operating for the same conditions the system response is improved, as shown in Figure 23. The rigid body damping ratio calculated from the rate of decrease of the peaks is improved from 0.13 to 0.27 by

the active damping control system. The modulation of the damping orifice area about the datum area of 100 mm^2 is also evident on this plot. In fact this shows the system increasing the orifice area during transition of the bumps to values above those of the basic system.

8. RECOMMENDATIONS FOR FURTHER WORK

The results obtained in this study show that benefits in terms of improved ride quality are possible using an active landing gear. Since the system studied includes significant nonlinearities the results have been obtained primarily in the time domain. This has been accomplished using a software package which is intended for detailed analysis of landing gear dynamics. Further study covering the fundamental analysis of the control law presented here and other possible schemes would be beneficial. Additional work is required so that the control system design can be optimised for sensor locations, feedback gains and overall performance objectives. This would include the trade-off between the relative r.m.s. contributions from the rigid body mode and the individual structural mode responses. The higher frequency flexible modes could be brought in if these are important.

The system has been evaluated at a range of speeds, but a full ground envelope investigation is needed covering a wider range of aircraft configurations. The cases where the response has been amplified in some regions of the fuselage needs to be investigated. Of significant interest in further system studies is the effect of the active landing gear on airframe loads and fatigue. It is likely that ride improvement by reducing fuselage accelerations will also benefit loads, but this needs to be verified. Once the design and performance benefits of the system are understood more thoroughly a comprehensive system definition study could be undertaken. The system model could then be refined and the results verified. The robustness of the system to variations in design assumptions should also be assessed.

Landing impact requirements conflict with the active landing gear system for ride quality improvement. Active landing gear control can be applied to the landing case, which would lead to a different system design. Since the two cases do not occur at the same time it could be that a system can be designed that will reduce the landing impact, then by suitable switching logic, reconfigure to a ride improvement mode. The active damping control could also permit the optimisation of energy absorption performance for all landing impact descent velocities.

9. CONCLUSION

An active landing gear system has been investigated that is effective in improving ride quality on the ground by reducing normal accelerations at the rigid body mode and first flexible mode frequencies. This has been achieved by active control of damping in the nose gear oleo. The main improvement to the rigid body response is obtained by reducing the basic damping orifice area, but this increases the response in the first flexible mode. The flexible mode response is restored near to that of the basic aircraft level by the active damping control system.

Fully active control of the nose gear oleo is not required in the example studied here to gain any significant further ride quality improvement, but it can reduce the flexible mode response to a level below that of the basic aircraft case. Other structural vibration modes at higher frequencies are affected by the system, but these have not been considered in the evaluation of the system. They are at fairly low amplitudes and are outside the frequency range normally associated with ride quality.

The performance of the active damping control system has been evaluated for a range of aircraft speeds and for random and discrete bump models of the runway surface. In general the peak and r.m.s. values of normal accelerations at all passenger cabin locations are reduced. There are some regions where the response is slightly amplified and these require further investigation. Overall, however, the system performance is good enough to suggest that useful benefit can be obtained from a relatively simple active control system.

ACKNOWLEDGEMENT

The authors wish to express their thanks to British Aerospace (Airbus) Limited for funding the development of the initial software package used for the work reported here. Special thanks are due to R.H.P. Davies, D.H. Jagger, M.W. Jones and M.A. Laceby of British Aerospace.

REFERENCES

1. McGehee, J.R., Dreher, R.C., "Experimental Investigation of Active Loads Control for Aircraft Landing Gear", NASA TP 2042, August 1982.

2. Freymann, R., "An Active Control Landing Gear for the Alleviation of Aircraft Taxi Ground Loads", Z. Flugwiss. Weltraumforsch, Vol. 11, No. 2, March-April 1987, pp 97-105.

3. International Organization for Standardization, "Guide for the Evaluation of Human Exposure to Whole Body Vibration", ISO 2631-1974(E), July 1974.

4. Shepherd, A., Catt, T., Cowling, D., "The Simulation of Aircraft Landing Gear Dynamics", *in* "18th Congress of the International Council of the Aeronautical Sciences", Beijing, China, September 1992, Paper ICAS-92-1.7.1.

5. Currey, N.S., "Aircraft Landing Gear Design: Principles and Practices", AIAA Education Series, 1988 (ISBN 0930403-41-X), pp 297-301.

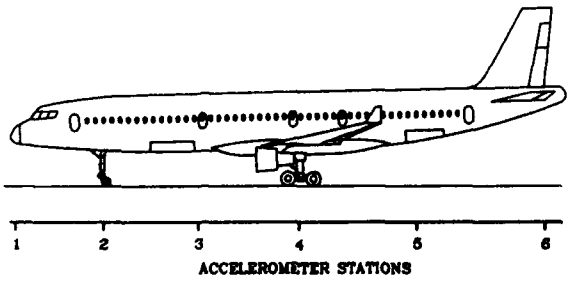

FIG. 1 AIRCRAFT CONFIGURATION AND ACCELERATION OUTPUT LOCATIONS

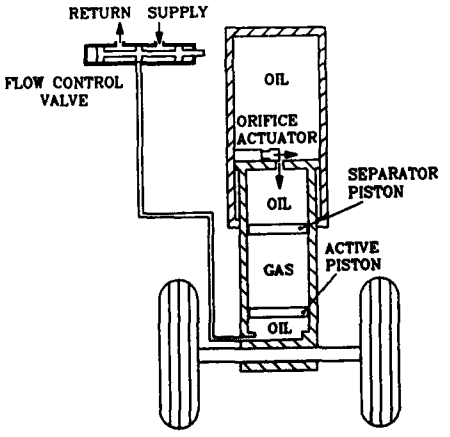

FIG. 2 OLEO ARRANGEMENT WITH ACTIVE SYSTEMS

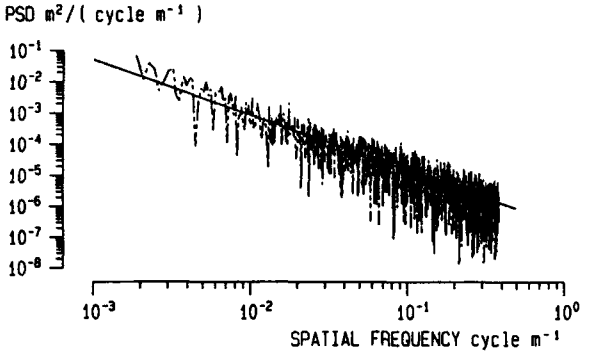

FIG. 3 POWER SPECTRAL DENSITY OF A PAVED RUNWAY

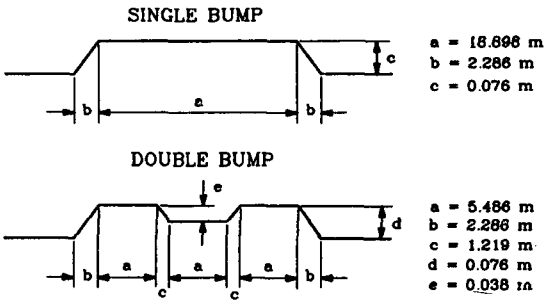

FIG. 4 RUNWAY BUMP PROFILES

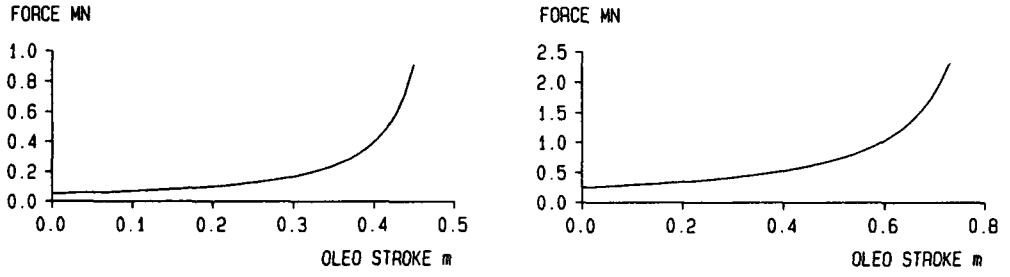

FIG. 5 NOSE AND MAIN GEAR OLEO STATIC FORCE CURVES

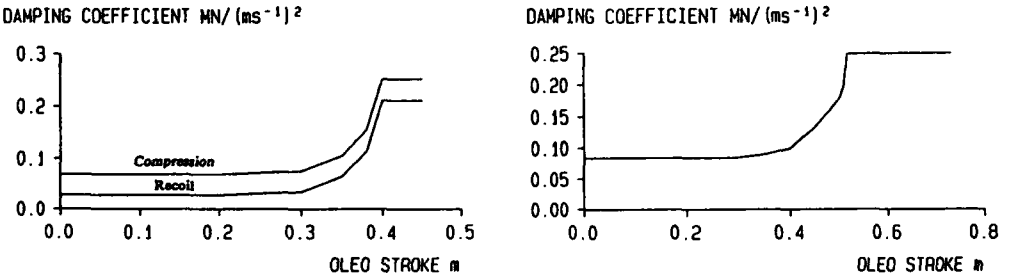

FIG. 6 NOSE AND MAIN GEAR OLEO DAMPING CHARACTERISTICS

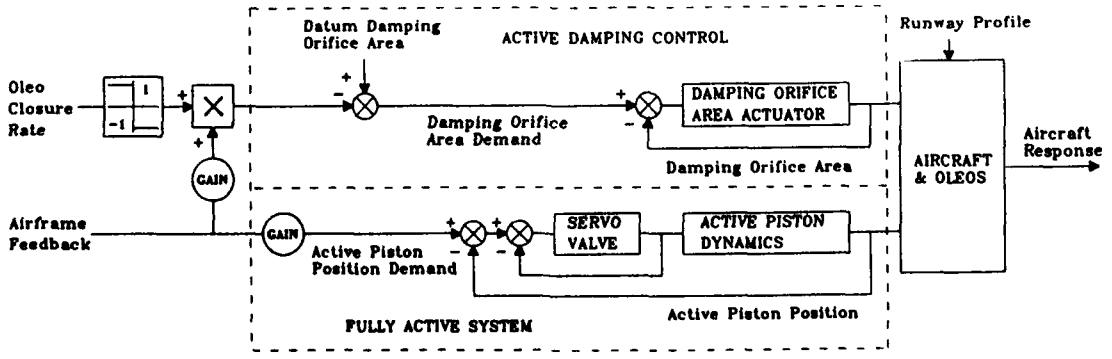

FIG. 7 ACTIVE LANDING GEAR CONTROL SYSTEM BLOCK DIAGRAM

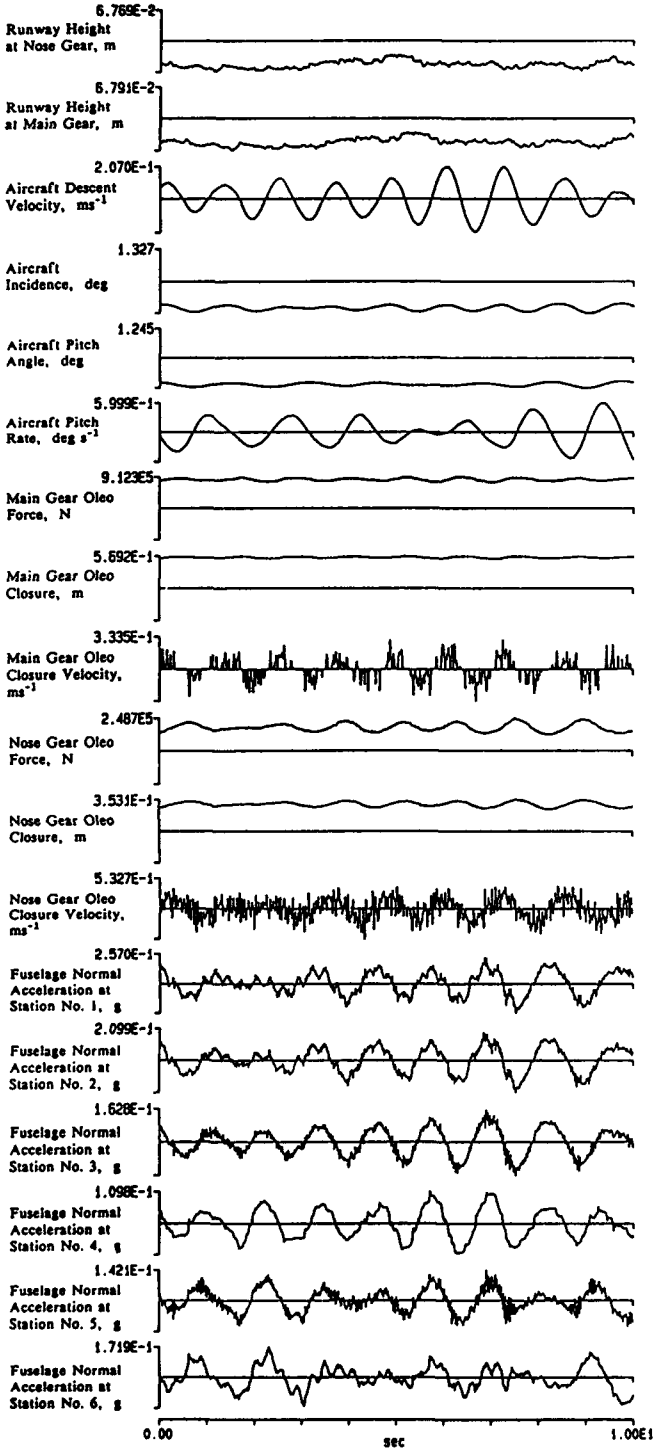

FIG. 8 BASIC AIRCRAFT RESPONSE TO RANDOM RUNWAY, 70 m/s

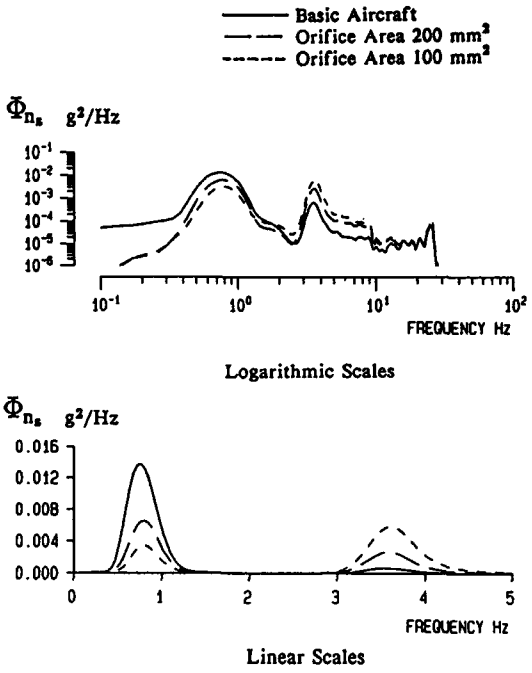

FIG. 9 EFFECT OF REDUCED DAMPING ORIFICE AREA ON PSD OF NOSE ACCELERATION

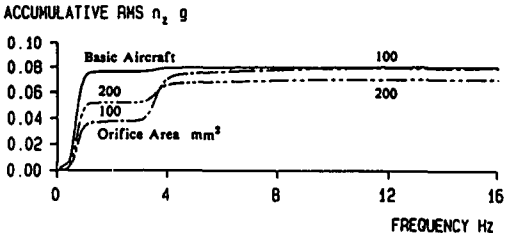

FIG. 10 EFFECT OF DAMPING ORIFICE AREA ON ACCUMULATIVE R.M.S. OF NOSE ACCELERATION

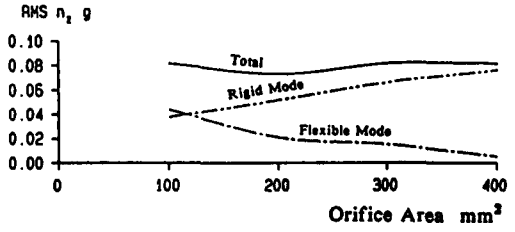

FIG. 11 EFFECT OF DAMPING ORIFICE AREA ON R.M.S. OF NOSE ACCELERATION SHOWING INDIVIDUAL MODE CONTRIBUTIONS

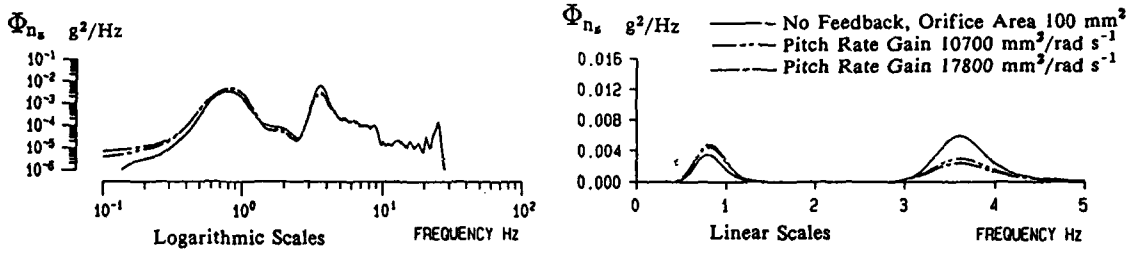

FIG. 12 EFFECT OF PITCH RATE FEEDBACK ON R.M.S. OF NOSE ACCELERATION

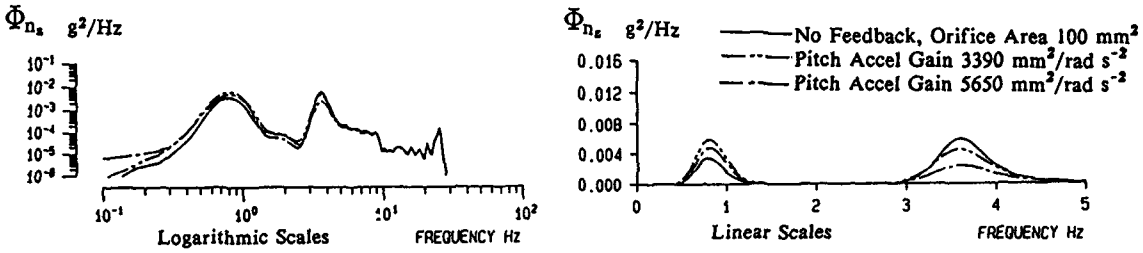

FIG. 13 EFFECT OF PITCH ACCELERATION FEEDBACK ON R.M.S. OF NOSE ACCELERATION

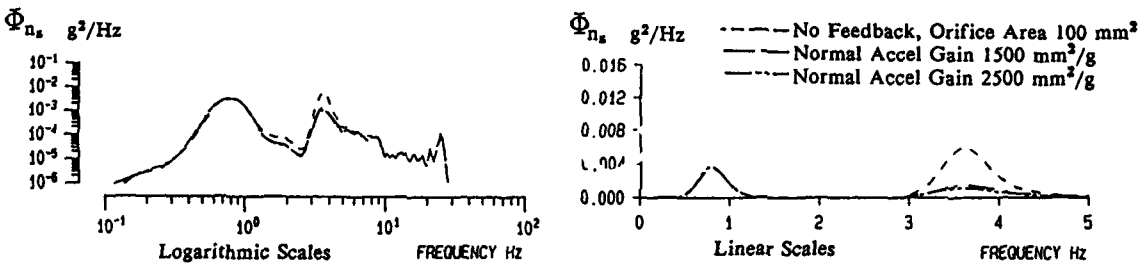

FIG. 14 EFFECT OF NORMAL ACCELERATION FEEDBACK ON R.M.S. OF NOSE ACCELERATION

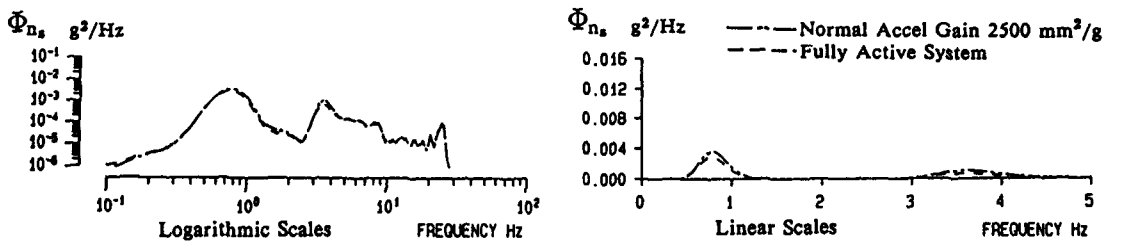

FIG. 15 EFFECT OF FULLY ACTIVE SYSTEM ON R.M.S. OF NOSE ACCELERATION

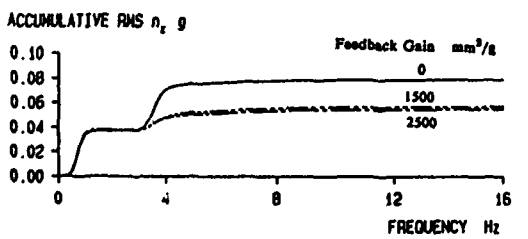

FIG. 16 EFFECT OF ACTIVE DAMPING CONTROL ON ACCUMULATIVE R.M.S. OF NOSE ACCELERATION

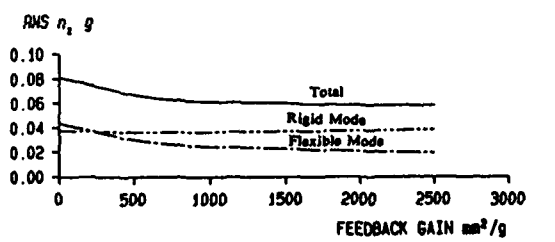

FIG. 17 EFFECT OF ACCELERATION FEEDBACK GAIN ON R.M.S. OF NOSE ACCELERATION SHOWING INDIVIDUAL MODE CONTRIBUTIONS

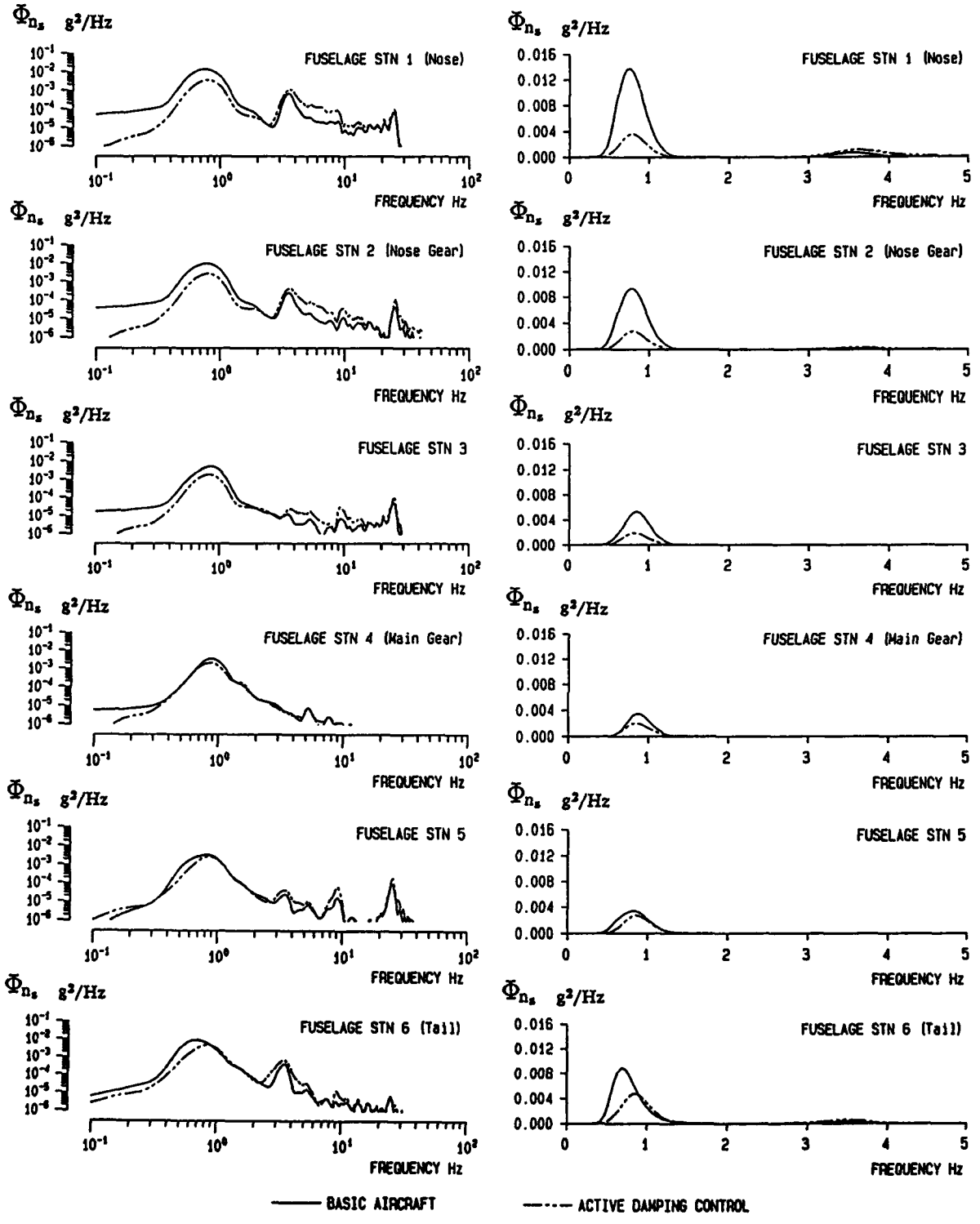

FIG. 18 PSD VARIATION ALONG FUSELAGE SHOWING COMPARISON WITH BASIC AIRCRAFT CASE

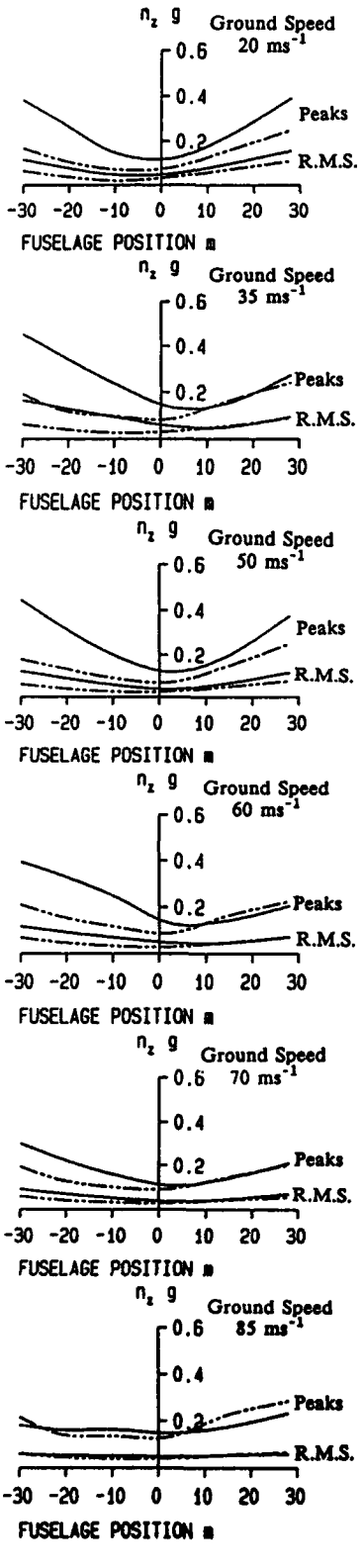

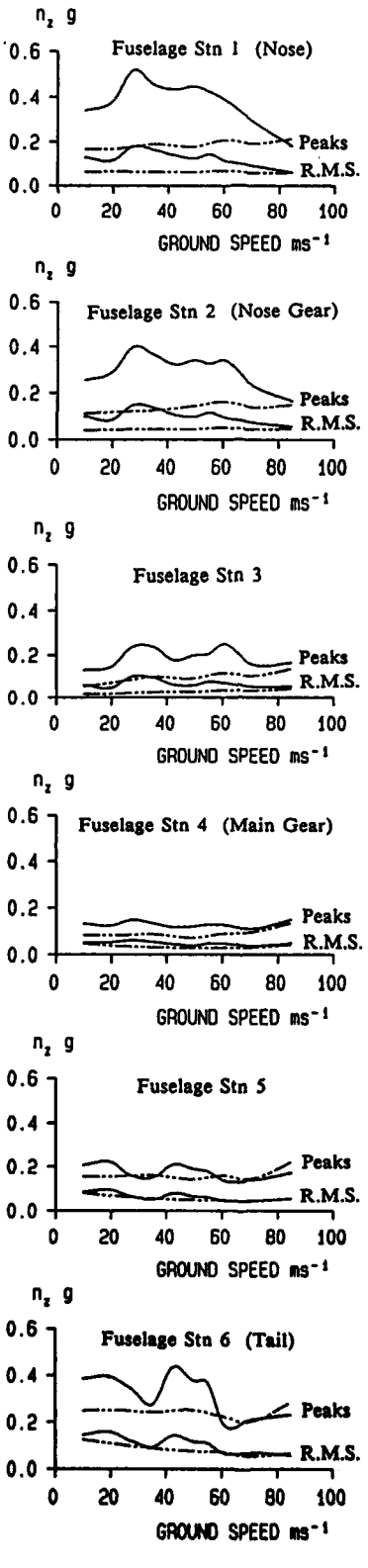

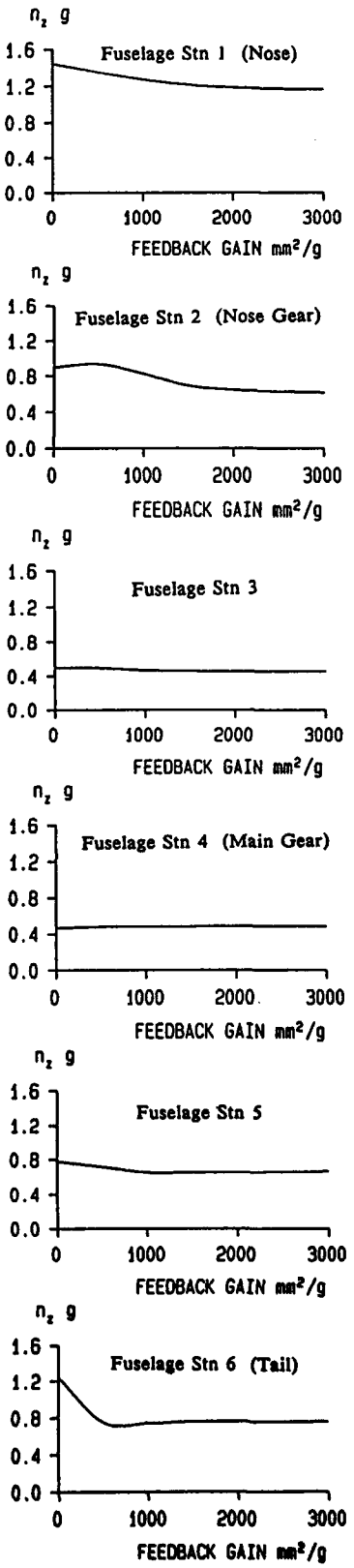

——— BASIC AIRCRAFT ——·—·— ACTIVE DAMPING CONTROL

FIG. 19
PEAK AND R.M.S. RESPONSE DISTRIBUTION ALONG FUSELAGE FOR DIFFERENT SPEEDS

FIG. 20
PEAK AND R.M.S. RESPONSE VARIATION WITH SPEED FOR DIFFERENT FUSELAGE LOCATIONS

FIG. 21
EFFECT OF FEEDBACK GAIN ON PEAK RESPONSES TO RUNWAY BUMPS FOR DIFFERENT FUSELAGE LOCATIONS

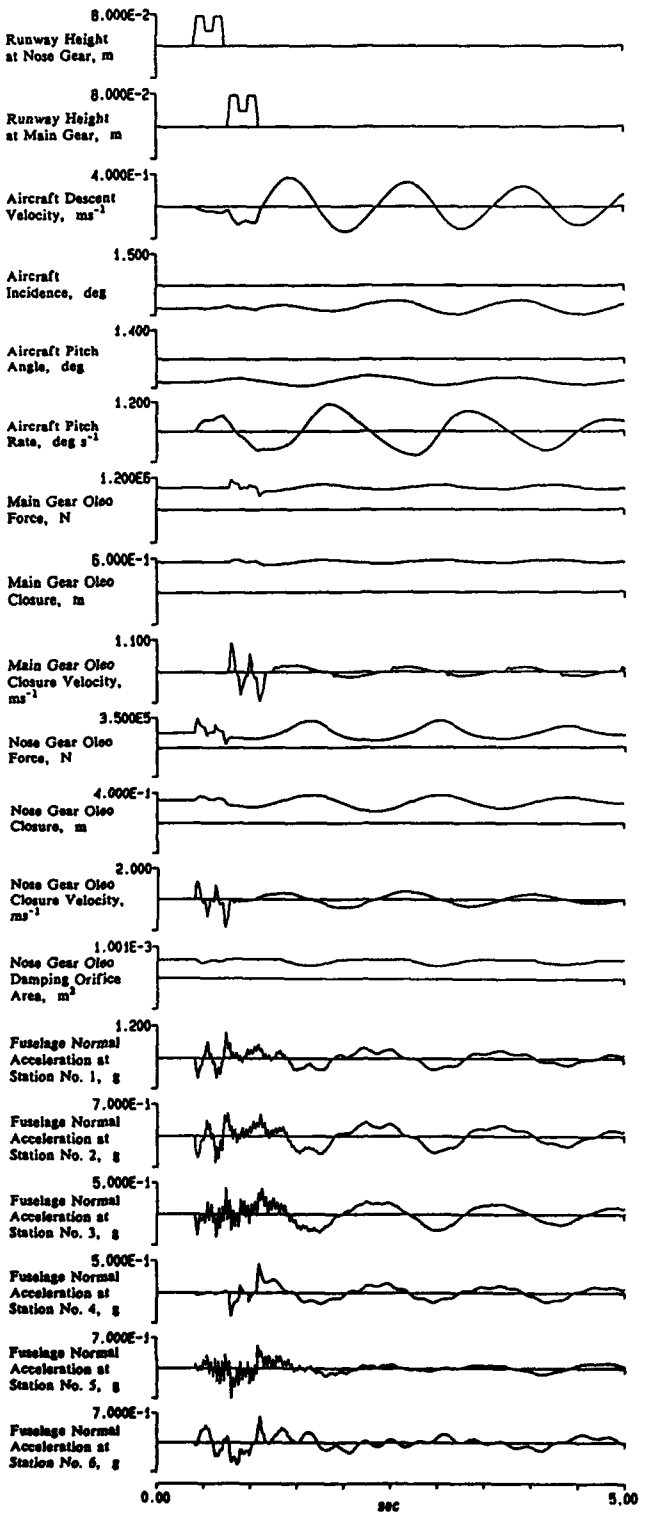

FIG. 22 RESPONSE TO RUNWAY DOUBLE BUMP OF BASIC AIRCRAFT

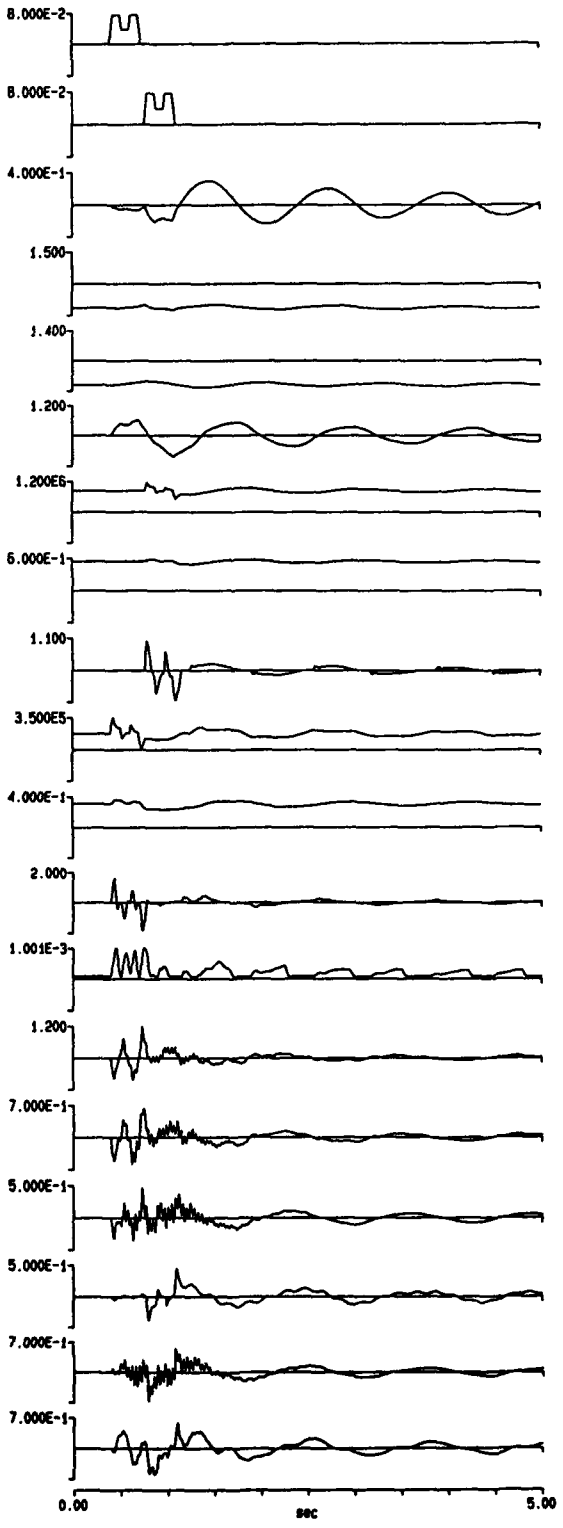

FIG. 23 RESPONSE TO RUNWAY DOUBLE BUMP WITH ACTIVE DAMPING CONTROL

ACTIVE DAMPING AUGMENTATION OF ELASTOMECHANICAL SYSTEMS USING PIEZOELECTRIC SENSORS AND ACTUATORS

by

Raymond Freymann and **Edmond Stümper**
Institut Supérieur de Technologie (IST)
6 rue Coudenhove-Kalergi
L-1359 Luxembourg
Grand-Duchy of Luxembourg

Summary

It will be shown in how far use can be made of piezoelectric elements, integrated as sensors and actuators in a closed control loop, to improve the modal damping behavior of elastomechanical systems. Focus will be pointed on some special characteristics of piezoelectric elements, such as their dynamic behavior, their energy transfer capabilities when being used as actuators and their geometric filtering possibilities when being used as sensors. The experimental part of the work will concentrate on the active damping augmentation in the low frequency range of a flexible beam-shaped structural system with a total length of 4 meters.

1. Introduction

It is a well known fact that large space structures ,due to their inherent low stiffness and damping properties, tend to execute hardly damped structural vibrations in the very low frequency range once the platform has been excited, e.g. by the firing of an attitude positioning engine. These vibrations may adversely affect the operability of a variety of systems integrated in the space structure. This fact calls for the implementation of additional stability augmentation systems in order to guarantee the satisfactory operation of the space platform at any time.

According to this task a noticable research effort has been placed during the last few years in the development of damping augmentation systems for space structures [1]. One very promising way to increase the structural stability consists in actively damping the elastomechanical system by the forces generated from piezoelectric elements, used as actuators in a closed control loop. The feasability of damping augmentation on the basis of piezoelectric actuating elements has already been demonstrated by the experimental results from the publications [2,3] , which appeared in 1979 and 1981, respectively. But the real boost was only given lately to the piezoelectric technology by some of the major space programs (e.g. SDI and space station) calling for enormously challenging requirements with regard to their pointing, shape control and microgravity capabilities. The increasing number of recent publications in this technological area clearly indicate the thus related problems and the progress achieved [4, 5, 6, 7].

It is the aim of this paper to add some new experiences and ideas to the framework already existing in this technical field. Thereby two main topics will be addressed. In a first part a detailed description of some special properties of piezoelectric elements will be given. Focus will be pointed on their force-strain characteristics, their adaptation to the elastomechanical structure to be controlled in order to allow for optimum energy transfer capabilities and finally their geometric filtering possibilities affected by the geometric shaping of the elements and their correct location on the basic structural system. The second part will concentrate on the tests performed on an actively controlled beam-shaped structure with a total length of 4 meters and a mass of 2 kg. It will be shown in how far modal damping augmentation could be achieved in the two fundamental bending eigenmodes of the structure with eigenfrequencies at 1.44 and 8.60 Hz by making use of an overall number of 35 piezoceramic transducers as actuators and two piezo-polymer elements (PVDF) as sensors.

This work was performed at the Institut Supérieur de Technologie in Luxembourg and financially supported by the Ministère de l'Education Nationale of Luxembourg under project No. MEN/IST/87/002.

2. List of symbols

A	m^2	cross sectional area
B	m	height of a beam
C	F	capacitance
D	m	width of a beam
D_r	kg m^2/s	modal damping factor
D_r^*	kg m^2/s	additional modal damping induced by the active damping augmentation system
E	N/m^2	modulus of elasticity
F	N	force
H, H^*		transfer behavior of an electronic compensation network
I	m^4	bending moment of inertia
K_r	kg m^2/s^2	generalized stiffness
L	m	length of a beam
M_r	kg m^2	generalized mass
Q	C	electrical charge
Q_r	kg m^2/s^2	generalized force
U	V	voltage
W	N m	energy
Y_1, Y_2, Y_3, Y_4		constant
b	m	width of a piezo-element
d	m	thickness of a piezo-element
d_{31}	m/V	piezo-constant
e	m	distance from the neutral axis
f	Hz	frequency
f_C		corner frequency
i	A	electric current
j		imaginary unit $\equiv \sqrt{-1}$
k	N m^2	amplification factor
k_{ACT}	N/V	actuator sensitivity
k_{SEN}	V m	sensor sensitivity
$\tilde{k}_{SEN}$	V/m	sensor sensitivity per unit area
l	m	length of a piezo-element
Δl	m	elongation
$\tilde{m}$	kg/m	mass per unit length
q_r		generalized coordinate
s	l/s	Laplace variable
t	s	time
w_0	m	normalized deformation
x	m	translatory coordinate
ε		strain

ω	1/s	circular eigenfrequency
Φ_r		eigenmode

Subscripts and abbreviations

$( )_{ACT}$	related to the actuator (system)
$( )_H$	related to the intersection point
$( )_{SEN}$	related to the sensor
$( )_b$	related to the beam structure
$( )_p$	related to the piezo-element
$( )_r$	related to the r-th eigenmode
$( )_{max}$	*maximum* value of
d/dt	derivative with respect to the time
$( )''$	second derivative with respect to a geometrical coordinate

3. Characteristics of piezoelectric transducers

The most commonly used materials for piezo-transducers are

* lead-zirkonate-titanate (PZT),
* barium-titanate ($BaTiO_3$),
* quartz,
* polivinylidene fluorid (PVDF).

Typical sizes of ceramic transducers, which can be supplied by different manufacturers, range from 0,5 mm * 0,5mm * 0,2 mm to 110 mm * 110 mm * 60 mm. Thin layer PVDF transducers can be provided in very different sizes ranging from 40 mm * 15 mm * 28 µm to 300 mm width on a continuous roll of "endless" length with a film thickness of 110 µm.

3.1 Basic equations

According to [8], the following equations can be formulated for piezoelectric plate systems, if the transversal piezo-effect, with elongations vertical to the direction of the (applied) electrical field (Fig. 1), is to be considered:

$$(1) \qquad Q = CU + d_{31}\frac{l}{d}\cdot F \ ,$$

$$(2) \qquad \varepsilon = \frac{\Delta l}{l} = -d_{31}\cdot\frac{1}{d}\cdot U - \frac{1}{b\cdot d\cdot E_p}\cdot F \ ,$$

with C as the capacitance of the piezo-transducer, the voltage U between the electrodes and the electrical charge Q, F as the force produced by the piezo-element with length l, width b and the material elasticity modulus E_p, ε denotes the strain and d_{31} the piezo-constant, which generally is of negative value.

In Eqs. (1) and (2) ε is positive in case of an elongation of the transducer, F is positive when a pressure force is exerted by the element and U is positive for an electrical field which is oriented to the grounded electrode.

From Eq. (2) it follows that the maximum values obtainable with regard to the force F and the strain ε for a defined voltage U are:

$$(3) \qquad F_{max}(U) = (F)_{\varepsilon=0} = -b\,E_p\,d_{31}\,U \ ,$$

$$(4) \qquad \varepsilon_{max}(U) = (\varepsilon)_{F=0} = -d_{31}\frac{1}{d}U \ .$$

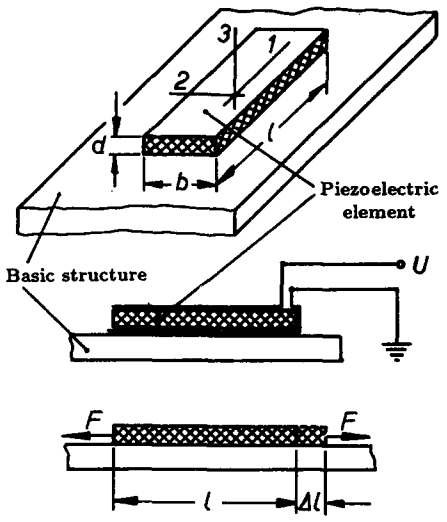

Fig. 1: Piezoelectric transducer

Since piezo-transducers consist out of electrically polarized materials, the electrical field applied to the elements must always be oriented in the direction of the polarization, else depolarization could occur with the effect of a degradation in the transducer properties. This entails that high voltages should only be applied in the negative voltage direction, positive voltages must be avoided at any time. Accordingly, the dynamic operation of the piezo-transducer requires the dynamic voltage to be biased by a negative offset voltage.

Eqs. (2,3,4) were validated by experimental investigations performed on different types of piezo-transducers. A fairly linear force-strain behavior for a given input voltage U as well as a linear behavior of F_{max} and ε_{max} as a function of the input voltage were determined (Fig. 2). However it has to be mentioned that this linear behavior could only be produced in the case of negative input voltages. For electrical fields applied which were oriented in the opposite direction of the polarization (positive input voltages), a nonlinear behavior of the piezo-element was experimentally detected. As a result of these investigations, Table 1 depicts some characteristic values of different piezo-materials.

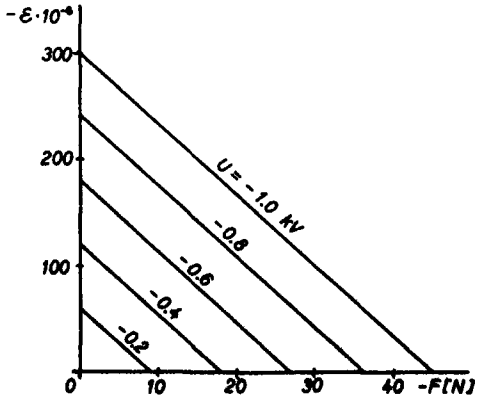

Fig. 2: Force-strain characteristics of a piezoelectric transducer

		PZT	$BaTiO_3$	PVDF
d_{31}	[m/V]	$-130 \cdot 10^{-12}$	$-45 \cdot 10^{-12}$	$-20 \cdot 10^{-12}$
E_P	[N/m²]	$8.2 \cdot 10^{10}$	$12 \cdot 7 \cdot 10^{10}$	$0.2 \cdot 10^{10}$
F_{max} 1)	[N]	33,6	18,1	2,3 3)
ε_{max} 2)		$260 \cdot 10^{-6}$	$90 \cdot 10^{-6}$	$720 \cdot 10^{-6}$
ρ	[kg/m³]	$7.55 \cdot 10^{3}$	$5.70 \cdot 10^{3}$	$1.75 \cdot 10^{3}$

1) piezo-element with b=3,2 mm at U=1 kV
2) piezo-element with d=0,5 mm at U=1 kV
3) multi-layer film with an equivalent thickness of 0,5 mm at U=1 kV

Table 1: Typical data of piezoelectric transducers

3.2 Frequency response behavior of piezoelectric transducers

Each change in the length of a piezo-electric transducer is coupled to an electrical charge exchange inducing a current i. Operating a piezoelectric element as an actuator thus entails that the high voltage power source, which is used to drive the transducer, must deliver a considerable electrical current if the piezo-element is actuated in the higher frequency range. Since this current is limited in practice it follows that the performance of the actuator will be reduced whenever a current i, exceeding the limit current i_{max}, is required.

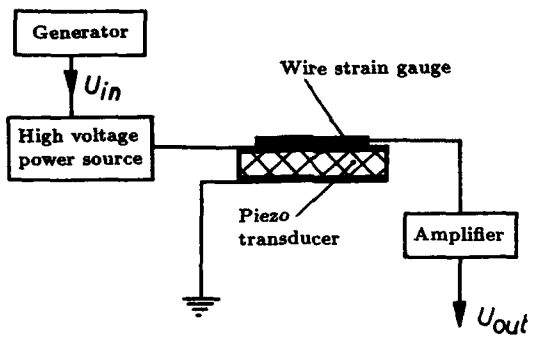

Fig. 3: Experimental determination of the strain of an unmounted piezo-transducer

This effect can easily be explained when considering an unmounted piezo-transducer, operated as shown in Fig. 3. From Eq. (1) we can deduce with $F \approx 0$:

$$(5) \qquad i = dQ / dt = C \cdot dU / dt \ .$$

This relation can be rewritten in the frequency domain as follows:

$$(6) \qquad i_0 = j \omega C U_0 \ ,$$

the index 0 characterizing the amplitude levels of the respective quantities. This Eq. shows that the current i is directly proportional to the capacitance of the transducer and the driving frequency. Moreover it follows from Eq. (2) with consideration of Eq. (6):

$$(7) \qquad \varepsilon_0 = -d_{31} \cdot d \cdot \frac{i_0}{j \omega C} \ ,$$

which indicates, as is also shown in Fig. 4, that the realizable values for the strain will drop by a rate of -6 dB/oct. if a

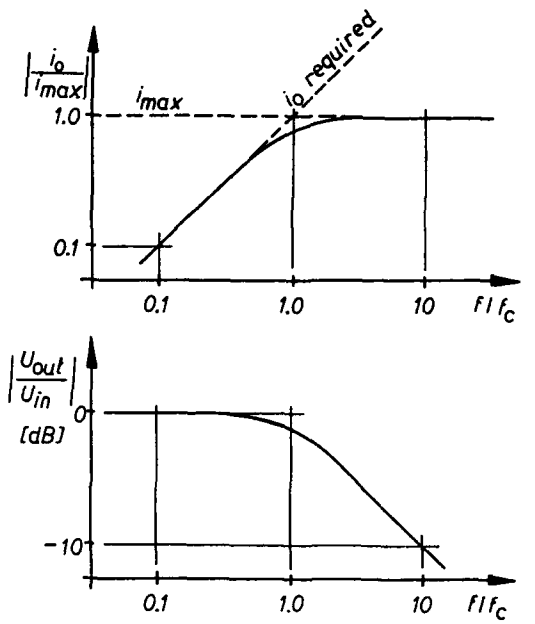

Fig. 4: Frequency response of a piezo-actuator

critical frequency f_c, at which the limit current i_{max} is reached, is exceeded. Accordingly, if a transducer has to be operated in the higher frequency range, it is of importance to select an element with a low capacitance in order to reach a correspondingly high value of f_c.

3.3 Adaptation of the piezoelectric actuator for optimized energy transfer capabilities

There is no doubt that if a piezo-element is used as an actuating device, the transducer is supposed to transfer a "considerable" amount of energy to or from the actuated structure. As will be shown, this requirement entails a thorough adaptation of the actuating system to the elastomechanical properties of the basic structural system.

The following simple reflections give an indication of the problem encountered. The energy W, transfered by the transducer to the basic structure along its elongation Δl, can be written as

$$(8) \qquad W = \int_0^{\Delta l} F \cdot dl \ .$$

If the piezo-element is glued on a "soft" structure, so that its extensional behavior approaches that of an unmounted, no force creating element, than the energy transfered will be nearly zero. This also applies to a transducer fitted to a "hard" structure, since even with the assumption of a high force level obtainable, the energy produced will be small due to the vanishing elongations.

To quantify the expressions of "hard" and "soft" the following experiment is performed. A piezo-transducer is glued on a bar, as shown in Fig. 5 . The forces F created by the element can be reduced to an equivalent loading set F´ and M, with $F = F'$ and $M = F \cdot e$, e being the distance from the median plane of the transducer to the elastic axis of the bar.

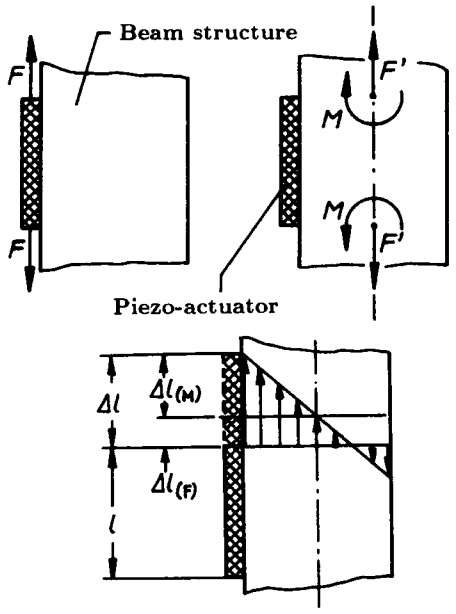

Fig. 5: Forces induced in a structure by a piezo-actuator

The bar, being subjected to the specified loading, will be deformed, thus entailing an elongation Δl of the piezo-transducer which can be formulated as

$$(9) \qquad \Delta l = (\Delta l)_{F'} + (\Delta l)_M \ .$$

In Eq. (9)

$$(10) \qquad (\Delta l)_{F'} = \frac{l}{E_b \cdot A_b} \cdot F$$

denotes the elongation due to the pair of forces F' and

$$(11) \qquad (\Delta l)_M = \frac{l \cdot e^2}{E_b \cdot I_b} \cdot F$$

the corresponding value related to the bending moment M. Assuming a bar with a solid section of height D and width B, we can write: $I_b = 1/12 \cdot B \cdot D^3$ and $A_b = B \cdot D$. Furthermore, if for the sake of simplification we put $e = D/2$, Eq. (9) yields:

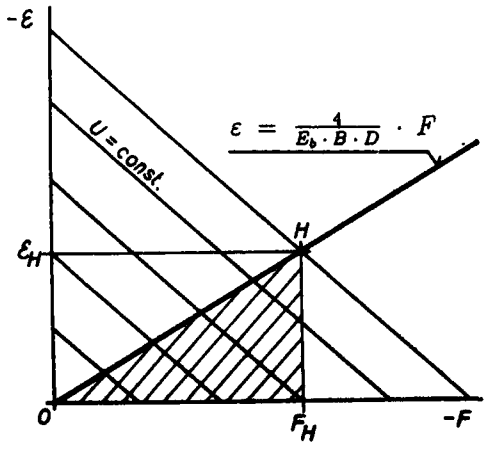

Fig. 6: Energy transfered by a piezo-actuator

$$(12) \qquad \Delta l = \frac{4 \cdot l}{E_b \cdot B \cdot D} \cdot F$$

or

$$(13) \qquad \varepsilon = \frac{4}{E_b \cdot B \cdot D} \cdot F \ .$$

Plotting the relation existing between ε and F, according to Eq. (13), in an ε/F-plot of transducer characteristics, as shown in Fig. 6, finally explains the situation. If a voltage is supplied to the piezo-transducer, its strain and force levels will be "adjusted" according to the ε/F-characteristic of the bar.

Accordingly a highest possible amount of energy

$$(14) \qquad W = \int_0^{\Delta l} F \cdot dl = l \cdot \int_0^{\varepsilon_H} F \cdot d\varepsilon = l \int_0^{\varepsilon_H} F_H / \varepsilon_H \cdot \varepsilon \cdot d\varepsilon = l/2 \cdot F_H \cdot \varepsilon_H$$

can be transfered by the transducer if the area of the triangle O-H-F_H, depicted in Fig. 6, is maximized. This situation is realized if the point of intersection H corresponds to the central point of the $\varepsilon_{max}/F_{max}$-line under consideration. Depending upon the structural parameters of the bar, or of the elasto-mechanical structure to be controlled, there may result a quite "powerful" actuating element from the requirements mentioned above. Practically this actuator can be realized or by one single "big" piezoceramic element (with sizes ranging up to 110 mm * 110 mm * 60 mm) or by a set of "smaller" piezo-elements, connected to one another in a parallel circuit, to form an actuating system.

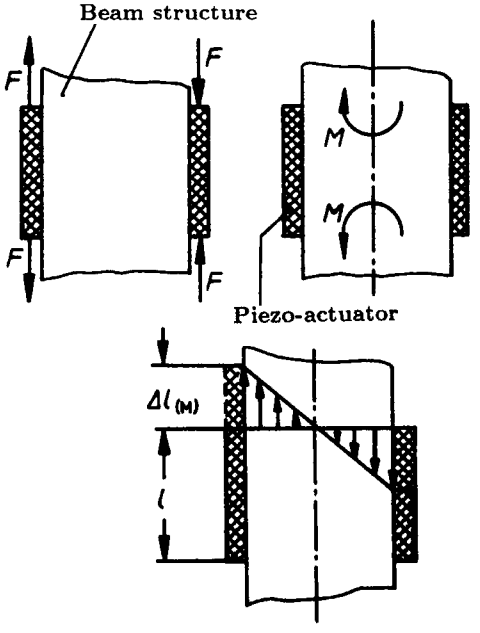

Fig. 7: Forces induced in a structure by a pair of oppositely activated actuators

Remark:
In the case where a pair of piezo-elements is fixed to both sides of the bar, as depicted in Fig. 7, thus creating a pure bending moment in the structure, the ε/F-characteristic of the bar changes - in comparison to Eq. (13) - to

$$(15) \quad \varepsilon = \frac{6}{E_b \cdot B \cdot D} \cdot F \quad .$$

This example demonstrates the importance of a thorough consideration of the arrangement of the actuating piezo-elements in all investigations in order to allow for an optimum "tuning" of the actuator configuration with regard to advantageous energy transfer capabilities.

3.4 Geometric filtering

According to Eq. (14), a piezoelectric actuator can only transfer a significant amount of energy to a structural system if both the actuator force as well as the local deformation (strain) at the actuator location are high enough. In the case of modal structural vibrations, we will find along a continuous structure areas with a minimum and a maximum of local deformations. Placing the actuators in areas of maximum local deformations will allow for a favorable energy transfer behavior whereas the location of actuators in areas of minimum local deformation will minimize the energy transfer from the actuators to the basic structure.

Accordingly, placing the piezoelectric elements in areas with a high local deformation in one particular eigenmode and a low deformation level in "other" modes does allow an efficient modal control of this particular mode under consideration with the further effect of "not disturbing" the dynamic response in the other modes. This approach of modal filtering is well known and has already been used in other applications [9].

It is evident that the reasoning, outlined above for the case of actuator systems, also applies to sensor elements. But beyond this rather simple geometric filtering technique, the piezo-technology offers further modal filtering possibilities, especially when piezo-polymer elements are used as sensor systems.

As was already mentioned, PVDF elements are available at any arbitrary length. Accordingly, they may not only be used as "point sensors" but also as "area sensors" covering a noticable portion of the structure to be controlled. As will be shown in the following, area sensors do offer further more sophisticated possibilities to achieve modal filtering characteristics.

Lets start from a beam shaped structure, hinged at both of its ends to a support, as depicted in Fig. 8. Its free vibrations (eigenmodes) can be formulated in the form

$$(16) \quad \Phi_r(x) = w_0 \cdot \sin r\Pi \frac{x}{L} \quad , (r = 1, 2, ..., N) \quad .$$

This leads to the following expressior for the curvature (strain):

$$(17) \quad \Phi_r''(x) = -w_0 \left[\frac{r \cdot \Pi}{L}\right]^2 \sin r\Pi \frac{x}{L}$$
$$= w_0'' \sin r\Pi \frac{x}{L} \quad .$$

Using a PVDF sensor with width b, length l << L and a sensitivity $\bar{k}_{SEN}$ per unit area, we get the following output voltage U from the sensor element if the sensor is fixed to the bar at x = L/2:

$$(18) \quad U_r = \bar{k}_{SEN} \cdot b \cdot l \cdot w_0'' \{\sin r \cdot \Pi/2\} \quad .$$

The expression in parantheses gives an indication of the relative modal feedback signal created by the sensor element in the different eigenmodes (r = 1, 2, ..., N). From Eq. (18) it follows:

$$U_1 = 1, U_2 = 0, U_3 = -1, U_4 = 0, U_5 = 1, \ldots .$$

This example indicates that, due to the positioning of the "point sensor" element at the particular location x = L/2, all feedback signals in modes with pair numbers (r = 2, 4, 6, ...) are nullified.

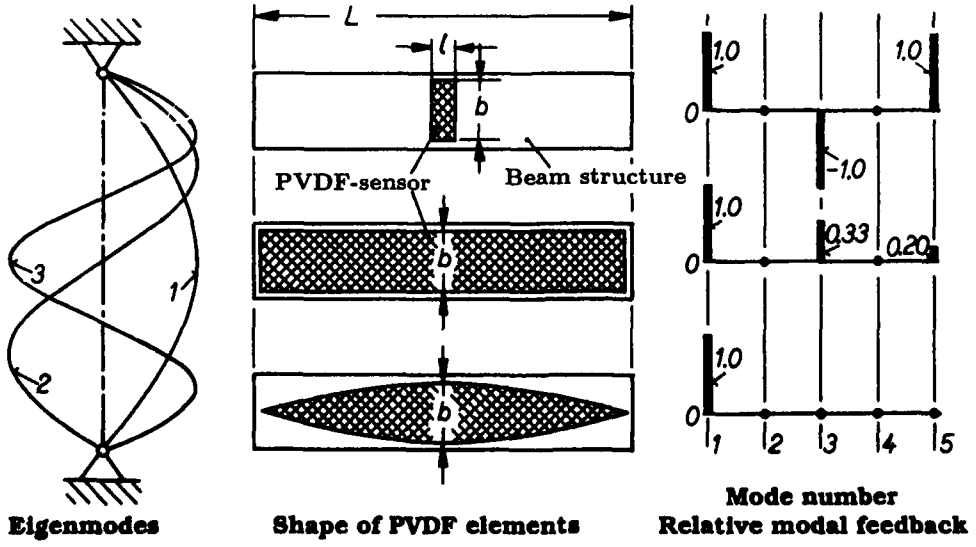

Fig. 8: Modal feedback created by "point" and "area" sensors

If an "area PVDF sensor" with width b and length L is now fixed to the structure, thus a rectangular shaped sensor element covering the whole length of the bar, we get the following modal output from the sensor:

$$(19a)\quad U_r = \bar{k}_{SEN} \cdot b \cdot w_0'' \int_0^L \sin r\Pi \frac{x}{L}\, dx$$

$$= \bar{k}_{SEN} \cdot 2/\Pi \cdot bLw_0'' \{\frac{1}{2r}(1 - \cos r\Pi)\} \quad .$$

Again the term enclosed in parantheses gives an indication of the relative modal feedback signals which are as follows:

$U_1 = 1,\ U_2 = 0,\ U_3 = 0.333,\ U_4 = 0,\ U_5 = 0.200, \ldots .$

This result clearly shows, that the "area sensor" lowers the feedback signal in the higher eigenmodes when compared to the "point sensor". Thus, in a real control system, the PVDF sensor element, covering the whole length of the beam shaped structure, will finally act as a low-pass filtering element.

These filtering characteristics can be further pronounced if a sensor element with variable width b = b(x) over its total length is considered . For a sinusoidally shaped PVDF element of length L, as shown in Fig. 8, we can write in analogy to Eq. (19 a):

$$(19b)\quad U_r = \bar{k}_{SEN} \cdot w_0'' \int_0^L b \sin\Pi\frac{x}{L} \cdot \sin r\Pi\frac{x}{L} \cdot dx$$

$$= \begin{cases} \bar{k}_{SEN} \cdot 1/2 \cdot bLw_0'' \cdot \{1\} & \text{for } r = 1, \\ \bar{k}_{SEN} \cdot 1/2 \cdot bLw_0'' \left\{\dfrac{\sin(\Pi - r\Pi)}{1 - r} - \dfrac{\sin(\Pi + r\Pi)}{1 + r}\right\} & \text{for } r > 1. \end{cases}$$

From Eq. (19b) we get the following values of relative modal feedback:

$U_1 = 1,\ U_2 = 0,\ U_3 = 0, \ldots\ U_r = 0, \ldots .$

Thus just a feedback signal in the first eigenmode is created by this specially shaped "area sensor", entailing that all the other eigenmodes will not be "disturbed".

This simple example clearly indicates just a few of the many possibilities offered by PVDF sensor elements to create filtering characteristics.

Having analyzed the basic properties of piezoelectric transducers, focus will now be pointed on the dynamic behavior of active-controlled structures.

4. Generalized equations of motion of active-controlled structures

According to [10, 11], the generalized equations of motion of flexible structural systems can be formulated as a set of N uncoupled equations of the form

$$(20)\quad M_r \ddot{q}_r(t) + D_r \dot{q}_r(t) + K_r(t)\, q_r(t) = Q_r(t) \quad , \qquad (r = 1, 2, \ldots, N),$$

with M_r, D_r, K_r denoting the generalized mass, the modal damping and the generalized stiffness of the r-th modal degree-of-freedom, respectively, q_r being the corresponding, generalized coordinate and Q_r the gerneralized external force.

Transforming Eq. (20) from the time to the frequency domain leads to

$$(21)\quad (-\omega^2 M_r + j\,\omega D_r + K_r)\, q_r = Q_r \quad , \qquad (r = 1, 2, \ldots, N).$$

For the sake of simplicity only a single actuator and a single sensor system, being formed by piezoelectric transducers attached to a beam structure (Fig.9), will be considered in the following. According to [11], the generalized force Q_r produced by the piezoelectric actuating system can be written as

$$(22)\quad Q_r = F \cdot e \cdot \Phi''_{r,ACT} \quad ,$$

F denoting the force induced by the piezoelectric actuator system and $\Phi''_{r,ACT}$ the curvature of the beam in the r-th eigenmode at the location of the actuator.

Moreover, the following equations can be formulated to describe the transfer behavior of the feedback circuit:

$$(23)\quad U_{SEN} = k_{SEN} \cdot \sum_{s=1}^{N} \Phi''_{s,SEN} \cdot q_s \quad ,$$

the sensor output voltage is proportional to the curvature of the beam at the location of the sensor,

$$(24)\quad F = k_{ACT} \cdot U_{ACT} \quad ,$$

the actuator force produced is proportional to the transducer input voltage, and

$$(25)\quad U_{ACT} = H \cdot U_{SEN} \quad ,$$

which defines the transfer characteristic of the electronic compensation network H.

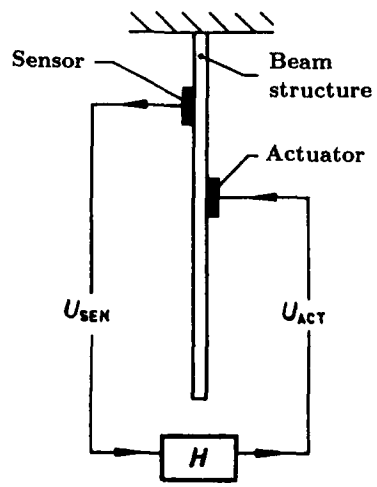

Fig. 9: Shematic control system layout

Introducing Eqs. (22) to (25) into Eq. (21) finally yields the following set of equations of motion in case of the active-controlled structure:

$$(26)\quad (-\omega^2 M_r + j\,\omega\, D_r + K_r - kH\,\Phi''_{r,ACT}\,\Phi''_{r,SEN})\cdot q_r - k\,H\,\Phi''_{r,ACT}\sum_{\substack{s=1\\ s\neq r}}^{N}\Phi''_{s,SEN}\cdot q_s = 0, \qquad (r = 1,2,\ldots,N),$$

with

$$(27)\quad k = e\,k_{ACT}\,k_{SEN}\ .$$

In the next chapter focus will be pointed on the layout of the active control system with regard to the creation of damping forces.

5. Control strategy

The aim to be followed consists in the active damping of so-called "critical" eigenmodes. From Eq. (26) it can be deduced that a practicable possibility to improve the modal damping behavior of an r-th critical eigenmode consists in

a) achieving a transfer behavior H^* of the feedback compensation network according to

$$(28)\quad H^* = -\,j\,H/\omega$$

b) to place the sensor/actuator pair at positions characterized by

$$(29)\quad \begin{cases} \Phi''_{r,ACT}\ \Phi''_{r,SEN} \dashrightarrow Maximum \\ \Phi''_{r,ACT}\ \Phi''_{s,SEN} \dashrightarrow 0 \end{cases}$$

Assuming that this can be realized, Eq. (26) can be reformulated as

$$(30)\quad [-\omega^2 M_r + j\,\omega\,(D_r + D_r^*) + K_r]\cdot q_r = 0,$$

with

$$(31)\quad D_r^* = k\cdot H^*\cdot \Phi''_{r,ACT}\cdot \Phi''_{r,SEN}\ .$$

Eq. (30) clearly shows that - at least on the basis of pure theoretical considerations - an increase in the modal damping of eigenmodes can be achieved by the rather simple means of a 90° phase shift in the compensation network and the realization of geometric filtering conditions [9, 12] in accordance with Eq. (29). It should already be mentioned here that these fundamentals will be fully validated by the experimental investigations to be described in the next chapter.

6. Experimental investigations

The active damping investigations were carried out on a vertically suspended cantilevered beam structure (Fig. 10) with

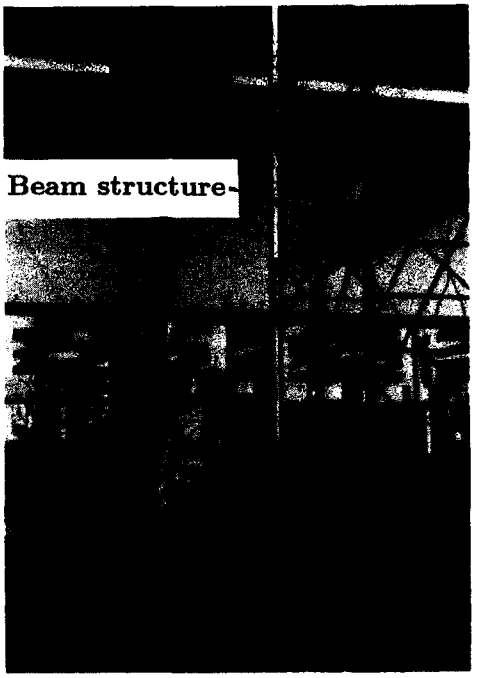

Fig. 10: Beam structure investigated

an overall length of 4 meters and a rectangular hollow section of 50 mm x 30 mm with a wall thickness of approximately 1.1 mm. The goal of the investigations was to increase the modal damping related to the first and second bending eigenmodes with eigenfrequencies at 1.44 and 8.60 Hz, respectively, by the implementation of two separate feedback loops. Both of the control loops comprised piezo-ceramic elements as actuators and thin layer PVDF transducers as sensors.

The following sections focus on the layout of the active damping control system.

6.1 Modal parameters of the beam structure

According to [10], the deformations in the bending eigenmodes of a cantilevered beam structure are defined by

$$(32)\quad \Phi_r(x) = Y_1 \sinh\cdot\alpha_r\cdot x/l + Y_2 \cosh\alpha_r\cdot x/l + Y_3 \sin\alpha_r\cdot x/l + Y_4 \cos\alpha_r\cdot x/l,$$

with

$$(33)\quad Y_1 = -Y_3 = -\frac{\sinh\alpha_r - \sin\alpha_r}{\cosh\alpha_r + \cos\alpha_r}$$

and

$$(34)\quad Y_2 = -Y_4 = 1\ ,$$

the values of α_r being: $\alpha_1 = 1.875$ for the first, $\alpha_2 = 4.694$ for the second and $\alpha_3 = 7.855$ for the third bending eigenmodes (Fig.11) which circular eigenfrequencies can be determined from

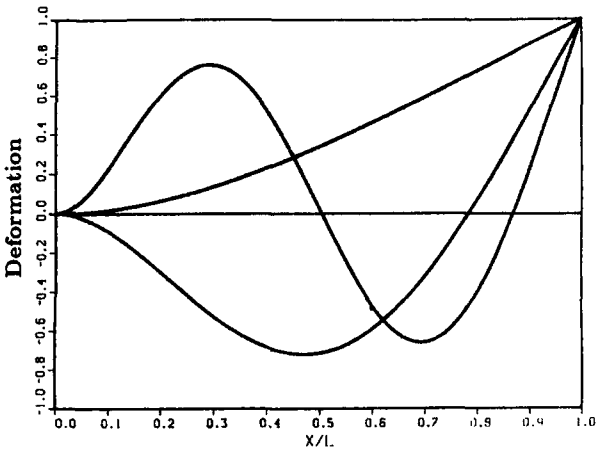

Fig. 11: Normalized eigenmodes of a beam structure cantilevered on one side

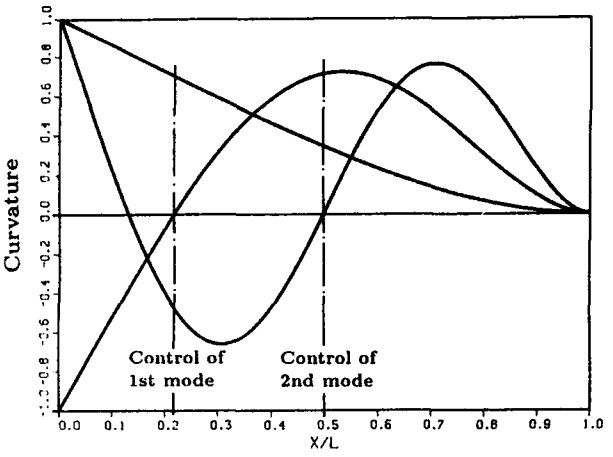

Fig. 12: Normalized modal curvatures

$$(35) \quad \omega_r = \alpha_r^2 \cdot \sqrt{\frac{E_b \cdot I_b}{\bar{m} \cdot L^4}} \,,$$

$\bar{m}$ denoting the mass per unit length of the beam. The measured eigenfrequencies, which were in a good agreement with the calculated values from Eq. (35), were at 1.44, 8.60 and 24.0 Hz. The corresponding damping factors identified were in the range of 0.58, 0.62 and 0.88 % of the critical damping.

6.2 Sensor/actuator placement

In order to provide satisfactory geometric filtering conditions, the sensors/actuators must be located in areas of the structure which satisfy Eq. (29). Since the curvature of the beam in the different eigenmodes is required for a closer analysis, Eq. (32) is derived two times with respect to the coordinate x, yielding:

$$(36) \quad \Phi_r''(x) = (\alpha_r/l)^2 \, [Y_1 \sinh \alpha_r \cdot x/l + Y_2 \cosh \alpha_r \cdot x/l - Y_3 \sin \alpha_r \cdot x/l - Y_4 \cos \alpha_r \cdot x/l].$$

The corresponding (normalized) characteristics are plotted in Fig. 12. With consideration of these results it was decided

- to place the actuator/sensor pair for control of the first bending eigenmode at 21 % of the overall beam length L, say at 0.84 m downwards from the fixed end of the structure,
- to place the actuator/sensor pair for control of the second bending eigenmode at the point of 50 %-L.

The point at 21 %-L is characterized by a significant curvature in the first mode and a zero curvature in the second mode. The non negligible curvature in the third eigenmode can be regarded as being uncritical since, due to the rather large frequency spacing, an efficient electronic filtering can be realized. The same reasoning applies for the 50 %-L point which shows a high value for the curvature in the second eigenmode, a zero curvature in the third mode and an uncritical curvature amplitude in the first mode when reduced by means of electronic filtering techniques.

The criteria for a best adaptation of the actuator system to the beam structure, worked out in section 3.3, indicated that by an in-line arrangement of 5 ceramic transducers 97 % of the highest possible energy transfer could be realized. Accordingly, 25 transducers arranged in 5 rows were fitted at the 21 %-L point for control of the first mode and 10 transducers, aligned in 2 rows, were arranged at 50%-L for control of the second mode. PVDF transducers with the size of 155 mm x 18 mm were used as sensors (Fig.13).

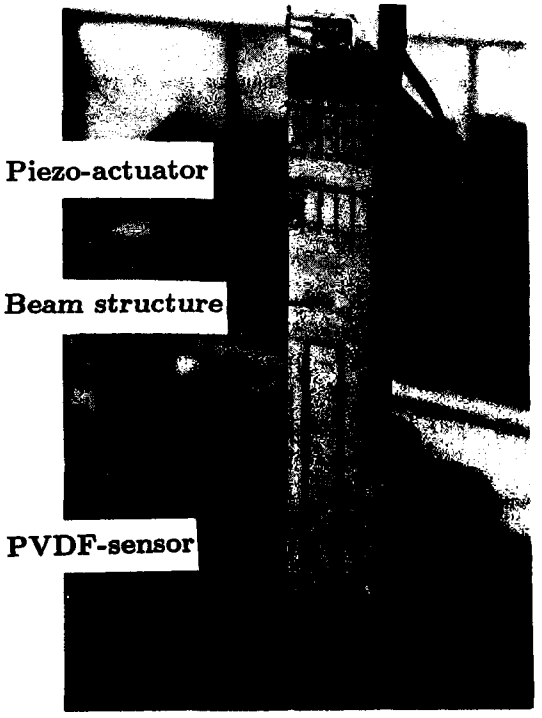

Fig. 13: Piezoceramic actuating system and PVDF sensor

6.3 Compensation network

In order to still improve the modal filtering yet realized by the skilfull placement of the actuators and sensors (geometric filtering) additional electronic filters are generally fitted into the compensation network. Typically, the implementation of low-pass filters reduces the excitation of higher frequency

eigenmodes and band-pass filtering elements are a powerful means for lowering the excitation of eigenmodes in the frequency neighborhood of the modes to be controlled [9, 13].

Fig. 14 gives a detailed information on the layout of the entire control system. The compensation network (Fig. 15) was realized in analogous technique featuring excellent possibilities for an easy manual setting of the filtering element parameters and the (numerous) amplification factors as well as of sign reversals.

6.4 Test results

In a first test the stability of the two control loops installed was investigated by drawing open loop Nyquist diagrams [14]. As a result, Fig. 16 depicts the plot obtained for the loop to control the first bending eigenmode. The pattern of the characteristic indicates a high stability of the active system with no increase in the amplitude at the frequencies related to the second and third eigenmodes of the beam structure. This indicates the high quality of the modal control achieved.

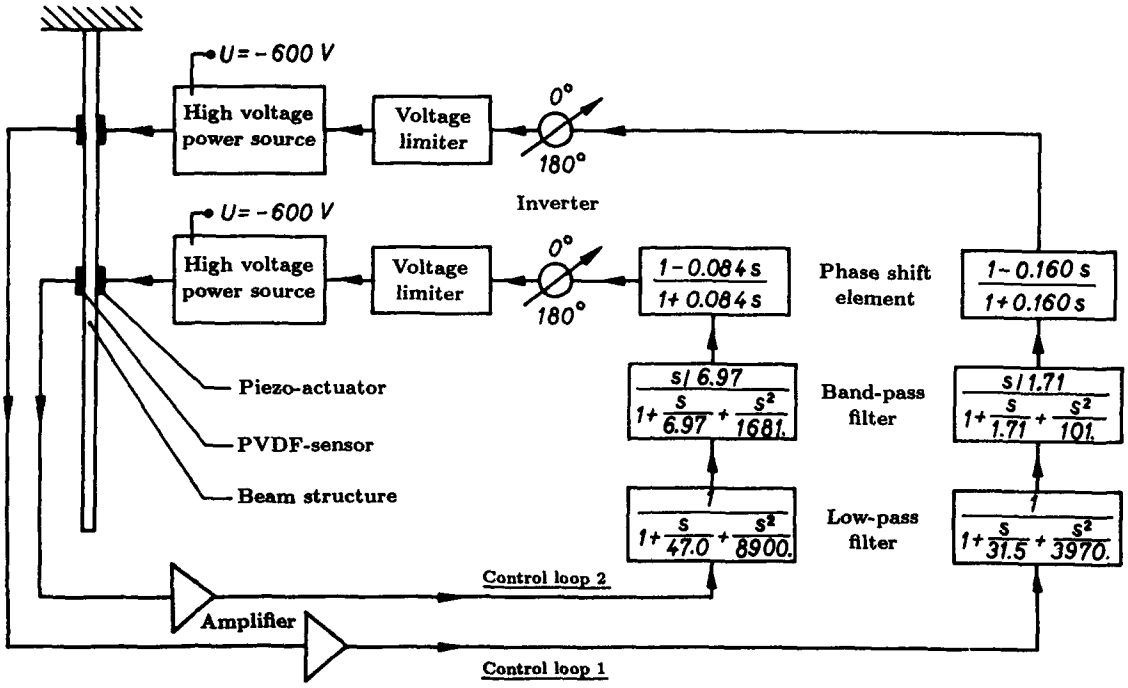

Fig. 14: Layout of the active damping augmentation control system

Finally it should be mentioned that the ceramic piezo-actuators were all operated at an offset voltage of -600 V (see section 3.1) and the dynamic voltage changes were limited around ± 600 V. This is the reason why some of the time plots, depicted in the next section, feature a square-wave shaped control signal in case the set voltage limits were exceeded.

Fig. 15: Electronic compensation network

A second test consisted in the determination of the modal damping provided by the active damping augmentation system. During this experiment the beam structure was one after

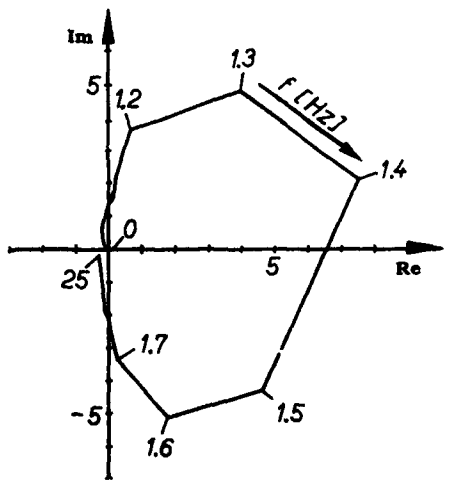

Fig. 16: Open loop Nyquist stability diagram related to the control loop achieving the damping augmentation of the first bending eigenmode

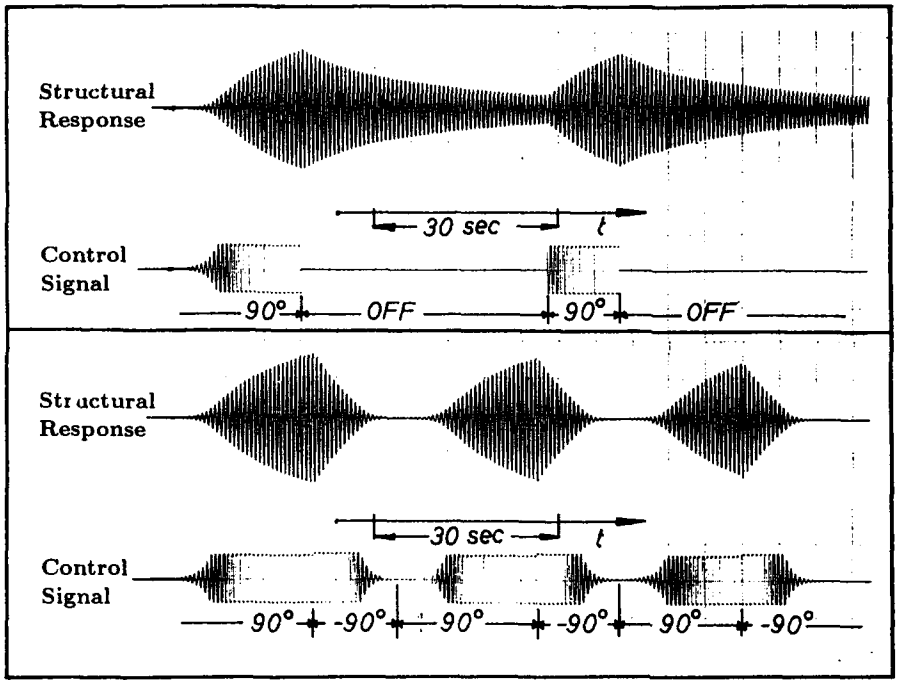

Fig. 17: **Decay time plots**

another excited in its eigenmodes by reversing the sign (180° phase shift) in the feedback loops of the control systems installed, which automatically entails the structure to become unstable. The structural amplitudes having reached a significant level, the control systems were or switched off or sign reversed, which returns the structure into a state of stability. Recording time plots of the decay curves of structural vibration (Fig. 17) allows an accurate determination of the modal damping achieved on basis of the so-called logarithmic decay criterion. The following modal damping values, related to mode 1, were taken from decay curves in case of

- the uncontrolled structure: 0.58 % of D_{crit} ,
- the actively damped beam: 2,7 % of D_{crit} .

A similar increase in the damping factor was also realized for the damping control of the second bending mode at 8.60 Hz.

In a third test the beam structure was randomly exited by an electrodynamic shaker in its relevant lateral bending direction (Fig. 18). The vibrational amplitudes of the beam were recorded in the case of the switched on and switched off

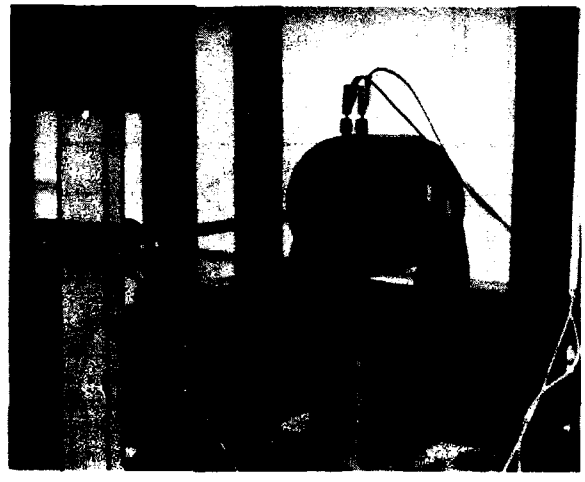

Fig. 18: **Electrodynamic shaker used for the excitation of the beam structure**

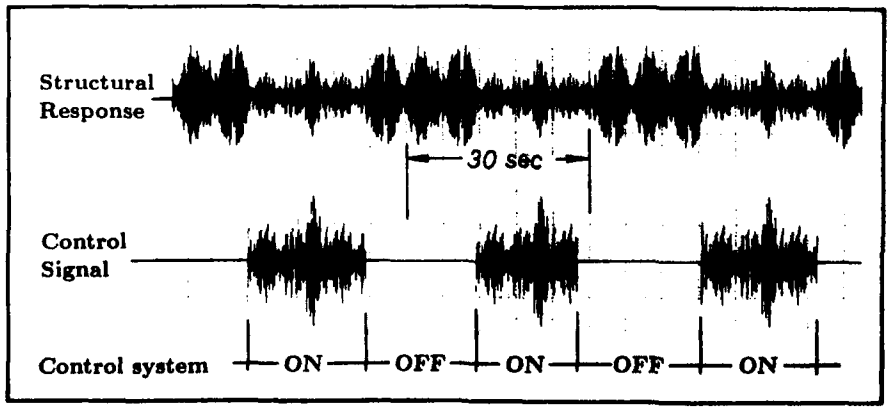

Fig. 19: **Typical time plots obtained from tests with an external random excitation**

control systems. A time plot of the results obtained is depicted in Fig. 19, the corresponding spectra are shown in Fig. 20. Both of the figures clearly indicate the efficiency of the control system installed.

With regard to the validation of the control criterion, described in chapter 5, which requires a layout of the compensation network with a 90° phase shift in the frequency-neighborhood of the eigenmodes to be damped, the frequency responses of the compensation networks installed were experimentally determined. The characteristics obtained, which are plotted in Fig. 21, show that the 90° phase requirement has been nearly fulfilled.

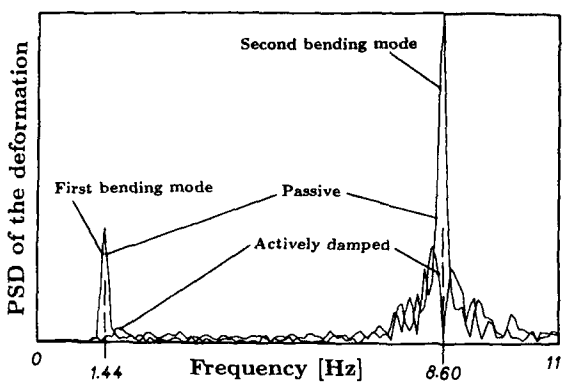

Fig. 20: Power spectral density of the structural deformations

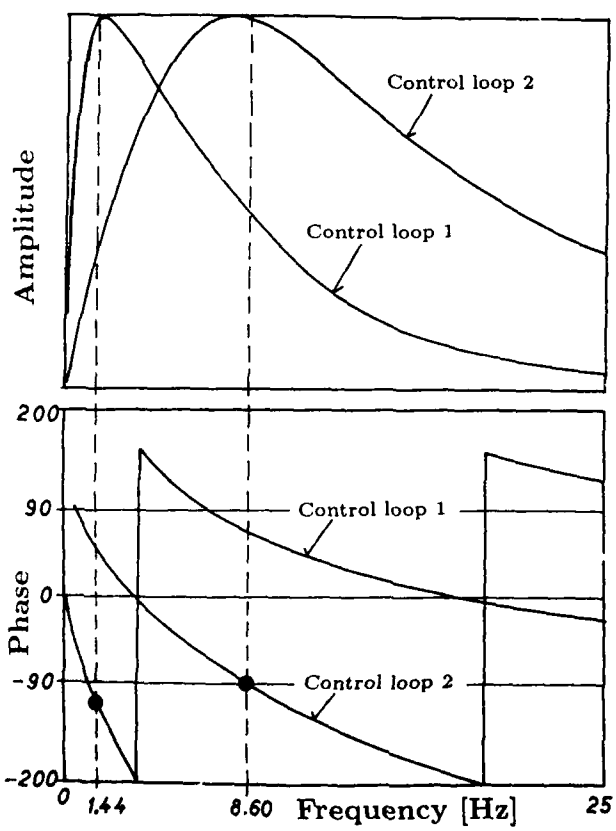

Fig. 21: Transfer characteristics of the compensation network

7. Conclusions

It was demonstrated that the piezo-technology is a powerful means to increase the (modal) damping of elastomechanical systems. Integrated in a closed loop (active) control system, piezoceramic transducers and PVDF elements, used as actuators and sensors, respectively, can cope with control problems in the frequency range below 1 Hz. This statement is of importance with regard to the application of the piezo-technology for the stability control of large flexible space structures.

It was shown that piezoceramic actuators, due to their linear behavior, when fed with voltages which are not opposed to their direction of polarization, are easy to be handled in analytical and experimental investigations. In order to get a high efficiency of the actuator systems, however, special care must be placed in the adaptation of the actuating system to the elastomechanical properties of the basic structure to be controlled.

Focus was pointed on how PVDF "point sensors " and "area sensors" can be used as filtering elements in order to realize an optimum control of so-called critical structural eigenmodes without affecting the remaining modes. This approach could entail further advantages, if applicable to "area actuating systems" as well, requiring the availability of powerful (multi-layer) PVDF actuating elements.

Finally it can be assumed that a further boost could be given to the piezo-technology by some of the new developments in the piezo-materials-area, entailing the supply of these "new" elements by a low-voltage power source with output-voltages in the range of only 0,2 kV [15].

8. References

[1] Damping 1986 Proceedings
Air Force Wright Aeronautical Laboratories - Report AFWAL-TR-86-3059 (1986)

[2] Forward, R.L.
Electronic Damping of Vibrations in Optical Structures
Applied Optics, Vol. 18 No. 5, pp. 690-697 (1979)

[3] Forward, R.L.
Electronic Damping of Orthogonal Bending Modes in a Cylindrical Mast
Journal of Spacecraft, Vol. 18 No. 1, pp. 11-17 (1981)

[4] Natori, M. et alii
Vibration Control of Truss Beam Structures Using Axial Force Actuators
AIAA-CP-882, Part 1, pp.491-499 (1988)

[5] Crawley, E.F.
Detailed Models of Piezoceramic Actuation of Beams
AIAA-CP-891, Part 4, pp. 2000-2010 (1989)

[6] Lee, C.K. et alii
Piezoelectric Modal sensors and Actuators Achieving Critical Active Damping on a Cantilever Plate
AIAA-CP-891, Part 4, pp. 2018-2026 (1989)

[7] Lee, C.K. et alii
Piezoelectric Strain Rate Sensor and Actuator Designs for Active Vibration Control
AIAA-CP-911, Part 3, pp. 2197-2207 (1991)

[8] Tichy, J.; Gautschi, G.
Piezoelektrische Meßtechnik
Springer Verlag Berlin, Heidelberg, New York (1980)

[9] Freymann, R.
Interactions Between an Aircraft Structure and Active Control Systems
Journal of Guidance, Control and Dynamics, Vol. 10 No.5, pp. 447-452 (1987)

[10] Försching, H.
Gundlagen der Aeroelastik
Springer-Verlag Berlin, Heidelberg, New York (1974)

[11] Freymann, R.
A Method for Determination of the Aeroelastic Behavior of Aircraft with Active Control Systems
DFVLR-Forschungsbericht 81-05 (1981)
ESA-TT-719 (1982)

[12] Freymann, R.
New Simplified Ways to Understand the Interaction Between Aircraft Structure and Active Control Systems
AIAA-CP-848, pp. 233-245 (1984)

[13] Freymann, R.
Dynamic Interactions Between Active Control Systems and a Flexible Aircraft Structure
AIAA-CP-864, pp. 517-524 (1986)

[14] Dorf, R.C.
Modern Control Systems
Addison-Wesley, Reading, 2nd Ed. (1976)

[15] Produkte für die Mikrostelltechnik
Gesamtkatalog 1990
Physik Instrumente, Waldbronn, Germany

control systems. A time plot of the results obtained is depicted in Fig. 19, the corresponding spectra are shown in Fig. 20. Both of the figures clearly indicate the efficiency of the control system installed.

With regard to the validation of the control criterion, described in chapter 5, which requires a layout of the compensation network with a 90° phase shift in the frequency-neighborhood of the eigenmodes to be damped, the frequency responses of the compensation networks installed were experimentally determined. The characteristics obtained, which are plotted in Fig. 21, show that the 90° phase requirement has been nearly fulfilled.

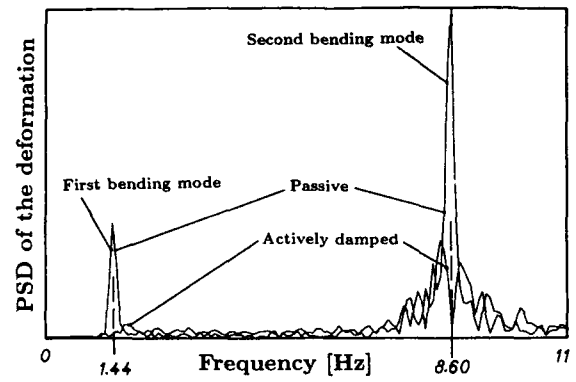

Fig. 20: Power spectral density of the structural deformations

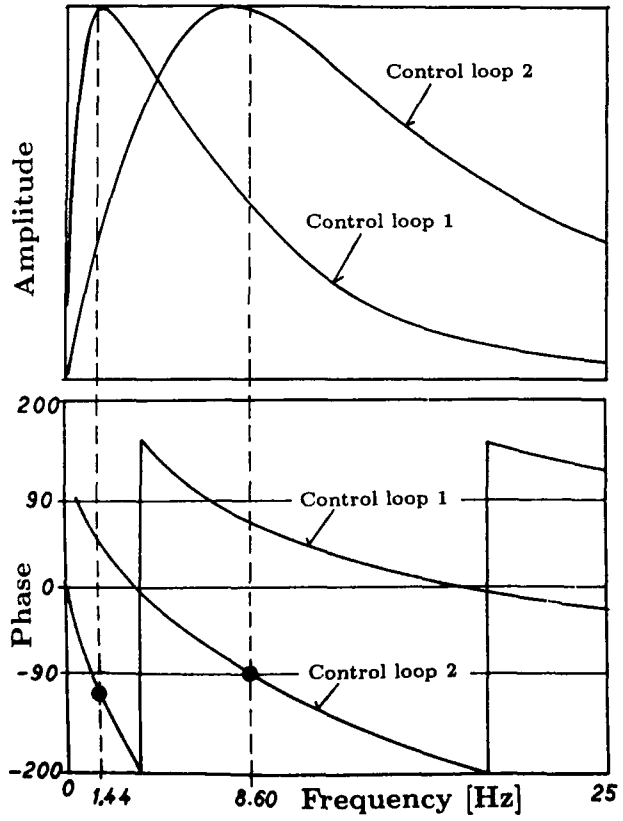

Fig. 21: Transfer characteristics of the compensation network

7. Conclusions

It was demonstrated that the piezo-technology is a powerful means to increase the (modal) damping of elastomechanical systems. Integrated in a closed loop (active) control system, piezoceramic transducers and PVDF elements, used as actuators and sensors, respectively, can cope with control problems in the frequency range below 1 Hz. This statement is of importance with regard to the application of the piezo-technology for the stability control of large flexible space structures.

It was shown that piezoceramic actuators, due to their linear behavior, when fed with voltages which are not opposed to their direction of polarization, are easy to be handled in analytical and experimental investigations. In order to get a high efficiency of the actuator systems, however, special care must be placed in the adaptation of the actuating system to the elastomechanical properties of the basic structure to be controlled.

Focus was pointed on how PVDF "point sensors " and "area sensors" can be used as filtering elements in order to realize an optimum control of so-called critical structural eigenmodes without affecting the remaining modes. This approach could entail further advantages, if applicable to "area actuating systems" as well, requiring the availability of powerful (multi-layer) PVDF actuating elements.

Finally it can be assumed that a further boost could be given to the piezo-technology by some of the new developments in the piezo-materials-area, entailing the supply of these "new" elements by a low-voltage power source with output-voltages in the range of only 0,2 kV [15].

8. References

[1] Damping 1986 Proceedings
Air Force Wright Aeronautical Laboratories - Report AFWAL-TR-86-3059 (1986)

[2] Forward, R.L.
Electronic Damping of Vibrations in Optical Structures
Applied Optics, Vol. 18 No. 5, pp. 690-697 (1979)

[3] Forward, R.L.
Electronic Damping of Orthogonal Bending Modes in a Cylindrical Mast
Journal of Spacecraft, Vol. 18 No. 1, pp. 11-17 (1981)

[4] Natori, M. et alii
Vibration Control of Truss Beam Structures Using Axial Force Actuators
AIAA-CP-882, Part 1, pp.491-499 (1988)

[5] Crawley, E.F.
Detailed Models of Piezoceramic Actuation of Beams
AIAA-CP-891, Part 4, pp. 2000-2010 (1989)

[6] Lee, C.K. et alii
Piezoelectric Modal sensors and Actuators Achieving Critical Active Damping on a Cantilever Plate
AIAA-CP-891, Part 4, pp. 2018-2026 (1989)

[7] Lee, C.K. et alii
Piezoelectric Strain Rate Sensor and Actuator Designs for Active Vibration Control
AIAA-CP-911, Part 3, pp. 2197-2207 (1991)

MULTIDIMENSIONAL INTELLIGENT CONTROL FOR SUPERLIGHT AIR VEHICLES

by

Aivars Smitchens
Wright Laboratory
Wright Patterson Air Force Base
Ohio, OH 45433-6553
United States

Anthony DeThomas, Ph.D.
Wright Laboratory
Wright Patterson Air Force Base, Ohio

Kurt Grevstad
The Boeing Company
Seattle, Washington

Doug Moore
Rockwell International
El Segundo, California

SUMMARY

Flexible wing technology has been explored in a number of design studies. Wind tunnel experiments generally affirm the results of these studies that a flexible, variable twist wing holds the potential for dramatic air vehicle performance improvements. However, the attendant control reversal, increase in control parameter nonlinearities, and the need for an active control system to suppress flutter has discouraged the application of this technology in production designs. Advancement of a robust control capability for damping structural modes; embedded sensors to provide required inputs to the control system for active flutter control and, possibly, battle damage tolerance; high-speed on-board computation; and other technologies promise the capability to exploit the benefits promised by more flexible structures. Current proposals to reduce air vehicle structural weight are briefly reviewed and implications on the control system are assessed. Even though control system concerns exist, they are resolvable and it may be timely to undertake the development and demonstration of an actively controlled flexible wing.

1.0 INTRODUCTION

Current and future tactical mission scenarios are placing greater emphasis on improvements in air vehicle agility combined with increased payload, range, time on station, and low vehicle signatures. These sought after aircraft capabilities require an overall weight reduction to provide the necessary increases in weapons carried, fuel capacity, and maneuverability without diminishing overall air vehicle performance.

The need for lighter weight structures motivates a wide range of innovative work in structures and materials, such as composites and advanced metallics. Currently, light weight structures, vehicle management systems, and the integration of innovative control effectors, such as vortex burst control, are the air vehicle elements with the greatest potential for weight reduction. Relaxed wing torsional stiffness, relaxed flutter margins, and relaxed structural design margins are some specific examples of weight reduction approaches under consideration.

Usually, a change in one area of air vehicle design propagates into other design areas. Such is also the case with the contemplated structural weight reduction approaches mentioned above. For example, relaxed torsional stiffness may result in control reversal; relaxed design margins may result in flutter in some parts of the flight envelope; and, some of the structural modes may be high energy modes with potential attendant structural life and even flight safety concerns. The use of active control to provide structural mode damping and flutter suppression continues to be considered a means of achieving weight reduction.

Integration of active control with the contemplated new structural design approaches may provide an effective means of realizing the sought after weight reductions. Even though active control applications have been previously explored and successfully applied, control system robustness concerns due to reduced separation between rigid body and structural modes; significantly increased modeling uncertainties; and flight safety concerns previously combined to discourage the flight control community from agreeing that these issues could be dealt with effectively within the other existing air vehicle design, manufacturing, and affordability ground rules. However, recent developments in control technologies and system integration capabilities seem to have potential for easing these concerns and contributing to a dramatic decrease in the air vehicle's weight.

Key control technologies include multivariable, adaptive, and nonlinear control designs and parameter identification methodologies. When applied to structures with embedded sensors and effectors, these methods have the potential to significantly reduce the structural weight required to handle flutter and maneuver loads on the vehicle. These new design methodologies also allow use of unconventional control effectors such as thrust vectoring and reversing, vortex control, and split surfaces, in a manner that permits smaller and lighter conventional surfaces, resulting in an overall reduction of aircraft weight.

Similarly, integrated, photonics based, vehicle management systems offer substantial weight saving by eliminating many subsystem components and by replacing the relatively heavy shielded copper wiring throughout the aircraft with lighter weight optical fibers. In addition to weight savings, photonics offers improved electro magnetic interference (EMI) immunity. Subsystem integration offers synergism benefits as well as vehicle and subsystem improvements in performance, reliability, maintainability, and life cycle costs.

This paper presents a control technologist's perspective on the implications of structural stiffness reduction and other approaches to weight reduction, the opportunities and challenges they pose, and the potential future direction of active control applications to flexible structures. Air vehicle elements with high potential for weight savings and the possibilities for capitalizing on these savings are presented in Section 2.0. Section 3.0 addresses the control system, the additional functional requirements which may need to be incorporated to provide active control of the structure as well as the air vehicle, and briefly considers control technology readiness. Our conclusions are presented in Section 4.0.

2.0 AIR VEHICLE WEIGHT CONTRIBUTORS

The takeoff gross weight of a manned aircraft includes the fuel fraction, payload, structure, systems, and many other elements. This paper considers only those air vehicle weight contributors with the highest potential for weight reduction through application and integration of advanced control: airframe structures, vehicle management systems, and innovative control effectors. The weight reduction potential in each of these areas is addressed in the following subsections.

2.1 STRUCTURES

Aircraft structures must endure the cumulative effect of a variety of takeoff, landing, maneuver, gust, and other flight loads. The structures on today's aircraft are designed to support these loads, with appropriate design margins, through the physical strength of the structural members. It may be practical to significantly reduce the total weight by applying adaptive, integrated, multivariable control techniques to the control and management of the vehicle structural members and control effectors. Additional weight reductions may be obtained through structural integration of airframe, engine, and exhaust nozzle components.

2.1.1 Wing Torsional Stiffness

Wing structures of today's aircraft are designed to ensure torsional stiffness so that wing twist is minimized and sufficient control power is maintained throughout the flight envelope. If torsional stiffness were not added, the aeroelastic twist caused by trailing edge control surface deflection would twist the wing in a direction which reduces lift and thus the rolling moment. This is illustrated in Figure 1. To ensure control power, a combination of increased surface deflection and torsional stiffness is used to preclude control power loss. This results in a heavier structure and requires larger control actuators and power, again adding to total aircraft weight.

The weight of the wing structure could be reduced on future aircraft if wing twist were exploited using advanced control methods. For example, leading edge control surfaces may be used to obtain an optimum camber for maneuvering and cruise or to offset the torsional deflection caused by the trailing edge controls. However, the effectiveness of leading edge surfaces, as control effectors, is small. If the wing flexibility were increased by removing the stiffness material and designing the wing for strength only, leading edge control effectors would have significant control effectiveness, particularly at higher dynamic pressures.

With relaxed torsional stiffness wings, large variations in control surface effectiveness can occur with flight condition, even resulting in control reversal at high dynamic pressures, as illustrated in Figure 2. By implementing a control system design which accounts for these control effectiveness variations, adequate control power can be maintained to meet the maneuverability and agility requirements. To meet the commanded roll rates, an advanced controller which blends and prioritizes the use of leading edge and other available surfaces, according to the effectiveness of each at the present flight condition, may be required.

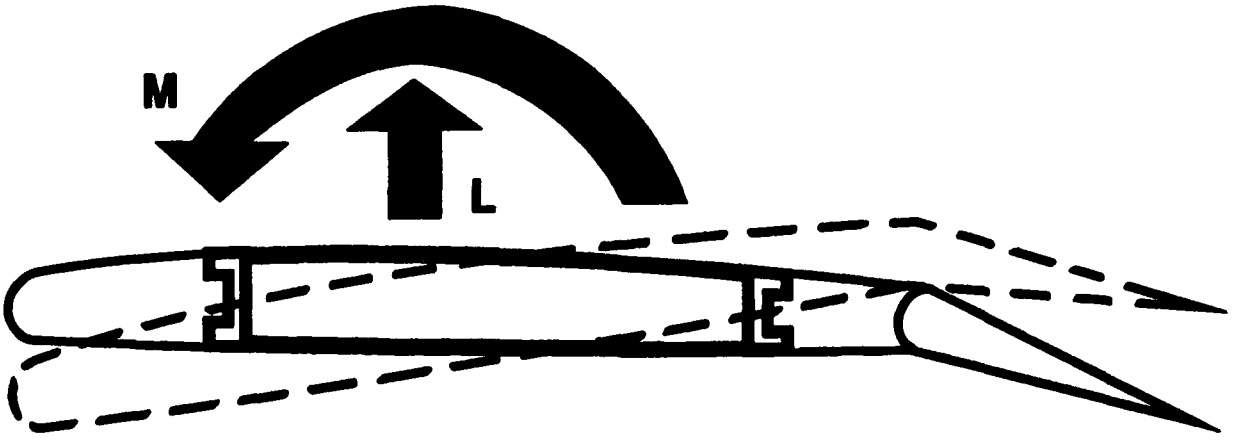

- TORSIONALLY STIFF STRUCTURE ASSURES AILERON EFFECTIVENESS
- RELAXED TORSIONAL STIFFNESS AFFECTS AILERON EFFECTIVENESS
  - MOMENT DUE TO CONTROL SURFACE DEFLECTION TWISTS WING, REDUCING LIFT
  - AT SOME DYNAMIC PRESSURE CONTROL REVERSAL MAY OCCUR

FIGURE 1 - AILERON AND FLEXIBLE WING INTERACTION

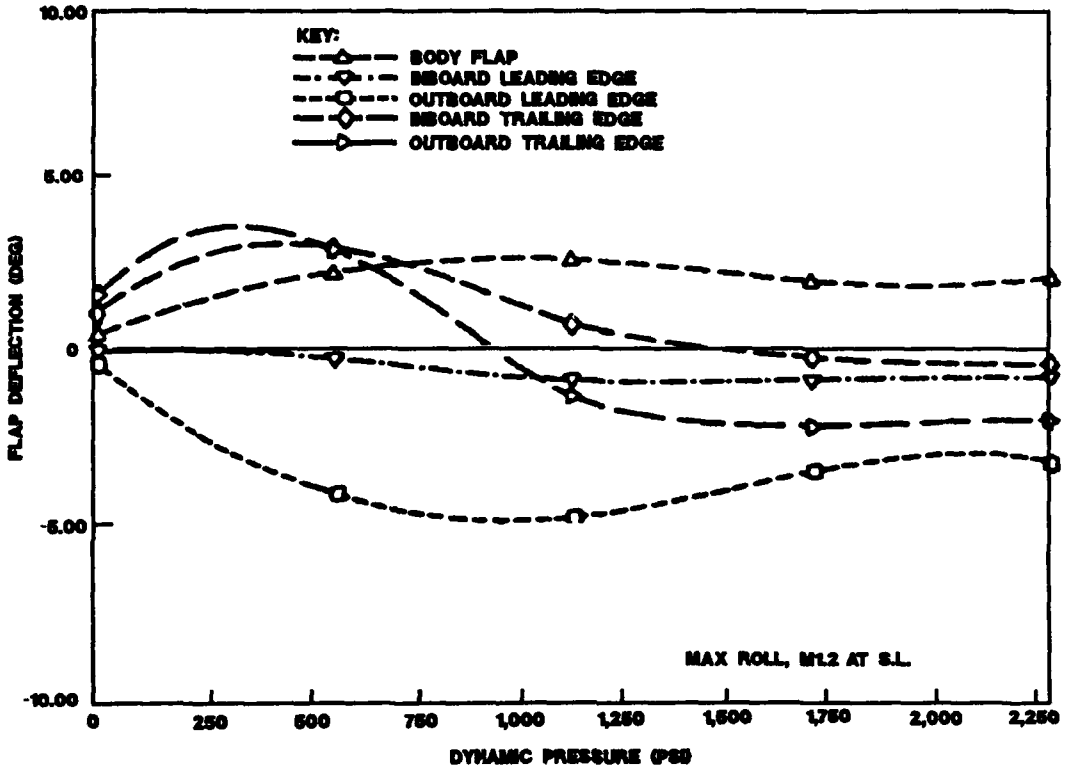

FIGURE 2 - CONTROL SURFACE DEFLECTIONS FOR MAXIMUM ROLL RATE OF A RELAXED STIFFNESS WING

2.1.2 Structural Strength for Load Carrying Capacity

Active control of the vehicle and structure to maintain loads within limits is another weight reduction alternative. That is, rather than adding material to provide structural strength for the maximum expected ultimate load, active control could be employed to maintain loads within specific limits. These limits could vary with fuel load, weapon stores, and flight condition. Additional limiting could also be implemented in the event battle damage is sustained or structural fatigue or other airframe stress limits are detected.

One suggested approach for sensing loads and detecting structural damage is to embed strain gages in the aircraft's skin or structural members. This would provide feedback to the flight control system so that maneuver loads would be controlled up to the structural limits with acceptably low risk of exceedance. Figure 3 illustrates a recent application of maneuver load control where an accelerometer was employed to maintain wing pivot bending moment at or below a specified level. Use of acceleration data combined with structural load data hold significant promise and are of interest to both the structures and flight control engineers, as well as air vehicle designers.

Also, innovative use of alternative control effectors could be relied on to ensure that wing bending moment and other structural limits are not exceeded if the proposed wing leading edge effectors can not fully meet the maneuvering control power requirements. Thrust vectoring and body flaps are only example alternative control effectors that should be considered.

Wind shear, gust, and turbulence loads are of concern and may need to be actively controlled in relaxed stiffness structures. The use of look ahead laser sensors to detect wires and other obstacles is being explored extensively. Similar technology could be used for air data sensing to characterize the gusts and turbulence of the air mass ahead of the aircraft. These data would then be used to provide appropriate load control responses before the gusts or turbulence are encountered. A logical extension of this dynamic loads control function would be to use the combined set of structural loads and air mass behavior data to control the accelerations at the pilot station and provide improved ride qualities.

2.1.3 Structural Stiffness for Flutter Suppression

Airframe weight may be further reduced by relaxing the stiffness that is typically included in the structure to preclude

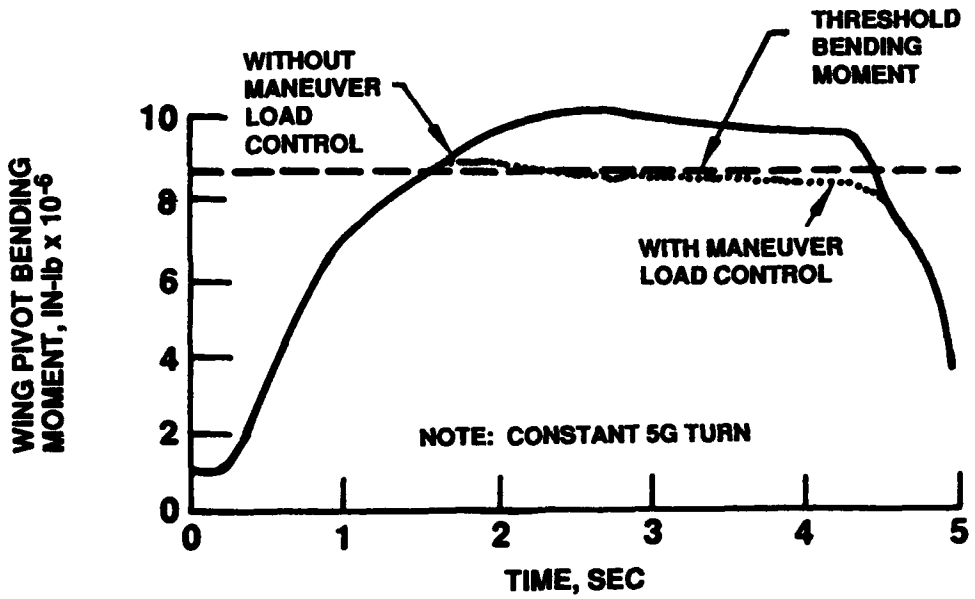

FIGURE 3 - MANEUVER LOAD CONTROL REDUCES WING PIVOT BENDING MOMENT

flutter. One suggested approach is to employ a distributed network of embedded sensors throughout the vehicle structure, in conjunction with adaptive multivariable control techniques, to suppress flutter of the relaxed stiffness, reduced weight structure. This distributed sensor network would provide the data necessary for real time identification of flexible mode frequencies and shapes, and would be used to close a control loop with adaptive feedback gains. The potentially large number of feedback sensors and actuators is likely to require some development and maturation of multi-input, multi-output control system design methods. Existing methods have the potential of being extendible to deal with added control requirements. Also, new design methods which promise improved capability to deal with complex control system nonlinearities are emerging.

2.1.4 Engine Exhaust Structural Integration

Today, exhaust nozzles are structurally supported by the engine. Loads from adjacent empennage surfaces are usually taken out forward to the first crossbody frame well ahead of the nozzle and airframe interface. A more efficient, lower weight load path would take advantage of nozzle structure to bring the loads more directly into the airframe. This structural integration may also have a favorable impact on aerodynamics by reducing the cross section area around the nozzle structure and on radar observability with elimination of the airframe to nozzle interface gaps. A variant to the airframe integrated nozzle is an airframe mounted nozzle. In this approach, the nozzle would be mounted to an aft structural cross member that also distributes airframe to empennage loads. This structural approach promises weight savings as well as advantages in maintainability and supportability.

2.1.5 Conceptual Design Study Results

To quantify the potential benefits of relaxed stiffness wings, three different wings were designed for different stiffness requirements and their weights were calculated. These studies focused primarily on exploitation of active control technology to solve the aileron control reversal problem and relied on wing twist and deflection to provide the control power desired.

For the actuator comparison, control power requirements were defined in terms of actuator hinge moment and hydraulic power requirements. Table 1 presents a comparison of hinge moment, actuator weight, and hydraulic horsepower required at maximum surface rates for the baseline and most flexible wing designs studied. The study used surface deflections required to meet roll performance requirements specified by widely accepted design criteria and showed that significant reductions in actuator weight and power could be obtained with a more flexible wing.

TABLE 1 - ACTUATOR REQUIREMENTS

CONTROL SURFACE	BASELINE WING DESIGN WITH STIFFNESS			ACTIVE FLEXIBLE WING		
	HINGE MOMENT PER SURFACE (IN-LB)	ACTUATOR WEIGHT (LB)	HYDRAULIC POWER AT MAX RATE (HP)	HINGE MOMENT PER SURFACE (IN-LB)	ACTUATOR WEIGHT (LB)	HYDRAULIC POWER AT MAX RATE (HP)
INBOARD TRAILING EDGE (2 PER A/C)	0.99×10^6	176	132	0.172×10^6	19	14
OUTBOARD TRAILING EDGE (2 PER A/C)	0.49×10^6	80	39	0.155×10^6	18	14
INBOARD LEADING EDGE (2 PER A/C)	0.20×10^6	20	16	0.172×10^6	19	14
OUTBOARD LEADING EDGE (2 PER A/C)	0.18×10^6	19	14	0.172×10^6	19	14
TOTAL PER A/C		590	402		50	224

KEY: IN: INCH; LB:POUND; A/C: AIRCRAFT; HP: HORSEPOWER; MAX:MAXIMUM

Benefits of actively controlled flexible wings were further explored to quantify aircraft takeoff gross weight (TOGW) reductions by using the structural and system weight changes as well as estimates of flexibility effects on drag due to lift. The resulting savings in structural weight from these analyses are presented in Table 2. Three design analysis points are presented: stiff wing, relaxed stiffness wing without maneuver load control, and a relaxed stiffness wing with active load control. When combined with the actuator weight savings, as seen in Figure 4, the potential benefit of relaxed stiffness technology based design is estimated to be a 15-30% TOGW reduction.

TABLE 2 - WING DESIGN COMPARISON

DESIGN	STRUCTURAL BOX WEIGHT (POUNDS/SIDE)	CONTROL SYSTEM IMPLICATIONS
CONVENTIONAL: TORSIONAL STIFFNESS FOR ROLL EFFECTIVENESS	1545	BASELINE DESIGN
RELAXED TORSIONAL STIFFNESS WING	563	- STRUCTURAL MODE COMPENSATION - CONTROL REVERSAL - EXTENSIVE PARAMETER NONLINEARITIES
RELAXED TORSIONAL STIFFNESS WING WITH MANEUVER LOAD CONTROL & ACTIVE FLUTTER SUPPRESSION	345	ABOVE PLUS: - ACTIVE FLUTTER CONTROL - LOAD CONTROL SENSORS & ALGORITHMS - PRECISE, WIDE BANDWIDTH ACTUATION

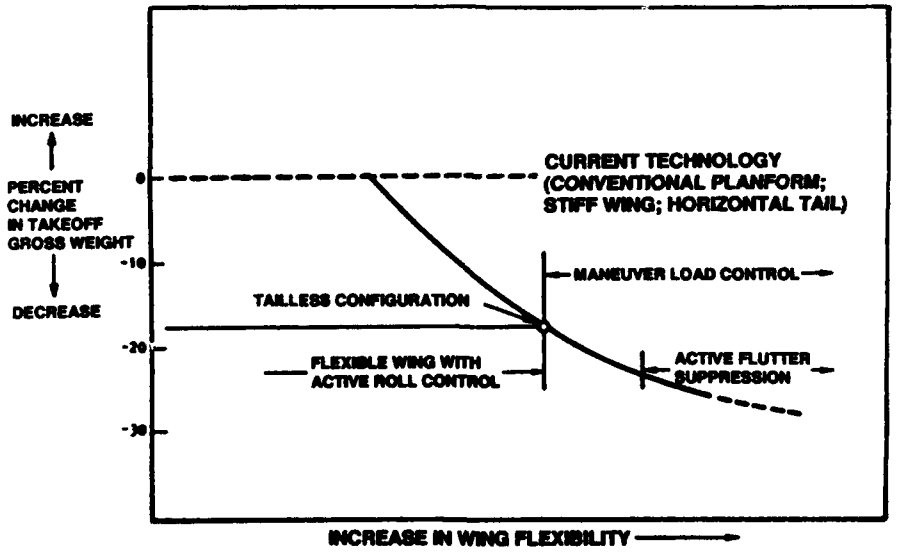

FIGURE 4 - FLEXIBLE STRUCTURE REDUCES TAKEOFF GROSS WEIGHT

2.2 VEHICLE SYSTEMS

The contemplated use of embedded load and other sensors and fiber optic signaling to provide structural and other feedback data to the flight control system merges well with the interest in fiber optics to reduce the weight of the vehicle management system (VMS). Two approaches may be employed to reduce the weight of the VMS using fiber optics. The first is to replace all electrical data transmission wires and low wattage power lines with optical fibers. The second is to integrate subsystems of the VMS to reduce the number of components and interconnections, thus reducing their weight and increasing their performance.

The use of fiber optics would also reduce the susceptibility of the VMS to EMI by replacing the electrical power and signal wires connecting sensors, control effectors, and cockpit displays with the computers. Fiber optics would also avoid the need to enclose the entire system of sensor and effector signal

paths and data buses with braided shielding, eliminating a large source of weight.

As systems become more integrated and more complex, the amount of data transmission and thus the amount of shielded wires increases. This is particularly evident in structures designs in which motion and load sensors would be distributed over the entire airframe, each requiring signal wiring to connect an individual sensor to data processing units or to remote bus terminals. With the introduction of photonic based control systems for vehicle management, the weight penalties attendant to the incorporation of structural sensors would be significantly mitigated. Industry studies comparing fly-by-wire and fly-by-light VMS equipped aircraft show that the weight savings range from 700 pounds for a fighter aircraft to as much as 4000 pounds for a transport aircraft.

Integration of the various aircraft subsystem control functions into a single integrated vehicle management system may produce additional weight savings. To a limited extent, this approach has been employed on some recent prototype fighters and extensions appear feasible. Traditionally, flight critical systems are designed as a family of independent systems, each having its own sensors, effectors, and computing sites. Integration of control functions into a single system, both functionally and physically, promises savings in weight due to reduction in the number of subsystem components and interconnections. Additional functional integration benefits may be gained in maintainability, reliability, and performance. Physical integration would eliminate components by sharing sensors, processors and buses, and reduce electrical power distribution and cooling requirements. Also, weight savings may result from integration of the electrical and hydraulic power subsystems into a more electric aircraft where much of the hydraulic plumbing and engine power extraction hardware may be removed from the aircraft. Another example is the integration of the separate environmental control and fuel subsystems into a single thermal management system utilizing an integrated closed environmental control system optimized to minimize bleed air and power extraction loads on the engine. These integration concepts are currently being explored aggressively.

2.3 CONTROL EFFECTORS

Flying qualities requirements of current and future tactical aircraft result in stringent requirements on the center of gravity placement and control surface sizing. High agility design goals result in the need to rapidly maneuver, resulting in the need for powerful control surfaces, effective to what, today, we would consider high angles of attack (AOA). Further, current design philosophy requires that the aircraft be easily controllable to high AOA and be able to recover from upsets using only aerodynamic controls. This requirement is the major driver for both balance and horizontal tail size.

These requirements, when coupled with low observability requirements, as exemplified by current designs, tend to result in increased tail sizes. Fins must be located at larger cant angles than would be desirable from a strictly aerodynamic standpoint. Also, the aggressive maneuvering needed for good agility requires very effective yaw and roll control devices. This results in large rudders and wing roll control surfaces, thereby increasing weight.
Future tactical aircraft will take advantage of emerging technologies in aircraft design, structures, materials, and control, some of which are currently under evaluation on models and on test aircraft. For example, thrust vectoring in pitch may be used to aid high AOA recovery, to allow further aft balance, thereby reducing trim drag, and to supplement pitch control during high AOA roll maneuvers. Horizontal tail size may be reduced, resulting in an overall weight saving on the aircraft. The benefits of combined pitch and yaw thrust vectoring are being evaluated on the X-31 and F-18 HARV (High Angle of Attack Research Vehicle).

Other emerging control technologies include vortex burst control, wing leading edge control surfaces, and split trailing edge controls. Asymmetric movement of vortices by forebody strakes or blowing to generate yaw control has been studied for some time in wind tunnels. This concept has the advantage of providing control at high AOA, where conventional rudders lose effectiveness, thereby reducing rudder and vertical tail size. Forebody blowing has recently been flight tested on the X-29. Both forebody blowing and moveable strakes will be evaluated on the F-18 HARV airplane.

Wing leading edge controls improve agility and high AOA stability when deflected symmetrically, thereby reducing empennage size. The same controls deflected asymmetrically will aid roll control at high AOA by controlling flow attachment, and at high speed, by using wing flexibility to distort the wing and provide roll control.

Split trailing edge controls can be used for yaw control, thus reducing or eliminating the need for vertical surfaces and thereby greatly enhancing vehicle signature. Split surface effectiveness is very nonlinear with deflection, necessitating nonlinear surface control.

Low observability requirements may place additional constraints on stability, control, and flying qualities design. Currently, vertical and horizontal tails provide control power. Tailless designs are being proposed to decrease signature characteristics, with yaw control for stability and maneuvering provided by thrust vectoring, split surfaces, and vortex control.

3.0 CONTROL SYSTEM IMPLICATIONS

3.1 CONTROL SYSTEM STRUCTURE

A top level control system representation for an advanced fighter aircraft is shown in Figure 5. This control system consists of multiple control loops, is highly integrated, and provides many cross paths, which are not explicitly shown, between sensors and effectors. This multiloop, highly integrated design approach is required to allow the aircraft to meet the large number of performance requirements and provide the control modes required in a high agility combat aircraft. For example, blending of thrust vectoring with aerodynamic control may be employed at high angles of attack to ensure sufficient pitch and lateral and directional control, good maneuverability in all control axes, and departure resistance. Typical pitch axis control effectors are the horizontal tail, pitch thrust vector, symmetric trailing-edge flaps, canards, and leading-edge flaps. Typical lateral and directional control effectors include differential trailing-edge flaps, rudders, nose yaw strakes, and yaw thrust vector angle. The control system, by appropriately blending these multiple effectors, enables the pilot to maneuver the aircraft as required, but presents a design challenge for selecting the control laws, control parameters, and gains to ensure the required controllability and flying qualities over the full flight envelope.

Existing, demonstrated control system design capability gives confidence that controls technology can be matured to permit addition of the control requirements posed by relaxed structural stiffness and battle damage tolerance. The structure of the control system would become somewhat more complex since more sensors and, possibly, effectors may be required. For example, inclusion of battle damage tolerance could require rapid identification of the extent of the damage, determination of still usable control effectors, estimation of control effectiveness, and even control law restructuring.

The key to choosing an appropriate control structure is to understand the physical process to be controlled. How nonlinear are physical phenomena? Are the sensors and control effectors available to effect the control function under consideration? Are the sensor accuracies and response times consistent with the dynamics of the control function? Much progress has been made under the Advanced Technology Wing (ATW), B-52 Load Alleviation and Mode Suppression (B-52 LAMS), and other research programs in developing an understanding of the characteristics and interactions of structural modes and aircraft attitude, propulsion, and maneuvering control functions. This work enables the control system designer to develop a sufficient understanding of flexible structure control dynamics and move towards the incorporation of flexible structures in operational aircraft and contribute to the realization of potential weight savings. Development of this understanding will require a cooperative effort of structures, control, materials, aeromechanics, and other technologists. It is hoped that the remainder of this paper, which focuses on principal enabling controls technology areas, would continue to expand the dialogue as we consider the various options for advancing the capability of combat aircraft.

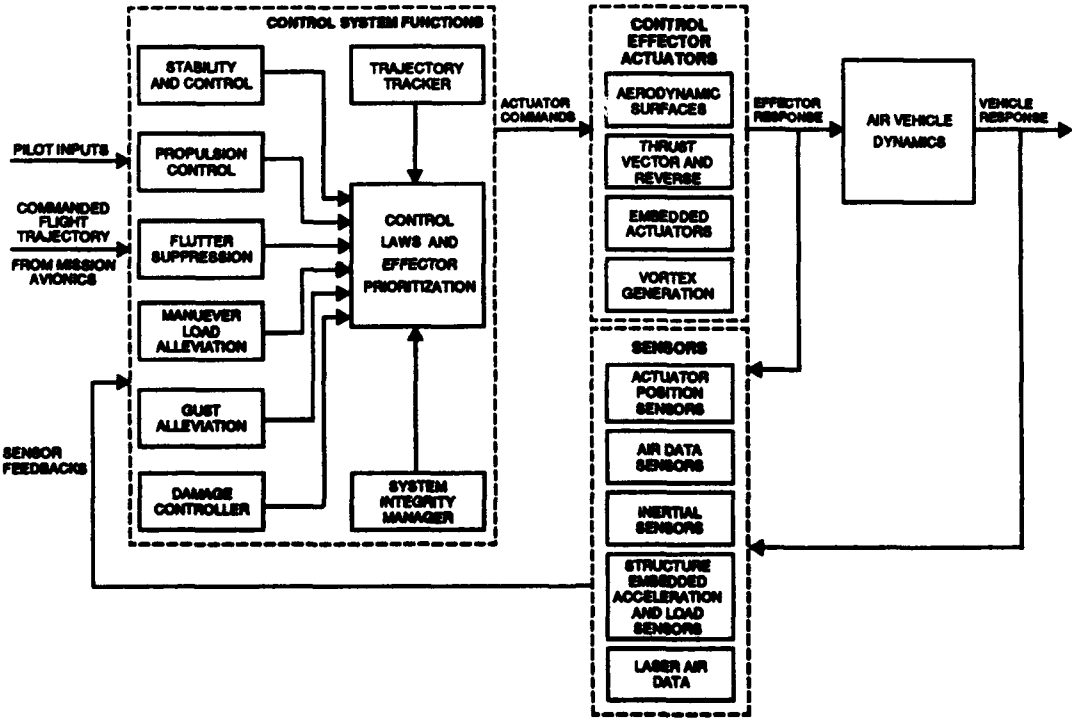

FIGURE 5 - TOP LEVEL CONTROL SYSTEM REPRESENTATION

3.2 STRUCTURAL AND FLUTTER MODE MODELING

To exploit the potential of flexible wings, either new or improved fidelity models of structural parameters and phenomena must be included in the total air vehicle model used for control system design. These include aeroservoelastic models of the entire aircraft; flutter suppression and load control sensor network responses, dynamics, and noise models; and the characteristics of the effector used to control the parameter of concern. Integration of these models in the total air vehicle design process will also be required to ensure control power for structural mode stabilization and maneuvering.

Successful control law designs for active control of flexible modes may require highly accurate finite element modeling methods and controller design methods that are robust, i.e., insensitive, to modeling errors. For feedback control purposes, the modeling accuracy required in a structural model, such as a finite element model of flexible mode frequencies and mode shapes, is likely to be much greater than that needed for stress analysis only. For example, in applying active control to flutter suppression, a small error in mode shape node location can change a transfer function's phase by 180 degrees, driving a feedback system unstable.

Near the wing control surface effectiveness reversal point, roll control may depend on alternate effectors such as differential thrust vectoring, tails, body flaps, or vortex control. Thus, control system design will also require integration in the aerodynamic database the effects of structural flexibility, possibly obtained from flexible wind tunnel models or computational fluid dynamic models, to more accurately represent the aircraft's characteristics.

In the Active Flexible Wing program, the aeroservoelastic model used had 10 symmetrical modes, 10 anti-symmetrical modes, 4 aerodynamic lags, third order actuator models, and a first order rigid body roll mode. There were 10 control surface deflection and turbulence inputs and 52 outputs in terms of acceleration, loads, surface position, hinge moments, and others. This linear, 172 state aeroservoelastic model benefited from two wind tunnel entries and ground vibration tests to tune and correlate it. This experience is cited primarily to underline the point that air vehicle flexible mode models are somewhat complex and require time and significant resources to develop. However, the time and technical resources required to develop the needed high fidelity structural and aerodynamic models to support engineering decisions in simultaneously matching loads, aerodynamics, flutter frequencies, flutter dynamic pressures and deflection shapes, and control algorithm design appear to be commensurate with the time and resources required to develop the structure itself.

3.3 STRUCTURAL MODE CONTROL SENSORS

Networks of very small, lightweight motion sensors distributed over the structure, such as strain gages or accelerometers embedded in or affixed to the skin or structure, may play a crucial role in enabling robust active control of flutter and dynamic loads. The more sensors that are available, the greater the potential for rejection of unwanted modes, or modal selectivity. However, each new sensor introduces potential failure modes as well as some maintenance and repair concerns. Therefore, it will be necessary to minimize the number of additional sensors and demonstrate, through analyses, design tests and flight validation, that the weight reduction capability is enabled by an affordable control system implementation.

Equally important is sensor location, which is a compromise between often conflicting sensing, maintenance, and other requirements. Sensor location for active structure and flutter control laws may not necessarily be the best when considering additional requirements. To minimize the total number of sensors required, the flexible vehicle model will need to be quite accurate relatively early in the total design process. This model will need to enable sensor location selection, preliminary control structure formulation, and failure mode analyses and safety assurance.

3.4 CONTROL ALGORITHMS

Several relaxed stiffness structure control algorithms need to be developed and demonstrated. Some specific examples include maneuver load control algorithms using distributed structural load sensing; active flutter control throughout the flight envelope; real time control parameter and structural mode identification; and damage tolerance.

By forming a weighted sum of the sensor network signals, with weights corresponding to the shape vector of the flexible mode, the controller would develop feedback signals proportional to one mode's excitation with minimal interference from other modes. This permits increased loop gain and active damping level achievable without destabilizing the other structural modes. This "spatial filtering" approach contrasts with traditional "temporal filtering," which separates modes based on their frequencies and possibly introducing phase lags which may destabilize the feedback loop.

It may not be practical to use existing control law structures because the physical processes tend to be highly nonlinear and time varying. In addition, self-repair capability and damage tolerance may require new gains subsequent to battle or other damage to the structure or control effectors.

Adaptive control, in combination with distributed sensing, may be a successful approach to active model damping, since the required gains may be sensitive to the mode shape, which can change significantly and rapidly with flight condition, fuel weight, and battle damage. While a potential drawback of adaptive control is the difficulty in proving that the adaptive gains will never cause instability, such systems do offer significant performance advantages. As an alternative to adaptive control, application of parameter identification algorithms to flexible structures to identify, in real time, the flexible mode frequencies and mode shapes as seen by the network of distributed sensors holds significant promise.

3.5 CONTROL COMPUTATION AND SIGNALING

3.5.1 Control Computation

Integration of maneuver, stabilization, load, and flexible structure control now appears practical due to the advances in microprocessor speed and memory capacity and demonstrated capability of digital flight control. Digital fly-by-wire control systems provide the basis for implementing structural load and flutter control, which, coupled with the speed and memory improvements of digital systems, allows consideration of controlling the higher frequency load and flutter phenomena. Digital controls today use 60-80 Hz frame rates to control 3-4 Hz aircraft stability modes and maneuver modes. Flutter controllers may need to control structural modes in the 6-20 Hz range requiring control system computer frame rates in the 200-400 Hz range for acceptable phase loss due to digital controller effects. One area of concern, which has not been adequately quantified at this time, deals with the computation speed required for real time parameter estimation of statically unstable combat aircraft to compensate for battle damage to the aircraft. Partitioning of the control system using modular components tailored to specific functions could resolve the potential requirement for extremely fast computation.

The mechanization of highly integrated control laws may also be a challenge from a flight safety standpoint. Embedded structural sensors could provide the capability for fatigue load assessment, maneuver limitations, or speed limitations due to flutter and advisories from damage assessment algorithms. If these functions are implemented as flight critical control modes, then the embedded sensors and control computations must be implemented so as not to compromise flight safety. Similarly, the forward looking laser sensor for active load control of a relaxed strength structure would become flight critical. Careful attention will need to be devoted to dealing with these flight criticality issues.

3.5.2 Signaling

A wide range of conventional sensors and signal transmission means are now available for implementing control systems. However, many different types of photonic sensors are under development, some of which may be useful in active structural mode control system applications. Of particular interest are embedded photonic structural sensor networks because light weight photonic fibers would not significantly increase the total vehicle weight due to the additional sensing requirements. The application of photonic systems also promises significant benefits in EMI immunity, improved performance, and potentially lower life cycle costs. Photonic components, however, present unique differences compared to their fly-by-wire equivalents that emphasize the need for extended validation testing. Some of these characteristics are photonic power sources, high reliability interconnects, and installation and maintenance of fiber optic systems. A great deal of activity is currently in progress to deal with these issues. However, the realization of active control of flexible structures, which is likely to be photonics based, may require a focused initiative in the photonics area.

3.6 CONTROL ACTUATION

Increased reliance on leading edge effectors, innovative force and moment generators, such as vortex burst control, or increasing the number of control surfaces by splitting the leading or trailing edge surfaces into independent sections, have benefits for active control similar to increasing the number of sensors. Sending weighted, simultaneous commands to the surfaces can maximize the control over a desired flexible mode while minimizing the excitation of other modes; this increases the amount of damping achievable without destabilizing other modes. Independent trim settings for these surfaces would also increase the controllability of the load distribution and structural deformation along the wing modes. Design trade studies indicate that current actuation technology seems adequate to support the expected actuation accuracy and response requirements. However, some attention may be required to design and develop actuation devices whose size is consistent with the expected cross sections of leading edge control.

Piezoelectric bending actuators for integration in composite smart structures may provide active structural mode damping beyond that available from aerodynamic control surfaces. These actuators, however, are in the early stages of development and the maturation schedules do not appear to be consistent with the anticipated pace of smart structure control.

3.7 DESIGN METHODS

The current aircraft and control system design process relies on conservative design, accurate structural modeling, and extensive verification and validation to ensure that structural modes do not compromise the performance or safety of the control system. This process is not likely to be modified by the added requirement to actively control a flexible structure. However, in the future, designers may have the freedom to allow structural frequencies to enter a currently forbidden region, even though their effects may be critical.

The proposed large number of feedback sensors and actuators pose stiff challenges to control law designers, who traditionally chose sensor-actuator gains only one at a time. One key enabling technology to design the envisioned control law structure is modern multivariable control design and analysis. Of particular importance is the ability of these design methods to handle large degrees of critical control parameter uncertainties and to provide complex nonlinear control functions. These design methods also promise to allow the control system designer to take full advantage of the advanced aircraft multiple sensors and effectors to meet the complex requirements which may be levied.

Multi-input multi-output design methods, including Mu synthesis, H-infinity, Linear Quadratic, direct optimization, and others, are maturing. To date, these design methods have been used successfully with about a dozen inputs or outputs and appear extendible to deal with the design problem posed by active control of flexible structures. In addition, positivity methods offer some help when sensors and actuators are collocated, such as the embedded piezoelectric actuators and load sensors in some proposed structures designs.

Conventional single-loop phase and gain margin methods could also be complemented with advanced multivariable stability analysis techniques, such as Mu synthesis and singular value tests, to deal with the totality of the control law design problem. It will also be necessary to demonstrate that these methods, nearly all based on linear system theory, behave gracefully under the inevitable nonlinearities such as actuator rate and position limiting.

Several nonlinear control methods based on fuzzy logic, neural networks, dynamic inversion, and other approaches are emerging and offer promise for coping with complex nonlinear feedback systems. Presently, they have been shown to provide good performance but generally lack a supporting stability analysis theory, thus requiring a design-by-simulation process. This design process does not end with the usual stability measures, such as poles, zeros, and stability margins, and pose a flight safety assurance issue which should not be intractable. On the other hand, designs based on linear control methods, both classical and modern, may perform poorly when typical nonlinearities, such as actuator limits, are introduced. Possibly, the nonlinear control methods could handle high-level control functions such as mode switching and responding to large commands, while linear feedback laws would operate near each equilibrium trim point.

While active control of flexible structures is by no means trivial, the design tools, methods, and a data base to enable control system design appear to be available. Cooperation between structures, aerodynamics, and control technologists will be essential to maturing the design methods, criteria, and tools essential to exploitation of relaxed stiffness structures. A focused flexible structures active control of initiative may well provide the opportunity for control system technologists to successfully combine these two very promising design approaches.

3.8 VERIFICATION AND VALIDATION

As the complexity of aircraft systems and control algorithms increase, performance and flight safety verification and validation become more critical. The verification and validation process consists of four major phases: analysis and simulation; pilot and hardware-in-the-loop simulation test and evaluation; vehicle ground test; and flight test, evaluation, and demonstration. This process has evolved over time and its application is refined by each successive development program. The soundness of this process and of each phase is well attested to by the numerous flight critical systems now in operation. Available information is convincing that application of this process to certification of relaxed stiffness structures control system would result in high performance and safe aircraft.

4.0 CONCLUSIONS

Through the application of advanced control, substantial reduction in aircraft gross takeoff weight may be obtained by reducing the weight of aircraft structures, vehicle management systems, and flight control effectors.

Flexible, relaxed stiffness wings have been explored in numerous analyses, simulations, design studies, and wind tunnel experiments. Results of this work show that wing control power can be increased through the use of leading and trailing edge surfaces in conjunction with increased wing flexibility. This increased control power and reduced structural weight of flexible wings may be exploited by the aircraft designer to improve structural efficiency and significantly increase range or payload.

Vehicle management systems offer a potential for aircraft weight reduction through the integration of subsystems and application of optical fibers and photonic sensors. Subsystem integration will reduce the number of components on the aircraft while adding synergistic performance improvements. For example, replacement of the relatively heavy shielded copper signal transmission and low wattage power lines with light weight optical fibers throughout the vehicle offers substantial savings in weight. Benefits from these advances in systems technology increase with the complexity of the structure and control systems.

Alternatives to conventional aerodynamic surfaces have been under investigation for some time and offer large potential for weight reduction, particularly when coupled with relaxed stiffness structures. Control effectors such as thrust vectoring and reversing and vortex burst control allow reductions in the size and weight of empennage surfaces, add maneuverability at high AOA, and enhance control in regimes of reduced surface effectiveness due to twist in flexible structure wings.

Potential control requirements of flexible wings have been considered in detail with the specific purpose of assessing control technology readiness to meet the accuracy and response demands of these structures. While active control of flexible structures poses a challenge, it is a challenge which can be met in the context of available design tools, methods, and design data.

The potential of actively controlled relaxed stiffness wings; highly integrated, photonics based vehicle management systems; and unconventional control effectors is a dramatic increase in the performance, range, or payload capability of combat aircraft which appears readily extendible to transport and other aircraft applications. A cooperative and concerted structures, materials, control, and aerodynamics endeavor to build and demonstrate the expected capabilities appears to be in order.

ACKNOWLEDGMENTS

The authors wish to acknowledge the valuable technical support of others in the preparation and development of this paper. Input and assistance were received from the following people in their respective fields of expertise:

Boeing Company: D. Gangsaas in overseeing the Boeing Company effort; D. L. Martin in photonics; J. D. Blight, R. L. Dailey, and B. F. Ray in controls; L. Turner and G. R. Trowbridge in systems; J. Petit in propulsion; and R. Ikegami in smart structures.

Dynamic Controls, Inc.: M. A. Ostgaard in flight control.

Rockwell International: Jose Aldana in vehicle management system .

Wright Laboratory: W. Baldwin and K. Bonnema in aeromechanics; and T. Harris and E. Pendleton in aircraft structures.

BIBLIOGRAPHY

1. Buttrill, Carey S., Bacon, Barton J., Heeg, Jennifer, Houck, Jacob A., and Wood, David, **Simulation and Model Reduction for the AFW Program**, AIAA-92-2081, Presented at the Dynamic Specialists Conference, Dallas, Texas April, 1992

2. Christhilf, David M. and Adams, William M, Jr., **Multifunction Tests of a Frequency Based Flutter Suppression System**, AIAA-92-2096, Presented at the Dynamic Specialists Conference, Dallas, Texas April, 1992

3. Chiu, s., Chand, S., Moore, D., Chuadhury, A., **A Fuzzy Logic Based Flexible Wing Aircraft Roll and Structural Torsion Moment Control**, Presented at the IEEE Int. Symposium on Intelligent Control, Philadelphia, Pennsylvania September 1990

4. Hoadley, S., and McGraw, S., **The Multiple Function Multi-input/Multi-output Digital Controller System for the AFW Wind Tunnel Model**, AIAA-92-2083, Presented at the Dynamic Specialists Conference, Dallas, Texas April, 1992

5. Klepl, Martin A., **A Flutter Suppression System Using Strain Gauges Applied to Active Flexible Wing Technology: Design and Test**, AIAA-92-2098, Presented at the Dynamic Specialists Conference, Dallas, Texas April, 1992

6. Moore, Doug, **Active Flexible Wing Wind Tunnel Test Report**, Rockwell International, North American Aircraft, NA-91-1547, August 1, 1991

7. Moore, Doug, **Maneuver Load Control Using Optimized Feedforward Commands**, AIAA-92-2100, Presented at the Dynamic Specialists Conference, Dallas, Texas April, 1992

8. Mukhopadhyay, Vivek, **Flutter Suppression Digital Control Law Design and Testing for the AFW Wind Tunnel Model**, AIAA-92-9295, Presented at the Dynamic Specialists Conference, Dallas, Texas April, 1992

9. Pendleton, Edmund, Lee, Mark and Wasserman, Lee, **Application of Active Flexible Wing Technology to the Agile Falcon**, Journal of Aircraft, Vol 29, No 3, May-June 1992, pg 444-451

10. Perry, Boyd III, Cole, Stanley, and Miller, Gerald A., **A Summary of the Active Flexible Wing Program**, AIAA-92-2080, Presented at the Dynamic Specialists Conference, Dallas, Texas April, 1992

11. Silva, Walter and Bennet, Robert, **Further Investigations of the Aeroelastic Behavior of the AFW Wind Tunnel Model Using Transonic Small Disturbance Theory**, AIAA-92-2082, Presented at the Dynamic Specialists Conference, Dallas, Texas April, 1992

12. Waszak, Martin R. and Srinathkumar, S., **Flutter Suppression for the Active Flexible Wing: Control System Design and Experimental Validation**, AIAA-92-2097, Presented at the Dynamic Specialists Conference, Dallas, Texas April, 1992

13. Woods-Vedleler, J. and Pototsky, A., **Rolling Maneuver Load Alleviation Using Active Controls**, AIAA-92-2099, Presented at the Dynamic Specialists Conference, Dallas, Texas April, 1992

REPORT DOCUMENTATION PAGE

1. Recipient's Reference	2. Originator's Reference	3. Further Reference	4. Security Classification of Document
	AGARD-CP-531	ISBN 92-835-0710-X	UNCLASSIFIED/ UNLIMITED

5. Originator Advisory Group for Aerospace Research and Development
North Atlantic Treaty Organization
7 Rue Ancelle, 92200 Neuilly sur Seine, France

6. Title SMART STRUCTURES FOR AIRCRAFT AND SPACECRAFT

7. Presented at the 75th Meeting of the AGARD Structures and Materials Panel, held in Lindau, Germany from 5th—7th October 1992.

8. Author(s)/Editor(s)	9. Date
Various	April 1993
10. Author's/Editor's Address	**11. Pages**
Various	404

12. Distribution Statement There are no restrictions on the distribution of this document. Information about the availability of this and other AGARD unclassified publications is given on the back cover.

13. Keywords/Descriptors

Aircraft	Engine condition monitoring
Spacecraft	Airframes
Active control	Maintenance
Fault diagnosis	Vibration damping

14. Abstract

The papers which are collected in this report give an excellent overview of the state-of-the-art of "Smart Structures" technology as well as detailed descriptions of specific applications. This technology offers extremely attractive advantages in the design, development and operation of aerospace structures.

AGARD Conference Proceedings 531 Advisory Group for Aerospace Research and Development, NATO SMART STRUCTURES FOR AIRCRAFT AND SPACECRAFT Published April 1993 404 pages The papers which are collected in this report give an excellent overview of the state-of-the-art of "Smart Structures" technology as well as detailed descriptions of specific applications. This technology offers extremely attractive advantages in the design, development and operation of aerospace structures. ISBN 92-835-0710-X	AGARD-CP-531 Aircraft Spacecraft Active control Fault diagnosis Engine condition monitoring Airframes Maintenance Vibration damping	AGARD Conference Proceedings 531 Advisory Group for Aerospace Research and Development, NATO SMART STRUCTURES FOR AIRCRAFT AND SPACECRAFT Published April 1993 404 pages The papers which are collected in this report give an excellent overview of the state-of-the-art of "Smart Structures" technology as well as detailed descriptions of specific applications. This technology offers extremely attractive advantages in the design, development and operation of aerospace structures. ISBN 92-835-0710-X	AGARD-CP-531 Aircraft Spacecraft Active control Fault diagnosis Engine condition monitoring Airframes Maintenance Vibration damping
AGARD Conference Proceedings 531 Advisory Group for Aerospace Research and Development, NATO SMART STRUCTURES FOR AIRCRAFT AND SPACECRAFT Published April 1993 404 pages The papers which are collected in this report give an excellent overview of the state-of-the-art of "Smart Structures" technology as well as detailed descriptions of specific applications. This technology offers extremely attractive advantages in the design, development and operation of aerospace structures. ISBN 92-835-0710-X	AGARD-CP-531 Aircraft Spacecraft Active control Fault diagnosis Engine condition monitoring Airframes Maintenance Vibration damping	AGARD Conference Proceedings 531 Advisory Group for Aerospace Research and Development, NATO SMART STRUCTURES FOR AIRCRAFT AND SPACECRAFT Published April 1993 404 pages The papers which are collected in this report give an excellent overview of the state-of-the-art of "Smart Structures" technology as well as detailed descriptions of specific applications. This technology offers extremely attractive advantages in the design, development and operation of aerospace structures. ISBN 92-835-0710-X	AGARD-CP-531 Aircraft Spacecraft Active control Fault diagnosis Engine condition monitoring Airframes Maintenance Vibration damping

AGARD

NATO OTAN

7 RUE ANCELLE · 92200 NEUILLY-SUR-SEINE

FRANCE

Télécopie (1)47.38.57.99 · Télex 610 176

DIFFUSION DES PUBLICATIONS
AGARD NON CLASSIFIEES

Aucun stock de publications n'a existé à AGARD. A partir de 1993, AGARD détiendra un stock limité des publications associées aux cycles de conférences et cours spéciaux ainsi que les AGARDographies et les rapports des groupes de travail, organisés et publiés à partir de 1993 inclus. Les demandes de renseignements doivent être adressées à AGARD par lettre ou par fax à l'adresse indiquée ci-dessus. *Veuillez ne pas téléphoner.* La diffusion initiale de toutes les publications de l'AGARD est effectuée auprès des pays membres de l'OTAN par l'intermédiaire des centres de distribution nationaux indiqués ci-dessous. Des exemplaires supplémentaires peuvent parfois être obtenus auprès de ces centres (à l'exception des Etats-Unis). Si vous souhaitez recevoir toutes les publications de l'AGARD, ou simplement celles qui concernent certains Panels, vous pouvez demander à être inclu sur la liste d'envoi de l'un de ces centres. Les publications de l'AGARD sont en vente auprès des agences indiquées ci-dessous, sous forme de photocopie ou de microfiche.

CENTRES DE DIFFUSION NATIONAUX

ALLEMAGNE
Fachinformationszentrum,
Karlsruhe
D-7514 Eggenstein-Leopoldshafen 2

BELGIQUE
Coordonnateur AGARD-VSL
Etat-Major de la Force Aérienne
Quartier Reine Elisabeth
Rue d'Evere, 1140 Bruxelles

CANADA
Directeur du Service des Renseignements Scientifiques
Ministère de la Défense Nationale
Ottawa, Ontario K1A 0K2

DANEMARK
Danish Defence Research Board
Ved Idraetsparken 4
2100 Copenhagen Ø

ESPAGNE
INTA (AGARD Publications)
Pintor Rosales 34
28008 Madrid

ETATS-UNIS
National Aeronautics and Space Administration
Langley Research Center
M/S 180
Hampton, Virginia 23665

FRANCE
O.N.E.R.A. (Direction)
29, Avenue de la Division Leclerc
92322 Châtillon Cedex

GRECE
Hellenic Air Force
Air War College
Scientific and Technical Library
Dekelia Air Force Base
Dekelia, Athens TGA 1010

ISLANDE
Director of Aviation
c/o Flugrad
Reykjavik

ITALIE
Aeronautica Militare
Ufficio del Delegato Nazionale all'AGARD
Aeroporto Pratica di Mare
00040 Pomezia (Roma)

LUXEMBOURG
Voir Belgique

NORVEGE
Norwegian Defence Research Establishment
Attn: Biblioteket
P.O. Box 25
N-2007 Kjeller

PAYS-BAS
Netherlands Delegation to AGARD
National Aerospace Laboratory NLR
P.O. Box 90502
1006 BM Amsterdam

PORTUGAL
Portuguese National Coordinator to AGARD
Gabinete de Estudos e Programas
CLAFA
Base de Alfragide
Alfragide
2700 Amadora

ROYAUME UNI
Defence Research Information Centre
Kentigern House
65 Brown Street
Glasgow G2 8EX

TURQUIE
Millî Savunma Başkanlığı (MSB)
ARGE Daire Başkanlığı (ARGE)
Ankara

Le centre de distribution national des Etats-Unis (NASA/Langley) ne détient PAS de stocks des publications de l'AGARD. *D'éventuelles demandes de photocopies doivent être formulées directement auprès du NASA Center for Aerospace Information (CASI) à l'adresse suivante:*

AGENCES DE VENTE

NASA Center for
Aerospace Information (CASI)
P.O. Box 8757
BWI Airport, Maryland 21240
United States

ESA/Information Retrieval Service
European Space Agency
10, rue Mario Nikis
75015 Paris
France

The British Library
Document Supply Division
Boston Spa, Wetherby
West Yorkshire LS23 7BQ
Royaume Uni

Les demandes de microfiches ou de photocopies de documents AGARD (y compris les demandes faites auprès du CASI) doivent comporter la dénomination AGARD, ainsi que le numéro de série d'AGARD (par exemple AGARD-AG-315). Des informations analogues, telles que le titre et la date de publication sont souhaitables. Veuiller noter qu'il y a lieu de spécifier AGARD-R-nnn et AGARD-AR-nnn lors de la commande des rapports AGARD et des rapports consultatifs AGARD respectivement. Des références bibliographiques complètes ainsi que des résumés des publications AGARD figurent dans les journaux suivants:

Scientifique and Technical Aerospace Reports (STAR)
publié par la NASA Scientific and Technical
Information Division
NASA Headquarters (NTT)
Washington D.C. 20546
Etats-Unis

Government Reports Announcements and Index (GRA&I)
publié par le National Technical Information Service
Springfield
Virginia 22161
Etats-Unis

(accessible également en mode interactif dans la base de données bibliographiques en ligne du NTIS, et sur CD-ROM)

Imprimé par Specialised Printing Services Limited
40 Chigwell Lane, Loughton, Essex IG10 3TZ

AGARD

NATO OTAN

7 RUE ANCELLE · 92200 NEUILLY-SUR-SEINE

FRANCE

Telefax (1)47.38.57.99 · Telex 610 176

DISTRIBUTION OF UNCLASSIFIED AGARD PUBLICATIONS

AGARD holds limited quantities of the publications that accompanied Lecture Series and Special Courses held in 1993 or later, and of AGARDographs and Working Group reports published from 1993 onward. For details, write or send a telefax to the address given above. *Please do not telephone.*

AGARD does not hold stocks of publications that accompanied earlier Lecture Series or Courses or of any other publications. Initial distribution of all AGARD publications is made to NATO nations through the National Distribution Centres listed below. Further copies are sometimes available from these centres (except in the United States). If you have a need to receive all AGARD publications, or just those relating to one or more specific AGARD Panels, they may be willing to include you (or your organisation) on their distribution list. AGARD publications may be purchased from the Sales Agencies listed below, in photocopy or microfiche form.

NATIONAL DISTRIBUTION CENTRES

BELGIUM
Coordonnateur AGARD — VSL
Etat-Major de la Force Aérienne
Quartier Reine Elisabeth
Rue

CANAD
Dir
Dep
Otti

DENMA
Dar
Ved
210

FRANCE
O.N
29 /
923

GERMA
Facl
Karl
D-7

GREECE
Hell
Air
Scie
Deke
Dekelia, Athens TGA 1010

ICELAND
Director of Aviation
c/o Flugrad
Reykjavik

ITALY
Aeronautica Militare
Ufficio del Delegato Nazionale all'AGARD
Aeroporto Pratica di Mare
00040 Pomezia (Roma)

LUXEMBOURG
See Belgium

NETHERLANDS
D
LR

olishment

AGARD

Ankara

UNITED KINGDOM
Defence Research Information Centre
Kentigern House
65 Brown Street
Glasgow G2 8EX

UNITED STATES
National Aeronautics and Space Administration (NASA)
Langley Research Center
M/S 180
Hampton, Virginia 23665

The United States National Distribution Centre (NASA/Langley) does NOT hold stocks of AGARD publications.
Applications for copies should be made direct to the NASA Center for Aerospace Information (CASI) at the address below.

SALES AGENCIES

NASA Center for
Aerospace Information (CASI)
P.O. Box 8757
BWI Airport, Maryland 21240
United States

ESA/Information Retrieval Service
European Space Agency
10, rue Mario Nikis
75015 Paris
France

The British Library
Document Supply Centre
Boston Spa, Wetherby
West Yorkshire LS23 7BQ
United Kingdom

Requests for microfiches or photocopies of AGARD documents (including requests to CASI) should include the word 'AGARD' and the AGARD serial number (for example AGARD-AG-315). Collateral information such as title and publication date is desirable. Note that AGARD Reports and Advisory Reports should be specified as AGARD-R-nnn and AGARD-AR-nnn, respectively. Full bibliographical references and abstracts of AGARD publications are given in the following journals:

Scientific and Technical Aerospace Reports (STAR)
published by NASA Scientific and Technical
Information Division
NASA Headquarters (NTT)
Washington D.C. 20546
United States

Government Reports Announcements and Index (GRA&I)
published by the National Technical Information Service
Springfield
Virginia 22161
United States
(also available online in the NTIS Bibliographic
Database or on CD-ROM)

Printed by Specialised Printing Services Limited
40 Chigwell Lane, Loughton, Essex IG10 3TZ

ISBN 92-835-0710-X